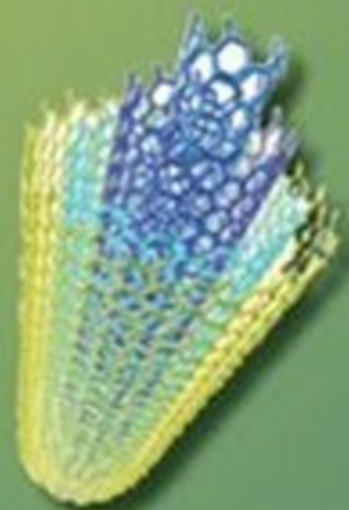



Wiley Series in Nanoscience and Nanotechnology
Arben Merkoçi, Series Editor

Biosensing Using Nanomaterials



Edited by
ARBEN MERKOÇI

 **WILEY**

BIOSENSING USING NANOMATERIALS

WILEY SERIES IN NANOSCIENCE AND NANOTECHNOLOGY

Arben Merkoçi, Series Editor

BIOSENSING USING NANOMATERIALS / Arben Merkoçi, Editor

BIOSENSING USING NANOMATERIALS

Edited by

Arben Merkoçi



WILEY

A JOHN WILEY & SONS, INC., PUBLICATION

Copyright © 2009 by John Wiley & Sons, Inc. All rights reserved.

Published by John Wiley & Sons, Inc., Hoboken, New Jersey.
Published simultaneously in Canada.

No part of this publication may be reproduced, stored in a retrieval system, or transmitted in any form or by any means, electronic, mechanical, photocopying, recording, scanning, or otherwise, except as permitted under Section 107 or 108 of the 1976 United States Copyright Act, without either the prior written permission of the Publisher, or authorization through payment of the appropriate per-copy fee to the Copyright Clearance Center, Inc., 222 Rosewood Drive, Danvers, MA 01923, (978) 750-8400, fax (978) 750-4470, or on the web at www.copyright.com. Requests to the Publisher for permission should be addressed to the Permissions Department, John Wiley & Sons, Inc., 111 River Street, Hoboken, NJ 07030, (201) 748-6011, fax (201) 748-6008, or online at <http://www.wiley.com/go/permission>.

Limit of Liability/Disclaimer of Warranty: While the publisher and author have used their best efforts in preparing this book, they make no representations or warranties with respect to the accuracy or completeness of the contents of this book and specifically disclaim any implied warranties of merchantability or fitness for a particular purpose. No warranty may be created or extended by sales representatives or written sales materials. The advice and strategies contained herein may not be suitable for your situation. You should consult with a professional where appropriate. Neither the publisher nor author shall be liable for any loss of profit or any other commercial damages, including but not limited to special, incidental, consequential, or other damages.

For general information on our other products and services or for technical support, please contact our Customer Care Department within the United States at (800) 762-2974, outside the United States at (317) 572-3993 or fax (317) 572-4002.

Wiley also publishes its books in a variety of electronic formats. Some content that appears in print may not be available in electronic formats. For more information about Wiley products, visit our web site at www.wiley.com.

Library of Congress Cataloging-in-Publication Data:

Merkoçi, A. (Arben)

Biosensing using nanomaterials / Arben Merkoçi.

p. cm. -- (Wiley series in nanoscience and nanotechnology)

Includes index.

ISBN 978-0-470-18309-0 (cloth)

1. Biosensors. 2. Nanostructured materials. I. Title.

R857.B54M47 2009

610.28'4--dc22

2009005618

Printed in the United States of America

10 9 8 7 6 5 4 3 2 1

CONTENTS

CONTRIBUTORS	xi
SERIES PREFACE	xv
PREFACE	xvii
PART I CARBON NANOTUBES	1
1. Carbon Nanotube–Based Sensors and Biosensors	3
<i>Richard G. Compton, Gregory G. Wildgoose, and Elicia L. S. Wong</i>	
1.1. Introduction to the Structure of Carbon Nanotubes	3
1.2. Electroanalysis Using CNT-Modified Electrodes	7
1.3. Advantageous Application of CNTs in Sensors: pH Sensing	13
1.4. Carbon Nanotube–Based Biosensors	18
1.5. Using CNTs in Biosensor Production for Medical Diagnostics and Environmental Applications	25
References	30
2. Isotropic Display of Biomolecules on CNT-Arrayed Nanostructures	39
<i>Mark R. Contarino, Gary Withey, and Irwin Chaiken</i>	
2.1. Introduction: CNT Arrays for Biosensing	40
2.2. Functionalization of CNTs: Controlling Display Through Covalent Attachment	41
2.3. Self-Assembling Interfaces: Anchor-Probe Approach	49
2.4. Molecular Wiring of Redox Enzymes	53
2.5. Multiplexing Biomolecules on Nanoscale CNT Arrays	54
2.6. Conclusions	59
References	60
3. Interaction of DNA with CNTs: Properties and Prospects for Electronic Sequencing	67
<i>Sheng Meng and Efthimios Kaxiras</i>	
3.1. Introduction	68
3.2. Structural Properties of Combined DNA–CNT Systems	70
3.3. Electronic Structure	79

3.4. Optical Properties	85
3.5. Biosensing and Sequencing of DNA Using CNTs	88
3.6. Summary	92
References	93
PART II NANOPARTICLES	97
4. Improved Electrochemistry of Biomolecules Using Nanomaterials	99
<i>Jianxiu Wang, Andrew J. Wain, Xu Zhu, and Feimeng Zhou</i>	
4.1. Introduction	100
4.2. CNT-Based Electrochemical Biosensors	100
4.3. Nanoparticle-Based Electrochemical Biosensors	110
4.4. Quantum Dot-Based Electrochemical Biosensors	122
4.5. Conclusions and Outlook	123
References	125
5. The Metal Nanoparticle Plasmon Band as a Powerful Tool for Chemo- and Biosensing	137
<i>Audrey Moores and Pascal Le Floch</i>	
5.1. Introduction	138
5.2. The SPB: An Optical Property of Metal NPs	143
5.3. Plasmon Band Variation Upon Aggregation of Nanoparticles	154
5.4. Plasmon Band Variation on the Environment or Ligand Alteration	164
5.5. Metal Nanoparticles as Labels	167
5.6. Conclusions	169
References	170
6. Gold Nanoparticles: A Versatile Label for Affinity Electrochemical Biosensors	177
<i>Adriano Ambrosi, Alfredo de la Escosura-Muñiz, Maria Teresa Castañeda, and Arben Merkoçi</i>	
6.1. Introduction	178
6.2. Synthesis of AuNPs	179
6.3. Characterization of AuNPs	179
6.4. AuNPs as Detecting Labels for Affinity Biosensors	181
6.5. Conclusions	191
References	192
7. Quantum Dots for the Development of Optical Biosensors Based on Fluorescence	199
<i>W. Russ Algar and Ulrich J. Krull</i>	
7.1. Introduction	200

7.2. Quantum Dots	205
7.3. Basic Photophysics and Quantum Confinement	207
7.4. Quantum Dot Surface Chemistry and Bioconjugation	212
7.5. Bioanalytical Applications of Quantum Dots as Fluorescent Labels	225
7.6. Fluorescence Resonance Energy Transfer and Quantum Dot Biosensing	232
7.7. Summary	238
References	239
8. Nanoparticle-Based Delivery and Biosensing Systems: An Example	247
<i>Almudena Muñoz Javier, Pablo del Pino, Stefan Kudera, and Wolfgang J. Parak</i>	
8.1. Introduction	247
8.2. Functional Colloidal Nanoparticles	250
8.3. Polyelectrolyte Capsules as a Functional Carrier System	256
8.4. Uptake of Capsules by Cells	259
8.5. Delivery and Sensing with Polyelectrolyte Capsules	262
8.6. Conclusions	270
References	270
9. Luminescent Quantum Dot FRET-Based Probes in Cellular and Biological Assays	275
<i>Lifang Shi, Nitsa Rosenzweig, and Zeev Rosenzweig</i>	
9.1. Introduction	275
9.2. Luminescent Quantum Dots	276
9.3. Fluorescence Resonance Energy Transfer	278
9.4. Quantum Dot FRET-Based Protease Probes	280
9.5. Summary and Conclusions	283
References	284
10. Quantum Dot–Polymer Bead Composites for Biological Sensing Applications	291
<i>Jonathan M. Behrendt and Andrew J. Sutherland</i>	
10.1. Introduction	291
10.2. Quantum Dot–Composite Construction	293
10.3. Applications of QD Composites	307
10.4. Future Directions	325
References	327
11. Quantum Dot Applications in Biomolecule Assays	333
<i>Ying Xu, Pingang He, and Yuzhi Fang</i>	
11.1. Introduction to QDs and Their Applications	333
11.2. Preparation of QDs for Conjugation with Biomolecules and Cells	337

11.3. Special Optoelectronic Properties in the Bioemployment of QDs	340
11.4. Employment of QDs as Biosensing Indicators	344
References	349
12. Nanoparticles and Inductively Coupled Plasma Mass Spectroscopy–Based Biosensing	355
<i>Arben Merkoçi, Roza Allabashi, and Alfredo de la Escosura-Muñiz</i>	
12.1. ICP-MS and Application Possibilities	355
12.2. Detection of Metal Ions	360
12.3. Detection of Nanoparticles	361
12.4. Analysis of Metal-Containing Biomolecules	363
12.5. Bioanalysis Based on Labeling with Metal Nanoparticles	364
12.6. Conclusions	372
References	373
PART III NANOSTRUCTURED SURFACES	377
13. Integration Between Template-Based Nanostructured Surfaces and Biosensors	379
<i>Walter Vastarella, Jan Maly, Mihaela Ilie, and Roberto Pilloton</i>	
13.1. Introduction	380
13.2. Nanosphere Lithography	380
13.3. Nanoelectrodes Ensemble for Biosensing Devices	390
13.4. Concluding Remarks	406
References	407
14. Nanostructured Affinity Surfaces for MALDI-TOF-MS–Based Protein Profiling and Biomarker Discovery	421
<i>R. M. Vallant, M. Rainer, M. Najam-Ul-Haq, R. Bakry, C. Petter, N. Heigl, G. K. Bonn, and C. W. Huck</i>	
14.1. Proteomics and Biomarkers	421
14.2. MALDI in Theory and Practice	422
14.3. Carbon Nanomaterials	429
14.4. Near-Infrared Diffuse Reflection Spectroscopy of Carbon Nanomaterials	448
References	451
PART IV NANOPORES	457
15. Biosensing with Nanopores	459
<i>Ivan Vlasiouk and Sergei Smirnov</i>	
15.1. Nanoporous Materials in Sensing	459

15.2. Nanochannel and Nanopore Fabrication	460
15.3. Surface Modification Chemistry	469
15.4. Nonelectrical Nanoporous Biosensors	472
15.5. Electrical Nanoporous Biosensors	474
15.6. Summary	486
References	486

INDEX	491
--------------	------------

CONTRIBUTORS

W. Russ Algar, Department of Chemical and Physical Sciences, University of Toronto Mississauga, Mississauga, Ontario, Canada

Roza Allabashi, University of Natural Resources and Applied Life Sciences, Vienna, Austria

Adriano Ambrosi, Nanobioelectronics and Biosensors Group, Institut Català de Nanotecnologia, Barcelona, Spain

R. Bakry, Institute of Analytical Chemistry and Radiochemistry, Leopold-Franzens University, Innsbruck, Austria

Jonathan M. Behrendt, Department of Chemical Engineering and Applied Chemistry, Aston University, Birmingham, United Kingdom

G. K. Bonn, Institute of Analytical Chemistry and Radiochemistry, Leopold-Franzens University, Innsbruck, Austria

Maria Teresa Castañeda, Nanobioelectronics and Biosensors Group, Institut Català de Nanotecnologia, Barcelona, Spain, and Grup de Sensors i Biosensors, Departamento de Química, Universitat Autònoma de Barcelona, Bellaterra, Catalonia, Spain; on leave from Departamento de Ciencias Básicas, Universidad Autónoma Metropolitana-Azcapotzalco, México D.F., México

Irwin Chaiken, Department of Biochemistry and Molecular Biology, Drexel University College of Medicine, Philadelphia, Pennsylvania

Richard G. Compton, Physical and Theoretical Chemistry Laboratory, Oxford University, Oxford, United Kingdom

Mark R. Contarino, School of Biomedical Engineering, Science and Health Systems, Drexel University, and Department of Biochemistry and Molecular Biology, Drexel University College of Medicine, Philadelphia, Pennsylvania

Alfredo de la Escosura-Muñiz, Nanobioelectronics and Biosensors Group, Institut Català de Nanotecnologia, Barcelona, Spain, and Instituto de Nanociencia de Aragón, Universidad de Zaragoza, Zaragoza, Spain

Pablo del Pino, Fachbereich Physik, Philipps Universität Marburg, Marburg, Germany

Yuzhi Fang, Department of Chemistry, East China Normal University, Shanghai, China

Pingang He, Department of Chemistry, East China Normal University, Shanghai, China

N. Heigl, Institute of Analytical Chemistry and Radiochemistry, Leopold-Franzens University, Innsbruck, Austria

C. W. Huck, Institute of Analytical Chemistry and Radiochemistry, Leopold-Franzens University, Innsbruck, Austria

Mihaela Ilie, Department of Applied Electronics and Information Engineering, LAPI, Universitatea Politehnica București, Bucharest, Romania

Efthimios Kaxiras, Department of Physics and School of Engineering and Applied Sciences, Harvard University, Cambridge, Massachusetts

Ulrich J. Krull, Department of Chemical and Physical Sciences, University of Toronto Mississauga, Mississauga, Ontario, Canada

Stefan Kudera, Department of New Materials and Biosystems, Max Planck Institute for Metals Research, and Department of Biophysical Chemistry, University of Heidelberg, Stuttgart, Germany

Pascal Le Floch, Hétéroéléments et Coordination, Ecole Polytechnique, Palaiseau, France

Jan Maly, Department of Biology, University of J.E. Purkyne, Usti nad Labem, Czech Republic

Sheng Meng, Department of Physics and School of Engineering and Applied Sciences, Harvard University, Cambridge, Massachusetts

Arben Merkoçi, ICREA and Nanobioelectronics and Biosensors Group, Institut Català de Nanotecnologia, Barcelona, Spain

Audrey Moores, Department of Chemistry, McGill University, Montreal, Quebec, Canada

Almudena Muñoz Javier, Fachbereich Physik, Philipps Universität Marburg, Marburg, Germany

M. Najam-Ul-Haq, Institute of Analytical Chemistry and Radiochemistry, Leopold-Franzens University, Innsbruck, Austria

Wolfgang J. Parak, Fachbereich Physik, Philipps Universität Marburg, Marburg, Germany

C. Petter, Institute of Analytical Chemistry and Radiochemistry, Leopold-Franzens University, Innsbruck, Austria

Roberto Pilloton, ENEA C.R. Casaccia, Rome, Italy

M. Rainer, Institute of Analytical Chemistry and Radiochemistry, Leopold-Franzens University, Innsbruck, Austria

Nitsa Rosenzweig, Department of Chemistry and the Advanced Materials Research Institute, University of New Orleans, New Orleans, Louisiana

Zeev Rosenzweig, Department of Chemistry and the Advanced Materials Research Institute, University of New Orleans, New Orleans, Louisiana

Lifang Shi, Department of Chemistry and the Advanced Materials Research Institute, University of New Orleans, New Orleans, Louisiana

Sergei Smirnov, Department of Chemistry and Biochemistry, New Mexico State University, Las Cruces, New Mexico

Andrew J. Sutherland, Department of Chemical Engineering and Applied Chemistry, Aston University, Birmingham, United Kingdom

R. M. Vallant, Institute of Analytical Chemistry and Radiochemistry, Leopold-Franzens University, Innsbruck, Austria

Walter Vastarella, ENEA C.R. Casaccia, Rome, Italy

Ivan Vlassiuk, Department of Physics and Astronomy, University of California, Irvine, California

Andrew J. Wain, Department of Chemistry and Biochemistry, California State University, Los Angeles, California

Jianxiu Wang, School of Chemistry and Chemical Engineering, Central South University, Changsha, Hunan, China

Gregory G. Wildgoose, Physical and Theoretical Chemistry Laboratory, Oxford University, Oxford, United Kingdom

Gary Withey, Engineering Division, Brown University, Providence, Rhode Island

Elicia L. S. Wong, Physical and Theoretical Chemistry Laboratory, Oxford University, Oxford, United Kingdom

Ying Xu, Department of Chemistry, East China Normal University, Shanghai, China

Feimeng Zhou, Department of Chemistry and Biochemistry, California State University, Los Angeles, California

Xu Zhu, School of Chemistry and Chemical Engineering, Central South University, Changsha, Hunan, China

SERIES PREFACE

Nanoscience and *nanotechnology* refer broadly to a field of applied science and technology whose unifying theme is the control of matter on the molecular level in scales smaller than 1 micrometer, normally 1 to 100 nanometers, and the fabrication of devices within that size range. Nanotechnology also refers to the manufacture of nano-sized systems that perform specific electrical, mechanical, biological, chemical, or computing tasks.

Nanotechnology is based on the fact that nanostructures, nanodevices, and nanosystems exhibit novel properties and functions as a result of their small size. It is a highly multidisciplinary field, drawing from such subjects as applied physics, materials science, colloidal science, device physics, supramolecular chemistry, and mechanical and electrical engineering. Given the inherent nanoscale functions of the biological components of living cells, it was inevitable that nanotechnology would also be related and applied to the life sciences through the application of nanoscaled tools to biological systems as well as the uses of biological systems as templates in the development of novel nanoscaled products. Much speculation exists related to what new science and technology may result from the synergy of the disciplines mentioned. Nanotechnology can be seen as an extension of existing sciences to the nanoscale level.

Two primary approaches are used in nanotechnology. In the bottom-up approach, materials and devices are built from molecular components which assemble themselves chemically by principles of molecular composition. In the top-down approach, nanoobjects are constructed from larger entities without atomic-level control. The impetus for nanotechnology comes from a renewed interest in colloidal science, coupled with a new generation of analytical tools such as the atomic force microscope and the scanning tunneling microscope. Combined with refined processes such as electron-beam lithography and molecular-beam epitaxy, these instruments allow the deliberate manipulation of nanostructures and have led to the observation of novel phenomena.

Examples of nanotechnology in modern use are the manufacture of polymers based on molecular structure and the design of computer chip layouts based on surface science. Despite the great promise of numerous nanotechnologies, such as quantum dots and nanotubes, real commercial applications have mainly used the advantages of colloidal nanoparticles in bulk form, such as in suntan lotion, cosmetics, protective coatings, and stain-resistant clothing.

Research in the field of nanoscience and technology is very active and is expected to remain so for the foreseeable future. The Wiley Series in Nanoscience and Nanotechnology will be focused on the following important topics:

- Basic nanoscience
- Nanotechnology tools
- Nanomaterials
- Nanobiosensors
- Nanobiotechnology
- Nanotechnology for environment.
- Nanotechnology and energy
- Nanotechnology and electronics/computers
- Nanotechnology and ethical issues

We welcome coverage of other topics in response to issues that arise in coming months. All topics will be edited by experts the various nanoscience and nanotechnology fields and will serve as a reference source for this new and exciting science and technology. Collaborations are welcome!

ARBEN MERKOÇI
Series Editor

Bellaterra, Catalonia, Spain
July 2008

PREFACE

The implementation of nanoscience and nanotechnology achievements in bioanalysis is the main objective of this book, whose aim is to explaining to readers several strategies related to the integration of nanomaterials with bioanalytical systems as one of the hottest topics of today's nanotechnology and nanoscience. Novel concepts are shown, together with practical aspects of nanoscale material's integration into biosensing systems. This integration is due to the capacity of nanomaterials to provide special optical or electrical properties as well as stability and to minimize surface fouling of the sensing systems where they are being integrated.

Various nanomaterials, including carbon nanotubes, nanoparticles, nanomagnetic beads, and nanocomposites, are being used to develop highly sensitive and robust biosensors and biosensing systems. The materials mentioned are attractive probe candidates because of their (1) small size (1 to 100 nm) and correspondingly large surface-to-volume ratio; (2) chemically tailorable physical properties, which relate directly to size, composition, and shape; (3) unusual target binding properties; and (4) overall structural robustness.

This is an interdisciplinary book dedicated to professionals who have an interest in the improving the current bioanalytical techniques and methodologies by implementing nanoscience and nanotechnology in general and nanomaterials in particular. The goal is to present the most recent scientific and technological advances as well as practical bioanalytical applications based on the use of nanomaterials. It will be an important reference source for a broad audience involved in the research, teaching, learning, and practice of nanomaterial integration into biosensing systems for clinical, environmental, and industrial applications.

Bioanalysis in general and biosensor fields in particular are showing special interest in nanobiomaterials. Nanomaterials bring several advantages to bioanalysis. Their immobilization on sensing devices generates novel interfaces that enable sensitive optical or electrochemical detection of molecular and biomolecular analytes. Moreover, they are being used as effective labels to amplify the analysis and to design novel biomaterial architectures with predesigned and controlled functions with interest for several applications. Achieving higher sensitivities and better and more reliable analysis are one of the objectives of DNA probes and immunoanalysis.

Carbon nanotubes (CNTs) represent one of the building blocks of nanotechnology. With one hundred times the tensile strength of steel, thermal conductivity better than that of all but the purest diamond, and electrical conductivity similar to that of copper but with the ability to carry much higher currents, CNTs seem to be a very interesting

material. Since their discovery in 1991, CNTs have generated great interest for future applications based on their field emission and electronic transport properties, high mechanical strength, and chemical properties. The structural and electronic properties of CNTs provide them with distinct properties for facilitating direct electrochemistry of proteins and enzymes compared to other types of materials used so far. The bioelectrochemistry and optical properties, along with some other interesting features of CNTs coupled to several bioanalytical procedures, are also presented.

Nanoparticles of a variety of shapes, sizes, and compositions are changing the bioanalytical measurement landscape continuously and so are also included. Nanoparticles can be used, for example, in quantification or codification purposes, due to their chemical behavior, which is similar to that of small molecules. They also provide novel platforms for improving the activity of DNA probes, antibodies, or enzymes. Nanoparticles may be expected to be superior in several ways to other materials commonly used in bioanalysis. They are more stable and cheaper, allow more flexibility, have faster binding kinetics (similar to those in a homogeneous solution), and have high sensitivity and high reaction rates for many types of multiplexed assays, ranging from immunoassays to DNA analysis.

Improving the current bioanalytical techniques and methodologies and finding novel concepts and applications in bioanalysis are two of the most important objectives of nanotechnology and nanoscience today. Advances in nanotechnology are affecting existing technologies and leading to the development of novel bioanalytical tools and techniques through improvements in precision and speed, lower sample requirements, and the ability to perform multiple detections in smaller devices. Novel biosensing systems that require less sample material are being developed so as to perform sophisticated tests at the point of care (e.g., blood analysis using a handheld device within a few minutes) and make possible the multiplex analysis (i.e., simultaneous and fast analysis of more than one variable). Analysis of the structure of living cells in real time and in the intact organism (*in vivo*) as opposed to using laboratory-prepared samples (*in vitro*), as well as molecular analysis (DNA, RNA, and protein analysis), including biosensors based on nanomaterials, represent challenges not only for basic research in nanotechnology but for the bioanalysis community, which is willing to see new input from this novel area of research that is developing so fast.

In this context the book introduces novel concepts that are being achieved in the area of bioanalysis based on the fact that nanomaterials are opening up new opportunities not only for basic research but overall, are offering new tools for real bioanalytical applications. The focus is on the latest tendencies in the field of nanoparticles, carbon nanotubes, and nanochannels: integration into bioanalytical systems, including sensors and biosensors.

The area of biosensing using nanotechnology is providing the information necessary for real applications of nanomaterials and related nanotechnologies. The book should act as a very interesting interface of information between complementary fields, thus opening up new opportunities for researchers and others. It will also support doctoral students and those involved in learning and teaching nanobiotechnological applications in bioanalysis.

How does the bionalytical community implement the spectacularly bright future offered us by nanoscience? What are the challenges facing bioanalysis in our nanoscale future? How do we move from an almost science fiction level toward real-world outcomes in nanotechnology? The bioanalytical community will be better able to respond to these questions in the future after reading this book, which not only compares nanomaterials to conventional materials but also gets inside the response mechanisms related to such improvements.

The book's fifteen chapters deal with the most successful nanomaterials used so far in biosensing: carbon nanotubes, nanoparticles, and nanochannels, including detection strategies ranging from optical to electrochemical techniques. Each chapter provides a theoretical overview topic of interest as well as a discussion of the published data with a selected list of references for further details. The book provides a comprehensive forum that integrates interdisciplinary research and development of interest to scientists, engineers, researchers, manufacturers, teachers, and students in order to present the most recent advances in the integration of nanomaterials with bioanalysis as they relate to everyday life. The book promotes the use of novel nanomaterials in biosensors and biosensing systems through introduction of the highest-quality research in the field of nanomaterial-based bioassay.

ARBEN MERKOÇI

Bellaterra, Catalonia, Spain
July 2008

PART I

CARBON NANOTUBES

Carbon Nanotube–Based Sensors and Biosensors

RICHARD G. COMPTON, GREGORY G. WILDGOOSE, and ELICIA L. S. WONG

Physical and Theoretical Chemistry Laboratory, Oxford University, Oxford, United Kingdom

- 1.1 Introduction to the structure of carbon nanotubes
- 1.2 Electroanalysis using CNT-modified electrodes
 - 1.2.1 Historical background
 - 1.2.2 Electron transfer at graphitic carbon electrodes: The role of edge-plane defects
 - 1.2.3 Exceptions to the rule that edge-plane defects are the important electroactive sites on CNTs
- 1.3 Advantageous application of CNTs in sensors: pH sensing
- 1.4 Carbon nanotube–based biosensors
 - 1.4.1 Introduction
 - 1.4.2 Surface functionalization of carbon nanotubes and configuration of a CNT-based electrochemical biosensor
- 1.5 Using CNTs in biosensor production for medical diagnostics and environmental applications
 - 1.5.1 Medical diagnostics
 - 1.5.2 Environmental applications

1.1 INTRODUCTION TO THE STRUCTURE OF CARBON NANOTUBES

In recent years carbon nanotubes (CNTs) have attracted, and continue to attract, considerable interest in a wide variety of scientific fields, not least that of the electroanalytical and bioelectroanalytical communities. However, before we summarize some of the main properties of CNTs that make them an interesting and often ideal material to use in electrochemical sensors and biosensors, let us begin by highlighting perhaps *the* most common misconception found in the literature concerning

CNTs: who should actually be credited with their discovery. Numerous examples can be found among the many thousands of carbon nanotube papers that begin with an erroneous introductory phrase along the lines of: “Since the discovery of CNTs in 1991 by S. Iijima . . .”, with subsequent sentences proceeding to list the much vaunted electrical and mechanical properties of CNTs. Certainly, Iijima’s 1991 high-profile publication in *Nature* [1] brought the idea of nanometer-sized carbon fibers *back* to the attention of a wider scientific audience, particularly as, after the excitement created over the discovery of fullerenes, scientists were starting to think about materials on the truly “nano” scale. In fact, Iijima and Ichihashi should more correctly be credited with the first convincing discovery of single-walled carbon nanotubes (consisting of a single sheet of graphite rolled into a seamless tube) in their 1993 paper [2]. The case for who discovered multiwalled carbon nanotubes is more complex, with the earliest possible claim dating from as far back as 1952! However, work from 1976 by Oberlin and Endo [3] and in 1978 by Wiles and Abrahamson [4] (subsequently republished in 1999 [5]) present arguably the earliest and clearest characterization of what would later be recognized as multiwalled CNTs. For a more detailed discussion of who should be credited with the discovery of CNTs, the interested reader is directed to the comprehensive editorial by Monthieux and Kuznetsov [6].

Structurally, CNTs can be approximated as rolled-up sheets of graphite. CNTs are formed in two principal types: single-walled carbon nanotubes (SWCNTs), which consist of a single tube of graphite, as shown in Figure 1.1, and multiwalled carbon nanotubes (MWCNTs), which consist of several concentric tubes of graphite fitted one inside the other. The diameters of CNTs can range from just a few nanometers in the case of SWCNTs to several tens of nanometers for MWCNTs. The lengths of the tubes are usually in the micrometer range.

Conceptually, the way in which the graphite sheet is rolled up to form each nanotube affects the electronic properties of that CNT. In general, any lattice point in the graphite sheet can be described as a vector position (n,m) relative to any given origin. The graphite sheet can then be rolled into a tube such that the lattice point chosen is coincident with the origin (Figure 1.1). The orientation of this *roll-up vector* relative to the graphite sheet determines whether the tube forms a chiral, armchair, or zigzag SWCNT, terms that describe the manner in which the fused rings of a graphite sheet are arranged at the termini of an idealized tube. Alternatively, SWCNTs are more precisely described in the literature by the roll-up vector coordinates as $[n,m]$ -SWCNTs. It has been shown that when $|n - m| = 3q$, where q is an integer, the CNT is metallic or semimetallic and the remaining CNTs are semiconducting [7,8]. Therefore, statistically, one-third of SWCNTs are metallic depending on the method and conditions used during their production [7] and can possess high conductivity, greater than that of metallic copper, due to the ballistic (unscattered) nature of electron transport along a SWCNT [9].

If one considers the structure of a perfect crystal of graphite, two crystallographic faces can be identified, as shown in Figure 1.2. One crystal face consists of a plane containing all the carbon atoms of one graphite sheet, which we call the *basal plane*; the other crystal face is a plane perpendicular to the basal plane, which we call the *edge plane*. By analogy to the structure of graphite, two regions on a CNT can be

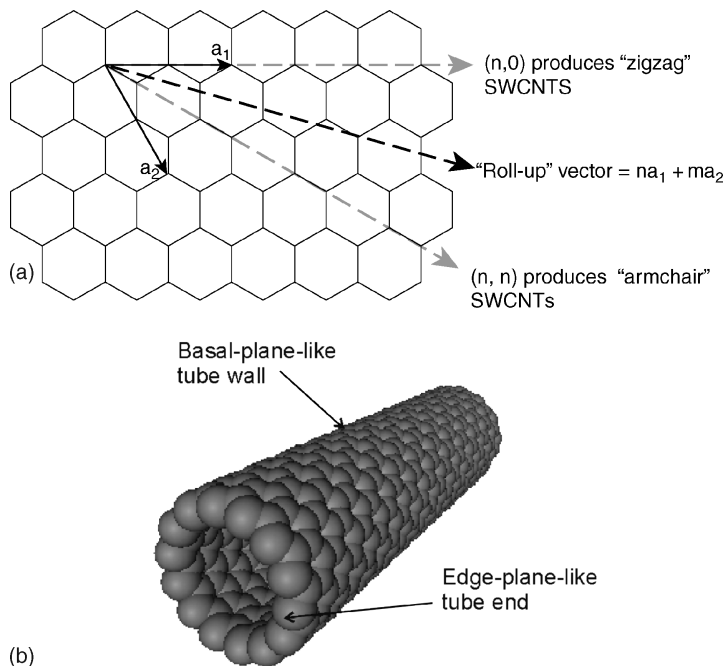


FIGURE 1.1 (a) How the lattice vectors \mathbf{a}_1 and \mathbf{a}_2 of a graphene sheet can be used to describe a “roll-up” vector to form a single-walled carbon nanotube; (b) space-filled model of a “zigzag” $(n,0)$ -SWCNT.

identified (and are labeled in Figure 1.1) as (1) basal-plane-like regions comprising smooth, continuous tube walls and (2) edge-plane-like regions where the rolled-up graphite sheets terminate, typically located at the tube ends and around holes and defect sites along tube walls. As we discuss in Section 1.2, it is these edge-plane-like defects that are crucial to an understanding of some of the surface chemistry and the electrochemical behavior of CNT (MWCNT, in particular)–based analytical and bioanalytical systems.

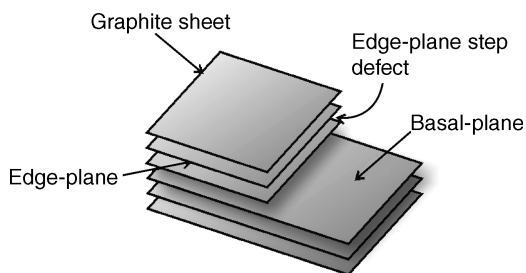


FIGURE 1.2 Crystal faces of a highly ordered crystal of graphite and the formation of an edge-plane step defect.

In the case of MWCNTs, a number of morphological variations are also possible, depending on the conditions and chosen method of CNT formation [e.g., chemical vapor deposition (CVD) or the high-voltage arc discharge method (ARC)] [10]. They can be formed as hollow-tube (h-MWCNTs), herringbone (hb-MWCNTs) [10], or bamboo-like (b-MWCNTs) [11]. The different internal structures of h-MWCNTs and b-MWCNTs are clearly visible in the high-resolution transmission electron microscopic images shown in Figure 1.3. In h-MWCNTs the graphitic tubes are oriented parallel to the tube axis and the central cavity remains open along the entire length of the h-MWCNT. The hb-MWCNTs and b-MWCNTs differ in that the graphitic tubes are oriented at an angle to the axis of the nanotube in both cases, but while the central cavity remains open in the hb-MWCNTs, in the b-MWCNTs the central cavity is periodically closed off into compartments similar to the structure of bamboo, from which the b-MWCNT name is derived. The interested reader is directed to a fascinating insight into the mechanism of b-MWCNT formation from metal nanoparticle catalyst “seeds” using the CVD method in real time by Lin et al. [12] using transmission electron microscopy. From Figure 1.3 it is also apparent that, due to the nonaxial arrangement of graphitic tubes in the hb-MWCNTs and b-MWCNTs, a greater number of edge-plane-like defect sites are formed along the length of the nanotubes compared to the h-MWCNTs.

In the case of MWCNTs it has recently been proposed that only the outer two or three graphitic tubes carry any significant current along the tube length except at the

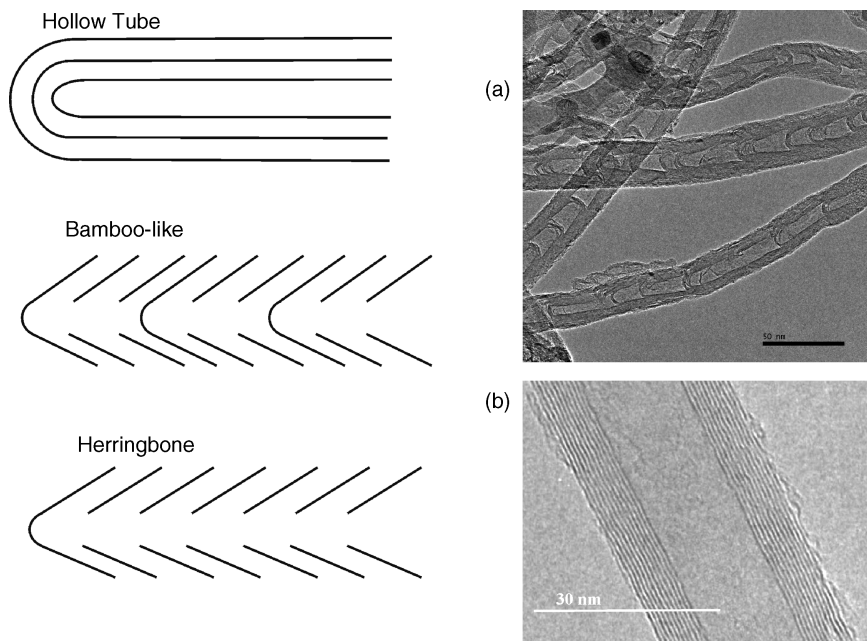


FIGURE 1.3 Three morphological variations of MWCNTs, and high-resolution transmission electron micrograph images of (a) bamboo-like and (b) hollow-tube MWCNTs.

ends of the tubes [13]. This is due to the mismatch and poor overlap of π -orbitals between different tubes within the multiwalled structure, where adjacent tubes may show different metallic or semiconducting properties. However, at the ends of the tubes, because of the higher energy density at these reactive edge-plane-like sites, intershell electron hopping is possible and the current is discharged by the entire ensemble of tube ends [13].

These inherent properties of CNTs, together with their high aspect ratio and the ability to incorporate them easily and rapidly onto or into an electrode substrate (as either random networks or as highly ordered and well-defined nanoscale structures such as vertical arrays, which are discussed in later sections), have resulted in CNTs being used in numerous electroanalytical and bioelectroanalytical applications and sensors. Furthermore, as the CNTs often possess chemical reactivity and surface functional groups similar to those of graphite, their properties can be tailored in an advantageous manner by chemically modifying the surface of the CNTs using an extraordinary variety of synthetic strategies, some of which are reviewed in later sections of this chapter.

1.2 ELECTROANALYSIS USING CNT-MODIFIED ELECTRODES

1.2.1 Historical Background

The first reported use of CNTs in electroanalysis was the pioneering work of Britto and co-workers in 1996 [14]. By incorporating CNTs into a paste electrode using bromoform as the binder, they were able to explore the electrochemical oxidation of dopamine. However, the number of papers using CNTs in electroanalysis exploded at around the turn of the twenty-first century, due in large part to the pioneering work of Joseph Wang, then at the University of New Mexico, whose article had, as of August 2007, received almost 260 citations [15]! By modifying a glassy carbon (GC) electrode with a sprinkling of CNTs, Wang et al. reported that the biologically important molecule nicotinamide adenine dinucleotide (NADH) could be detected at a much lower potential than at a bare GC electrode in the absence of nanotubes [16]. This work inspired a new trend within the electroanalytical community, and the race was on to modify electrode substrates, usually but not always a GC electrode, with CNTs which were then found to allow the “electrocatalytic” detection of literally hundreds of inorganic and biological analytes, such as insulin [17], uric acid [18], catechol [19], morphine [20], brucine [21], cytochrome *c* [22], galactose [23], glucose [24], nitric oxide [25], and horseradish peroxidase [26], as well as NADH [16] and hydrogen peroxide [27], the latter two of which comprise important substrates, cofactors, and products for more than 800 enzymes. The list of analytes that could be detected electrocatalytically at these CNT-modified electrodes was (and perhaps still is) increasing at a rate of more than a dozen or more new analytes each week.

The apparent electrocatalytic benefit of using a CNT-modified electrode was typically manifested by a lower detection limit, increased sensitivity, and in particular,

a lower overpotential at which the analyte was detected compared to the unmodified electrode substrate [28]. However, at the time, very few researchers were asking what the underlying physical cause of this apparent electrocatalytic behavior could be attributed to—it was as if this effect was considered to be due to some intrinsic, almost “magical” property of the CNTs themselves! This question prompted further investigation of the electrochemical behavior of CNTs [29–31]. In order to understand the electrocatalytic behavior observed at CNT-modified electrodes, it is first necessary to understand the electrochemical behavior of an analogous electrode substrate: graphite, in particular where on a graphite electrode the electroactive sites for electron transfer are located.

1.2.2 Electron Transfer at Graphitic Carbon Electrodes: The Role of Edge-Plane Defects

Over the past three decades there has been a strong interest in understanding the fundamentals of electron transfer at graphite electrodes. To do this, it is necessary to fabricate an electrode that has a well-defined structure, and as such, most research is usually carried out on highly ordered pyrolytic graphite (HOPG) electrodes. The basal-plane crystal face of a HOPG consists principally of atomically flat terraces of graphite. However, the main difficulty faced when trying to understand electron transfer at graphite electrode surfaces is that these surfaces are inherently spatially heterogeneous. Even the most carefully prepared surface of a HOPG possesses step defects (on a well-prepared surface these defects can comprise as little as 0.2% of the total surface coverage [32]) which reveal thin bands of the edge-plane face of the HOPG crystal, the height of which varies as multiples of 0.335 nm. These nanobands of edge-plane regions break up the large, flat, basal-plane terraces into islands up to 1 to 10 μm in size, depending on the quality of the HOPG crystal and the surface preparation [33–35]. The rates of electron transfer at these two crystal faces are very different. Therefore, any attempt to simulate the electrochemical and coupled mass transport processes at such spatially heterogeneous electrode surfaces normally requires that we solve prohibitively computationally demanding three-dimensional problems.

In Recent work by Davies et al. within the Compton group, a method of modeling such spatially heterogeneous electrode surfaces using a diffusion domain approximation was developed [29,36,37]. The mathematical and computational details of this model are left to the interested reader, but the resulting benefit of this powerful approach is that the physical model that one is attempting to simulate is reduced from an almost intractable three-dimensional problem to a much more manageable two-dimensional problem [29,36,37]. By simulating experimental data obtained at a HOPG electrode using standard redox probes such as ferrocyanide/ferricyanide and hexamineruthenium(III)/(II), Davies et al. suggested that while the electron transfer rate at the edge-plane step defects on the HOPG surface, k_{edge}^0 , was relatively fast (typically on the order of 10^{-2} cm/s), the electron transfer on the basal-plane regions of the HOPG surface was occurring so slowly ($k_{\text{basal}}^0 < 10^{-9}$ cm/s) as to be almost zero. In other words, the entire faradaic electron transfer process occurs solely,

or almost solely, at the edge-plane sites, while the basal-plane remains effectively electrochemically inert [29,37]!

Having made these strong claims, Davies et al. proceeded to design an elegant experiment by which they could generate data that would support their hypothesis convincingly. The obvious approach would be to compare the voltammetric response of a bare HOPG electrode with the response at the same electrode that has the edge-plane sites blocked with an insulating layer, and record the lack of any faradaic voltammetric response at such an electrode. Unfortunately, this approach has been prohibitively difficult to achieve. However, the alternative approach, insulating the basal-plane and leaving only the edge-plane sites exposed, is relatively straightforward, thanks to a method adapted from the work of Penner et al. [38–40]. By electrodepositing MoO_2 only along the edge-plane step defects on a HOPG electrode, then covering up the basal-plane terraces with an insulating polymer, and finally removing the MoO_2 with dilute acid to expose just the edge-plane nanobands, Davies et al. were able to investigate the voltammetry arising solely from these edge-plane regions of the graphite crystal (see Figure 1.4) [29,41].

In this way they could decouple the electron transfer at the basal- and edge-plane sites. The voltammetric response to standard redox probes, produced by revealing only the edge-plane nanobands on the HOPG surface, was almost indistinguishable from that of the bare HOPG surface, providing conclusive experimental evidence that the basal-plane regions of a graphite electrode are indeed electrochemically inert, and that the edge-plane sites on such an electrode surface are *the* active sites for electron transfer [29,41].

Many other graphitic electrode materials, such as carbon powder, carbon fiber, and in particular carbon nanotubes, are constructed from essentially the same building blocks as HOPG: namely, graphene sheets. Therefore, it was proposed by Davies et al. that if edge-plane defects on HOPG are *the* sites of electron transfer, the same is probably true for other forms of graphitic materials, including carbon nanotubes. (More specifically, we are limiting this argument to MWCNTs. In the case of SWCNTs, the smaller size of the nanotubes requires greater curvature of the walls of the tubes, reducing the overlap between neighboring p-orbitals in the delocalized π -electronic structure, and therefore possibly imparting more chemical and electrochemical reactivity to the tube walls.)

These insights prompted Banks et al. to repeat some of the original experiments which had claimed that CNTs were apparently electrocatalytic, except that in addition to comparing the voltammetry at a CNT-modified and blank GC electrode, they performed additional control experiments comparing the CNT-modified GC response to that of basal-plane pyrolytic graphite (BPPG) and edge-plane pyrolytic graphite (EPPG) electrode surfaces [29,30,42–44]. In *almost* every case the “electrocatalytic” response of the CNT-modified GC, both in terms of the reduction in the required overpotential at which each analyte could be detected and the lower detection limits obtained, was identical to that of an EPPG electrode (Figure 1.5) [45]. Thus, the apparent electrocatalytic behavior of CNT-modified electrodes was confirmed as being due simply to increasing the number of edge-plane sites on the electrode surface. By modifying the electrode substrate with CNTs, one is in effect converting

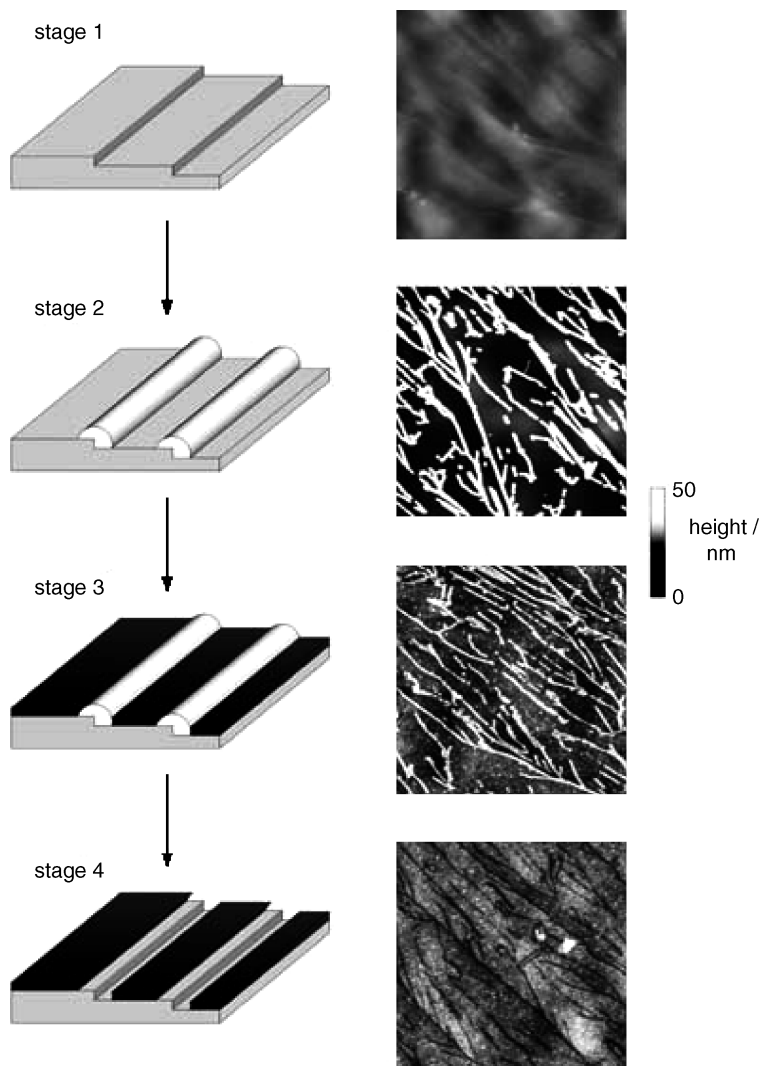


FIGURE 1.4 Four stages used to fabricate “nanotrenches.” Only the edge-plane sites on an HOPG surface are shown. (From ref. 41, with permission. Copyright © 2005 Wiley-VCH Verlag GmbH & Co. KGaA.)

the electrode substrate surface into something that more closely resembles an EPPG electrode, albeit in a rather expensive fashion! Furthermore, the work of Banks and Compton showed that in most cases, EPPG electrodes are in fact *the* electrode material of choice for the electroanalysis of a wide range of analytes [43].

Further confirmation that the electroactive sites on CNTs were located at the edge-plane-like tube ends was provided by Jurkschat et al. [46]. In this work, MoO_2

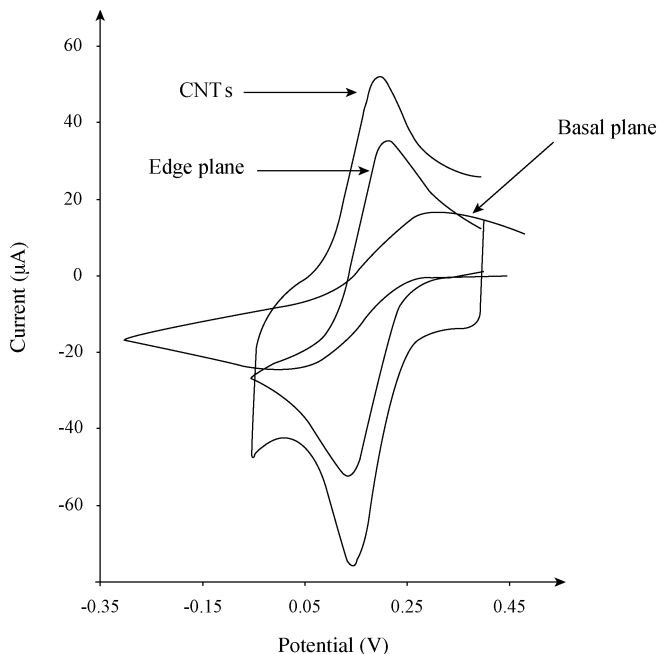


FIGURE 1.5 Overlaid voltammetric response of an EPPG, BPPG and MWCNT modified BPPG electrode in a 1 mM solution of potassium ferrocyanide with 0.1 M KCl as supporting electrolyte. (Adapted from ref. 42, with permission.)

was electrodeposited onto an h-MWCNT-modified electrode in a manner similar to the work described above on HOPG surfaces. Again, the MoO_2 is deposited only on the electroactive sites. High-resolution transmission electron microscopy was performed on the MoO_2 -modified h-MWCNTs, which revealed that the deposits of MoO_2 were found only at the ends of the tubes, forming *nanoplugs* of MoO_2 (Figure 1.6) [46].

1.2.3 Exceptions to the Rule That Edge-Plane Defects Are the Important Electroactive Sites on CNTs

There are currently only three known exceptions to the rule that it is the edge-plane-like sites on MWCNTs that are responsible for any electrocatalytic detection of a given analyte. These are the detection of halothane, hydrazine, and most important for biosensors, hydrogen peroxide. All three of these analytes are detected at lower overpotentials at an h-MWCNT-, b-MWCNT-, or SWCNT-modified GC electrode than at an EPPG electrode and with a larger peak current and hence lower limit of detection and sensitivity. However, the CNTs used in these experiments were all made using the chemical vapor deposition method, and as such, contain remains of the metal nanoparticle catalysts, such as iron and copper, used to grow the nanotubes.

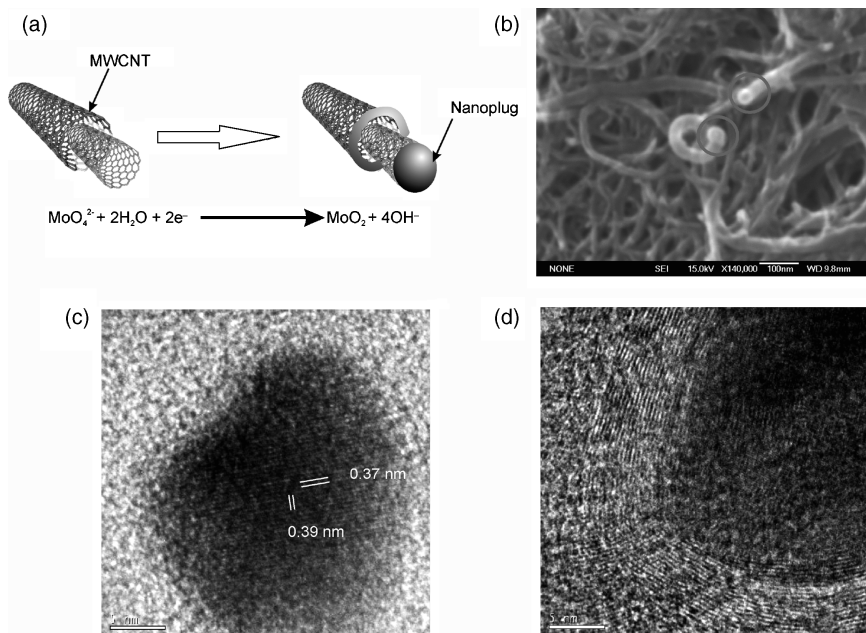


FIGURE 1.6 (a) Electrodeposited nanoplug; (b) SEM image of the nanoplug decorated h-MWCNTs (nanoplugs circled); (c) HRTEM image of a nanoplug at the end of a MWCNT showing the MoO_2 lattice spacings; (d) same as (c) but with a different focus showing the fringes of the carbon sheets at the end of the nanotube and the darker mass of the MoO_2 nanoplug. (From ref. 46, with permission. Copyright © 2006 Wiley-VCH Verlag GmbH & Co. KGaA.)

It was found that most common purification methods, such as washing the CNTs in mixtures of concentrated mineral acids, did not remove all of these metal impurities; the residual metal nanoparticles were found to be occluded within the walls of the h-MWCNTs and b-MWCNTs, which prevents their complete removal by such chemical methods [47–49].

Further control experiments were performed using iron oxide microparticles abrasively immobilized onto a BPPG or EPPG electrode, which demonstrated that in the cases of hydrazine and hydrogen peroxide, it was the occluded iron/iron oxide nanoparticle impurities in the CNTs that were responsible for the electrocatalysis observed [47,48]. In the case of halothane, residual metallic copper nanoparticle impurities also occluded within the walls of the h-MWCNTs and b-MWCNTs were shown to be the electroactive sites [50].

In summary, the authors recommend that caution be employed when claiming any electrocatalytic detection of analytes using CNTs. In all cases the appropriate control experiments using EPPG electrodes should be performed. In rare cases where the CNT-modified electrode is still behaving in an electrocatalytic manner, further control experiments should be performed to elucidate the physical origins of this phenomenon.

1.3 ADVANTAGEOUS APPLICATION OF CNTs IN SENSORS: pH SENSING

Having shown in Section 1.2, that for most electroanalytical applications EPPG electrodes are often superior to CNT-modified electrodes as electrode substrates of choice, the obvious question is: Why is there still such an intense interest in using CNTs in electroanalysis and bioelectroanalysis? Reassuringly, the use of CNTs in sensors and biosensors still offers many practical and analytical benefits. The small size of the CNTs allows the prospect of sensor miniaturization down to the nanoscale, possibly allowing the study of many intracellular processes in vivo without causing substantial damage to the structural integrity of the cells being studied [51,52]. Their high aspect ratio imparts many benefits, such as the ability to construct vertically aligned arrays of CNTs, or *nanoarrays*, with correspondingly improved sensitivity and lower detection limits of target analytes [53–55]. Alternatively, their high aspect ratio and the hydrophobic nature of the native CNTs allows one to encapsulate them in certain types of protein or enzyme. The nanotube then acts as a molecular “wire,” allowing us to probe the electron-transfer properties of redox active sites buried deep in the hydrophobic interior of the protein or enzyme, which would otherwise be inaccessible using conventional electrodes (where the electrons would be required to tunnel over large distances, typically greater than 10 to 13 Å, through the protein structure to reach the active site) [54,56–59]. Finally, CNTs (MWCNTs in particular) possess a chemical reactivity similar to that of graphite itself. Thus, one can fabricate chemically modified CNTs using the same vast range of techniques that have been developed for the modification of graphite electrodes, and thereby “tailor” the properties of the CNT-based sensor in a controlled fashion, to impart the desired beneficial behavior of the sensor toward the system under investigation.

The range of modification techniques is vast—being limited more by the imagination of the researcher than anything else—but several common methods are abundant in the literature, including (but not limited to): (1) physical adsorption (including layer-by-layer assembly and self-assembled monolayer formation), (2) radical attack, (3) electrophilic attack, (4) nucleophilic attack, (5) esterification/amidification, (6) intercalation (full or partial), (7) agglomeration, and finally, (8) forming carbon nanotube paste electrodes with the modifying species incorporated into the binder. Of these methods, the ones most commonly employed in bioanalysis are methods of physisorbing biological species onto CNTs or covalently attaching them through the formation of esters or amides. The latter is facilitated by both the presence of surface carboxyl groups, which naturally decorate the edge-plane defects on CNTs, and an abundance of available amine groups on the hydrophilic exterior or terminus of many enzymes or protein structures. The surface coverage of carboxyl groups on the CNTs can be increased by various methods, such as stirring a suspension of nanotubes in a mixture of concentrated mineral acids (e.g., a 3 : 1 mixture of sulfuric and nitric acids), which in turn increases the efficiency of any coupling reaction to the biological species of interest. Furthermore, the large surface area and structure of CNTs make them ideal supports for various metal nanoparticles and quantum dots for both sensing and catalyst

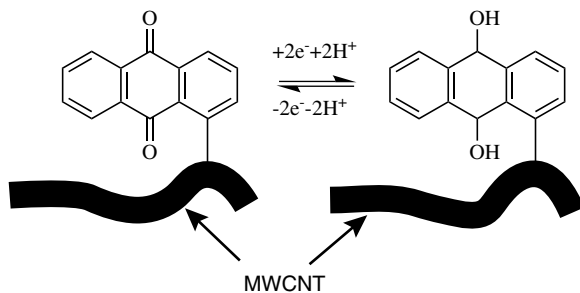


FIGURE 1.7 Two-electron, two-proton redox couple of the anthraquinone/anthrahydroquinone modified MWCNTs. (From ref. 62, with permission. Copyright © 2004 Wiley-VCH Verlag GmbH & Co. KGaA.)

applications, which are dealt with in other chapters of this book and are reviewed by, for example, Wildgoose et al. [60].

The area of chemically modified CNTs for electroanalysis and bioelectroanalysis has also been subject to substantial review, and we shall not repeat the exercise here except to direct the interested reader to references 51–52, 61. Nevertheless, one noteworthy aspect of using chemically modified CNTs that has recently arisen from the authors' own work is the observation that the pK_a values of chemical species attached to CNT surfaces can differ markedly from that of species in solution. This effect has important implications in two areas of bioanalytical importance: (1) in designing syntheses, for example, involving the formation of esters or amides to the surface carboxyl groups on CNTs (either those that occur naturally or those that have been introduced by prior chemical modification), where a consideration of relative pK_a values of both reactants can be crucial in determining a successful synthetic outcome; and (2) in the design and construction of sensors that respond to changes in the pH of the solution, which is one of the most important, but often overlooked, analytical measurements that can have a huge effect in biological systems.

Heald et al. reported the covalent chemical modification of MWCNTs with anthraquinone radicals generated via the chemical, as opposed to electrochemical, reduction of 1-anthraquinonediazonium chloride with aqueous hypophosphorous acid (50% v/v H_3PO_2) [62]. The anthraquinone-modified MWCNTs (AQ-MWCNTs) exhibited a quasireversible voltammetric response, corresponding to the two-electron, two-proton anthraquinone/anthrahydroquinone redox couple shown in Figure 1.7. Due to the concomitant proton and electron transfer, the peak potential of the anthraquinone/anthrahydroquinone couple depends on the solution pH according to a modified form of the Nernst equation: For

$$AQ\text{-MWCNTs} + 2e^- + 2H^+ \rightarrow AQH_2\text{-MWCNTs}$$

$$E = E_f^0 - \frac{2.303RTm}{nF} \log \frac{[AQH_2\text{-MWCNTs}]}{[AQ\text{-MWCNTs}][H^+]}$$

$$[AQH_2\text{-MWCNTs}] = [AQ\text{-MWCNTs}] \quad \text{pH} = -\log([H^+])$$

Therefore,

$$E = E_f^0 - 0.059 \text{ pH at } 298 \text{ K}$$

In the expressions above R , T , and F are the universal gas constant ($\text{J/mol} \cdot \text{K}$), temperature (K), and the Faraday constant (C/mol), respectively; n and m are the number of electrons and protons transferred, respectively (in this case $n = m = 2$); and E and E_f^0 (V) are the peak potential and the formal potential of the anthraquinone/anthrahydroquinone redox couple, respectively. Heald et al. reported that the AQ-MWCNTs exhibited a linear shift in peak potential, with an almost nernstian gradient of -56 mV per decade increase in pH over the entire pH range studied, from pH 1.0 to pH 14.0 (Figure 1.8) [62].

Note that in solution, the $\text{p}K_a$ value corresponding to the removal of the first proton from the anthrahydroquinone molecule is about 10, while the $\text{p}K_a$ for removal of the second proton is around 12. Thus, a plot of peak potential versus pH for anthraquinone in solution would show deviations from linearity around pH 10 and again around pH 12. The fact that the AQ-MWCNTs exhibit a linear response over the entire pH region up to pH 14 indicates that the $\text{p}K_a$ of the anthrahydroquinone molecules attached to the MWCNT surface has been altered to beyond pH 14, one of the largest reported shifts in $\text{p}K_a$ on any carbon surface. Thus, Heald et al. proposed that this advantageous effect could be exploited to develop the AQ-MWCNTs into a reliable, calibration-less, pH sensor which has subsequently been patent protected [63]. Later, Masheter et al. extended the derivatization method of Heald et al. to study the shifts in $\text{p}K_a$ of anthraquinone-modified CNTs of different morphologies, b-MWCNTs, h-MWCNTs and SWCNTs and used these to explore where on the CNT surface the reactive sites for the attachment of the anthraquinonyl radical were likely to be [64]. In the case of the MWCNTs it was concluded that the majority of anthraquinonyl radicals modify the edge-plane-like sites at the tube ends, whereas a greater degree of sidewall functionalization occurs for the SWCNTs, reflecting their greater reactivity [64]. Interestingly, the shift in the $\text{p}K_a$ of the anthrahydroquinone species covalently attached to CNTs compared to the solution-phase $\text{p}K_a$ values was found to depend on the morphology of the CNTs.

To explore this further, Masheter et al. covalently attached the anthraquinone species to the surface of graphite powder forming AQ-carbon and also attached anthraquinone-2-carboxylic acid to aniline groups covalently attached to the surface of the CNTs and graphite, forming AQ-AN-carbon or AQ-AN-CNTs (Figure 1.9) [64]. This coupling method has the effect of attaching the anthraquinone center to the graphitic surface through a "spacer" molecule, extending the anthraquinone group farther from the surface of the carbon material into the solution phase. The effect on the $\text{p}K_a$ values of the anthrahydroquinone groups is summarized in Table 1.1. The differences in the $\text{p}K_a$ values are attributed to the anthraquinone groups found in different molecular environments (solvation spheres, solvent ordering/disordering etc.) on the surface of each material, which is influenced directly by the morphology of the CNTs or graphite powder [64].

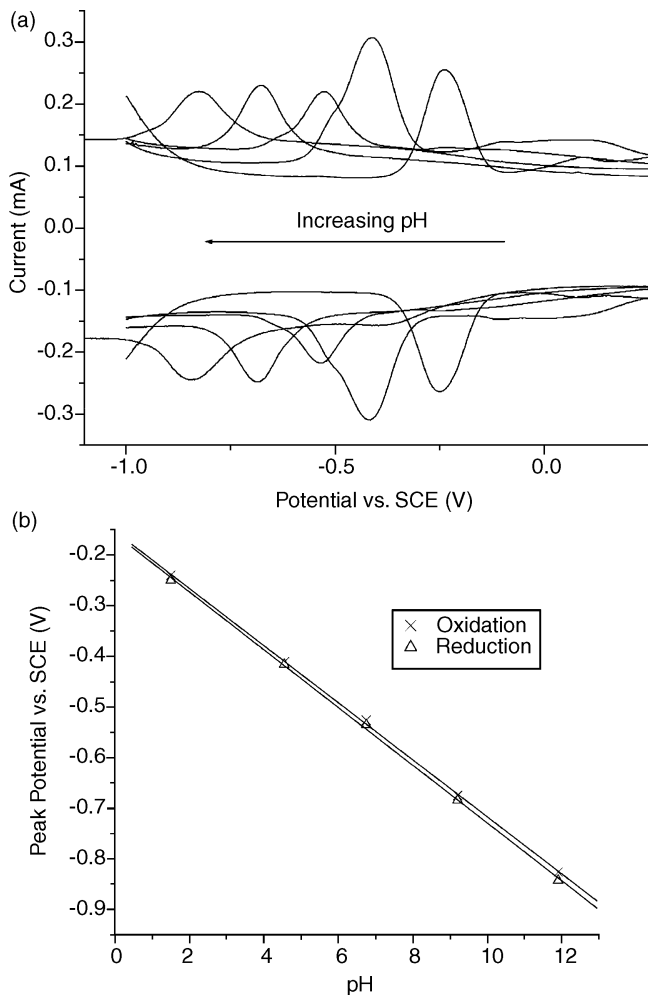


FIGURE 1.8 (a) Overlaid oxidative and reductive square wave voltammograms for AQ-MWCNTs at pH 1.0, 4.6, 6.8, 9.2, and 12.0, at 293 K; (b) plot of peak potential vs. pH from the square-wave voltammetry of AQ-MWCNTs over the pH range pH 1.0 to 12.0 at 293 K. (From ref. 62, with permission. Copyright © 2004 Wiley-VCH Verlag GmbH & Co. KGaA.)

Finally, Abiman et al. studied the shift in pK_a of 4-carboxyphenyl groups attached covalently to graphite and glassy carbon surfaces [65]. In the solution phase 4-carboxybenzene has a pK_a of 4.20 at 298 K. On the surface of glassy carbon the pK_a was found to shift to 3.25, while on the surface of graphite the pK_a was shifted in the opposite direction, to 6.45 [65]. The thermodynamic parameters controlling these shifts were investigated and it was found that the degree and direction of the shift in pK_a are dominated by the entropy change upon ionization of the carboxyl groups. This, in turn, can be related to the different hydrophobicity and hydrophilicity of

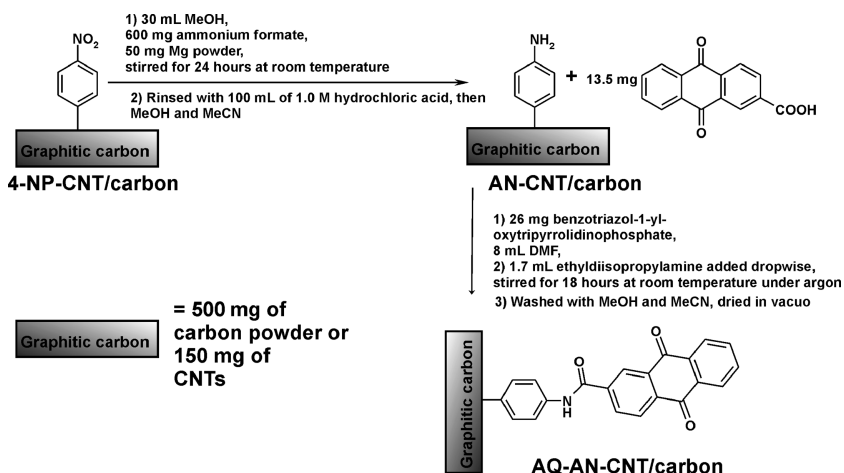


FIGURE 1.9 Derivatization of graphitic carbon with anthraquinone-2-carboxylic acid. (From ref. 64, with permission. Copyright © 2007 Royal Society of Chemistry.)

graphite and glassy carbon, and reflects the role of the solvent ordering and disordering around the interface, as intimated earlier by Masheter et al. [64]. Thus, when designing synthetic strategies to modify CNTs with biological species for bioanalysis involving the formation of ester or amide linkages, researchers should be aware that the pK_a values of the carboxyl, hydroxyl, or amino groups on the CNT surface may differ markedly from their value in bulk solution. This, in turn, will affect the choice of reagents and synthetic strategy used to produce the successful modification desired. Having introduced the reader to the use of CNTs in electroanalysis, and highlighted the many pitfalls to be avoided, we now turn our attention to the use of CNTs in bioelectroanalysis and biosensors.

TABLE 1.1 Peak Potential Variation with Increasing pH and the pK_a Values Observed for AQ-Modified CNTs and Graphite Powder^a

Material	Shift in Peak Potential per pH Unit Below the		
	pK_a Value/mV per pH Unit	pK_{a1}	pK_{a2}
Anthraquinone in solution	58	10	12
AQ-h-MWCNT	55		13
AQ-b-MWCNT	58		>14
AQ-SWCNT	57		>14
AQ-carbon	60		>14
AQ-AN-h-MWCNT	58		12
AQ-AN-b-MWCNT	54		13
AQ-AN-SWCNT	58		>14
AQ-AN-carbon	57	10	12

Source: From ref. 64, with permission. Copyright © 2007 Royal Society of Chemistry.

^aNote that where both protons are lost simultaneously, only one pK_a value is reported.

1.4 CARBON NANOTUBE-BASED BIOSENSORS

1.4.1 Introduction

Biosensors represent a plausible and exciting application in the field of nanobiotechnology. The most widespread biosensors, which have made their most significant commercial inroads, are perhaps the portable glucose sensors used by diabetic patients to measure blood glucose level. These are available from high-street chemists and have been around for more than three decades. Small commercially available handheld devices such as the FreeStyle Lite from Abbott Diabetes Care employ an enzyme (glucose oxidase) that catalyzes the oxidation of glucose. In doing so, it transfers an electron between the target analyte and the enzyme in close proximity to an electrode within the device, which is then converted into a measure of blood glucose concentration. The deceptively simple, and extremely portable, glucose biosensor has effectively met the needs of 1 to 2% of the world's population that have diabetes, thus generating high market demand for such sensors and fueling the development of the associated biosensor technologies.

So questions arise as to what exciting features these devices possess that mark its attractiveness to the marketplace. Biosensors are simple analytical devices that combine the high sensitivity and specificity of a biological molecule with the versatility of a range of different physical transducers (Figure 1.10) to convert a biological response or biorecognition event into a readable digital electronic signal. Therefore, a typical biosensor consists of three parts: (1) a biological, biologically derived, or biomimetic sensing element; (2) a physical transducer; and (3) a detector. The sensing elements or receptors employed can exploit the bioaffinity interactions, as is the case with antibodies, cell receptors, nucleic acids, imprinted polymers, or catalytic reactions as would be carried out by whole organisms, tissue sample cells, organelles, or

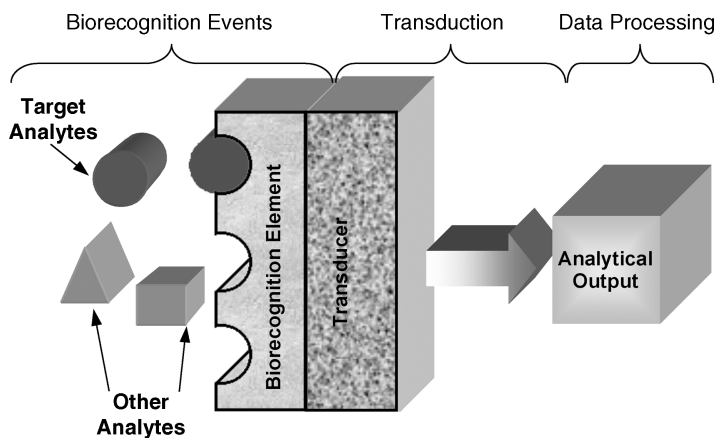


FIGURE 1.10 Biosensor that consists of a biorecognition layer on a transducer attached to an analytical output. (Adapted and modified from ref. 66, with permission. Copyright © 2007 World Scientific Publishing.)

enzymes. Biosensors can be classified into various groups according to signal transduction or biorecognition events. On the basis of transducing elements, biosensors can be categorized as piezoelectric, optical, or electrochemical sensors [66].

Piezoelectric transducers interconvert mechanical deformation when an electrical potential is applied to measure mass or viscoelastic effects through the use of acoustic waves, surface acoustic waves, or Love waves. Optical transducers exploit properties such as simple light absorption, fluorescence, bio- or chemiluminescence, and refractive index to transduce the biological responses. Electrochemical transducers utilize current or electrical charge to translate the recognition events. Regardless of the transducing elements, the main advantages offered by the biosensors over conventional analytical techniques are the possibility of miniaturization, for the sensing to be conducted on-site, and the ability to measure the target analytes in complex matrices with minimal sample preparation. Although many of the biosensors developed might not be able to compete with conventional analytical methods in terms of accuracy and reproducibility, they can be used in view of providing enough information for routine testing and screening of samples rapidly and with ease.

For biosensors to be workable, several requirements need to be satisfied. First, an easy-to-construct sensing yet reproducible interface is required to output a reliable assay signal. Second, the transducing element and method of detection need to be (1) highly specific to the recognition events to an extent that they can differentiate and/or exclude all the nonspecific interaction, (2) highly sensitive with a relatively high signal-to-noise ratio to minimize a false-positive or false-negative outcome, (3) low cost by using the least amount of expensive sensing or labeling materials, and (4) user friendly. Third, the ability to withstand extreme conditions (i.e., sustain sterilization under autoclaving conditions) is also ideal. Finally, the next generation of biosensors will also require arrayable designs that can be functionalized and monitored in a multiplex fashion (see Figure 1.11).

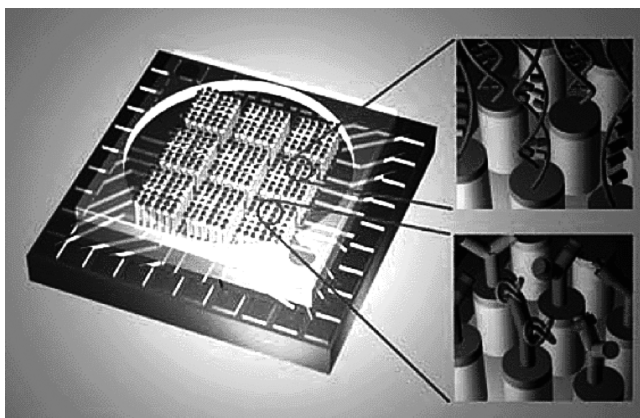


FIGURE 1.11 Ultrasensitive multiplex electronic biosensor based on CNT array. The insets on the right represent application in DNA (top) and antigen (bottom). (Adapted and modified from www.cict.nasa.gov.)

To fulfill all or most of the prerequisites mentioned above, researchers have begun to investigate a novel class of nanomaterials to enhance the response of biosensors. One-dimensional nanostructures are particularly attractive for bioelectronic detection because of their high surface-to-volume ratio and novel electron transport properties. Their electronic conductance is strongly influenced by minor surface perturbations (such as those associated with the binding of macromolecules). The extreme smallness of these nanomaterials would allow packing of a huge number of sensing elements onto a small footprint of an array device. In particular, CNTs have attracted much attention (owing to their excellent electrical, mechanical, optical, and thermal properties [67–69]) since their discovery and have paved the way to new and improved sensing devices. For example, an extremely important challenge in amperometric enzyme electrodes is the establishment of satisfactory electrical communication between the active site of the enzyme and the electrode surface. The redox center of most enzymes is electrically insulated by a glycoprotein shell. Because the enzyme is embedded deep within the shell, it cannot be oxidized or reduced at an electrode at any potential. The possibility of direct electron transfer between enzymes and electrode surfaces could result in the development of superior reagentless biosensing devices, as it eliminates the need for co-substrates or mediators and allows efficient transduction of the biorecognition event. In fact, both Gooding's [70] and Willner's [71] groups have reported the direct electrochemistry of enzymes and proteins at CNT-modified electrodes. The enhanced electrochemical response obtained at CNT-modified electrodes is due largely to the small size of CNTs. In effect, CNTs have the ability to reduce the distance between the redox site of a protein and the electrode. Since the rate of electron transfer is inversely dependent on the exponential distance between the redox center and the electrode, the overall rate of the electrochemical process is subsequently enhanced. In addition, CNTs are also used in the modification of electrode surfaces or to modify biological receptor molecules such as proteins (enzyme electrodes) [72–75], antibodies (immunosensor) [76], or oligonucleotides (nucleic acid sensing devices) [74,77].

With regard to different transducing elements, the piezoelectric method is generally used to study the adsorption properties of biomaterials to CNTs [78]. There is also a report on the use of surface-acoustic waves to enhance the alignment of thiolated CNTs on gold electrodes [79]. The information obtained by using the piezoelectric technique is extremely helpful in characterizing and aligning CNTs, but its use in any biosensing application is limited. Current biological sensing techniques that rely on optical detection principles using CNTs are inherently complex, requiring multiple preparative steps, multiple reagents, signal amplification, and complex data analysis. Although the techniques are highly sensitive and specific, they are generally more difficult to miniaturize. However, a recent report on the development of a near-infrared optical biosensor which uses the modulation of SWCNTs' fluorescence emission in response to changes in glucose concentration is extremely promising [80]. The advantage of a near-infrared optical biosensor is its potential for implantation into thick tissue or whole-blood media, where the transduction signal is allowed to penetrate up to a greater distance. Such a passive, optically responsive biosensor may

allow the realization of continuous analyte detection *in vivo* using an external, miniaturized excitation and detection device [80].

Electrochemical CNT-based biosensors are studied widely, owing to the remarkable ability of CNTs to enhance the electrochemical reactivity of biomolecules and to promote the electron-transfer reactions of proteins [70,71]. These properties make CNTs extremely attractive for a wide range of electrochemical biosensors, ranging from amperometric enzyme electrodes to DNA biosensors. In this section, state-of-the-art designs of electrochemical CNT-based biosensors are discussed, along with practical examples of such devices.

1.4.2 Surface Functionalization of Carbon Nanotubes and Configuration of a CNT-Based Electrochemical Biosensor

Immobilization of biomolecules onto CNTs has been pursued in the past, motivated by the prospects of using CNTs as new types of biosensor materials. A prerequisite for research in this area is the development of chemical methods to immobilize biological molecules onto CNTs in a reliable manner. The successful realization of CNT-based biosensors also requires proper control of their chemical and physical properties as well as their functionalization and surface immobilization to the physical transducer. There are several ways to functionalize the surface of CNTs, but these can be generalized into two main domains: (1) noncovalent functionalization and (2) covalent modification.

Functionalization of CNTs by noncovalent methods is used primarily to preserve the *sp*² nanotube structure, and thus CNTs' electronic characteristics. Common methods of noncovalent functionalization of CNTs include encapsulation, adsorption (physical and chemical), and the exploitation of hydrophobic interactions. The selective opening at the capped region (ends) of nanotubes by oxidants [81,82] has promoted extensive experiments involving the filling of the inner hollow cavity. For example, metallothionein proteins have been encapsulated inside open nanotubes using wet techniques [74,77,83]. The opened nanotubes were prepared by refluxing the closed tubes with nitric acid for 24 hours to purify and open the tube at the capped region, followed by washing with distilled water and drying *in vacuo*. Then the opened nanotubes were suspended in an aqueous protein solution for 24 hours [83]. Several proteins were also found to adsorb on CNTs via hydrophobic interactions between the nanotubes and the hydrophobic domains of the proteins [84,85]. Antibody and DNA molecules have also been observed to adsorb onto CNTs via nonspecific interactions [77].

A recent innovative approach to noncovalent biofunctionalization of CNTs involves the irreversible adsorption of the pyrene moiety of the aqueous bifunctional small molecule 1-pyrenebutanoic acid succinimidyl ester (see Figure 1.12) onto the inherently hydrophobic surfaces of CNTs in an organic solvent [73]. The pyrenyl group, being highly aromatic in nature, is known to interact strongly with the basalplane of graphite via π -stacking [86] and is believed to interact strongly with CNTs in a similar manner. Subsequently, the proteins, which are generally rich in surface amines, are attached to the surface-immobilized ester through carbodiimide coupling to form an amide bond. Yet another inventive strategy for the noncovalent immobilization of enzyme onto CNTs is achieved through layer-by-layer assembly.

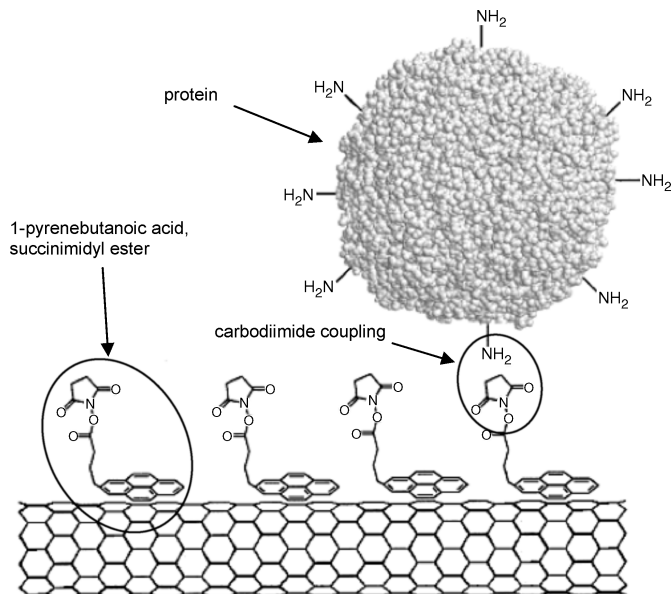


FIGURE 1.12 Anchored succinimidyl ester to form amide bonds for protein immobilization. (From ref. 73, with permission. Copyright © 2001 American Chemical Society.)

Stepwise layer-by-layer assembly of multilayer enzyme films on a CNT template was performed using alternate electrostatic deposition of oppositely charged polyion [poly(diallyldimethylammonium chloride)] and enzyme (alkaline phosphatase) [87]. The enzyme in the film is accessible by the substrate of the enzyme (α -naphthyl phosphate), and the entire layer-by-layer assembly enables signal amplification for ultrasensitive detection of nucleic acids (down to 80 DNA copies) [87].

While the biomolecules can be linked to the carbon nanotubes via noncovalent attachment, the use of covalent chemistry is expected to provide the best stability, accessibility, and selectivity. Although covalent functionalization will unavoidably lead to a disruption of the carbon nanotube–delocalized π -system, this offers a convenient and controllable means of tethering molecular species. Covalent immobilization of biological molecules to CNTs is often achieved using oxidized CNTs. An overview of the covalent attachment process is as follows: CNTs are oxidized either by sonicating [70] or refluxing [75] in concentrated acid solution, resulting in the formation of carboxylic acid groups at the ends and sidewalls of the CNTs. The resulting carboxylic acids on the surface of the CNTs are then reacted with amino functional groups of the biological receptors via carbodiimide coupling. As an example, successful attachments of bovine serum albumin (BSA) protein [75] and glucose oxidase enzyme [88] to the sidewalls of CNTs via amide linkages have been demonstrated. End-wall attachment of the biomolecules, such as glucose oxidase [71] and microperoxidase MP-11 [70], to CNTs has also been shown. Recently, bienzymatic (glucose oxidase and horseradish peroxidase) modification and assembly of CNTs covalently linked with a poly(amidoamine) (PAMAM) dendrimer have been demonstrated [89]. This is achieved by using amidation reaction to link the dendrimer

to the CNTs, followed by the reduction of Schiff bases formed between the CNT-linked dendrimer and bienzymes using sodium borohydride [89].

We have discussed the functionalization of CNTs, but questions arise as to how one links the CNTs onto the electrochemical transducer. Most common approaches can be generalized into three categories: (1) CNT-coated electrodes, (2) CNT-biocomposite electrodes, and (3) CNT-aligned electrodes. The simplest route to CNT-coated electrodes is through drop coating of a random tangle of nanotubes onto the electrode surface. First, the CNTs are randomly dispersed with the aid of sonication in a solvent, deposited on the electrode surface, and allowed to dry under ambient conditions or under an infrared lamp. The dispersion of CNTs in aqueous solution can be facilitated by an appropriate surfactant, such as dihexadecyl hydrogen phosphate [90]. Instead of aqueous media, various organic solvents, such as dimethylformamide (DMF), have been used as the dispersing solvent. The CNT-coated electrodes are then immersed in a buffered solution containing a dilute amount of the biomolecule of interest, which allows for physisorption of the biomolecules onto the CNT-coated electrodes. Proteins with an accessible redox active center close to their surface, such as cytochrome *c* [22,91] and horseradish peroxidase [92], have been immobilized successfully onto CNT-coated glassy carbon electrodes. Even proteins with a redox active center embedded deep within the glycoprotein shell, such as glucose oxidase, still exhibit well-behaved reversible redox response after adsorption onto the CNT-coated glassy carbon electrode [93]. One other approach in preparing CNT-coated electrodes is through the use of Nafion, a perfluorinated sulfonic acid ionomer with good ion-exchange and biocompatibility properties that is very effective as a protective coating for glucose sensors [94,95]. Successful immobilization of glucose oxidase onto a Nafion/CNT-coated electrode has been demonstrated, and the electrode was shown to benefit greatly from the antifouling and discriminative properties of the Nafion film, exhibiting efficient electrocatalytic action toward hydrogen peroxides [96].

CNT-biocomposite electrodes are also used commonly in the preparation of CNT-based electrochemical biosensors, which consist of a mixture of CNTs, binder, and biomolecules. The main advantage of CNT-biocomposite electrodes over CNT-coated electrodes is the renewable sensing surface offered by the CNT-biocomposite designs. Conventional CNT-biocomposite electrodes are made from CNT carbon paste electrodes, constructed by mixing carbon powder with different binders, commonly mineral oil [97,98] or bromoform, in conjunction with CNTs and biomolecules. Such composite electrodes combine the ability of CNTs to promote electron-transfer reactions with the electrical conductivity of the paste electrode materials. A binderless CNT-biocomposite electrode has been fabricated by mixing glucose oxidase with CNTs, followed by packing this mixture firmly into a 300- μm polyimide tubing before inserting the entire setup into a 21-gauge needle, forming a microsensor for glucose [99].

Another innovative improvement in the construction of CNT-biocomposite electrodes, which provides more mechanical strength to the biosensors, involves the use of CNTs and Teflon composite materials [100]. The use of Teflon as a binder for graphite particles has shown it to be extremely useful for various electrochemical sensing applications. Unlike the early CNT carbon paste biocomposite electrodes, the new CNT-Teflon biocomposite devices rely on the use of CNTs as the sole conductive component, rather than utilizing it as the modifier in connection with another electrode

surface. The bulk of the resulting CNT–Teflon electrode serves as a “reservoir” for the enzyme, in a manner similar to their graphite-based counterparts [100]. Prominent electrocatalytic activity of CNTs toward hydrogen peroxide is still observed using the CNT–Teflon–glucose oxidase biocomposite design.

Both the CNT-coated and CNT–biocomposite electrodes result in an unknown spatial relationship between the biological molecules and the CNTs. As a result, an effective way to counter this limitation is to align the shortened CNTs perpendicular to an electrode surface, which gives rise to CNT vertically aligned electrodes. This vertical alignment not only improves the electrical contact between the sensing element and the physical transducer, but also ensures that the sensor is free of impurities originating from the solvents or binders. Another major advantage of such an assembly is the ability to construct arrays of CNT nanoelectrodes in which the vertical CNT arrays exhibit high electrocatalytic activity coupled with fast electron transfer [101,102]. For example, Gooding et al. [70] and Potolsky et al. [71] refer to the vertical CNT arrays as CNT “nanoforests” that can act as molecular wires to allow electrical communication between the underlying electrodes and redox proteins. Their data suggest that the CNT nanoforests behave in an electrically similar fashion to metal wires, conducting electrons from an external circuit to the redox sites of enzymes. The CNT-aligned electrodes are prepared by linking the carboxylated open ends of nanotubes chemically to self-assembled monolayers of cysteamine on a gold surface (see Figure 1.13) [70,71].

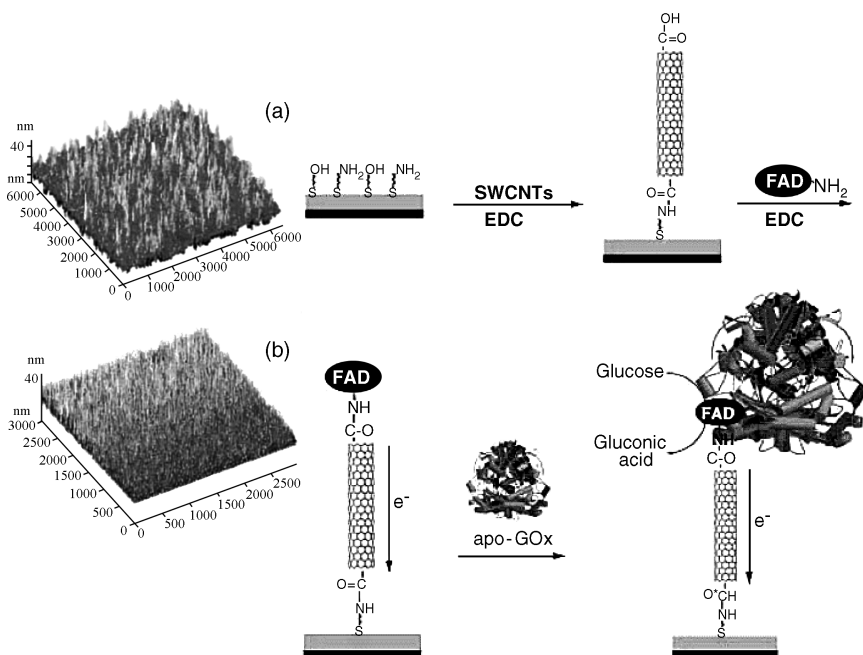


FIGURE 1.13 Construction of SWCNT-based glucose oxidase (GOx) electrode (FAD, flavin adenine dinucleotide, an enzyme cofactor), and AFM images of SWCNT covalently linked to a cysteamine monolayer associated with an Au electrode after 90 and 180 minutes of coupling. (From ref. 71, with permission. Copyright © 2004 Wiley-VCH Verlag GmbH & Co. KGaA.)

One limitation of such an assembly is that the highly conductive CNT nanoforests are linked in series with a layer of insulating cysteamine that can impede the electron transfer. Therefore, recent advances on growing the CNTs [103] directly on metallic substrates such as platinum electrodes have been investigated to eliminate this barrier layer [104]. In this approach the CNT array was grown by the chemical vapor deposition (CVD) method on a platinum electrode [104]. Successful attachment of glucose oxidase onto the CNT arrays grown on platinum and its ability to monitor glucose has also been demonstrated [105].

1.5 USING CNTs IN BIOSENSOR PRODUCTION FOR MEDICAL DIAGNOSTICS AND ENVIRONMENTAL APPLICATIONS

In the arena of medical diagnostics and environmental applications, nanotechnology-based biosensors could be used, for example, to replace more costly and tedious laboratory methods for monitoring a patient's blood for proteins, chemicals, and pathogens, and also for monitoring pollutants in the environment. In this section, different types of CNT-based electrochemical biosensors used in the fields of medical diagnostics and environmental applications are discussed. Most commonly used CNT-based electrochemical biosensors are generalized into three categories: immunochemical, enzymatic, and DNA-based biosensors.

1.5.1 Medical Diagnostics

Early diagnosis of cancer is vital to increase the chances of successful treatment of the disease. This requires extremely sensitive methods to detect the cancer biomarkers, such as mutated genomic sequences, present at ultralow levels during early stages of the disease. In particular, clinical measurement of collections of cancer biomarkers shows great promise for highly reliable predictions for early cancer detection. Point-of-care DNA screening for early cancer detection will require low-cost methodology for rapid detection of mutated genomic sequences with high selectivity, and sensitivity, while maintaining minimum sample amount and operational simplicity. DNA electrochemical biosensors, based on nucleic acid recognition processes, are currently being developed toward the goal of rapid, simple, and inexpensive testing of genetic and infectious diseases. Electrochemical hybridization biosensors rely on the immobilization of a single-stranded DNA probe onto the transducer surface that converts the formation of double-stranded DNA into a useful electrical signal.

An impressive number of inventive strategies for electrochemical DNA sensing have emerged. Recently published review articles by Kerman et al. [106], Drummond et al. [107], Wang [108], and Gooding [109] summarized the state of the art and recent trends in electrochemical DNA biosensor technology. The most common strategy for the electrochemical detection of hybridization is through the use of a redox-active label where there is a change in affinity of the redox molecule toward the probe single-stranded-DNA-modified interface before and after exposure to the target DNA. An alternative strategy to using redox-active-labeled systems is the label-free approach, which relies on the intrinsic redox-active properties (e.g., direct oxidation)

of DNA bases (guanine or adenine). In both cases, amplification of the current signal arising from the hybridization event between the probe and the target is desirable to achieve low detection limits.

The performance of DNA hybridization biosensors can greatly benefit from the use of CNTs. Such improvements are attributed to enhanced detection of the target guanine as well as to the use of CNT carrier platforms. For the label-free electrochemical detection methods, a novel approach to amplifying the guanine oxidation current is through the use of MWCNTs [110]. The advantage of CNT-modified glassy carbon electrodes has been illustrated in comparison with the common unmodified glassy carbon, carbon paste, and graphite pencil electrodes. For example, a significantly enhanced guanine oxidation current is observed when the direct electrochemistry of guanine is performed at a MWCNT-modified glassy carbon electrode compared to an unmodified glassy carbon electrode using cyclic voltammetry (CV) [90]. Wang et al. [110] reported an 11-fold increase in the guanine oxidation current using CV at an end-functionalized MWCNT-DNA-modified glassy carbon electrode for the detection of DNA sequences related to the breast cancer *BRCA1* gene compared to a MWCNT-free glassy carbon electrode. In addition to glassy carbon electrodes, similar enhancement of the guanine DNA response was reported at MWCNT paste electrodes [111]. Further enhancement of the guanine oxidation current is demonstrated by Kerman et al. [112]. The group designed a label-free DNA biosensor using sidewall- and end-functionalized MWCNT, as shown in Figure 1.14. The efficient electron-transfer ability of MWCNTs, and a larger surface area for DNA immobilization through sidewall- and end-functionalized MWCNTs, further lowered the detection limit, to levels that are compatible with the demand of genetic testing [112].

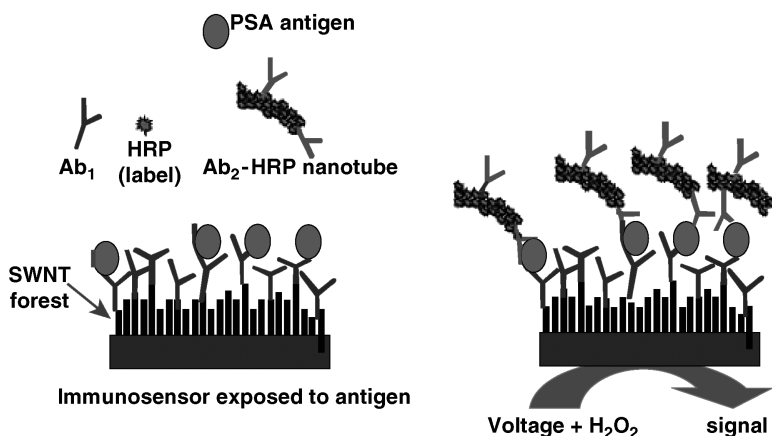


FIGURE 1.14 Surface construct of the SWCNT immunosensor that has been equilibrated with an antigen after binding with the antigen is shown in the left. While the right hand diagram depicted the immunosensor after treating with HRP CNT-Ab₂ to obtain amplification by providing numerous enzyme labels per binding event. HRP, horseradish peroxidase, Ab, antibody. (Reproduced in part from ref. 114. with permission. Copyright © 2006 American Chemical Society.)

For assaying using a redox-active-labeled system, the hybridization is transduced by a change in the magnitude of the label's electrochemical current after hybridization. The labels range from redox-active DNA-specific molecules (DNA groove binders or intercalators) to enzymes and metal nanoparticles. Enzyme labels hold great promise for the electrochemical detection of DNA hybridization, since their biocatalytic activity provides the amplification essential for monitoring at low target levels. Coupling the catalytic amplification of enzyme tags with additional amplification properties of CNTs is desirable to enhance the sensitivity of DNA bioassays. As an example, Wang et al. [113] demonstrated the strong accumulation of multiple alkaline phosphatase (ALP) onto CNT-modified electrodes. This allowed the transduction of target DNA at extremely low levels using chronopotentiometry to measure the products of the enzymatic reaction. In this case, CNTs play a role in amplification of the transduction process. An even more sensitive protocol for detecting DNA was also described recently based on coupling of several CNT-derived amplification processes. In this instance, the CNTs play a *dual* amplification role in both recognition and transduction events. The protocol involves a sandwich hybridization between magnetic beads and ALP-derived CNTs, followed by enzymatic amplification (addition of substrate) and finally, the chronopotentiometric stripping detection of the product at the CNT-modified electrode.

Recently, the combination of electrochemical immunosensors using SWCNT forest platforms with multilabel secondary antibody–nanotube bioconjugates for highly sensitive detection of a cancer biomarker in serum and tissue lysates has been described [114]. This is achieved through self-assembly of 20 to 30-nm-long terminally carboxylated SWCNT into nanoforests standing in upright bundles on Nafion/iron oxide-decorated conductive surfaces, followed by attachment of antibodies to SWCNT nanoforest platforms. This approach provided a detection limit of 100 aM for prostate-specific antigen in 10 μ L of undiluted calf serum and shows excellent promise for clinical screening of cancer biomarkers using biosensing technology.

α -Fetoprotein (AFP) is another tumor marker of interest. In healthy human serum, the average concentration of AFP is typically below 25 ng/mL, and an elevated AFP concentration in adult plasma may be an early indication of some cancerous diseases. Recently, a new immunosensor consisting of gold nanoparticles and Azure I–MWCNT composite membranes for the detection of AFP was reported (see Figure 1.15 for the assembly of the this AFP biosensor) [115]. The immunosensor is fabricated by coating Azure I on MWCNT-modified glassy carbon electrode, followed by adsorption of gold nanoparticles onto the Azure I–MWCNT surface by electrostatic interactions. Subsequently, AFP antibodies were assembled onto the surface of gold nanoparticles. Finally, horseradish peroxidase was employed to prevent nonspecific binding and to amplify the amperometric signal of the antigen–antibody reaction. This immunosensor showed high sensitivity with a low detection limit of 0.04 ng/mL, owing to the synergistic augmentation provided by Azure I and the MWCNTs in facilitating electron-transfer processes.

In addition to the cancer biomarkers, detection of glucose is one of the most frequently performed routine analyses in the medical field. High demand for such

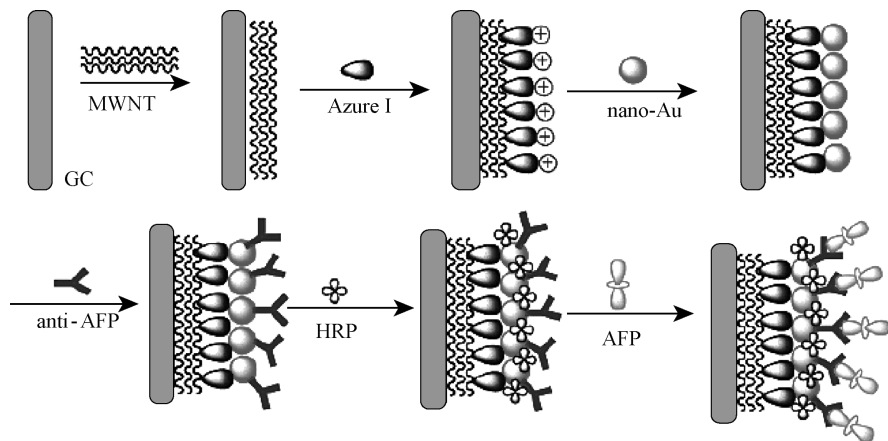


FIGURE 1.15 Fabrication of an AFP immunosensor. (From ref. 115. with permission. Copyright © 2007 American Chemical Society.)

detection in body fluids arises from the need to lower the mortality of a population diagnosed with diabetes. Glucose sensors normally incorporate glucose oxidase (GOx), which catalyzes the oxidation of glucose using oxygen as an electron acceptor. The hydrogen peroxide generated is then detected electrochemically at the electrode surface. A remarkable amount of innovative designs for CNT-based electrochemical glucose sensors are reported in the literature. Generally, there are three construction methodologies of CNT-based glucose biosensors: biocomposite casting, electropolymerization, and nanoparticle decorations.

A new glucose biosensor has been fabricated by immobilizing GOx into a sol-gel composite at the surface of a BPPG electrode modified with MWCNTs [116]. The CNT/sol-gel GOx biocomposite electrode gave a detection limit of 50 μM , a sensitivity of 196 nA/mM, and a response time of less than 5 s. Instead of sol-gel, Nafion had also been used as a GOx immobilization medium. In this case, the glucose biosensor is fabricated by casting a mixture of sonicated Nafion solution consisting GOx and MWCNTS onto a glassy carbon electrode. [117]. The CNT/GOx/Nafion glassy carbon electrode displayed a sensitivity of 330 nA/mM, a detection limit of 4 μM , and a response time of less than 3 seconds.

Immobilization of GOx into an electropolymerized matrix is an alternative method for the fabrication of CNT-based glucose sensors. Conducting polymers such as poly-*o*-aminophenol (POAP) [118] and polypyrrole (PPy) [101,119] are used in the construction of these glucose biosensors. The electropolymerization of the conducting polymers and immobilization of GOx is achieved using either performing cyclic voltammetry [118] or by holding the working electrode at a fixed potential for a fixed amount of time [119] in a mixture containing the polymers and GOx. The resulting conducting polymer/GOx/MWCNT biosensors lead to attractive, low-potential detection of the hydrogen peroxide liberated. The glucose biosensors fabricated

using this technique offer higher sensitivity than the casting method; for example, a sensitivity of 735 nA/mM is obtained using POAP as the conducting polymers in the construction of the glucose biosensor [118].

An even better sensitivity, up to 256 μ A/mM [120], can be achieved through the incorporation of metal nanoparticle into the CNT-based glucose biosensor, as the nanoparticles exhibit enhanced catalytic activity, good biocompatibility, and a large surface area. As an example, platinum nanoparticles with a diameter of 2 to 3 nm were prepared and used in combination with SWCNTs for the construction of electrochemical glucose biosensors, with remarkably improved sensitivity toward hydrogen peroxide [121]. The biosensor is constructed by drop-casting a solution containing SWCNT and Pt nanoparticles in Nafion on a glassy carbon electrode before further adsorption of GOx onto the SWCNT/Pt/Nafion-modified electrode. Nafion was used to solubilize the SWCNTs and it also displayed strong interactions with Pt nanoparticles to form a network that connected Pt nanoparticles to the electrode surface. A high sensitivity of 2.1 μ A/mM is obtained for this construct. An even higher sensitivity of 256 μ A/mM is reported when Cu nanoparticles (4 to 8 nm in diameter) were used [120].

In addition to glucose, dopamine is another molecule of clinical interest, as a deficiency of dopamine in the brain is believed to cause schizophrenia and Parkinson's disease. A modified carbon paste electrode is prepared by incorporating thionine–Nafion supported on MWCNT [122]. The thionine–Nafion/MWCNT carbon paste electrode possess an efficient electrocatalytic activity for the electrochemical oxidation of dopamine. As a result, this dopamine biosensor shows good sensitivity for submicromolar detection of dopamine and good selectivity in clinical and pharmaceutical preparations. Besides using thionine–Nafion, conducting polymers have also been employed as the biosensing element in CNT–modified electrodes. As an example, a polypyrrole–MWCNT nanocomposite film is used for the detection of dopamine via impedance measurements [123]. The composite film shows a notably larger affinity to dopamine in neutral phosphate buffer and gives a low limit of 1.7 nM with good selectivity and stability.

Recently, a new electrochemical method was reported for the selective determination of dopamine with laccase/MWCNT-based biosensors prepared by cross-linking laccase into a MWCNT layer confined on a glassy carbon electrode [124]. A combination of the chemical properties inherent in dopamine, coupled with the multifunctional catalytic properties of laccase and the excellent electrochemical properties of CNTs enables laccase/MWCNT-based biosensors to behave extremely well toward the selective determination of dopamine. A laccase/MWCNT-based biosensor is able to detect dopamine with the coexistence of physiological levels of interferents such as ascorbic acid and 3,4-dihydroxyphenylacetic acid [124].

1.5.2 Environmental Applications

Although commercial pressures drive the development of biosensors in the medical and pharmaceutical sectors, public concern for the environment has also stimulated

the application of biosensors to measure pollutants and other environmental hazards. CNTs are used to improve the operational characteristic of the biosensors, as they provide a larger surface area and offer good catalytic activity.

Organophosphorous insecticides constitute a very large class of chemical pesticides, and toxicity is associated primarily with the capacity of the chemical to inhibit acetylcholinesterase enzyme activity within nerve tissue. Recently, an enzyme-based biosensor using CNTs which is sensitive to several organophosphate pesticides has been developed [125]. This enzyme-based biosensor measures the hydrogen peroxide produced during the catalysis of acetylcholine by acetylcholinesterase–choline oxidase enzymes to detect organophosphorous compounds with high sensitivity, large linear range, and low detection limits. Such characteristics are attributed to the catalytic behavior of CNTs to promote the redox reaction.

One other attractive method to detect organophosphorous pesticides involves the use of enzyme organophosphorous hydrolase, which converts organophosphorous compounds into *p*-nitrophenol that can be oxidized at a CNT-modified electrode as demonstrated by Wang's group [126]. These CNT-modified electrodes gave a stable amperometric signal for *p*-nitrophenol over a duration of about 60 minutes and can detect paraoxon and parathion as low as 0.15 and 0.8 μM , respectively.

Besides organophosphorous compounds, CNT-modified electrodes have also been used to sense phenolic compounds. Phenolic compounds occur naturally in many vegetables and fruits. However, it is crucial to monitor the phenolic content in food samples and in the environment, as some of the phenols are toxic. A CNT/Nafion-modified glassy carbon electrode has been developed for the detection of phenol in solution. To increase the sensitivity of the phenolic biosensor, enzymes are incorporated into the CNT-modified electrode. One example is the adsorption of the enzyme tyrosinase onto a CNT-modified glassy carbon electrode [127]. Tyrosinase catalyzes the oxidation of phenolic compounds to quinones, which can be detected electrochemically at the electrode. Another example is a CNT paste electrode modified with polyphenoloxidase, which enables the sensing of various phenolic compounds, including phenol, catequine, and catechol in real pharmaceutical products [97].

REFERENCES

1. Iijima S. Helical microtubules of graphitic carbon. *Nature*. 1991;354(6348):56.
2. Iijima S, Ichihashi T. Single-shell carbon nanotubes of 1-nm diameter. *Nature*. 1993;363:603.
3. Oberlin A, Endo M. Filamentous growth of carbon through benzene decomposition. *J. Cryst. Growth*. 1976;32:335.
4. Wiles PG, Abrahamson J. Carbon fibre layers on arc electrodes: I. Their properties and cool-down behaviour. *Carbon*. 1978;16:341.
5. Abrahamson J, Wiles PG, Rhoades BL. Structure of carbon fibres on carbon arc anodes. *Carbon*. 1999;37:1873.
6. Monthieux M, Kuznetsov VL. Who should be given credit for the discovery of carbon nanotubes? *Carbon*. 2006;44:1621.

7. Jishi RA, Dresselhaus MS, Dresselhaus G. Symmetry properties of chiral carbon nanotubes. *Phys. Rev. B*. 1993;47:16671.
8. Strano MS, Dyke CA, Usrey ML, et al. Electronic structure control of single-walled carbon nanotube functionalization. *Science*. 2003;301:1519.
9. Li J, Stevens R, Delzeit L, et al. Electronic properties of multiwalled carbon nanotubes in an embedded vertical array. *Appl. Phys. Lett.* 2002;81:910.
10. Leonhardt A, Ritschel M, Bartsch K, Graff A, Taschner C, Fink J. Chemical vapour deposition: a promising method for production of different kinds of carbon nanotubes. *J. Phys. IV: Proc.* 2001;11:Pr3445.
11. Wang YY, Tang GY, Koeck FAM, Brown B, Garguilo JM, Nemanich RJ. Experimental studies of the formation process and morphologies of carbon nanotubes with bamboo mode structures. *Diamond Rel. Mater.* 2004;13:1287.
12. Lin M, Tang JPY, Boothroyd C, Loh KP, Tok ES, Foo Y-L. Dynamical observation of bamboo-like carbon nanotube growth. *Nano Lett.* 2007;7:2234.
13. Bourlon B, Miko C, Forró L, Glatli DC, Bachtold A. Determination of the intershell conductance in multiwalled carbon nanotubes. *Phys. Rev. Lett.* 2004;93:176806.
14. Britto PJ, Santhanam KSV, Ajayan PM. Carbon nanotube electrode for oxidation of dopamine. *Bioelectrochem. Bioenerg.* 1996;41:121.
15. ISI Web of Knowledge Citation Index.
16. Musameh M, Wang J, Merkoci A, Lin Y. Low-potential stable NADH detection at carbon-nanotube-modified glassy carbon electrodes. *Electrochem. Commun.* 2002;4:743.
17. Wang J, Musameh M. Electrochemical detection of trace insulin at carbon-nanotube-modified electrodes. *Anal. Chim. Acta.* 2004;511:33.
18. Ye JS, Wen Y, Zhang WD, Gan LM, Xu GQ, Sheu FS. Selective voltammetric detection of uric acid in the presence of ascorbic acid at well-aligned carbon nanotube electrode. *Electroanalysis.* 2003;15:1693.
19. Xu Z, Chen X, Qu X, Dong S. Electrocatalytic oxidation of catechol at multiwalled carbon nanotubes modified electrode. *Electroanalysis.* 2004;16:684.
20. Salimi A, Hallaj R, Khayatian G-R. Amperometric detection of morphine at preheated glassy carbon electrode modified with multiwall carbon nanotubes. *Electroanalysis.* 2005;17:873.
21. Wang SF, Xu Q. Square wave voltammetry determination of brucine at multiwall carbon nanotube-modified glassy carbon electrodes. *Anal. Lett.* 2005;38:657.
22. Wang JX, Li MX, Shi ZJ, Li NQ, Gu ZN. Direct electrochemistry of cytochrome *c* at a glassy carbon electrode modified with single-wall carbon nanotubes. *Anal. Chem.* 2002;74(9):1993.
23. Deo RP, Wang J. Electrochemical detection of carbohydrates at carbon-nanotube modified glassy-carbon electrodes. *Electrochem. Commun.* 2004;6:284.
24. Ye JS, Wen Y, Zhang WD, Gan LM, Xu GQ, Sheu FS. Nonenzymatic glucose detection using multi-walled carbon nanotube electrodes. *Electrochem. Commun.* 2004;6:66.
25. Wu FH, Zhao G-C, Wei X-W. Electrocatalytic oxidation of nitric oxide at multiwalled carbon nanotubes modified electrode. *Electrochem. Commun.* 2002;4:690.
26. Cai C-X, Chen J. Direct electrochemistry of horseradish peroxidase at a carbon nanotube electrode. *Huaxue Xuebao.* 2004;62(3):335.

27. Valentini F, Orlanducci S, Terranova ML, Amine A, Palleschi G. Carbon nanotubes as electrode materials for the assembling of new electrochemical biosensors. *Sens. Actuators B*. 2004;B100(1–2):117.
28. Banks CE, Compton RG. New electrodes for old: from carbon nanotubes to edge plane pyrolytic graphite. *Analyst*. 2006;131:15.
29. Banks CE, Davies TJ, Wildgoose GG, Compton RG. Electrocatalysis at graphite and carbon nanotube modified electrodes: edge-plane sites and tube ends are the reactive sites. *Chem. Commun*. 2005;7:829.
30. Banks CE, Moore RR, Davies TJ, Compton RG. Investigation of modified basal plane pyrolytic graphite electrodes: definitive evidence for the electrocatalytic properties of the ends of carbon nanotubes. *Chem. Commun*. 2004;16:1804.
31. Moore RR, Banks CE, Compton RG. Basal plane pyrolytic graphite modified electrodes: comparison of carbon nanotubes and graphite powder as electrocatalysts. *Anal. Chem*. 2004;76(10):2677.
32. McDermott MT, McCreery RL. Scanning tunneling microscopy of ordered graphite and glassy carbon surfaces: electronic control of quinone adsorption. *Langmuir*. 1994;10:4307.
33. Moore AW. *Chemistry and Physics of Carbon*, Vol. 11. Marcel Dekker, New York, 1973.
34. McCreery RL. Carbon electrodes: structural effects on electron transfer kinetics. In: Bard AJ, ed. *Electroanalytical Chemistry: A Series of Advances*, Vol. 17. Marcel Dekker, New York, 1991, p. 221.
35. Chang H, Bard AJ. Observation and characterization by scanning tunneling microscopy of structures generated by cleaving highly oriented pyrolytic graphite. *Langmuir*. 1991;7:1143.
36. Davies TJ, Banks CE, Compton RG. Voltammetry at spatially heterogeneous electrodes. *J. Solid State Electrochem*. 2005;9(12):797.
37. Davies TJ, Moore RR, Banks CE, Compton RG. The cyclic voltammetric response of electrochemically heterogeneous surfaces. *J. Electroanal. Chem*. 2004; 574(1):123.
38. Zach MP, Ng KH, Penner RM. Molybdenum nanowires by electrodeposition. *Science*. 2000;290:2120.
39. Zach MP, Inazu K, Ng KH, Hemminger JC, Penner RM. Synthesis of molybdenum nanowires with millimeter-scale lengths using electrochemical step edge decoration. *Chem. Mater*. 2002;14:3206.
40. Walter EC, Zach MP, Favier F, et al. Metal nanowire arrays by electrodeposition. *ChemPhysChem*. 2003;4:131.
41. Davies TJ, Hyde ME, Compton RG. Nanotrench arrays reveal insight into graphite electrochemistry. *Angew. Chem. Int. Ed*. 2005;44(32):5121.
42. Banks CE, Compton RG. Edge plane pyrolytic graphite electrodes in electroanalysis: an overview. *Anal. Sci*. 2005;21(11):1263.
43. Banks CE, Compton RG. New electrodes for old: from carbon nanotubes to edge plane pyrolytic graphite. *Analyst*. 2006;131(1):15.
44. Banks CE, Compton RG. Exploring the electrocatalytic sites of carbon nanotubes for NADH detection: an edge plane pyrolytic graphite electrode study. *Analyst*. 2005;130(9):1232.

45. Moore RR, Banks CE, Compton RG. Electrocatalytic detection of thiols using an edge plane pyrolytic graphite electrode. *Analyst*. 2004;129:755.
46. Jurkschat K, Wilkins SJ, Salter CJ, et al. Multiwalled carbon nanotubes with molybdenum dioxide nanoplungs: new chemical nanoarchitectures by electrochemical modification. *Small*. 2006;2(1):95.
47. Šljukić B, Banks CE, Compton RG. Iron oxide particles are the active sites for hydrogen peroxide sensing at multiwalled carbon nanotube modified electrodes. *Nano Lett*. 2006;6(7):1556.
48. Banks CE, Crossley A, Salter C, Wilkins SJ, Compton RG. Carbon nanotubes contain metal impurities which are responsible for the “electrocatalysis” seen at some nanotube-modified electrodes. *Angew. Chem. Int. Ed.* 2006;45(16):2533.
49. Jurkschat K, Ji X, Crossley A, Compton RG, Banks CE. Super-washing does not leave single walled carbon nanotubes iron-free. *Analyst*. 2007;132(1):21.
50. Dai X, Wildgoose GG, Compton RG. Apparent ‘electrocatalytic’ activity of multiwalled carbon nanotubes in the detection of the anaesthetic halothane: occluded copper nanoparticles. *Analyst*. 2006;131(8):901.
51. Lin Y, Taylor S, Li H, et al. Advances toward bioapplications of carbon nanotubes. *J. Mater. Chem.* 2004;14(4):527.
52. Wildgoose GG, Banks CE, Leventis HC, Compton RG. Chemically modified carbon nanotubes for use in electroanalysis. *Microchim. Acta.* 2006;152(3–4):187.
53. Gooding JJ. Nanostructuring electrodes with carbon nanotubes: a review on electrochemistry and applications for sensing. *Electrochim. Acta.* 2005;50(15):3049.
54. Gooding JJ. Toward the next generation of enzyme biosensors: communication with enzymes using carbon nanotubes. *Nanotechnol. Biol. Med.* 2007;21/1.
55. Li J, Koehne JE, Cassell AM, et al. Inlaid multi-walled carbon nanotube nanoelectrode arrays for electroanalysis. *Electroanalysis*. 2005;17(1):15.
56. Pumera M, Sanchez S, Ichinose I, Tang J. Electrochemical nanobiosensors. *Sens. Actuators B.* 2007;B123(2):1195.
57. Cui D. Advances and prospects on biomolecules functionalized carbon nanotubes. *J. Nanosci. Nanotechnol.* 2007;7(4–5):1298.
58. Kane RS, Stroock AD. Nanobiotechnology: protein–nanomaterial interactions. *Biotechnol. Prog.* 2007;23(2):316.
59. Guiseppi-Elie A, Shukla NK, Brahim S. Nanobiosensors: carbon nanotubes in bioelectrochemistry. *Nanotechnol. Biol. Med.* 2007;27/1.
60. Wildgoose GG, Banks CE, Compton RG. Metal nanoparticles and related materials supported on carbon nanotubes: methods and applications. *Small*. 2006;2(2):182.
61. Khabashesku VN, Pulikkathara MX. Chemical modification of carbon nanotubes. *Mendeleev Commun.* 2006(2):61.
62. Heald CGR, Wildgoose GG, Jiang L, Jones TGJ, Compton RG. Chemical derivatization of multiwalled carbon nanotubes using diazonium salts. *ChemPhysChem*. 2004;5 (11): 1794.
63. Jiang L, Jones TGJ, Compton R, et al. [Schlumberger Holdings Limited, Virgin I. (Brit.)] assignee. An electrochemical sensor for gas analysis in well bore. U.S. patents 20,04-2325,2,409,902, 20,040,108, 2005.

64. Masheter AT, Abiman P, Wildgoose GG, et al. Investigating the reactive sites and the anomalously large changes in surface pK_a values of chemically modified carbon nanotubes of different morphologies. *J. Mater. Chem.* 2007;17(25):2616.
65. Abiman P, Crossley A, Wildgoose GG, Jones JH, Compton RG. Investigating the thermodynamic causes behind the anomalously large shifts in pK_a values of benzoic acid-modified graphite and glassy carbon surfaces. *Langmuir.* 2007; 23(14):7847.
66. Wong ELS. Recent trends in DNA biosensing technologies. *Biophys. Rev. Lett.* 2007;2 (2):167.
67. Zhang Y, Iijima S. Elastic response of carbon nanotube bundles to visible light. *Phys. Rev. Lett.* 1999;82(17):3472.
68. Ajayan PM, Terrones M, de la Guardia A, et al. Nanotubes in a flash: ignition and reconstruction. *Science.* 2002;296(5568):705.
69. Li ZM, Tang ZK, Liu HJ, et al. Polarized absorption spectra of single-walled 4 angstrom carbon nanotubes aligned in channels of an AlPO 4-5 single crystal. *Phys. Rev. Lett.* 2001;8712(12).
70. Gooding JJ, Wibowo R, Liu JQ, et al. Protein electrochemistry using aligned carbon nanotube arrays. *J. Am. Chem. Soc.* 2003;125(30):9006.
71. Patolsky F, Weizmann Y, Willner I. Long-range electrical contacting of redox enzymes by SWCNT connectors. *Angew. Chem. Int. Ed.* 2004;43(16):2113.
72. Besteman K, Lee JO, Wiertz FGM, Heering HA, Dekker C. Enzyme-coated carbon nanotubes as single-molecule biosensors. *Nano Lett.* 2003;3(6):727.
73. Chen RJ, Zhang YG, Wang DW, Dai HJ. Noncovalent sidewall functionalization of single-walled carbon nanotubes for protein immobilization. *J. Am. Chem. Soc.* 2001;123(16):3838.
74. Guo ZJ, Sadler PJ, Tsang SC. Immobilization and visualization of DNA and proteins on carbon nanotubes. *Adv. Mater.* 1998;10(9):701.
75. Huang WJ, Taylor S, Fu KF, et al. Attaching proteins to carbon nanotubes via diimide-activated amidation. *Nano Lett.* 2002;2(4):311.
76. Erlanger BF, Chen BX, Zhu M, Brus L. Binding of an anti-fullerene IgG monoclonal antibody to single wall carbon nanotubes. *Nano Lett.* 2001;1(9):465.
77. Tsang SC, Guo ZJ, Chen YK, et al. Immobilization of platinated and iodinated oligonucleotides on carbon nanotubes. *Angew. Chem. Int. Ed.* 1997;36(20):2198.
78. Chen RJ, Choi HC, Bangsaruntip S, et al. An investigation of the mechanisms of electronic sensing of protein adsorption on carbon nanotube devices. *J. Am. Chem. Soc.* 2004;126(5):1563.
79. Smorodin T, Beierlein U, Ebbecke J, Wixforth A. Surface-acoustic-wave-enhanced alignment of thiolated carbon nanotubes on gold electrodes. *Small.* 2005;1(12):1188.
80. Barone PW, Baik S, Heller DA, Strano MS. Near-infrared optical sensors based on single-walled carbon nanotubes. *Nat. Mater.* 2005;4(1):86.
81. Hiura H, Ebbesen TW, Tanigaki K. Opening and purification of carbon nanotubes in high yields. *Adv. Mater.* 1995;7(3):275.
82. Tsang SC, Chen YK, Harris PJF, Green MLH. A simple chemical method of opening and filling carbon nanotubes. *Nature.* 1994;372(6502):159.

83. Tsang SC, Davis JJ, Green MLH, et al. Immobilization of small proteins in carbon nanotubes: high-resolution transmission electron-microscopy study and catalytic activity. *J. Chem. Soc. Chem. Commun.* 1995 (17) 1803.
84. Balavoine F, Schultz P, Richard C, Mallouh V, Ebbesen TW, Mioskowski C. Helical crystallization of proteins on carbon nanotubes: a first step towards the development of new biosensors. *Angew. Chem. Int. Ed.* 1999;38(13–14):1912.
85. Chen RJ, Bangsaruntip S, Drouvalakis KA, et al. Noncovalent functionalization of carbon nanotubes for highly specific electronic biosensors. *Proc. Natl. Acad. Sci. USA.* 2003;100(9):4984.
86. Jaegfeldt H, Kuwana T, Johansson G. Electrochemical stability of catechols with a pyrene side-chain strongly adsorbed on graphite-electrodes for catalytic-oxidation of dihydro-nicotinamide adenine-dinucleotide. *J. Am. Chem. Soc.* 1983;105(7):1805.
87. Munge B, Liu GD, Collins G, Wang J. Multiple enzyme layers on carbon nanotubes for electrochemical detection down to 80 DNA copies. *Anal. Chem.* 2005;77(14):4662.
88. Azamian BR, Davis JJ, Coleman KS, Bagshaw CB, Green MLH. Bioelectrochemical single-walled carbon nanotubes. *J. Am. Chem. Soc.* 2002;124(43):12664.
89. Zeng YL, Huang YF, Jiang JH, et al. Functionalization of multi-walled carbon nanotubes with poly(amidoamine) dendrimer for mediator-free glucose biosensor. *Electrochem. Commun.* 2007;9(1):185.
90. Wu KB, Sun YY, Hu SS. Development of an amperometric indole-3-acetic acid sensor based on carbon nanotubes film coated glassy carbon electrode. *Sens. Actuators B.* 2003;96(3):658.
91. Wang G, Xu JJ, Chen HY. Interfacing cytochrome *c* to electrodes with a DNA–carbon nanotube composite film. *Electrochem. Commun.* 2002;4(6):506.
92. Yamamoto K, Shi G, Zhou TS, et al. Study of carbon nanotubes: HRP modified electrode and its application for novel on-line biosensors. *Analyst.* 2003;128(3):249.
93. Guiseppi-Elie A, Lei CH, Baughman RH. Direct electron transfer of glucose oxidase on carbon nanotubes. *Nanotechnology.* 2002;13(5):559.
94. Harrison DJ, Turner RFB, Baltes HP. Characterization of perfluorosulfonic acid polymer coated enzyme electrodes and a miniaturized integrated potentiostat for glucose analysis in whole-blood. *Anal. Chem.* 1988;60(19):2002.
95. Turner RFB, Harrison DJ, Rajotte RV. Preliminary in vivo biocompatibility studies on perfluorosulfonic acid polymer membranes for biosensor applications. *Biomaterials.* 1991;12(4):361.
96. Wang J, Musameh M, Lin YH. Solubilization of carbon nanotubes by Nafion toward the preparation of amperometric biosensors. *J. Am. Chem. Soc.* 2003;125(9):2408.
97. Rubianes MD, Rivas GA. Enzymatic biosensors based on carbon nanotubes paste electrodes. *Electroanalysis.* 2005;17(1):73.
98. Valentini F, Amine A, Orlanducci S, Terranova ML, Pallechi G. Carbon nanotube purification: preparation and characterization of carbon nanotube paste electrodes. *Anal. Chem.* 2003;75(20):5413.
99. Wang J, Musameh M. Enzyme-dispersed carbon-nanotube electrodes: a needle micro-sensor for monitoring glucose. *Analyst.* 2003;128(11):1382.
100. Wang J, Liu GD, Merkoci A. Electrochemical coding technology for simultaneous detection of multiple DNA targets. *J. Am. Chem. Soc.* 2003;125(11):3214.

101. Gao M, Dai LM, Wallace GG. Biosensors based on aligned carbon nanotubes coated with inherently conducting polymers. *Electroanalysis*. 2003;15(13):1089.
102. Li J, Cassell A, Delzeit L, Han J, Meyyappan M. Novel three-dimensional electrodes: electrochemical properties of carbon nanotube ensembles. *J. Phys. Chem. B*. 2002;106 (36):9299.
103. Dai HJ. Carbon nanotubes: synthesis, integration, and properties. *Acc. Chem. Res*. 2002;35(12):1035.
104. Ren ZF, Huang ZP, Xu JW, et al. Synthesis of large arrays of well-aligned carbon nanotubes on glass. *Science*. 1998;282(5391):1105.
105. Sotiropoulou S, Chaniotakis NA. Carbon nanotube array-based biosensor. *Anal. Bioanal. Chem.* 2003;375(1):103.
106. Kerman K, Kobayashi M, Tamiya E. Recent trends in electrochemical DNA biosensor technology. *Meas. Sci. Technol.* 2004;15(2):R1.
107. Drummond TG, Hill MG, Barton JK. Electrochemical DNA sensors. *Nat. Biotechnol.* 2003;21(10):1192.
108. Wang J. Electrochemical nucleic acid biosensors. *Anal. Chim. Acta.* 2002;469(1):63.
109. Gooding JJ. Electrochemical DNA hybridization biosensors. *Electroanalysis*. 2002;14(17):1149.
110. Wang J, Kawde AN, Musameh M. Carbon-nanotube-modified glassy carbon electrodes for amplified label-free electrochemical detection of DNA hybridization. *Analyst*. 2003;128(7):912.
111. Pedano ML, Rivas GA. Adsorption and electrooxidation of nucleic acids at carbon nanotubes paste electrodes. *Electrochem. Commun.* 2004;6(1):10.
112. Kerman K, Morita Y, Takamura Y, Ozsoz M, Tamiya E. DNA-directed attachment of carbon nanotubes for enhanced label-free electrochemical detection of DNA hybridization. *Electroanalysis*. 2004;16(20):1667.
113. Wang J, Liu GD, Jan MR. Ultrasensitive electrical biosensing of proteins and DNA: carbon-nanotube derived amplification of the recognition and transduction events. *J. Am. Chem. Soc.* 2004;126(10):3010.
114. Yu X, Munge B, Patel V, et al. Carbon nanotube amplification strategies for highly sensitive immunodetection of cancer biomarkers. *J. Am. Chem. Soc.* 2006;128(34):11199.
115. Li N, Yuan R, Chai Y, Chen S, An H, Li W. New antibody immobilization strategy based on gold nanoparticles and Azure I/multi-walled carbon nanotube composite membranes for an amperometric enzyme immunosensor. *J. Phys. Chem. C*. 2007;111 (24):8443.
116. Salimi A, Compton RG, Hallaj R. Glucose biosensor prepared by glucose oxidase-encapsulated sol-gel and carbon-nanotube-modified basal plane pyrolytic graphite electrode. *Anal. Biochem.* 2004;333(1):49.
117. Tsai YC, Li SC, Chen JM. Cast thin film biosensor design based on a Nafion backbone, a multiwalled carbon nanotube conduit, and a glucose oxidase function. *Langmuir*. 2005;21(8):3653.
118. Ye JS, Wen Y, Zhang WD, Cui HF, Xu GQ, Sheu FS. Electrochemical biosensing platforms using phthalocyanine-functionalized carbon nanotube electrode. *Electroanalysis*. 2005;17(1):89.

119. Wang J, Musameh M. Carbon-nanotubes doped polypyrrole glucose biosensor. *Anal. Chim. Acta.* 2005;539(1–2):209.
120. Male KB, Hrapovic S, Liu YL, Wang DS, Luong JHT. Electrochemical detection of carbohydrates using copper nanoparticles and carbon nanotubes. *Anal. Chim. Acta.* 2004;516:35.
121. Hrapovic S, Liu YL, Male KB, Luong JHT. Electrochemical biosensing platform using platinum nanoparticles and carbon nanotubes. *Anal. Chem.* 2004;76:1083.
122. Shahrokhian S, Zare-Mehrjardi HR. Application of thionin–Nafion supported on multi-walled carbon nanotube for preparation of a modified electrode in simultaneous voltammetric detection of dopamine and ascorbic acid. *Electrochim. Acta.* 2007;52:6310.
123. Tu XM, Xie QJ, Jiang SY, Yao SZ. Electrochemical quartz crystal impedance study on the overoxidation of polypyrrole–carbon nanotubes composite film for amperometric detection of dopamine. *Biosens. Bioelectron.* 2007;22:2819.
124. Xiang L, Lin YQ, Yu P, Su L, Mao LQ. Laccase-catalyzed oxidation and intramolecular cyclization of dopamine: a new method for selective determination of dopamine with laccase/carbon nanotube-based electrochemical biosensors. *Electrochim. Acta* 2007;52:4144.
125. Lin YH, Lu F, Wang J. Disposable carbon nanotube modified screen-printed biosensor for amperometric detection of organophosphorus pesticides and nerve agents. *Electroanalysis.* 2004;16(1–2):145.
126. Deo RP, Wang J, Block I, et al. Determination of organophosphate pesticides at a carbon nanotube/organophosphorus hydrolase electrochemical biosensor. *Anal. Chim. Acta.* 2005;530(2):185.
127. Zhao Q, Guan LH, Gu ZN, Zhuang QK. Determination of phenolic compounds based on the tyrosinase-single walled carbon nanotubes sensor. *Electroanalysis.* 2005;17(1):85.

Isotropic Display of Biomolecules on CNT-Arrayed Nanostructures

MARK R. CONTARINO

School of Biomedical Engineering, Science and Health Systems, Drexel University, and Department of Biochemistry and Molecular Biology, Drexel University College of Medicine, Philadelphia, Pennsylvania

GARY WITHEY

Engineering Division, Brown University, Providence, Rhode Island

IRWIN CHAIKEN

Department of Biochemistry and Molecular Biology, Drexel University College of Medicine, Philadelphia, Pennsylvania

- 2.1 Introduction: CNT arrays for biosensing
- 2.2 Functionalization of CNTs: controlling display through covalent attachment
 - 2.2.1 Immobilization sites on CNT arrays
 - 2.2.2 Oriented immobilization of biomolecular probes
 - 2.2.3 Solvent accessibility
- 2.3 Self-assembling interfaces: anchor-probe approach
 - 2.3.1 DNA–RNA–PNA
 - 2.3.2 Biotin–streptavidin
 - 2.3.3 Antibody–antigen
 - 2.3.4 Recombinant affinity tags
- 2.4 Molecular wiring of redox enzymes
 - 2.4.1 Cofactor Reconstitution: apoenzymes
 - 2.4.2 Metallizing Peptides: chelating coiled coils
- 2.5 Multiplexing biomolecules on nanoscale CNT arrays
 - 2.5.1 Site addressability
 - 2.5.2 Pathways toward multiplexing using DNA
- 2.6 Conclusions

2.1 INTRODUCTION: CNT ARRAYS FOR BIOSENSING

Carbon nanotubes (CNTs) can form a conductive, semiconductive, or insulating nanoscale material [64]. Of these types, the metallic variety is best suited for conducting biologically derived signals in an electrochemical biosensor. Electrochemical biosensors are generally based on enzymatic catalysis of a substrate conversion that produces a flow of ions. These sensors are constructed of three electrodes: a reference electrode, an active electrode (the CNT array), and a sink electrode. Often, a counterelectrode is used as an ion source. The target analyte participates in the reaction that takes place on the active electrode surface, and the ions produced create a potential that is subtracted from the reference electrode to generate a signal. An array of metallic CNTs alone will not guarantee a successful electrochemical biosensor, as there are many other factors in play. In this chapter we focus on interfacing CNT array nanostructures with biomolecules at an active electrode surface to achieve maximum performance of amperometric biosensors.

Several design goals in building the ideal CNT array biosensor are represented schematically in Figure 2.1. Oriented immobilization schemes ensure that the isotropic display of biomolecules is in a functional state; maintenance of solvent accessibility allows immobilized biomolecules to interact with solution-based targets without steric hindrance from the CNT surfaces. Self-assembly and regeneration enables experimental repeats and automation on the same sensor surface, and multiplexing facilitates the detection of scalable target species on the same platform.

Impressive advances in the discovery and controlled growth of CNTs provide a major focus for device development in current nanotechnology. Since the discovery of CNTs [35], or perhaps the more applicable “rediscovery” of CNTs [54], many

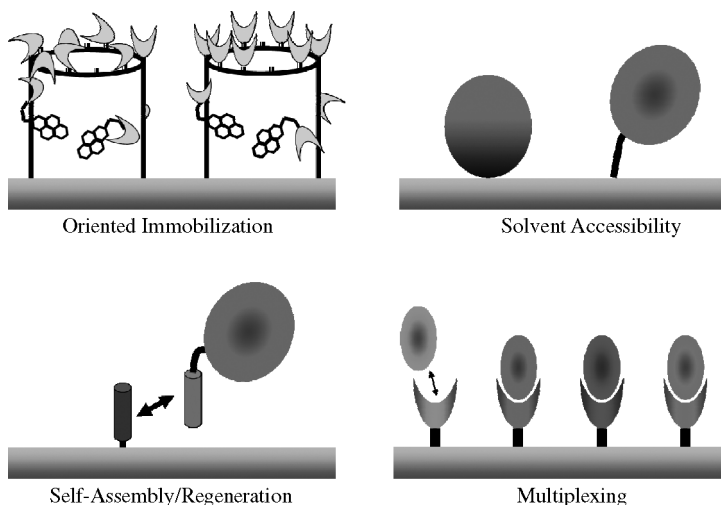


FIGURE 2.1 Guiding principles for nanoscale biosensors.

synthesis techniques have been devised that produce CNTs in bulk scale quantities, including arc discharge [20,36], laser ablation [79], and chemical vapor deposition (CVD) [49]. The controlled growth of CNTs into ordered compositions forms the basis for many array-based CNT biosensors, and a template-based form of CVD growth has been the leading synthesis technique.

Highly ordered arrays of vertically oriented CNTs are typically grown via thermal decomposition of carbon precursors onto seeded metallic nanoparticles within a nanoscale anodic aluminum oxide (AAO) template. The anodizing voltage used to create the pores in the AAO template forces the CNTs to grow in predefined geometries. AAO template nanotubes are characterized by a narrow size distribution, large-scale periodicity, and high densities, with diameters ranging from ten to hundreds of nanometers and lengths up to 100 μm .

Higher-ordered CNT arrays are also possible, including Y-junction CNTs within the nanopore array [48]. Meng et al. extended the capability of AAO template synthesis by creating controllable, hierarchical Y-junction CNTs and Ni nanowires via sequential reduction in anodizing voltage [53]. Similarly, Au Bouchon reported orthogonal multibranching growth via plasma-enhanced CVD and a self-seeding Ni catalyst [1]. Wei devised a scheme for multibranching through control of the gas flux and composition, avoiding templates or additives [86]. These advances have yet to flourish in CNT array biosensors, but the ability to create these branched CNT structures may provide opportunities for more advanced biosensor capabilities in the future.

Beyond the benefit of highly controlled geometrical arrays of metallic nanotubes, CNTs grown in AAO templates are also electrically insulated from each other [47,96]. This feature may ultimately enable high-density multiplexed CNT array biosensors using individual CNTs in parallel as a sensing platform. This is a particularly difficult challenge; the thermal noise limits sensitivity and necessitates that many individual nanotubes within the array be wired together via metallic deposition. These ordered CNT compositions provide an opportunity to form conductive arrays to detect biologically derived electronic signals with high sensitivity and specificity [37,74,91].

2.2 FUNCTIONALIZATION OF CNTs: CONTROLLING DISPLAY THROUGH COVALENT ATTACHMENT

The rapid progress in biomolecule-functionalized CNTs plays a central role in the interdisciplinary field of CNT-based nanobioelectronics and nanobiotechnology. To interface individual CNTs to soluble biologically significant targets, it is crucial that multifunctional molecular linkers be developed. For this reason, the attachment of biomolecules to CNTs has been a strong focus in biosensor technology [37]. The two potential biomolecule immobilization sites, the sidewalls and the tips of the CNT surfaces, are crucial to the function of nanotubes and biomolecules acting in concert. Biomolecules have a wider variety of attachment sites than CNTs, and knowing the basics can ensure successful CNT array interfacing in electrochemical biosensors.

2.2.1 Immobilization Sites on CNT Arrays

There are several means of attaching biomolecular recognition elements to the two distinct regions of a CNT, specifically the tips and the sidewalls. To date, it remains undetermined which of these two surfaces is more useful for biomolecule immobilization. In applications where physical access to the sidewalls is limited, such as densely packed arrays of CNTs, tip conjugation may be preferred. However, the high aspect ratio of CNTs presents a much larger surface for conjugation to the sidewalls relative to the tips, and therefore more area for biomolecule attachment. In other biosensors that have a single CNT spanning two electrodes, such as in a field-effect transistor, these CNT biosensors leave no option other than sidewall conjugation. Tasis et al. examined the covalent and noncovalent approaches for linking to functionalized and solubilized nanotubes, with particular emphasis on the change of inherent CNT properties upon modification [77]. However, solubilized nanotubes may not be truly representative of the field of nanosensors as a whole, since many applications use arrays of CNTs grown directly on the biosensor substrate.

2.2.1.1 Tip-Directed Attachments CNTs can be visualized as graphene sheets of carbon that are rolled to form a tube. Where the perfect rolled hexagonal lattice of carbon is interrupted, the dangling bonds can be oxidized to form a carboxylic acid ($-\text{COOH}$), which is a useful group for covalent modifications. Tsang et al. reported a simple method for using nitric acid to open nanotubes selectively at regions of high curvature (i.e., the tips) to increase the number of reactive carboxylic acids [82]. These carboxylic acids are more densely located at the tips of the CNT, but may also be present in the defects in the sidewalls, as depicted in Figure 2.2. Several oxidation methods are now reported, most often a 6 M $\text{NaSO}_4/2$ M HNO_3 acid mixture, often in combination with sonication to increase the rate of formation of tip and sidewall

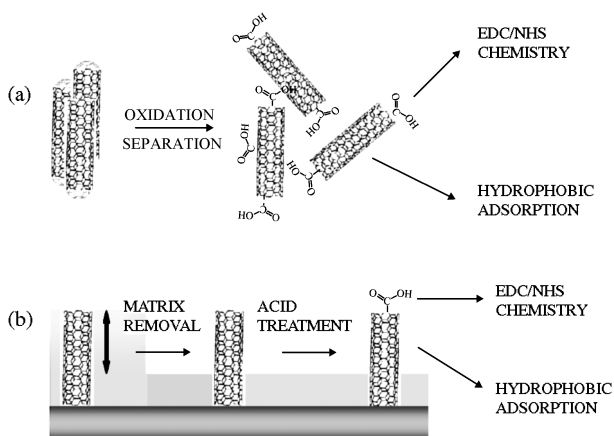


FIGURE 2.2 CNT configurations in (a) bulk and (b) template synthesis used in biosensing, and common routes for biomolecule immobilization.

carboxylic acids [93,94]. Nyugen et al. reported a simple method of air oxidation followed by a 12% HCl rinse to remove the metallic nanoparticles that are used to seed vertically aligned CNTs in CVD production [55]. Because many nanoparticles can transition between electronic states (e.g., $\text{Fe}^{2+} \leftrightarrow \text{Fe}^{3+}$), these metal structures tend to foul the specific electrochemical signatures of biomolecules. On the other hand, these same catalyst particles may actually be one factor responsible for the enhanced signals observed from CNT biosensors [71].

The most common reaction used to functionalize tips of CNTs with biomolecules is the zero-length heterobifunctional cross-linker 1-ethyl-3-(3-dimethylaminopropyl) carbodiimide hydrochloride (EDC). This forms a covalent peptide bond between carboxylic acids on the CNT tips and amines ($-\text{NH}_2$) that are present on many biomolecules. It is common practice to add *N*-hydroxysuccinimide ester (NHS) or its water-soluble analog sulfo-NHS to increase the efficiency of the linkage via stabilization of the reactive intermediate, as outlined in Figure 2.3. The resulting peptide bond is rather stable but is susceptible to hydrolytic cleavage in aqueous solutions over time. EDC/NHS can also be used to attach other heterobifunctional molecules with one amine and one additional reactive group to enable virtually any other chemical ligation route. For example, the heterobifunctional cross-linker 2-(2-pyridinyldithio) ethanamine hydrochloride (PDEA), featuring one amine and one pyridinyldithiol group, can be used to covalently bridge the carboxyl on the CNT tip and a thiol moiety on a biomolecule.

Beyond EDC/NHS covalent chemistries, a 1,3-dipolar cycloaddition of azo-methine ylides, generated between an α amino acid and an aldehyde, covalently functionalizes CNTs at 130°C [24,25]. This process cannot be used in conjunction with biomolecules that cannot withstand the thermal treatment. Aryldiazonium salts ($-\text{N}\equiv\text{N}$) can also functionalize CNTs in the presence of ionic liquids and K_2CO_3 in a mild chemical process [29]. Unfortunately, this methodology is not species selective and will target groups that are very common in biomolecules, including amines ($-\text{NH}_2$), alcohols ($-\text{OH}$), sulfhydryls ($-\text{SH}$), and aldehydes ($-\text{COH}$).

2.2.1.2 Sidewall-Directed Attachments The cylindrical sidewalls of the CNTs are very hydrophobic and can be modified through the adsorption of any nonpolar species. A wealth of research has been published on the sidewall functionalization of CNTs in an attempt to increase their aqueous solubility, which is important for biomolecule immobilization procedures. A good candidate for sidewall functionalization is the molecule 1-pyrenebutanoic acid, succinimidyl ester (P-130). This heterobifunctional molecule effectively adsorbs irreversibly to the hexagonal lattice via a pyrene moiety, forming a π -stacking interaction of the sp_2 orbitals between the curved hexagonal lattice of the CNT sidewalls and the pyrene group. The other end of P-130 presents a reactive succinimidyl ester for further functionalization to amine-containing biomolecules similar to the EDC/NHS tip-conjugation method. Through hydrophobic interaction with the sidewall, P-130 linkage avoids the alteration of CNT conductive properties that is unavoidable in tip-directed methods that involve strong acid treatments [10]. Acid exposure to create reactive tip functionalities will introduce greater interruptions

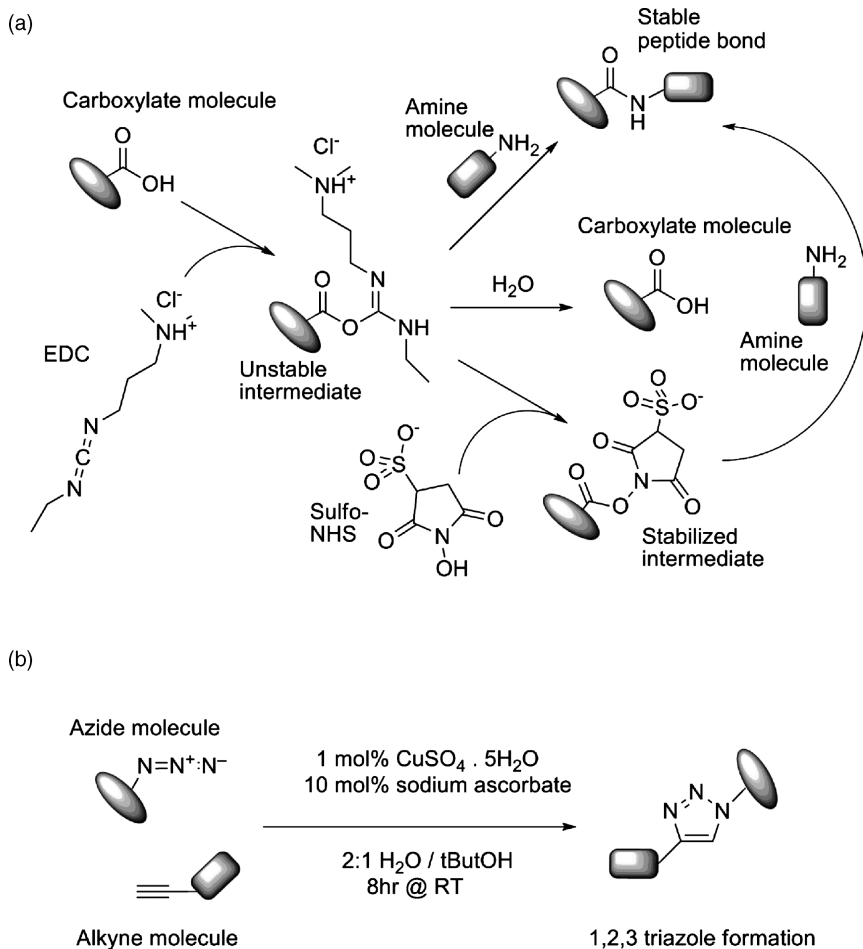


FIGURE 2.3 Covalent chemistries for cross-linking biomolecules with sensor substrates: (a) EDC/NHS reaction for linking amines to carboxyls; (b) click reaction for linking azides to alkynes via a copper-catalyzed 1,3-dipolar cycloaddition.

within the crystalline nanotube sidewalls and reduce charge transfer through the nanostructure.

Another useful reaction, the gold standard of “click” chemistry, is a copper catalyzed Huisgen 1,3-dipolar cycloaddition between azides and alkynes. Using a hydrophobic interaction between the sidewalls and a benzene ring, an adsorbed cross-linker is able to display a reactive alkyne for subsequent ligation with azide-modified polystyrene via a 1,2,3-triazole to the sidewalls of CNTs [46]. The rate of electron transfer through triazole linkages has been studied and can achieve rates greater than 60,000 per second in certain assemblies [19]. This approach may therefore provide a functional organic bridge for electron flow into CNTs. Furthermore, the

copper-catalyzed reaction can be carried out at room temperature, enabling covalent, species-selective linkages between biomolecules and the CNT array.

2.2.2 Oriented Immobilization of Biomolecular Probes

At the nanoscale, every molecule counts. In order to have accurate nanoscale biosensors, the biological element must remain in an active functional state. An overarching goal of biosensor design is the orientation of biological elements by immobilization through a single location, not the stochastic ensemble that is often the case. The most direct path to achieving uniform orientation of biological elements is through covalent-bond formation. However, direct covalent immobilization of biomolecules may result in a decrease or total loss of target recognition in some cases, manifesting itself in high variability between nanoscale biosensors.

CNTs have just two chemically distinguishable regions for attachment, but biomolecules are not that simplistic. When interfacing biomolecules with inorganic biosensor elements such as CNTs, knowledge of potential attachment sites on those biomolecules is a must. Nucleic acids, synthetic analogs, peptides, and proteins represent a diverse library of biosensor recognition elements, and the tools to functionalize CNTs with these molecules are of crucial importance. The following sections will serve as a guide for biomolecule attachments, potential chemical routes, and limitations but is by no means exhaustive. For a more detailed reference, the author highly recommends Hermanson's *Bioconjugate Techniques*.

2.2.2.1 Nucleic Acids EDC/NHS chemistries can be applied to orient DNA/RNA recognition elements, as they can readily be modified to feature a single reactive group in their sequence that does not interfere with their complementary DNA/RNA targets. Commercial synthesis is a mature technology, and common end modifications include amines and thiols ($-SH$) that are not naturally present in DNA/RNA. A variety of commercially available cross-linkers (e. g., Pierce Biotechnologies) can be used to attach CNTs covalently to these modified nucleic acids with different spacer lengths. Biotinylation (see Section 2.3.2) of nucleic acids is also a commercially available option, or alternatively, is readily achieved with a variety of cross-linkers. As a rule of thumb, the acceptable range of DNA/RNA lengths for a stable and specific interaction between stands is roughly 20 to 25 base pairings. Shorter strands may not possess the desired interaction strength, while longer strands may favor other assemblies than 1 : 1 complementary pairing, especially in RNA.

DNA has also been shown to coil helically around the sidewalls of CNTs without chemical modification. This sequence-dependent coiling of double-stranded DNA around CNTs serves to facilitate their geometrical separation by anion-exchange chromatography [97] and size-exclusion chromatography [33]. These techniques are applied to sort nanotubes into distinct, application-specific populations by homogenizing their electronic properties within complex populations. Array-based biosensors may borrow this trait and tailor DNA sequences to contain a specific region to coil around the sidewalls of CNTs while still presenting a complementary sequence to capture the desired nucleic acid target.

2.2.2.2 Peptides Peptides are made from a combination of the 20 amino acids, and sometimes nonnative amino acids, and this complexity can provide more functionality than that of their nucleic acid counterparts. Peptides also have some control over their moieties for covalent immobilization, although less than that of DNA/RNA. At each end of the amino acid chain there is a single amine and a single carboxyl at the N-terminus and C-terminus, respectively. Potentially reactive moieties also exist in the side chains of several amino acids (amino acid–reactive moiety): lysine–amine, aspartic acid–carboxyl, and glutamic acid–carboxyl. To limit the attachment site to a single moiety, terminal cysteines may be introduced to provide a reactive thiol group for further covalent linkage via a maleimide, iodoacetyl, or pyridyldithiol group. The cysteine’s thiol group can also covalently bind noble metal surfaces such as gold nanoparticles [11]. Cysteines may not always be the best option; cyclized peptides can require disulfides for proper function, and these peptides would be unable to attach covalently through thiols.

Peptides may also link selectively through hydrophobic interaction with CNT nanostructures. Wang et al. used phage display to discover peptides rich in histidine and tryptophan residues and having a selective affinity for CNTs by favoring a central hydrophobic sequence with short hydrophilic termini [84]. This noncovalent means may serve as a short consensus sequence that could assemble longer peptides and recombinant proteins to CNT sidewalls.

2.2.2.3 Peptide Nucleic Acids Another possibility is the use of peptide nucleic acids (PNAs), which are similar to DNA with the same A–T,G–C base pairings, but replace the polyphosphate sugar backbone with a poly-N-(2-aminoethyl)glycine backbone linked together by peptide bonds [5,56]. PNA has two main advantages over DNA. Since it is a nonnative molecule, it is not recognized by enzymes that cleave DNA/RNA or proteins/peptides. In addition, PNA has a stronger DNA-binding capacity, due to the elimination of electrostatic repulsion between the negatively charged phosphate backbones of each strand. Thus, shorter PNA sequences can be used in complex environments to achieve the same interaction strength of longer DNA/RNA sequences. Like proteins, PNA contains a single amine at the N-terminus and a single carboxylic acid at the C-terminus, but these moieties are found nowhere else in its sequence. EDC/NHS chemistries will orient PNA on CNT array biosensors through the N-terminus [70,87] provided that the hydrophobic sidewalls of CNTs do not interact with the PNA, as has been reported with DNA [97] and peptides [84].

2.2.2.4 Proteins Proteins represent more challenging opportunities as recognition elements in CNT biosensors. They have a defined recognition area determined by the complex arrangement of their lengthy ($n > 100$) amino acid sequence. Hydrophobic adsorption to the sidewalls can diminish activity or even render the protein ineffective, specifically for biosensor applications [91]. The standard EDC/NHS chemistry is by far the most commonly employed means and will attach proteins covalently through any exposed lysine residue. Unfortunately, since lysine is a charged residue, it is often present in abundant quantities on the solvent-exposed surface of proteins. As in hydrophobic adsorption, the result is a randomly oriented recognition

element that may decrease or even completely abolish its native recognition capacity at the single molecule level.

Covalent immobilization through nonabundant residues, such as the thiol moiety on the side chain of the amino acid cysteine, can be achieved readily via maleimide, iodoacetyl, or pyridyldithiol chemistries. Although cysteine residues present a single reactive thiol group and their overall content is low, these residues are often critical for protein function and are rarely exposed to the solvent. Their innate ability to form disulfides helps to stabilize the structure of proteins and their potential complexes with other proteins. Formation of disulfides from two free thiols between proteins can also activate cellular machinery [30]. In this way, covalent attachment through these thiols may reduce downstream function in more complex biosensors. Regardless of these limitations, many proteins can have their disulfides reduced to active thiols with the addition of a reduction agent such as DTT, BME, or TCEP and be covalently attached by this means. It is important to note that with the exception of TCEP in conjunction with maleimide reactions, the reduction agent must be removed from the reaction mixture prior to covalent bond formation.

2.2.2.5 Recombinant Engineering of Specific Protein Functionalities

Recent progress in single molecule atomic force microscopy has led to the increased use of mutants with cysteines expressed at the N- or C-termini, facilitating an oriented thiol linkage of molecular-engineered proteins. For example, a de novo designed 4- α -helix bundle carboprotein has been engineered recombinantly to contain a terminal sequence of multiple cysteines that can be used to link them covalently to sensor surfaces [3]. Redox enzymes can also employ a multithiol linkage strategy to orient themselves on sensor surfaces [28].

Aside from the inclusion of additional cysteines, one alternative is to incorporate a nonnatural amino acid that displays a single chemically reactive species, such as an azide or an alkyne, via auxotrophic expression. This technique takes a genetically modified cell that cannot produce a particular DNA-encoded amino acid (e.g., methionine), and the cellular machinery replaces it with an alternative, noncanonical amino acid in the peptide chain. Upon auxotrophic protein expression, methionines coded in the sequences are replaced by homoazidoalanine or an amino acid featuring an alkyne on its side chain, as seen in Figure 2.4. These moieties are readily “clicked” to form specific and stable triazole linkages. Using auxotroph bacteria, Kiick et al. pioneered such azide incorporation into engineered sites within recombinant proteins that were capable of the click reaction [41]. Link et al. improved this process using extremely pure CuBr as the catalysis for copper-catalyzed triazole formation on bacterial cell surface glycoproteins [50].

2.2.3 Solvent Accessibility

Oriented covalent immobilization may not be the only requirement for functional display of biomolecules on CNT arrays. As an example, many redox enzymes require substrates to bind to a definitive site on the enzyme for substrate conversion and electronic signal acquisition. If the attachment site on the biomolecule is near or within

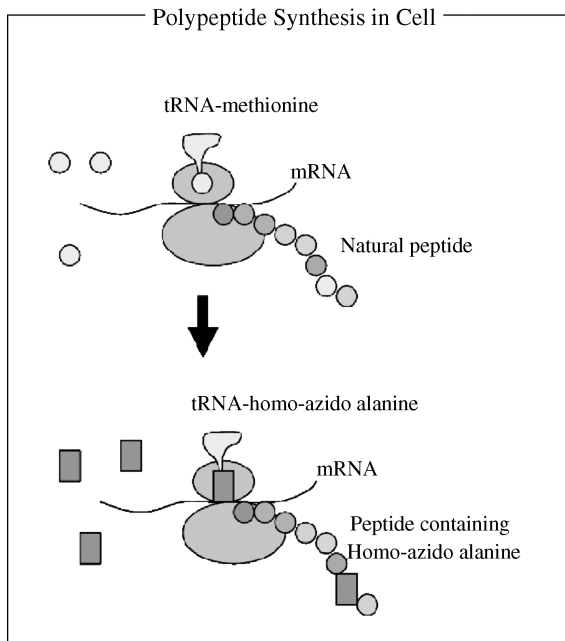


FIGURE 2.4 Autotrophic expression of the nonnative amino acid homoazido alanine. The tRNA that would typically insert a methionine now inserts a homoazido alanine in order to display an azide functionality within the sequence of the recombinantly produced protein or peptide.

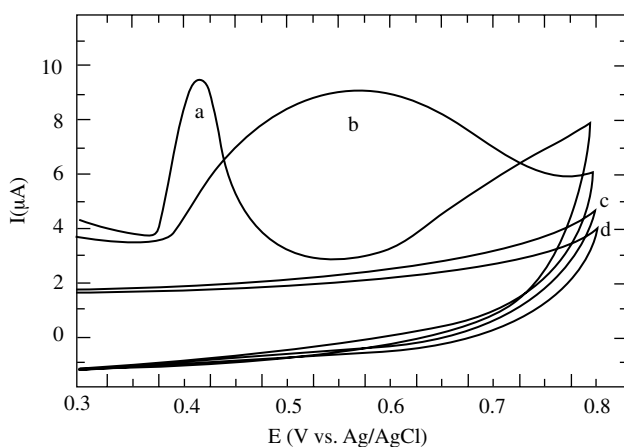


FIGURE 2.5 Cyclic voltammetry of two redox protein–CNT electrode conjugates in the presence of 50 mM glucose. The redox protein linked to the tips (a) produces a very defined peak around the expected redox potential (0.42 V vs. Ag/AgCl), while the sidewall-adsorbed protein (b) produces a broader peak at a slightly higher potential (0.58 V vs. Ag/AgCl). A control electrode (c) was capped and coated with surfactant to block protein attachment and has no distinguishable peak. On a second control electrode (d), no redox protein is added. (From ref. 91, with permission.)

this crucial catalytic site, the substrate may not be converted because it cannot access this region freely. The result of this blockage at the protein's active site is a reduction or complete loss of bioelectrocatalytic signal, which in turn would lead to decreased performance and greater variability between biosensors.

For instance, when the redox protein glucose oxidase was attached to either the tips or the sidewalls on a CNT array biosensor, dramatically different redox events were observed with cyclic voltammetry experimentation, as seen in Figure 2.5. The tip-directed scheme has a much narrower redox peak, whereas the sidewall scheme has significant broadening in its corresponding peak. This result may be partially explained by the fact that the tip immobilization scheme allows for a more uniform substrate access to the enzyme's binding site, whereas the sidewall immobilization did not allow for such uniform substrate access in solvent [91].

2.3 SELF-ASSEMBLING INTERFACES: ANCHOR-PROBE APPROACH

Beyond the need to control the isotropic display of biological recognition elements lies the capability to reuse the sensor in an automated fashion. A disposable sensor most will probably not require regeneration, but most CNT biosensors have not yet reached this level of cost efficiency. Complete sensor regeneration also allows for repeat experiments on the same sensor as well as computer automation for varied experimental conditions.

Biological recognition is a reversible, noncovalent process that can be defined mathematically in terms of affinity for one molecule to interact with another. Driven by intermolecular forces (electrostatic, van der Waals, hydrogen bonding) in a solvent, affinity is a function of the rate at which molecules associate and subsequently dissociate from their complexation. Use of capture interfaces for biosensors would ideally feature a fast association rate and a slow dissociation rate, ensuring efficient capture with minimal target leaching. The target species should remain in place until its desired time of release.

Regeneration of the sensor surface is not without limitations. The immobilized capture interface may not completely withstand the regeneration conditions. That is, there may be a decrease in activity for the capture interface over time. Incomplete regeneration, on the other hand, leads to "memory effects"; a small amount of material remains captured on the biosensor, decreasing the total signal to a given amount of target substrate. Furthermore, nonspecific accumulation of material on the CNT and capture interface may reduce the response to a given target over multiple cycles.

One approach to incorporating self assembling interfaces on CNT array biosensors can be described as an anchor-probe self-assembly scheme. In this scheme, the anchor is covalently linked via isotropic display to a specific region of the CNT surface. The probe component is able to noncovalently recognize the anchor component and bind with high affinity and selectivity. Through this means, sensor surfaces can be constructed, deconstructed, and reconstructed for multiple experimental cycles as envisioned in Figure 2.6.

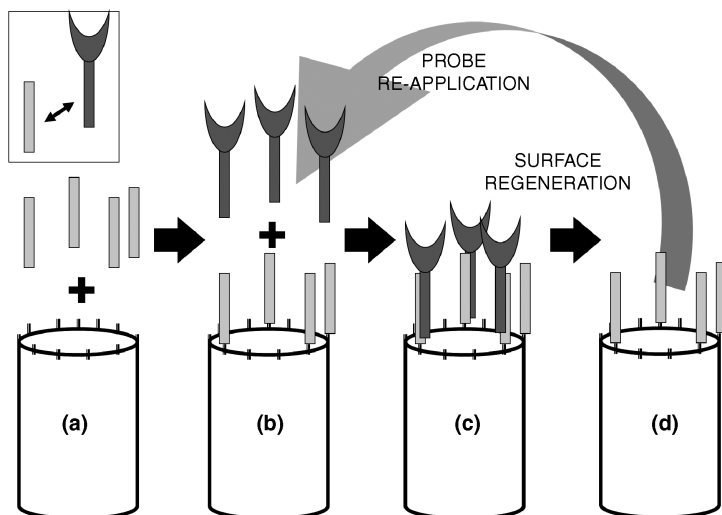


FIGURE 2.6 Self-assembly and regeneration of a CNT sensor surface using an anchor-probe strategy. (a) Oriented covalent attachment of the anchor (light gray) to the CNT tips enables a recognition surface for the probe (dark gray). (b) Upon addition of the probe in solution, self-assembly is able to display the target molecule isotropically through the capture component. (c) The biological component is free to access the solvent and its native target. Upon addition of a regeneration solution that disrupts biological assembly, the capture probe is washed from the surface (d) and can be reapplied for further experimentation.

2.3.1 DNA–RNA–PNA

DNA and RNA provide the ideal candidates for biomolecule capture and display on CNT interfaces. Simply by raising the temperature, complete dissociation of nucleic acid strands can be achieved. The specific temperature is dependent on the A–T, C–G pairings and can be calculated by the length of the oligo-DNA or oligo-RNA pairings:

$$\begin{aligned} \text{For } < 20 \text{ nucleotide : } & T_m = 2l_n \\ \text{For } 20\text{--}35 \text{ nucleotides : } & T_m = 1.46l_n \end{aligned}$$

Where T_m is the melting temperature and l_n is the effective length of primer = $2 \times (\text{no. of G} + \text{C}) + (\text{no. of A} + \text{T})$. Disruption of the hydrogen bonding with chaotropic agents such as concentrated urea or guanidine hydrochloride may provide an alternative means to weaken or even dissociate the complementary strands on a biosensor surface if high temperatures are to be avoided. For example, for each 1% formamide, T_m is reduced by about 0.6°C , while the presence of 6 M urea reduces T_m by about 30°C .

2.3.2 Biotin–Streptavidin

What if there were a way to have a strong interaction between two molecules that would serve as a generic capture moiety? Nature has already provided us with these

tools. Perhaps the most commonly employed biological recognition pairing is that of the small protein streptavidin and the small molecule biotin (also known as vitamin H). This interaction is virtually irreversible, possessing an extraordinarily high affinity, $K_D \sim 10^{-15}$. Unfortunately, this strong interaction makes biotin–streptavidin separation difficult and hinders the ability to regenerate the biosensor surface. Mutations of the streptavidin protein have brought about marked advances, decreasing the stoichiometry (the number of binding sites) to biotin from four to one, and decreasing the affinity to its biotin target for complete regeneration capabilities.

2.3.3 Antibody–Antigen

Researchers have borrowed from the immune system and its capability to produce antibodies that can be directed to bind to virtually every biological target (antigens). Biosensors commonly employ the high affinity of antibodies toward their antigen as a biological recognition element. The IgG form is the most commonly used antibody and is found in two flavors, polyclonal and monoclonal. A *polyclonal antibody* is produced by the injection of antigen into live animals and purification from blood or serum. These antibodies can bind a specific antigen in multiple locations and result in randomly oriented capture. *Monoclonal antibodies*, produced in cellular factories, are directed to interact with a single distinct location, or epitope, of a target. Thus, monoclonal antibodies are useful for oriented capture and target display of proteins in biosensors, attributing the same affinity to a single target. The regeneration of antibody–antigen interactions is readily achieved with a combination of high–salt and low–pH solutions. However, these biomolecules are rather large (ca. 150 kDa) and have variable affinity between antibody–antigen pairings, resulting in different regeneration conditions. This has not stopped multiplexed biosensors from using antibody arrays [17,44]; their specificity toward any desired target is unmatched.

2.3.4 Recombinant Affinity Tags

There have been many advances in protein chemistry for the production and purification of proteins in sufficient quantity and purity for bioanalysis. Tailoring the purification method to isolate a single protein species by its individual biophysical characteristics is extremely time consuming; thus, simplified conditions were created for ease of purification via affinity tags. These genetically expressed affinity tags employ specialized amino acid sequences in either peptide (short) or protein (long) form, which can reversibly capture or release expressed targets under standardized buffer conditions. This technology was driven largely by the requirements of structural biology, as milligrams of protein are often required to determine native structure by crystallographic analysis. Biosensors now borrow this ever-expanding technology to undergo multiple experimental cycles by regenerating a sensor surface, bringing automation to sensor technology through the use of self-assembling interfaces.

Table 2.1 depicts the most commonly used recombinant-expressed affinity tags. They vary in size, sequence, noncovalent recognition elements, and affinities. Since

TABLE 2.1 Commonly Employed Affinity Tags and Relevant Characteristics That Can Be Used to Self-Assemble Biological Elements, Including Recombinantly Produced Redox Enzymes, to CNT Array Amperometric Biosensors

Name	Recombinant Probe			Anchor ^d			Refs.
	Molecular Mass (Da)	Recognition Element	Number of Sites	Affinity	Regeneration		
Biotin	244	Streptavidin	4	10 ⁻¹⁵	Excess Biotin	27	
Polyhistidine, (His) _x	841	Ni/Co-NTA	1	—	Excess imidazole	61	
FLAG (DYKDDDDK)	1,013	Antibody	2	10 ⁻⁸	Low pH	68	
HA (YPYDVPDYA)	1,102	Antibody	2	10 ⁻⁷	EDTA	4,31,32,42,62	
c-myc (EQKLISEEDL)	1,203	Antibody	2	10 ⁻⁸	Low pH	58	
V5 (GKPIPNLLGLDST)	1,422	Antibody	2	10 ⁻⁹	Low pH	22	
S-tag (KETAAAKFERQHMDS)	1,749	S-protein	—	—	Low pH	39	
StrepTagII (WHPQFEK)	1,058	Streptavidin	4	10 ⁻⁵	—	78	
		Streptactin	—	10 ⁻⁶	—	65	
		Streptavidin	—	10 ⁻⁹	—	45	
		Streptavidin	—	10 ⁻⁸	—	45	
Nanotag 9 (DVEAWELGAR)	1,145	Antibody	2	—	—	—	
Nanotag 15 (VEAWELGARVPLVET)	1,784	Ca ²⁺ -calmodulin	1	10 ⁻⁹	EDTA	75	
T7-tag (MASMTGGQQMG)	1,098	Streptavidin	4	10 ⁻⁹	50 mM NaOH	38	
CBP (calmodulin-binding peptide)	4,300	R/K-rich peptide	1	10 ⁻⁵ to 10 ⁻¹¹	5 M GndHCl, 0.05% SDS	81	
SBPtag (streptavidin-binding protein tag)	2,300–5,400	Streptavidin	4	10 ⁻¹⁵	8 M GndHCl, 1% SDS	9,13,38	
Coiled coil (E-rich peptide)		<i>lac</i> operator	—	—	—	80	
BCCP (biotin carboxy carrier peptide)	8,600	Phenylarsine oxide	1	—	—	78	
Ubiquitin	11,700	Reduced glutathione	1	—	—	72	
Thioredoxin	26,000	Amylose	1	—	Excess maltose	40	
GST (glutathione-S-transferase)	42,000	Antibody	5	—	Low pH	57	
MBP (maltose-binding protein)	45,000	Albumin	2	—	Low pH	2	
Protein A (antibody-binding protein)	45,000						
Protein G (antibody-binding protein)	22,000						

^dThis component is linked covalently to the surface of the sensor and can self-assemble the probe component.

the affinity tag is genetically encoded within the protein, the protein is always captured via the same location, usually at the beginning (N-terminus) or end of the sequence (C-terminus), although some tags can be expressed internally. This eliminates the inherent variability of covalent protein immobilization through surface residues while allowing uniform access to other molecules. The smaller tags are generally preferred for protein purification, as they do not interfere with native protein function. However, larger affinity tags may offer unique capabilities beyond simply purification and uniform access. Larger tags afford a spacer between the noncovalent recognition site attached to the protein and that attached to the biosensor, resulting in enhanced solvent access and increased protein solubility. The downside of the largest tags is that for amperometric applications, the gap between the redox enzyme and the electrode may hinder efficient electronic communication.

2.4 MOLECULAR WIRING OF REDOX ENZYMES

The use of specific proteins called *redox enzymes* as the source of electronic signals in response to a specific ligand or other physiological signal is fundamental for amperometric biosensors [83]. Contact with sensor surfaces may alter or even destroy native protein conformations, significantly altering redox capabilities. Nanoscale surfaces such as nanoparticles and CNTs may limit these detrimental effects because of (1) regions of high curvature that energetically limit biomolecule adsorption, and (2) reduced steric hindrance of the substrate to its binding site on the enzyme.

Covalently functionalizing redox enzymes with a conductive spacer to span electrode surfaces with the use of interdigitated redox mediators such as ferrocene has been shown to increase amperometric signals [66]. Unfortunately, this heterogeneous contact of the enzyme at random orientations with respect to the active site can result in decreased rates of electron transfer [25,92,95]. Thus, the conductive spacers used to link enzymes to the sensor substrates in amperometric biosensors should be linked in an isotropically controlled manner. Two pathways toward achieving isotropic enzyme display on carbon nanotubes are discussed: reconstitution of enzymes around tethered cofactors, and metallized peptide wiring of enzymes.

2.4.1 Cofactor Reconstitution: Apoenzymes

Beyond the preservation of active conformation upon immobilization, another challenge in using redox enzymes in biosensing is channeling the electron transfer to the electrode. These electroactive molecules lack efficient pathways for the transport of electrons from their embedded redox sites to an electrode. Enzymes that are redox active typically incorporate organic molecules called *cofactors* near the active site of the enzyme. These act as electron transporters in the catalytic reduction and oxidation of biologically relevant targets in amperometric biosensors. Enzymes stripped of these cofactors (*apoenzymes*) can be reconstituted directly onto cofactor-functionalized gold nanoparticles, molecular wires, and carbon nanotubes [88,89,92]. Employing this strategy essentially plugs the electrode into the enzyme, facilitating

electrical communication between the redox proteins and the electrodes. This self-assembly methodology is an important development in the progress of amperometric biosensors that can produce electron transfer rates that exceed the rates at which the enzyme converts its substrate under native *in vivo* conditions.

2.4.2 Metallizing Peptides: Chelating Coiled Coils

The coiled-coil motif represents a well-characterized, simple, ubiquitous conformational scaffold in proteins, involving two or more supercoiled α -helices. In living organisms, coiled coils drive molecular recognition and downstream function in diverse biological systems. This motif is commonly found in cytoskeletal architecture and function [12,34,73], cellular transport and secretion [18], DNA-binding proteins [21,59,63], and viral and bacteriological membrane fusion elements [6,7,16,51].

Coiled-coil peptide dimers commonly consist of repeat sequences of seven residues, denoted as $(a b c d e f g)_n$. By changing the number of heptad repeats, the size of the interface and the strength of interaction can be controlled [14]. At positions a and d are hydrophobic residues that are central to the interface between the helices. Positions e and g are typically charged and form electrostatic interactions between coils, providing specificity between helical subunits and helping to stabilize the tertiary structure. The remaining residues (b , c and f) are more exposed to solvent and variable, and thus can be engineered for specific tasks, such as controlling solubility and/or conductance. For example, histidine residues located in the b and f (i and $i + 4$) positions chelate divalent metal ions, effectively creating a metallopeptide [11,23,43,95]. The coiled-coil interaction is stable and enables repeated cycles of dissociation and reassembly, a characteristic that supports their impact in automated, repetitive assays in optical biosensor platforms [8,11,14,15,69].

Coiled coils that have been metallized with multiple cobalt groups perform as conductive wires when linked to a redox enzyme [95], as shown in Figure 2.7. Pertaining to CNTs, coiled coils have been used to reversibly self-assemble gold nanoparticles in an anchor-probe methodology as in Figure 2.8 [11]. Combined with recombinant production of functional proteins with a probe coil sequence tag [15], metallized coiled coils may provide a pathway forward for isotropically, regenerable displayed enzymes that are wired to CNT biosensors.

2.5 MULTIPLEXING BIOMOLECULES ON NANOSCALE CNT ARRAYS

The ability to detect multiple biospecies on a single CNT biosensor array is an important focus to many researchers. These *lab-on-chip* (LOC) devices would potentially monitor several molecular signatures simultaneously. For example, biomolecular signatures that mark a disease state such as cancer may not be predicted accurately by tracking a single biomolecule. The ability to monitor global changes in multiple DNA, RNA, and protein targets at the same time drives the field of multiplexed biosensors [67] and provides unique challenges to those specific biosensors built on CNT arrays.

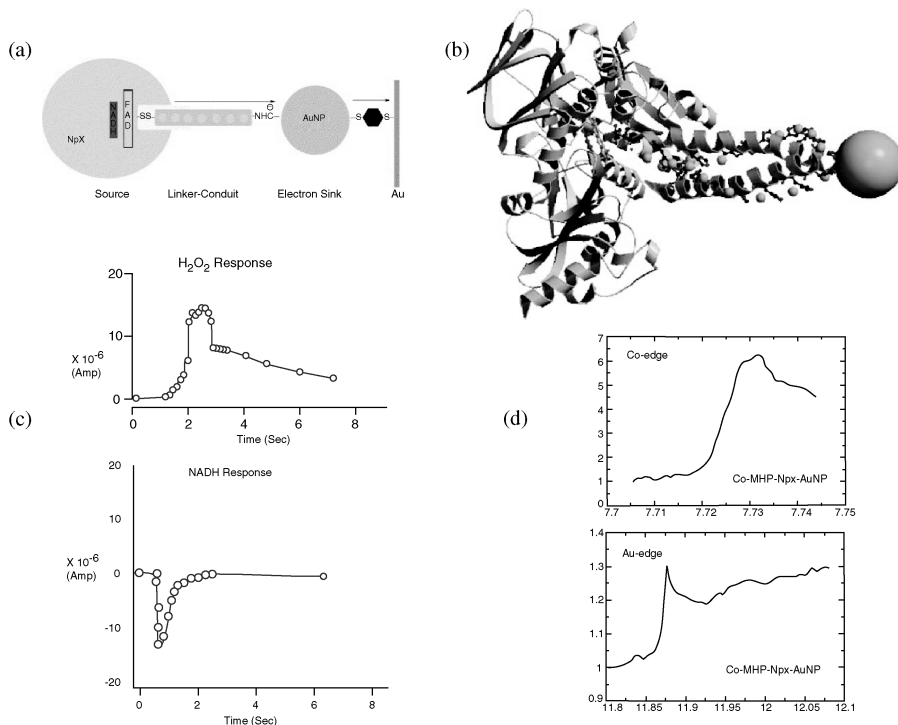


FIGURE 2.7 (a) Assembly consisting of the redox enzyme (Npx), metallized coiled-coil peptide (MHP), and a gold nanoparticle (AuNP) immobilized onto an electrode. The assembly was formed through stepwise linkage of each component with adsorption of the AuNP-linked complex reconstituted onto a dithiol monolayer associated with an Au electrode. (b) Model of the assembly based on the atomic coordinates of the Npx and the leucine zipper region of GCN4. The peptide coordinates cobalts (small spheres) through histidine residues at every i and $i + 4$ positions. AuNP was modeled as a sphere, to scale with the biological molecules, with a diameter of 14 Å. (c) Plots of the currents generated from addition of H₂O₂ (top) and NADH (bottom) vs. time. H₂O₂ results in surface and cobalt oxidation, nonspecific to the enzyme, while NADH is dependent on enzyme binding, exhibiting fast time constants with opposite current flows, as expected. (d) EXAFS on a solution of the washed assembly containing cobalt-metallized MHP, redox enzyme Npx, and a gold nanoparticle, AuNP. Scans were performed across the cobalt edge and gold edge, confirming the presence of both metals in the assembly, cobalt coordinated to the peptide and gold from the nanoparticle that is linked to the peptide. (Adapted from ref. 95, with permission.)

2.5.1 Site Addressability

The first step in multiplexing is controlling the “where” of the biomolecule detection reaction: that is, the distinct location to which each signal detected can be attributed. Ultimately, this has to be achieved by the controlled deposition of a single species at the micrometer and, potentially, nanometer scale. Two processes that may provide

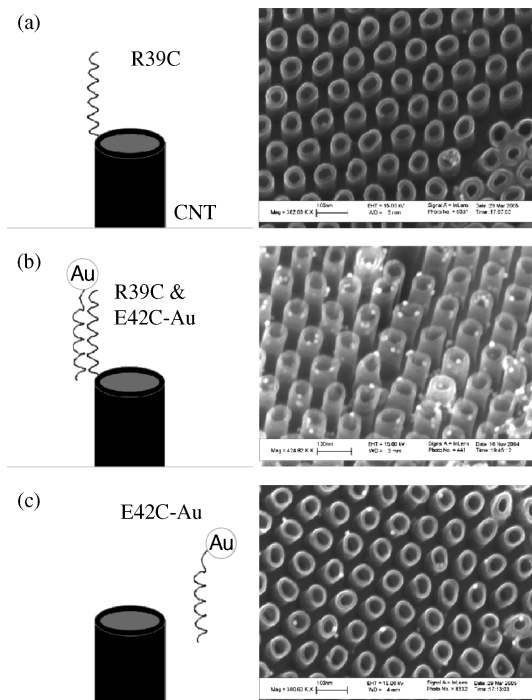


FIGURE 2.8 SEM image of the covalent immobilization of anchor coiled-coil peptide (R39C) in H_2O onto etched tips of the CNT array. (a) Upon addition of the Au-labeled capture peptide (E42C) again in H_2O , the tips of the carbon nanotubes demonstrate site-specific assembly of the coiled coil peptides. (b) Without the covalent attachment of the anchor peptide, Au-labeled E42C shows minimal nonspecific adsorption to the CNT array following simple substrate washing with H_2O . (c) Control image of unlabeled Au nanoparticles and R39C indicates that interaction is specific between R39C and E42C, not R39C and the nanoparticle. (From ref. [11], with permission.)

pathways forward in this respect are presented: micro/nanofluidics and dip pen nanolithography.

2.5.1.1 Micro and Nanofluidics Perhaps the most straightforward approach to immobilizing biomolecules onto distinct sites of a CNT array would be to deliver the biomolecule solution specifically and exclusively to that precise location. Traditional top-down lithography techniques are now able to produce one, and two-dimensional features in the nanometer realm. Thus, fluidic channels can deliver reagents to distinct locales and functionalize specific regions on CNT arrays. Additionally, regeneration of the biomolecules captured at specific regions on a CNT array or the entire surface would enable the reuse of a CNT biosensor. However, this route for multiplexing would require a different fluidic channel for each biological target and may prove cost inefficient for multiplexing a set of biological detection elements of any considerable number.

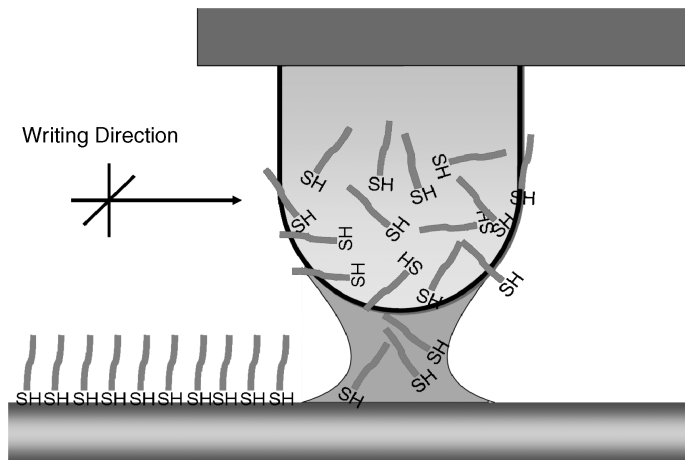


FIGURE 2.9 Dip pen nanolithography (DPN) in the deposition of alkanethiols onto a gold surface. The spatial resolution of molecular deposition is determined by tip geometry, contact time, humidity, and initial species concentration.

2.5.1.2 Dip Pen Nanolithography While conventional microarrays are spotted to micrometer-sized locations, the precision nanoscale deposition of selective species is an important challenge in reducing the size of multiplexed CNT biosensors. Dip pen nanolithography (DPN) affords the ability to do just this, tailoring chemical composition and surface structure with a sub-100-nm precision [26,60]. It works exactly like a stylus dipped into ink, with the exception that the stylus is an AFM tip of nanometer dimensions. DPN readily deposits self-assembled monolayers (SAMs) of different alkanethiols onto gold sensor surfaces for further covalent attachment, as illustrated in Figure 2.9. This technique has been used to control the template assembly of SWNTs onto gold surfaces into higher-ordered structures [85].

DPN is also extremely useful for patterning biological and soft organic structures onto surfaces; these molecules can be deposited in either ambient or inert environments without ionization or radiation exposure. Biomolecules can be deposited in buffered solutions with retention of activity upon immobilization. When spotting biomolecule solutions, the DPN method can produce nanoscale spotted features which are much smaller than conventional spotted bioarrays [26,60]. Thus, DPN may provide a tool to functionalize individual CNTs on an oriented array, provided that the center-to-center CNT spacing is greater than that of the atomic force microscopy stylus dimensions.

2.5.2 Pathways Toward Multiplexing Using DNA

To date, the majority of progress with multiplexing on CNT array biosensors is accomplished with self-assembling DNA linkers. Dual self-assembly and recognition capabilities have been achieved on a single nanotube within an array through the tip- and sidewall-specific attachment of amine- and pyrene-terminated oligonucleotides,

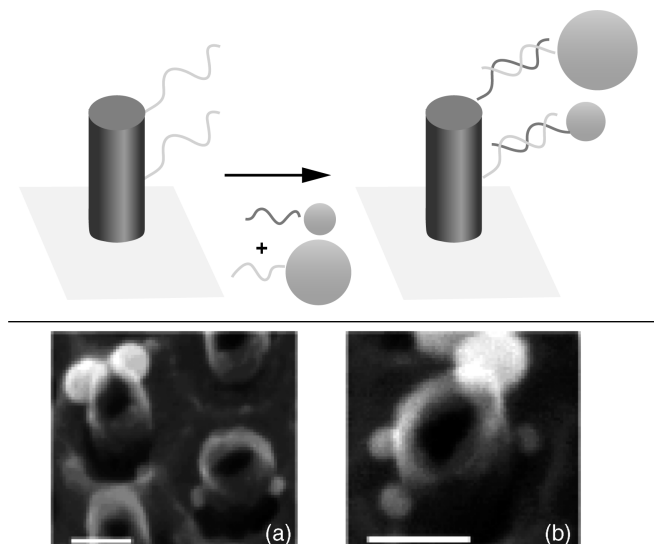


FIGURE 2.10 Site-specific delivery of DNA oligonucleotides and appended Au nanoparticles. SEM images correspond to nanoparticles introduced through parallel hybridization following the serial attachment of two DNA single strands. The 30-nm particles represent sites where amide coupling of tip-immobilized strands occurred, and the 15-nm particles represent sites where sidewall-immobilized strands were adsorbed via pyrene functionality. All scale bars represent 50 nm. (From ref. 76, with permission.)

respectively, as presented in Figure 2.10. EDC/NHS chemistries attach one anchor to the oxidized tips, while P-130 was used to immobilize the second anchor onto the sidewalls of the CNT. Site-specific, complementary hybridization of nanoparticle-labeled oligonucleotides was visualized by scanning electron microscopy. Thus, this route can be applied to build functionality to attach two different biospecies onto a CNT array biosensor, although simultaneous electrochemical recognition will be complicated if the redox peaks are similar for each enzyme.

The detection of two components is a start, but multiplexing on CNT arrays is not limited to the detection of two components. Withey et al. have employed a tip-specific strategy using DNA linkers that is truly scalable for multiplexing biospecies on CNT arrays. Simultaneous detection of five biologically relevant molecules was achieved via the capture and display of redox enzymes tagged with oligonucleotides, as shown in Figure 2.11. The CNT tips were reacted with EDC/NHS with amine-terminated DNA anchors. Amine groups on the enzymes were conjugated to complementary thiol-terminated DNA probes via the heterobifunctional cross-linker SIAB. Five redox-active enzymes—glucose oxidase (GOx), alcohol dehydrogenase (ADH), galactose oxidase (GO), lactate oxidase (LAX), and hemoglobin (Hb)—were used to form a multiplexed amperometric biosensor capable of monitoring solution levels of glucose, ethanol, galactose, lactic acid, and nitrous oxide, respectively.

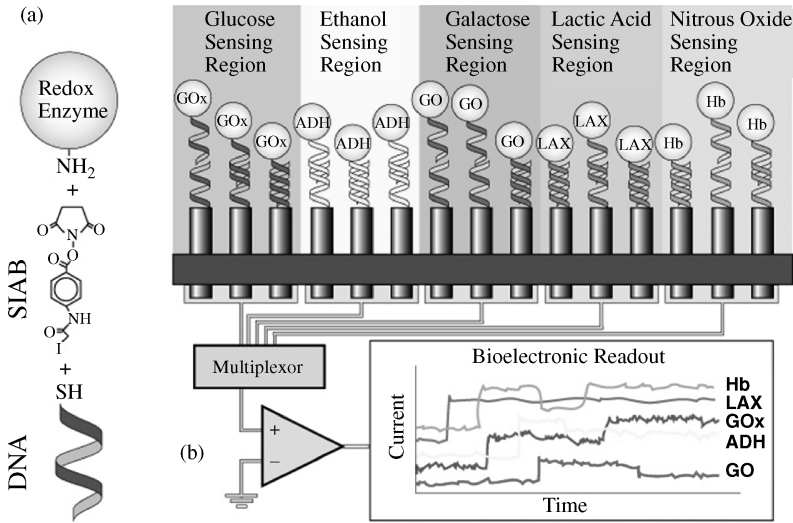


FIGURE 2.11 Site-addressable assembly of multiple enzymes to specific regions of a CNT array electrode. (a) The cross-linking of enzyme–ssDNA conjugates using the heterobifunctional cross-linker SIAB. An NHS ester reacts with an amine group on the enzyme while the iodoacetyl functional group reacts with a thiolated DNA oligo. (b) Parallel hybridization of the five enzymes to distinct regions of a CNT array electrode using differing oligonucleotide pairings. The CNTs are exposed from the aluminum oxide template on both sides. The top side is biofunctionalized, while electrical contacts are made to the bottom side by gold evaporation. Electrochemical currents originating from the enzymes indicate the corresponding substrate concentrations. (From ref. 90, with permission.)

Furthermore, the signals were enhanced using zinc and magnesium coordinated with anchor-probe DNA at high pH [90].

Although this scheme does not immobilize the enzyme at a single location, it does satisfy the remaining three guiding principles in nanoscale biosensor design: solvent accessibility, self-assembly and regeneration, and multiplexing. Oriented enzyme immobilization could be achieved readily using recombinant enzyme production as outlined in Section 2.2.2.5.

2.6 CONCLUSIONS

Successful implementation of advanced interfaces has provided marked progress within the field of CNT array biosensors. Homogeneous display of biomolecular ligands on CNTs is a key process in forming functionalized arrays, and the use of self-assembling interfaces on CNT arrays provides the additional benefits of solvent access for target capture, sensor surface regeneration, and ordered molecular wiring. A coordinated display of biomolecular elements organized by self-assembly will continue to enhance the utility of CNTs in biosensing arenas, as well as provide insights for other future applications of this versatile nanostructure.

REFERENCES

1. Aubuchon JF, Chen LH, Daraio C, Jin S. Multi-branching carbon nanotubes via self-seeded catalysts. *Nano Lett.* 2006;6:324–328.
2. Bjorck L, Kronvall G. Purification and some properties of streptococcal protein G, a novel IgG-binding reagent. *J. Immunol.* 1984;133:969–974.
3. Brask J, Wackerbarth H, Jensen KJ, Zhang J, Chorkendorff I, Ulstrup J. Monolayer assemblies of a de novo designed 4- α -helix bundle carboprotein and its sulfur anchor fragment on Au(111) surfaces addressed by voltammetry and in situ scanning tunneling microscopy. *J. Am. Chem. Soc.* 2003;125:94–104.
4. Brizzard BL, Chubet RG, Vizard DL. Immunoaffinity purification of FLAG epitope-tagged bacterial alkaline phosphatase using a novel monoclonal antibody and peptide elution. *Biotechniques.* 1994;16:730–735.
5. Buchardt O, Egholm M, Berg RH, Nielsen PE. Peptide nucleic acids and their potential applications in biotechnology. *Trends Biotechnol.* 1993;11:384–386.
6. Carr CM, Kim PS. A spring-loaded mechanism for the conformational change of influenza hemagglutinin. *Cell.* 1993;73:823–832.
7. Chambers P, Pringle CR, Easton AJ. Heptad repeat sequences are located adjacent to hydrophobic regions in several types of virus fusion glycoproteins. *J. Gen. Virol.* 1990; 71 (Pt.12):3075–3080.
8. Chao H, Houston M.E. Jr, Grothe S, Kay C.M, O'Connor-McCourt M, Irvin RT, Hodges RS. Kinetic study on the formation of a de novo designed heterodimeric coiledcoil: use of surface plasmon resonance to monitor the association and dissociation of polypeptide chains. *Biochemistry.* 1996;35:12175–12185.
9. Chapman-Smith A, Turner DL, Cronan JE Jr., Morris TW, Wallace JC. Expression, biotinylation and purification of a biotin-domain peptide from the biotin-carboxy carrier protein of *Escherichia coli* acetyl-CoA carboxylase. *Biochem J.* 1994;302(Pt. 3):881–887.
10. Chen RJ, Zhang Y, Wang D, Dai H. Noncovalent sidewall functionalization of single-walled carbon nanotubes for protein immobilization. *J. Am. Chem. Soc.* 2001;123: 3838–3839.
11. Contarino MR, Sergi M, Harrington AE, Lazareck A, Xu, J, Chaiken I. Modular, self-assembling peptide linkers for stable and regenerable carbon nanotube biosensor interfaces. *J. Mol. Recognit.* 2006;19:363–371.
12. Crick FH, Is alpha-keratin a coiled coil? *Nature.* 1952;170:882–883.
13. Cronan JE Jr. Biotinylation of proteins in vivo: a post-translational modification to label, purify, and study proteins. *J. Biol. Chem.* 1990;265:10327–10333.
14. De Crescenzo G, Litowski JR, Hodges RS, O'Connor-McCourt M. Real-time monitoring of the interactions of two-stranded de novo designed coiled-coils: effect of chain length on the kinetic and thermodynamic constants of binding. *Biochemistry.* 2003;42:1754–1763.
15. De Crescenzo G, Pham P, Durocher Y, O'Connor-McCourt M. Transforming growth factor-beta (TGF-beta) binding to the extracellular domain of the type II TGF-beta receptor: receptor capture on a biosensor surface using a new coiled-coil capture system demonstrates that avidity contributes significantly to high affinity binding. *J. Mol. Biol.* 2003;328:1173–1183.

16. de Groot RJ, Luytjes W, Horzinek MC, van der Zeijst BA, Spaan WJ, Lenstra JA. Evidence for a coiled-coil structure in the spike proteins of coronaviruses. *J. Mol. Biol.* 1987;196:963–966.
17. de Wildt RM, Mundy CR, Gorick BD, Tomlinson IM. Antibody arrays for high-throughput screening of antibody–antigen interactions. *Nat. Biotechnol.* 2000;18:989–994.
18. Delehay RM, Frankel G. Coiled-coil proteins associated with type III secretion systems: a versatile domain revisited. *Mol. Microbiol.* 2002;45:905–916.
19. Devaraj NK, Decreau RA, Ebina W, Collman JP, Chidsey CE. Rate of interfacial electron transfer through the 1,2,3-triazole linkage. *J. Phys. Chem. B.* 2006;110:15955–15962.
20. Ebbesen TW, Ajayan PM. Large-scale synthesis of carbon nanotubes. *Nature.* 1992;358:220.
21. Ellenberger TE, Brandl CJ, Struhl K, Harrison SC. The GCN4 basic region leucine zipper binds DNA as a dimer of uninterrupted alpha helices: crystal structure of the protein–DNA complex. *Cell* 1992;71:1223–1237.
22. Evan G, Lewis GK, Ramsay G, Bishop JM. Isolation of monoclonal antibodies specific for human *c-myc* proto-oncogene product. *Mol. Cell Biochem.* 1985;5:3610–3616.
23. Gelinsky M, Vahrenkamp H. Zinc complexes of a helical 22-mer peptide with two histidine donors. *Eur. J. Inorg. Chem.* 2002;9:2458–2462.
24. Georgakilas V, Kordatos K, Prato M, Guldi DM, Holzinger M, Hirsch A. Organic functionalization of carbon nanotubes. *J. Am. Chem. Soc.* 2002;124:760–761.
25. Georgakilas V, Tagmatarchis N, Pantarotto D, Bianco A, Briand JP, Prato M. Amino acid functionalisation of water soluble carbon nanotubes. *Chem. Commun. (Camb):* 2002;3050–3051
26. Ginger DS, Zhang H, Mirkin CA. The evolution of dip-pen nanolithography. *Angew. Chem. Int. Ed. Engl.* 2004;43:30–45.
27. Green NM. Avidin. *Adv. Protein. Chem.* 1975;29:85–133.
28. Gwenin CD, Kalaji M, Williams PA, Jones RM. The orientationally controlled assembly of genetically modified enzymes in an amperometric biosensor. *Biosens. Bioelectron.* 2007;22:2869–2875.
29. Heald CG, Wildgoose GG, Jiang L, Jones TG, Compton RG. Chemical derivatisation of multiwalled carbon nanotubes using diazonium salts. *Chemphyschem.* 2004;5:1794–1799.
30. Hogg PJ. Disulfide bonds as switches for protein function. *Trends. Biochem. Sci.* 2003;28:210–214.
31. Hopp T, Prickett K, Price V, et al. A short polypeptide marker sequence useful for recombinant protein identification and purification. *Bio/Technology* 1988;6:1204–1210.
32. Hopp TP, Gallis B, Prickett KS. Metal-binding properties of a calcium-dependent monoclonal antibody. *Mol. Immunol.* 1996;33:601–608.
33. Huang X, McLean RS, Zheng M. High-resolution length sorting and purification of DNA-wrapped carbon nanotubes by size-exclusion chromatography. *Anal. Chem.* 2005;77:6225–6228.
34. Hunter I, Schulthess T, Engel J. Laminin chain assembly by triple and double stranded coiled-coil structures. *J. Biol. Chem.* 1992;267:6006–6011.
35. Iijima, S. Helical microtubules of graphitic carbon. *Nature.* 1991;354:56–58.

36. Journet C, Maser W, Bernier P, et al. Large-scale production of single-walled carbon nanotubes by the electric-arc technique. *Nature*. 1997;388:756–758.
37. Katz E, Willner I. Biomolecule-functionalized carbon nanotubes: applications in nanobioelectronics. *ChemPhyschem*. 2004;5:1084–1104.
38. Keefe AD, Wilson DS, Seelig B, Szostak JW. One-step purification of recombinant proteins using a nanomolar-affinity streptavidin-binding peptide, the SBP-Tag. *Protein Expr. Purif.* 2001;23:440–446.
39. Keleman K, Rajagopalan S, Cleppien D, et al. Comm sorts robo to control axon guidance at the *Drosophila* midline. *Cell*. 2002;110:415–427.
40. Kellermann OK, Ferenci T. Maltose-binding protein from *Escherichia coli*. *Methods Enzymol.* 1982;90(Pt. E):459–463.
41. Kiick KL, Saxon E, Tirrell DA, Bertozzi CR. Incorporation of azides into recombinant proteins for chemoselective modification by the Staudinger ligation. *Proc. Natl. Acad. Sci. USA*. 2002;99:19–24.
42. Knappik A, Pluckthun A. An improved affinity tag based on the FLAG peptide for the detection and purification of recombinant antibody fragments. *Biotechniques*. 1994;17:754–761.
43. Krantz B, Sosnick T. Engineered metal binding sites map the heterogeneous folding landscape of a coiled coil. *Nature*. 2001;8:1042–1047.
44. Kusnezow W, Hoheisel JD. Antibody microarrays: promises and problems. *Biotechniques*. 2002; (Suppl):14–23.
45. Lamla T, Erdmann VA. The Nano-tag, a streptavidin-binding peptide for the purification and detection of recombinant proteins. *Protein Expr. Purif.* 2004;33:39–47.
46. Li H, Cheng F, Duft AM, Adronov A. Functionalization of single-walled carbon nanotubes with well-defined polystyrene by “click” coupling. *J. Am. Chem. Soc.* 2005;127:14518–14524.
47. Li J, Padadopoulos C, Xu J, Highly-ordered carbon nanotube arrays for electronics applications. *Appl. Phys. Lett.* 1999;75:367–369.
48. Li J, Papadopoulos C, Xu J. Nanoelectronics: growing Y-junction carbon nanotubes. *Nature*. 1999;402:253.
49. Li WZ, Xie SS, Qian LX, et al. Large-scale synthesis of aligned carbon nanotubes. *Science*. 1996;274:1701–1703.
50. Link AJ, Vink MK, Tirrell DA. Presentation and detection of azide functionality in bacterial cell surface proteins. *J. Am. Chem. Soc.* 2004;126:10598–10602.
51. Matthews JM, Young TF, Tucker SP, Mackay JP. The core of the respiratory syncytial virus fusion protein is a trimeric coiled coil. *J. Virol.* 2000;74:5911–5920.
52. Medvedev DM, Daizadeh I, Stuchebrukhov AA. Electron transfer tunneling pathways in bovine heart cytochrome *c* oxidase. *J. Am. Chem. Soc.* 2000;122: 6571–6582.
53. Meng G, Jung YJ, Cao A, Vajtai R, Ajayan PM. Controlled fabrication of hierarchically branched nanopores, nanotubes, and nanowires. *Proc. Natl. Acad. Sci. USA*. 2005;102:7074–7078.
54. Monthieux M, Kuznetsov VL. Who should be given the credit for the discovery of carbon nanotubes? *Carbon*. 2006;44:1621.
55. Nguyen CV, Delziet L, Matthews K, Chen B, Meyyappan M. Purification process for vertically aligned carbon nanofibers. *J. Nanosci. Nanotechnol.* 2003;3:121–125.

56. Nielsen PE, Egholm M, Berg RH, Buchardt O. Sequence-selective recognition of DNA by strand displacement with a thymine-substituted polyamide. *Science*. 1991;254:1497–1500.
57. Nilsson B, Abrahmsen L. Fusions to staphylococcal protein A. *Methods Enzymol*. 1990;185:144–161.
58. Niman H, Houghten R, Walker L, et al. Generation of protein-reactive antibodies by short peptides is an event of high frequency: implications for the structural basis of immune recognition. *Proc. Natl. Acad. Sci. USA*. 1983;80:4949–4953.
59. O'Shea EK, Klemm JD, Kim PS, Alber T. X-ray structure of the GCN4 leucine zipper, a two-stranded, parallel coiled coil. *Science*. 1991;254:539–544.
60. Piner RD, Zhu J, Xu F, Hong S, Mirkin CA. "Dip-Pen" nanolithography. *Science*. 1999;283:661–663.
61. Porath J, Carlsson J, Olsson I, Belfrage G. Metal chelate affinity chromatography, a new approach to protein fractionation. *Nature*. 1975;258:598–599.
62. Prickett KS, Amberg DC, Hopp TP. A calcium-dependent antibody for identification and purification of recombinant proteins. *Biotechniques*. 1989;7:580–589.
63. Rasmussen R, Benvegna D, O'Shea EK, Kim PS, Alber T. X-ray scattering indicates that the leucine zipper is a coiled coil. *Proc. Natl. Acad. Sci. USA*. 1991;88:561–564.
64. Saito R, Dresselhaus MS, Dresselhaus G. *Physical Properties of Carbon Nanotubes*. Imperial College Press, London, 1998.
65. Schmidt TG, Koepke J, Frank R, Skerra A. Molecular interaction between the strep-tag affinity peptide and its cognate target, streptavidin. *J. Mol. Biol*. 1996;255:753–766.
66. Schuhmann W, Ohara TJ, Schmidt H, Heller A. Electron transfer between glucose oxidase and electrodes via redox mediators bound with flexible chains to the enzyme surface. *J. Am. Chem. Soc*. 1991;113:1394–1397.
67. Schweitzer B, Predki P, Snyder M. Microarrays to characterize protein interactions on a whole-proteome scale. *Proteomics* 2003;3:2190–2199.
68. Sergi M, Zurawski J, Cocklin S, Chaiken I. Proteins, recognition networks and developing interfaces for macromolecular biosensing. *J. Mol. Recognit*. 2004;17:198–208.
69. Sergi M, Zurawski J, Cocklin S, Chaiken IM. Proteins, recognition networks and developing interfaces for macromolecular biosensing. *J. Mole. Recognit*. 2004;17:198–208.
70. Singh KV, Pandey RR, Wang X, et al. Covalent functionalization of single walled carbon nanotubes with peptide nucleic acid: nanocomponents for molecular level electronics. *Carbon*. 2006;44:1730–1739.
71. Slijukic B, Banks CE, Compton RG. Iron oxide particles are the active sites for hydrogen peroxide sensing at multiwalled carbon nanotube modified electrodes. *Nano Lett*. 2006;6:1556–1558.
72. Smith DB, Johnson KS. Single-step purification of polypeptides expressed in *Escherichia coli* as fusions with glutathione S-transferase. *Gene*. 1988;67:31–40.
73. Sodek J, Hodges RS, Smillie LB, Jurasek L. Amino-acid sequence of rabbit skeletal tropomyosin and its coiled-coil structure. *Proc. Natl. Acad. Sci. USA*. 1972;69:3800–3804.
74. Sotiropoulou S, Chaniotakis NA. Carbon nanotube array-based biosensor. *Anal. Bioanal. Chem*. 2003;375:103–105.
75. Stofko-Hahn RE, Carr DW, Scott JD. A single step purification for recombinant proteins: characterization of a microtubule associated protein (MAP 2) fragment which

- associates with the type II cAMP-dependent protein kinase. *FEBS. Lett.* 1992;302:274–278.
76. Taft BJ, Lazareck AD, Withey GD, Yin A, Xu JM, Kelley SO. Site-specific assembly of DNA and appended cargo on arrayed carbon nanotubes. *J. Am. Chem. Soc.* 2004;126:12750–12751.
 77. Tasis D, Tagmatarchis N, Georgakilas V, Prato M. Soluble carbon nanotubes. *Chemistry.* 2003;9:4000–4008.
 78. Terpe K. Overview of tag protein fusions: from molecular and biochemical fundamentals to commercial systems. *Appl. Microbiol. Biotechnol.* 2003;60:523–533.
 79. Thess A, Lee R, Nikolaev P, et al. Crystalline ropes of metallic carbon nanotubes. *Science.* 1996;273:483–487.
 80. Tomlinson E, Palaniyappan N, Tooth D, Layfield R. Methods for the purification of ubiquitinated proteins. *Proteomics.* 2007;7:1016–1022.
 81. Tripet B, Yu L, Bautista DL, Wong WY, Irvin RT, Hodges RS. Engineering a de novo-designed coiled-coil heterodimerization domain off the rapid detection, purification and characterization of recombinantly expressed peptides and proteins. *Protein Eng.* 1996;9:1029–1042.
 82. Tsang S, Chen Y, Harris J, Green M. A simple chemical method of opening and filling carbon nanotubes. *Nature.* 1994;372:159–162.
 83. Wang J, Kawde AN, Jan MR. Carbon-nanotube-modified electrodes for amplified enzyme-based electrical detection of DNA hybridization. *Biosens. Bioelectron.* 2004;20:995–1000.
 84. Wang S, Humphreys E, Chung S, et al. Peptides with selective affinity for carbon nanotubes. *Nat. Mater.* 2003;2:196–200.
 85. Wang Y, Maspoch D, Zou S, Schatz GC, Smalley RE, Mirkin CA. Controlling the shape, orientation, and linkage of carbon nanotube features with nano affinity templates. *Proc. Natl. Acad. Sci. USA.* 2006;103:2026–2031.
 86. Wei D, Liu Y, Cao L, et al. A new method to synthesize complicated multi-branched carbon nanotubes with controlled architecture and composition. *Nano Lett.* 2006;6:186–192.
 87. Williams KA, Veenhuizen PT, de la Torre BG, Eritja R, Dekker C. Nanotechnology: carbon nanotubes with DNA recognition. *Nature.* 2002;420:761.
 88. Willner B, Katz E, Willner I. Electrical contacting of redox proteins by nanotechnological means. *Curr. Opin. Biotechnol.* 2006;17:589–596.
 89. Willner I, Willner B, Katz E. Biomolecule-nanoparticle hybrid systems for bioelectronic applications. *Bioelectrochemistry.* 2007;70:2–11.
 90. Withey GD, Kim JH, Xu JM. Wiring efficiency of a metallizable DNA linker for site-addressable nanobioelectronic assembly. *Nanotechnology.* 2007;18:424025–424034.
 91. Withey GD, Lazareck AD, Tzolov MB, et al. Ultra-high redox enzyme signal transduction using highly ordered carbon nanotube array electrodes. *Biosens. Bioelectron.* 2006;21:1560–1565.
 92. Xiao Y, Patolsky F, Katz E, Hainfeld JF, Willner I. “Plugging into Enzymes”: nanowiring of redox enzymes by a gold nanoparticle. *Science.* 2003;299:1877–1881.
 93. King Y, Li L, Chusuei CC, Hull RV. Sonochemical oxidation of multiwalled carbon nanotubes. *Langmuir.* 2005;21:4185–4190.
 94. Yang DQ, Rochette JF, Sacher E. Functionalization of multiwalled carbon nanotubes by mild aqueous sonication. *J. Phys. Chem. B.* 2005;109:7788–7794.

95. Yeh JI, Zimmt MB, Zimmerman AL. Nanowiring of a redox enzyme by metallized peptides. *Biosens. Bioelectron.* 2005;21:973–978.
96. Yuan Z, Huang H, Liu L, Fan S. Controlled growth of carbon nanotubes in diameter and shape using template-synthesis method. *Chem. Phys. Lett.* 2001;345:39–43.
97. Zheng M, Jagota A, Strano MS, et al. Structure-based carbon nanotube sorting by sequence-dependent DNA assembly. *Science.* 2003;302:1545–1548.

Interaction of DNA with CNTs: Properties and Prospects for Electronic Sequencing

SHENG MENG and EFTHIMIOS KAXIRAS

Department of Physics and School of Engineering and Applied Sciences,
Harvard University, Cambridge, Massachusetts

- 3.1 Introduction
- 3.2 Structural properties of combined DNA–CNT systems
 - 3.2.1 single nucleotide on a CNT
 - 3.2.2 DNA oligomers on a CNT
 - 3.2.3 Helix of DNA on a CNT
 - 3.2.4 Integration of DNA and a CNT array
 - 3.2.5 DNA inside CNT pores
- 3.3 Electronic structure
 - 3.3.1 Polarization and charge transfer
 - 3.3.2 Density of states
 - 3.3.3 STM images
- 3.4 Optical properties
- 3.5 Biosensing and sequencing of DNA using CNTs
 - 3.5.1 Gaseous sensing using DNA–CNT
 - 3.5.2 Field-effect transistor and optical shift for DNA detection
 - 3.5.3 Monitoring morphology changes of dsDNA
 - 3.5.4 DNA sequencing
- 3.6 Summary

3.1 INTRODUCTION

The interaction between DNA and carbon nanotubes (CNTs) is a subject of intense current interest. Both DNA strands and CNTs are prototypical one-dimensional structures; the first plays a central role in biology, and the second holds promise for an equally pivotal role in nanotechnology applications. Single-stranded DNA (ssDNA) and CNTs have complementary structural features that make it possible to assemble them into a stable hybrid structure: ssDNA is a flexible, amphiphilic biopolymer, whereas CNTs are stiff, strongly hydrophobic nanorods. Indeed, ssDNA of different lengths, either small oligomers consisting of tens of bases [1,2] or long genomic strands (ca.100 bases) [3], wrap-around single-walled CNTs, forming tight helices, as observed by atomic force microscopy (AFM). Similarly, double-stranded DNA (dsDNA) [4,5] and fragmented dsDNA (a hybrid of both ssDNA and dsDNA) [6] can also be associated with a CNT, although less efficiently. In addition, as predicted theoretically [7,8] and confirmed experimentally [9] by high-resolution transmission electron microscopy (TEM), DNA can be encapsulated into the CNT interior.

Although the structures of DNA and CNTs, each in its natural form and environment, are well established (e.g., the B-DNA form in solution [10] or isolated CNTs [11]), the molecular structure for the combined DNA–CNT systems is not well characterized, and the nature of their interaction remains elusive [1–4,12–17]. This has motivated many studies and possible applications. For instance, it has been inferred from optical spectra that double-stranded DNA experiences a conformational transformation from the B-form to the Z-form on the CNT surface with the increase in ion concentration [4]. Due to their intriguing properties, including 100-fold-higher tensile strength than steel, excellent thermal conductivity comparable to that of diamond, and tunable electric conductance, CNTs have been proposed as the template for DNA encapsulation [9], intracellular DNA transport [13], DNA hybridization [17], and electrochemical DNA detection [12]. A different set of applications involves ssDNA wrapping around CNTs in a diameter- and sequence-dependent manner, which would make it possible to dissolve the naturally hydrophobic single [18] or multiwalled CNTs in water [19] and to sort them by their chirality [1,2]. Finally, DNA-decorated CNTs have been examined as a chemical sensor to discriminate odors in air [14] and glucose in solution [5], while DNA strands in contact with a CNT array have been proposed as the basis for electronic switches involving electron transport in both components [15] and for high- k -dielectric field-effect transistors (FETs) [20].

There is also an increasing interest in the use of CNTs for supporting and detecting DNA through electronic [16] and optical means [4,17], which could lead to ground-breaking, ultrafast DNA sequencing at low cost (see Figure 3.1 for a hypothetical setup), approaching the target of \$1000 per genome. Previous studies show that electronic detection of DNA bases using transverse conductance measurements depends sensitively on the tip-base distance and relative orientation, factors that can overwhelm the signal dependence on base identity and severely limit the efficacy of single-base detection methods [21–23]. These difficulties may

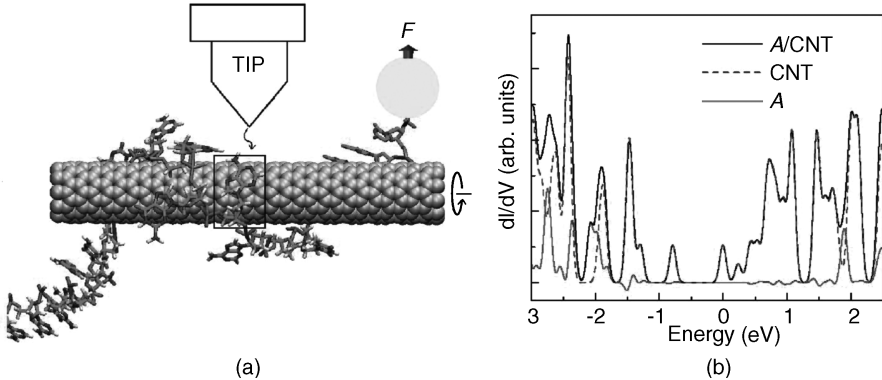


FIGURE 3.1 (a) Theoretical proposal for a setup for electronic DNA sequencing using partially DNA-wrapped CNTs and a probe with atomic-scale resolution, such as scanning tunneling spectroscopy. (b) The differential current–voltage curves are shown for the combined system (black line) and bare CNT (dashed); their difference (gray) corresponds to the measured signal for the DNA base under the tip (the example corresponds to the base A).

be overcome in the combined DNA–CNT system, since as we discuss later, attaching DNA on a CNT fixes the geometry of nucleotide (both the base–CNT distance and base orientation) on the CNT wall. Indeed, recent success in detecting DNA conformational changes [4] and hybridization [17] by near-infrared fluorescence of CNTs or CNT-field-effect transistors [16] opened the door for DNA sequencing based on its electronic structure.

To this end, what is currently missing for practical DNA detection and sequencing on CNTs is a detailed understanding of the nature of the DNA–CNT interaction and its dependence on the nucleotide identity. The DNA–CNT hybrid is a complicated, dynamic structure in which the four types of bases [the two purines, adenine (A) and guanine (G), and the two pyrimidines, cytosine (C) and thymine (T)] interact with the CNT in the presence of thermal fluctuations. Individual DNA bases can be stabilized on CNTs through mainly weak van der Waals interaction to the graphitic CNT wall. This interaction is perturbed by the sugar and phosphate groups in the DNA backbone, the counterions that bind to DNA, and the water molecules from solution. Even if the idea of using CNT as a template to hold and fix the DNA bases for electronic detection appears promising, many issues remain to be resolved before it is proven practical. The fundamental aspects of the DNA–CNT interaction include binding geometries, base orientation, mutual polarization, charge transfer, DNA association and dissociation, dynamical structure evolution, and response to electric and optical signals; all these need to be addressed at the molecular level. The dependence of these properties on the base identity, once explicitly resolved, may lead to the development of new DNA sequencing methods. We review here the properties of DNA–CNT systems and discuss the prospects for DNA detection and sequencing using electronic signals from CNTs.

3.2 STRUCTURAL PROPERTIES OF COMBINED DNA–CNT SYSTEMS

3.2.1 Single Nucleotide on a CNT

The first step in attempting to understand the DNA–CNT interaction is to establish the possible binding geometries in a DNA–CNT system, beginning with the structure of a single nucleotide adsorbed on the CNT surface [24]. To study this local interaction, we have used nucleosides, consisting of a base, a deoxyribose sugar group, and terminated by OH at the 3' and 5' ends. The phosphate group of a nucleotide is not included (in the following we identify nucleotides by the same symbols as the bases). We use the semiconducting (10,0) nanotube, which is abundant during synthesis and has a diameter of 7.9 Å, as a representative example of CNTs. We determined the energetically favorable configurations of the bases on the nanotube with the CHARMM program [25] using standard force fields [26] for atoms comprising the nucleosides and force fields of aromatic carbon atoms for those belonging to the CNT.

Compared to the planar structure of graphite, CNTs have a curved structure that perturbs only slightly the nucleoside adsorption positions but results in many inequivalent adsorption geometries. We performed an extensive search of the potential energy surface of each adsorbed nucleoside using the successive confinement method [27]. The potential energy surfaces of biomolecules are extremely complicated [28] and currently preclude direct exploration with *ab initio* methods. The search returned approximately 1000 distinct potential energy minima for each base–CNT system, with the global energy minimum structures shown in Figure 3.2(a). The room-temperature populations of each minimum range from 10^{-10} to 50%. Despite the numerous configurations, we found that very few of them are dominant, with significant room-temperature populations. For instance, there are four most stable configurations for C, with populations 25.2, 6.8, 4.3, and 3.2% [shown in Figure 3.2(b)]. Similarly, there are three dominant configurations for A, with populations of 28.4, 27.6,

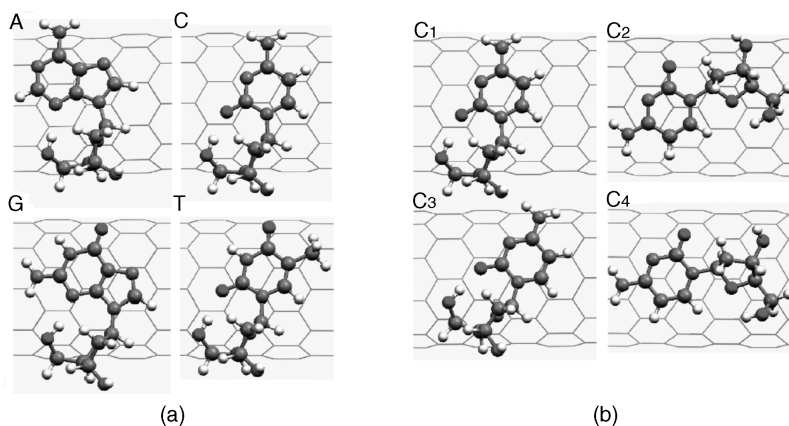


FIGURE 3.2 (a) The most stable configuration for a single nucleoside adsorption on the (10,0) CNT; (b) the four most stable configurations for adsorption of C on the CNT.

and 10.1%; three configurations for G (populations: 45.9, 20.8, and 7.2%), and four for T (populations: 11.2, 5.0, 4.1, and 2.0%). Together, these three to four structures represent the majority of the total population of configurations. The rest of the population contains more than 800 configurations. Therefore, it is reasonable to focus only on the dominant configurations in our evaluation of the DNA–CNT interactions. This is particularly true when we show later that the various configurations make a negligible difference in the DNA–CNT interaction.

The preferred configurations for each base have certain similarities, but all are different from their ideal geometries upon adsorption on a planar graphene layer. The nucleoside binds on carbon nanotubes through its base unit, located 3.3 Å away from the CNT wall. Whereas the base unit remains planar without significant bending, the sugar residue is more flexible. It lies farther away from the CNT, usually having its OC₄ plane perpendicular to the CNT wall with the O atom pointing toward it (Figure 3.2). On a graphene layer, the N and C atoms of A are found to occupy the hollow sites of the hexagonal rings, resembling AB stacking between adjacent layers in graphite [29]. Here, however, because of the curvature of the CNT, the C and N atoms of the base do not necessarily reside on the top of hexagonal C rings; instead, they can shift positions to maximize the attraction between C, N, and O atoms in the base and C atoms in the CNT. For guanine and cytosine on graphene, there is already a significant deviation from AB stacking [30]; they are further displaced on the CNT wall, with G being closest to that on the graphene structure, shifted by only about 0.8 Å along one C–C bond and slightly rotated. Moreover, because the CNT structure is highly asymmetric with a long axis, the orientation of a base with respect to the tube axis can be very different. For instance, in the four preferred geometries for C, two are rotated by about 90° relative to the most stable configuration (Figure 3.2). Interestingly, all four of the most stable configurations involving nucleoside adsorption on the CNT have the sugar-base direction pointing perpendicular to the tube axis or slightly tilted.

The force-field approach discussed so far relies on empirically derived dispersion interactions. In the context of the quantum approach, it is the explicit polarization of electronic charge that contributes to interaction between the nucleosides and the CNT. The structures obtained from the force-field calculations were further optimized using density functional theory in the local density approximation (LDA) for the exchange–correlation functional [31]. The structural relaxation was carried to the point where the forces calculated on each atom have a magnitude smaller than 0.005 eV/Å. The local structure, that is, covalent bond lengths and bond angles, shows little deviation from that obtained with the force field (of order 0.02 Å and 1°), while the optimal CNT–base distance is reduced by about 0.3 Å. The base adsorption induces a very small distortion of the CNT geometry, consisting of a 0.02-Å depression on the adsorption side and a 0.007-Å protrusion on the opposite side. The interaction energy calculated is 0.43 to 0.46 eV for the four nucleosides. This value is very close to the LDA calculation of adenine on graphite (0.46 eV) [29], but is significantly lower than the van der Waals energy of 0.70 to 0.85 eV from the CHARMM calculations (0.70 eV for C, 0.77 eV for T, 0.81 eV for A, and 0.85 eV for G). In comparison, the experimental value extracted from thermal desorption spectroscopy for adenine on graphite is

1.01 eV [32], which is reasonably close to the sum of the dispersion and electronic interaction energies (1.13 eV).

3.2.2 DNA Oligomers on a CNT

After examining the interaction between a single nucleoside and CNT, the next natural step is the interaction of a nucleotide strand with CNT, where the competition between the base–base and the base–CNT interactions comes into play. Using classic molecular dynamics (MD) simulations based on CHARMM force fields, we have investigated the interaction between CNTs and DNA oligomers, that is, short DNA strands consisting of a few bases and up to tens of DNA bases. The simulation box, of dimensions $25 \text{ \AA} \times 25 \text{ \AA} \times 43.4 \text{ \AA}$, comprises a DNA oligomer, a CNT (10,0), and about 700 water molecules with sodium counterions to neutralize the DNA backbone. We employ the TIP3P water model and periodic boundary conditions [33]. Constant pressure and constant temperature are controlled by the Berendsen barostat and the Nose–Hoover thermostat [34], respectively, toward the target values of 1 bar and 300 to 400 K. The particle-mesh Ewald method with cubic spline interpolation [35] is used to evaluate electrostatic energies and forces. A time step of 2 fs is used, and the OH vibrations are frozen using the SHAKE algorithm. The full trajectory is recorded every 1 ps after an equilibration of 20 to 200 ps.

Figure 3.3 shows the association dynamics of a ssDNA oligomer consisting of six adenine bases [poly(dA6)] with the CNT, at 300 K during a period of 3 ns. Initially, each base is 5 to 9 Å away from the nanotube outer surface. Here the base–CNT distance is defined as the distance between the center of mass of the individual base and the CNT wall. After 5 ps, one base at one of the two ends of the strand (base 1) quickly starts to attach on the CNT surface, as evidenced by a base–CNT distance of 3.4 Å. The other bases gradually approach the CNT wall. At time $t = 0.545 \text{ ns}$ and $t = 0.575 \text{ ns}$, respectively, the fourth and fifth bases counted from the same end of ssDNA attach to the CNT surface and are stabilized there. The rest of the DNA bases either stack on top of these CNT-attached bases (e.g., base 6) or are stacked among themselves (bases 2 and 3), forming a bubble on the CNT, as shown in the snapshot at 0.6 ns. Similar events take place at $t = 0.7$ to 0.8 ns for bases 2 and 3, when the base stacking is broken and both bases adsorb on the CNT surface. At this time, the system reaches steady state, where five of six bases form a close contact with the CNT surface, lying flat at a distance of 3.4 Å, which helps optimize the van der Waals attraction between the base and the CNT. Occasionally, some bases flip up, resulting in the base plane being aligned vertically with the CNT wall, which is followed by a larger oscillation in the base–CNT distance above 4 Å. The last base, base 6, at the other end of the ssDNA strand, forms a very stable stacking on base 5 during the $t = 0.8$ to 1.9 ns time interval [Figure 3.3(d)]. This stacking is not broken until 1.9 ns. After that, the DNA oligomer forms a stable horseshoe-like structure with all bases stacked on the CNT wall without self-stacking, which lasts for at least another nanosecond. The large deviation in the base–CNT distance for base 4 is due to its frequent flipping up and back onto the CNT wall. During the ssDNA–CNT association

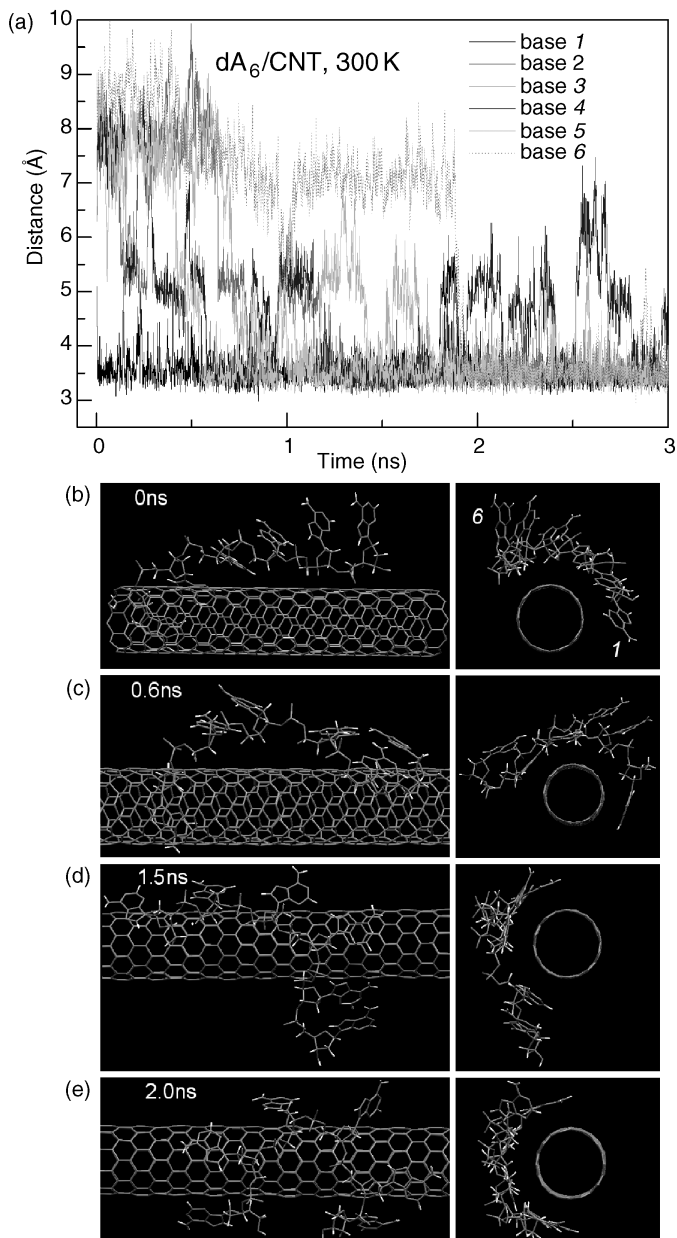


FIGURE 3.3 (a) Distance between the center of mass of each base in the ssDNA oligomer dA_6 and the CNT wall as a function of the simulation time; (b–e) snapshots from the simulation trajectory at times of 0, 0.6, 1.5, and 2.0 ns, respectively. Two views from directions vertical and parallel to the CNT axis are shown. For clarity, water molecules and counterions are not shown.

process, there is a stepwise decrease in the base–CNT distance; the terraces correspond to metastable intermediate states in which some bases are stacked between themselves.

The association of ssDNA on CNT walls in aqueous solution is due to both the hydrophobic effect and the vdW interaction, with the latter playing a dominant role. The interaction energy between the DNA base plane and the CNT wall is much larger than the self-stacking energy of bases: In Figure 3.4(a) we compare base–base interaction and a base–CNT stacking energy during the simulation, for the case of adenine. The A–CNT interaction energy is around 0.50 eV, larger than the A–A stacking energy by roughly a factor of 2. The presence of the sugar and phosphate group adds about another 0.3 eV to the total van der Waals interaction energy between the nucleotide and the CNT (not shown in this figure). The hydrophobic effect comes from the fact that the bases in DNA strands are hydrophobic and are likely to form a hybrid with the highly hydrophobic CNTs.

The process above is observed for other ssDNA strands of different sequence and length and should be considered as a general characteristic for ssDNA–CNT association. There exist, however, many stable ssDNA–CNT structures, among which the horseshoe structure is one of the most stable, observed for other oligomers, including poly(dG6) and poly(dC6). Other stable structures include the DNA strand linearly aligned along the nanotube axis, the S-shaped structure on the CNT wall, or a part of a helix structure. In our simulations, a six-base strand is too short to form a full period of a helix on the CNT. We also find that the base–CNT stacking and base–base stacking coexist in the stable ssDNA–CNT structures. The stacking of bases among themselves can occur either at the end of the ssDNA strand or in the middle, forming “bubbles” 5 to 8 Å high on the CNT. There is a relatively large barrier for these structures to develop optimal contact with the CNT (all bases lying flat and close to the CNT wall); therefore, they can be considered as “metastable” states, and do not unfold fully in our short simulations at the nanosecond scale.

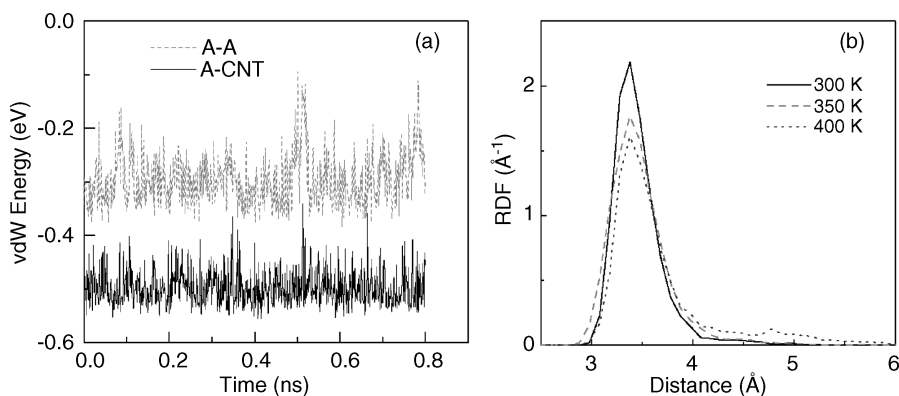


FIGURE 3.4 (a) Van der Waals interaction energy between base and CNT and between base and base in the simulation of dA₆/CNT in water; (b) radial distribution function of dA₆/CNT at different temperatures.

At different temperatures, the bound DNA–CNT structure exhibits different stability. When increasing the temperature, some bases are more likely to deviate from the optimal adsorption position and to detach from the CNT wall. Figure 3.4(b) shows the radial distribution function of the center of mass of each base around the CNT wall at different temperatures, averaged over all six bases in a 1-ns trajectory starting from the same configuration, which is the optimal contact between each DNA base and CNT. These results indicate that the higher the temperature, the less tight the ssDNA structure around the CNT, as is evident from the increasing values in the tail of the distribution (larger distances). The probability for a base to stay at the CNT surface actually decreases from 97% at 300 K to 81% at 400 K.

3.2.3 Helix of DNA on a CNT

The longer ssDNA strand will bind on the CNT surface in the same manner as DNA oligomers. Due to its extent, some new structural characteristics arise. The most striking feature is perhaps the formation of a stable, tight helical structure of ssDNA on the CNT along the tube axis, as seen in experiment: Zheng et al. [1] first observed that a relatively short ssDNA strand with 30 to 90 bases can effectively disperse the indissoluble CNT bundles in water after ultrasound sonication. In high-resolution AFM images, the dispersed CNT samples show clearly the helical ssDNA structure upon a single CNT with a constant periodicity along its axis (Figure 3.5). The dispersion effect comes from the fact that the binding energy between ssDNA and CNT is slightly larger than the CNT–CNT binding, and that the backbone of ssDNA after base–CNT binding is hydrophilic enough to make the ssDNA–CNT complex soluble. The dispersion process depends on the sequence and length of DNA used and, more important, on the CNT diameter and chirality [2]. This demonstration of successful dispersion of CNTs using DNA sequences provides a unique way of separating and sorting CNTs efficiently according to their diameter and electronic properties, which is essential in being able to employ CNTs in practical nanotech-

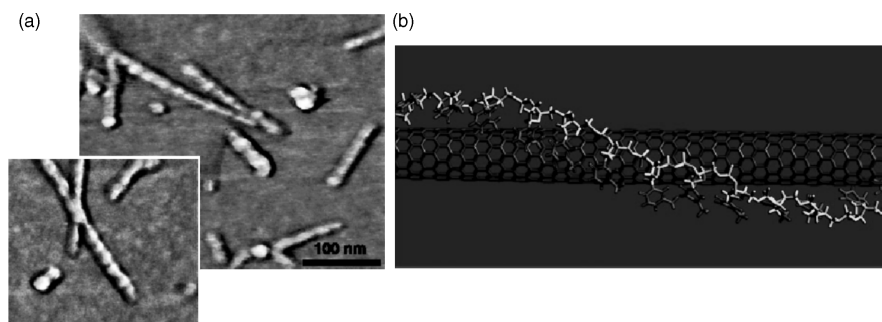


FIGURE 3.5 Helical ssDNA structure wrapping around CNT: (a) AFM images; (b) model from molecular simulations for poly(dT) on CNT(10,0). [(a) Adapted from ref. 2, with permission. Copyright © 2003 American Association for the Advancement of Science. (b) From ref. 1, with permission. Copyright © 2003 Nature Publishing Group.]

nology applications. Computer simulations showed that ssDNA spontaneously wraps into helices from the 3' end to the 5' end, driven by electrostatic and torsional interactions within the sugar–phosphate backbone [36]. We discuss below how even a long genomic ssDNA strand could bind on a CNT, effectively forming a rigid helix whose period is characteristic for the individual DNA–CNT complex [3]. The critical issue in achieving this is removal of the complementary DNA (cDNA) strands from the aqueous solution to assure that all DNA molecules are in single-stranded form. In the same way, ssDNA may disperse CNT bundles into the solution as a whole, without breaking each bundle further into individual CNTs [37].

Double-stranded DNA [4,5] and long RNA homopolymer strands [38] or strands extracted from natural microorganisms [1] could also wrap around CNT effectively. Computer simulations [39] revealed that the hydrophobic end groups, rather than the hydrophilic backbone of the dsDNA, bind on CNTs; the binding mode changes on charged CNTs: The backbone is attracted to a positively charged CNT but there is no dsDNA binding on a negatively charged CNT. By monitoring the shift of peak positions in the optical fluorescence spectrum, a recent study [4] revealed that the dsDNA helix on the CNT gradually switches its configuration from that resembling the B-form of dsDNA to the Z-form, due to the increase in ionic concentration (Figure 3.6).

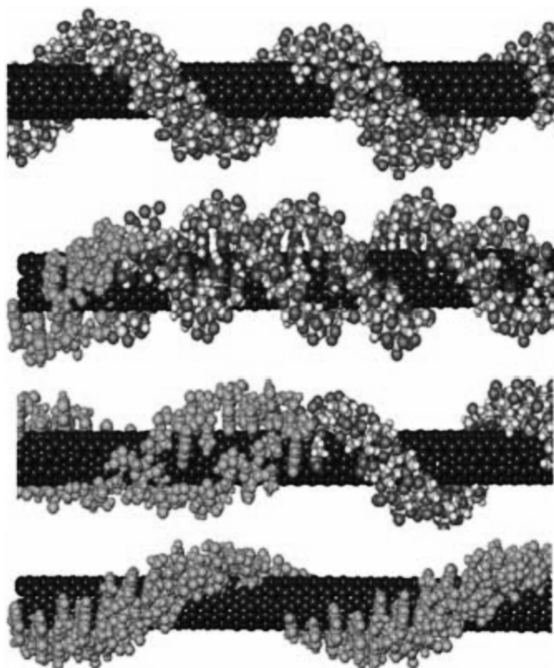


FIGURE 3.6 The dsDNA helix on CNT changes continually from the right-handed B-form to the left-handed Z-form upon the increase of ionic concentration in the solution. (Adapted from ref. 4, with permission. Copyright © 2006 American Association for the Advancement of Science.)

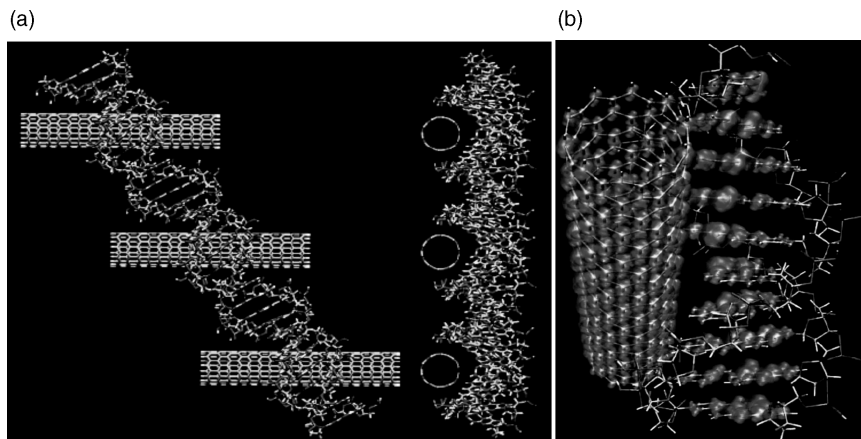


FIGURE 3.7 CNT array in contact with dsDNA: (a) CNTs are incorporated into the major groove of dsDNA; (b) charge density distribution of an electronic state that is 0.7 eV below the HOMO, involving charge distribution on both the DNA and the CNT components.

3.2.4 Integration of DNA and a CNT Array

DNA could effectively disperse CNTs into an aqueous solution either as an individual single tube or as bundles [37], where there may be many DNA stands wrapped around the same CNT or the same bundle. On the other hand, it is interesting to consider the possibility of a single DNA molecule binding and connecting several CNTs, in particular a CNT array. The reasons for considering this are: (1) with multiple signal channels, a CNT array could provide a means of sequencing DNA more effectively [12]; and (2) the DNA-connected and assembled CNTs could form useful components of devices for novel electronic applications. A recent study of such a system considered a (10,0) CNT array bound into the major groove of dsDNA [15] (see Figure 3.7). The DNA–CNT interaction reveals effective electronic coupling between the two components, demonstrated by the electronic density distribution of a state 0.7 eV below the highest occupied molecular orbital (HOMO). Interestingly, this contact results in the HOMO state localized exclusively on the CNT and the LUMO (lowest unoccupied molecular orbital) state localized exclusively on the DNA component. A nanoscale electronic switch device, which involves electronic transport in the two perpendicular directions, could be the result of this coupling. Similar contact is also found for the ssDNA as a “molecular wire” connecting a CNT array [12].

3.2.5 DNA Inside CNT Pores

DNA strands could not only bind strongly on the outer surface of CNTs, they could also enter the inner pore of CNTs. The insertion of DNA into nanotubes is interesting because of its relevance to drug delivery and to DNA translocation experiments through nanopores [40], which may be a promising method for DNA detection through

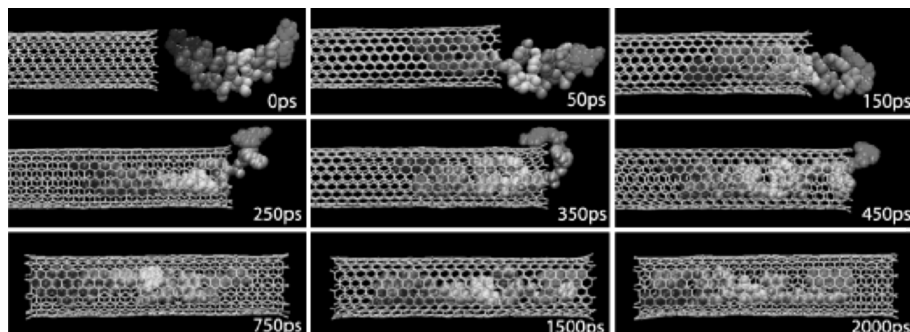


FIGURE 3.8 Insertion dynamics of a ssDNA (dA_8) into the CNT (10,10) from molecular dynamics simulations. (Adapted from *Annual Review of Materials Research*, Vol. 34, p. 123, with permission. Copyright © 2004 Annual Reviews.)

electrical means. DNA insertion into CNT was first considered in MD simulations by Gao et al. [7]. Figure 3.8 shows the dynamics of a ssDNA (8 Å bases) entering a (10,10) nanotube [8]. Initially, CNT and DNA are separated by 6 Å and aligned along the tube axis. The bases start to fill into the nanotube quickly; at time $t = 50$ ps, the first three bases have entered the inner pore of the CNT. The process continues until six out of eight bases fill up the nanotube, at around $t = 200$ ps. The entrance of the last two bases is somewhat hindered during $t = 250$ to 500 ps, due to their interaction with the tube end and the outer surface of CNT. Afterward, the full ssDNA is encapsulated within the inner pore of CNT and reaches the equilibrium state. The van der Waals interaction between the base and the CNT wall is found to be dominant during this insertion process; this is evidenced by the fact that no ssDNA insertion is observed when this interaction is artificially reduced by half. On the other hand, hydrophobic interactions also contribute because polypeptide molecules, which have similar van der Waals interaction with the CNT wall but are less hydrophobic, are hindered in the encapsulation process. The tube size plays a critical role for the DNA insertion: The diameter of the (8,8) CNT (10.8 Å) may be the critical size for ssDNA insertion, below which ssDNA does not enter the CNT pore. The insertion process is also slightly sequence dependent, with purine nucleotides being easier than pyrimidine nucleotides to encapsulate. Finally, double-stranded DNA could also be inserted into the nanotube pores with larger diameters (>27 Å), with the hydrogen bonds between the two complementary strands being partially broken. It was subsequently confirmed by TEM experiments [9] that a DNA strand can indeed be encapsulated into single-walled CNT pores, as observed. The critical issue there is to use radio-frequency and direct-current electric fields for the DNA solution in order to stretch the randomly coiled DNA strands and to irradiate DNA into the CNT coated on the electrode.

Very interestingly, a recent study based on molecular dynamics simulations suggests that the single-stranded RNA molecules can be transported effectively through a transmembrane carbon nanotube (14,14) within a few nanoseconds [41]. The realistic system comprises bare or edge-decorated nanotubes embedded into a dodecane membrane or a lipid bilayer in the aqueous solution. The RNA transport

undergoes repeated stacking and unstacking processes, due to the influence of the steric interaction with the head groups of membrane molecules and the hydrophobic CNT wall. Inside the CNT pore, the RNA structure is reorganized with its backbone solved by water near the CNT axis and its bases aligned with the CNT inner wall.

3.3 ELECTRONIC STRUCTURE

3.3.1 Polarization and Charge Transfer

An essential aspect of the DNA–CNT interaction, and a cornerstone of ultrafast DNA sequencing approaches based on such a combined system, is the electronic structure of its components. The electronic properties of the DNA–CNT can be studied through first-principles quantum mechanical calculations at the single-nucleotide level [24,42]. The interaction between nucleosides and a CNT is illustrated in Figure 3.9(a): In this figure, the density isosurfaces of the charge density difference upon adsorption of nucleoside *A* on the CNT is shown as a representative example of the CNT–nucleoside interaction. The interaction mainly involves the π orbitals of the base atoms, especially the NH_2 group at its end and of the carbon atoms in the CNT. The sugar group of the nucleoside, on the other hand, shows little perturbation in its electronic cloud, mainly in the region proximate to the CNT.

The mutual polarization of π orbitals in the DNA base and the CNT is more obvious in the planar-averaged charge density along the normal to the base plane, shown in Figure 3.9(b). Upon adsorption, the base plane of adenine is positively charged with electron accumulation (near the base) and depletion (near the CNT) in the region between the two components. Integrating this one-dimensional charge distribution in the base and the CNT region, respectively, reveals a net charge transfer of $0.017e$ from *A* to CNT, assuming that the two components are partitioned by the zero difference-density plane close to the CNT wall. This net charge transfer of $0.017e$ from the base to the CNT is rather small compared to that for a typical chemical bond, but is consistent with the weak van der Waals type of interaction between nucleosides and the CNT in this physisorbed system. Moreover, small though it is, this net charge transfer may produce an enhanced sensitivity in the CNT walls for the detection of molecules attached to it, through measuring, for instance, the shift of Raman peaks in the CNT vibrational modes [43].

A detailed analysis of the contributions to the total energy of the system reveals that the attraction between the nucleoside and the CNT is due to exchange–correlation (XC) interactions. Figure 3.10 shows the total energy and the decomposed XC energy and kinetic energy of Kohn–Sham particles as functions of the distance between the DNA base *A* and the CNT wall. We find that the total energy has a minimum at $d = 3.0 \text{ \AA}$, where the XC energy is negative and the kinetic energy is positive, indicating that the nucleoside–CNT attraction arises from XC effects. Beyond the equilibrium distance, the kinetic energy is lowered and has a minimum at $d = 3.75 \text{ \AA}$, while the XC energy keeps increasing and even becomes repulsive in the range $d = 4$ to 5.5 \AA . Similar results were found for *A* adsorbed on graphite [29] and on Cu(110) [44].

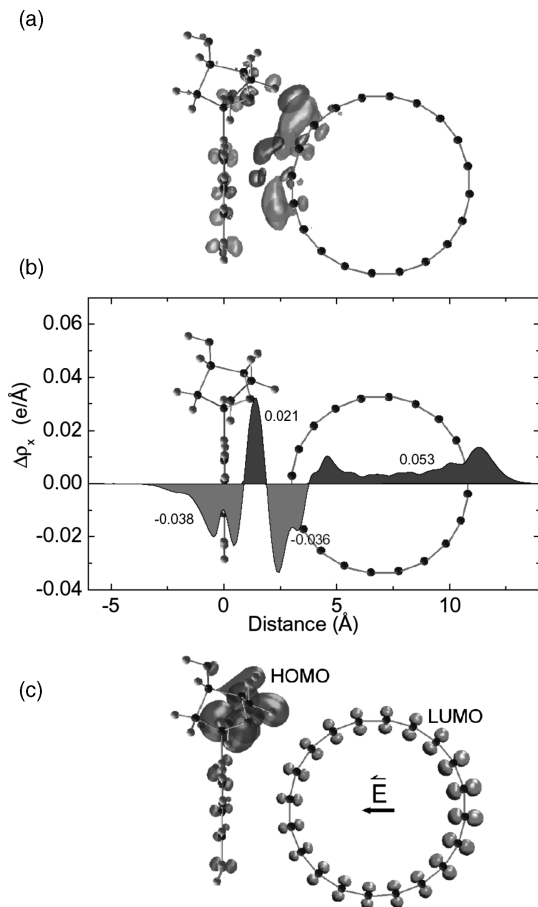


FIGURE 3.9 (a) Isosurfaces of the charge-density difference at levels of $\pm 0.002 e/\text{\AA}^3$ in superposition to the atomic structure for A-nucleoside on CNT. The charge-density difference is obtained by subtracting the charge density of the individual A-nucleoside and CNT systems, each fixed at their respective configurations when they are part of the A/CNT complex, from the total charge density of the A/CNT combined system: $\Delta\rho = \rho[A/CNT] - \rho[A] - \rho[CNT]$, where ρ is the charge density. Electron accumulation and depletion regions are shown in black and gray, respectively. (b) Planar-averaged charge density along the normal direction to the base plane, illustrating the mutual polarization of π orbitals. (c) Isosurface of the density of the HOMO and LUMO states of the combined A/CNT system in the presence of an external electric field of $+0.5 \text{ V/\AA}$.

In electric measurements of the DNA–CNT system, a gate voltage is usually applied to control the conductance [16], while the STM tip itself introduces a field on the order of 0.1 V/\AA . It is therefore interesting to investigate the response of the CNT–DNA system to the applied electric field. We studied this effect by treating the field as a planar dipole layer in the middle of the vacuum region. The external field affects the interaction energy significantly, which depends sensitively on the polarity,

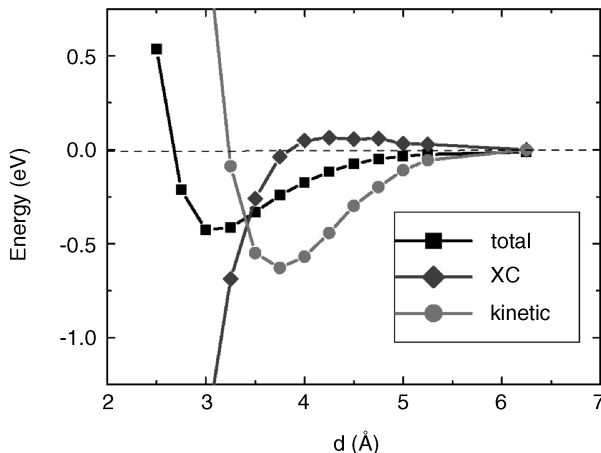


FIGURE 3.10 Relative total energy, decomposed exchange–correlation (XC) energy, and kinetic energy of Kohn–Sham orbits as functions of the base–CNT distance (d) for the DNA base A adsorption on CNT (10,0).

while it leaves almost unchanged the structural features of the system. Taking A–CNT as an example, we find that although a negative field $E_{\text{ext}} = -0.5 \text{ V/\AA}$ (which corresponds to the CNT being negatively charged) hardly changes the adsorption energy (0.436 eV), this energy increases significantly to 0.621, 0.928, and 1.817 eV under external fields of $E_{\text{ext}} = +0.25$, $+0.5$, and $+1.0 \text{ V/\AA}$ (corresponding to the CNT being positively charged). Here the adsorption energy is defined as the energy difference between the total system under E_{ext} with respect to the energy of the CNT under E_{ext} and the free nucleoside. The increase in binding energy under positive electric field is due to the fact that a positive field facilitates the polarization and charge transfer from the base to the CNT. The base–CNT distance, on the other hand, changes only slightly: it is 0.04 Å larger than the zero field value for $E_{\text{ext}} = -0.5 \text{ V/\AA}$ and 0.04 Å smaller for $E_{\text{ext}} = +1.0 \text{ V/\AA}$, respectively. The most prominent change in structure comes from the angle that the NH_2 group at the end of the base makes with the base plane [Figure 3.9(c)]. This angle changes from -27° at $E_{\text{ext}} = -0.5 \text{ V/\AA}$ to $+25^\circ$ at $E_{\text{ext}} = +1.0 \text{ V/\AA}$, indicating the softness of the C– NH_2 bond. The configuration under positive field resembles that on Cu(110) [44]. Other nucleosides have the same behavior given their similarity in structure. Therefore, the applied electric field stabilizes the DNA bases on the CNT without disturbing the zero-field adsorption geometry. The more profound effect of the electric field lies in the change of electronic structure; for instance, the HOMO and LUMO become spatially separated under an external field of $E_{\text{ext}} = +0.5 \text{ V/\AA}$, with the first localized on the nucleoside A and the second on the CNT, as indicated in Figure 3.9(c).

We have discussed in some detail the DNA–CNT interaction at the single-base level. In reality, when a DNA strand comes into close contact with a CNT, the interaction between them can be approximated as the superposition of the interactions of individual base–CNT units, which depends on the base identity. This is exemplified

by the overlap of charge distribution on both components in the dsDNA–CNT structure in Figure 3.7. The polarizability of the combined DNA–CNT system might be screened by the bound DNA strand, depending on the DNA density and geometry and on the nanotube diameter and chirality. We expect that thermal fluctuations of counterions and water will average out to a zero net contribution to the local field around the DNA–CNT system.

3.3.2 Density of States

The electronic density of states (DOS) describes the energy-level distribution of electrons and is a quantity directly accessible to experimental measurements: for example, through the differential current–voltage (dI/dV) in scanning tunneling spectroscopy (Figure 3.1). The characteristic features of the electronic structure for single DNA nucleoside adsorption on CNT is shown in the DOS plot of Figure 3.1(b) and in more detail in Figure 3.11. In Figure 3.1(b), the DOS peaks for the combined nucleoside–CNT system differ significantly from those of the bare CNT. The energy gap calculated for the CNT is 0.8 eV [45]. The difference in DOS between the bare CNT and the combined CNT–nucleoside system [Δ DOS, red curve in Figure 3.1(b) and all curves in Figure 3.11(a) and (b)] has features that extend through the entire range of energies; those close to the Fermi level are the most relevant for our discussion. These features can serve as the signal to identify DNA bases in current–voltage measurements or photoelectron spectroscopy. This “electronic fingerprint” is independent of the relative orientation of the nucleoside and the CNT, as shown in Figure 3.11; the Δ DOS for the three to four dominant configurations of the four nucleosides on CNT have essentially the same features. However, the Δ DOS peaks for *different* bases differ significantly from each other, which is encouraging as far as base identification is concerned. In Figure 3.11(c) and (d) we show the positions of the first peak below and above the Fermi level in the Δ DOS plots for A, C, G, and T adsorbed on the CNT. These two peaks correspond to the HOMO and LUMO of the bases, respectively. The spatial distribution of the corresponding wavefunctions for all four DNA bases is shown in Figure 3.12. We found that in the DOS plots of Figure 3.11(a) and (b), the HOMO and LUMO positions of the different bases are clearly distinguishable, while for a given base, the different adsorption geometries produce essentially indistinguishable peaks.

When a gate voltage is applied, the HOMO and LUMO peaks of the bases shift continuously with respect to the CNT DOS features. The latter change little under small gate voltage or electric field. For example, the bandgap of the CNT shrinks by only 0.03 eV for a field of $E_{\text{ext}} = 0.5 \text{ V/\AA}$ relative to its zero-field value. As is evident from Figure 3.11(c) and (d), it is possible to induce a shift of the DNA base peaks relative to the CNT features with external voltage so as to facilitate experimental measurements. The CNT HOMO and LUMO orbitals serve as a definitive, easily distinguishable reference in evaluating DOS features of the adsorbed DNA nucleosides. The HOMO and LUMO peaks of all DNA bases shift monotonically with applied external field, by about 0.7 eV for $E_{\text{ext}} = 0.25 \text{ V/\AA}$. Interestingly, when the external field is sufficiently large, the HOMO of all four bases falls within the bandgap

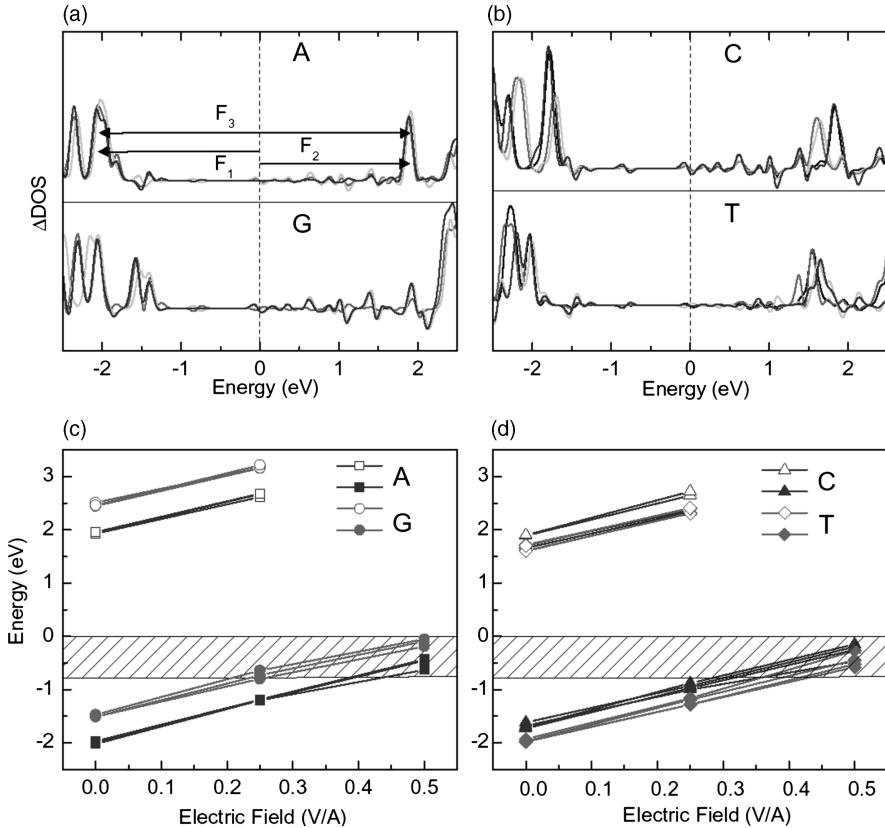


FIGURE 3.11 Density of states. (a), (b) DOS difference, Δ DOS, for the dominant nucleoside configurations on the nanotube. The zero of the energy scale is set to the conduction band minimum of the CNT. The features F_1 , F_2 , and F_3 energy separations between different orbitals, are identified. (c), (d) Variation of the HOMO energy level (open symbols) and the LUMO energy level (open symbols) of the four nucleosides on CNT, as a function of the magnitude of applied electric field. The shaded area is the energy gap of the CNT.

of the CNT [Figure 3.11(c) and (d)], which should enhance the sensitivity of experimental measurements to the type of base. At the highest field we studied, $E_{\text{ext}} = 0.5 \text{ V/\AA}$, the bandgap of the combined CNT–DNA systems is 0.51 eV for A, 0.45 eV for T, 0.27 eV for C, and 0.11 eV for G, on average, sufficiently different from each other to be clearly distinguished.

3.3.3 STM Images

For a direct real-space identification of DNA bases on CNT, a scanning tunneling microscopy (STM) image would be useful. We have simulated the STM images based on the Tersoff–Hamann theory [46]. The STM images in Figure 3.13 correspond to an

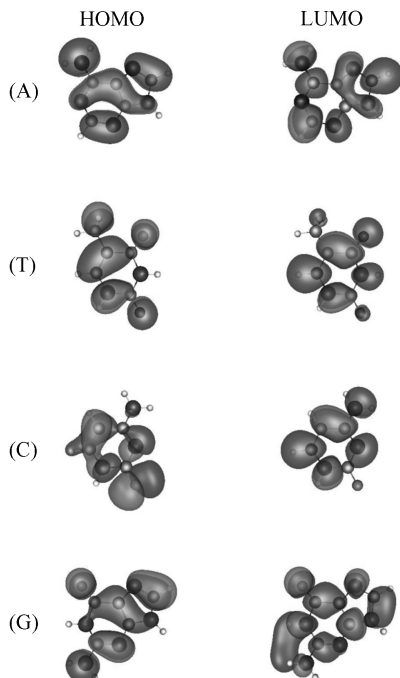


FIGURE 3.12 Wavefunctions of the HOMO and LUMO states for the four DNA bases. Black and gray clouds indicate positive and negative values.

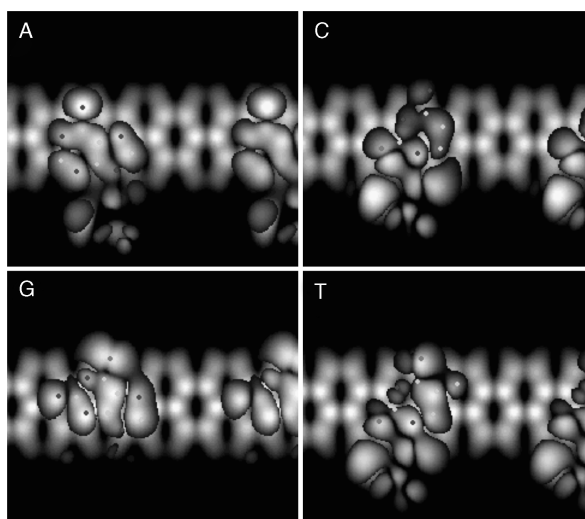


FIGURE 3.13 Simulated STM images of DNA bases on the (10,0) CNT. Small dots indicate the positions of the heavy atoms in the bases (light gray for C, black for N, and dark gray for O).

applied voltage of +1.4 V, which integrates the charge densities of states within the energy range -1.4 to 0 eV below the HOMO (including HOMO). It is clear that the STM images for the four DNA nucleoside have different spatial characteristics, which, with sufficient image resolution, could provide identification of the four bases directly. The STM images have a correspondence to the wavefunctions of DNA bases shown in Figure 3.12, as long as the energies of those states fall in the correct range of -1.4 to 0 V below the HOMO of the CNT.

3.4 OPTICAL PROPERTIES

The combination of DNA and CNT structures exhibits interesting optical properties that are accessible by standard optical measurements, including Raman, infrared–visible–ultraviolet (UV) absorption, dichroism, and fluorescence spectroscopy. The advantage is that as CNTs show rich and characteristic optical signatures, the changes in these easily measurable optical signals resulting from the presence of DNA strands wrapped around the CNT could be used as an identifier for the attached DNA strand. It would be helpful if these changes are sequence dependent and if they were sensitive at the single-base level. If the level of sensitivity can be established, these considerations suggest the development of novel DNA detection and sequencing methods based on optical signals.

The simplest system for addressing this issue is a DNA homopolymer wrapped around a CNT. Hughes et al. [47] have recently measured the UV–visible absorption of ssDNA homopolymers consisting of about 30 bases wrapped around CNTs in aqueous solution. Different DNA homopolymers show significant differences in optical absorption (both magnitude and peak positions) in the ultraviolet range 200 to 300 nm. The difference between absorption by the DNA–CNT combined system and the isolated, bare CNT, which constitutes the absorption signature of the DNA strand attached to the CNT wall, is shown in Figure 3.14 for the DNA homopolymers poly(dA), poly(dC), poly(dG), and poly(dT). There are significant differences from case to case in terms of absorption peak positions and their relative intensity. For instance, there are two peaks for A, at 266 and 213 nm, with the second having twice the intensity of the first; there are also two peaks, at 275 and 204 nm, for C, with the first peak showing higher intensity.

In the experimental measurements, there are significant changes in the spectrum of DNA on the CNT compared with that of free ssDNA in solution. For example, the first peak, centered at 260 nm, for free poly(dA) is red-shifted to 266 nm when A is adsorbed on CNT, and the peak at 203 nm is shifted to 213 nm. Similar changes are found in the various spectra of the other three bases. For poly(dC), the broad peak at 230 to 250 nm diminishes, the peak at 200 nm is reduced by half, while the peak at the longest wavelength (310 nm) does not change. For G, the peak at 275 nm remains constant while the peak at 248 nm is reduced by half and the peak at 200 nm increases slightly after adsorption on CNT. For T, there is no apparent change for the peak at 270 nm, while the adsorption in the range 210 to 240 nm is reduced significantly. The origin for these spectrum changes on DNA binding on CNT must be related to

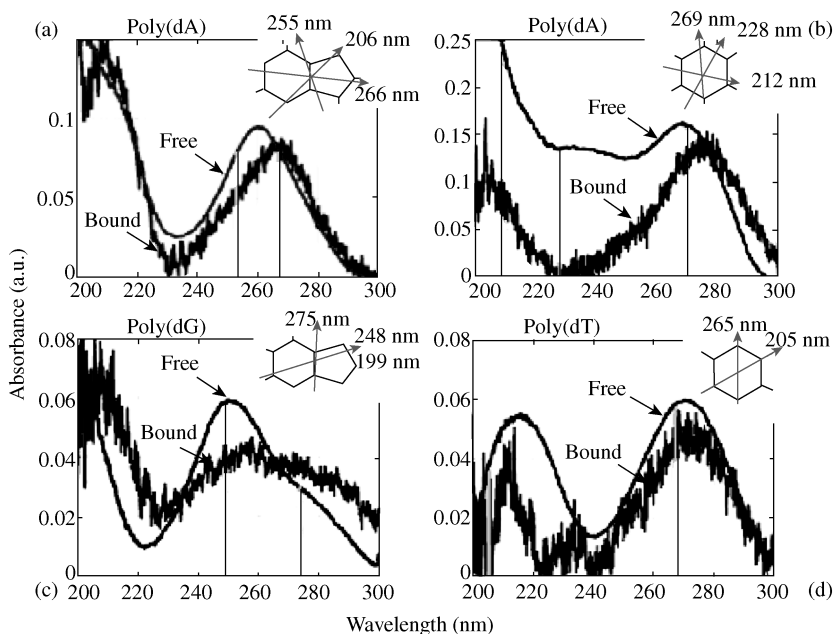


FIGURE 3.14 Optical adsorption of ssDNA homopolymer on CNT (thick lines) and in free solution (thin lines). (From ref. 47, with permission. Copyright © 2007 American Chemical Society.)

corresponding changes in electronic structure, which can be elucidated only through detailed theoretical calculations.

To address this issue, we have calculated orientation-dependent absorption spectra of DNA bases adsorbed on single-walled CNTs [48], as shown in Figure 3.15. We compare the spectrum of the DNA base along each polarization direction of incident light (the direction of the electric field vector) with the spectrum measured experimentally for the combined ssDNA–CNT systems. From these comparisons, all the features described above can be reproduced accurately in our calculations by considering the absorption of the base along a certain light-polarization direction only. CNTs have a dominant, intrinsic, and diameter-independent absorption peak in the ultraviolet region at 236 nm with polarization perpendicular to their axis [49]. Therefore, only photons with polarization parallel to the CNT axis are available to interact with the attached DNA bases, or equivalently, the nanotube produces a local electric field aligned along its axis (the *hypochroism effect*). This explains why the absorption spectra of the DNA bases change when they are attached to the nanotube wall: The direction of tube axis is indeed the preferred direction for UV absorption by the bases.

Consequently, the agreement of the calculated changes in absorption with the experimental results strongly suggests that there is a preferred absorption direction for the bases on the CNT, a desirable feature favoring ultrafast DNA sequencing based on optical properties of this system. This result is further supported by the comparison

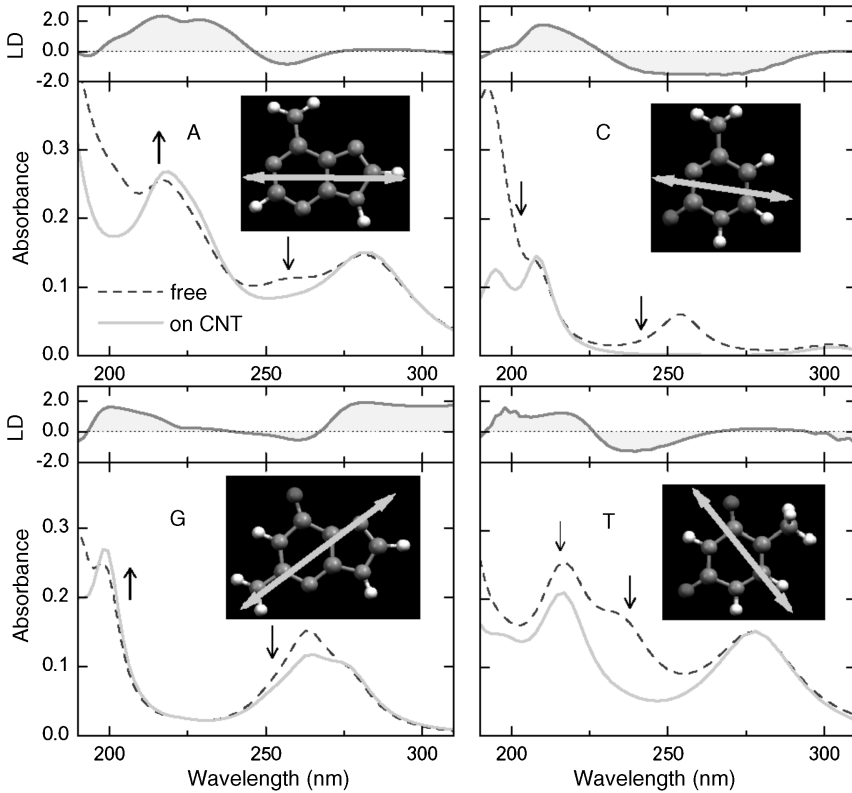


FIGURE 3.15 Absorption spectrum of DNA bases averaged over all field directions (dashed lines) and along a particular direction (indicated by double-headed arrows in the insets) that mimics the nanotube axis (solid line). These spectra reproduce adequately the experimentally measured spectra in solution. Vertical arrows indicate intensity changes in experimental spectra after base adsorption on the CNT. Linear dichroism spectra that best match experiment are also shown on top of each panel.

between the calculated linear dichroism curves and the measured ones [50]. In the insets of Figure 3.15 the lines show the direction of the CNT axis along which the experimental absorbance spectra of ssDNA wrapped on CNTs are best reproduced. The orientations of the nanotube axis relative to the bases as determined from this approach agree well with the global energy-minimum structures from force-field calculations, the only exception being T. Specifically, the directions of the nanotube axis from absorbance spectra, linear dichroism, and structural optimization are: 89° , 105° , 98° for A; -100° , -84° , -90° for C; -58° , -30° , -61° for G; and 39° , 40° , 75° for T. Overall, the agreement between experiment and theory is very reasonable given the complicated nature of both the experimental measurements and theoretical results. This provides a way to determine the base orientation relative to the nanotube axis in the DNA–CNT system from the optical absorption data.

Besides determining the base orientations, the optical spectra of the DNA–CNT systems are also used for identifying the types of enriched CNTs [2], sensing sugar in solutions [5], detecting DNA hybridization [17], and monitoring morphology changes of DNA on CNTs [4], as discussed in more detail below.

3.5 BIOSENSING AND SEQUENCING OF DNA USING CNTs

3.5.1 Gaseous Sensing Using DNA–CNT

One of the most successful applications of DNA–CNT systems has been the detection of chemical substances [51]. In such applications, the presence of certain molecules can be converted into electric signals: DNA is used as the chemical recognition site and single-walled CNT field-effect transistors (FETs) as the electronic readout unit. The fundamental principles here are that CNTs, as either a metallic system or a narrow bandgap semiconductor, can conduct electricity and be used in a FET, and that the conductivity of CNTs is strongly influenced by the presence of functional groups, either covalently bound to the CNT walls or ends, or physically adsorbed on the CNT wall, especially wrapped DNA. Gaseous molecules or other chemicals induce a change in the configuration or electronic structure of the bound DNA, due to its large structural variability, which in turn results in a change in the conductivity of the CNT–FET. We discuss next two specific applications of this type.

Figure 3.16(a) shows schematically the device setup made of ssDNA–CNT [14]. The chemical formula of some ordinary gases to be detected is shown in (b), and results are demonstrated in Figure 3.16(c)–(e). Due to its chemically inert nature, the bare CNT is not sensitive enough to have a detectable conductivity change when the gas odors of propionic acid, trimethylamine, and methanol are passing through the device channels. The situation changes, however, for the ssDNA-decorated CNTs, which exhibit a sensitive interaction between the gases and the ssDNA on the CNT. Conductivity changes due to the various gas odors differ in sign and in magnitude, and can be tuned by choosing different DNA base sequences. For example, propionic acid and methanol give positive (increase) and negative changes (decrease) in electric conductivity of the CNT wrapped with a ssDNA sequence of 5′GAGTCTGTGGAGGAGGTAGTC3′ [Figure 3.16(e)], making this ssDNA–CNT structure a sensitive detector. The sensing device is robust and sustains at least 50 gas exposure cycles. It is rapid in response and recovers in seconds in airflow. All these attributes make this device promising as an electronic “nose” or “tongue” for molecular detection, disease diagnosis, and home security applications. Recently, a counterpart DNA–CNT device for detecting glucose in a biology-relevant environment in the presence of the glucose oxidase enzyme was developed [5].

3.5.2 Field-Effect Transistor and Optical Shift for DNA Detection

An even more challenging issue is the detection of DNA strands using bare or DNA-decorated CNTs. There are, however, some successful examples of DNA detection

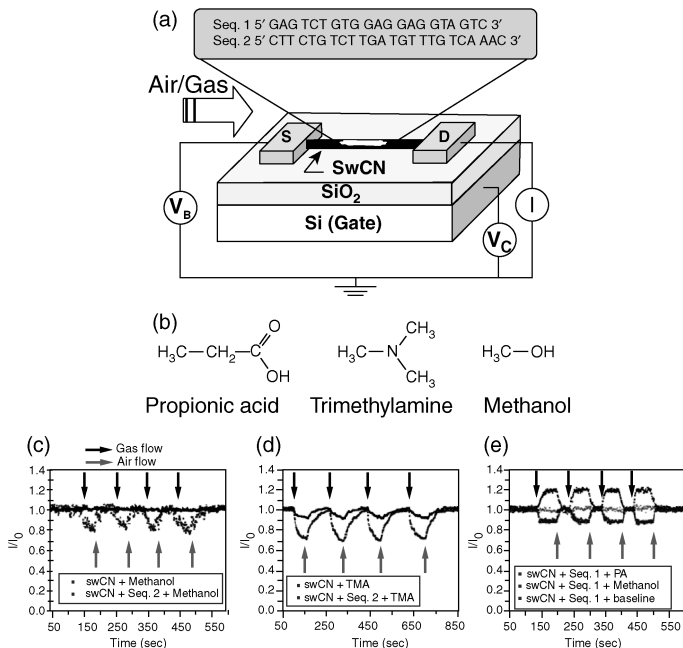


FIGURE 3.16 ssDNA-CNT as a chemical sensor: (a) device setup; (b) molecules to be detected; (c–e) responses in conductivity to gaseous flows and recovery in air using bare and DNA-decorated CNTs. Two different ssDNA sequences are employed as shown in (a). PA, propionic acid; TMA, trimethylamine. (Adapted from *Nano Letters*, Vol. 5, p. 1174, with permission. Copyright © 2005 American Chemical Society.)

using devices made of ssDNA-CNT, through either electric [12,16] or optical means [17]. For instance, the source-drain conductance measurement of the CNT FET device shows a large shift (decrease) in conductivity for the bare and the ssDNA-wrapped CNTs [16]. The conductivity is lowered further in the presence of other DNA strands; the complementary strand (cDNA) to that incubated onto the CNTs shows the largest reduction in conductance, while a noncomplementary strand (ncDNA) shows fewer pronounced changes or no change at all. This conductivity drop also depends sensitively on the concentration of ssDNA in solution at picomolar to micromolar levels. Therefore, this simple device could be used effectively for label-free detection of the cDNA and its concentration. This method has been demonstrated to have a sensitivity at the level of single-nucleotide mismatch between the two strands. The sensitive dependence of signals on the counterion concentration suggests that the reduction in conductivity upon ssDNA immobilization and hybridization relies on the screening effect of charges around the CNT from the added ssDNA.

The same idea was demonstrated for the detection of DNA hybridization through bandgap fluorescence measurements of the CNTs [17]. The addition of cDNA in the ssDNA-wrapped CNT solution resulted in a 2-meV increase in the emission energy of bandgap fluorescence peak of the nanotube, whereas for a ncDNA strand there is little

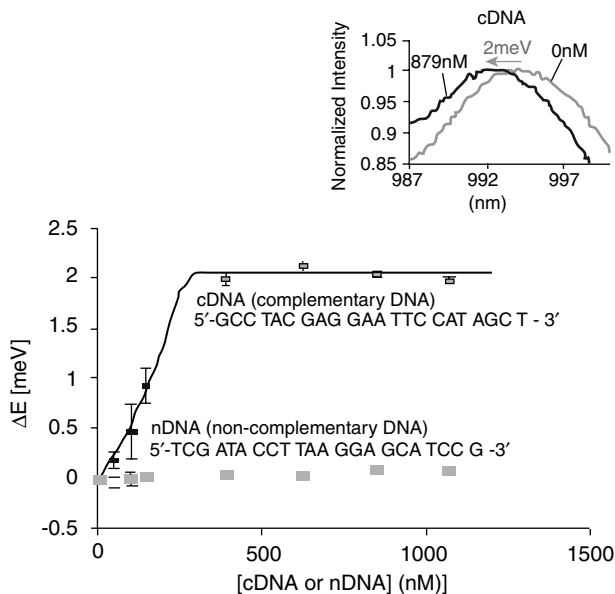


FIGURE 3.17 Optical DNA detection. Addition of complementary DNA (cDNA) strand to the ssDNA-wrapped CNT solution causes an energy increase in the CNT bandgap fluorescence peak, while there is no detectable change for adding noncomplementary strands. The peak shift is dependent on the cDNA concentration. Insert: sample spectra showing a blue shift in the fluorescence peak with cDNA addition. (From ref. 17, with permission. Copyright © 2006 American Chemical Society.)

or no shift (Figure 3.17). Again, this shift of the peak depends almost linearly on the concentration of cDNA from 1 to 400 nM. The energy shift observed in experiments can be interpreted as an increase in the exciton binding energy due to the increased surface area of the CNT covered by ssDNA upon hybridization. This energy shift in the CNT bandgap fluorescence provides an easy way to detect cDNA in solution and to monitor the DNA hybridization process by an optical means. Electronic or optical DNA detection using ssDNA-decorated CNTs has the advantages of being label-free, low cost, highly sensitive, simple, and of high accuracy, and represents an important step toward practical molecular diagnostics.

3.5.3 Monitoring Morphology Changes of dsDNA

As mentioned earlier, the change of the dsDNA from the right-handed B-like form to the left-handed Z-like form can also be monitored by measuring the optical responses (fluorescence and circular dichroism) of DNA strands on a (6,5) CNT (Figure 3.6), as a response to the increase in divalent metal cation concentration [4]. The assumption is that the surface area of CNT covered by dsDNA increases during the transition from the B to the Z form; thus, the exciton-binding energy of the CNT increases. This is

interesting because it provides an inexpensive way to detect molecular structures in the NANO–BIO hybrid complex at the nanoscale.

3.5.4 DNA Sequencing

All methods discussed so far measure the effects of a DNA strand as a whole. They are very useful for detection of DNA strands, but in terms of DNA sequencing, one has to go a step further and determine explicitly the effect on CNT properties of changes in electronic or optical signals corresponding to a *single nucleotide*. We discussed in Section 3.3 the fact that the four nucleosides introduce characteristic peaks in the density of states of the DNA–CNT complex, which points to the possibility of employing these characteristics for DNA single-base detection and DNA sequencing. The setup we envisaged for this purpose is shown in Figure 3.1: A fragment of ssDNA is brought into close contact with the CNT and wraps around it partially. A force can be exerted on one end of the DNA: for example, by attaching to a bead that can be manipulated by optical [52] or magnetic means [53]. This will lead to a situation in which a few (even a single) base is in intimate contact with the CNT. By pulling the ssDNA fragment, the bases along it will interact successively with the CNT, allowing for measurements of the interaction. A setup in which the CNT can rotate in synchronization with the DNA pulling process may facilitate the motion.

Inspired by the calculations of the DOS of the nucleoside–CNT complex, the present authors and collaborators have proposed measuring the electronic structure to identify bases by a probe sensitive to local electronic states, such as scanning tunneling spectroscopy, using a stationary STM tip in the geometry similar to that described by Kong et al. [54]. This type of method has a high resolution of about 2 Å and is used routinely to investigate the local electronic structure of adsorbates on semiconductor surfaces. For example, local density of states of aniline ($C_6H_5NH_2$) on Si(100) was clearly measured [55]. To maximize the sensitivity of such measurements, it is desirable to have a semiconducting CNT as the substrate. Such a setup also overcomes the difficulty in the older proposals of distinguishing DNA bases by measuring the transverse conductance of an electrode–ssDNA–electrode junction, where it was found that transverse conductance cannot be used to distinguish nucleotides because ssDNA is too flexible when in the neighborhood of the electrode [21]. In our case the DNA bases are bound on the CNT at a constant distance of 3.4 Å from the CNT wall and with a definitive orientation, as we have shown in Sections 3.2 and 3.4, forming a very stable and robust DNA–CNT complex, which would constrain the DNA–electrode geometry in a desired, well-controlled manner. The device proposed in Figure 3.1 serves only as an idealized case in point to illustrate the key concepts. We note that there may exist several equivalent experimental setups toward the same goal. For instance, sequentially embedding the ssDNA–CNT structure into a nanopore and measuring the transverse conductance from the CNT to the nanopore wall could be an equally promising approach.

To test the validity of the proposed detection of DNA bases, we evaluated the efficiency of base identification using data generated from the Δ DOS calculations as

input to a neural network classifier, which was trained to produce as output the label of the DNA base (A, C, G, or T). Specifically, we extracted six simple representative features (F_i , $i = 1$ to 6) in an energy window from -3 to 3 eV around the Fermi level:

- F_1 : location of the base HOMO
- F_2 : location of the base LUMO
- F_3 : bandgap of the base (LUMO–HOMO distance)
- F_4 : number of prominent peaks below the Fermi level
- F_5 : location of the highest occupied peak
- F_6 : integral of the occupied states from -3 to 3 eV

Features F_1 , F_2 , and F_3 are indicated in Figure 3.11 for A/CNT. We produced a robust scheme for identifying the bases by employing artificial neural networks [56] and find that the network can deliver 100% efficiency even after taking into consideration the measurement errors (e.g., an error of ± 0.10 eV in energy). For practical applications it is important to evaluate the significance of each feature individually. To this end, we tested the discriminating ability of each of the six features defined and found that the location of base HOMO–LUMO (F_1/F_2) and the HOMO–LUMO gap (F_3) are the most informative features, while the number of occupied states (F_4) and the location of the highest peak (F_5) are less so. The HOMO–LUMO gaps alone, which are 3.93 to 4.02 eV for A, 3.34 to 3.62 eV for C, 3.93 to 4.02 eV for G, and 3.58 to 3.69 eV for T, could easily discriminate A and G from C and T. Certain features are complementary, and combinations of just two features can actually yield 100% efficiency. For instance, if the location of HOMO (-2.02 eV for A, -1.68 eV for C, -1.51 eV for G, and -1.98 eV for T), which is well defined in experiments with respect to the DOS peaks of the CNT, is used in addition to the HOMO–LUMO gap, A is easily discriminated from G (and C from T), resulting in 100% efficiency for the combination of features F_1 to F_3 . The external field magnifies these differences, making the base classification even more robust. With a field of 0.25 eV/Å, several triplets of features produce 100% efficiency in base identification.

3.6 SUMMARY

We have reviewed the fundamental aspects of DNA interaction with CNTs and have discussed the prospects of DNA sensing and sequencing using DNA–CNT complexes. Due to the large variety in structures of the two components, such as different diameters, chiralities, conducting properties, single- or multiwalled CNTs, isolated CNTs or bundles of CNTs, and single- or double-stranded DNA as well as different forms, various lengths, and different sequences, the combined DNA–CNT system exhibits a truly rich variety of artificial nanostructures, for which wide applications can be envisaged. Among them, the most significant might be the robust helical structure formed by wrapping DNA around a CNT, which has characteristic structural and

electronic features, that may enable ultrafast DNA sequencing. To this end, the most important properties of the DNA–CNT complex are:

- Long genomic single-stranded DNA can wrap around a single-walled CNT, forming a tight, stable helix. The lateral periodicity remains constant for any single ssDNA–CNT, but is dependent on the CNT diameter and the DNA sequence.
- The bases in the ssDNA are almost fixed in geometry bound on the CNT. They are stabilized at 3.4 Å away from the CNT wall through mainly van der Waals attraction and the hydrophobic effect. Although a very large number of nonequivalent configurations may be present, only a few of them are dominant. Moreover, each type of base prefers to have a definite orientation with respect to the CNT axis: 90° for A, 80° for C, 120° for G, and 40° for T.
- Because DNA bases are attached rigidly to the CNT, the noise in transverse conductance measurements can be minimized. Our quantum mechanical calculations show that the four types of nucleotides introduce distinct characteristic features in the local density of states. These features are easily recognizable and produce 100% accuracy in our artificial neural network for DNA base identification.

Based on these observations, we suggest that the DNA–CNT system is very promising in terms of DNA detection and DNA sequencing through electronic means, upon which a low-cost, ultrafast, accurate, and largely parallel DNA sequencing method could eventually be built. In addition, this system can be the basis for diverse applications, combining the robustness of CNTs with the flexibility of DNA in a unique building block that blends artificial and natural materials at the nanometer scale.

Acknowledgments

It is a pleasure to acknowledge the numerous original contributions to the work reviewed here by our collaborators: P. Maragakis, G. Lu, C. Papaloukas, and W. L. Wang. The original work was supported in part by grants from the U.S. Department of Energy and the Harvard University Center for the Environment. We are indebted to M. Fyta, M. Hughes, F. Albertorio, J. Golovchenko, and D. Branton for helpful discussions.

REFERENCES

1. Zheng M, Jagota A, Semke ED, et al. DNA-assisted dispersion and separation of carbon nanotubes. *Nat. Mater.* 2003;2:338–342.
2. Zheng M, Jagota A, Strano MS, et al. Structure-based carbon nanotube sorting by sequence-dependent DNA assembly. *Science.* 2003;302:1545–1548.
3. Gigliotti B, Sakizzie B, Bethune DS, Shelby RM, Cha JN. Sequence-independent helical wrapping of single-walled carbon nanotubes by long genomic DNA. *Nano Lett.* 2006;6:159–164.

4. Heller DA, Jeng ES, Yeung TK, et al. Optical detection of DNA conformational polymorphism on single-walled carbon nanotubes. *Science*. 2006;311:508–511.
5. Xu Y, Pehrsson PE, Chen L, Zhang R, Zhao W. Double-stranded DNA single-walled carbon nanotube hybrids for optical hydrogen peroxide and glucose sensing. *J. Phys. Chem. C*. 2007;111:8638–8643.
6. Gladchenko GO, Karachevtsev MV, et al. Interaction of fragmented double-stranded DNA with carbon nanotubes in aqueous solution. *Mol. Phys.* 2006;104:3193–3201.
7. Gao HJ, Kong Y, Cui D, Ozkan CS. Spontaneous insertion of DNA oligonucleotides into carbon nanotubes. *Nano Lett.* 2003;3:471–473.
8. Gao HJ, Kong Y. Simulation of DNA–nanotube interactions. *Annu. Rev. Mater. Res.* 2004;34:123–150.
9. Okada T, Kaneko T, Hatakeyama R, Tohji K. Electrically triggered insertion of single-stranded DNA into single-walled carbon nanotubes. *Chem. Phys. Lett.* 2006;417:288–292.
10. Watson JD, Crick FHC. Molecular structure of nucleic acids: a structure for deoxyribose nucleic acid. *Nature (London)*. 1953;171:737–738.
11. Iijima S. Helical microtubules of graphitic carbon. *Nature (London)*. 1991;354:56–58.
12. Li J, Ng HT, Cassell A, et al. Carbon nanotube nanoelectrode array for ultrasensitive DNA detection. *Nano Lett.* 2003;3:597–602.
13. Kam NWS, Liu ZA, Dai HJ. Carbon nanotubes as intracellular transporters for proteins and DNA: an investigation of the uptake mechanism and pathway. *Angew. Chem. Int. Ed.* 2006;45:577–581.
14. Staii C, Johnson AT, Chen M, Gelperin A. DNA-decorated carbon nanotubes for chemical sensing. *Nano Lett.* 2005;5:1774–1778.
15. Lu G, Maragakis P, Kaxiras E. Carbon nanotube interaction with DNA. *Nano Lett.* 2005;5:897–900.
16. Star A, Tu E, Niemann J, Gabriel JP, Joiner CS, Valcke C. Label-free detection of DNA hybridization using carbon nanotube network field-effect transistors. *Proc. Natl. Acad. Sci. USA*. 2006;103:921–926.
17. Jeng ES, Moll AE, Roy AC, Gastala JB, Strano MS. Detection of DNA hybridization using the near-infrared band-gap fluorescence of single-walled carbon nanotubes. *Nano Lett.* 2006;6:371–375.
18. Nakashima N, Okuzono S, Murakami H, Nakai T, Yoshikawa K. DNA dissolves single-walled carbon nanotubes in water. *Chem. Lett.* 2003;32:456–457.
19. Takahashi H, Numao S, Bandow S, Iijima S. AFM imaging of wrapped multiwall carbon nanotube in DNA. *Chem. Phys. Lett.* 2006;418:535–539.
20. Lu Y, Bangsaruntip S, Wang X, Zhang L, Nishi Y, Dai HJ. DNA functionalization of carbon nanotubes for ultrathin atomic layer deposition of high kappa dielectrics for nanotube transistors with 60 mV/decade switching. *J. Am. Chem. Soc.* 2006;128:3518–3519.
21. Zhan XG, Krstic PS, Zikic R, Wells JC, Fuentes-Cabrera M. First-principles transversal DNA conductance deconstructed. *Biophys. J.* 2006;91:L4–L6.
22. Zwolak M, Di Ventra M. Electronic signature of DNA nucleotides via transverse transport. *Nano Lett.* 2005;5:421–424.
23. Lagerqvist J, Zwolak M, Di Ventra M. Fast DNA sequencing via transverse electronic transport. *Nano Lett.* 2006;6:779–782.

24. Meng S, Maragakis P, Papaloukas C, Kaxiras E. DNA nucleoside interaction and identification with carbon nanotubes. *Nano Lett.* 2007;7:45–50.
25. Brooks BR, Bruccoleri RE, Olafson BD, States DJ, Swaminathan S, Karplus M. CHARMM: a program for macromolecular energy, minimization, and dynamics calculations. *J. Comp. Chem.* 1983;4:187–217.
26. MacKerell AD Jr., Bashford D, Bellott RL, et al. All-atom empirical potential for molecular modeling and dynamics studies of proteins. *J. Phys. Chem. B.* 1998;102:3586–3616.
27. Krivov SV, Chekmarev SF, Karplus M. Potential energy surfaces and conformational transitions in biomolecules: a successive confinement approach applied to a solvated tetrapeptide. *Phys. Rev. Lett.* 2002;88:038101.
28. (a) Elber R, Karplus M. Multiple conformational states of proteins: a molecular-dynamics analysis of myoglobin. *Science* 1987;235:318–321. (b) Wales DJ, Scheraga HA. Review: Chemistry—global optimization of clusters, crystals, and biomolecules. *Science* 1999;285:1368–1372. (c) Wales DJ. A microscopic basis for the global appearance of energy landscapes. *Science* 2001;293:2067–2070.
29. Ortmann F, Schmidt WG, Bechstedt F. Attracted by long-range electron correlation: adenine on graphite. *Phys. Rev. Lett.* 2005;95:186101.
30. Gowtham S, Scheicher RH, Ahuja R, Pandey R, Karna SP. Physisorption of nucleobases on graphene: density-functional calculations. *Phys. Rev. B.* 2007;76:033401.
31. For these calculations we employed a periodic supercell with dimensions of $20 \text{ \AA} \times 20 \text{ \AA} \times 12.78 \text{ \AA}$. Larger supercells show minor differences in the structural and electronic features: a sampling of a $1 \times 1 \times 3$ k -point mesh in reciprocal space is used to generate the charge density and the density of states. Gaussian smearing of electronic eigenvalues with a width of 0.1 eV is employed.
32. Freund JE. Ph.D. dissertation. Ludwig-Maximilians Universität München, 1998.
33. Jorgensen WL, Chandrasekhar J, Madura JD, Impey RW, Klein ML. Comparison of simple potential functions for simulating liquid water. *J. Chem. Phys.* 1983;79:926–935.
34. Berendsen HJC, Postma JPM, Nola AD, Haak JR. Molecular-dynamics with coupling to an external bath. *J. Chem. Phys.* 1984;81:3684–3690.
35. Darden T, York D, Pedersen L. Particle mesh Ewald: an $N \log(N)$ method for Ewald sums in large systems. *J. Chem. Phys.* 1993;98:10089–10092.
36. Johnson RR, Johnson ATC, Klein ML. Probing the structure of DNA–carbon nanotube hybrids with molecular dynamics. *Nano Lett.* 2008;8:69–75.
37. Cathcart H, Quinn S, Nicolosi V, Kelly JM, Blau WJ, Coleman JN. Spontaneous debundling of single-walled carbon nanotubes in DNA-based dispersions. *J. Phys. Chem. C.* 2007;111:66–74.
38. Ishibashi A, Yamaguchi Y, Murakami H, Nakashima N. Layer-by-layer assembly of RNA/single-walled carbon nanotube nanocomposites. *Chem. Phys. Lett.* 2006;419:574–577.
39. Zhao XC, Johnson JK. Simulation of adsorption of DNA on carbon nanotubes. *J. Am. Chem. Soc.* 2007;129:10438–10445.
40. Li JL, Gershow M, Stein D, Brandin E, Golovchenko JA. DNA molecules and configurations in a solid-state nanopore microscope. *Nat. Mater.* 2003;2:611–615.
41. Zimmerli U, Koumoutsakos P. Simulations of electrophoretic RNA transport through transmembrane carbon nanotubes. *Biophys. J.* 2008;94:2546–2557.
42. Enyashin AN, Gemming S, Seifert G. DNA-wrapped carbon nanotubes. *Nanotechnology.* 2007;18:245702.

43. Fantini C, Jorio A, Santos AP, Peressinotto VST, Pimenta MA. Characterization of DNA-wrapped carbon nanotubes by resonance Raman and optical absorption spectroscopies. *Chem. Phys. Lett.* 2007;439:138–142.
44. Preuss M, Schmidt WG, Bechstedt F. Coulombic amino group-metal bonding: adsorption of adenine on Cu(110). *Phys. Rev. Lett.* 2005;94:236102.
45. Ebbsen TW. *Carbon Nanotubes: Preparation and Properties*. CRC Press, Boca Raton, FL, 1997.
46. Tersoff J, Hamann DR. Theory of the scanning tunneling microscope. *Phys. Rev. B.* 1985;31:805–813.
47. Hughes ME, Brandin E, Golovchenko JA. Optical absorption of DNA–carbon nanotube structures. *Nano Lett.* 2007;7:1191–1194.
48. Meng S, Wang WL, Maragakis P, Kaxiras E. Determination of DNA-base orientation on carbon nanotubes through directional optical absorbance. *Nano Lett.* 2007;7:2312–2316.
49. Murakami Y, Einarsson E, Edamura T, Maruyama S. Polarization dependence of the optical absorption of single-walled carbon nanotubes. *Phys. Rev. Lett.* 2005;94:087402.
50. Rajendra J, Rodger A. The binding of single-stranded DNA and PNA to single-walled carbon nanotubes probed by flow linear dichroism. *Chem. Eur. J.* 2005;11:4841–4847.
51. Daniel S, Rao TP, Rao KS, et al. A review of DNA functionalized/grafted carbon nanotubes and their characterization. *Sens. Actuators B.* 2007;122:672–682.
52. Chu S. Laser manipulation of atoms and particles. *Science.* 1991;253:861–866.
53. Smith SB, Finzi L, Bustamante C. Direct mechanical measurements of the elasticity of single dna-molecules by using magnetic beads. *Science.* 1992;258:1122–1126.
54. Kong J, LeRoy BJ, Lemay SG, Dekker C. Integration of a gate electrode into carbon nanotube devices for scanning tunneling microscopy. *Appl. Phys. Lett.* 2005;86:112106.
55. Rummel RM, Ziegler C. Room temperature adsorption of aniline (C₆H₅NH₂) on Si(100) (2 × 1) observed with scanning tunneling microscopy. *Surf. Sci.* 1998;418:303–313.
56. Rumelhart DE, Hinton GE, Williams RJ. Learning representations by back-propagating errors. *Nature.* 1986;323:533–536.

NANOPARTICLES

Improved Electrochemistry of Biomolecules Using Nanomaterials

JIANXIU WANG

School of Chemistry and Chemical Engineering, Central South University, Changsha, Hunan, China

ANDREW J. WAIN

Department of Chemistry and Biochemistry, California State University, Los Angeles, California

XU ZHU

School of Chemistry and Chemical Engineering, Central South University, Changsha, Hunan, China

FEIMENG ZHOU

Department of Chemistry and Biochemistry, California State University, Los Angeles, California

- 4.1 Introduction
- 4.2 CNT-based electrochemical biosensors
 - 4.2.1 Improved voltammetric signals of biologically important small molecules at CNT-modified electrodes
 - 4.2.2 Direct electrochemistry or electrocatalysis of biomacromolecules at CNT-modified electrodes
 - 4.2.3 Highly aligned CNT arrays for biological applications
- 4.3 Nanoparticle-based electrochemical biosensors
 - 4.3.1 Improved voltammetric signals of biologically important small molecules at gold nanoparticle-modified electrodes
 - 4.3.2 Direct electrochemistry or electrocatalysis of biomacromolecules at gold nanoparticle-modified electrodes
 - 4.3.3 Highly aligned metal arrays for biological applications
 - 4.3.4 Nanoparticles and nanotechnology used in conjunction with scanning electrochemical microscopy

- 4.4 Quantum dot–based electrochemical biosensors
 - 4.4.1 Improved voltammetric signals of biologically important small molecules at quantum dot–modified electrodes
 - 4.4.2 Direct electrochemistry or electrocatalysis of biomacromolecules at quantum dot–modified electrodes
- 4.5 Conclusions and outlook

4.1 INTRODUCTION

Nanomaterials, with particle sizes falling in the range 1 to 100 nm, behave differently from bulk materials in their physical, chemical, and electronic properties, and are associated with unusual phenomena such as quantum size effects, surface effects and macro-quantum tunneling effects [1]. Due to their unique, and in many cases, desirable properties, the discovery of nanomaterials has sparked a surge of interest, leading to a great deal of intense research in this area. *Nanotechnology*, the creation of functional materials, devices, and systems through the control of nanoscale materials [2], has recently become one of the most influential fields at the forefront of analytical chemistry [1–5]. The emergence of nanostructured materials with tailored composition, structure, and properties has opened new horizons for the exploitation of innovative biosensors. The comparable dimensions of nanomaterials and biomacromolecules has allowed the integration of biological systems with nanoscale structures, leading to novel hybrid nanobiomaterials with synergetic properties and functions [6]. The compatibility of carbon nanotubes (CNTs), for example, with biomaterials has yielded hybrid systems possessing fascinating properties for the development of new nanoscale devices, with applications in biological, medical, and electronic fields [7,8]. Furthermore, the unique catalytic properties of such nanomaterials can result in a substantial signal amplification for the transduction of biomolecular interactions [9]. Consequently, with the integration of nanomaterials into their construction, the analytical performance of biosensors has shown remarkable improvement. The use of these nanomaterials has also facilitated the effective utilization of existing detection methods and provided many new signal transduction schemes, paving the way for the design of innovative and powerful nanomaterial-based biosensors with excellent sensitivity, high selectivity, and long-term stability.

This contribution addresses recent advances in carbon nanotube–, gold nanoparticle–, and quantum dot–based electrochemical biosensors, with emphasis placed on novel approaches to the development of biosensors together with the performance characteristics, advantages, and representative applications of such biosensors.

4.2 CNT-BASED ELECTROCHEMICAL BIOSENSORS

Since their discovery in 1991 [10], CNTs have generated a frenzy of excitement, due to their unique properties, such as remarkable tensile strength, superb electrical

conductivity, and high chemical stability [11]. Numerous novel applications of carbon nanotubes have been investigated, including, but not limited to, field emitters [12], nanoelectronic devices [13], nanotube actuators [14], batteries [15], probe tips for scanning probe microscopy [16], chemical and biological sensors [17], gas storage devices [18], and nanotube-reinforced materials [19]. Depending on their atomic structures, carbon nanotubes can behave as metals or semiconductors [20]. As a consequence, CNTs can serve as an excellent substrate or modifier to promote electron-transfer reactions [21]. Carbon nanotube-based electrochemical probes also exhibit numerous advantages, such as nanoscopic sizes, high aspect ratio (ranging from 100 to 1000), specific catalytic activity, high sensitivity, stability, and selectivity.

4.2.1 Improved Voltammetric Signals of Biologically Important Small Molecules at CNT-Modified Electrodes

Britto et al. first constructed CNT electrodes by mixing CNTs and bromoform and then packing the paste inside a glass tube [22]. The as-prepared electrode was used to examine the oxidation of dopamine (DA) (Figure 4.1). As shown in Figure 4.1(a), good reversibility with a peak potential separation of 30 mV was obtained at the CNT electrode, which was notably superior to that at a carbon paste electrode [Figure 4.1 (b)]. Due to the catalytically active surface, larger background currents are observed in Figure 4.1(a). Treatment of the CNT electrode with homogenized brain tissue had little influence on the voltammetric behavior of DA, indicating that the oxidation of

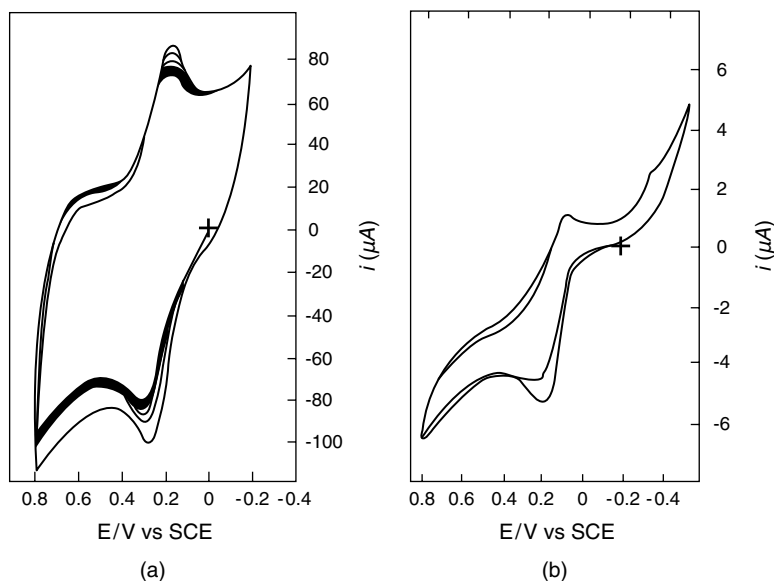


FIGURE 4.1 (a) Cyclic voltammetry of 5 mM dopamine in phosphate buffer solution (pH 7.4) at a carbon nanotube electrode (sweep rate, 20 mV/s); (b) cyclic voltammetric curve of 1 mM dopamine in phosphate buffer solution (pH 7.4) at a carbon paste electrode (sweep rate, 20 mV/s). (Adapted from ref. 22, with permission. Copyright © 1996 Elsevier Science B.V.)

dopamine occurs predominantly inside the tubes, where the electrolysis product is stabilized. The better performance of CNT electrodes may be interpreted on the basis of their unique properties, such as high aspect ratio, a multitude of active sites on the tube surface and ends, and their specific electronic structure. In particular, the presence of edge plane-like defects on the surface of CNTs has been strongly associated with their enhanced activity [23–26].

Later, Ajayan et al. used a multiwalled carbon nanotube (MWNT) microelectrode for the electrocatalytic reduction of dissolved oxygen [27]. The reduction of oxygen is important since many biological processes require the presence of oxygen and its ability to transport electrons, and the reduction of oxygen leads to the generation of reactive oxygen species [28]. The microelectrode was constructed by mixing carbon nanotubes with liquid paraffin and then curing at 50°C for 30 minutes. In H₂SO₄ solution, a well-defined reduction peak of dissolved oxygen at –0.31 V was obtained at the carbon nanotube electrode. The same reduction at a carbon paste electrode occurred at the more negative potential of –0.48 V and was ill defined, indicating the electrocatalytic nature of the nanotube microelectrode. Even more significant electrocatalytic oxygen reduction was found to take place at metal (Ag or Pd)-deposited CNT electrodes.

Li et al. first reported the electrochemical behavior of single-walled carbon nanotubes (SWNTs) functionalized with carboxylic acid groups [29]. The SWNT film was prepared by solvent evaporation of a volatile suspension of SWNTs, placed onto the electrode surface. The preparation of the modified electrodes made by solution casting proved economical, simple, and convenient compared with that of the other carbon nanotube electrodes mentioned above [22,27,30]. A pair of stable voltammetric peaks was observed, corresponding to the reduction and reoxidation of the carboxylic acid groups on the tube surface based on x-ray photoelectron spectroscopy and infrared band assignments. The electrode process involved a four-electron reduction of SWNT–COOH to SWNT–CH(OH)₂, with the rate-determining step being one-electron reduction to SWNT–C(OH)₂. Favorable electrocatalytic activity toward the oxidation of several biomolecules was observed at the SWNT film. Generally, chemical or electrochemical oxidation of the CNTs results in the formation of oxide functionalities such as esters and hydroxyl and diphenol groups on the tube surface and tube ends, which are known to activate the electrodes [31,32].

However, the relatively low density of these oxygen-containing moieties on the tubes restricts their potential applications in electrochemistry. To mimic the redox properties inherent in the SWNTs themselves and to increase the number of active sites on the tube surfaces, Mao et al. synthesized triptycene orthoquinone (TOQ) and attached this oxygen-containing compound onto the tube surface through hydrophobic or charge-transfer interactions (Figure 4.2) [33]. The electrode exhibited a pair of symmetric redox peaks, similar to that at the SWNT-modified electrode in the absence of TOQ. Extraordinary electrocatalytic activity toward the oxidation of biological thiols, such as homocysteine, cysteine, and glutathione at a low potential of 0.0 V vs. Ag/AgCl, was observed, with sensitivity almost 10 times higher than that at the native SWNT-modified electrode. Such an enhancement highlights the importance of surface chemistry in electrocatalysis and provides a new method for the sensitive determination of biological molecules.

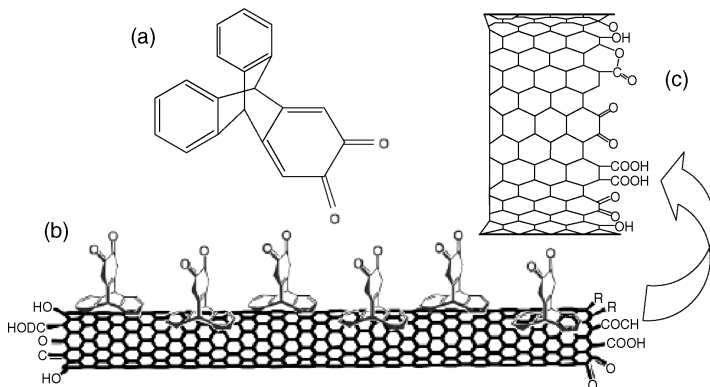


FIGURE 4.2 (a) Structure of triptycene orthoquinone (TOQ); (b) schematic illustration of attachment of TOQ onto carbon nanotubes; (c) enlarged tube ends with oxygen-containing moieties. (From ref. 33, with permission. Copyright © 2005 American Chemical Society.)

Over the past few years, one of us has investigated the improved voltammetric response of several neurotransmitters and their metabolites, such as 3,4-dihydroxyphenylacetic acid (DOPAC), norepinephrine (NE), and uric acid (UA) [34–37]. Scanning electron micrograph (SEM) images indicate that SWNT films formed by solution casting are composed primarily of many disordered SWNT bundles, which demonstrate a high level of electrocatalytic activity toward the oxidation of DOPAC, NE, and UA. One well-defined redox couple was obtained for DOPAC with a peak current that increased linearly with the concentration of DOPAC in the range 1.0×10^{-6} to 1.2×10^{-4} M and a detection limit of 4.0×10^{-7} M. A two-electron oxidation mechanism was proposed in which *o*-quinone is formed, followed by a dimerization reaction. The rate constant for the dimerization reaction was calculated to be $2.10 \times 10^3 \text{ dm}^3/\text{mol} \cdot \text{s}$. Selective determination of biologically important species in complex sample media can also be accomplished at SWNT-modified electrodes. In a mixed solution of DOPAC and 5-hydroxytryptamine (5HT), a convoluted anodic peak corresponding to the oxidation of both DOPAC and 5HT was observed at bare glassy carbon (GC) electrodes. However, two separate oxidation peaks were clearly resolved at the SWNT-modified electrode, with a peak potential separation of 162 mV. Furthermore, the SWNT-modified electrode has a favorable electrocatalytic activity toward NE and UA and can separate the electrochemical responses of UA, NE, and ascorbic acid (AA). The results above demonstrate the wealth of possible applications of carbon nanotubes in biosensors.

Due to the enhanced electron transfer associated with carbon nanotubes, other applications of these structures as a potential electrode material have also been exploited. A carbon nanotube powder microelectrode (CNTPME) was prepared by filling a cavity at the tip of a Pt microelectrode with carbon nanotube powder [38]. Anodic pretreatment of the electrode resulted in the formation of shorter tubes and an increased double-layer capacity. Due to the wetting of the nanotubes, facilitated by the electrochemical treatment [39], the electrode was found to strongly adsorb $\text{Os}(\text{bpy})_3^{2+}$. The as-prepared CNTPME– $\text{Os}(\text{bpy})_3^{2+}$ adduct

exhibited high electrocatalytic activity toward nitrite reduction, aiding the effective construction of high-quality nitrite sensors. Wang et al. reported the electrochemical detection of trace insulin at CNT-modified electrodes [40]. The substantial lowering of the oxidation potential is accompanied by a significantly larger current signal at the CNT-modified electrode. Subsequent amperometric analysis of insulin offers favorable signal-to-noise characteristics with good linearity, high reproducibility, and fast response time. Zhao and co-workers investigated the electrocatalytic response of tryptophan at a MWNT-modified electrode [41]. This modified electrode has been used successfully in the determination of tryptophan in composite amino acid injections, with excellent repeatability and high sensitivity.

β -Nicotinamide adenine dinucleotide (NAD^+), a cofactor associated with a plethora of enzymatic reactions of NAD^+/NADH -dependent dehydrogenases [42], has been studied extensively for the development of amperometric biosensors based on its electrochemical oxidation [43,44]. However, the large overpotential for NADH oxidation and the occurrence of surface fouling due to the accumulation of oxidation products are common problems encountered at conventional electrodes [45,46]. CNTs can reduce the overpotential for NADH oxidation and minimize the surface passivation effects [42]. Compared with traditional carbon electrodes, a substantial decrease of 490 mV in the overpotential of NADH oxidation was observed at the CNT-modified electrodes. The CNT-modified electrodes thus allow highly sensitive, low-potential, stable amperometric NADH sensing, demonstrating great promise for the construction of dehydrogenase-based amperometric biosensors. An even more significant diminution of the overpotential for NADH oxidation (more than 600 mV) was reported at an ordered CNT electrode [47].

Filling the carbon nanotubes with toluene improves the performance of these nanoreactors and renders them with some interesting properties. Zhang et al. investigated the electrochemical behavior of empty and toluene-filled nanotubes [48]. The toluene-filled nanotube film was demonstrated to catalyze the electrochemical response of dopamine and epinephrine, while empty MWNT films exhibited less or no electrocatalytic behavior with these biomolecules.

Fabrication of nanotube and nanoparticle hybrid materials with particular properties is an area under pursuit [49]. The functionalization of CNTs by metal nanoparticles greatly enhances their suitability for use in analytical methodologies. Various protocols have been employed to functionalize CNTs by metal nanoparticles, such as physical evaporation [50,51], solid-state reaction with metal salts [52,53], electroless deposition [54,55], and electrochemical deposition [56].

Given the vast array of electroactive species present in biological systems, CNTs may find potential application in the selective determination of biologically important species in complex sample media (e.g., blood and urine samples). As described above, nanotubes have proven particularly advantageous when the redox potentials of the analyte species normally overlap. UA, the primary end product of purine metabolism, often coexists with AA in biological fluids. Ye et al. reported the selective voltammetric determination of UA in the presence of a high concentration of AA at well-aligned CNT electrodes [57]. In this case, due to the different catalytic activity toward the oxidation of UA and AA, the modified electrode is capable of resolving the overlapping voltammetric responses into two well-defined peaks. β -Cyclodextrin

(β -CD)-coated electrodes incorporating CNTs were also prepared for the detection of UA in the presence of a high AA concentration [58]. The combination of β -CD with CNTs further enhanced the sensitivity toward UA due to the formation of a supramolecular complex between UA and β -CD. The composite electrode could be used for the determination of UA in human urine samples without pretreatment. Furthermore, simultaneous measurement of DA and AA has been reported at CNT-modified electrodes [59,60], and more recently, selective detection of AA *in vivo* was realized using a MWNT-modified carbon fiber microelectrode [61].

4.2.2 Direct Electrochemistry or Electrocatalysis of Biomacromolecules at CNT-Modified Electrodes

Due to their unique electronic properties, CNTs can serve as excellent substrates to enhance electron-transfer kinetics at the electrode–solution interface [22]. Davis was the first to show that MWNTs could be used for the electrochemical detection of proteins [62]. The CNT electrode was prepared by packing the tubes into a glass capillary with mineral oil, deionized water, and bromoform, the latter being removed before use. Although direct electrochemistry of cytochrome *c* and azurin was realized through the use of MWNTs, such a CNT electrode is time consuming to prepare, and the electrochemical response is weak. To overcome these problems, our group prepared a CNT-modified electrode by casting an aliquot of a CNT suspension onto substrate surfaces. The as-prepared electrode facilitates well the electron-transfer reactions of cytochrome *c*, catalase (Ct), and DNA [37,63–65]. For example, Ct at a bare gold electrode essentially exhibits no voltammetric response within a typical potential window. However, a quasireversible redox process of Ct was obtained at the modified electrode [Figure 4.3(A)]. The redox wave corresponds to the Fe (III)/Fe(II) redox center of the heme group of the Ct adsorbate. Compared to other

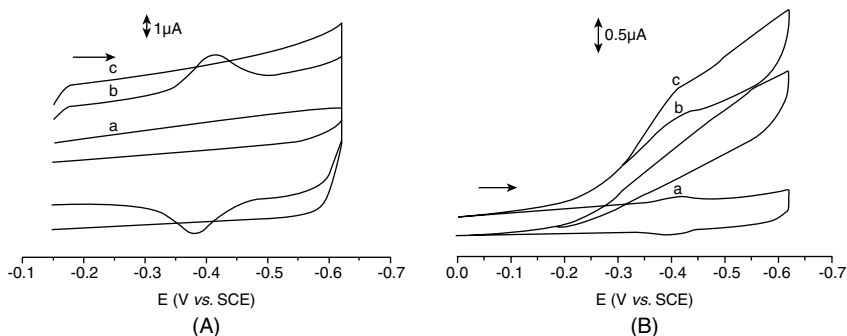


FIGURE 4.3 (A) Cyclic voltammograms of catalase (adsorbed from a 5×10^{-5} M Ct solution) at a bare gold electrode (curve a) and a SWNT-modified gold electrode (curve b). Curve c is a voltammogram acquired at a SWNT-modified gold electrode in the absence of catalase. (B) Cyclic voltammograms of catalase at a SWNT-modified gold electrode covered with Ct in the absence of H_2O_2 (curve a) and in the presence of 7.0×10^{-4} M (curve b) and 1.1×10^{-3} M H_2O_2 (curve c). The electrolyte solution used was a 0.05 M phosphate buffer (pH 5.9) and the scan rate employed was 0.1 V/s. The arrow indicates the scan direction. (From ref. 64, with permission. Copyright © 2004 Wiley-Interscience.)

types of carbonaceous electrode materials (e.g., graphite and carbon soot), the electron-transfer rate of the Ct redox reaction was greatly enhanced at the SWNT-modified electrode. The catalytic activity of Ct was still retained upon adsorption onto the SWNT-modified electrode, which was verified by the characteristic electrocatalytic redox wave upon the addition of H_2O_2 or O_2 ($E_r C'_i$ mechanism) [Figure 4.3(B)] and reflectance Fourier transfer–infrared measurements. The results above provide an attractive route for the development of enzyme electrodes and biosensors.

In connection with the direct electrochemical investigation of biomacromolecules at CNT-modified electrodes, several other groups have carried out some interesting work. Dong's group investigated the direct electron transfer of several enzymes on CNTs [66–69]. Glucose oxidase (GOD) was entrapped in a composite of CNTs and the polysaccharide chitosan, and the direct electron transfer of GOD was achieved at the modified electrode [66]. The electron-transfer rate of GOD confined in the composite film is higher than that of GOD or FAD (flavin adenine dinucleotide, the active site of GOD) adsorbed on the CNTs, suggesting that the composite matrix greatly facilitates electron transfer between the enzyme and the electrode. The as-prepared electrode could be used as a glucose biosensor with high sensitivity and stability. In a second paper, the direct electrochemistry of microperoxidase (MP-11) was recorded at a Pt microelectrode modified with MWNTs [67]. The immobilized MP-11 retains its bioactivity and can be used to catalyze the reduction of O_2 and H_2O_2 . Due to the favorable microenvironment provided by a sol–gel-derived ceramic–CNT nanocomposite film, direct electron transfer of horseradish peroxidase (HRP) was also facilitated [69]. The nanocomposite film was formed by coating a mixed suspension of methyltrimethoxysilane and MWNTs onto a GC electrode surface. Atomic force microscopy (AFM) images indicated that the well-dispersed MWNTs could interact with silicate particles through a hydrophobic interaction.

CNT length-controlled electrical communication of an enzyme redox center with an electrode surface was reported by Willner et al. [7]. Functionalized and surfactant-protected SWNTs were coupled to a mixed monolayer of thioethanol and cysteamine assembled onto a gold electrode. Utilization of the mixed monolayer prevented the nonspecific adsorption of SWNTs, leaving the SWNT columns perpendicular with respect to the underlying electrode surface. After the sidewalls of SWNTs had been blocked with Triton X-100 and polyethylene glycol (PEG), FAD cofactor (1) was attached to the free edges of the standing SWNTs, followed by reconstitution of the apo-glucose oxidase on the FAD units (Figure 4.4). The nanotube serves as a nanoconnector, and electron transfer between FAD units and the electrode is controlled by the nanotube length. Interfacial electron-transfer rate constants of 83, 42, 19, and 12 s^{-1} were obtained for SWNT assemblies of 25-, 50-, 100-, and 150-nm average length, respectively. This ability to tailor the electrical properties of such nanomaterial conduits is no doubt advantageous with regard to their application in biosensing.

The construction of nanohybrid films based on the utilization of carbon nanotubes as the matrix to attach metal nanoparticles has gained increasing attention in terms of their application, due to good biocompatibility and high surface activity. Smyth et al. investigated the direct electrochemistry of GOD immobilized with a chitosan film containing gold nanoparticles on the surface of a CNT-modified electrode [70].

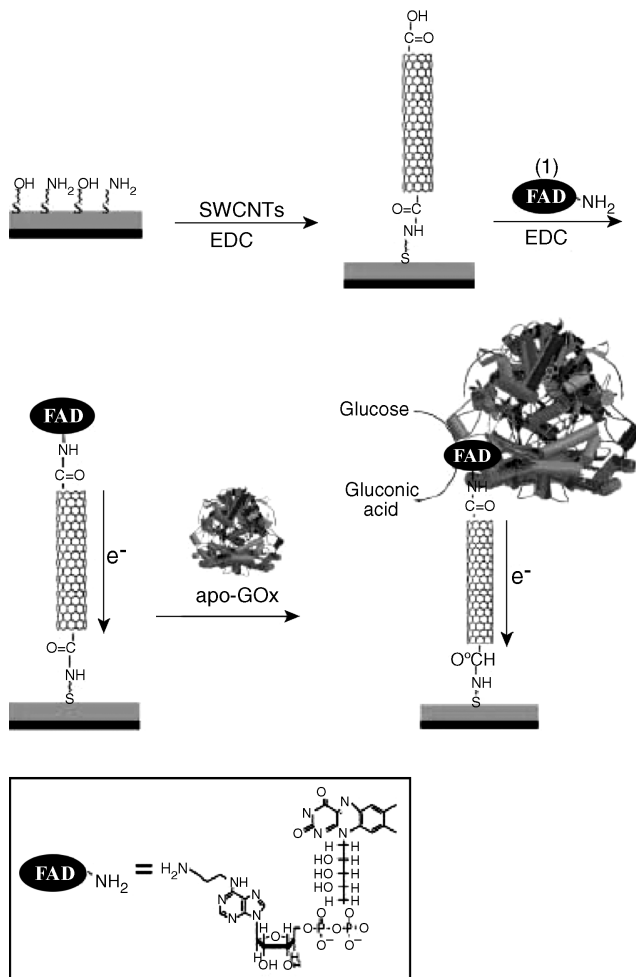


FIGURE 4.4 Assembly of the SWNT electrically contacted glucose oxidase electrode. (From ref. 7, with permission. Copyright © 2004 Wiley-Interscience.)

The immobilized GOD retains its bioactivity due to the presence of the gold nanoparticles/chitosan film, while the CNTs can facilitate electron transfer between GOD and the electrode surface. Direct electron transfer of microperoxidase-11 (MP-11, the heme-containing polypeptide of cytochrome *c*) covalently immobilized onto a nanohybrid film of MWNTs and gold nanoparticles (GNPs) was also reported [71]. The adherence of GNPs onto the MWNT surface was achieved by immersing the MWNT-modified GC electrode made by solution casting into a gold colloidal solution. The GNPs that adhered were derivatized with cysteamine, and MP-11 was then covalently attached onto the surface of the GNP-MWNT-GC electrode. The formal potential of the MP-11 at this surface was found to be shifted in comparison with other systems [72,73], which may originate from the interaction

between the microenvironment and the protein [74,75]. Novel composite quantum dot (QD)–CNT electrodes for the electrochemical biosensing of glucose have also been prepared [76]. The assembly of CdTe QDs with CNTs combines the semiconductivity of QDs together with the excellent electrical conductivity and biocompatibility of carbon nanotubes. Hence, higher performance was obtained at the CdTe–CNT electrode compared with that at the GC electrode modified with CdTe QDs or CNTs alone. The sensing platform based on QD–CNT electrodes could find potential applications in clinical, environmental, and food analysis.

An assembly of layer-by-layer (LBL) films of heme proteins and SWNTs with controllable layer thickness was fabricated based on the alternative adsorption of positively charged hemoglobin (Hb) or myoglobin (Mb) and negatively charged CNTs onto a pyrolytic graphite electrode [77]. In comparison with cast films of proteins and CNTs, the layer-by-layer assembly ensures a higher fraction of electroactive proteins and better controllability in film construction. The proteins entrapped in the film retained their near-native structure, suggesting a new type of biosensor application. Li et al. reported the fabrication of protein–polyion multilayers by the electrostatic LBL assembly of glucose oxidase and poly(diallyldimethylammonium chloride) on CNT templates [78]. Protein biosensing was realized at these assembled nanoshell bioreactors. The approach could be extended to other biological molecules, such as antibody, antigen, and DNA, for wide bioassay applications.

4.2.3 Highly Aligned CNT Arrays for Biological Applications

As mentioned above, the majority of studies in this field have focused on the use of CNT electrodes prepared by drop casting for biosensing. Although economical, simple, and convenient, drop coating usually results in a random tangle of nanotubes and an unknown spatial relationship between the redox proteins and the nanotubes [79]. To address this issue, Gooding and colleagues studied protein electrochemistry at aligned CNT arrays [79]. The scheme for fabrication of aligned CNT arrays and subsequent microperoxidase MP-11 attachment is shown in Figure 4.5. Shortened SWNTs were dispersed in dimethylformamide and then the terminal carboxyl groups were converted into active carbodiimide esters using dicyclohexyl carbodiimide [80]. Next, the tubes were attached at one end to amine moieties at the termini of a cysteamine-modified gold electrode through amide bond formation. Finally, MP-11 was attached covalently to the free ends of the tubes aligned normal to the electrode surface. The efficiency of the nanotubes acting as molecular wires for direct electrochemistry of the attached enzyme was demonstrated. The as-prepared arrays have also been used for probing the direct electron transfer between the redox active centers of GOD and FAD and electrode surfaces [81].

Highly aligned MWCT tower arrays were synthesized on silicon substrates via a thermally driven chemical vapor deposition method [82]. Each tower (1 mm × 1 mm) comprised approximately 25 million nanotubes aggregated together in parallel based on environmental scanning electron microscopy (ESEM) observations. The surface of each tower was approximated at 6000 mm². These arrays could easily be peeled off the silicon substrate and used as electrode materials for highly sensitive

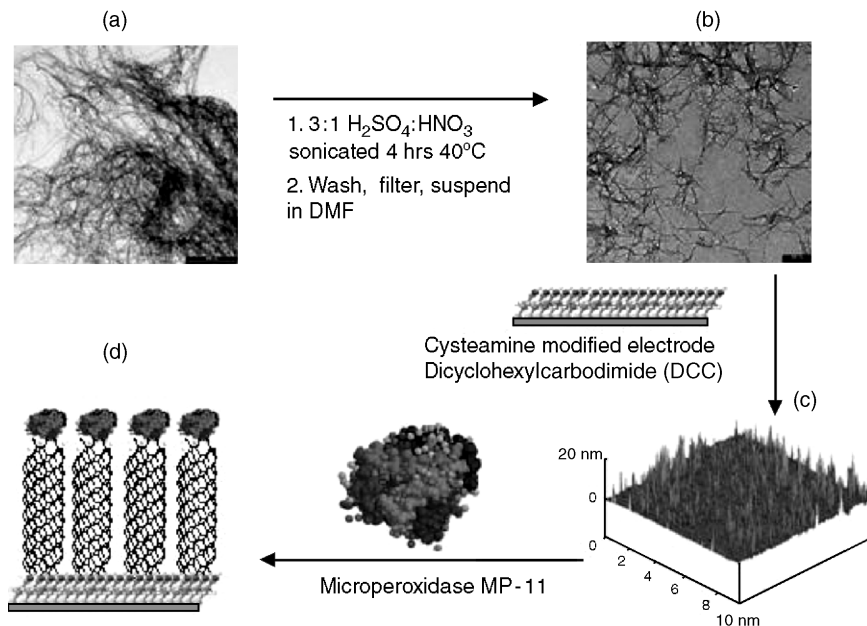


FIGURE 4.5 Steps involved in the fabrication of aligned SWNT arrays for direct electron transfer with enzymes such as microperoxidase MP-11. (Adapted from ref. 79, with permission. Copyright © 2003 American Chemical Society.)

chemical and biosensor applications. Moreover, large-scale production of aligned MWNT arrays has been achieved by a simple pyrolytic method [83]. These aligned CNTs with tunable surface characteristics could find practical applications in sensors and electronics. For example, single-stranded DNA or glucose oxidase could be immobilized onto these active materials and the sensing of target DNA with specific sequence or glucose could be realized with high sensitivity and selectivity.

Rusling and co-workers constructed an amperometric immunosensor in which an antibody was strongly adsorbed onto SWNT forests [84]. The forests were constructed from carboxyl functionalized and shortened SWNTs onto Nafion/iron oxide-coated pyrolytic graphite electrodes. The successful adsorption of the antibody was characterized by AFM. In the presence of a mediator, hydroquinone, biotin-HRP, and biotin could be detected with detection limits of 2.5 nM and 16 μM , respectively, suggesting that immunosensors based on the use of the oriented assemblies of SWNTs are particularly effective as nano-biosensing arrays. The tumor marker, carcinoembryonic antigen (CEA), was also detected using SWNT field-effect transistors (SWNT-FETs) [85]. Construction of SWNT-FETs was achieved using CNTs produced by a patterned catalyst growth method. The CEA antibody, a recognition element for CEA, was immobilized on the sidewalls of the CNTs and the binding of tumor markers to these antibody-functionalized SWNT-FETs resulted in a sharp

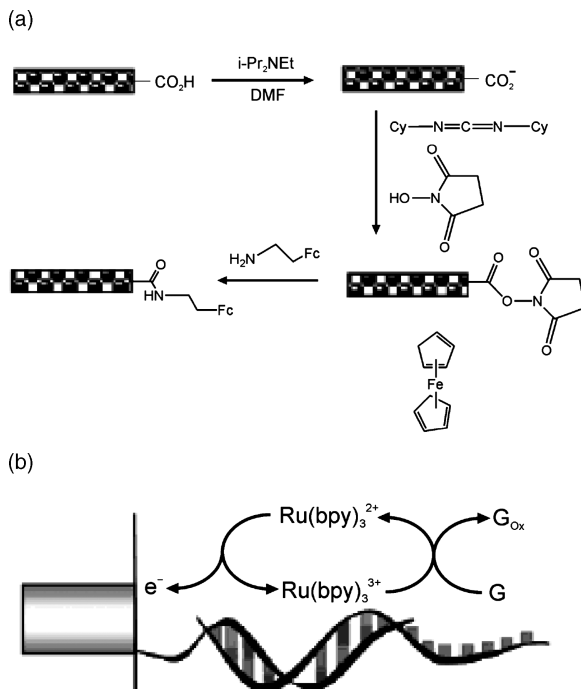


FIGURE 4.6 (a) Functionalization process of the amine-terminated ferrocene derivative to CNT ends by carbodiimide chemistry; (b) mechanism of $\text{Ru}(\text{bpy})_3^{2+}$ -mediated guanine oxidation. (Adapted from ref. 86, with permission. Copyright © 2003 American Chemical Society.)

decrease in conductance, providing the key to the construction of highly sensitive, label-free SWNT-FET-based tumor sensors.

CNT-based nanoelectrode arrays have proven useful for ultrasensitive DNA detection [86]. A well-aligned array embedded in a SiO_2 matrix was fabricated via a bottom-up protocol; the carboxylate groups at the open ends of carbon nanotubes were derivatized with amine-terminated ferrocene derivatives or oligonucleotide probes. Target concentrations below a few attomoles can be detected via the $\text{Ru}(\text{bpy})_3^{2+}$ -mediated oxidation of guanine (Figure 4.6).

4.3 NANOPARTICLE-BASED ELECTROCHEMICAL BIOSENSORS

Metal nanoparticles have been studied extensively due to their unusual physical and chemical properties, in addition to their variety and relative ease of preparation [87]. Among the various metal nanoparticle types, gold nanoparticles are the most commonly used. GNPs exhibit excellent catalytic activity due to their high surface area and their interface-dominated properties [88,89]. Modification of electrode

surfaces with GNPs renders the substrate with unusual properties inherent in the nanomaterial modifier.

4.3.1 Improved Voltammetric Signals of Biologically Important Small Molecules at Gold Nanoparticle-Modified Electrodes

The utilization of gold nanoparticles assembled onto different substrates leads to extraordinary electrocatalytic activity toward oxygen reduction, and the catalytic behavior of these nanoparticles depends on their size and the conducting support used for their deposition and immobilization [90]. Ohsaka et al. investigated the electroreduction of oxygen using citrate-stabilized GNPs anchored onto cysteamine and 1,4-benzenedimethanethiol self-assemblies via amino and mercapto terminal groups, respectively [90]. The modified electrode demonstrated efficient catalysis of the reduction of oxygen to hydrogen peroxide due to the active sites on the GNPs. In similar work undertaken by Yoshihara and co-workers, the electrocatalytic reduction of oxygen in acidic media was conducted at GNPs deposited on boron-doped diamond films [91]. Again, remarkable electrocatalysis was observed, which has potential applications in oxygen sensing and energy conversion.

Due to the important roles of nitric oxide (NO) in physiology and pathology, the development of various nanomaterial-based electrochemical sensors selective toward NO has generated a great deal of attention. Oyama and co-workers demonstrated the high catalytic activity of gold nanoparticle arrays grown directly on nanostructured indium tin oxide (ITO) electrodes toward the electrooxidation of NO [92]. The arrays were prepared by a two-step seed-mediated growth approach for the direct attachment and subsequent growth of mono-dispersed gold nanoparticles on ITO surfaces. The first step involved the physical adsorption of Au precursor solution onto the active sites of a nanostructured ITO surface and subsequent chemical reduction of the Au complex to gold nanoparticles by NaBH₄. In the second step, the gradual growth of gold nanoparticles was realized via chemical reduction of gold ions in a HAuCl₄ solution by the immobilized gold nanoseed particles. As indicated by SEM imaging, the size of the gold nanospheres could be modulated by variation of the growth time and the as-prepared arrays demonstrated potential use in NO sensing. The electrocatalytic oxidation of NO was also reported at gold colloids assembled on cysteine-modified platinum electrodes [93] and polyelectrolyte-gold nanoparticle hybrid films assembled on ITO electrodes [88]. The above-mentioned GNP arrays prepared by the seed-mediated growth approach could be further extended to complex sample media determination or derivatized with other species for higher-performance biosensor construction. In a second paper by Oyama et al., the gold nanoparticle arrays were utilized for the simultaneous determination of dopamine and serotonin [94]. The GNP arrays could be further derivatized with 3-mercaptopropionic acid (MPA), which was also carried out by Oyama et al., allowing a three-dimensional MPA monolayer on a gold nanoparticle array to be fabricated [95]. The three-dimensional MPA monolayers showed higher electrocatalytic activity toward DA and UA than either the gold nanoparticle arrays on ITO or the two-dimensional MPA monolayers assembled on planar gold electrodes. Furthermore, poisoning of the

electrode surfaces by the oxidation products observed on two-dimensional MPA monolayers was inhibited at the three-dimensional monolayers. Alternatively, thiol-capped and networked core-shell gold nanoparticles were constructed on GC electrode surfaces [96]. Differing from that reported by Oyama et al. [95], the catalytically active gold nanoparticle cores were entirely capped with thiolate monolayers, resulting in a networked assembly. The network fabrication involved exchange of 1,9-nonanedithiol (NDT) with decanethiolate (DT)-capped gold nanoparticles, cross-linking, nucleation, and subsequent growth of a thin film. The assembly exhibited high catalytic activity toward the oxidation of carbon monoxide, which demonstrated its potential application in areas as diverse as air purification, new fuel-cell technology, and automobile exhaust conversion [96–98].

Enzymatic sensors based on the utilization of gold nanoparticles assembled onto GC electrodes for the detection of hydrogen peroxide [99], xanthine and hypoxanthine [100], cholesterol [101], and glucose [102] have been proposed. The addition of albumin facilitates the dispersion of gold nanoparticles, resulting in higher electrocatalytic activity toward hydrogen peroxide, dopamine, and hydroquinone [103]. Due to the clinical significance in patient therapy, the determination of glucose in serum samples was accomplished at an electrodeposited chitosan–GOD–gold nanoparticle hybrid film on a Prussian Blue (PB)–modified electrode [104]. The application of a deposition potential allows formation of a chitosan hydrogel with the incorporation of GOD and GNPs. In comparison with films constructed by manual dropping, even and uniformly dispersed composite films were fabricated, due largely to H₂ evolution during deposition, which resulted in the generation of a nanopore architecture. Satisfactory results for glucose determination in serum samples were achieved and were in good agreement with those obtained by spectrophotometric methods commonly used in clinical laboratories. As an alternative, glucose biosensing may be performed at films constructed with GNP–FAD semisynthetic cofactor units reconstituted into apo-GOD [105].

As we have seen above, attaching gold nanoparticles to carbon nanotube sidewalls is of great interest for obtaining gold nanoparticle–CNT hybrids [55,106]. Carbon nanotubes can be used as a support for a three-dimensional electrocatalytic layer containing dispersed metal nanoparticles that specifically catalyze the reduction of oxygen [106] and the oxidation of AA [107].

4.3.2 Direct Electrochemistry or Electrocatalysis of Biomacromolecules at Gold Nanoparticle-Modified Electrodes

Wang et al. studied the direct electrochemistry of cytochrome *c* at a novel electrochemical interface constructed by self-assembling gold nanoparticles onto a three-dimensional silica gel network on a gold electrode [108]. These nanoparticles provided the necessary conduction pathways from cytochrome *c* to the electrode surface, inhibited the adsorption of cytochrome *c* onto the bare electrode, and aided the favorable orientation of cytochrome *c*, thus reducing the effective electron-transfer distance. These attractive features indicate that colloidal GNPs may be useful as

building blocks for macroscopic metal surfaces with biological applications. In a second paper by the same group, the direct electron transfer between Hb and a GC electrode facilitated by lipid-protected gold nanoparticles was investigated [109]. The lipid-protected gold nanoparticles demonstrated good biocompatibility and high stability (for at least eight months).

Due to the composite nature and the feasibility of incorporating colloidal nanoparticles, carbon paste has become a widely used material for the development of biosensors. Ju and colleagues systematically investigated the incorporation and direct electrochemistry of Mb, GOD, cytochrome *c*, and horseradish peroxidase by immobilizing these redox-active species onto colloidal GNP-modified carbon paste electrodes [110–112].

Gold nanoparticles can be assembled onto other substrates, such as screen-printed rhodium-graphite electrodes, porous calcium carbonate microspheres (CaCO_3), and ITO (see above). The as-prepared biocompatible matrices can be used for biomacromolecule interrogation. Oyama and co-workers demonstrated that when biocompatible gold nanoparticles and ITO were combined for Mb immobilization, stable and well-behaved voltammetry for Mb could be obtained [113,114]. Three-dimensional superstructures, multilayer arrays consisting of GNPs cross-linked by MP-11, were assembled on transparent ITO-conductive glass supports [115]. The array exhibited three-dimensional conductivity, indicating that the MP-11 in the superstructure was coupled electronically with the electrode. Electron transfer between cytochrome P450_{scc} and gold nanoparticles immobilized on screen-printed rhodium-graphite electrodes has also been realized [116]. Porous calcium carbonate microspheres (CaCO_3), a biocompatible structure, may also serve as an immobilized matrix for the assembly of GNPs through electrostatic interactions [117]. The resulting multifunctional GNPs- CaCO_3 hybrid material was used for HRP assemblies and biosensor fabrication. The improved performance of the biosensor originating from the synergic effect of the CaCO_3 microspheres and GNPs was ascribed to the fact that the hybrid material can provide a biocompatible environment for HRP to orient the heme edge toward its electron donor or acceptor and facilitate the electron transfer process [117,118].

Taking advantage of the specific recognition between antigens (Ag) and antibodies (Ab), immunoassays have been widely used in clinical analyses [119,120]. Due to their high surface area and excellent biocompatibility, GNPs have been used successfully in such immunoassays as an immobilized matrix for higher loading density and better retained immunoactivity [121]. Yang et al. assembled recombinant dust mite allergen Der f2 molecules onto a GNP-modified GC electrode and the interaction of the allergen with a murine monoclonal antibody was monitored by electrochemical impedance spectroscopy (EIS) (Figure 4.7) [122]. As the Ab concentration was increased, the interfacial electron transfer of the redox probe was retarded accordingly, indicating that more Ab molecules had become bound to the immobilized allergen. The active sites of the gold colloid monolayer allowed the immobilization of a greater allergen density with retained immunoactivity, while in the subsequent EIS sensing, the gold nanoparticles served as an electron-conducting conduit. Human chorionic

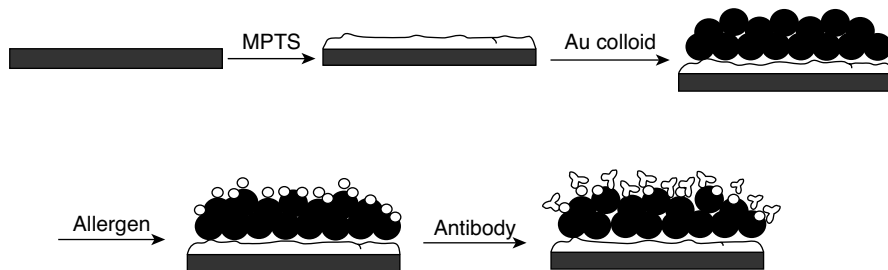


FIGURE 4.7 Stepwise immunoassay assembly. The GC substrate was first modified with (3-mercaptopropyl)trimethoxysilane (MPTS) before GNP immobilization. (From ref. 122, with permission. Copyright © 2006 Elsevier Science B.V.)

gonadotrophin (hCG), a diagnostic marker of pregnancy and tumors, was determined via encapsulation of a HRP-labeled hCG antibody in the composite membrane of a colloidal nanoparticle and titania sol-gel [123]. The composite architecture provided a hydrophilic interface for bioactivity retention and improved stability of the immobilized biomolecules. The formation of the immunoconjugate between the hCG antigen and HRP-labeled hCG antibody hindered the direct electron transfer between HRP and the substrate surface. Thus, a reagentless electrochemical immunoassay for hCG in serum samples was presented with a detection limit of 0.3 mIU/mL. The combined utilization of magnetic beads with GNP labels for the development of renewable electrochemical immunosensors was reported by Lin et al. [124]. Sensing of target immunoglobulin G (IgG) in the sample solution was accomplished by examining the electrochemical stripping signals of the GNP tracers capsulated to the surface of magnetic beads by a “sandwich” immunoassay, thus avoiding the use of an enzyme label and substrate. Such nanoparticle-based electrochemical magnetic immunosensors offer great promise for disease diagnostics and biosecurity. Other groups also carried out some interesting work on electrochemical immunoassays for the human tumor markers CEA [125] and carbohydrate antigen 19-9 [126].

The use of colloidal GNPs for gene analysis was found to improve the sensitivity and sequence specificity of one approach [127–132]. Ozsoz et al. constructed an electrochemical genosensor based on the hybridization of target DNA to GNP-tagged capture probes at a disposable pencil graphite electrode surface [133]. Differentiation of heterozygous and homozygous factor V Leiden mutations from polymerase chain reaction–amplified real samples was accomplished via examining the oxidation signal of Au colloids. Enhanced electrochemical detection of DNA hybridization utilizing gold nanoparticle tags coupled with subsequent silver deposition was also reported (Figure 4.8) [134]. The oxidative silver-dissolution signal was used to transduce the hybridization event. Layer-by-layer adsorption of polyelectrolyte poly(allylamine hydrochloride) and poly(styrenesulfonate) (PSS) was used for surface-charge control to minimize the background silver deposition on the gold electrode. Alternatively, magnetically induced electrochemical detection of DNA hybridization

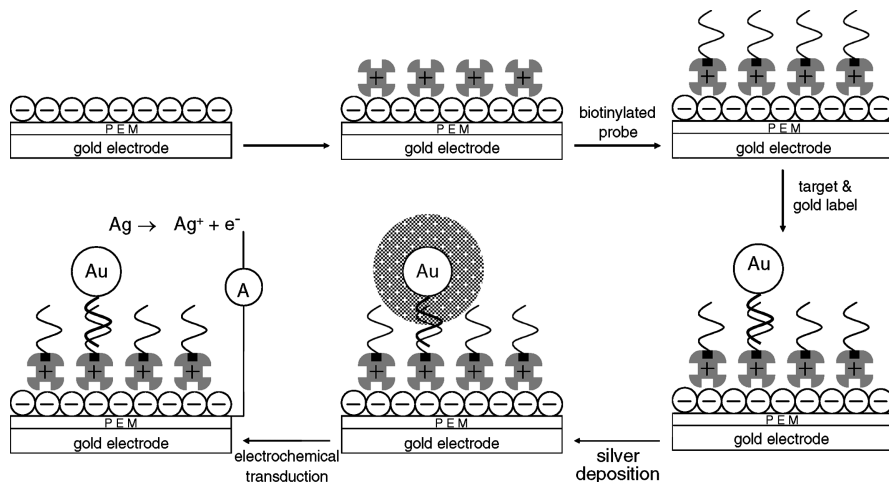


FIGURE 4.8 Electrochemical DNA-hybridization detection using a silver-enhanced GNP label on a gold electrode modified with a polyelectrolyte membrane (PEM), streptavidin, and the biotinylated probe. (From ref. 134, with permission. Copyright © 2003 American Chemical Society.)

based on the stripping detection of metal tags was proposed [135]. The protocol of utilizing magnetic collection of the magnetic bead–DNA hybrid–metal tracer assembly onto the electrode surface removes unwanted constituents or interfering species in gene analysis, thus offering high sensitivity and selectivity. The interested reader is directed to reviews focusing on integrated GNP–biomolecule hybrid systems for bioanalytical applications and for the fabrication of bioelectronic devices [6,136].

Recently, our group developed a voltammetric scheme for amplified sandwich assays of both oligonucleotide and polynucleotide samples via the oxidation of ferrocene (Fc)-capped gold nanoparticle–streptavidin conjugates [131]. The biotin–streptavidin complexation leads to the attachment of the conjugates onto the biotinylated detection probe of a sandwich DNA complex. Since each gold nanoparticle is decorated with over 100 Fc moieties, the voltammetric signal is greatly enhanced. It is also worthy to note that some of the streptavidin molecules are linked to one gold nanoparticle, while many more are linked to two gold nanoparticles. Consequently, the voltammetric signal is augmented further. The present method can measure oligonucleotide sample concentrations as low as 2.0 pM. The feasibility of this approach for real sample analysis was demonstrated by measurement of polymerase chain reaction (PCR) products of the hepatitis B virus (HBV) pre-S gene extracted from serum samples. This amplified voltammetric method offers an ideal platform for detection of metallothioneins and oligopeptides immobilized onto surfaces [137], as well as for DNA hybridizations in a direct hybridization format [138]. Amplified voltammetric detection of wide-type p53 from normal and cancer cell lysates has also been carried out, and concentrations as low as 2.2 pM

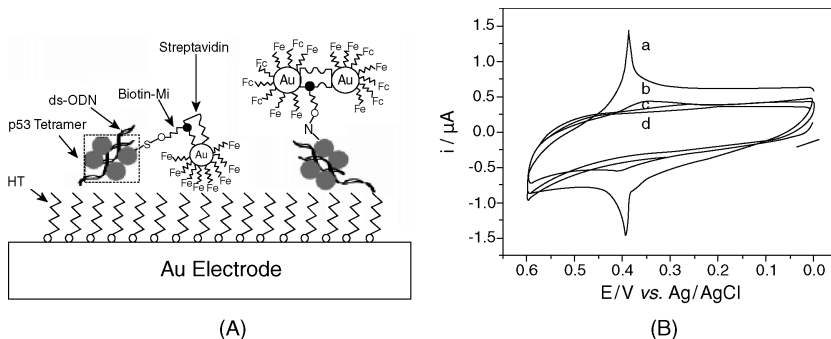


FIGURE 4.9 (A) Capture of p53 by dsODN-modified electrodes and the following amplified voltammetric detection of p53 via oxidation of the ferrocene tags on the GNP–streptavidin conjugates. (B) CVs recorded at consensus dsODN-modified electrodes that had been exposed to a normal cell lysate diluted threefold with buffer (curve a) and a colorectal cancer cell lysate (curve b). Curves c and d depict CVs recorded at electrodes modified with a 25-mer ssODN exposed to the same normal and colorectal cancer cell lysates, respectively. (Adapted from ref. 139, with permission. Copyright © 2008 American Chemical Society.)

were detected [139]. Double-stranded oligonucleotides containing the consensus sites were immobilized onto gold electrodes to capture wide-type p53. The cysteine residues on the exterior of the p53 molecules were derivatized for the attachment of gold nanoparticle/streptavidin conjugates capped with multiple ferrocene tags [Figure 4.9(A)]. Substantially lower (50 to 182 times) wide-type p53 concentrations in the three cancer cell lines (two colorectal cancers and one lung cancer) were obtained relative to that in the normal cell lysate [Figure 4.9(B)]. Furthermore, comparison of the total p53 concentration in these cancer cell lysates, determined by enzyme-linked immunosorbant assay (ELISA), with that of the wild-type p53 determined above indicated that the mutated p53 gene was overwhelmingly predominant in these samples. The method described herein is therefore amenable to the quantification of wide-type functional p53 levels in normal and cancerous cells and is highly complementary to ELISA.

Relying on gold nanoparticle labels, the biological binding event between the *Escherichia coli* single-stranded DNA binding protein, SSB, and DNA was utilized for the electrochemical detection of DNA hybridization [140]. SSB is a product of the *E. coli ssb* gene that plays important roles in DNA repair, replication, and recombination [141]. The binding of gold nanoparticle-tagged SSB with single-stranded oligonucleotides immobilized onto a biotin-modified carbon paste electrode (BCPE) was monitored by examining the gold oxidation signal. The lack of significant binding between the gold nanoparticle-tagged SSB and double-stranded hybrid-modified electrodes resulted in a diminished electrochemical response (Figure 4.10). The work presents a novel hybridization detection protocol with the combination of the recognition ability of a protein and the oxidation signal of metal nanoparticles.

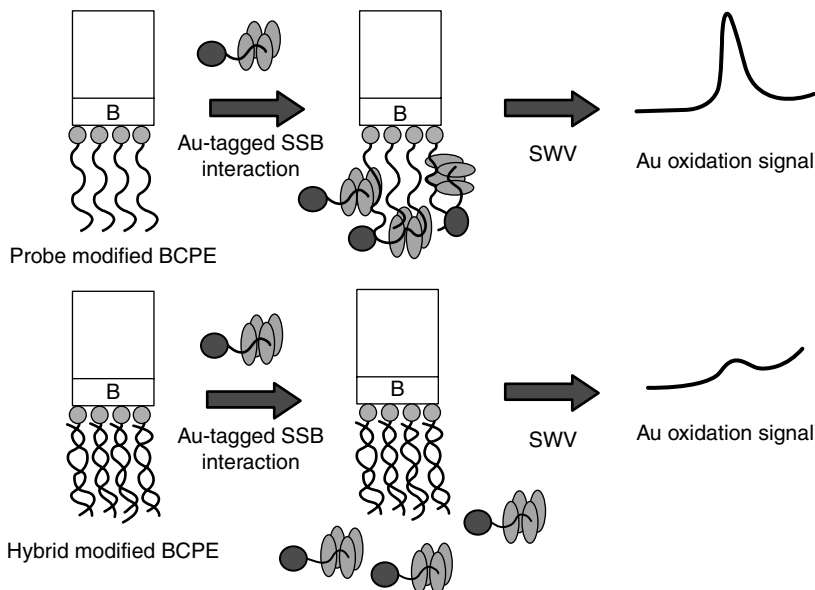


FIGURE 4.10 Hybridization detection protocol. Au-tagged SSB can bind to the single-stranded probe and thus amplify the Au oxidation signal. However, only a low Au signal can be obtained from the double-stranded hybrid after interaction with SSB. (Reprinted from ref. 140, with permission. Copyright © 2004 Elsevier Science B.V.)

4.3.3 Highly Aligned Metal Arrays for Biological Applications

Gold nanotube arrays were synthesized via electroless metal deposition within the pores of polycarbonate nanoporous particle track-etched membranes [142]. It was proposed that the growth of such gold nanotube arrays involves a progressive nucleation mechanism beginning with the formation of gold sticks. Longer growth time resulted in a more dense structure, with the formation of bundles of nanowires that gradually became longer and narrower. Due to the large surface area of the nanotube arrays, these structures could be utilized as ideal electrode materials for the assembly of novel electrochemical sensors and biosensors.

Well-oriented nanowells (ONWs) were fabricated using electron-beam nanolithographic technology [143]. AFM imaging revealed an array of ONWs with a diameter of 100 nm, allowing only one or a few biomolecules to be attached to the nanosized gold dots. Electrochemical detection of DNA hybridization was achieved inside the nanowells with a two-order-of-magnitude enhancement in sensitivity as compared to bare gold microelectrodes. Such ONW arrays have several advantages in terms of biosensor applications, such as minimization of unwanted nonspecific binding, increase in the S/N ratio, implementation of high-throughput detection, and wide use in other integrated biosensor systems [144–146]. The combination of self-assembly techniques with electron-beam lithography for the fabrication of

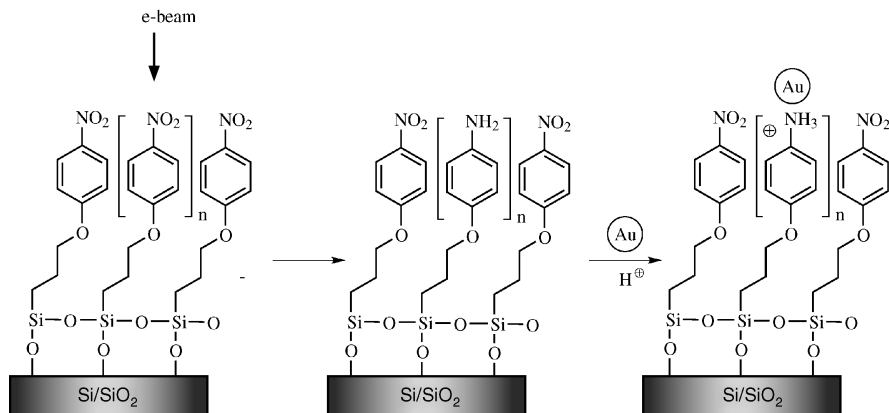


FIGURE 4.11 GNP pattern fabrication on silica surfaces (GNPs not to scale). (From ref. 147, with permission. Copyright © 2004 American Chemical Society.)

nanopatterned arrays of gold nanoparticles has also been presented [147]. The utilization of direct-write electron-beam lithography permits the localized conversion of nitro-terminated monolayers into amino functionalities. Subsequent reaction of citrate-coated GNPs with the amine regions allows well-defined surface architectures of GNPs to be formed; At unirradiated NO_2 -terminated regions, no such assembly takes place, due to the lack of any strong affinity between the NO_2 groups and the citrate-passivated gold nanoparticles (see Figure 4.11). This technique opens up many opportunities for applications in biosensors, electronics, and optical devices. A similar technique based on the concept of electron-beam-induced genotoxic damage for the construction of GNP patterns was also reported [148].

The synthesis and application of other metal arrays have also been an area of research under intense pursuit. Through the LBL technique and subsequent electroless reduction of metal ions, our group constructed two-dimensional well-ordered silver arrays [149]. Briefly, the polyelectrolytes (PEs) poly(diallyldimethylammonium chloride) (PDADMAC) and PSS were adsorbed in alternating layers onto polystyrene (PS) nanospheres via electrostatic interactions, and the resulting PE-coated PS nanospheres were assembled onto a silicon wafer. Next, the PS sphere cores were extracted with toluene, leaving well-ordered interconnected PDADMAC/PSS thin shells on the surface. Finally, silver ions that had penetrated the PE shell could be reduced to produce a metallic network. The construction of nanoring arrays was also achieved by treating a hexagonally close-packed PS nanosphere array with a silane reagent before sonication in toluene [150]. The formation of a siloxane film within the interstitial voids prevents complete removal of the PS particles and results in a nanostructured array of PS–silane rings to which gold or DNA-capped gold nanoparticles could be attached. Such metal arrays could find potential applications in a variety of nanoelectronic devices and chemical and biological sensors. Our group has also fabricated polyaniline honeycombs using

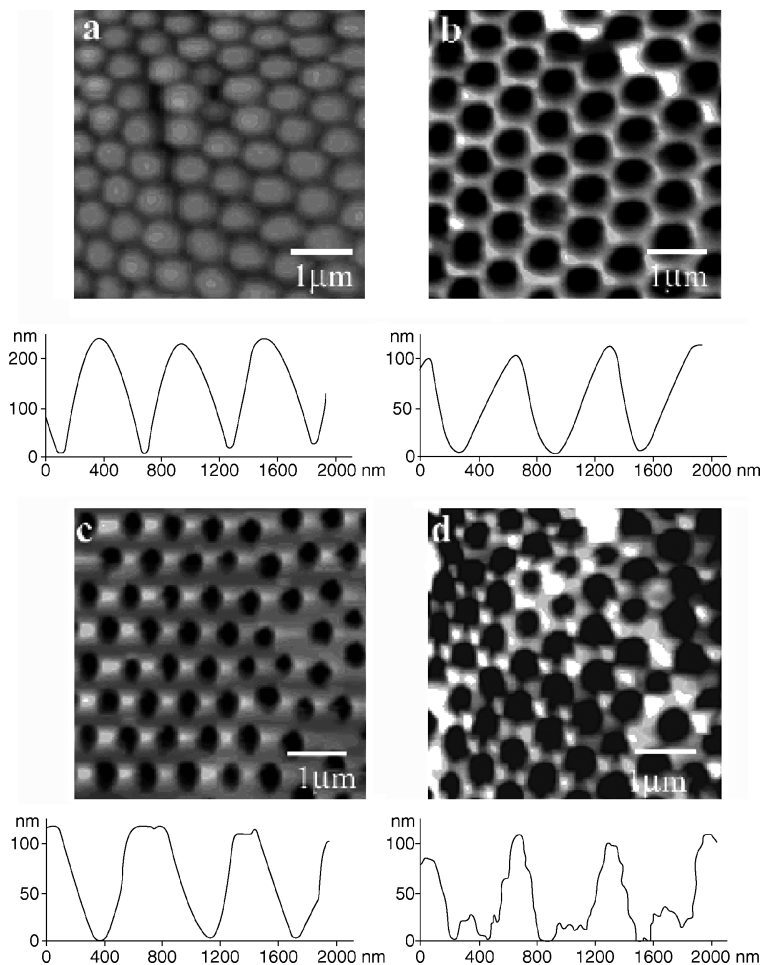


FIGURE 4.12 AFM images of (a) a gold surface covered with a close-packed two-layer polyelectrolyte coated PS particle assembly, (b) a polyaniline honeycomb film generated by electropolymerization of aniline in the interstitial voids of (a) following core extraction, (c) a polyaniline honeycomb film produced using a four-layer polyelectrolyte-PS particle assembly, and (d) a polyaniline honeycomb film templated with a bare PS particle assembly. Representative cross-sectional contours are also presented, to show the regularity of the patterns. (From ref. 151, with permission. Copyright © 2002 American Chemical Society.)

nanosphere lithography followed by electropolymerization of aniline in the interstitial voids of the nanosphere arrays [151] (Figure 4.12). Control of the pore size could be achieved by varying the number of aniline layers coated onto the surface of the PS nanospheres.

4.3.4 Nanoparticles and Nanotechnology Used in Conjunction with Scanning Electrochemical Microscopy

The ability to carry out high-throughput sample analysis using multiplexed detection is fast becoming a prerequisite for modern biosensors, and this is commonly achieved via the spatially resolved imaging of localized events on miniaturized detector arrays. The utilization of nanomaterials has not only improved this aspect of biosensing with regard to sensitivity, selectivity, and resolution, but has opened new avenues in terms of novel detection strategies. Scanning electrochemical microscopy (SECM) is finding an increasing number of biological applications [152], and the advent of nanomaterials has further broadened its scope. In SECM, an ultramicroelectrode is used to probe surface morphology and activity by measuring the local concentration profiles of species at the surface and/or in an adjacent electrolyte solution, either amperometrically or potentiometrically [153]. Arrays of biomolecules can be immobilized onto substrate surfaces, and their presence can be detected with spatial resolution (typically, submicrometer to micrometer), and the use of nanomaterials may facilitate or enhance signal transduction.

Our group used SECM for the sensitive detection of DNA hybridization by imaging localized DNA spots immobilized on microarray surfaces [132,154]. In one example, streptavidin–gold nanoparticles were attached to biotinylated target DNA which were subsequently stained with silver. Since the surface conductivity of the regions where DNA hybridization occurs is increased by silver staining, a SECM-positive feedback results. On the other hand, noncomplementary sequences of the biotinylated target do not hybridize to the surface-confined aminated probes, inhibiting the attachment of the streptavidin–colloidal gold conjugate and subsequent silver staining. Consequently, a SECM-negative feedback response is obtained. The feasibility of the method for reading a microarray with a detection level of 30 amol per spot was demonstrated [132]. A similar methodology was applied to the detection of protein spots on poly(vinylidene difluoride) (PVDF) membranes, the latter material being employed due to its high protein-binding capacity [155]. Spots of bovine serum albumin (BSA) were immobilized onto the PVDF membrane and were subsequently tagged with silver nanoparticles via physisorption or electrostatic interactions. The protein spots were thus identified as regions of positive feedback on the resulting SECM image. This technique was recently adapted to allow the visualization of proteins following gel electrophoresis [156]. Gels containing BSA were electroblotted onto PVDF membranes which were then stained with silver nanoparticles and imaged as above. The detection limit of 0.5 ng/mm² of BSA for this technique is a significant improvement on some common gel staining procedures, and the method requires less complex equipment and sample handling procedures than do the more sensitive radioactive labeling protocols.

Nanotechnology and nanomaterials also continue to play a significant role in the development of the SECM technique, which has led to improved sensitivity, selectivity, and resolution, allowing for new applications in the field of biosensing. For example, the development of nanostructured platinum microelectrodes has notably enhanced the reliable detection of hydrogen peroxide, thus advancing SECM to allow

for the imaging of peroxide-releasing enzymes [157,158]. Mesoporous SECM tips were fabricated by first assembling a three-dimensional template of surfactant rods onto the surface of a platinum microdisk electrode followed by electrodeposition of platinum into the surrounding voids. Subsequent removal of the surfactant template revealed a film with a hexagonal array of cylindrical pores, with a typical pore size and separation of 2.5 nm. Such a procedure is analogous to the nanosphere lithography, as shown in Figure 4.12. As a consequence of the high surface area of the mesoporous film, these electrodes were afforded electrocatalytic activity toward the oxidation of hydrogen peroxide. The application of these SECM tips was demonstrated by imaging of the hydrogen peroxide concentration profiles generated by monolayers of GOD immobilized with polyphenol [157] and attached to electrogenerated polypyrrole microspots [158]. In addition, the construction of nanoscale tips for simultaneous AFM–SECM imaging has permitted biosensor visualization [159–161]. The use of these complementary scanning probe microscopic techniques allows for topographical imaging of patterns of immobilized enzymes while mapping their activity amperometrically. The relevance of this hybrid methodology to biosensing applications has been demonstrated with deposited arrays of GOD [159,161] and HRP [160].

Fabrication of microelectrodes from single CNTs has also been reported [30]. Carbon nanotubes with diameters of 80 to 200 nm were cut to the desired length and connected to sharpened Pt wires. The sides of the nanotubes were insulated electrically with polyphenol, leaving an electroactive tip (Figure 4.13). Sigmoidal voltammetry was observed using an electrochemical probe, characteristic of radial diffusion to an ultramicroelectrode. Taking advantage of their geometrical shape, mechanical strength, and electrical conductivity, the microelectrodes could find their potential applications in SECM [162] and bioelectrochemistry.

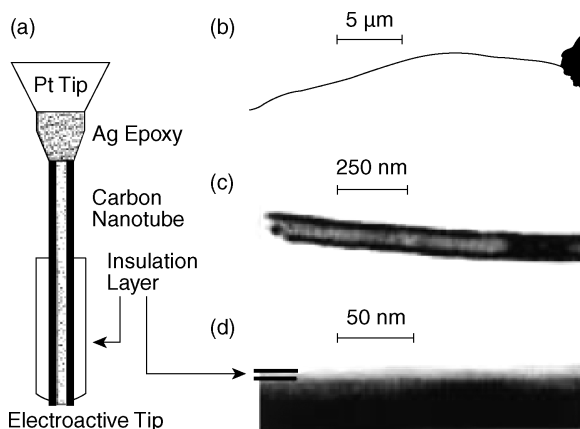


FIGURE 4.13 (a) Partially insulated CNT electrode. (b–d) TEM images of mounted nanotubular electrodes showing (b) a 30- μm -long electrode; (c) the tip of a $\sim 100\text{-nm}$ -diameter uninsulated nanoelectrode; (d) a $\sim 10\text{-nm}$ -thick insulation layer of polyphenol on a $\sim 220\text{-nm}$ -diameter nanotube. (From ref. 30, with permission. Copyright © 1999 American Chemical Society.)

On a theme similar to that of the scanning probe microscopic techniques described above, which essentially involve interrogations at nanoscale junctions, experiments have also been undertaken with biomolecules across nanogaps [163–165]. In one example, biotin-labeled peptide molecules were attached covalently to a silicon substrate, spanning a 40-nm gap between two planar gold electrodes, deposited using electron-beam lithography [163]. The capture of streptavidin-tagged gold nanoparticles in this interelectrode region resulted in an increase in conductivity, thus indicating successful binding. The same approach was employed to investigate biomolecular interactions between biotin and anti-biotin antibodies. A related signal transduction scheme involved immobilizing GOD onto polyelectrolyte bridges, linking two nanoelectrodes separated by a few tens of nanometers [164]. The conductance of these polymer nanojunctions was shown to increase with additions of glucose due to the generation of hydrogen peroxide by GOD, with a fast response time, thus demonstrating the potential of such a nanoscale device in the field of glucose sensing.

4.4 QUANTUM DOT–BASED ELECTROCHEMICAL BIOSENSORS

Quantum dots (QDs) are semiconductor particles with sizes in the nanometer and subnanometer range. Their unique optical properties, such as light absorption and photoluminescence, and electronic properties are size dependent, and due to their excellent biocompatibility, they can be used as fluorescent probes [166,167] and in electrochemical sensors for biological detection [168–174].

4.4.1 Improved Voltammetric Signals of Biologically Important Small Molecules at Quantum Dot–Modified Electrodes

Jin et al. constructed a uricase–ZnS QD/L-cysteamine assembly for reagentless amperometric UA biosensing [175]. The free carboxyl groups on the surface of ZnS QDs are responsible for the covalent binding of L-cysteamine and then uricase. The high electrocatalytic performance and anti-interference ability of the biosensor are proposed to originate from the unique properties of the carboxyl group functionalized QDs, such as solubility, biocompatibility, conductivity, and more binding sites for higher enzyme loading. In another report by the same author, a QD-modified acetylcholinesterase biosensor was proposed for the determination of trichlorfon [176].

4.4.2 Direct Electrochemistry or Electrocatalysis of Biomacromolecules at Quantum Dot–Modified Electrodes

Li and colleagues investigated the direct electrochemistry of GOD and Hb immobilized with CdS nanoparticles on graphite electrodes [168,169]. The CdS nanoparticles play an important role in facilitating the electron exchange between these heme-containing proteins and the electrode surface. Direct electrochemistry of Hb can

also be performed by immobilizing Hb in Nafion/(CdSe–ZnS) films [170]. The Hb immobilized in such films can retain its bioactivity and catalyze the reduction of NO and H₂O₂. Preparation of PVP-capped CdS QDs modified electrodes, and their application to the determination of Hb has also been reported [177,178].

QDs may be used as electrical tags for multiplexed bioanalysis. Such nanocrystal tracers have been utilized successfully for enhanced electrochemical detection of DNA hybridization [171], electrical coding of single-nucleotide polymorphisms [172], electrochemical sandwich immunoassays of proteins [174], lectin–sugar interactions [179], and multianalyte electrochemical detection [173]. Regarding the multianalyte QD/aptamer-based devices [173], the sensing protocol involves the binding of mixed monolayers of thiolated thrombin- and lysozyme-binding aptamers with thrombin–CdS and lysozyme–PbS conjugates, respectively, displacement of the tagged proteins with the mixed samples of lysozyme and thrombin, and electrochemical detection of the displaced CdS and PbS nanocrystal tracers (Figure 4.14). A detection limit at the attomole level was achieved, which is notably lower than that of the commonly used single-analyte devices [180–183]. Such a nanoparticle-based electrochemical biosensor could be used for the determination of various disease biomarkers at ultratrace levels for early diagnosis.

In another work by Wang et al., carbon nanotubes were used as carrier platforms for loading CdS nanocrystal tracers for amplified electrochemical detection of DNA hybridization [184]. The analytical protocol relies on the immobilization of the biotinylated DNA capture probe, P₁, on the streptavidin-covered microwell, and subsequent dual hybridization with the target and the SWNT–CdS–streptavidin–labeled detection probe, P₂, respectively (Figure 4.15). The combination of using carbon nanotubes as a matrix for the attachment of a large number of nanocrystal tracers and the subsequent ultrasensitive electrochemical stripping detection greatly enhanced the sensitivity of the method. In comparison with the sensing protocol based on single-particle tags [185], such an assembly dramatically lowered the detection level by approximately 500-fold.

4.5 CONCLUSIONS AND OUTLOOK

The unique properties of nanomaterials have attracted much attention in electrochemistry and offer significant promise for the construction of a wide variety of electrochemical biosensors with desirable analytical features. In this review, a range of examples encompassing carbon nanotube-, gold nanoparticle-, and quantum dot-based electrochemical biosensors have been highlighted. Particular emphasis has been directed to the use of carbon nanotubes and gold nanoparticles for the development of novel electrochemical biosensors, since these represent, by far, the most widely studied materials. It has been clearly established that improved voltammetric responses of small molecules and direct electrochemistry or electrocatalysis of biomacromolecules may be achieved at nanomaterial-modified electrodes. Nevertheless, due to limitations imposed by the random orientation of the nanostructures and the unknown spatial relationship between redox species and the

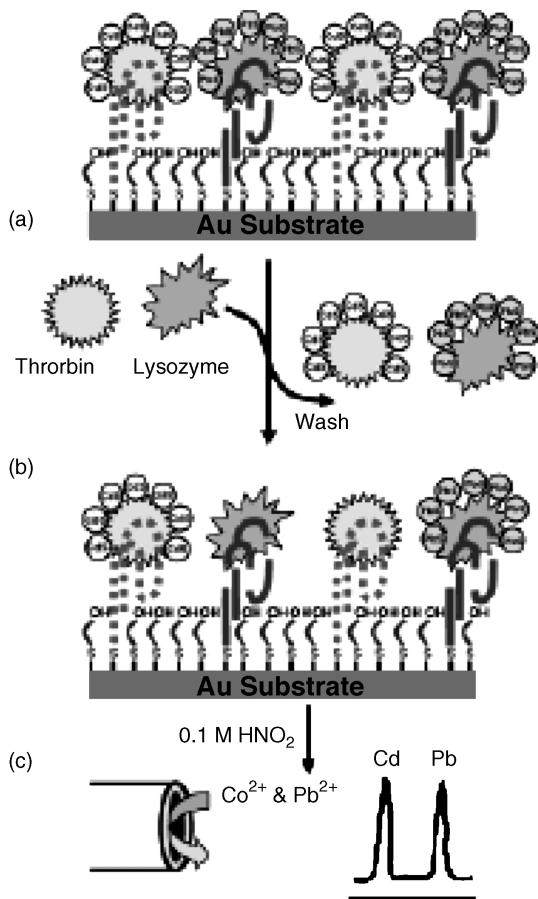


FIGURE 4.14 Operation of the aptamer–QD-based dual-analyte biosensor, involving displacement of the tagged proteins by the target analytes: (a) mixed monolayer of thiolated aptamers on gold substrates with the bound protein–QD conjugates; (b) sample addition and displacement of the tagged proteins; (c) dissolution of the remaining captured nanocrystals followed by their electrochemical-stripping detection at a coated glassy carbon electrode. (From ref. 173, with permission. Copyright © 2006 American Chemical Society.)

nanomaterials, highly aligned nanoarrays or nanopatterns for biological applications have also been developed to address this. Furthermore, the attractive features of nanomaterials have notably affected the practice of SECM and its application to the imaging of immobilized biomolecules, and the novel techniques developed demonstrate real potential for the future of bisensing.

From the examples described throughout the chapter, it is evident that the integration of nanomaterials or innovative nanodevices with electrochemistry has given rise to new opportunities for remarkable improvements in the analytical figures of merit of a range of biosensors. Such nanomaterial-based electrochemical

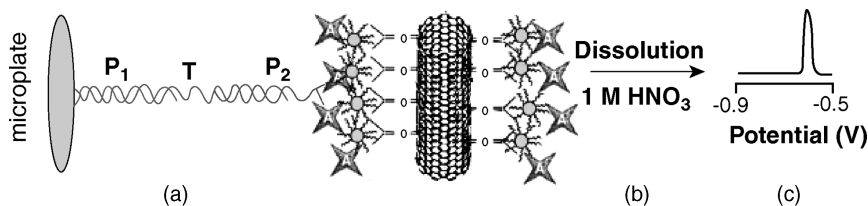


FIGURE 4.15 Analytical protocol: (a) dual hybridization event of the sandwich hybridization assay, leading to capturing of the CdS-loaded CNT tags in the microwell; (b) dissolution of the CdS tracer; (c) stripping voltammetric detection of cadmium at a mercury-coated glassy carbon electrode. P₁, DNA probe 1; T, DNA target; P₂, DNA probe 2. (From ref. 184, with permission. Copyright © 2003 Elsevier Science B.V.)

devices are expected to hold great promise for many important applications, such as gene and protein analyses, disease diagnostics, sensitive detection of biologically important small molecules, and development of miniaturized biosensors for highly selective and sensitive assays. With the development of nanotechnology along with progress in existing detection methods, powerful sensor arrays for parallel and real-time monitoring of multiple analytes are becoming readily attainable. Undoubtedly, biosensors have become increasingly important to various disciplines, and with the construction of a wide range of new nanostructures, a multitude of applications featuring these materials in electrochemical fields is expected in the near future.

Acknowledgments

We thank the NIH-RIMI Program (P20 MD001824-01), the Dreyfus Teacher-Scholar Award (TH-01-025), an NSF-RUI grant (0555244), and the National Natural Science Foundation of China (No. 20775093 and 20225517) for supporting our work.

REFERENCES

1. Chen J, Miao Y, He N, Wu X, Li S. Nanotechnology and biosensors. *Biotechnol. Adv.* 2004;22:505–518.
2. Wang J. Nanomaterial-based electrochemical biosensors. *Analyst.* 2005;130:421–426.
3. Vo-Dinh T, Cullum BM, Stokes DL. Nanosensors and biochips: frontiers in biomolecular diagnostics. *Sens. Actuators B.* 2001;74:2–11.
4. Haruyama T. Micro- and nanobiotechnology for biosensing cellular responses. *Adv. Drug Deliv. Rev.* 2003;55:393–401.
5. Jain KK. Nanodiagnosics: application of nanotechnology in molecular diagnostics. *Expert Rev. Mol. Diagn.* 2003;3:153–161.
6. Katz E, Willner I. Nanobiotechnology: integrated nanoparticle-biomolecule hybrid systems: synthesis, properties, and applications. *Angew. Chem. Int. Ed.* 2004;43:6042–6108.

7. Patolsky F, Weizmann Y, Willner I. Long-range electrical contacting of redox enzymes by SWCNT connectors. *Angew. Chem. Int. Ed.* 2004;43:2113–2117.
8. Willner I. Tech sight: Biomaterials for sensors, fuel cells, and circuitry. *Science.* 2002;298:2407–2408.
9. Wang J. Nanomaterial-based amplified transduction of biomolecular interactions. *Small.* 2005;1:1036–1043.
10. Iijima S. Helical microtubules of graphitic carbon. *Nature.* 1991;354:56–58.
11. Iijima S, Ichihashi T. Single-shell carbon nanotubes of 1-nm diameter. *Nature.* 1993;363:603–605.
12. De Heer WA, Chatelain A, Ugarte D. A carbon nanotube field-emission electron source. *Science.* 1995;270:1179–1180.
13. Collins PG, Zettl A, Bando H, Thess A, Smalley RE. Nanotube nanodevice. *Science.* 1997;278:100–103.
14. Baughman RH, Cui CX, Zakhidov AA, et al. Carbon nanotube actuators. *Science.* 1999;284:1340–1344.
15. Che GL, Lakschmi BB, Fisher ER, Martin CR. Carbon nanotubule membranes for electrochemical energy storage and production. *Nature.* 1998;393:346–349.
16. Wong SS, Joselevich E, Woolley AT, Cheung CL, Lieber CM. Covalently functionalized nanotubes as nanometer-sized probes in chemistry and biology. *Nature.* 1998;394:52–55.
17. Davis JJ, Coleman KS, Azamian BR, Bagshaw CB, Green MLH. Chemical and biochemical sensing with modified single walled carbon nanotubes. *Chem. Eur. J.* 2003;9:3732–3739.
18. Sankaran M, Viswanathan B. The role of heteroatoms in carbon nanotubes for hydrogen storage. *Carbon.* 2006;44:2816–2821.
19. Dresselhaus MS. Down the straight and narrow. *Nature.* 1992;358:195–196.
20. Wildöer JWG, Venema LC, Rinzler AG, Smalley RE, Dekker C. Electronic structure of atomically resolved carbon nanotubes. *Nature.* 1998;391:59–62.
21. Wildgoose GG, Banks CE, Leventis HC, Compton RG. Chemically modified carbon nanotubes for use in electroanalysis. *Microchim. Acta.* 2006;152:187–214.
22. Britto PJ, Santhanam KSV, Ajayan PM. Carbon nanotube electrode for oxidation of dopamine. *Bioelectrochem. Bioenerg.* 1996;41:121–125.
23. Banks CE, Compton RG. New electrodes for old: from carbon nanotubes to edge plane pyrolytic graphite. *Analyst.* 2006;131:15–21.
24. Banks CE, Davies TJ, Wildgoose GG, Compton RG. Electrocatalysis at graphite and carbon nanotube modified electrodes: edge-plane sites and tube ends are the reactive sites. *Chem. Commun.* 2005;7:829–841.
25. Banks CE, Compton RG. Exploring the electrocatalytic sites of carbon nanotubes for NADH detection: an edge plane pyrolytic graphite electrode study. *Analyst.* 2005;130:1232–1239.
26. Banks CE, Moore RR, Davies TJ, Compton RG. Investigation of modified basal plane pyrolytic graphite electrodes: definitive evidence for the electrocatalytic properties of the ends of carbon nanotubes. *Chem. Commun.* 2004;16:1804–1805.
27. Britto PJ, Santhanam KSV, Rubio A, Alonso JA, Ajayan PM. Improved charge transfer at carbon nanotube electrodes. *Adv. Mater.* 1999;11:154–157.
28. Fridovich I. The biology of oxygen radicals. *Science.* 1978;201:875–880.

29. Luo HX, Shi ZJ, Li NQ, Gu ZN, Zhuang QK. Investigation of the electrochemical and electrocatalytic behavior of single-wall carbon nanotube film on a glassy carbon electrode. *Anal. Chem.* 2001;73:915–920.
30. Campbell JK, Sun L, Crooks RM. Electrochemistry using single carbon nanotubes. *J. Am. Chem. Soc.* 1999;121:3779–3780.
31. Chen P, McCreery RL. Control of electron transfer kinetics at glassy carbon electrodes by specific surface modification. *Anal. Chem.* 1996;68:3958–3965.
32. Guo T, McCreery RL. Surface chemistry and electron-transfer kinetics of hydrogen-modified glassy carbon electrodes. *Anal. Chem.* 1999;71:1553–1560.
33. Gong KP, Zhu XZ, Zhao R, Xiong SX, Mao LQ, Chen CF. Rational attachment of synthetic triptycene orthoquinone onto carbon nanotubes for electrocatalysis and sensitive detection of thiols. *Anal. Chem.* 2005;77:8158–8165.
34. Wang JX, Li MX, Shi ZJ, Li NQ, Gu ZN. Electrocatalytic oxidation of 3,4-dihydroxyphenylacetic acid at a glassy carbon electrode modified with single-wall carbon nanotubes. *Electrochim. Acta.* 2001;47:651–657.
35. Wang JX, Li MX, Shi ZJ, Li NQ, Gu ZN. Electrocatalytic oxidation of norepinephrine at a glassy carbon electrode modified with single-wall carbon nanotubes. *Electroanalysis.* 2002;14:225–230.
36. Wang JX, Li MX, Shi ZJ, Li NQ, Gu ZN. Investigation of the electrocatalytic behavior of single-wall carbon nanotube films on a Au electrode. *Microchem. J.* 2002;73:325–333.
37. Li NQ, Wang JX, Li MX. Electrochemistry at carbon nanotube electrodes. *Rev. Anal. Chem.* 2003;22:19–33.
38. Liu PF, Hu JH. Carbon nanotube powder microelectrodes for nitrite detection. *Sens. Actuators B.* 2002;84:194–199.
39. Barisci JN, Wallace GG, Baughman RH. Electrochemical characterization of single-wall carbon nanotube electrodes. *J. Electrochem. Soc.* 2000;147:4580–4583.
40. Wang J, Musameh M. Electrochemical detection of trace insulin at carbon nanotube-modified electrodes. *Anal. Chim. Acta.* 2004;511:33–36.
41. Wu FH, Zhao GC, Wei XW, Yang ZS. Electrocatalysis of tryptophan at multi-walled carbon nanotube modified electrode. *Microchim. Acta.* 2004;144:243–247.
42. Musameh M, Wang J, Merkoci A, Lin YH. Low-potential stable NADH detection at carbon-nanotube-modified glassy carbon electrodes. *Electrochem. Commun.* 2002;4:743–746.
43. Lobo MJ, Miranda AJ, Tunon P. Amperometric biosensors based on NAD(P)-dependent dehydrogenase enzymes. *Electroanalysis.* 1997;9:191–202.
44. Gorton L, Dominguez E. Electrocatalytic oxidation of NAD(P) H at mediator-modified electrodes. *Rev. Mol. Biotechnol.* 2002;82:371–392.
45. Blaedel WJ, Jenkins RA. Electrochemical oxidation of reduced nicotinamide adenine dinucleotide. *Anal. Chem.* 1975;47:1337–1343.
46. Wang J, Angnes L, Martinez T. Scanning tunneling microscopic probing of surface fouling during the oxidation of nicotinamide coenzymes. *Bioelectrochem. Bioenerg.* 1992;29:215–221.
47. Chen J, Bao JC, Cai CX, Lu TH. Direct electrochemical oxidation of dihydronicotinamide adenine dinucleotide (NADH) at an ordered carbon nanotubes electrode. *Chin. Chem. Lett.* 2003;14:1171–1174.

48. Zhang HM, Wang XB, Wan LJ, Liu YQ, Bai CL. Electrochemical behavior of multi-wall carbon nanotubes and electrocatalysis of toluene-filled nanotube film on gold electrode. *Electrochim. Acta.* 2004;49:715–719.
49. Wildgoose GG, Banks CE, Compton RG. Metal nanoparticles and related materials supported on carbon nanotubes: methods and applications. *Small.* 2006;2:182–193.
50. Kong J, Chapline M, Dai H. Functionalized carbon nanotubes for molecular hydrogen sensors. *Adv. Mater.* 2001;13:1384–1386.
51. Bezryadin A, Lau CN, Tinkham M. Quantum suppression of superconductivity in ultrathin nanowires. *Nature.* 2000;404:971–974.
52. Steigerwalt ES, Deluga GA, Lukehart CM. Pt–Ru/carbon fiber nanocomposites: synthesis, characterization, and performance as anode catalysts of direct methanol fuel cells: a search for exceptional performance. *J. Phys. Chem. B.* 2002;106:760–766.
53. Hermans S, Sloan J, Shephard DS, Johnson BFG, Green MLH. Bimetallic nanoparticles aligned at the tips of carbon nanotubes. *Chem. Commun.* 2002;276–277.
54. Li J, Moskovits M, Haslett T. Nanoscale electroless metal deposition in aligned carbon nanotubes. *Chem. Mater.* 1998;10:1963–1967.
55. Choi HC, Shim M, Bangsaruntip S, Dai H. Spontaneous reduction of metal ions on the sidewalls of carbon nanotubes. *J. Am. Chem. Soc.* 2002;124:9058–9059.
56. Ye JS, Cui HF, Wen Y, Zhang WD, Xu GQ, Sheu FS. Electrodeposition of platinum nanoparticles on multi-walled carbon nanotubes for electrocatalytic oxidation of methanol. *Microchim. Acta.* 2006;152:267–275.
57. Ye JS, Wen Y, Zhang WD, Gan LM, Xu GQ, Sheu FS. Selective voltammetric detection of uric acid in the presence of ascorbic acid at well-aligned carbon nanotube electrode. *Electroanalysis.* 2003;15:1693–1698.
58. Wang ZH, Wang YM, Luo GA. A selective voltammetric method for uric acid detection at β -cyclodextrin modified electrode incorporating carbon nanotubes. *Analyst.* 2002;127:1353–1358.
59. Wang ZH, Liu J, Liang QL, Wang YM, Luo GA. Carbon nanotube-modified electrodes for the simultaneous determination of dopamine and ascorbic acid. *Analyst.* 2002;127:653–658.
60. Hu CG, Wang WL, Feng B, Wang H. Simultaneous measurement of dopamine and ascorbic acid at CNT electrode. *Int. J. Mod. Phys. B.* 2005;19:607–610.
61. Zhang M, Liu K, Xiang L, Lin Y, Su L, Mao L. Carbon nanotube-modified carbon fiber microelectrodes for in vivo voltammetric measurement of ascorbic acid in rat brain. *Anal. Chem.* 2007;79:6559–6565.
62. Davis JJ, Coles RJ, Hill HAO. Protein electrochemistry at carbon nanotube electrodes. *J. Electroanal. Chem.* 1997;440:279–282.
63. Wang JX, Li MX, Shi ZJ, Li NQ, Gu ZN. Direct electrochemistry of cytochrome *c* at a glassy carbon electrode modified with single-wall carbon nanotubes. *Anal. Chem.* 2002;74:1993–1997.
64. Wang L, Wang JX, Zhou FM. Direct electrochemistry of catalase at a gold electrode modified with single-wall carbon nanotubes. *Electroanalysis.* 2004;16:627–632.
65. Wang JX, Li MX, Shi ZJ, Li NQ, Gu ZN. Electrochemistry of DNA at single-wall carbon nanotubes. *Electroanalysis.* 2004;16:140–144.

66. Liu Y, Wang MK, Zhao F, Xu ZA, Dong SJ. The direct electron transfer of glucose oxidase and glucose biosensor based on carbon nanotubes/chitosan matrix. *Biosens. Bioelectron.* 2005;21:984–988.
67. Wang MK, Zhao F, Liu Y, Dong SJ. Direct electrochemistry of microperoxidase at Pt microelectrodes modified with carbon nanotubes. *Biosens. Bioelectron.* 2005;21:159–166.
68. Wang MK, Shen Y, Liu Y, et al. Direct electrochemistry of microperoxidase 11 using carbon nanotube modified electrodes. *J. Electroanal. Chem.* 2005;578:121–127.
69. Chen HJ, Dong SJ. Direct electrochemistry and electrocatalysis of horseradish peroxidase immobilized in sol–gel-derived ceramic–carbon nanotube nanocomposite film. *Biosens. Bioelectron.* 2007;22:1811–1815.
70. Luo XL, Killard AJ, Smyth MR. Reagentless glucose biosensor based on the direct electrochemistry of glucose oxidase on carbon nanotube-modified electrodes. *Electroanalysis.* 2006;18:1131–1134.
71. Liu Y, Wang MK, Zhao F, Guo ZH, Chen HJ, Dong SJ. Direct electron transfer and electrocatalysis of microperoxidase immobilized on nanohybrid film. *J. Electroanal. Chem.* 2005;581:1–10.
72. Santuel R, Reinhard L, Brunori M. Direct electrochemistry of the undecapeptide from cytochrome *c* (microperoxidase) at a glassy carbon electrode. *J. Am. Chem. Soc.* 1988;110:8536–8537.
73. Laviron E. General expression of the linear potential sweep voltammogram in the case of diffusionless electrochemical systems. *J. Electroanal. Chem.* 1979;101:19–28.
74. Zhang Z, Rusling JF. Electron transfer between myoglobin and electrodes in thin films of phosphatidylcholines and dihexadecylphosphate. *Biophys. Chem.* 1997;63:133–146.
75. Nassar AEF, Zhang Z, Hu N, Rusling JF, Kumosinski TF. Proton-coupled electron transfer from electrodes to myoglobin in ordered biomembrane-like films. *J. Phys. Chem. B.* 1997;101:2224–2231.
76. Liu Q, Lu XB, Li J, Yao X, Li JH. Direct electrochemistry of glucose oxidase and electrochemical biosensing of glucose on quantum dots/carbon nanotubes electrodes. *Biosens. Bioelectron.* 2007;22:3203–3209.
77. Zhao LY, Liu HY, Hu NF. Assembly of layer-by-layer films of heme proteins and single-walled carbon nanotubes: electrochemistry and electrocatalysis. *Anal. Bioanal. Chem.* 2006;384:414–422.
78. Liu GD, Lin YH. Carbon nanotube-templated assembly of protein. *J. Nanosci. Nanotechnol.* 2006;6:948–953.
79. Gooding JJ, Wibowo R, Liu JQ, et al. Protein electrochemistry using aligned carbon nanotube arrays. *J. Am. Chem. Soc.* 2003;125:9006–9007.
80. Liu Z, Shen Z, Zhu T, et al. Organizing single-walled carbon nanotubes on gold using a wet chemical self-assembling technique. *Langmuir.* 2000;16:3569–3573.
81. Liu JQ, Chou A, Rahmat W, Paddon-Row MN, Gooding JJ. Achieving direct electrical connection to glucose oxidase using aligned single walled carbon nanotube arrays. *Electroanalysis.* 2005;17:38–46.
82. Yun YH, Shanov V, Schulz MJ, et al. High sensitivity carbon nanotube tower electrodes. *Sens. Actuators B.* 2006;120:298–304.

83. Qu LT, He PG, Li LC, Gao M, Wallace G, Dai LM. Aligned/micropatterned carbon nanotube arrays: surface functionalization and electrochemical sensing. *Proc. SPIE.* 2005;5732(Quantum Sensing and Nanophotonic Devices II):84–92.
84. O'Connor M, Kim SN, Killard AJ, et al. Mediated amperometric immunosensing using single walled carbon nanotube forests. *Analyst.* 2004;129:1176–1180.
85. Park DW, Kim YH, Kim BS, et al. Detection of tumor markers using single-walled carbon nanotube field effect transistors. *J. Nanosci. Nanotechnol.* 2006;6:3499–3502.
86. Li J, Ng HT, Cassell A, et al. Carbon nanotube nanoelectrode array for ultrasensitive DNA detection. *Nano Lett.* 2003;3:597–602.
87. Hernández-Santos D, González-García MB, García AC. Metal-nanoparticles based electroanalysis. *Electroanalysis.* 2002;14:1225–1235.
88. Yu A, Liang Z, Cho J, Caruso F. Nanostructured electrochemical sensor based on dense gold nanoparticle films. *Nano Lett.* 2003;3:1203–1207.
89. Welch CM, Compton RG. The use of nanoparticles in electroanalysis: a review. *Anal. Bioanal. Chem.* 2006;384:601–619.
90. Raj CR, Abdelrahman AI, Ohsaka T. Gold nanoparticle-assisted electroreduction of oxygen. *Electrochem. Commun.* 2005;7:888–893.
91. Zhang YR, Asahina S, Yoshihara S, Shirakashi T. Oxygen reduction on Au nanoparticle deposited boron-doped diamond films. *Electrochim. Acta.* 2003;48:741–747.
92. Zhang JD, Oyama M. Gold nanoparticle arrays directly grown on nanostructured indium tin oxide electrodes: characterization and electroanalytical application. *Anal. Chim. Acta.* 2005;540:299–306.
93. Zhu M, Liu M, Shi G, et al. Novel nitric oxide microsensor and its application to the study of smooth muscle cells. *Anal. Chim. Acta.* 2002;455:199–206.
94. Goyal RN, Gupta VK, Oyama M, Bachheti N. Gold nanoparticles modified indium tin oxide electrode for the simultaneous determination of dopamine and serotonin: application in pharmaceutical formulations and biological fluids. *Talanta.* 2007;72:976–983.
95. Zhang JD, Oyama M. Electrocatalytic activity of three-dimensional monolayer of 3-mercaptopropionic acid assembled on gold nanoparticle arrays. *Electrochem. Commun.* 2007;9:459–464.
96. Maye MM, Lou YB, Zhong CJ. Core-shell gold nanoparticle assembly as novel electrocatalyst of CO oxidation. *Langmuir.* 2000;16:7520–7523.
97. Haruta M. Size- and support-dependency in the catalysis of gold. *Catal. Today.* 1997;36:153–166.
98. Bond GC. Catalysis by gold. *Catal. Rev.* 1999;41:319–388.
99. Zhao J, Henkens RW, Stonehuerner J, O'Daly JP, Crumbliss AL. Direct electron transfer at horseradish peroxidase-colloidal gold modified electrodes. *J. Electroanal. Chem.* 1992;327:109–119.
100. Zhao J, O'Daly JP, Henkens RW, Stonehuerner J, Crumbliss AL. A xanthine oxidase/colloidal gold enzyme electrode for amperometric biosensor applications. *Biosens. Bioelectron.* 1996;11:493–502.
101. Crumbliss AL, Stonehuerner J, Henkens RW, Zhar J, O'Daly JP. A carrageenan hydrogel stabilized colloidal gold multi-enzyme biosensor electrode utilizing immobilized

- horseradish peroxidase and cholesterol oxidase/cholesterol esterase to detect cholesterol in serum and whole blood. *Biosens. Bioelectron.* 1993;8:331–337.
102. Crumbliss AL, Perine SC, Stonehuerner J, et al. Colloidal gold as a biocompatible immobilization matrix suitable for the fabrication of enzyme electrodes by electrodeposition. *Biotechnol Bioeng.* 1992;40:483–490.
 103. Miscoria SA, Barrera GD, Rivas GA. Enzymatic biosensor based on carbon paste electrodes modified with gold nanoparticles and polyphenol oxidase. *Electroanalysis.* 2005;17:1578–1582.
 104. Xue MH, Xu Q, Zhou M, Zhu JJ. In situ immobilization of glucose oxidase in chitosan–gold nanoparticle hybrid film on Prussian Blue modified electrode for high-sensitivity glucose detection. *Electrochem. Commun.* 2006;8:1468–1474.
 105. Willner I, Willner B. Functional nanoparticle architectures for sensoric, optoelectronic, and bioelectronic applications. *Pure Appl. Chem.* 2002;74:1773–1783.
 106. Alexeyeva N, Laaksonen T, Kontturi K, Mirkhalaf F, Schiffrin DJ, Tammeveski K. Oxygen reduction on gold nanoparticle/multi-walled carbon nanotubes modified glassy carbon electrodes in acid solution. *Electrochem. Commun.* 2006;8:1475–1480.
 107. Lee KP, Gopalan AL, Santhosh P, Manesh KM, Kim JH, Kim KS. Fabrication and electrocatalysis of self-assembly directed gold nanoparticles anchored carbon nanotubes modified electrode. *J. Nanosci. Nanotechnol.* 2006;6:1575–1583.
 108. Wang L, Wang EK. Direct electron transfer between cytochrome *c* and a gold nanoparticles modified electrode. *Electrochem. Commun.* 2004;6:49–54.
 109. Han XJ, Cheng WL, Zhang ZL, Dong SJ, Wang EK. Direct electron transfer between hemoglobin and a glassy carbon electrode facilitated by lipid-protected gold nanoparticles. *Biochim. Biophys. Acta.* 2002;1556:273–277.
 110. Liu SQ, Ju HX. Reagentless glucose biosensor based on direct electron transfer of glucose oxidase immobilized on colloidal gold modified carbon paste electrode. *Biosens. Bioelectron.* 2003;19:177–183.
 111. Liu SQ, Ju HX. Electrocatalysis via direct electrochemistry of myoglobin immobilized on colloidal gold nanoparticles. *Electroanalysis.* 2003;15:1488–1493.
 112. Liu SQ, Ju HX. Renewable reagentless hydrogen peroxide sensor based on direct electron transfer of horseradish peroxidase immobilized on colloidal gold-modified electrode. *Anal. Biochem.* 2002;307:110–116.
 113. Zhang JD, Oyama M. Gold nanoparticle-attached ITO as a biocompatible matrix for myoglobin immobilization: direct electrochemistry and catalysis to hydrogen peroxide. *J. Electroanal. Chem.* 2005;577:273–279.
 114. Fan LZ, Yang SF, Yang SH. Electroactive endohedral metallofullerene film electrodes in aqueous solutions. *J. Electroanal. Chem.* 2005;574:273–283.
 115. Patolsky F, Gabriel T, Willner I. Controlled electrocatalysis by microperoxidase-11 and Au-nanoparticle superstructures on conductive supports. *J. Electroanal. Chem.* 1999;479:69–73.
 116. Shumyantseva VV, Carrara S, Bavastrello V, et al. Direct electron transfer between cytochrome P450_{scd} and gold nanoparticles on screen-printed rhodium-graphite electrodes. *Biosens. Bioelectron.* 2005;21:217–222.
 117. Cai WY, Xu Q, Zhao XN, Zhu JJ, Chen HY. Porous gold–nanoparticle–CaCO₃ hybrid material: preparation, characterization, and application for horseradish peroxidase assembly and direct electrochemistry. *Chem. Mater.* 2006;18:279–284.

118. Albery WJ, Eddowes MJ, Hill HAO, Hillman AR. Mechanism of the reduction and oxidation reaction of cytochrome *c* at a modified gold electrode. *J. Am. Chem. Soc.* 1981;103:3904–3910.
119. Biswas S. Assessment of immunometric parameters in malaria: role of enzyme immunoassay. *J. Immunoassay Immunochem.* 2006;27:341–350.
120. Diaz-Gonzalez M, Garcia MB, Costa-Garcia A. Recent advances in electrochemical enzyme immunoassays. *Electroanalysis.* 2005;17:1909–1918.
121. Thanh NTK, Rosenaweig Z. Development of an aggregation-based immunoassay for anti-protein A using gold nanoparticles. *Anal. Chem.* 2002;74:1624–1628.
122. Huang HZ, Liu ZG, Yang XR. Application of electrochemical impedance spectroscopy for monitoring allergen–antibody reactions using gold nanoparticle-based biomolecular immobilization method. *Anal. Biochem.* 2006;356:208–214.
123. Chen J, Tang JH, Yan F, Ju HX. A gold nanoparticles/sol–gel composite architecture for encapsulation of immunoconjugate for reagentless electrochemical immunoassay. *Biomaterials.* 2006;27:2313–2321.
124. Liu G, Lin Y. A renewable electrochemical magnetic immunosensor based on gold nanoparticle labels. *J. Nanosci. Nanotechnol.* 2005;5:1060–1065.
125. Tang DQ, Zhang DJ, Tang DY, Ai H. One-step electrochemical immunoassay for carcinoembryonic antigen in human via back-filling immobilization of gold nanoparticles on DNA-modified gold electrodes. *Electroanalysis.* 2006;18:2194–2201.
126. Du D, Xu XX, Wang SF, Zhang AD. Reagentless amperometric carbohydrate antigen 19-9 immunosensor based on direct electrochemistry of immobilized horseradish peroxidase. *Talanta.* 2007;71:1257–1262.
127. Patolsky F, Ranjit KT, Lichtenstein A, Willner I. Dendritic amplification of DNA analysis by oligonucleotide-functionalized Au-nanoparticles. *Chem. Commun.* 2000; 1025–1026.
128. Han S, Lin J, Satjapipat M, Baca AJ, Zhou F. A three-dimensional heterogeneous DNA sensing surface formed by attaching oligodeoxynucleotide-capped gold nanoparticles onto a gold-coated quartz crystal. *Chem. Commun.* 2001;609–610.
129. Storhoff JJ, Elghanian R, Mucic RC, Mirkin CA, Letsinger RL. One-pot colorimetric differentiation of polynucleotides with single base imperfections using gold nanoparticle probes. *J. Am. Chem. Soc.* 1998;120:1959–1964.
130. Wang J, Xu DK, Kawde AN, Polsky R. Metal nanoparticle-based electrochemical stripping potentiometric detection of DNA hybridization. *Anal. Chem.* 2001;73: 5576–5581.
131. Wang J, Li JH, Baca AJ, et al. Amplified voltammetric detection of DNA hybridization via oxidation of ferrocene caps on gold nanoparticle/streptavidin conjugates. *Anal. Chem.* 2003;75:3941–3945.
132. Wang J, Song FY, Zhou F. Silver-enhanced imaging of DNA hybridization at DNA microarrays with scanning electrochemical microscopy. *Langmuir.* 2002;18:6653–6658.
133. Ozsoz M, Erdem A, Kerman K, et al. Electrochemical genosensor based on colloidal gold nanoparticles for the detection of factor V Leiden mutation using disposable pencil graphite electrodes. *Anal. Chem.* 2003;75:2181–2187.
134. Lee TMH, Li L-L, Hsing I-M. Enhanced electrochemical detection of DNA hybridization based on electrode-surface modification. *Langmuir.* 2003;19:4338–4343.

135. Wang J, Xu DK, Polsky R. Magnetically-induced solid-state electrochemical detection of DNA hybridization. *J. Am. Chem. Soc.* 2002;124:4208–4209.
136. Bakker E. Electrochemical sensors. *Anal. Chem.* 2004;76:3285–3298.
137. Jimenez O, Chikneyan SZ, Baca A, Wang J, Zhou F. Sensitive detection of sulfhydryl groups in surface-confined metallothioneins and related species via ferrocene-capped gold nanoparticle/streptavidin conjugates. *Environ. Sci. Technol.* 2005;39:1209–1213.
138. Baca AJ, Zhou F, Wang J, et al. Attachment of ferrocene-capped gold nanoparticle/streptavidin conjugates onto electrode surfaces covered with biotinylated biomolecules for enhanced voltammetric analysis. *Electroanalysis.* 2003;16:73–80.
139. Wang JX, Zhu X, Tu QY, et al. Capture of p53 by electrodes modified with consensus DNA duplexes and amplified voltammetric detection using ferrocene-capped gold nanoparticle/streptavidin conjugates. *Anal. Chem.* 2008;80:769–774.
140. Kerman K, Morita Y, Takamura Y, Ozsoz M, Tamiya E. Modification of *Escherichia coli* single-stranded DNA binding protein with gold nanoparticles for electrochemical detection of DNA hybridization. *Anal. Chim. Acta.* 2004;510:169–174.
141. Chase JW, Williams KR. Single-stranded DNA binding proteins required for DNA replication. *Annu. Rev. Biochem.* 1986;55:103–136.
142. Curulli A, Valentini F, Padeletti G, et al. Gold nanotubules arrays as new materials for sensing and biosensing: Synthesis and characterization. *Sens. Actuators B.* 2005;111–112:526–531.
143. Lee HY, Park JW, Kim JM, Jung HS, Kawai T. Well-oriented nanowell array metrics for integrated digital nanobiosensors. *Appl. Phys. Lett.* 2006;89:113901/1–113901/3
144. Jung HS, Park JW, Kim JM, Lee HY, Kawai T. Amperometric immunosensor for direct detection based upon functional lipid vesicles immobilized on nanowell array electrode. *Langmuir.* 2005;21:6025–6029.
145. Goral VN, Zaytseva NV, Baeumner AJ. Electrochemical microfluidic biosensor for the detection of nucleic acid sequences. *Lab Chip.* 2006;6:414–421.
146. Gales C, Rebois RV, Hogue M, et al. Real-time monitoring of receptor and G-protein interactions in living cells. *Nat. Methods.* 2005;2:177–184.
147. Mendes PM, Jacke S, Critchley K, et al. Evans SD, Fitzmaurice D. Gold nanoparticle patterning of silicon wafers using chemical e-beam lithography. *Langmuir.* 2004;20:3766–3768.
148. Lin H-Y, Tsai L-C, Chi P-Y, Chen C-D. DNA as an electron-beam-sensitive reagent for nanopatterning. *Adv. Mater.* 2006;18:1517–1520.
149. Han SB, Shi XY, Zhou FM. Polyelectrolyte hollow sphere lithographic patterning of surface: construction of 2-dimensional well-ordered metal arrays. *Nano Lett.* 2002;2:97–100.
150. Wang Y, Han S, Briseno AL, Sanedrin RJ, Zhou F. A modified nanosphere lithographic method for the fabrication of aminosilane/polystyrene nanoring arrays and the subsequent attachment of gold or DNA-capped gold nanoparticles. *J. Mater. Chem.* 2004;14:1–8.
151. Han S, Briseno AL, Shi X, Mah D, Zhou F. Polyelectrolyte-coated nanosphere lithographic patterning of surfaces: fabrication and characterization of electropolymerized thin polyaniline honeycomb films. *J. Phys. Chem. B.* 2002;106:6465–6472.

152. Gyurcsányia RE, Jágorszka G, Kissb G, Tóth K. Chemical imaging of biological systems with the scanning electrochemical microscope. *Bioelectrochemistry*. 2004;63:207–215.
153. Bard AJ, Fan F-RF, Kwak J, Lev O. Scanning electrochemical microscopy. Introduction and principles. *Anal. Chem.* 1989;61:132–138.
154. Wain AJ, Zhou F. Scanning electrochemical microscopy imaging of DNA microarrays using methylene blue as a redox-active intercalator. *Langmuir*. 2008;24:5155–5160.
155. Carano M, Lion N, Abid J-P, Girault HH. Detection of proteins on poly(vinylidene difluoride) membranes by scanning electrochemical microscopy. *Electrochem. Commun.* 2004;6:1217–1221.
156. Zhang M, Wittstock G, Shao Y, Girault HH. Scanning electrochemical microscopy as a readout tool for protein electrophoresis. *Anal. Chem.* 2007;79:4833–4839.
157. Evans SAG, Elliott JM, Andrews LM, Bartlett PN, Doyle PJ, Denuault G. Detection of hydrogen peroxide at mesoporous platinum microelectrodes. *Anal. Chem.* 2002;74:1322–1326.
158. Evans SAG, Brakha K, Billon M, Mailley P, Denuault G. Scanning electrochemical microscopy (SECM): localized glucose oxidase immobilization via the direct electrochemical microspotting of polypyrrole–biotin films. *Electrochem. Commun.* 2005;7:135–140.
159. Hirata Y, Yabuki S, Mizutani F. Application of integrated SECM ultra-micro-electrode and AFM force probe to biosensor surfaces. *Bioelectrochemistry*. 2004;63:217–224.
160. Kranz C, Kueng A, Lugstein A, Bertagnolli E, Mizaikoff B. Mapping of enzyme activity by detection of enzymatic products during AFM imaging with integrated SECM–AFM probes. *Ultramicroscopy*. 2004;100:127–134.
161. Kueng A, Kranz C, Lugstein A, Bertagnolli E, Mizaikoff B. Integrated AFM–SECM in tapping mode: simultaneous topographical and electrochemical imaging of enzyme activity. *Angew. Chem. Int. Ed.* 2003;42:3238–3240.
162. Hafner JH, Cheung C-L, Oosterkamp TH, Lieber CM. High-yield assembly of individual single-walled carbon nanotube tips for scanning probe microscopies. *J. Phys. Chem. B.* 2001;104:743–746.
163. Haguet V, Martin D, Marcon J, et al. Combined nanogap nanoparticles nanosensor for electrical detection of biomolecular interactions between polypeptides. *Appl. Phys. Lett.* 2004;84:1213–1215.
164. Forzani ES, Zhang H, Nagahara LA, Amlani I, Tsui R, Tao N. A conducting polymer nanojunction sensor for glucose detection. *Nano Lett.* 2004;4:1785–1788.
165. Bi S, Liu B, Fan F-RF, Bard AJ. Electrochemical studies of guanosine in DMF and detection of its radical cation in a scanning electrochemical microscopy nanogap experiment. *J. Am. Chem. Soc.* 2005;127:3690–3691.
166. Chan WC, Nie S. Quantum dot bioconjugates for ultrasensitive nonisotopic detection. *Science*. 1998;281:2016–2018.
167. Bruchez MJ, Moronne M, Gin P, Weiss S, Alivisatos AP. Semiconductor nanocrystals as fluorescent biological labels. *Science*. 1998;281:2013–2016.
168. Huang YX, Zhang WJ, Xiao H, Li GX. An electrochemical investigation of glucose oxidase at a US nanoparticles modified electrode. *Biosens. Bioelectron.* 2005;21:817–821.

169. Zhou H, Gan X, Liu T, Yang QL, Li GX. Effect of nano cadmium sulfide on the electron transfer reactivity and peroxidase activity of hemoglobin. *J. Biochem. Biophys. Methods.* 2005;64:38–45.
170. Lu Q, Hu SS, Pang DW, He ZK. Direct electrochemistry and electrocatalysis with hemoglobin in water-soluble quantum dots film on glassy carbon electrode. *Chem. Commun.* 2005;2584–2585.
171. Wang J, Liu GD, Merkoci A. Electrochemical coding technology for simultaneous detection of multiple DNA targets. *J. Am. Chem. Soc.* 2003;125:3214–3215.
172. Liu GD, Lee TMH, Wang J. Nanocrystal-based bioelectronic coding of single nucleotide polymorphisms. *J. Am. Chem. Soc.* 2005;127:38–39.
173. Hansen JA, Wang J, Kawde AN, Xiang Y, Gothelf KV, Collins G. Quantum-dot/apptamer-based ultrasensitive multi-analyte electrochemical biosensor. *J. Am. Chem. Soc.* 2006;128:2228–2229.
174. Liu GD, Wang J, Kim J, Jan MR. Electrochemical coding for multiplexed immunoassays of proteins. *Anal. Chem.* 2004;76:7126–7130.
175. Zhang FF, Li CX, Li XH, et al. ZnS quantum dots derived a reagentless uric acid biosensor. *Talanta.* 2006;68:1353–1358.
176. Li XH, Xie ZH, Min H, et al. Development of quantum dots modified acetylcholinesterase biosensor for the detection of trichlorfon. *Electroanalysis.* 2006;18:2163–2167.
177. Liu MC, Shi GY, Zhang L, Cheng YX, Jin LT. Quantum dots modified electrode and its application in electroanalysis of hemoglobin. *Electrochem. Commun.* 2006;8:305–310.
178. Li P, Liu MC, Zhang CL, Cheng YX, Zhang L, Jin LT. Preparation of PVP-capped CdS quantum dot modified electrode and its application to the determination of hemoglobin. *Acta Chim. Sinica.* 2005;63:1075–1080.
179. Dai Z, Kawde A-N, Xiang Y, et al. Nanoparticle-based sensing of glycan–lectin interactions. *J. Am. Chem. Soc.* 2006;128:10018–10019.
180. Rodriguez MC, Kawde A-N, Wang J. Aptamer biosensor for label-free impedance spectroscopy detection of proteins based on recognition-induced switching of the surface charge. *Chem. Commun.* 2005;4267–4269.
181. Nutio R, Li Y. Structure-switching signaling aptamers. *J. Am. Chem. Soc.* 2003;125:4771–4778.
182. Pavlov V, Xiao Y, Shlyabovskiy B, Willner I. Aptamer-functionalized Au nanoparticles for the amplified optical detection of thrombin. *J. Am. Chem. Soc.* 2004;126:11768–11769.
183. Baldrich K, Acero JL, Reekmans G, Laureyn W, O’Sullivan CK. Aptasensor development: elucidation of critical parameters for optimal aptamer performance. *Anal. Chem.* 2004;76:7053–7063.
184. Wang J, Liu GD, Rasul Jan M, Zhu QY. Electrochemical detection of DNA hybridization based on carbon-nanotubes loaded with CdS tags. *Electrochem. Commun.* 2003;5:1000–1004.
185. Wang J, Liu G, Polsky R, Merkoçi A. Electrochemical stripping detection of DNA hybridization based on cadmium sulfide nanoparticle tags. *Electrochem. Commun.* 2002;4:722–726.

The Metal Nanoparticle Plasmon Band as a Powerful Tool for Chemo- and Biosensing

AUDREY MOORES

Department of Chemistry, McGill University, Montreal, Quebec, Canada

PASCAL LE FLOCH

Hétéroéléments et Coordination, Ecole Polytechnique, Palaiseau, France

- 5.1 Introduction
 - 5.1.1 Plasmonics: principles and surface plasmon resonance/surface plasmon band comparison
 - 5.1.2 Metal nanoparticles: definition, synthesis, and applications
 - 5.1.3 Chapter outline
- 5.2 The SPB: an optical property of metal NPs
 - 5.2.1 Absorption of light by nanoparticles
 - 5.2.2 Scattering of light by nanoparticles
 - 5.2.3 Factors affecting the position of the surface plasmon band
- 5.3. Plasmon band variation upon aggregation of nanoparticles
 - 5.3.1 Pioneer works
 - 5.3.2 Further developments in DNA detection
 - 5.3.3 Protein detection
 - 5.3.4 Detection of other biomolecules
 - 5.3.5 Sensing of metal cations
- 5.4 Plasmon band variation on the environment or ligand alteration
 - 5.4.1 Biosensing by alteration of the dielectric medium
 - 5.4.2 Chemosensing by ligand-exchange mechanisms
- 5.5 Metal nanoparticles as labels
- 5.6. Conclusions

5.1 INTRODUCTION

Metal nanoparticles (NPs) seem to have fascinated humans since their first syntheses during antiquity [1]. Indeed, solutions and solids containing metal NPs of gold, silver, or copper feature beautiful bright colors due to a physical property called the surface plasmon band (SPB). Under photoexcitation, conduction electrons inside a metal nanoparticle oscillate collectively, which causes strong absorption in the visible spectrum and thus appearance of color [2]. This aesthetic property has been exploited extensively for centuries: for instance, for coloration of glass [3] or pottery painting (Figure 5.1) [4].

Among the most astonishing achievements, one can cite the famous Lycurgus cup, crafted by the Romans in the fourth century, on display at the British Museum (see Figure 5.6) in London [5] or the bright red color of church and cathedral stained glass produced during the Middle Ages [6]. Many more applications of this optical property have arisen recently, leading to a plethoric bibliography. In the frame of this chapter, we focus on its use for sensing molecules, most of them being biologically relevant. Basically, metal nanoparticles constitute interesting sensing tools since they provide a physical output (e.g., a shift in color) from a chemical input (a chemically induced modification of the parameters of the particle). In early applications, the position of the SPB of the NPs in solution (in other words, the solution colors) was used as a probe, but in the most recent advances the SPB can be used in a more elaborate way, as an enhancer of another signal, such as a Raman signal, to give rise to a complete new field of science, surface-enhanced Raman spectroscopy (SERS). Today, thanks to those techniques, single-molecule detection is within reach, and we can hope to design rapidly portable, user-friendly detectors in living samples without amplification. Molecules detected range from small molecules featuring a thiol or phosphine functionality to DNA strands, proteins, or antibodies. Since the alchemists who mistook gold colloidal solutions for an elixir of youth [7], noble-metal NPs have never had a brighter future in health sciences.

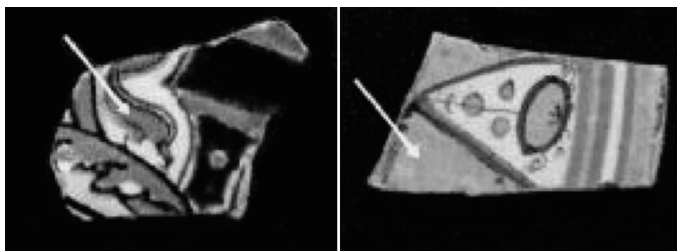


FIGURE 5.1 Fragment of pottery that contains copper (left arrow) and silver (right arrow) nanoparticles. (From ref. 4, with permission. Copyright © 2003, American Institute of Physics.)

5.1.1 Plasmonics: Principles and Surface Plasmon Resonance/Surface Plasmon Band Comparison

The term *plasmonics* has recently been crafted to define the field dealing with optical phenomena related to the electromagnetic response of metals [8]. Any metal interacting with an electromagnetic field at optical frequencies produces an optical response at the nanoscale at a distinct frequency. This response is the result of oscillations, called *plasmon polaritons* or *plasmons*, of conduction electrons acting as a free electron gas. Those properties have found major applications in two principal cases: at the surface of bulk metal or inside a nanoparticle of metal.

1. At its surface, a bulk piece of metal under electromagnetic excitation produces evanescent waves (plasmons) that interact with the incoming wave; for a given wavelength, extinction is observed by reflection [Figure 5.2(a)]. This phenomenon is the basis of the surface plasmon resonance (SPR), spectroscopy that has had outstanding success [8–12] since it was found in 1983 to be a powerful tool for biosensing [13]. In a typical experiment [8,14] the sample to analyze is excited by a laser at a given wavelength and angle. A detector collects the signal produced by reflection. The sample can be scanned at a fixed angle and variable wavelength, or the contrary. In conditions corresponding to the SPR, the reflectance goes through a minimum.
2. A three-dimensionally confined electron gas of the type found in metal nanoparticles (of subwavelength size) can also oscillate in resonance with an incoming optical signal [Figure 5.2(b)]. This leads to an overall absorption and scattering phenomenon commonly called the surface plasmon band (SPB), whose precise physical aspect is explained fully in Section 5.2. The SPB does not require a complex setup to be observed; it is visible with the naked eye from very low concentrations, and a simple ultraviolet–visible (UV–vis) spectrometer can easily provide a measured result of the phenomenon. This explains one

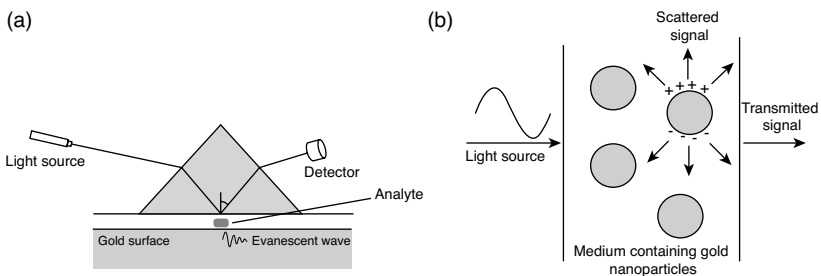


FIGURE 5.2 Schematics of SPR and SPB. (a) In a typical SPR experimental, the incoming wave is shed onto a gold surface. It interacts with the evanescent waves present at the surface, causing a perturbation of the reflected signal. The presence of an analyte at the surface of gold can be sensed. (b) In a typical SPB experiment, light is shed on a medium containing nanoparticles. The signal interacts with each nanoparticle electronic cloud, resulting in an overall scattering of the signal. This signal can be modified by the presence of an analyte (see below).

of the great advantages of SPB-based detection systems: They allow the design of cheap, portable, user-friendly devices which compete effectively with systems based on SPR spectroscopy, which requires a complex setup of laser and detectors, despite an earlier start in the history of plasmonic sensing.

We want to stress that the denomination of SPR and SPB can easily lead to confusion. They both refer to a surface, but this surface is both different in nature and in its role in the phenomenon. In the SPR case, the surface is a macroscopic two-dimensional interface between a metal and a dielectric and is the location of the phenomenon; in the SPB case, the surface is nanometric in size, not flat, not perfectly defined, and more important, is the place where surface charges appear and lead to a restoring force for the electron gas. Another confusion can arise from the fact that by convention only the first phenomenon is called resonance, although both are resonance phenomena. In the SPR case it is resonance between the incoming wave and evanescent waves at the surface of the metal; in the SPB, it is resonance between the incoming wave and the cloud of conduction electrons inside the nanodomain [15]. To be complete, we note here that in some publications the SPB is referred to as *localized surface plasmon resonance* (LSPR). In this chapter we limit our analysis to applications in sensing the SPB of metal NPs. Direct exploitations of this phenomenon are presented as well as cases where it is used to enhance another signal or to improve SPR spectroscopy (typically, in cases where metal NPs interact with a metal film). We do not address the wide domain of SPR spectroscopy itself, but the reader can refer to one of the many reviews available [8–12].

5.1.2 Metal Nanoparticles: Definition, Synthesis, and Applications

Nanoparticles (NPs) are defined as particles composed of a certain number of atoms, ranging from 3 to 10^7 [2]. Because of their size, they feature properties that are neither those of molecules nor those of bulk material. In particular, the properties of the material at this size become strongly dependent on the material's size and shape [16]. The SPB results in a strong, broad band observed in absorption in the UV–vis spectrum for metallic NPs larger than 2 nm. For smaller clusters, no SPB is observed [17]. All metals feature this property [2], but only the series Au–Ag–Cu exhibits one intense enough to have enabled applications in sensing.

Nanoparticles can be synthesized in solution: In the case of gold, salts of Au(III) are typically dissolved in water and reduced with NaBH_4 in the presence of a ligand to confine the particle at the size wanted [18,19]. Many variations of this procedure have been designed, some being mono [20] or biphasic [19], some favoring specific shapes by allowing the growth of only some of the facets of the nanocrystal [21,22], some occurring in purely organic medium and starting from Au(I) precursor [23]. Photochemical methods have also been reported [24,25]. The synthesis allows us to have some control on the size of the particles, their monodispersity (homogeneity in size), their shape, and their surface functionality. After the synthesis, ligand place-exchange reactions can be performed to achieve new functionalities at the

surface [26–28]. The particles in solutions can thus be used as such or engineered inside a material [29] or onto a surface [30]. Photochemical methods are also available [31], or they can be prepared directly on a substrate. One of the most popular of the direct methods, conceived by Van Duyné’s group, is called *nanosphere lithography* (Figure 5.3). In this technique, latex nanospheres are packed on a wafer to be used as a mask. Metal is then deposited. In the interstices between the nanospheres, metal forms a layer directed onto the wafer. After removal of the nanomasks, a pattern of triangular nanoparticles remains on the surface [32]. This method allows fine control over the particle sizes, and “naked particles” (i.e., particles without surface functionalities) are reachable. These methods allowed the most recent breakthroughs in plasmonics [33–35]. This very powerful strategy is somewhat limited by the number of particles synthesized, since it is a two-dimensional method. A few reviews are available for the reader interested in metal nanoparticle synthesis [1,16,36–39].

Among the numerous applications of metal nanoparticles, detection is one of the most prolific, thanks to their remarkable properties, such as a high surface-to-volume ratio, chemical versatility, tailorable and powerful optical properties, and structural stability [40]. More specifically, the cross section for elastic scattering of light from a 50-nm gold nanocrystal can be a million-fold larger than the cross section of emission or absorption from any other molecular chromophore [41]. Because of that property, scientists have in hand detection methods that will probably sometimes make it possible to avoid polymerase chain reaction (PCR), a method used to amplify nucleic acid expression prior to detection which is time consuming, costly, and little portable. Four mechanisms have been used for sensing with plasmonic particles: (1) nanoparticle aggregation (Section 5.3), (2) local dielectric medium constant change (Section 5.4.1), (3) charge-transfer interaction between particles and their ligands (Section 5.4.2), and (4) use of particles as labels (Section 5.5) [42]. Detection

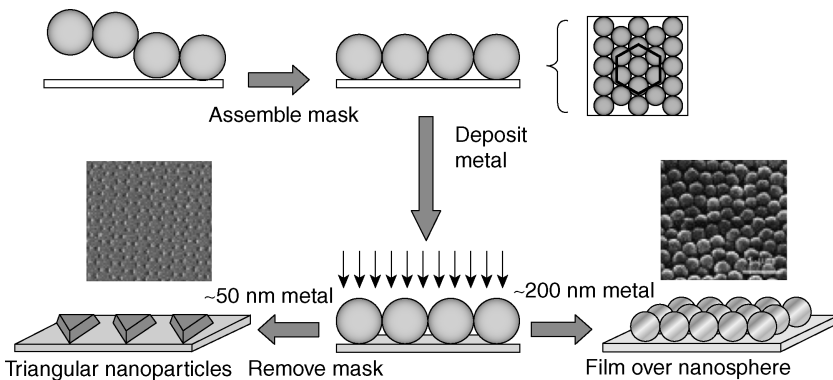


FIGURE 5.3 Nanosphere lithographic fabrication of nanoparticle arrays and film over nanosphere surfaces. (From ref. 32, with permission. Copyright © 2005 Elsevier.)

methods that rely on plasmonic nanoparticles have already reached commercialization, with, for example, the two-color nucleic acid microarray of Genicon Science [43]. Such newly crafted words as *nanodiagnosis* or *nanomedicine* indicate how important those methods have become for biologists [40]. The reader may be interested in the plethora of literature that is available on subjects touching on plasmonic particles applied to detection. Astruc et al. published a very complete review on all aspects of the physics, chemistry, and biology of gold nanoparticles [1], which was complemented by a tutorial review by Enstis and El-Sayed [16]. Numerous reviews have recently been published on various aspects of metal nanoparticle optics [44–46]; applications of the SPB [47]; nanoparticles applied to biology [40,48–50], especially to biosensing [13,32,41,43,51–56]; or surface-enhanced methods [57–60]. Other properties of metal nanoparticles not involving the SPB have been used for sensing [61–63].

The next step to take in nanomedicine is application *in vivo* (i.e., inside a living organism). As a consequence, recent studies have been launched to evaluate the cellular uptake and the cytotoxicity of some plasmonic nanoparticles, with an emphasis on gold nanoparticles [64,65]. Connor et al. reported that a library of gold nanoparticles of sizes ranging from 4 to 18 nm, and capping ligands such as biotin hexadecyltrimethyl-ammonium bromide (CTAB) and citrate, were easily taken up by some leukemia cells, but no cytotoxicity was observed [66]. Other studies have shown minor toxicity for cell nucleus targeted particles [67]. In a similar approach, Takahashi et al. efficiently replaced CTAB by phosphatidylcholine onto gold nanorods to provide cyto-compatible nanorods [68]. Very recently, Huff et al. showed that CTAB nanorods were also bio-compatible and could be taken up by cellular nucleus [69]. Further studies are desired to understand the role of factors such as shape or other ligands, the long-term impact of nanoparticles in cells, potential degradation metabolisms, and accumulation schemes in organisms, but this remains extremely promising. The question of cytotoxicity of metals different from gold has also been raised. Silver, although a better scatterer than gold at the particulate state [70], cannot be used as such *in vivo* because they could not be stabilized adequately [71]. Such a problem could be circumvented by protecting silver particles with a layer of gold in a strategy developed by Mirkin and explained in Section 5.2.3.4 [71].

Apart from diagnosis and sensing, metal nanoparticle plasmonics have shown great potential for therapeutic strategies. Takahashi et al. recently induced a release of DNA plasmid on demand by pulsed infrared light using the SPB [72]. Plasmonic particles could be used as an antenna to enhance a field, leading to phenomena such as SERS. The SPB was employed in a similar fashion to create local heating, used for therapeutic application. Since 2003, several studies have been published on the use of excited plasmonic particles to degrade cancer cells thermally. The West, Halas, and Hirsch groups chose gold nanoshells that feature an SPB in the near infrared (Figure 5.4). Indeed, transmission through living tissues is optimal in this region [73]. Once inside the target tumor, the particles are excited under 820-nm radiation, which results in heat production around the particles. Tests on cells and in mice have been successful [74–77]. This approach counts among the most novel frontiers in nanotherapy [49].

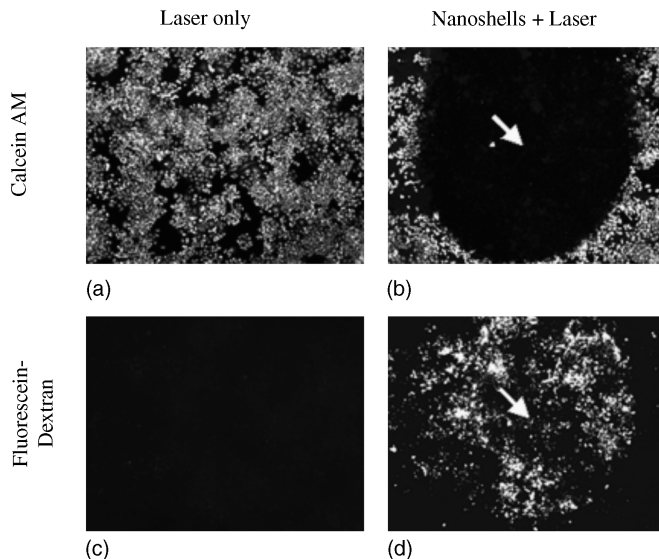


FIGURE 5.4 Cells irradiated in the absence of nanoshells maintained both viability, as depicted by calcein fluorescence (a), and membrane integrity, as indicated by a lack of intracellular fluorescein dextran uptake (c). Cells irradiated with nanoshells possess well-defined circular zones of cell death in the calcein AM study (b) and cellular uptake of fluorescein dextran from increased membrane permeability (d). (From ref. 74, with permission. Copyright © 2003 National Academy of Sciences USA.)

5.1.3 Chapter Outline

In the present review we introduce the physical theory explaining the SPB in Section 5.2. Both the absorption and the scattering properties are discussed. Factors affecting the SPB, such as the dielectric medium, ligands, and stabilizing agents, size and shape, and nanoparticle composition, are then discussed and placed in perspective with the role they play for detection. In Sections 5.3, 5.4, and 5.5 we detail various strategies developed for detection involving the SPB. Section 5.3 is dedicated to detection using nanoparticle aggregation–deaggregation events. In Section 5.4 we summarize the advances in using nanoparticle as labels, especially using their scattering properties. In Section 5.5 we overview detection methods relying on modification of the medium or the ligands stabilizing the nanoparticles. In this review we do not discuss the numerous surface-enhanced spectroscopies, such as SERS, although they use the SPB properties. Several reviews are available to the reader [59,60,78,79].

5.2 THE SPB: AN OPTICAL PROPERTY OF METAL NPS

The SPB has been studied extensively for the past 100 years or so. Many descriptions of it were given by both chemists and physicists, and we would like to describe

them briefly. The book of Kreibig and Vollmer is the most extensive and precise opus on the subject of optical behavior of metal clusters, while Liebsch's book offers a solid background in plasmonic physics in general [2,80]. For a more concise and illustrative outlook, we refer to Liz-Marzán's recent review, focusing on Mie and effective medium theory [44]. In this section we summarize the physics behind the phenomenon, using the two traditional theories: the Drude–Maxwell model and the theory exposed by Mie. For a more extensive description, we direct the reader to the article by Moores and Goettmann [45].

5.2.1 Absorption of Light by Nanoparticles

The SPB is a phenomenon due to the presence of NPs that is observed in transmission or in scattering. This macroscopic feature can be explained by the collective resonance of the conduction electrons of the nanoparticle (the d electrons in gold and silver) [16] under the effect of an incoming wave. To set up the problem, one needs to have a good model for describing the wave on one side and the particles on the other. The model for the propagating wave is obviously the Maxwell theory, while the particle electrons are described using Drude's theory of free electrons. This will provide a dielectric constant ϵ for the particles, a crucial parameter that appears in the Maxwell equations.

Let's consider a metal defined with a dielectric constant ϵ_∞ . The Maxwell equations describing the propagation of an electromagnetic wave of frequency ω in that metal [81] link the electric field \mathbf{E} , the magnetic induction \mathbf{B} , the electric polarization \mathbf{P} , the electric displacement \mathbf{D} , the magnetization \mathbf{M} , the permittivity ϵ_0 of free space, the permeability μ_0 of free space, ϵ_∞ , the electrical current \mathbf{j} , the conductivity of the metal $\sigma(\omega)$, and the current density ρ in the medium studied. From those equations, one can extract an equation ruling a periodical electric field in that medium [$\mathbf{E}(\omega) = \mathbf{E}_0 e^{-i\omega t}$ is taken as a convention]:

$$\nabla^2 \mathbf{E} = -\mu_0 \epsilon_0 \omega^2 \left[\epsilon_\infty + \frac{i\sigma(\omega)}{\omega \epsilon_0} \right] \mathbf{E} \quad (5.1)$$

$$\nabla^2 \mathbf{E} = -\mu_0 \epsilon_0 \omega^2 \mathbf{E} \quad (5.2)$$

$$\epsilon(\omega) = \epsilon_\infty + \frac{i\sigma(\omega)}{\omega \epsilon_0} \quad (5.3)$$

Equation (5.1) is a propagation equation. It has the same form as that of a wave propagating in the free space [equation (5.2)], but with ϵ_0 replaced by $\epsilon(\omega)$ [expressed in equation (5.3)]. $\epsilon(\omega)$ is the frequency-dependent dielectric constant of the metal in the presence of a wave. Incident light causes a change in the metal behavior that is thus taken into account. This value is complex, which expresses the fact that the wave and the response are not necessarily in phase. Unlike the free-space problem [equation (5.2)], equation (5.1) is difficult to solve, for it requires $\epsilon(\omega)$ and $\sigma(\omega)$ to be fully expressed. Of course, experimental values were determined for them and could be used, but many models were also developed. Among them, the Drude theory

describes the mechanics of the electrons inside a metal. In this theory, electrons are considered as free and independent. The motion of a whole cloud is then the sum of the motion of the individual electrons: The coupling between them is thus considered as maximum, electrons acting all in phase [2]. The motion of one electron is described by

$$m_e \frac{dv}{dt} + m_e \Gamma v = e \mathbf{E} \quad (5.4)$$

where m_e stands for the effective mass of the electron (taking into account the presence of a positively charge background), v the electron speed, and e the charge of the electron. The second term represents damping due to various factors, such as free-electron inelastic collisions but also electron phonon coupling, defects, and impurities [17]; Γ is the damping constant. The second member is the force due to the electric field. Compared to that of the electric field, the force exerted on the electrons by the magnetic field is negligible. This approximation is justified since electrons are moving very slowly compared to light. It is stated again that $\mathbf{E}(\omega) = \mathbf{E}_0 e^{-i\omega t}$. Then v will also be sinusoidal ($v = v_0 e^{-i\omega t}$) and equation (5.4) becomes

$$(-i\omega m_e + m_e \Gamma) v_0 e^{-i\omega t} = e \mathbf{E}_0 e^{-i\omega t} \quad (5.5)$$

Hence,

$$v_0 = \frac{e}{m_e \Gamma - i\omega m_e} \mathbf{E}_0 \quad (5.6)$$

Then \mathbf{j} ($= env$ by definition, $\mathbf{j} = j_0 e^{-i\omega t}$) can be expressed as resulting from the individual motion of all electrons, with n the electron density:

$$j_0 = env_0 = \frac{ne^2}{m_e \Gamma - i\omega m_e} \mathbf{E}_0 = \sigma(\omega) \mathbf{E}_0 \quad (5.7)$$

The last identity is simply the expression of the Joule rule [45] and results in the conductivity $\sigma(\omega)$ then having the form

$$\sigma(\omega) = \frac{ne^2}{m_e \Gamma - i\omega m_e} \quad (5.8)$$

Together, equations (5.3) and (5.8) provide the dielectric constant $\epsilon(\omega)$ as a function of known constants: ϵ_∞ , n , e , m_e , and ϵ_0 , of the frequency ω and of Γ :

$$\epsilon(\omega) = \epsilon_\infty - \frac{\omega_p^2}{\omega^2 + i\omega\Gamma} = \epsilon_\infty - \frac{\omega_p^2}{\omega^2 + \Gamma^2} + i \frac{\omega_p^2 \Gamma}{\omega(\omega^2 + \Gamma^2)} \quad (5.9)$$

where ω_p is used to simplify the expression of $\epsilon(\omega)$; its expression is

$$\omega_p^2 = \frac{ne^2}{\epsilon_0 m_e} \tag{5.10}$$

For the determination of Γ , experimental data are generally used [17,82,83].

Now that we have an expression for $\epsilon(\omega)$, we can address the problem of the nanoparticles. Since $\epsilon(\omega)$ was determined here for bulk metal, several postulates then become wrong but are kept as approximations; for example, $\rho = 0$, as in small particles the electron density is no longer uniform. Charges will accumulate at particle edges, as we will discuss further.

Two other approximations are made here: Because NPs are very small in regard to the wavelength, all the electrons confined in a nanoparticle see approximately the same field at a given time t [2]. The electric field is considered as independent of the position (quasistatic approximation). The displacement of the electron cloud under the effect of the electric field leads to the creation of surface charges, positive where the cloud is lacking, negative where it is concentrated (Figure 5.5) [2]. This aspect of the problem justifies the use of the term *surface* in the designation of the global phenomenon: the *surface* plasmon band. But one has to keep it mind that all the electrons present are moving collectively while under the effect of the field. Such collective oscillations are said to be plasmon polaritons [3], as opposed to the free plasmon occurring in bulk metal [2]. This dipolar charge repartition imposes a new force on the electron cloud, which tends to restore it to its original position. The position, x , of an electron placed in the oscillating cloud of a nanoparticle is then governed by

$$m_e \frac{d^2x}{dt^2} + m_e \Gamma \frac{dx}{dt} + Kx = eE \tag{5.11}$$

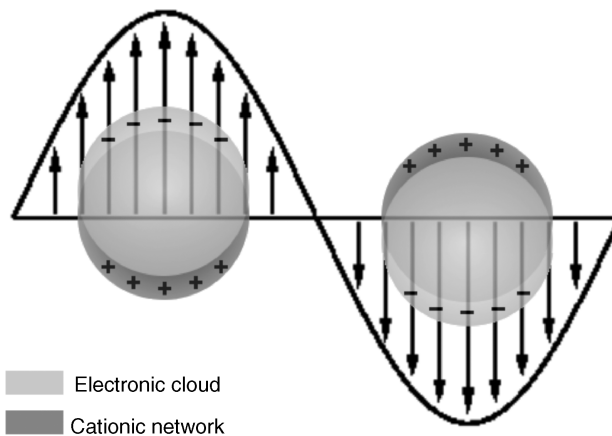


FIGURE 5.5 Electronic cloud displacements in nanoparticles under the effect of an electromagnetic wave.

where K is the restoring force; k will not be expressed here. This equation describes the movement of a forced, damped harmonic oscillator. This problem is equivalent to that of classical mechanical oscillators.

Another way of watching the problem is to say that the electric field seen by the nanoparticle is the external one altered by the effect of the polarizability of the medium. Using the boundary condition in a spherical particle, the internal field \mathbf{E}_i in a nanoparticle surrounded by vacuum is expressed as [2,85]

$$\mathbf{E}_i = \mathbf{E}_0 \frac{3}{\varepsilon(\omega) + 2} \quad (5.12)$$

This gives a condition of resonance which occurs when \mathbf{E}_i is maximum, hence when $|\varepsilon(\omega) + 2|$; that is, $|\varepsilon_1(\omega) + 2|^2 + |\varepsilon_2(\omega)|^2$ is minimum [$\varepsilon(\omega) = \varepsilon_1(\omega) + i\varepsilon_2(\omega)$]. Thus, ω_M the resonance frequency, verifies that $\varepsilon_1(\omega_M) = -2$. With the relation (11), considering that $\varepsilon_\infty = 1$ and $\Gamma \ll \omega$, the following relation is obtained:

$$\varepsilon_1(\omega_M) = 1 - \frac{\omega_P^2}{\omega_M^2} = -2 \quad \text{hence} \quad \omega_M = \frac{\omega_P}{\sqrt{3}} \quad (5.13)$$

The description we have made of the phenomenon thus far is very simple: We envisaged one isolated spherical nanoparticle in vacuum with several hypotheses, such as $\varepsilon_\infty = 1$ and $\Gamma \ll \omega$. This is wrong, of course, but the virtue of this model is to provide good insight into what happens physically: The electron cloud oscillates under the effect of incident light. The restoring force is provided by the surface charges formed at the edge. The value of the resonance frequency is given with a good approximation by equation (5.13) [2].

5.2.2 Scattering of Light by Nanoparticles

There is one other way to explain the SPB property in simple terms. The electron cloud of a nanoparticle oscillates under photoexcitation. We detailed in Section 5.2.1 the forces that play on the cloud of electrons (electric field, restoring force, and damping). Hence, electrons in this context are accelerated and thus emit a wave themselves, since any electric charge that accelerates produces electromagnetic radiation, according to Maxwell's equation [81]. This wave is emitted in all directions, thus scattering the energy of the unidirectional incoming wave. At resonance this phenomenon reaches its climax and a maximum of the incoming energy is scattered and thus not transmitted. This explains the absorbance spectrum of plasmonic particles, which we discussed above. The light thus scattered has the same wavelength as the incident light [85]. In fact, the scattering approach problem was historically the first used to rationalize the SPB. In 1908, Mie used Maxwell's equations to spherical particles embedded in a medium, boundary

conditions being chosen adequately [86]. He thus obtained an expression of the cross section C_{ext} :

$$C_{\text{ext}} = \frac{24\pi^2 R^3 \epsilon_m^{2/3}}{\lambda} \frac{\epsilon_2}{(\epsilon_1 + 2\epsilon_m)^2 + \epsilon_2^2} \quad (5.14)$$

where λ is the wavelength and ϵ_m the dielectric constant of the surrounding medium), which reaches a maximum at resonance for $\epsilon_1 = -2\epsilon_m$. We find here the condition furnished by the Drude treatment [equation (5.13)] stating that $\epsilon_m = 1$.

The Lycurgus cup (Section 5.1) is a good illustration of the scattering properties of nanoparticles. Its walls are made of a dichroic glass (i.e., they feature two different colors, depending on light exposure). Gold and silver alloy nanoparticles embedded in the glass absorb light by transmission to give a red color when the cup is lightened from inside, while light scattered by the same particles makes the cup look green when light is shed from outside (Figure 5.6) [87].

Most other properties of a scattering peak are comparable to the absorption peak, such as the dependence of the peak sensitivity on the dielectric medium, recently shown to be linear [88]. Nanosized tips have been used as scatterers for microscopy [8]. The scattering properties have been exploited for sensing, where the particles are in fact used as labels, in a fashion similar to that for fluorescent probes. This is described further in Section 5.4.



FIGURE 5.6 The Lycurgus Cup: on the left it appears green, because it is lit from outside and scattering effects are dominating; on the right, light from inside allows to see the red color typical of absorption phenomenon by nanoparticles. (From ref. 15, with permission from the British Museum, London. Copyright © Trustees of the British Museum.)

5.2.3 Factors Affecting the Position of the Surface Plasmon Band

As illustrated by equation (5.9), the expression of the dielectric constant $\epsilon(\omega)$ depends on the electron density inside the particle n and the damping effects represented by Γ , but also on the dielectric constant of the surrounding medium, ϵ_0 . The position, shape, and intensity of the SPB depend on them strongly. Here we develop how the plasmon band position is affected by the dielectric constant of the surrounding medium, the electronic interactions between the stabilizing ligands and the NP, which alters the electron density inside the NP and the size of the NPs. Obviously, the nature of the metal inside the particle comes into play as well and will be discussed.

5.2.3.1 Dielectric Medium The nature of the medium surrounding the nanoparticles has a great impact on the position of the plasmon band, as expressed in the Mie equation [equation (5.14)]. This property is probably the one used most for sensing purposes. Several methods exist for modifying the dielectric medium around the nanoparticles. The first is to change the matter directly surrounding the particle itself; the second is to change the distance between two consecutive particles. Mulvaney's group has launched pioneer studies on the field and evidenced the shift of the SPB position with a change of surrounding solvents. By using gold nanoparticles stabilized with a polymeric comb that prevented aggregation upon solvent transfer, they showed that the position of the plasmonic band shifts toward the lower-energy region while the solvent refractive index increases [89]. His work was completed by a theoretical analysis using the Mie theory. The same group then coated gold nanoparticles with silica to provide a core-shell structure with a silica layer of various thicknesses. In solution, the position of the SPB of those hybrid systems depended on the thickness of the layer [90]. These silica-coated nanoparticles were used to provide thin films deposited on glass. The color of those films depended on the thickness of the silica layer, which affected the distance between two consecutive particles (Figure 5.7) [91]. As the distance decreased, the color of the film shifted from red to blue. This is the same phenomenon that we observe when aggregating nanoparticles in solution (see Section 5.3.1). This red-to-blue color shift can be rationalized by a red shift of the SPB (considered in absorption). The position of the SPB was also found to depend on the number of layers of particles in the film. Recently, complete theoretical analyses of the sensitivity of metal nanoparticle SPB to the dielectric environment have been released, in both the absorption [92] and the scattering context [89]. Mock et al. also studied this dependence on silver particles of various shapes [93].

As pointed out earlier, the dielectric medium is also altered by the distance between two consecutive nanoparticles. This problem has been studied in the case of pairs of nanoparticles deposited on a substrate, usually by nanolithography (see Section 5.1.2) [94,95]. When the interparticle distance drops below twice the mean diameter of the particle, a dramatic shift is observed in the SPB. This effect is explained by dipole-dipole interaction between the two particles. As the particles come closer, their SPB position shifts toward the red region of the spectrum. In solution, reversible

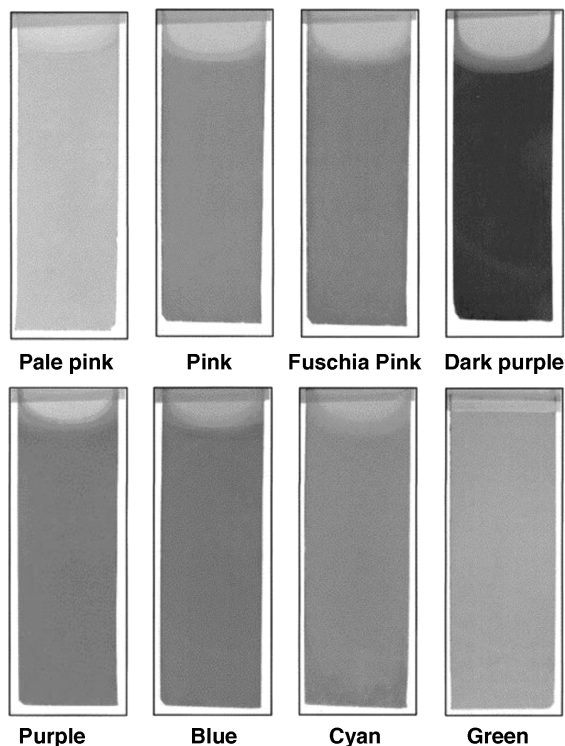


FIGURE 5.7 Transmitted color of the films after deposition from a ruby red gold sol as a function of the silica shell thickness. Top left going across: 15-nm gold particles coated with silica shells of thickness 17.5, 12.5, 4.6, 2.9, and 1.5 nm, then with mercaptopropionate and citrate ions. The bottom right is a thin, sputter-coated gold film. (From ref. 19, with permission. Copyright © 2001 American Chemical Society.)

aggregation and deaggregation of nanoparticles induced by chemical means has a similar effect. Scrimin and Pasquato grafted gold nanoparticles stabilized with dithiol that could be cleaved or rejoined chemically. A red shift of the solutions was observed when the particles aggregate [97]. Nanoparticles of various shapes feature similar behaviors. Thomas and Kamat noticed that addition of a mercaptocarboxylic acid onto a solution of gold nanorod triggered a hydrogen-bonding agglomeration that highly favors alignment of the nanorods, as shown in Figure 5.8 [97]. A subsequent red shift of the longitudinal mode of the SBP is observed. They used this self-assembly property to design a detection system that would specifically sense sulfur-containing amino acids. Upon addition, those analytes cover the tips of the rods, trigger an aggregation by hydrogen bonding specifically in the longitudinal direction, and observe the extinction of only the longitudinal mode of resonance [98]. This system allowed very specific detection of cysteine and glutathione in the presence of other amino acids. The dependence of the SPB on the aggregation state of the NPs has been used intensively for sensing purposes, as we will see in Section 5.3.3.

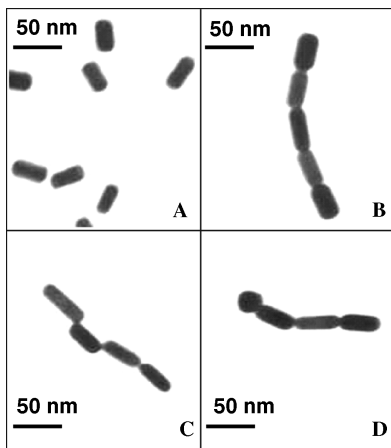


FIGURE 5.8 TEM images of gold nanorods functionalized (A) in the absence of mercaptopropionic acid, and (B–D) in the presence of mercaptopropionic acid, which occupies favorably the tips of the nanorods. (From ref. 97, with permission. Copyright © 2004 American Chemical Society.)

5.2.3.2 Ligands and Stabilizing Agents Metal NPs in colloidal solutions have a natural tendency to agglomerate and form bigger particles, so that they lower their surface tension [1]. To ensure kinetic stability, metal particles in solution need to be covered by stabilizers (or ligands) that protect their surface. The nature of the interaction between the stabilizers and the surface could be either a coordination chemistry type, meaning that the ligand and a metal atom at the surface exchange electrons to form a bond, or a purely electrostatic type. Amines [99], thiols [19], and phosphines [100] are common ligands for metal nanoparticle stabilization. The stabilizers form a shell around the particle that has a strong impact on the dielectric medium. But also by electronic exchange between the metal core and the ligands, through mechanisms that are well known in coordination chemistry, the electronic density inside the particle can be altered directly [29,101]. In other words, the ligands can partially oxidize or reduce the surface atoms, and thus the particle core. The frequency of the SPB, given by equations (5.10) and (5.13), varies as the square root of n , the electron density inside the NP. As a consequence, the plasmon band position is red-shifted when the electronic density drops. Henglein et al. studied this dependence in the 1990s in both oxidation [102–104] and reduction [105]. Other groups studied this phenomenon using electrochemistry [106,107].

5.2.3.3 Size and Shape The dependence of the SPB position on the size of the particle is obvious from equation (5.14), since the cross section of the particle is linearly dependent on R , the radius of the particle. This is a specificity of nanosized materials, bulk materials having optical properties dependent only on their composition. In simple words, the mean free path of electrons in gold or silver being about 50 nm, an electron of a particle of that size or smaller is more likely to encounter the

“wall” of the particle than another electron, which perturbs the dynamics of the system [108]. Consequently, the position of the SPB of noble-metal nanoparticles undergoes a blue shift as the size of the particles decreases, as evidenced experimentally [109,110] and rationalized theoretically [111]. Alteration of the synthetic methods of NPs makes it possible to reach an entire size range of particles. Changing the size is a very powerful means of finely tuning the properties desired for the sensing device being designed. For similar reasons, changes in the particle shape have a dramatic effect on the position of the SPB and thus on the color of the colloidal solution. The variety of particle shapes has challenged human imagination, and nanospheres, nanorods [21,112,113], nanotriangles [114,115], nanooctahedra [116], nanocubes [22,117], nanorices [118], nanodisks [119], nanowires [120], nanostars [121], triangular prisms [119,122] and many more have been reported (Figure 5.9) [123,124].

Orendorff et al. have studied the scattering properties of nanoparticles of various sizes [120]. On reducing the symmetry of a particle, additional modes of resonance appear. For example, a sphere differs from a rod in that in the first case, one peak is observed versus two in the second case [113,125]. For the rod, two resonances are observed, corresponding to oscillations of electrons along either the small axis of the particle (transverse mode) or the long one (longitudinal mode). The latter is red-shifted with respect to the former. Nanorods have been used for sensing systems, in which case the longitudinal mode shift was utilized, as explained in Section 5.2.3.1 [98]. The two modes allow fine tuning of the system for the applications envisioned. A very complete

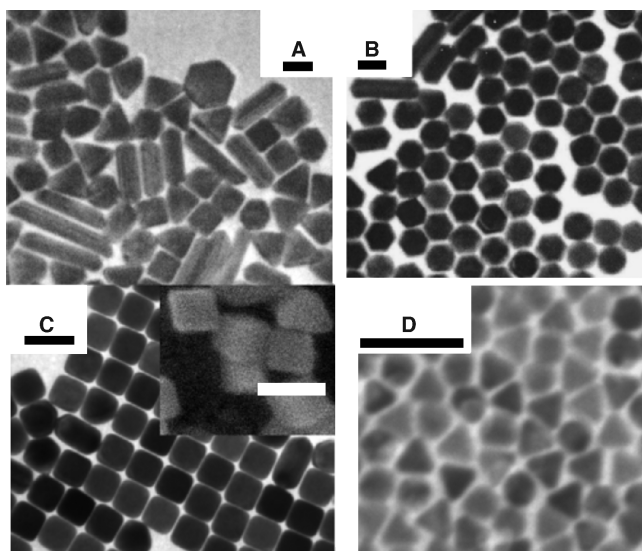


FIGURE 5.9 TEM (inset SEM) images of Au nanoparticles synthesized under different conditions: (A) triangles and rods are visible; (B) hexagons are dominant; (C) cubes are formed; (D) triangles and spherical particles are observed. (From ref. 122, with permission. Copyright © 2004 American Chemical Society.)

study published recently by Noguez shows that the SPB undergoes a blue shift when the particle become more symmetrical (i.e., with fewer facets) [127]. Another interesting point regarding sensing is that shapes featuring tips such as stars or triangles possess an enhanced field around the tips, which provides a great potential for surface plasmon resonance-enhanced spectroscopies [127].

5.2.3.4 Nanoparticle Composition Metal nanoparticle composition obviously has a strong effect on the optical response. Among metals with a strong plasmonic response, Cu, Ag, and Au behave differently, and silver nanoparticles differ from gold ones by a sharper SPB signal [101], a different window, and a fourfold larger extinction coefficient [70]. The variation of the position of the SPB in Au–Ag alloy nanoparticles of various compositions is visible in Figure 5.10. A red shift is observed on going from pure silver to pure gold. When arranged into an array, silver particles can produce remarkably narrow plasmonic bands [128].

In recent years, nanotechnology has made it possible to reach nanoparticles of alloys of several metals [129–132], but also core–shell structures [90,133] (hybrid structures made of a core of one material and an envelope of another). Such designs are very valuable for tuning the properties of the sensing device made from them [134]. Core–shell structures are particularly successful, since the core can be chosen for

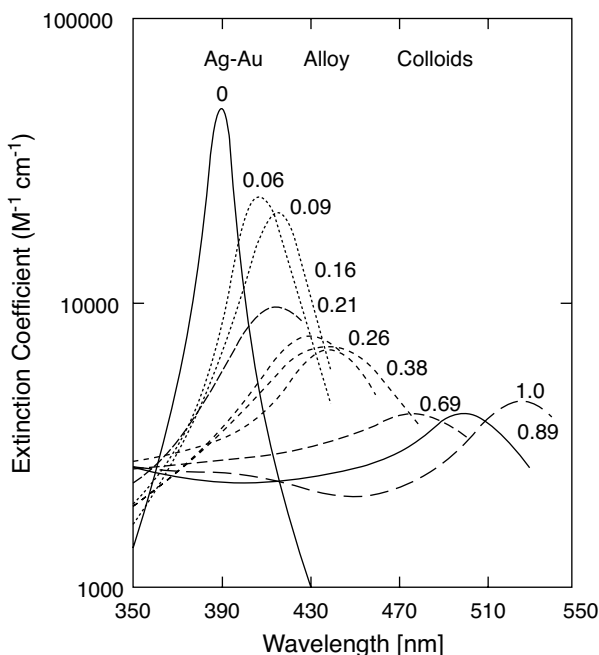


FIGURE 5.10 Calculated spectra of 6-nm particles of Ag–Au alloys of various composition in water using full Mie equations (0 corresponds to full Ag, 1 to full Au). (From ref. 101, with permission. Copyright © 1996 American Chemical Society.)

certain desired physical features, and the shell, for protection of otherwise unstable nanoparticles. For example, the Mirkin group developed a synthesis of DNA-modified core-shell Ag-Au nanoparticles. This system is very interesting because it combines the advantage of the powerful SPB provided by the silver core with the stability and easy of DNA functionalization that the gold cover allowed [71]. The shell of the structure can also be chosen to alter the position of the SPB. In another example, silica beads (of diameter 96 nm) have been covered with a gold layer (of thickness 22 nm) [135]. This design enables optical resonance in the near-infrared region, where optical transmission through living tissue is optimal [73]. It also allows functionalization of the core-shell in the same way as do classical gold nanoparticles. Since 2003, applications of those core-shell structures have been published for sensing, for example, in whole blood [136]. In the case of core-shell structure, both the dielectric medium and electronic effects are required to describe the SPB alteration.

5.3 PLASMON BAND VARIATION UPON AGGREGATION OF NANOPARTICLES

In Section 5.2.3.1 we described how the aggregation state of particles has direct consequences on the dielectric index of the surrounding medium around the particles and thus affects the SPB position. Nanoparticles are easy to functionalize with various recognition molecules, and this fact can be used to induce an aggregation or deaggregation event (see Figure 5.11). This idea has been used intensively in a wide variety of applications, ranging from DNA and protein recognition to environmentally relevant cation sensing. Very recently, it has even been exploited for pH sensing in an alkaline medium [137].

5.3.1 Pioneer Works

As described in Section 5.4, the first example of the use of nanoparticles as colorful labels was proposed by Leuvering et al. as early as 1980. They designed a “sandwich” immunoassay using antibody-functionalized gold nanoparticles. Interestingly, in the course of their studies, they evidenced a naked-eye visible color change from red to

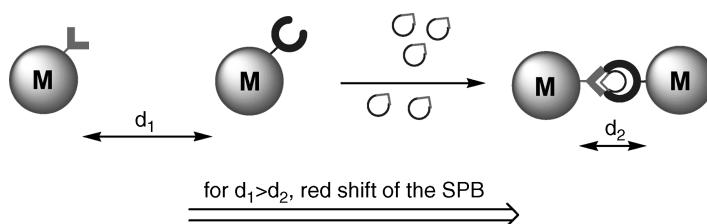


FIGURE 5.11 Principle of detection by aggregation: the presence of the analyte to sense-induce an aggregation event by molecular recognition (M = Ag or Au).

blue due to the presence of human chorionic gonadotrophin (hCG) in a solution of antibody conjugated gold nanoparticles [138]. This shift was caused by aggregation of the particles, and Leuvering et al. saw the potential of that aggregation as a probing event. With a diameter of 50 nm and functionalized with the anti-hCG, the particles feature a red color in solution. Addition of hCG and incubation induce binding of the hCG to several anti-hCGs, causing aggregation of the particles and appearance of a blue color. The change can be monitored by UV–vis spectroscopy. Further work showed good selectivity of that method and applicability for naked-eye detection of hCG in urines [139]. This methodology was then used for detection of estrogen. It is an interesting problem since estrogen is a monovalent immunoresponsive molecule, meaning that simultaneous conjugation with two antibody-attached nanoparticles is impossible. This limitation was circumvented by complexing the estrogen onto a multivalent carrier, bovine serum albumine. This colorimetric detection method of estrogen was adapted for urine and plasmon media [140]. The work led to clinical testing on rubella hemagglutinin with excellent selectivity and sensitivity [141].

In 1996, Mirkin et al. engineered the first DNA strand–sensing method using plasmon active nanoparticles. The detection was based on the change of position of the plasmon band of a colloidal solution (and thus on a change of color) triggered by aggregation of the particles. Aggregation was controlled by DNA hybridization [142]. They coordinated 13-nm gold nanoparticles with oligonucleotides (single-stranded DNA) terminated with a thiol function. Two batches were prepared, one with DNA strands that we will name A and the other with B, and then mixed together. In the presence of a free duplex containing on one end a strand complementary to A, on the other a strand complementary to B, the DNA strands hybridized and the distance between two consecutive nanoparticles was reduced dramatically. The natural consequence was a change in color from bright red for nonaggregated NPs to purple for aggregated NPs (Figure 5.12).

Interestingly, the presence of nanoparticles changed the dynamics of DNA strand hybridization. Upon heating the aggregated mixture to 80°C, denaturation of the double strand occurs, but in the presence of nanoparticles, the transition observed was much sharper than in their absence [144]. This property was used to provide a system capable of detecting a single base mismatch or deletion [146,147]. Storhoff et al. further investigated the optical properties of those hybrid nanoparticles by changing the distance between consecutive particles in the aggregate. This parameter can easily be tuned by changing the length of the DNA stands used as spacers (Figure 5.12) [146]. The size of the nanoparticles is also a parameter that can improve the sensitivity: Larger particles (50 and even 100 nm), with a better extinction coefficient, gave better results and quantitative detection down to 1 nM [147]. A further development allowed the design of detection on a solid support: Test solutions could be spotted on silica gel plates, which enhanced the color change and allowed a permanent record of the test [145]. The advantages of their method on other known biosensors are numerous: its sensitivity, its selectivity (one base end replacement, one deletion or insertion, is enough to have the test failed) [145], its user friendliness (the color shift is eye visible), and the fact that it occurs in real time. This study was a milestone both in the domain of biosensing, allowing naked-eye detection of DNA strands and seeding

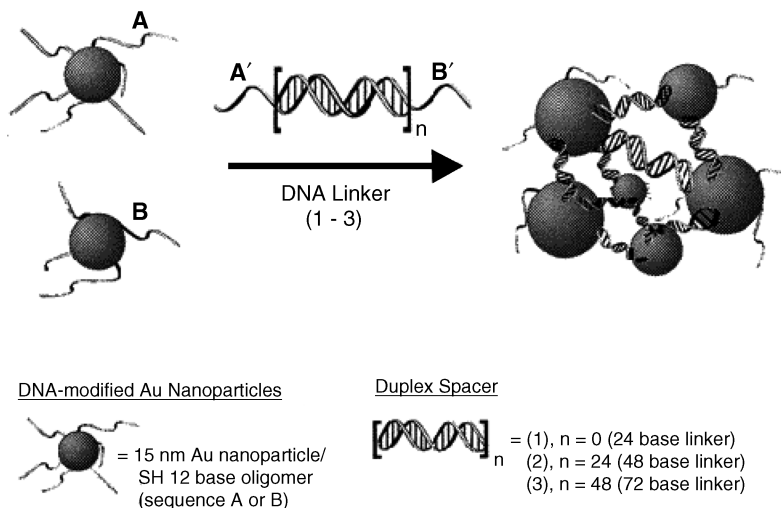


FIGURE 5.12 Principle of DNA detection using nanoparticle aggregation: A strand and B strand substituted nanoparticles, mixed in the presence of a DNA linker featuring an A'-duplex-B' structure, leading to aggregation. (From ref. 143, with permission. Copyright © 2000 American Chemical Society.)

a concept that will be used for sensing of various biomolecules, and also for nanoparticle optics, since controlled and reversible NP aggregation had been problematic before that work. Since then, the field of material science has also exploited intensively this concept of DNA-driven assembly of nanoobjects [148–150]. Also, detection using color change induced by nanoparticle aggregation has flourished, providing applications for sensing all sorts of biomolecules, but also metal cations, as described below [51].

5.3.2 Further Developments in DNA Detection

To foster user-friendly medical diagnosis, Taton et al. investigated the possibility of producing a heterogeneous (i.e., solid-based) DNA-sensing device with improved sensitivity [151]. They used sandwich assay strategies, in which strand A is attached to a support and strand B is hybridized on the nanoparticles. In the presence of a target DNA A'B', a pink color characteristic of the nanoparticles appeared.

In 2003, Sato et al. developed a DNA-sensing method which, contrary to the Taton et al. system, did not involve cross-linking hybridization (Figure 5.13) [152]. In this work they used a DNA-functionalized gold nanoparticle solution with a high salt concentration. In the presence of the complementary strand, DNA duplexes form at the particle surface and considerably reduce both the electrostatic and steric repulsion between nanoparticles in solution; aggregates then form. The aggregation behavior was investigated by varying the salt (NaCl) concentration from 0.1 to 2.5 M. Single DNA strand-functionalized nanoparticles showed no aggregation behavior in

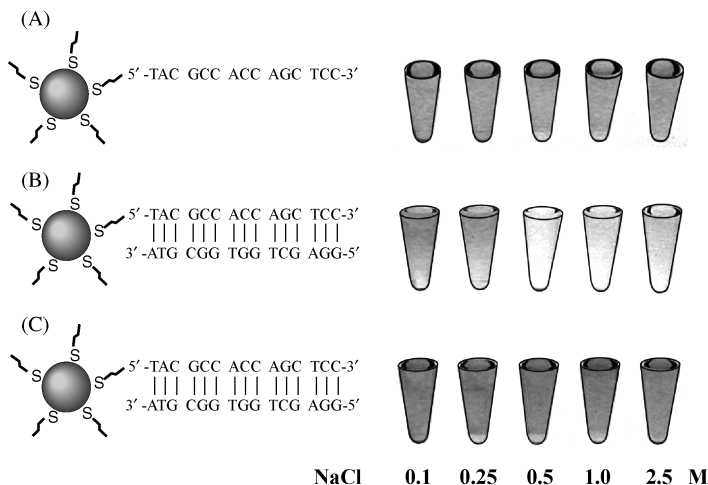


FIGURE 5.13 Aggregation behaviors of DNA–gold nanoparticles at various NaCl concentrations at room temperature: (A) without a target DNA; (B) with the complementary target; (C) with a target containing a single-base mismatch at its 5' terminus. The final concentrations of the particle, the probe DNA, and the targets were 2.3, 500, and 500 nM, respectively. (From ref. 152, with permission. Copyright © 2003 American Chemical Society.)

that range because of the strong electrostatic repulsion between the particles. In the presence of the perfect complementary strand, duplexes form and the electrostatic repulsion drops. Above a threshold at 0.5 M NaCl concentration, this drop results in aggregation of the particles [Figure 5.13(B)]. The detection is very fast (<3 minutes). The detection method proved selective to single-base mismatch [Figure 5.13(C)] but less sensitive (500 nM) than in the Taton et al. system. Methods that do not require prefunctionalization of the nanoparticle surface were also designed [153,154].

5.3.3 Protein Detection

Since the pioneering work of Leuvering et al. in the 1980s on gonadotrophin or estrogen reported in Section 5.3.1 [138–140], protein detection has proved very successful. The principle of detection exemplified by DNA sensing served as a template for the development of protein sensing. Here an antigen–protein couple is used as the specific probe to trigger an aggregation event. The high specificity of this binding allows very high selectivity of the sensors devised. It must be emphasized that this binding mode has been used extensively for nanoparticle assembly [155,156]. As early as 1998, Sastry et al. developed a colorimetric assay based on the Mirkin strategy. Avidin-stabilized gold and silver nanoparticles aggregated in the presence of complementary biotin, leading to color change in the solution [157]. In 2001, Otsuka et al. studied a system that allowed reversible aggregation of particles. Nine-nanometer gold nanoparticles have been coated with a poly(ethylene glycol) polymer and then functionalized with a lectin-specific antigen, β -D-lactopyranoside (Lac).

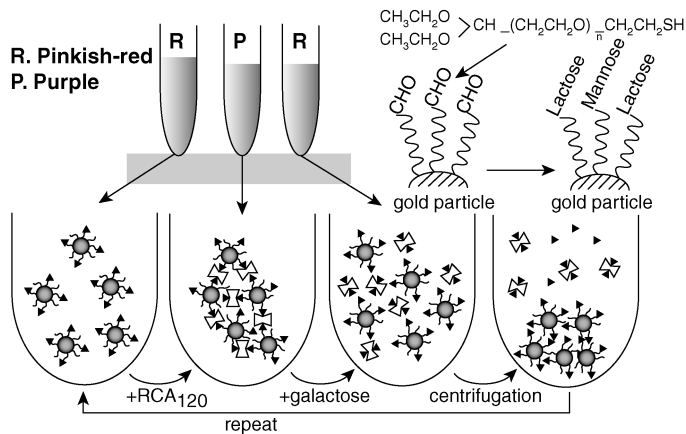


FIGURE 5.14 Reversible aggregated behavior of Lac-functionalized gold nanoparticles by sequential addition of RCA₁₂₀ lectin and galactose with actual concomitant change in color from pinkish red to purple to pinkish red. (From ref. 158, with permission. Copyright © 2001 American Chemical Society.)

When exposed to the bivalent lectin *Recinus communis* agglutinin (RCA₁₂₀), the particles agglomerate and the solution shifts from red to purple (Figure 5.14). This binding proved reversible. In the presence of an excess of galactose, for which RCA₁₂₀ has a strong affinity, deaggregation occurs and the original color is recovered. Detection down to 5 $\mu\text{g/mL}$ has been shown [158]. Along that line, work by Thanh and Rosenzweig in 2002 proved the concept feasible for detection in a serum medium. A detection level of 1 $\mu\text{g/mL}$ was measured [159]. Protein A was used as a model, and the effect of pH and temperature on the aggregation phenomenon was discussed. In 2003, access to antigen sensors in whole blood was achieved based on the SPB of gold nanoshells: silica beads covered with a gold layer [160]. In 2006, Russell's group showed that silver nanoparticles (16 nm of diameter) functionalized with a mannose derivative specific to concanavalin A (Con A) were well suited for quantitative detection (between 0.08 and 0.26 μM); gold nanoparticles of the same size and with the same functionalization proved the most sensitive, with a limit of 0.04 μM . Interestingly, a mixture of lactose-stabilized gold nanoparticles with mannose-stabilized silver nanoparticles could detect both RCA₁₂₀ and Con A with a selective aggregation of the respective nanoparticles [161,162]. In 2007, Mirkin's group published an interesting example of endonuclease inhibitor sensing using a similar strategy [163]. In 2005, Zare's group demonstrated that plasmonic particles were good candidates for detection of conformational changes in proteins. This interesting breakthrough was performed with cytochrome *c*-stabilized gold nanoparticles subjected to pH changes. Indeed, low pH is known to induce an unfolding of cytochrome *c*. The nanoparticle thus surrounded by unfolded nanoparticles aggregated. Those phenomena are reversible, since an increase in pH could allow the protein to fold back and the particle to deaggregate. It was proved that the change of pH on a "bare" gold nanoparticle had no effect on the SPB. The color of the solution was once again

a probe to follow the phenomenon. This is the first time that a simple colorimetric assay has been designed to track protein folding [164]. The aggregation strategy also resulted in its use to for detect serum or blood. Hirsch et al. used a silica–gold core–shell structure functionalized with antibody (rabbit IgG). Those particles absorb at 720 nm. In the presence of the analyte, aggregation occurs and a red shift, as well as a broadening of the SPB, is observed. This event is detectable in serum medium and in whole blood. The detection sensitivity was down to 0.8 ng/mL within 10 to 30 minutes [136]. More recently, two original strategies that do not involve particle prefunctionalization have been developed for protein detection. In the first, Wei et al. used the specificity of aptamers, a small DNA or RNA strand that possesses a strong ability for detection of a protein (here, thrombin). The thrombin-specific aptamer could efficiently stabilize gold nanoparticles and keep them deaggregated in a salted solution (Figure 5.15). In the presence of thrombin, the aptamer folds and binds to the protein; the particles are not longer protected, and aggregate. This system is extremely specific, since it relies on aptamer–protein interaction. It has a detection limit of 83 nM [165].

In the second system, adenosine 5'-triphosphate (ATP)-capped gold nanoparticles were used to sense a protein: calf intestine alkaline phosphatase (CIAP). ATP is a charged molecule that protects the particles from aggregation. In the presence of CIAP, ATP is converted to adenosine, which does not bear any charge and thus allows the particles to aggregate [166]. The latter two examples are very similar in spirit to the non-cross-linking strategy developed by Sato et al. [152] and described in Section 5.3.2.

In Section 5.2.3.1 we described the aggregation phenomenon of nanorods [97]. This work has been used to devise a sensing method for sulfur-containing amino acids (cysteine) and small peptides (glutathione) [98]. Gold nanorods were synthesized by photochemical methods and stabilized by hexadecyltrimethylammonium bromide (CTAB) [24]. In the presence of cysteine and glutathione, two molecules that possess

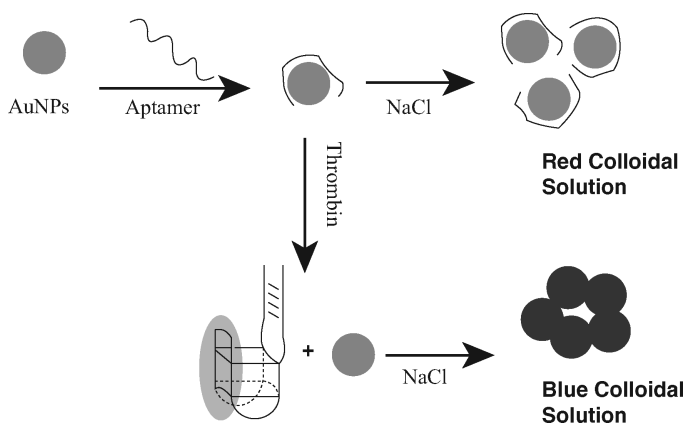
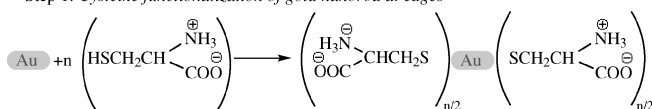
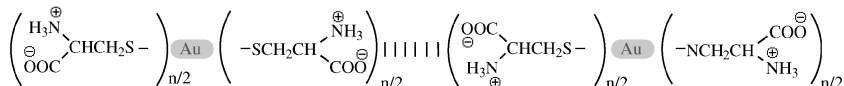
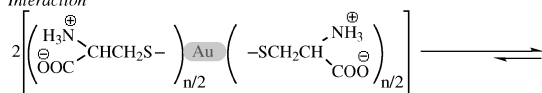


FIGURE 5.15 Aptamer-based colorimetric sensing of thrombin using unmodified AuNP probes. (From ref. 165, with permission from the Royal Society of Chemistry.)

Step 1: Cysteine functionalization of gold nanorod at edges



Step 2: Uniaxial dimerization of gold nanorod through two point electrostatic Interaction



Step 3: Oligomerization of gold nanorod through end to end self-assembly

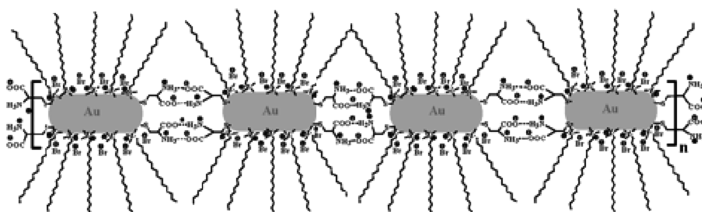


FIGURE 5.16 Mechanism of self-assembly of Au nanorods. (From ref. 98 with permission. Copyright © 2005 American Chemical Society.)

both a thiol and an amino acid functionality, the nanorods organize and assemble in their longitudinal direction (Figure 5.16). Indeed, thiol groups displace CTAB in the rod surface, with a greater affinity for the edges and their $\{111\}$ faces. The amino acid functionalities, in their zwitterionic form, then assemble by hydrogen interactions. Only the longitudinal mode of the plasmonic response of the solution was affected, and detection proved highly selective compared to that of other amino acids. The sensitivity was about 2 and $10 \mu\text{M}$ for cysteine and glutathione, respectively. Detection with nanorods offers an advantage over detection with spherical nanoparticles: Monofunctional molecules containing functional groups such as amines or carboxylic acids do not influence the plasmon absorption of Au nanorods. This was a crucial advantage for the selective detection of cysteine and glutathione.

5.3.4 Detection of Other Biomolecules

The powerful detection method based on aggregation and deaggregation of plasmonic nanoparticles was extended to all sorts of biorelevant molecules. Detection of hydrogen peroxide, an important intermediate in the food-processing, pharmaceutical, and environmental industries, was achieved with an indirect method involving unmodified citrate-stabilized nanoparticles and horseradish peroxidase. In this study, Wu et al. used a substrate, *o*-phenylenediamine, which is oxidized specifically

with hydrogen peroxide in the presence of a biocatalyst, horseradish peroxidase. Upon formation of the enzymatic product azoaniline, the unmodified gold nanoparticles aggregated and a color shift could be observed. A linear response was observed between 1.3 and 41 μM , allowing quantitative sensing [167]. Glucose detection was also an important subject of studies due to its impact on diabetes follow-up, and noninvasive, in-physiological-fluid methods are highly desired.

In 2004, Aslan et al. developed an indirect strategy using 10-nm gold nanoparticles (Figure 5.17) [168]. The nanoparticles were coated with dextran and subsequently aggregated using the four-valent protein Concanavalin A (Con A). The resulting UV-vis spectrum showed a red shift and a broadening of the plasmon band. When added to the solution, glucose competes successfully with dextran for binding with Con A, and nanoparticles deaggregate and a blue shift is observed. This system allows glucose detection from 1 mM and a linear response between 1 and 40 mM, which is relevant for blood detection. The same system was developed by the group on 5-nm silver particles [169]. Con A–dextran silver nanoparticles were observed to dissociate from a glucose concentration of 47 nM. These two studies offer a very good example of how the same strategy can be applied effectively to different ranges of sensing sensitivity by tuning the nanoparticle size, the metal, or the nature of the ligand.

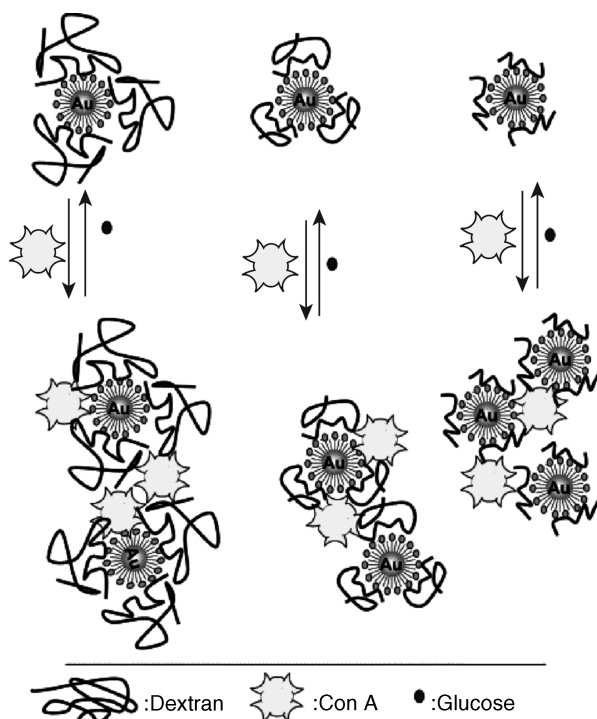


FIGURE 5.17 Glucose-sensing mechanism: the dissociation of Con A–aggregated dextran-coated gold nanoparticles. (From ref. 168, with permission. Copyright © 2004 Elsevier.)

5.3.5 Sensing of Metal Cations

The design described above, which uses plasmonic particle aggregation for biosensing, was subsequently adapted to allow colorimetric detection of metal cations. Colorimetric sensing of water pollutants such as Pb^{2+} , Hg^{2+} , Cd^{2+} , Ca^{2+} , or alkali metal cations is highly desirable for environmental applications. Conventional molecular dyes are often limited in sensitivity ($0.5 \mu\text{M}$), due to their extinction coefficient [170], a drawback that the nanoparticle-aggregation approach can circumvent. The technique consists of the stabilization of gold nanoparticles with a long alkyl chain thiol bearing a specific functionality at the end of the molecule. This functionality will either cause aggregation of the particles in the presence of the cation to be detected or, alternatively, deaggregation of existing aggregates, formed, for example, by hydrogen bonding. Both phenomena induce naked-eye color change. In 2001, Kin et al. could detect Pb^{2+} , Cd^{2+} , and Hg^{2+} (but not Zn^{2+}) at $400 \mu\text{M}$ concentrations using carboxylic acid-functionalized gold nanoparticles [170]. The particles aggregate in the presence of the analyte to be detected by chelation of the cations with carboxylates, causing a red-to-blue color change. The aggregation could be reversed upon addition of a highly chelating ligand such as EDTA. In 2002, Obare et al. achieved selective detection of lithium cations using phenanthroline-functionalized nanoparticles, which bind Li^+ selectively in water in a 2:1 fashion [171]. In the same year, Lin et al. used a similar strategy for potassium using 15-crown-5 as a selective binder [172]. K^+ was detected selectively even in the presence of such competitive analytes as Li^+ , Cs^+ , NH_4^+ , Ca^{2+} , and Na^+ . The concentration range of K^+ was 0.09 to 0.48 mM. More recently, biomolecules such as l-cysteine were used as a sensing functionality for copper cation detection, in a selective manner with respect to Cd^{2+} , Co^{3+} , Cr^{3+} , Fe^{3+} , Ni^{2+} , Zn^{2+} , and Ag^+ [173]. L-Cysteine binds to Cu^{2+} with a stoichiometry of 2:1. The detection limits could be lowered to $10 \mu\text{M}$ due to the high sensitive of cysteine to Cu^{2+} . In 2006, Lin et al. achieved a very good sensitivity of $1 \mu\text{M}$ for detection of Pb^{2+} using deaggregation of gold nanoparticles instead of aggregation. The response also proved to be fast (1 second) and selective over 12 metal cations. The gold nanoparticles were functionalized with two different functionalities: a 15-crown-5 ether and a carboxylic acid. Each crown ether molecule traps one molecule of water that can bind two carboxylic acids by hydrogen bonding, thus directing nanoparticle aggregation as shown in Figure 5.18(a). This aggregation is disrupted in the presence of Pb^{2+} , leading to a blue-to-red color change [174].

Lie and Lu have developed a strategy using DNAzyme as a functionality directing the aggregation of gold nanoparticles for Pb^{2+} -sensing purposes [175,176]. DNAzymes are DNA enzymes chosen as a metal-binding moiety for their specificity for metals such as Pb^{2+} , Cu^{2+} , and Zn^{2+} . Figure 5.18(b), pathway 1 shows a duplex of DNAzyme, termed 17E, and a complementary strand, called a substrate strand or Sub_{Au} . In the presence of an analyte, here Pb^{2+} , the enzyme carries out a catalytic cleavage of Sub_{Au} . A sensor was designed from this recognition unit: Sub_{Au} was extended and some gold nanoparticles were functionalized with DNA strands complementary to those extensions (DNA_{Au}). DNAzyme 17E, extended substrate strand Sub_{Au} ,

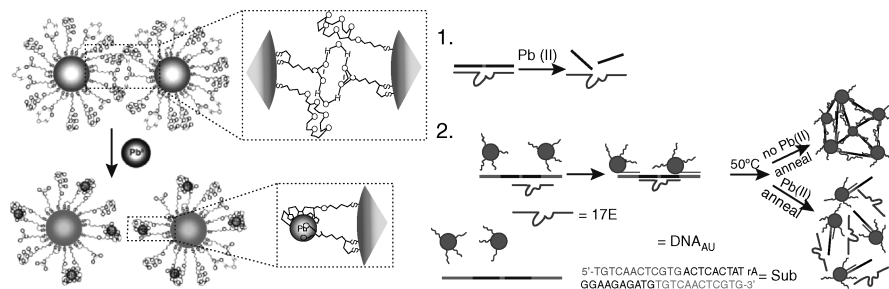


FIGURE 5.18 (a) Proposed methodology for the recognition of Pb^{2+} cations by 15-crown-5 ether/carboxylate functionalized gold nanoparticles. (b) 1, Cleavage of the upper strand (17DS) by the lower strand (DNAzyme) (17E) in the presence of Pb^{2+} ; 2, proposed methodology for the recognition of Pb^{2+} cations using DNAzyme-directed assembly of gold nanoparticles. [(A) From ref. 175, with permission. Copyright © Wiley-VCH Verlag GmbH & Co.KGaA. (B) Adapted from ref. 175 with permission. Copyright © 2001 American Chemical Society.]

and complementary strands DNA_{Au} attached to gold nanoparticles were mixed and annealed at 50°C before cooling down. This procedure results in the formation of aggregates shown in Figure 5.18(b) pathway 2. Aggregates are blue in color. In the presence of Pb^{2+} during the process, 17E cleaves Sub_{Au}, gold nanoparticles do not assemble, and the red color remains [175]. As such, this unoptimized sensor can detect Pb^{2+} at concentrations ranging between 100 nM and 4 μM, which is a significant improvement over the systems described previously. It now allows detection for environmental applications, as 480 nM is recognized as the toxic level for human beings [175]. Very interestingly, the research team synthesized a mutant of the DNAzyme, 17Ec, that proved totally inactive for catalytic cleavage with Pb^{2+} ; however, when using a 1:20 mixture of 17E and 17Ec in place of pure 17E, the sensitivity could be tuned to the range 10 to 200 μM. This approach is the first step toward quantitative detection of Pb^{2+} in colorimetric assays. Researchers also used TLC-based detection with this system to allow easy, portable assay-type sensing. Mg^{2+} , Ca^{2+} , Mn^{2+} , Co^{2+} , Ni^{2+} , Cu^{2+} , Zn^{2+} , and Cd^{2+} were also tested and were not detected, nor did they interfere with the detection of Pb^{2+} [175]. Further improvement in the method, especially by changing the nanoparticle size to 42 nm in diameter and changing the distance between consecutive nanoparticles in the aggregates, allowed much faster detection (8 minutes) at temperatures close to room temperature (35°C) [178]. Quantitative detection is possible between 0.4 and 2 μM. More recent studies showed how Pb^{2+} could not only prevent aggregation but could also induce disassembly of preexisting aggregates in the presence of a well-chosen free DNA strand, allowing “light-up” detection: detection by color appearance in the presence of the analyte as opposed to color disappearance [176]. Huang and Chang recently published a colorimetric Hg^{2+} -sensing method based on similar principles. Mercaptopropionic acid-stabilized gold nanoparticles 13 nm in size, in a buffer solution of Tris borate, aggregated in the presence of Hg^{2+} ions [179]. The method was proved selective and sensitive down to 100 μM. A dramatic improvement was

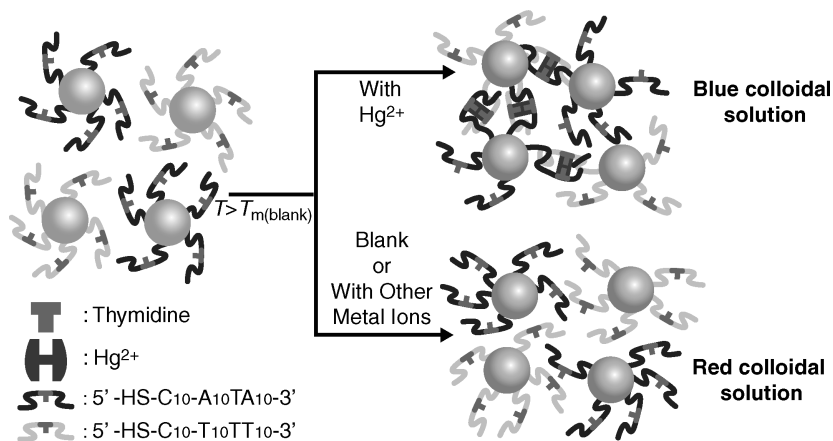


FIGURE 5.19 Colorimetric detection of mercuric ion (Hg^{2+}) using DNA-Au NPs. (From ref. 180, with permission. Copyright © Wiley-VCH Verlag GmbH & Co. KGaA.)

made recently in the field of Hg^{2+} detection with plasmonic particles by Lee et al., who used DNA-stabilized Au NPs (Figure 5.19). Two sets of particles were functionalized with strands that are complementary except for one single thymine–thymine mismatch. Hg^{2+} is indeed known to coordinate specifically to the bases that make up a thymine–thymine mismatch. Measuring the melting transition temperature for those systems in the presence or absence of the cation to be detected provides a powerful and sensitive method for detecting Hg^{2+} . Good selectivity versus other environmentally relevant metal cations and excellent sensitivity down to 100 nM were demonstrated [180].

Plasmonic particle aggregation/deaggregation–based detection is a very powerful sensing means since it provides a field-portable, inexpensive, environmentally benign, rapid, reliable, tunable, naked-eye, and assay type of sensing method. Semiquantitative to quantitative methods are now within reach. The versatility of nanoparticle functionalization allows good selectivity and a high extinction coefficient for gold nanoparticles ranging from 10 to 50 nm, which account for good sensitivity, making those systems competitive with fluorescence-based methods.

5.4 PLASMON BAND VARIATION ON THE ENVIRONMENT OR LIGAND ALTERATION

Fewer sensing methodologies that rely on a change in the plasmonic particle environment have been developed than methods using aggregation phenomena. As explained in Sections 5.2.3.1 and 5.3.2, the dielectric medium surrounding a nanoparticle, as well as the electronic exchanges between the particle and its stabilizing ligands, have a significant impact on the position of the SPB. Various methods exploiting these properties have been developed in the past decade or so. In

these methods, the sensing event is the binding of an analyte either to the surface of a plasmonic particle, resulting in a modification often of both the electronic density inside the particle and a change in the dielectric medium, or to a ligand preinstalled on the particle, causing a change in the dielectric medium. This event causes a shift of the SPB. In the following we first present methods that rely on pure alteration of the dielectric medium and then methods that rely on ligand exchange.

5.4.1 Biosensing by Alteration of the Dielectric Medium

The first breakthrough in the field was made by Englebienne in 1998. He was then studying sandwich assay methodologies relying on aggregation mechanisms with various antigens, but realized that contrary to his expectations, monovalent biomolecules induced a SPB shift. In this case the SPB shift could not be caused by aggregation, but rather, relied on a modification of the area surrounding the particles [181]. Detection at the nanogram level was achieved and the technique proved useful for kinetics measurements and compatible for automated, high-throughput analyzers. Since then, methods have been developed that use immobilized nanoparticles on surfaces, thus providing the advantage of a user-friendly device. In such systems, interparticle distances are fixed so that it can only be the adsorption of analytes onto particles that triggers a detectable shift of the SPB observed, since the binding event between a ligand on the particle and the analyte causes dielectrical medium modification [182]. In 2000, Okamoto et al. deposited presynthesized gold nanoparticles onto glass substrate to sense various solvents, measuring both the position and the intensity of the SPB [183]. The position of the SPB proved strongly dependent on the solvent in which the layer of naked particles was immersed. In the same year, Himmelhaus and Takei used a slightly different strategy to engineer a biosensor: a dense monolayer of latex beads was covered with a thin layer of gold. The resulting layer presents a good extinction coefficient. It was functionalized with biotin and used to sense avidin [184]. These two examples had reasonable sensitivity and the detection event could be recorded with a simple UV-vis spectrometer with very simple apparatus, which proved to have a significant advantage over other methods, such as surface plasmon resonance (using gold film). Van Duyne's group used their method, called *nanosphere lithography* (NSL), to pattern a surface with an array of triangular gold or silver nanoparticles (Figure 5.3) [185]. The nanoparticles were functionalized with biotin receptors. Upon binding, biotin modified the dielectric environment close to the particles and could thus be detected by a shift in the SPB position. Sensitivity was increased further by completing the sensing method with streptavidin to form a sandwich assay. The latter system was a significant breakthrough in the field, allowing detection sensitivity down to 1 pM [42]. More recently, in 2005, this methodology was used to detect biomarkers for Alzheimer disease, for the first time in conditions compatible with in vivo concentration [34]. Following the same trend, Nath and Chilkoti published work on coating a glass substrate with nanoparticles using self-assembled monolayers [186]. The nanoparticles are functionalized so as to bind a given protein: namely, streptavidin. Again, the alteration of the dielectric medium around the nanoparticle is responsible for an SPB shift. User-friendly and sensitive protein sensors

based on the SPB response of nanoparticles stabilized on various substrates (glass [186,187] quartz [188]) were thus designed. In a more recent application, silica-coated gold nanorods were used in a similar fashion [189]. One must also emphasize that functionalized gold nanoparticles have also been used as a complement to metallic films utilized for DNA assay [190,191]. Indeed, the surface plasmon band of a metallic film observed in transmission is a well-known optical phenomenon that has also been used for detection, especially of biological targets [193].

5.4.2 Chemosensing by Ligand-Exchange Mechanisms

In addition to the impact of the dielectric environment on the position of the SPB that we noted in Section 5.2.3.2, electronic exchange between particles and ligands chemisorbed on them also plays a major role. Since ligands can easily be replaced at the surface of nanoparticles, provided that the replacing ligand is in excess, this strategy was used as a sensing probe. Thiols, carbon disulfide, disulfides, and phosphine sensors have been developed that take advantage of the affinity of gold and silver particles for these species. In a first example, Henglein et al., using silver nanoparticles in solution, detected various sulfur-containing molecules in the range of

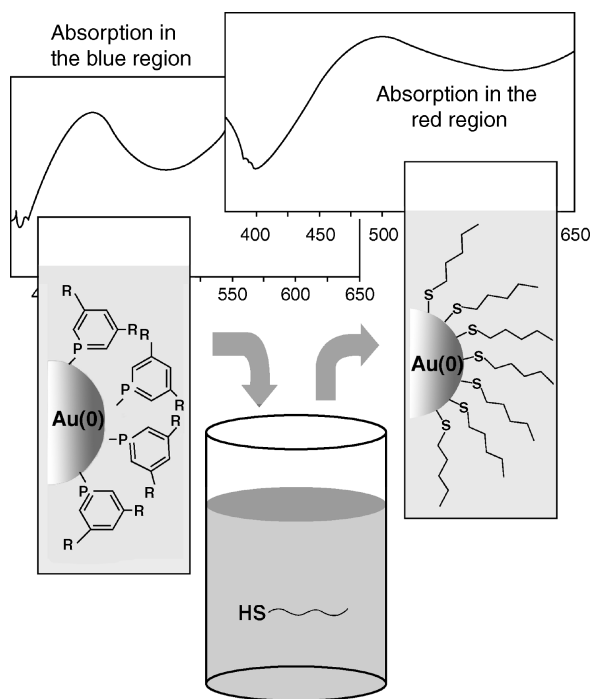


FIGURE 5.20 Gold nanoparticles immobilized in a silica mesoporous thin layer for detection of dodecanethiol. (From ref. 29, with permission. Copyright © Wiley-VCH Verlag GmbH & Co. KGaA.)

10 μM [194] and iodine from 2 μM [105]. Gases have also been detected [195]. More recently, our group used gold nanoparticles immobilized in a mesoporous film, with a low metal loading, so that the analyte to be detected is in large excess even at low concentrations (Figure 5.20) [29]. The films synthesized are transparent to visible light, so the SPB of the particles can be measured by absorption. NPs are stabilized there by a special ligand, the phosphinine, which enables selective detection of trimethylphosphine, characterized by a blue shift, or of thiols, which led to a red shift. Sensitivity down to 5 ppm in 1 minute was achieved for dodecanethiol.

5.5 METAL NANOPARTICLES AS LABELS

In past sections we reviewed sensing systems involving a change in the SPB properties of nanoparticles. In this section we focus on strategies in which the optical properties of particles are not altered by the sensing events, but rather, are used as such. Because of their beautiful, intense color, plasmon resonant particles were early thought of as ideal labels for molecules. In the first applications, the color of particles observed by absorption was used, but quickly, the scattering properties showed their great potential. Indeed, they offer a lot of advantages compared to such labels as radioactive molecules, which have a short life and induce safety and waste disposal issues, or fluorescent dyes, which they surpass as chromophores since their visible-region extinction coefficient can be several orders of magnitude higher [170]. Another crucial advantage is the capability to engineer dyes of various colors simply by changing the particle size or composition [196].

In 1980, Leuvering et al. designed a sandwich type of assay for the detection of antibodies [197]. Gold and silver nanoparticles of 60 and 50 nm of mean diameter, respectively, were conjugated with the antibody complementary to human placental lactogen (hPL). Solid support plate wells were also functionalized with the same antibody. Some solutions containing lactogen hPL, or blank solutions, were incubated in the functionalized wells before the conjugated nanoparticles were incubated under the same conditions. Wells were then washed. In wells where the lactogen hPL was present, they could bond both the solid support and the nanoparticles. After washing, nanoparticle presence was detectable by simple UV-vis analysis, carbon rod atomic absorption spectroscopy (CRAAS), or even by the naked eye at sufficient concentration. The sensitivity of the systems was 1.4 pM with CRAAS and 170 pM for naked-eye detection. Immunoassays of human chorionic gonadotrophin were also reported using the same methodology [140,197]. Further studies by the same group led to the design of various biomolecule sensing methodology by aggregation of nanoparticles (see Section 5.3.1). Aggregation proved a very powerful method, but it would not allow detection with the naked eye below 1 nM. Labeling seemed an interesting approach, as it allows signal amplification through various strategies. Mirkin's group chose silver amplification, which consists of treating the sensing plates with Ag(I) cations and hydroquinone after the sensing event has occurred. Hydroquinone reduces silver into metal at the surface of particles, providing a dark signal when particles are present. This very powerful method allowed the development of scanometric

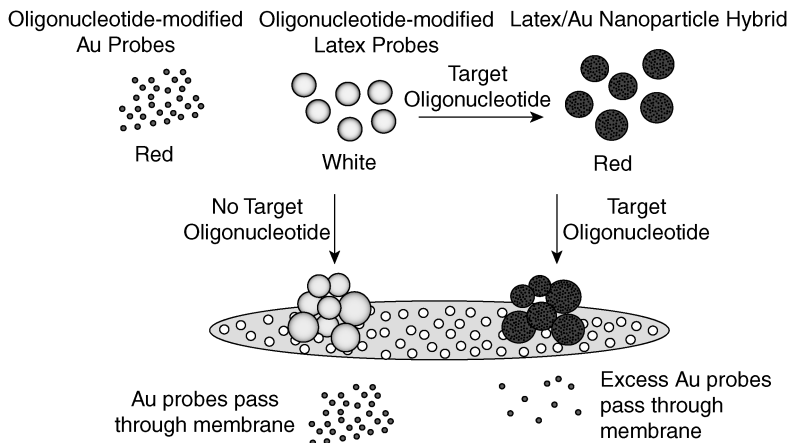


FIGURE 5.21 Gold nanoparticle–latex microsphere-based colorimetric DNA detection method. (From ref. 201, with permission from IUPAC.)

methods using a flatbed scanner as a reader [151,198–200]. Amplification has also been achieved by using methods to “concentrate” the particles. The first approach, described in 2000 by Mirkin’s group, was to functionalize latex beads with one of the two DNA strands utilized for detection (Figure 5.21). In the presence of gold nanoparticles functionalized with the complementary strand, gold NPs aggregate around the bigger latex bead. Excess nanoparticles could be removed by filtration. Here the test was positive if the red color of the gold nanoparticles appears in the filtrate. It must be emphasized that the sensing event here is not the aggregation of particles but their mere presence (attached to latex beads). The detection limit reaches 500 pM for DNA single strands for that system [201]. In a similar spirit, it proved possible to use magnetic nanoparticles in place of the latex beads. Magnetic particles can be concentrated magnetically, allowing a sensitivity of 500 pM (10 DNA strands in solution) [200,202]. Further work was directed toward the synthesis of particles with similar sensing capabilities but a different color, to permit multiplexing. This was achieved with core–shell Ag–Au nanoparticles featuring a yellow color when well dispersed in a solution and a black color when aggregated [71].

In 1998, Yguerabide and Yguerabide used the properties of plasmonic particles to scatter light as a tool for making labels after discovering that “light-scattering gold nanoparticles suspension has the same appearance as a fluorescing solution” [85]. Indeed gold, silver, and copper nanoparticles scatter colored light when illuminated with white light, and they do so in a very intense fashion. For example, a 60-nm gold nanoparticle is equivalent to 3×10^5 fluorescein molecules. Such particles can be detected in solutions of concentrations down to 10^{-16} M [85,196]. Light-scattering resonant particles were very quickly used for ultrasensitive DNA detection onto a solid platform via sandwich assays; again, target DNA strand A’B’ could be detected by a solid support functionalized with A and nanoparticles hybridized with B [203]. This method was developed in 2001 by Thaxton et al., who showed how two sets of

particles of various sizes—and thus various colors—could selectively detect two distinct DNA strands. This methodology was then commercialized by Genicon Sciences for DNA microarray analysis with 10-fold increased sensitivity over that of fluorescent probes [43]. The following year Bao and et al. used another DNA assay using gold light scatterers. DNA strands were functionalized with biotin molecules and kept in solution. Also, a surface was functionalized with DNA strands to analyze. The solution was added to the surface and recognition could happen. After washing with biotin, hybridized nanoparticles were introduced and bound specifically to DNA duplexes. Scanning of the surface made it possible to detect the binding event. This method proved sensitive down to tens of pg/ μ L [204]. More recently, comparable methodologies were used successfully for the detection of genetically modified organism markers [205] and DNA detection with very cheap gold functionalization [206].

The scattering properties of plasmonic nanoparticles quickly showed applications for imaging. In 2000, Schultz and co-workers introduced the use of silver-enhanced gold nanoparticles as scatterers for detecting single molecules spatially in a biological sample [207]. Using dark-field microscopy, a mode of microscopy where only the light emitted by the sample is collected, not the exciting light, the particles were visible individually under white light excitation, and their presence could account for a recognition event depending on an appropriate functionalization of the particles. This work evidenced detection of specific genes in chromosomes or at specific sites in tissues (e.g., muscles). Plasmonic nanoparticles offer a significant advantage over fluorescent molecules or quantum dots, which are generally used in the context of imaging; they have a higher light yield and are independent of time considerations (no blinking or photobleaching). More recently, interesting breakthroughs have been made in the domain of imaging with plasmonic particles. Yu et al. modified the surface of nanorods to make them cyto-benign and evidenced detection of cell surface biomarkers [208]. Applications of plasmonic labels to cancer cell recognition or marking have been developed by Huang et al. [209]. Of considerable interest for monitoring cellular functions, Kumar and co-workers engineered intracellular multifunctional labels based on gold nanoparticles [210]. Actin filaments inside fibroblast cells were targeted and filament rearrangements could be followed. A recent report from Orendorff et al. demonstrated that using particles of various shapes easily provides particles of different colors, with great potential for multiplexing imaging in a close future [120].

5.6 CONCLUSIONS

Throughout this chapter, we demonstrated that Cu, Ag, and Au nanoparticles possess powerful characteristics that make them very interesting probes for sensing applications. They are relatively cheap to produce, are very easily stabilized and functionalized, possess optical properties that compare or surpass those of fluorescent molecules, and their signal is stable in time and can be tuned using various factors, such as aggregation state, direct environment, and shape. Moreover, the

reading methodologies for the probing event are extremely simple, since the naked eye or a simple UV–vis spectrometer is usually sufficient. Commercial SPB-based sensors have already been developed, and field-portable detectors of environmentally relevant cations and pathogens are within reach. Applications for detection and therapy *in vivo* are active research areas and one can soon hope to obtain methodologies for tracking a marker inside a cell and potentially to perform delivery or thermotherapy. As we also discussed, further studies are necessary to allow enhanced sensitivity in all the techniques developed, but single molecule detection is potentially attainable.

Acknowledgments

The authors would like to thank the Ecole Polytechnique, the CNRS, the Canada Research Chair Foundation, the Canadian Foundation for Innovation, and McGill University for their financial support. Frédéric Goettmann is acknowledged for fruitful discussions on the principles of the SPB.

REFERENCES

1. Daniel MC, Astruc D. *Chem. Rev.* 2004;104:293–346.
2. Kreibig U, Vollmer M. *Optical Properties of Metal Clusters*. Springer-Verlag, Berlin, 1995.
3. Gonella F, Mazzoldi P. In Nalwa HS, ed. *Handbook of Nanostructured Materials and Nanotechnology*, Academic Press, San Diego, CA, 2000, pp. 81–158.
4. Padovani S, Sada C, Mazzoldi P, et al. *J. Appl. Phys.* 2003;93:10058–10063.
5. http://www.britishmuseum.org/explore/highlights/highlight_objects/pe_mla/t/the_lycurgus_cup.aspx, British Museum, London, accessed April 2008.
6. Chang K. *The New York Times*, Feb. 22, 2005.
7. Rabelais F. La vie tres horricque du grand Gargantua pere de Pantagruel. Francoys Juste, Lyon, devant Nostre Dame de Confort, 1802.
8. Novotny L, Hecht B. *Principles of Nano-optics*. Cambridge University Press, Cambridge, UK, 2006.
9. Campbell CT, Kim G. *Biomaterials*. 2007;28:2380–2392.
10. Pirondini L, Dalcanale E. *Chem. Soc. Rev.* 2007;36:695–706.
11. Shankaran DR, Gobi KV, Miura N. *Sens. Actuators B*. 2007;121:158–177.
12. Yuk JS, Ha KS. *Exp. Mol. Med.* 2005;37:1–10.
13. Liedberg B, Nylander C, Lunstrom I. *Sens. Actuators*. 1983;4:299–304.
14. Fendler JH. In Pileni M-P, ed. *Exploitation of Self Assembled Nanostructures in Optical Biosensors*, Wiley-VCH; Weinheim, Germany, 2005, pp. 279–293.
15. Zhao J, Zhang XY, Yonzon CR, Haes AJ, Van Duyne RP. *Nanomedicine*. 2006;1: 219–228.
16. Eustis S, El-Sayed MA. *Chem. Soc. Rev.* 2006;35:209–217.
17. Alvarez MM, Houry JT, Schaaff TG, Shafiguillin MN, Vezmar I, Whetten RL. *J. Phys. Chem. B*. 1997;101:3706–3712.

18. Brust M, Fink J, Bethell D, Schiffrin DJ, Kiely C. *J. Chem. Soc. Chem. Commun.* 1995;1655–1656.
19. Brust M, Walker M, Bethell D, Schiffrin DJ, Whyman R. *J. Chem. Soc. Chem. Commun.* 1994;801–802.
20. Turkevich J, Stevenson PC, Hillier J. *Discuss. Faraday Soc.* 1951;11:55–75.
21. Gole A, Murphy CJ. *Chem. Mater.* 2004;16:3633–3640.
22. Yu DB, Yam VWW. *J. Am. Chem. Soc.* 2004;126:13200–13201.
23. Moores A, Goettmann F, Sanchez C, Le Floch P. *Chem. Commun.* 2004;2842–2843.
24. Kim F, Song JH, Yang P. *J. Am. Chem. Soc.* 2002;124:14316–14317.
25. Nishioka K, Niidome Y, Yamada S. *Langmuir.* 2007;23:10353–10356.
26. Hostetler MJ, Green SJ, Stokes JJ, Murray RW. *J. Am. Chem. Soc.* 1996;118:4212–4213.
27. Warner MG, Reed SM, Hutchison JE. *Chem. Mater.* 2000;12:3316–3320.
28. Rucareanu S, Gandubert VJ, Lennox RB. *Chem. Mater.* 2006;18:4674–4680.
29. Goettmann F, Moores A, Boissiere C, Le Floch P, Sanchez C. *Small.* 2005;1:636–639.
30. Hamamoto K, Micheletto R, Oyama M, Umar AA, Kawai S, Kawakami Y. *J. Opt. A Pure Appl. Opt.* 2006;8:268–271.
31. Kim F, Song JH, Yang PD. *J. Am. Chem. Soc.* 2002;124:14316–14317.
32. Yonzon CR, Stuart DA, Zhang XY, McFarland AD, Haynes CL, Van Duyne RP. *Talanta.* 2005;67:438–448.
33. Sherry LJ, Jin RC, Mirkin CA, Schatz GC, Van Duyne RP. *Nano Lett.* 2006;6:2060–2065.
34. Haes AJ, Chang L, Klein WL, Van Duyne RP. *J. Am. Chem. Soc.* 2005;127:2264–2271.
35. Haes AJ, Hall WP, Chang L, Klein WL, Van Duyne RP. *Nano Lett.* 2004;4:1029–1034.
36. Katz E, Willner I. *Angew. Chem. Int. Edt.* 2004;43:6042–6108.
37. Park J, Joo J, Kwon SG, Jang Y, Hyeon T. *Angew. Chem. Int. Edt.* 2007;46:4630–4660.
38. Pellegrino T, Kudera S, Liedl T, Javier AM, Manna M, Parak WJ. *Small.* 2005;1:48–63.
39. Richards R, Bönemann H, In Kumar CSSR, Holmes J, Leuschner C, eds. *Nanofabrication Towards Biomedical Applications.* Wiley-VCH, Weinheim, Germany, 2005, pp. 3–32.
40. Leary SP, Liu CY, Apuzzo MLJ. *Neurosurgery.* 2006;58:805–822.
41. Alivisatos P. *Nat. Biotechnol.* 2004;22:47–52.
42. Haes A, Van Duyne R. *J. Am. Chem. Soc.* 2002;10596–10604.
43. Thaxton CS, Mirkin CA, In Niemeyer CM, Mirkin CA, eds. *Nanobiotechnology,* Wiley-VCH, Weinheim, Germany, 2004, pp. 288–307.
44. Liz-Marzan LM. *Mater. Today.* 2004;7:26–31.
45. Moores A, Goettmann F. *New J. Chem.* 2006;30:1121–1132.
46. Shi JJ, Zhu YF, Zhang XR, Baeyens WRG, Garcia-Campana AM. *Trac-Trends Anal. Chem.* 2004;23:351–360.
47. Hutter E, Fendler J. *Adv. Mater.* 2004;1685–1706.
48. Leary SP, Liu CY, Yu C, Apuzzo MLJ. *Neurosurgery.* 2005;57:606–633.
49. Leary SP, Liu CY, Apuzzo MLI. *Neurosurgery.* 2006; 58; 1009–1025.
50. Liao HW, Nehl CL, Hafner JH. *Nanomedicine.* 2006;1:201–208.
51. Rosi NL, Mirkin CA. *Chem. Rev.* 2005;105:1547–1562.
52. Azzazy HME, Mansour MMH, Kazmierczak SC. *Clin. Chem.* 2006;52:1238–1246.

53. Bally M, Halter M, Voros J, Grandin HM. *Surf. Interface Anal.* 2006;38:1442–1458.
54. Fritzsche W, Taton TA. *Nanotechnology.* 2003;14:R63–R73.
55. Liang S, Pierce DT, Amiot C, Zhao XJ. *Synth. React. Inorg. Met. Org. Nano-Met. Chem.* 2005;35:661–668.
56. West JL, Halas NJ. *Annu. Rev. Biomed. Eng.* 2003;5:285–292.
57. Haes AJ, Van Duyne RP. *Anal. Bioanal. Chem.* 2004;379:920–930.
58. Haes AJ, Van Duyne RP. *Expert Rev. Mol. Diagn.* 2004;4:527–537.
59. Willets KA, Van Duyne RP. *Ann. Rev. Phys. Chem.* 2007;58:267–297.
60. Yonzon CR, Zhang X, Zhao J, Van Duyne RP. *Spectroscopy.* 2007;22:42–56.
61. Astruc D, Daniel MC, Ruiz J. *Chem. Commun.* 2004;2637–2649.
62. Aranzaes JR, Belin C, Astruc D. *Chem. Commun.* 2007;3456–3458.
63. Daniel MC, Aranzaes JR, Nlate S, Astruc D. *J. Inorg. Organomet. Polym. Mater.* 2005;15:107–119.
64. Thomas M, Klibanov AM. *Proc. Natl. Acad. Sci. USA.* 2003;100:9138–9143.
65. Tkachenko AG, Xie H, Liu Y, et al. *Bioconjugate Chem.* 2004;15:482–490.
66. Connor EE, Mwamuka J, Gole A, Murphy CJ, Wyatt MD. *Small.* 2005;1:325–327.
67. Tkachenko AG, Xie H, Coleman D, et al. *J. Am. Chem. Soc.* 2003;125:4700–4701.
68. Takahashi H, Niidome Y, Niidome T, Kaneko K, Kawasaki H, Yamada S. *Langmuir.* 2006;22:2–5.
69. Huff TB, Hansen MN, Zhao Y, Cheng JX, Wei A. *Langmuir.* 2007;23:1596–1599.
70. Link S, Wang ZL, El-Sayed MA. *J. Phys. Chem. B.* 1999;103:3529–3533.
71. Cao YW, Jin R, Mirkin CA. *J. Am. Chem. Soc.* 2001;123:7961–7962.
72. Takahashi H, Niidome Y, Yamada S. *Chem. Commun.* 2005;2247–2249.
73. Weissleder R. *Nat. Biotechnol.* 2001;19:316–317.
74. Hirsch LR, Stafford RJ, Bankson JA, et al. *Proc. Natl. Acad. Sci. USA.* 2003;100:13549–13554.
75. Krpetic Z, Porta F, Scari G. *Gold Bull.* 2006;39:66–68.
76. Loo C, Lin A, Hirsch L, Lee, et al. *Technol. Cancer Res. Treat.* 2004;3:33–40.
77. O’Neal DP, Hirsch LR, Halas NJ, Payne JD, West JL. *Cancer Lett.* 2004;209:171–176.
78. Dieringer JA, McFarland AD, Shah NC, et al. *Faraday Discuss.* 2006;132:9–26.
79. El-Kouedi M, Keating CD, In Niemeyer CM, Mirkin CA, eds. *Nanobiotechnology*, Wiley-VCH, Weinheim, Germany 2004, pp. 429–443.
80. Liebsch A. *Electronic Excitations at the Metal Surfaces*. Plenum Press, New York, 1997.
81. Bohren GF, Huffman DR. *Absorption and Scattering of Light by Small Particles*. Wiley, New York, 1983.
82. Ung T, Liz-Marzan LM, Mulvaney P. *J. Phys. Chem. B.* 2001;105:3441–3452.
83. Lica GC, Zelakiewicz BS, Constantinescu M, Tong Y. *J. Phys. Chem. B.* 2004;108:19896–19900.
84. Jackson JD. *Classical Electrodynamics*, 3rd ed. Wiley, New York, 1999.
85. Yguerabide J, Yguerabide EE. *Anal. Biochem.* 1998;262:137–156.
86. Mie G. *Ann. Phys.* 1908;25:377–445.
87. Barber DJ, Freestone IC. *Archaeometry.* 1990;32:33–45.

88. Miller MM, Lazarides AA. *J. Opt. A Pure Appl. Opt.* 2006;8:S239–S249.
89. Underwood S, Mulvaney P. *Langmuir*. 1994;10:3427–3430.
90. Liz-Marzan LM, Giersig M, Mulvaney P. *Langmuir*. 1996;12:4329–4335.
91. Ung T, Liz-Marzan LM, Mulvaney P. *J. Phys. Chem. B*. 2001;105:3441–3452.
92. Miller MM, Lazarides AA. *J. Phys. Chem. B*. 2005;109:21556–21565.
93. Mock JJ, Smith DR, Schultz S. *Nano Lett.* 2003;3:485–491.
94. Atay T, Song JH, Nurmikko AV. *Nano Lett.* 2004;4:1627–1631.
95. Rechberger W, Hohenau A, Leitner A, Krenn JR, Lamprecht B, Aussenegg FR. *Opt. Commun.* 2003;220:137–141.
96. Guarise C, Pasquato L, Scrimin P. *Langmuir*. 2005;21:5537–5541.
97. Thomas KG, Barazzouk S, Itty Ipe B, Joseph STS, Kamat PV. *J. Phys. Chem. B*. 2004;108:13066–13068.
98. Sudeep PK, Joseph STS, Thomas KG. *J. Am. Chem. Soc.* 2005;127:6516–6517.
99. Brown LO, Hutchison JE. *J. Phys. Chem. B*. 2001;105:8911–8916.
100. Weare WW, Reed SM, Warner MG, Hutchison JE. *J. Am. Chem. Soc.* 2000;122:12890–12891.
101. Mulvaney P. *Langmuir*. 1996;12:788–800.
102. Linnert T, Mulvaney P, Henglein A. *J. Phys. Chem.* 1993;97:679–682.
103. Henglein A, Mulvaney P, Linnert T. *Faraday Discuss.* 1991;31–44.
104. Henglein A. *Chem. Mater.* 1998;10:444–450.
105. Henglein A. *J. Phys. Chem.* 1993;97:5457–5471.
106. Chapman R, Mulvaney P. *Chem. Phys. Lett.* 2001;349:358–362.
107. Lica GC, Zelakiewicz BS, Constantinescu M, Tong YY. *J. Phys. Chem. B*. 2004;108:19896–19900.
108. Kreibitz U, Fragstein CV. *Z. Physik.* 1969;224:307–323.
109. Tiggesbaumer J, Koller L, Meiwesbroer KH, Liebsch A. *Phys. Rev. A*. 1993;48:R1749–R1752.
110. Tiggesbaumer J, Koller L, Lutz HO, Meiwesbroer KH. *Chem. Phys. Lett.* 1992;190:42–47.
111. Liebsch A. *Phys. Rev. B*. 1993;48:11317–11328.
112. Perez-Juste J, Pastoriza-Santos I, Liz-Marzan LM, Mulvaney P. *Coord. Chem. Rev.* 2005;249:1870–1901.
113. Link S, Mohamed MB, El-Sayed MA. *J. Phys. Chem. B*. 1999;103:3073–3077.
114. Rai A, Singh A, Ahmad A, Sastry M. *Langmuir*. 2006;22:736–741.
115. Shankar SS, Rai A, Ankamwar B, Singh A, Ahmad A, Sastry M. *Nat. Mater.* 2004;3:482–488.
116. Seo D, Park JC, Song H. *J. Am. Chem. Soc.* 2006;128:14863–14870.
117. Sun YG, Xia YN. *Science*. 2002;298:2176–2179.
118. Wang H, Brandl DW, Le F, Nordlander P, Halas NJ. *Nano Lett.* 2006;6:827–832.
119. Hao E, Schatz GC, Hupp JT. *J. Fluoresc.* 2004;14:331–341.
120. Orendorff CJ, Sau TK, Murphy CJ. *Small*. 2006;2:636–639.
121. Nehl CL, Liao HW, Hafner JH. *Nano. Lett.* 2006;6:683–688.

122. Sau TK, Murphy CJ. *J. Am. Chem. Soc.* 2004;126:8648–8649.
123. Pileni MP. *Nat. Mater.* 2003;2:145–150.
124. Wiley B, Sun YG, Chen JY, et al. *MRS Bull.* 2005;30:356–361.
125. Gans R. *Ann. Phys.* 1915;270.
126. Noguez C. *J. Phys. Chem. C.* 2007;111:3806–3819.
127. Hao E, Bailey RC, Schatz GC, Hupp JT, Li SY. *Nano Lett.* 2004;4:327–330.
128. Zou SL, Schatz GC. *J. Chem. Phys.* 2004;121:12606–12612.
129. Devarajan S, Bera P, Sampath S. *J. Colloid Interface Sci.* 2005;290:117–129.
130. Hostetler MJ, Zhong CJ, Yen BKH, et al. *J. Am. Chem. Soc.* 1998;120:9396–9397.
131. Kariuki NN, Luo J, Maye MM, et al. *Langmuir.* 2004;20:11240–11246.
132. Wu ML, Lai LB. *Colloids Surf. A.* 2004;244:149–157.
133. Wilcoxon JP, Provencio PP. *J. Am. Chem. Soc.* 2004;126:6402–6408.
134. Lee KS, El-Sayed MA. *J. Phys. Chem. B.* 2006;110:19220–19225.
135. Averitt RD. *Phys. Rev. Lett.* 1997;78:4217–4220.
136. Hirsch LR, Jackson JB, Lee A, Halas NJ, West JL. *Anal. Chem.* 2003;75:2377–2381.
137. Lim JK, Joo SW. *Appl. Spectrosc.* 2006;60:847–852.
138. Leuvinger JHW, Thal P, Vanderwaart M, Schuurs A. *J. Immunol. Methods.* 1981;45:183–194.
139. Leuvinger JHW, Thal P, Schuurs A. *J. Immunol. Methods.* 1983;62:175–184.
140. Leuvinger JHW, Thal P, White DD, Schuurs A. *J. Immunol. Methods.* 1983;62:163–174.
141. Wielaard F, Denissen A, van der Veen L, Rutjes I. *J. Virol. Methods.* 1987;17:149–158.
142. Mirkin CA, Letsinger RL, Mucic RC, Storhoff JJ. *Nature.* 1996;382:607–609.
143. Storhoff JJ, Lazarides AA, Mucic RC, Mirkin CA, Letsinger RL, Schatz C. *J. Am. Chem Soc.* 2000;122:4640–4650.
144. Elghanian R, Storhoff JJ, Mucic RC, Letsinger RL, Mirkin CA. *Science.* 1997;277:1078–1081.
145. Storhoff JJ, Elghanian R, Mucic RC, Mirkin CA, Letsinger RL. *J. Am. Chem. Soc.* 1998;120:1959–1964.
146. Storhoff JJ, Lazarides AA, Mucic RC, Mirkin CA, Letsinger RL, Schatz C. *J. Am. Chem Soc.* 2000;122:4640–4650.
147. Reynolds RA, Mirkin CA, Letsinger RL. *J. Am. Chem. Soc.* 2000;122:3795–3796.
148. Sadasivan S, Dujardin E, Li M, Johnson CJ, Mann S. *Small.* 2005;1:103–106.
149. Aldaye FA, Sleiman HF. *J. Am. Chem. Soc.* 2007;129:4130–4131.
150. Aldaye FA, Sleiman HF. *Angew. Chem. Int. Edt.* 2006;45:2204–2209.
151. Taton TA, Mirkin CA, Letsinger RL. *Science.* 2000;289:1757–1760.
152. Sato K, Hosokawa K, Maeda M. *J. Am. Chem. Soc.* 2003;125:8102–8103.
153. Li HX, Rothberg LJ. *J. Am. Chem. Soc.* 2004;126:10958–10961.
154. Li H, Rothberg L. *Proc. Natl. Acad. Sci. USA.* 2004;101:14036–14039.
155. Mann S, Shenton W, Li M, Connolly S, Fitzmaurice D. *Adv. Mater.* 2000;12:147–150.
156. Niemeyer CM, Burger W, Peplies J. *Angew. Chem. Int. Ed.* 1998;37:2265–2268.
157. Sastry M, Lala N, Patil V, Chavan SP, Chittiboyina AG. *Langmuir.* 1998;14:4138–4142.
158. Otsuka H, Akiyama Y, Nagasaki Y, Kataoka K. *J. Am. Chem. Soc.* 2001;123:8226–8230.

159. Thanh NTK, Rosenzweig Z. *Anal. Chem.* 2002;74:1624–1628.
160. Hirsch LR, Jackson JB, Lee A, Halas NJ, West J. *Anal. Chem.* 2003;75:2377–2381.
161. Hone DC, Haines AH, Russell DA. *Langmuir.* 2003;19:7141–7144.
162. Schofield CL, Haines AH, Field RA, Russell DA. *Langmuir.* 2006;22:6707–6711.
163. Xu X, Han MS, Mirkin CA. *Angew. Chem. Int. Edt.* 2007;46:3468–3470.
164. Chah S, Hammond MR, Zare RN. *Chem. Biol.* 2005;12:323–328.
165. Wei H, Li B, Li J, Wang E, Dong S. *Chem. Commun.* 2007;3735–3737.
166. Zhao W, Chiunan W, Lam JCF, Brook MA, Li Y. *Chem. Commun.* 2007;3729–3731.
167. Wu ZS, Zhang SB, Guo MM, Chen CR, Shen GL, Yu RQ. *Anal. Chim. Acta.* 2007;584:122–128.
168. Aslan K, Lakowicz JR, Geddes CD. *Anal. Biochem.* 2004;330:145–155.
169. Zhang J, Roll D, Geddes CD, Lakowicz JR. *J. Phys. Chem. B.* 2004;108:12210–12214.
170. Kim Y, Johnson RC, Hupp JT. *Nano Lett.* 2001;1:165–167.
171. Obare SO, Hollowell RE, Murphy CJ. *Langmuir.* 2002;18:10407–10410.
172. Lin SY, Liu SW, Lin CM, Chen CH. *Anal. Chem.* 2002;74:330–335.
173. Yang WR, Gooding JJ, He ZC, Li Q, Chen GN. *J. Nanosci. Nanotechnol.* 2007;7:712–716.
174. Lin S-Y, Wu S-H, Chen C-H. *Angew. Chem. Int. Edt.* 2006;45:4948–4951.
175. Liu J, Lu Y. *J. Am. Chem. Soc.* 2003;125:6642–6643.
176. Liu J, Lu Y. *J. Am. Chem. Soc.* 2005;127:12677–12683.
177. Liu JW, Lu Y. *Chem. Mater.* 2004;16:3231–3238.
178. Liu J, Lu Y. *J. Am. Chem. Soc.* 2004;126:12298–12305.
179. Huang C-C, Chang H-T. *Chem. Commun.* 2007;1215–1217.
180. Lee J-S, Han MS, Mirkin CA. *Angew. Chem. Int. Edt.* 2007;46:4093–4096.
181. Englebienne P. *Analyst.* 1998;123:1599–1603.
182. Haes AJ, Van Duyne RP. *J. Am. Chem. Soc.* 2002;124:10596–10604.
183. Okamoto T, Yamaguchi I, Kobayashi T. *Opt. Lett.* 2000;25:372–374.
184. Himmelhaus M, Takei H. *Sens. Actuators B.* 2000;63:24–30.
185. Malinsky MD, Kelly KL, Schatz GC, Van Duyne RP. *J. Am. Chem. Soc.* 2001;123:1471–1482.
186. Nath N, Chilkoti A. *Anal. Chem.* 2002;74:504–509.
187. Nath N, Chilkoti A. *Anal. Chem.* 2004;76:5370–5378.
188. Frederix F, Friedt JM, Choi KH. *Anal. Chem.* 2003;75:6894–6900.
189. Wang C, Ma Z, Wang T, Su Z. *Adv. Funct. Mater.* 2006;16:1673–1678.
190. He L, Musick MD, Nicewarner SR. *J. Am. Chem. Soc.* 2000;122:9071–9077.
191. Hutter E, Pileni MP. *J. Phys. Chem. B.* 2003;107:6497–6499.
192. Tokareva I, Minko S, Fendler JH, Hutter E. *J. Am. Chem. Soc.* 2004;126:15950–15951.
193. Homola J. *Anal. Bioanal. Chem.* 2003;377:528–539.
194. Henglein A, Meisel D. *J. Phys. Chem. B.* 1998;102:8364–8366.
195. Hilger A, Cuppers N, Tenfelde M, Kreibig U. *Eur. Phys. J. D.* 2000;10:115–118.
196. Yguerabide J, Yguerabide EE. *Anal. Biochem.* 1998;262:157–176.

197. Leuvering JHW, Thal PJHM, Van der Waart M, Schuurs AHW. *J. Immunoassay.* 1980;1:77–91.
198. Nam JM, Stoeva SI, Mirkin CA. *J. Am. Chem. Soc.* 2004;126:5932–5933.
199. Stoeva SI, Lee JS, Smith JE, Rosen ST, Mirkin CA. *J. Am. Chem. Soc.* 2006;128:8378–8379.
200. Stoeva SI, Lee JS, Thaxton CS, Mirkin CA. *Angew. Chem. Int. Edt.* 2006;45:3303–3306.
201. Reynolds RA, Mirkin CA, Letsinger RL. *Pure Appl. Chem.* 2000;72:229–235.
202. Nam JM, Stoeva SI, Mirkin CA. *J. Am. Chem. Soc.* 2004;126:5932–5933.
203. Taton TA, Lu G, Mirkin CA. *J. Am. Chem. Soc.* 2001;123:5164–5165.
204. Bao P, Frutos AG, Greef C, et al. *Anal. Chem.* 2002;74:1792–1797.
205. Kalogianni DP, Koraki T, Christopoulos TK, Ioannou PC. *Biosens. Bioelectron.* 2006;21:1069–1076.
206. Mehrabi M, Wilson R. *Small.* 2007;3:1491–1495.
207. Schultz S, Smith DR, Mock JJ, Schultz DA. *Proc. Natl. Acad. Sci. USA.* 2000;97:996–1001.
208. Yu C, Varghese L, Irudayaraj J. *Langmuir.* 2007;23:9114–9119.
209. Huang X, El-Sayed IH, Qian W, El-Sayed MA. *Nano Lett.* 2007;7:1591–1597.
210. Kumar S, Harrison N, Richards-Kortum R, Sokolov K. *Nano Lett.* 2007;7:1338–1343.

Gold Nanoparticles: A Versatile Label for Affinity Electrochemical Biosensors

ADRIANO AMBROSI

Nanobioelectronics and Biosensors Group, Institut Català de Nanotecnologia, Barcelona, Spain

ALFREDO DE LA ESCOSURA-MUÑIZ

Nanobioelectronics and Biosensors Group, Institut Català de Nanotecnologia, Barcelona, Spain, and Instituto de Nanociencia de Aragón, Universidad de Zaragoza, Zaragoza, Spain

MARIA TERESA CASTAÑEDA

Nanobioelectronics and Biosensors Group, Institut Català de Nanotecnologia, Barcelona, Spain, and Grup de Sensors i Biosensors, Departamento de Química, Universitat Autònoma de Barcelona, Bellaterra, Catalonia, Spain; on leave from Departamento de Ciencias Básicas, Universidad Autónoma Metropolitana-Azcapotzalco, México D.F., México

ARBEN MERKOÇI

ICREA and Nanobioelectronics and Biosensors Group, Institut Català de Nanotecnologia, Barcelona, Spain

- 6.1 Introduction
- 6.2 Synthesis of AuNPs
- 6.3 Characterization of AuNPs
 - 6.3.1 Electrochemical techniques
 - 6.3.2 Optical techniques
- 6.4 AuNPs as detecting labels for affinity biosensors
 - 6.4.1 DNA analysis
 - 6.4.2 Protein analysis
- 6.5 Conclusion

6.1 INTRODUCTION

Nanomaterials are of utmost importance and are characterized as materials having a length scale less than about 100 nm. Individual nanostructures involve clusters, nanoparticles (NPs), nanocrystals, carbon nanofibers, nanowires, and carbon nanotubes, while collections of nanostructures involve arrays, assemblies, and superlattices of individual nanostructures [1]. Nanosized particles of noble metals, especially gold nanoparticles (AuNPs), have received great attention due to their attractive electronic, optical, and thermal as well as catalytic properties and potential applications in the fields of physics, chemistry, biology, medicine, and material science and their different interdisciplinary fields [2], and therefore the synthesis and characterization of AuNPs have attracted considerable attention from a fundamental and practical point of view. A variety of methods have been developed to prepare AuNPs, and many reviews [3,4] are now available.

The preparation of AuNPs generally involves the chemical reduction of gold salt in the aqueous organic phase or in two phases. However, the high surface energy of AuNPs makes them extremely reactive, and this causes aggregation if their surfaces are not protected or passivated. Thus, special precautions have to be taken to avoid aggregation or precipitation. Typically, AuNPs are prepared by chemical reduction of the corresponding metal salts in the presence of a stabilizer that binds to their surface to impart high stability and rich linking chemistry and to provide the desired charge and solubility properties. Some of the methods commonly used for surface passivation include protection by self-assembled monolayers, the most popular being citrate [5] and thiol-functionalized organics [6]; encapsulation in the H₂O pools of reverse microemulsions [7]; and dispersion in polymeric matrixes [8]. Although the synthesis of AuNPs is making great progress, finding ways to control the size, morphology, and surface chemistry of AuNPs is still a great challenge. Recently, designing novel protectors for AuNPs have been the focus of intense research because the surface chemistry of AuNPs will play a key role in future application fields, such as nanosensors, biosensors, catalysis, nanodevices, and nanoelectrochemistry.

From an electroanalytical point of view, more attention has been paid to AuNPs because of their good biological compatibility, excellent conducting capability, and high surface-to-volume ratio. These features provide excellent prospects for interfacing biological recognition events with electronic signal transduction and make AuNPs extremely suitable for developing novel and improved electrochemical sensing and biosensing systems [9].

AuNPs, especially, present excellent biocompatibility and display unique structural, electronic, magnetic, optical, and catalytic properties, which have made them a very attractive material for biosensors, chemical sensors, and electrocatalysis is. In recent years, many research articles describing the use of AuNPs for electrochemical applications such as bioassays, biosensors, chemical sensors, and electrocatalysis have been published. Several reviews are available which deal partially with the use of AuNPs for amperometric or voltammetric electrochemical biosensors [10–13]. In this chapter we focus on the use of AuNPs as labels in electrochemical affinity biosensors and bioassays (DNA and protein analysis) employing a specific adopted electrochemical technique with direct and indirect detection strategies.

6.2 SYNTHESIS OF AuNPs

In 1857, Faraday published a comprehensive study on the preparation and properties of colloidal gold [14]. A variety of methods have been developed for synthesis of AuNPs, especially by chemical reduction; among them, sodium citrate reduction of chloroauric acid at 100°C, developed by Turkevich [15], remains the most commonly used method [16].

Brown et al. reported a generally applicable technique for synthesizing colloidal Au particles. In this approach, Au^{3+} is reduced on the surface of preformed 12-nm-diameter AuNPs by introduction of boiling sodium citrate, producing particles highly uniform in size and shape [17]. AuNPs have also been fabricated by electrochemically reducing chloroauric acid on the surface of NH_2 -HSM film, using potential step technology. The AuNPs deposited had an average diameter of 80 nm and showed high electroactivity [18]. Recently, Lung et al. reported the preparation of AuNPs by arc discharge in water as an alternative, cheap, effective, and environmentally friendly method [19]. Kim et al. developed a novel synthesis of AuNPs using alcohol ionic liquids. Such liquids served simultaneously as both reductants and protective agents, thereby simplifying the process of nanoparticle preparation significantly [20]. Currently, synthesis of novel AuNPs with unique properties and with applications in a wide variety of areas is the subject of substantial research [21–25].

In addition to their striking optical properties, AuNPs are important because they can be stabilized with a wide variety of molecules by taking advantage of well-known chemistry involving alkanethiol adsorption on gold [26]. The attractive physicochemical properties of AuNPs are strongly affected by their shape and size [27]. Ouacha et al. [28] reported the laser-assisted growth of AuNPs and concluded that this is a powerful method for controlling the shape of AuNPs, irrespective of size. On the other hand, the size and properties of AuNPs are highly dependent on their preparation conditions [29]. Synthesis of AuNPs of different shapes and sizes has been reported by Dos Santos et al. [30]. Alekseeva et al. [31] reported the synthesis of gold nanorods (NRs) based on seed-mediated growth in the presence of a soft surfactant template, cetyltrimethylammonium bromide. The catalytic, optical, electrical, magnetic, and electrochemical properties that exhibit AuNPs have made them an integral part of research in nanoscience [32].

6.3 CHARACTERIZATION OF AuNPs

6.3.1 Electrochemical Techniques

Electrochemical techniques such as cyclic voltammetry, differential pulse voltammetry (DPV), and chronoamperometry have been shown to be appropriate for characterization of AuNPs. Quinn et al. have studied DPV responses of thiolate monolayer-protected Au clusters (Au_{147} MPCs). They showed 15 evenly spaced voltammetric peaks characteristic of charge injection into the metal core. This was clear confirmation that MPCs behave as multivalent redox species in which the number of observable charge states is limited by the size of the potential window

available [33]. Hernández and co-workers synthesized AuNPs in a water-in-oil microemulsion. After the synthesis, the nanoparticles were cleaned by depositing a PbO_2 film in 0.1 M NaOH + 1 mM Pb(II). The characterization of the nanoparticles was carried out by recording the lead under potential deposition voltammetric profile in the same solution [34]. Stripping analysis is a powerful electroanalytical technique for trace metal measurements. Its remarkable sensitivity is attributed to the preconcentration step, during which the target metals are accumulated onto the working electrode. This technique has been used by many research groups for the characterization of AuNPs [35].

6.3.2 Optical Techniques

The development of scanning tunneling microscopy (STM) and subsequently other scanning probe microscopy (SPM), such as atomic force microscopy (AFM), one of the more recently developed technologies, have opened up new possibilities for the characterization, measurement, and manipulation of NPs [36,37]. Combined with other techniques, such as transmission electron microscopy (TEM) [38–40] high-resolution transmission electron microscopy (HRTEM) [41], scanning electron microscopy (SEM) [42–44], high-resolution scanning electron microscopy (HRSEM) [36], energy-dispersive x-ray spectrometry (EDS), extended x-ray absorption fine-structure (EXAFS) [45], Fourier transform infrared spectroscopy (FT-IR) [46,47], reflection absorption infrared spectroscopy (RAIRS), fluorescent microscopy, x-ray diffraction spectroscopy (XRD), and x-ray photoelectron spectroscopy (XPS), it is possible to study the AuNPs to a great detail. Inductively coupled plasma mass spectrometry (ICPMS) have also been used to detect AuNPs [48]. Ultraviolet–visible spectroscopy can also be used to determine the size and concentration of AuNPs [49] (Figure 6.1).

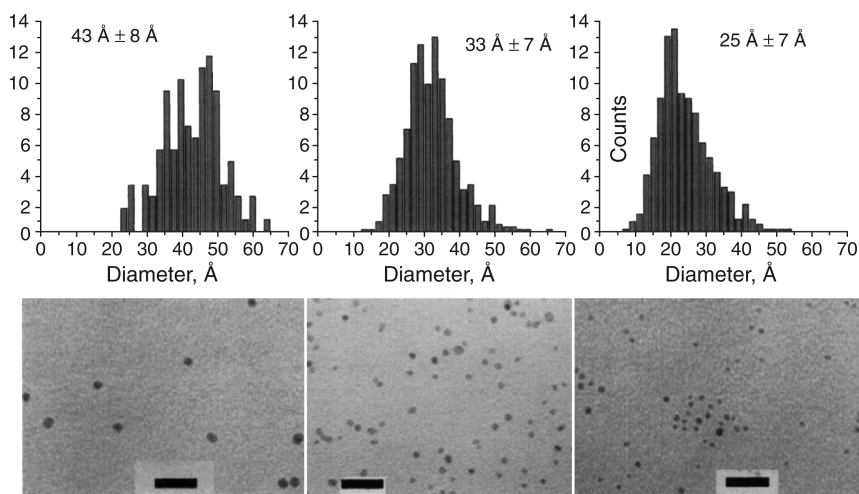


FIGURE 6.1 Particle-size dependence on Au/thiol ratio (changes from 6:1 to 3:1 to 1:1 from left to right) as observed by TEM. The scale bar is 20 nm. (From ref. 40, with permission.)

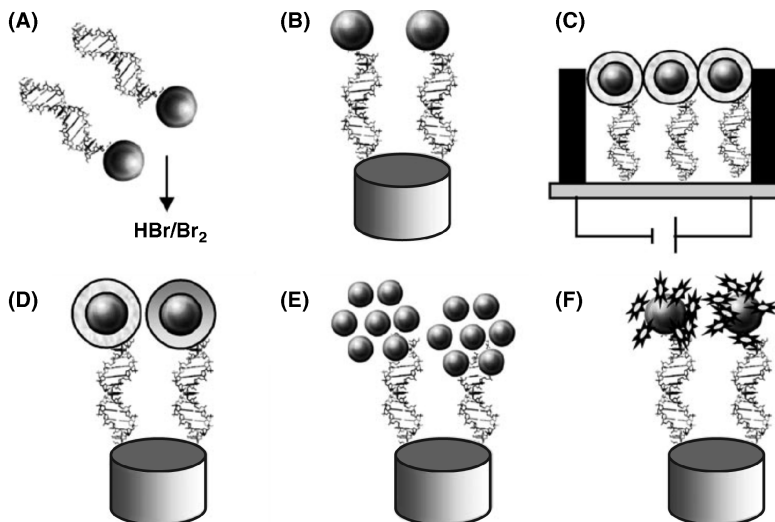


FIGURE 6.2 Schematic (not in scale) of the various strategies used for the integration of gold nanoparticles (AuNPs) into DNA-sensing systems: (A) previous dissolving of AuNP using a HBr/Br₂ mixture followed by Au(III) ion detection; (B) direct detection of AuNPs anchored onto the surface of the genosensor; (C) conductometric detection; (D) enhancement with silver or gold followed by detection; (E) AuNPs as carriers of other AuNPs; (F) AuNPs as carriers of other electroactive labels. (From ref. 60, with permission.)

6.4 AuNPs AS DETECTING LABELS FOR AFFINITY BIOSENSORS

Affinity biosensors can be defined as devices that rely on the use of receptor molecules, such as antibodies, nucleic acids, and membrane receptors, to recognize and bind a particular target irreversibly [50,51]. The high specificity and affinity of biochemical binding reactions (such as DNA hybridization and antibody–antigen complexation) lead to highly selective and sensitive sensing devices. Alternative and recently developed biorecognition elements include RNA and DNA aptamers [52], molecularly imprinted polymers [53], and templated surfaces [54]. In the following sections we describe in detail only the use of AuNPs as labels in sensing devices and assays in conjunction with DNA (Figure 6.2) and antibodies as recognition elements.

6.4.1 DNA Analysis

The use of nucleic acid technologies has significantly improved the diagnostic procedures in life sciences. The detection of DNA has a particular interest in genetics, pathology, criminology, pharmacogenetics, food safety, and many other fields. The development of electrical DNA hybridization biosensors has attracted considerable research effort [55,56]. Electrochemical DNA biosensors are attractive devices, especially for converting DNA hybridization event into an analytical signal for

obtaining sequence-specific information in connection with clinical, environmental, or forensic investigations. Such fast on-site monitoring schemes are required for quick preventive action and early diagnosis [57,58]. Nucleic acid hybridization is a process in which inconsonant nucleic acid strands with specific organization of nucleotide bases exhibiting complementary pairing with each other under specific given reaction conditions forms a stable duplex molecule. This phenomenon is possible because of the biochemical property of base pairing, which allows fragments of known sequences to find complementary matching sequences in an unknown DNA sample [59]. The AuNPs offer elegant ways of interfacing DNA recognition events with electrochemical signal transduction and of amplifying the resulting electrical response. AuNP-based amplification schemes have led to improved sensitivity of bioelectronic assays by several orders of magnitude [60].

6.4.1.1 Potentiometric Stripping Analysis Potentiometric stripping analysis (PSA) is an alternative stripping technique used for the electrochemical detection of nanoparticles after their dissolution. In this technique, just like stripping voltammetry, deposited reaction products or adsorbed substances are stripped from the electrode. The stripping itself can be done either by using a chemical reaction or by using an external current, and during the stripping process, the potential is recorded and processed. From the response (dt/dE vs. E), the amount of stripped material can be determined from the peak size, and the nature of the species can be deduced from the peak potential. In this way, Wang et al. [61], pioneered a nanoparticle-based electrochemical detection of DNA hybridization based on PSA detection of the colloidal gold tag. Signal amplification, and lowering the detection limits to the nanomolar and picomolar domains, were achieved by precipitation of gold or silver [62], respectively, onto the colloidal gold label.

A selective and sensitive gold nanoparticle and PSA-based method was reported by Hanaee et al. [63] for the detection of hepatitis B virus DNA sequences using magnetic beads as platforms. After separation of noncomplementary sequences, hybridized magnetic beads were treated with streptavidin-modified gold followed by silver enhancement at a gold screen-printed electrode (Figure 6.3). High selectivity and high sensitivity were obtained using PSA of silver ions that were deposited on gold nanoparticles, estimating a detection limit of the DNA strand of about 0.7 ng/mL. Kawde et al. [64] reported other work combining catalytic enhancement and PSA detection for a DNA assay. The assay is based on oligonucleotides functionalized with polymeric beads carrying numerous gold nanoparticle tags. This is combined with a catalytic enlargement of the multiple gold tags and an ultrasensitive chronopotentiometric stripping analysis of the dissolved gold tags on screen-printed carbon electrodes. Such amplified electrical transduction allows detection of DNA targets down to the 300-amol level.

6.4.1.2 Conductometric Analysis Conductometric biosensing systems are based on the fact that the specific biological interaction occurring on a supporting surface may vary the resistance or conductance of the substrate. A drawback

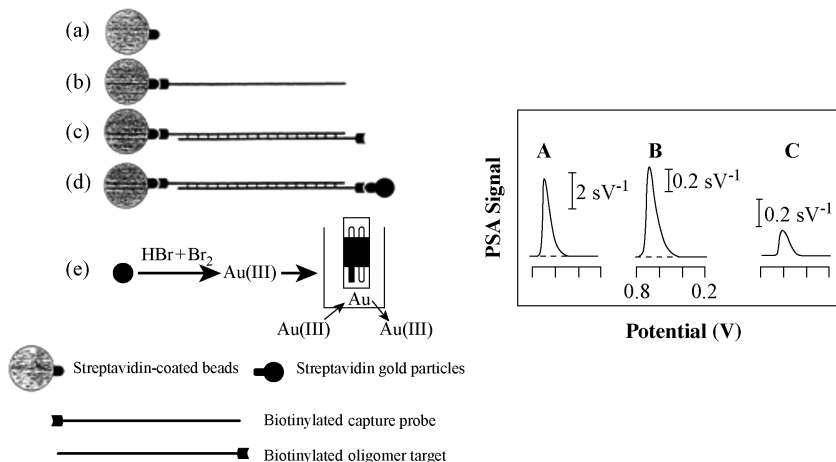


FIGURE 6.3 (Left) Analytical protocol: (a) introduction of streptavidin-coated beads; (b) immobilization of a biotinylated probe onto magnetic beads; (c) addition of biotinylated target—the hybridization event; (d) addition and capture of streptavidin–gold nanoparticles; (e) dissolution of gold tag and PSA detection. (Right) (A) Chronopotentiometric stripping response of $5 \mu\text{L}$ of 10-nm colloidal gold particles (3.45×10^8 particles/mL); gold oxidation time, 3 min; deposition time, 2 min at -0.8 V ; (B) chronopotentiometric stripping response of $100 \text{ ng/mL Au(III)}$, following 1-s (---) and 2-min (—) deposition; (C) chronopotentiometric stripping analysis of 4 ng/mL Au(III) ; 2-min deposition at -0.8 V . Stripping current, $+5.0 \mu\text{A}$. (From ref. 61, with permission.)

associated with conductometric biosensors is that it is difficult to overcome problems with nonspecificity, as the resistance of a solution is determined by the migration of all ions present. Therefore, in a complex matrix such as a biological sample, the high ionic strength of the medium may mask the comparatively small net conductivity change caused by the biointeraction. In this context, metal nanoparticles represent an excellent labeling system able to generate significant resistance changes upon the binding event.

This approach was followed by Mirkin and co-workers in 2002. They developed a conductometric sensor device for DNA analysis immobilizing short “capture” oligonucleotide strands between two fixed microelectrodes (gap $20 \mu\text{m}$). The specific binding occurs with the target oligonucleotide in solution, which also has recognition elements complementary to oligonucleotide-modified AuNPs. The latter, therefore, after the incubation, fill the electrode gaps, varying the conductance. The sensitivity of the device was increased further by means of a catalytic Au-promoted deposition of Ag, with hydroquinone reaching a limit of detection of 0.5 pM of target DNA [65].

6.4.1.3 Voltammetric Analysis Voltammetric techniques certainly represent the most widely used methods in electrochemical analysis, including sensing applications based on metal and semiconductor nanoparticles. This is due to its relatively low cost and the enormous diffusion of the related instruments required for such techniques

in addition to the enhanced sensitivities achieved in the last decades by means of new electrode materials. Solid-state detection of NPs has been used in numerous DNA analysis exploiting the intrinsic electrochemical properties of the metal NPs used as tracers. Wang's group and ours used magnetic particles as a platform to perform the immunological interactions or the DNA hybridization events. After specific interaction with the secondary NP-labeled probe, these magnetic particles were collected onto the electrode surface by means of a permanent magnet either positioned below the screen-printed electrode surface [66–68], or inserted inside the electrode body to detect DNA [69,70] and protein. DPV analyses were performed to quantify the metal NPs collected through the biospecific interaction, and that are related to the target analyte concentration (DNA/protein). Very low limits of detection were achieved using this magnetic particle collection, reaching the lowest value of a 150-pg/mL DNA segment related to the breast cancer gene [66] and 260 pg/mL to the human IgG protein.

Similar approaches were adopted to collect streptavidin-coated beads with an immobilized biotinylated-DNA probe and DNA target by means of a biotin-modified carbon paste electrode. Only after this collection was the specific Au-labeled single-stranded DNA-binding protein (SSB) added. The oxidation of AuNPs was followed by square-wave voltammetry (SWV). This approach allowed the authors to reach a limit of detection of 2.17 pM of target DNA [71].

Related to DNA analysis using AuNPs as labels, an electrochemical DNA detection method was proposed by Authier et al. [72] for the sensitive quantification of an amplified 406-base pair human cytomegalovirus DNA sequence (hCMV DNA). The assay relies on the hybridization of the single-stranded target hCMV DNA with an oligonucleotide-modified AuNP probe, followed by release of the gold metal atoms anchored on the hybrids by oxidative metal dissolution using a 0.1 M HBr solution containing 1×10^{-4} M of Br_2 . Indirect determination of the solubilized gold(III) ions by anodic stripping voltammetry at a sandwich-type screen-printed microband electrode allowing the detection of a 5 pM amplified hCMV DNA fragment has been reported.

6.4.1.4 Impedimetric Analysis Electrochemical impedance spectroscopy (EIS) is a very powerful tool for the analysis of interfacial capacitance and resistance changes occurring at conductive or semiconductive surfaces. A perturbing sinusoidal voltage signal is applied to the electrochemical cell, and the resulting current response is measured. Electrochemical transformations occurring at the electrode–electrolyte interface can be modeled by extracting components of the electronic equivalent circuits that correspond to the experimental impedance spectra [73].

Metal NPs have recently been adopted in impedimetric-based biosensing applications, with the main goal to amplify electrical signals generated by biorecognition events occurring at the electrode surface. AuNPs were used recently by Bonanni et al. in a DNA-sensing device for impedimetric signal amplification. They used streptavidin-coated gold nanoparticles specifically to bind the target biotinylated oligomer after the hybridization event. The probe oligomer was adsorbed onto a graphite–epoxy composite electrode (GECE) surface, and the

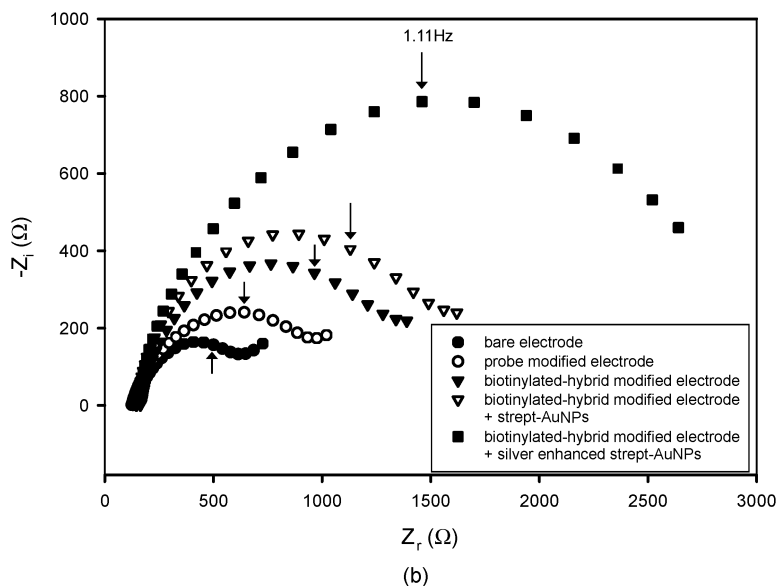
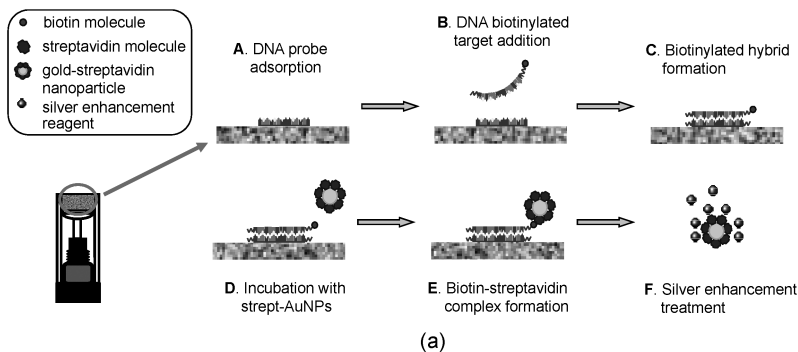


FIGURE 6.4 (a) Analytical protocol; (b) Nyquist diagrams for EIS measurements of: filled circles, bare GEC electrode; open circles, probe-modified electrode; filled triangles, biotinylated-hybrid-modified electrode; open triangles, biotinylated-hybrid-modified electrode + strept-AuNPs; filled squares, biotinylated-hybrid-modified electrode + silver-enhanced strept-AuNPs. All measurements were performed in 0.1 PBS buffer solution containing 10 mM $K_3[Fe(CN)_6]/K_4[Fe(CN)_6]$. The arrow in each spectrum denotes the frequency (ac) of 1.11 Hz. (From ref. 74, with permission.)

impedance measurement was performed in a solution containing the redox marker ferrocyanide/ferricyanide. In their work, a silver enhancement treatment was performed at the end to visualize the hybridization extension on the electrode surface by SEM, offering, moreover, a further signal amplification strategy [74] (Figure 6.4).

The same silver enhancement method has, in fact, been used by Moreno-Hagelsieb et al. to amplify the capacitance signal between interdigitated aluminum electrodes

imprinted over an oxidized silicon wafer. This type of electrode surface reduces the nonspecific precipitation of silver that occurs on conventional noble-metal electrodes. A change in capacitance by a factor of at least 2, using DNA solutions down to 0.2 nM spotted on the electrodes, was observed [75].

6.4.2 Protein Analysis

Immunosensors are affinity ligand-based biosensors in which the immunochemical reaction is coupled to a transducer [76]. These biosensors use antibodies (Abs) as the biospecific sensing element and are based on the ability to form complexes with the corresponding antigen [77]. Immunoassays are among the most specific and sensitive analytical techniques. They provide extremely low detection limits and can be used for a wide range of substances [78]. As research moves into the era of proteomic, such assays become extremely useful for identifying and quantifying proteins. Immunoassays, based on the specific reaction of Abs with the target substances (Ags) to be detected, have been used widely for the measurement of targets of low concentration in clinical biofluid specimen such as urine and blood and for the detection of trace amounts of drugs and chemicals, such as pesticides in biological and environmental samples [79].

The recent development of immunoassay techniques focused in most cases on decreased analysis times, improved assay sensitivity, simplification and automation of the assay procedures, and low-volume analysis. Among types of immunosensors, electrochemical immunosensors are attractive tools and have received considerable attention because they are easy and economical to mass-produce, are robust, and achieve excellent detection limits with small analyte volumes [80,81]. Furthermore, the availability of a variety of new materials with unique properties at nanoscale dimension, such as AuNPs, has attracted widespread attention in their utilization for bioassays, especially for electrochemical detection [82,83]. Different strategies have been employed to amplify the transducing signals of antibody–antigen interactions. Recently, several novel strategies have been proposed to develop electrochemical immunosensors and immunoassays with high sensitivity using AuNPs as labels based on different approaches, depending on the application and the electrochemical technique used [84–86].

6.4.2.1 Potentiometric Analysis Potentiometric measurements involve determination of the potential difference between either an indicator or a reference electrode or two reference electrodes separated by a permselective membrane when there is no significant current flowing between them. Ion-selective electrodes (ISEs) based on thin films or selective membranes as recognition elements for pH, F^- , I^- , CN^- , Na^+ , K^+ , Ca^{2+} , NH_4^+ , Pb^{2+} , Cd^{2+} , Cu^{2+} , etc. or even gases (e.g., CO_2 , NH_3) are the most commonly reported. Recently, some emerging novel possibilities of potentiometric immunosensing based on nanoparticle labeling and ion-selective microelectrodes (ISEs) with very low detection limits were announced. This work indicates that ISEs with improved detection limits may be attractive for the detection of bioassays.

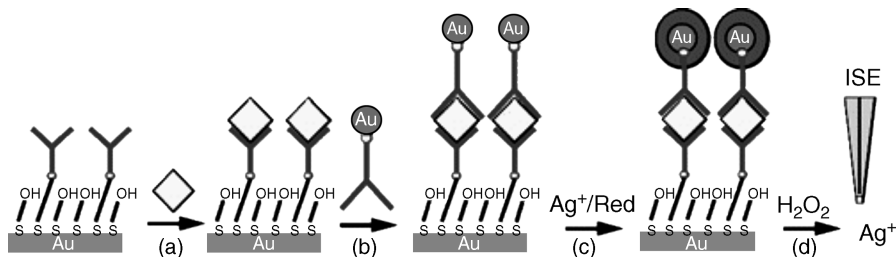


FIGURE 6.5 Potentiometric detection of sandwich immunoassay: (a) antigen addition; (b) capture of gold nanoparticle-labeled anti-mouse IgG antibody; (c) catalytic deposition of silver ions on conjugated Au nanoparticles; (d) silver dissolution and potentiometric detection using a Ag^+ -selective electrode (ISE). (From ref. 87, with permission.)

Bakker's group pioneered the use of potentiometry for ultrasensitive nanoparticle-based detection of protein interactions [87]. In particular, a silver ion-selective electrode (Ag -ISE) was used as an effective transducer for sandwich immunoassays in connection with the capture and silver enlargement of gold nanoparticle tracers (Figure 6.5). This approach may form the basis for highly sensitive bioaffinity assays. An interesting application of these potentiometric biosensors has been reported by Tang et al. [88] for the detection of hepatitis B surface antigen (HBsAg) by self-assembling gold nanoparticles to a thiol-containing sol-gel network. A cleaned gold electrode was first immersed in a hydrolyzed (3-mercaptopropyl)trimethoxysilane sol-gel solution to assemble a three-dimensional silica gel, and then gold nanoparticles were absorbed onto the thiol groups of the sol-gel network. Finally, hepatitis B surface antibody was assembled onto the surface of the gold nanoparticles. The self-assembling procedure was characterized by cyclic voltammetry and electrochemical impedance spectroscopy. Detection is based on the change in potentiometric response in pH 7.4 buffer solution before and after the antigen-antibody reaction. The linear range obtained was from 4 to 960 ng/mL, with a detection limit of 1.9 ng/mL and a lifetime of one month.

6.4.2.2 Conductometric Analysis The use of AuNPs was exploited by Kim et al., who developed a disposable immunochromatographic sensor for on-site quantitative determination of human serum albumin. The conductometric measurement was carried out in a membrane strip sensor based on two interdigitated silver electrodes screen-printed on a nitrocellulose membrane. Twenty-nanometer AuNPs modified with polyaniline (a conducting polymer) were used for signal generation [89]. Velev and Kaler reported a conductive immunosensor using antibody-functionalized latex spheres and a microelectrode gap (Figure 6.6). A sandwich immunoassay led to the binding of a secondary gold-nanoparticle-labeled antibody on latex spheres located in the gap, followed by catalytic deposition of a silver layer "bridging" the two electrodes. Such a formation of conductive paths across interdigitated electrodes led to a measurable conductive signal and enabled ultrasensitive detection of human IgG down to the 0.2 pM level [90]. The method holds promise for creating miniaturized on-chip protein arrays.

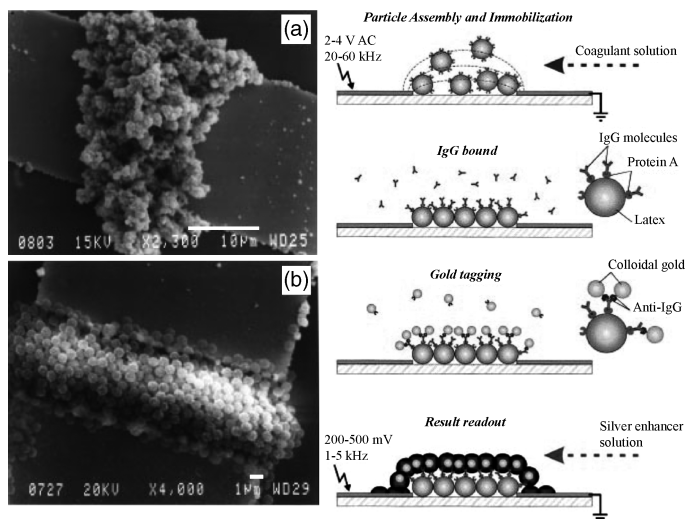


FIGURE 6.6 Main stages of sensor assembly and functioning. The procedure is illustrated by an immunoglobulin test (right). SEM micrographs of gold-tagged and silver-enhanced latex bridges between electrodes in IgG-specific experiments: (a) protein A–functionalized latexes heavily coated by deposited metal that short-circuits the electrodes; (b) nonfunctionalized particles in negative control patches only marginally tagged by deposited metal. The bridge remains nonconductive (left). (From ref. 90, with permission.)

6.4.2.3 Voltammetric Analysis In a pioneering work in the field of NP detection in aqueous medium carried out in 1995, direct stripping solid-state detection of gold nanoparticles (AuNPs) on a carbon paste electrode was performed using both unlabeled and antibody-labeled AuNPs by means of differential pulse anodic stripping voltammetry (DPASV). Detection limits of 1.78×10^{-8} M and 1.38×10^{-8} M for AuNPs and immunogold (antibody-conjugated AuNPs), respectively, were reached [91].

One of the first studies of indirect detection of AuNPs by voltammetric stripping analysis was reported by Dequaire et al. [92]. They developed a sensitive electrochemical immunoassay for immunoglobulin G (IgG) using AuNPs as labels. After an oxidative gold label metal dissolution step in an acidic solution, gold(III) ions were determined indirectly by anodic stripping voltammetry at a single-use carbon-based screen-printed electrode, making it possible to detect IgG at concentration levels of 3×10^{-12} M. The high performance level of the method is related to the sensitive ASV determination of gold(III) at a screen-printed electrode [the detection limit of gold(III) is around 5×10^{-9} M], due to the release of a large number of gold(III) ions from each AuNP anchored on the immunocomplex.

To avoid the acid-dissolution step, Liu and Lin developed an electrochemical magnetic immunosensor based on magnetic beads and gold nanoparticle labels. The captured gold nanoparticles labels on the immunosensor surface were quantified directly by electrochemical stripping analysis. The stripping signal of gold

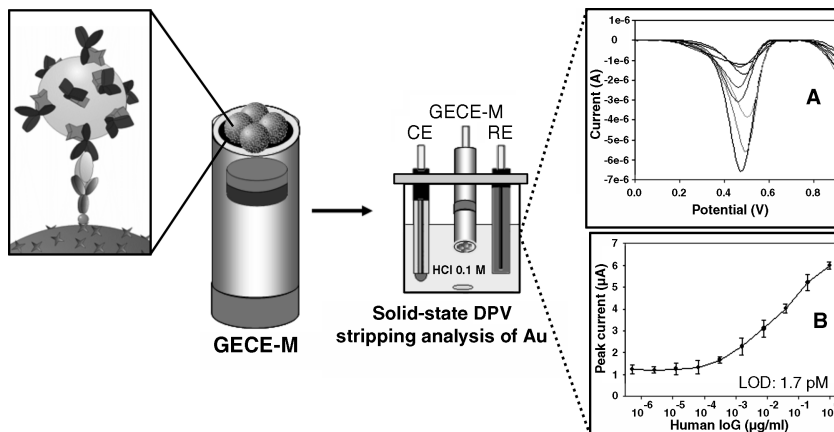


FIGURE 6.7 Electrochemical analysis procedure consisting of the deposition of MB-AuNP immunocomplex sample onto the GECE surface; introduction of the electrode in the measurement cell containing 0.1 M HCl as electrolyte buffer; electrochemical analysis consisting of a preconcentration step at 1.25 V for 150 s, followed by a DP cathodic scan from 1.25 to 0 V, and measurement of the peak current at 0.45 V (step potential 10 mV, amplitude 50 mV, scan rate 33 mV/s vs. Ag/AgCl). (A) Typical DPV curves corresponding to AuNPs analysis for human IgG concentrations of 2.5×10^{-6} , 1.3×10^{-5} , 3.2×10^{-4} , 1.6×10^{-3} , 0.008, 0.04, 0.2, and 1 $\mu\text{g/mL}$; (B) human IgG calibration curve recorded using the DPV analysis of AuNP. (Adapted from ref. 94.)

nanoparticles is related to the concentration of target IgG in the sample solution. A detection limit of 0.02 $\mu\text{g/mL}$ of IgG was obtained under optimum experimental conditions [93].

Ambrosi et al. reported double-codified gold nanolabels for simultaneous electrochemical and optical immunoassays. A built-in-magnet graphite-epoxy-composite electrode allowed a sensibly enhanced adsorption and electrochemical quantification of the specifically captured gold nanoparticle labels on the paramagnetic bead surface (Figure 6.7). The detection limits for this double-codified nanoparticle-based assay were 52 and 260 μg of human IgG/mL for the spectrophotometric (horseradish peroxidase [HRP]-based) and electrochemical (AuNP-based) detections, respectively, much lower than those typically achieved by ELISA tests [94].

The analytical signal in the detection of nanoparticles can be enhanced by catalytic deposition of another metal on the surface of the nanoparticle, followed by the stripping and detection of this metal. An example of this approach was reported by Mao et al. [95]. They developed a novel electrochemical protocol for the quantification of human IgG based on the precipitation of copper on gold nanoparticle tags and subsequent ASV detection of the dissolved copper, obtaining a detection limit of 0.5 ng/mL .

Another catalytic approach was reported by Chu et al. [96] based on the precipitation of silver on AuNPs labels using a silver enhancement solution and chemical reduction of silver ions to silver metal onto the surface of the AuNPs. After silver metal

dissolution in a 0.1 M HNO₃/0.6 M KNO₃ solution, silver ions were determined by anodic stripping voltammetry at a GCE. The method was evaluated for a noncompetitive heterogeneous immunoassay of IgG as a model, achieving a detection limit of 1 ng/mL, which is competitive with colorimetric enzyme linked immunosorbent assay (ELISA). The high performance of the method is attributed to the sensitive ASV determination of silver (I) at a glassy-carbon electrode (detection limit of 5×10^{-9} M) and to the catalytic precipitation of a large amount of silver on the colloidal gold-labeled antibody.

Recently, Mao et al. presented a new method based on cyclic accumulation of gold nanoparticles for detecting human immunoglobulin G (IgG) by ASV. The dissociation reaction between dethiobiotin and avidin in the presence of biotin provides an efficient means for the cyclic accumulation of gold nanoparticles used for the final analytical quantification. The anodic peak current increases gradually with the increasing accumulation cycles. Five cycles of accumulation are sufficient for the assay. The low background of the method proposed is a distinct advantage, providing a possibility for determining at least 0.1 ng/mL human IgG [97].

An electrochemical immunoassay method based on Au nanoparticle-labeled immunocomplex enlargement was reported by Zhou et al.. When the aggregates formed from nano-Au labeled goat/anti-human C-3 and nano-Au-labeled rabbit/anti-goat IgG were immobilized on the electrode surface by the sandwich method (antibody-antigen-aggregate), the electrochemical signal of the electrode was enlarged greatly [98]. The immunosensor reported could quantitatively determine complement C-3 in the range of 0.12, similar to 117.3 ng/mL, and the detection limit was 0.02 ng/mL. Liao and Huang reported an amplified electrochemical immunoassay by autocatalytic deposition of Au³⁺ onto gold nanoparticle labels. By coupling the autocatalytic deposition with square-wave stripping voltammetry, enlarged gold nanoparticles were used as labels on goat/anti-rabbit immunoglobulin G (GaRIgG-Au), and thus the rabbit immunoglobulin G (RIgG) analyte could be determined quantitatively. The detection limit was 0.25 pg/mL (1.6 fM), which is three orders of magnitude lower than that obtained by conventional immunoassay using the same gold nanoparticle labels [99].

Recently, Das et al. reported an ultrasensitive electrochemical immunosensor using the gold nanoparticle labels as electrocatalysts. In this case, the gold nanoparticle labels were attached to the immunosensor surface (indium tin oxide as substrate electrode) by sandwich immunoreaction; signal amplification was achieved by catalytic reduction of *p*-nitrophenol (NP) to *p*-aminophenol (AP) and chemical reduction of *p*-quinone imine to AP by NaBH₄. Such dual-amplification events gave a 1 fg/mL detection limit, and its linear range of measurement ranged from 1 fg/mL to 10 μg/mL, which covered a 10-fold concentration range [100].

6.4.2.4 Impedimetric Analysis The most widely reported use of Au nanoparticles in impedance sensors involves their incorporation into an ensemble substrate onto which a protein, oligonucleotide, or other probe molecule is immobilized. However, recent studies have also described various strategies for the use of impedance sensing that involved Au-nanoparticle conjugation in the solution phase rather

than prior modification of the sensing interface. In one approach, impedance sensing included an extra step of analyte conjugation to 10-nm-diameter Au nanoparticles, with signal amplification occurring only when the Au nanoparticles become embedded in the sensing interface. This approach was demonstrated using the model system fluorescein/antifluorescein, with fluorescein bound to the flat Au substrate using EDC/NHSS linker chemistry. The analyte (goat antifluorescein) was conjugated to Au nanoparticles in solution prior to detection. A change in the impedance at the sensing interface was observed when the antibody was conjugated to Au nanoparticles but not for the bare antibody [101]. Signal amplification was significantly higher with a redox probe (impedance detection) than without a redox probe (capacitance detection).

In biosensors, the use of nanomaterials has been envisioned to create successive amplification steps [102]. This type of approach was recently demonstrated with a different type of solution-phase Au-nanoparticle conjugation, utilizing a strategy that might be termed an impedance-sandwich assay. In this approach, anti-protein A IgG was bound to an Au-electrode surface and then exposed to protein A of varying concentrations. Following protein A binding, the sensing interface was exposed to a solution containing IgG antibodies conjugated to 13-nm-diameter Au nanoparticles. Without this amplification step, the LOD of protein A was reported to be 1 ng/mL, and the LOD was reduced by one order of magnitude by the amplification step. The authors reported that their sensitivity was about 100 times better than that obtained with conventional ELISA tests [103]. One advantage of this approach is that the protein-antibody conjugate can be prepared in advance and stored for about one month without loss of activity. Another group recently reported the use of solution-phase Au-nanoparticle conjugation for amplifying the signal from an impedance biosensor. The sensing interface was an Au electrode onto which Au nanoparticles were attached using 1,6-hexanedithiol, followed by immobilization of rabbit anti-IgG. After binding the hIgG analyte and blocking nonreacted surface sites with bovine serum albumin (BSA), the impedance signal was amplified by binding Au-colloid-labeled goat anti-hIgG that was synthesized in advance [104]. This approach was motivated by the relatively small impedance change sometimes observed upon antigen recognition by a surface-immobilized antibody. Without amplification, the impedance change upon binding of hIgG was about $100 \Omega \cdot \text{cm}^2$, whereas with amplification the impedance change was several thousand $\Omega \cdot \text{cm}^2$. The authors reported an LOD for human IgG of 4.1 ng/L and a linear concentration range of about 15 to 330 ng/L.

6.5 CONCLUSIONS

In this review, some recent advances have been addressed in the synthesis and electrochemical applications of AuNPs, emphasizing their importance as label in affinity electrochemical biosensors. A variety of sensitive bioanalytical detection methods based on the unique electrochemical properties of AuNPs have been developed. The attractive properties of the AuNPs make them a very promising material for the development of different electrochemical biosensors based on the immobilization of biomolecules such as DNA and antibodies. New challenges and

requirements for the design of an ideal electrochemical genosensor or immunosensor include a high-sensitivity, high-specificity protocol that can be carried out in a relatively short time while offering low detection limits.

Improvements using enhancement strategies seem to be a compromise between signal augmentation and reproducibility. Enhancements strategies using precipitation of gold or silver onto AuNPs or the use of AuNPs as carriers of other AuNPs or electroactive labels require careful attention, so as to avoid irreproducibility problems. The electrochemical detection of AuNPs using stripping methods can be improved further. The use of microelectrodes including arrays will probably improve the detection limits, allowing their use in the study of other biomolecular interactions. The potential for detecting single molecule interactions by detecting individual gold colloid labels opens the way to new applications. The electrochemical properties of AuNPs make them extremely easy to detect using simple instrumentation. In addition, these electrochemical properties may allow the design of simple, inexpensive electrochemical detection systems for ultrasensitive molecular diagnostic applications.

Acknowledgments

We wish to acknowledge MEC (Madrid) for projects MAT2008–03079/NAN and Consolider Nanobiomed and the Juan de la Cierva scholarship (A. de la Escosura).

REFERENCES

1. Rao CNR, Cheetham AK. Science and technology of nanomaterials: current status and future prospects. *J. Mater. Chem.* 2001;11:2887–2894.
2. Rashid MH, Bhattacharjee RR, Kotal A, Mandal TK. Synthesis of spongy gold nanocrystals with pronounced catalytic activities. *Langmuir.* 2006;22:7141–7149.
3. Schmid G, Bäumle M, Geerkens M, Heim I, Osemann C, Sawitowski T. Current and future applications of nanoclusters. *Chem. Soc. Rev.* 1999;28:179–191.
4. Daniel MC, Astruc D. Gold nanoparticles: assembly, supramolecular chemistry, quantum-size-related properties, and applications toward biology, catalysis, and nanotechnology. *Chem. Rev.* 2004;104:293–298.
5. Frens G. *Nature (Phys Sci.)* 1973;241:20–25.
6. Ullman A. Formation and structure of self-assembled Monolayers. *Chem. Rev.* 1996;96:1533–1539.
7. Petit C, Lixon P, Pileni M. Synthesis in situ of silver nanocluster in AOT reverse micelles. *J. Phys. Chem. B.* 1993;97:12974–12979.
8. Suslick KS, Fang M, Hyeon T. Sonochemical synthesis of iron colloids. *J. Am. Chem. Soc.* 1996;118:11960–11967.
9. Wang J. Nanomaterial-based electrochemical biosensors. *Analyst.* 2005;130:421–431.
10. Pumera M, Sánchez S, Ichinose I, Tang J. Electrochemical nanobiosensors. *Sens. Actuators B.* 2007;123:1195–1205.
11. Guo S, Wang E. Synthesis and electrochemical applications of gold nanoparticles. *Anal. Chim. Acta.* 2007;598:181–192.

12. Katz E, Willner I. Integrated nanoparticle–biomolecule hybrid systems: synthesis, properties, and applications. *Angew. Chem. Int. Ed.* 2004;43:6042–6094.
13. Wang J. Nanoparticle-based electrochemical DNA detection. *Anal. Chim. Acta.* 2003;500:247–258.
14. Faraday M. Experimental relations to gold (and other metals) to light. *Philos. Trans. R. Soc. London.* 1857;147:145–181.
15. Turkevich J, Stevenson PC, Hiller J. A study of the nucleation and growth processes in the synthesis of colloidal gold. *Discuss. Faraday Soc.* 1951;11:55–75.
16. Kimling J, Maier M, Okenve B, Kotaidis V, Ballot H, Plech A. Turkevich method for gold nanoparticles synthesis revisited. *Phys. Chem. B.* 2006;110:15700–15707.
17. Brown KR, Walter DG, Natan MJ. Seeding of colloidal Au nanoparticle solutions: 2. Improved control of particle size and shape. *Chem. Mater.* 2000;12:306–313.
18. Yu JJ, Lu S, Li JW, Zhao F-Q, Zeng B-Z. Characterization of gold nanoparticles electrochemically deposited on amine-functionalized mesoporous silica films and electrocatalytic oxidation of glucose. *J. Solid State Electrochem.* 2007;11:1211–1219.
19. Lung JK, Huang J-C, Tien D-C, et al. Preparation of gold nanoparticles by arc discharge in water. *J. Alloys Compounds.* 2007;434–435:655–658.
20. Kim K-S, Choi S, Cha J-H, Yeon S-H, Lee H. Facile one-pot synthesis of gold nanoparticles using alcohol ionic liquids. *J. Mater. Chem.* 2006;16:1315–1317.
21. Panda BR, Chattopadhyay A. Synthesis of Au Nanoparticles at “all” pH by H₂O₂ reduction of HAuCl₄. *J. Nanosci. Nanotechnol.* 2007;7:1911–1915.
22. Luo Y, Sun X. Sunlight-driving formation and characterization of size-controlled gold nanoparticles. *J. Nanosci. Nanotechnol.* 2007;7:708–711.
23. Liang Z, Zhang J, Wang L, Song S, Fan C, Li G. A Centrifugation-based method for preparation of gold nanoparticles and its application in Biodetection. *Int. J. Mol. Sci.* 2007;8:526–532.
24. Sinani VA, Podsiadlo P, Lee J, Kotov NA, Kempa K. Gold nanoparticles with stable yellow–green luminescence. *Int. J. Nanotechnol.* 2007;4:239–251.
25. Vasilev K, Zhu T, Glasser G, Knoll W, Kreiter M. Preparation of gold nanoparticles in an aqueous medium using 2-mercaptosuccinic acid as both reduction and capping agent. *J. Nanosci. Nanotechnol.* 2008;8:2062–2068.
26. Love JC, Estroff LA, Kriebel JK, Nuzzo RG, Whitesides GM. Self-assembled monolayers of thiolates on metals as a form of nanotechnology. *Chem. Rev.* 2005;105:1103–1169.
27. Liz-Marzan LM. Nanometals: formation and color. *Mater. Today.* 2004;7:26–31.
28. Ouacha H, Hendrich C, Hubenthal F, Träger G. Laser-assisted growth of gold nanoparticles: shaping and optical characterization. *Appl. Phys. B.* 2005;81:663–668.
29. Miscoria SA, Barrera GD, Rivas GA. Enzymatic biosensor based on carbon paste electrodes modified with gold nanoparticles and polyphenol oxidase. *Electroanalysis.* 2005;17:1578–1582.
30. Dos Santos DS Jr., Álvarez-Puebla RA, Oliveira ON Jr., Aroca RF. Controlling the size and shape of gold nanoparticles in fulvic acid colloidal solutions and their optical characterization using SERS. *J. Mater. Chem.* 2005;15:3045–3049.
31. Alekseeva AV, Bogatyrev VA, Dykman LA, et al. Preparation and optical scattering characterization of gold nanorods and their application to a dot-immunogold assay. *Appl. Opt.* 2005;44:6285–6295.

32. Burda C, Chen X, Narayanan R, El-Sayed MA. Chemistry and properties of nanocrystals of different shapes. *Chem. Rev.* 2005;105:1025–1102.
33. Quinn BM, Liljeroth P, Ruiz V, Laaksonen T, Kontturi K. Electrochemical resolution of 15 oxidation states for monolayer protected gold nanoparticles. *J. Am. Chem. Soc.* 2003;125:6644–6645.
34. Hernández J, Solla-Gullón J, Herrero E. Gold nanoparticles synthesized in a water-in-oil microemulsion: electrochemical characterization and effect of the surface structure on the oxygen reduction reaction. *J. Electroanal. Chem.* 2004;574:185–196.
35. Wang J. *Analytical Electrochemistry*, 3rd ed. Wiley, New York, 2006.
36. Dmitruk N, Barlas T, Dmytruk A, Korovin A, Romanyuk V. Synthesis of 1D regular arrays of gold nanoparticles and modeling of their optical properties. *J. Nanosci. Nanotechnol.* 2008;8:564–571.
37. Chirea M, García-Morales V, Manzanares JA, Pereira C, Gulaboski R, Silva F. Electrochemical characterization of polyelectrolyte/gold nanoparticle multilayers self-assembled on gold electrodes. *J. Phys. Chem. B.* 2005;109:21808–21817.
38. Rayavaraoy RG, Petersen W, Ungureanu C, Post JN, Van Leeuwen TG, Manohar S. Synthesis and bioconjugation of gold nanoparticles as potential molecular probes for light-based imaging techniques. *Int. J. Biomed. Imaging.* 2007;2007:29817–29826.
39. Jiang P, Xie S-S, Yao J-N, Pang S-J, Gao H-J. The stability of self-organized 1-nonanethiol-capped gold nanoparticle monolayer. *J. Phys. D.* 2001;34:2255–2259.
40. Frenkel AI, Nemzer S, Pister I, et al. Size-controlled synthesis and characterization of thiol-stabilized gold nanoparticles. *J. Chem. Phys.* 2005;123:184701–184711.
41. Cárdenas-Triviño G, Segura RA, Reyes-Gasga J. Palladium nanoparticles from solvated atoms—stability and HRTEM characterization. *Colloid. Polym. Sci.* 2004;282:1206–1212.
42. Luo Y, Sun X. Sunlight-driving formation and characterization of size-controlled gold nanoparticles. *J. Nanosci. Nanotechnol.* 2007;7:708–711.
43. Vasilev K, Zhu T, Glasser G, Knoll W, Kreiter M. Preparation of gold nanoparticles in an aqueous medium using 2-mercaptosuccinic acid as both reduction and capping agent. *J. Nanosci. Nanotechnol.* 2008;8:2062–2068.
44. Dmitruk N, Barlas T, Dmytruk A, Korovin A, Romanyuk V. Synthesis of 1D regular arrays of gold nanoparticles and modeling of their optical properties. *J. Nanosci. Nanotechnol.* 2008;8:564–571.
45. Frenkel AI, Nemzer S, Pister I, et al. Size-controlled synthesis and characterization of thiol-stabilized gold nanoparticles. *J. Chem. Phys.* 2005;123:184701.
46. Tannenbaum R, Zubris M, David K, Ciprari D, Jacob K, Jasiuk I, Dan N. FTIR characterization of the reactive interface of cobalt oxide nanoparticles embedded in polymeric matrices. *J. Phys. Chem. B* 2006; 110:2227–2232.
47. Jiang P, Xie S-S, Yao J-N, Pang S-J, Gao H-J. The stability of self-organized 1-nonanethiol-capped gold nanoparticle monolayer. *J. Phys. D.* 2001;34:2255–2259.
48. Merkoçi A, Aldavert M, Tarrasón G, Eritja R, Alegret S. Toward an ICPMS-linked DNA assay based on gold nanoparticles immunconnected through peptide sequences. *Anal. Chem.* 2005;77:6500–6503.
49. Haiss W, Thanh NTK, Aveyard J, Fernig DG. Determination of size and concentration of gold nanoparticles from UV–vis spectra. *Anal. Chem.* 2007;79:4215–4221.

50. Textor M, Kuennemann E, Knoll W. Combined affinity and catalytic biosensor: in situ enzymatic activity monitoring of surface-bound enzymes. *J. Am. Chem. Soc.* 2005;127:13084–13085.
51. Cosnier S. Affinity biosensors based on electropolymerized films. *Electroanalysis.* 2005;17:1701–1715.
52. Xu DK, Xu DW, Yu XB, Liu ZH, He W, Ma ZQ. Label-free electrochemical detection for aptamer-based array electrodes. *Anal. Chem.* 2005;77:5107–5113.
53. Hayden O, Bindeus R, Haderspock C, Mann KJ, Wirl B, Dickert FL. Study on the molecular imprinted polymers with recognition properties towards to dibenzoyl-L-tartaric acid prepared by photo-polymerization method. photo-polymerization conditions. *Sens. Actuators B.* 2003;91:316–319.
54. Rick J, Chou T-C. Using protein templates to direct the formation of thin-film polymer surfaces. *Biosens. Bioelectron.* 2006;22:544–549.
55. Gooding JJ. Electrochemical DNA hybridization biosensors. *Electroanalysis.* 2002;14:1149–1156.
56. Palecek E, Fojta M. Detecting DNA hybridization and damage. *Anal. Chem.* 2001;73:75A.
57. Wang J. Nanomaterial-based electrochemical biosensors, *Analyst.* 2005;130:421–435.
58. Wang J. Electrochemical nucleic acid biosensors *Anal. Chim. Acta.* 2002;469:63–74.
59. Bej AK. *Nucleic Acid Analysis: Principles and Bioapplications.* Wiley-Liss, New York, 1996, pp. 1–29.
60. Castañeda MT, Alegret S, Merkoçi A. Electrochemical sensing of DNA using gold nanoparticles *Electroanalysis.* 2007;19:743–753.
61. Wang J, Xu D, Kawde AN, Polsky R. Metal nanoparticle-based electrochemical stripping potentiometric detection of DNA hybridization. *Anal. Chem.* 2001;73:5576–5581.
62. Wang J, Xu D. Silver-Enhanced colloidal gold electrochemical stripping detection of DNA hybridization. *Langmuir.* 2001;17:5739–5746.
63. Hanaee H, Ghourchian H, Ziaee AA. Nanoparticle-based electrochemical detection of hepatitis B virus using stripping chronopotentiometry. *Anal. Biochem.* 2007; 370:195–200.
64. Kawde AN, Wang J. Amplified electrical transduction of DNA hybridization based on polymeric beads loaded with multiple gold nanoparticle tags. *Electroanalysis.* 2004;16:101–106.
65. Park SJ, Taton TA, Mirkin CA. Array-based electrical detection of DNA with nanoparticle probes. *Science.* 2002;295:1503–1507.
66. Wang J, Xu D, Polsky R. Magnetically-induced solid-state electrochemical detection of DNA hybridization. *J. Am. Chem. Soc.* 2002;124:4208–4216.
67. Wang J, Liu G, Polsky R, Merkoçi A. Electrochemical stripping detection of DNA hybridization based on cadmium sulfide nanoparticle tags. *Electrochem. Commun.* 2002;4:722–728.
68. Liu G, Lin Y. A renewable electrochemical magnetic immunosensor based on gold nanoparticle labels. *J. Nanosci. Nanotechnol.* 2005;5:1060–1067.
69. Castañeda MT, Merkoçi A, Pumera M, Alegret S. Electrochemical genosensors for biomedical applications based on gold nanoparticles. *Biosens. Bioelectron.* 2007; 22:1961–1969.

70. Pumera M, Castañeda MT, Pividori MI, Eritja R, Merkoçi A, Alegret S. Magnetically triggered direct electrochemical detection of DNA hybridization using Au₆₇ quantum dot as electrical tracer. *Langmuir*. 2005;21:9625–9630.
71. Kerman K, Morita Y, Takamura Y, Ozsoz M, Tamiya E. Modification of *Escherichia coli* single-stranded DNA binding protein with gold nanoparticles for electrochemical detection of DNA hybridization. *Anal. Chim. Acta*. 2004;510:169–174.
72. Authier L, Grossiord C, Brossier P, Limoges B. Gold nanoparticle-based quantitative electrochemical detection of amplified human cytomegalovirus DNA using disposable microband electrodes. *Anal. Chem*. 2001;73:4450–4456.
73. Bard AJ, Faulkner LR. *Electrochemical Methods: Fundamentals and Applications*. Wiley, New York, 1980, p. 369.
74. Bonanni A, Esplandiù MJ, del Valle M. Signal amplification for impedimetric genosensing using gold–streptavidin nanoparticles. *Electrochim. Acta*. 2008;53:4022–4029.
75. Moreno-Hagelsieb L, Lobert PE, Pampin R, Bourgeois D, Remacle J, Flandre D. Sensitive DNA electrical detection based on interdigitated Al/Al₂O₃ microelectrodes. *Sens. Actuators B*. 2004;98:269–276.
76. Lippa PB, Sokoll LJ, Chan DW. Immunosensors: principles and applications to clinical chemistry. *Clin. Chim. Acta*. 2001;314:1–26.
77. Chan WCW, Maxwell DJ, Gao XH, Bailey RE, Han MY, Nie SA. Luminescent quantum dots for multiplexed biological detection and imaging. *Curr. Opin. Biotechnol*. 2002;13:40–46.
78. Bakker E, Qin Y. Electrochemical sensors. *Anal. Chem*. 2006;78:3965–3986.
79. Lin J, Ju H. Electrochemical and chemiluminescent immunosensors for tumor markers. *Biosens. Bioelectron*. 2005;20:1461–1469.
80. Warsinke A, Benkert A, Scheller FW. Electrochemical immunoassays. *Fresenius J. Anal. Chem*. 2000;366:622–637.
81. Ghindilis AL, Atanasov P, Wilkinst M, Wilkins E. Immunosensors, electrochemical sensing and other engineering approaches. *Biosens. Bioelectron*. 1998;13:113–118.
82. Wang J. Nanoparticle-based electrochemical bioassays of proteins. *Electroanalysis*. 2007;19:769–783.
83. Wang J. Nanomaterial-based amplified transduction of biomolecular interactions, *Small*. 2005;1:1036–1043.
84. Wang J. Electrochemical biosensors: towards point-of-care cancer diagnostics. *Biosens. Bioelectron*. 2006;21:1887–1898.
85. Luo X, Morrín A, Killard AJ, Smyth MR. Application of nanoparticles in electrochemical sensors and biosensors. *Electroanalysis*. 2006;18:319–329.
86. Katz E, Willner I. Integrated nanoparticle–biomolecule hybrid systems: synthesis, properties, and applications. *Angew. Chem. Int. Ed*. 2004;43:6042–6091.
87. Chumbimuni-Torres YK, Dai Z, Rubinova N, et al. Potentiometric biosensing of proteins with ultrasensitive ion-selective microelectrodes and nanoparticle labels. *J. Am. Chem. Soc*. 2006;128:13676–13681.
88. Tang D, Yuan R, Chai Y, Zhong X, Liu Y, Dai J. Electrochemical detection of hepatitis B surface antigen using colloidal gold nanoparticles modified by a sol–gel network interface. *Clin. Biochem*. 2006;39:309–317.

89. Kim JH, Cho JH, Cha GS, Lee CW, Paek SH. Conductimetric membrane strip immunosensor with polyaniline-bound gold colloids as signal generator. *Biosens. Bioelectron.* 2000;14:907–913.
90. Velev OD, Kaler EW. In situ assembly of colloidal particles into miniaturized biosensors. *Langmuir.* 1999;15:3693–3698.
91. Gonzalez-Garcia MB, Costa-Garcia A. Adsorptive stripping voltammetric behaviour of colloidal gold and immunogold on carbon paste electrode. *Bioelectrochem. Bioenerg.* 1995;38:389–396.
92. Dequaire M, Degrand C, Limoges B. An electrochemical metalloimmunoassay based on a colloidal gold label. *Anal. Chem.* 2000;72:5521–5529.
93. Liu G, Lin Y. A renewable electrochemical magnetic immunosensor based on gold nanoparticle labels. *J. Nanosci. Nanotechnol.* 2005;5:1060.
94. Ambrosi A, Castañeda MT, Killard AJ, Smyth MR, Alegret S, Merkoci A. Double-codified gold nanolabels for enhanced immunoanalysis. *Anal. Chem.* 2007;79:5232–5240.
95. Mao X, Jiang J, Luo Y, Shen G, Yu R. Copper-enhanced gold nanoparticle tags for electrochemical stripping detection of human IgG. *Talanta.* 2007;73:420–427.
96. Chu X, Fu X, Chen K, Shen GL, Yu RQ. An electrochemical stripping metalloimmunoassay based on silver-enhanced gold nanoparticle label. *Biosens. Bioelectron.* 2005;20:1805–1810.
97. Mao X, Jiang JH, Chen JW, Huang Y, Shen GL, Yu RQ. Cyclic accumulation of nanoparticles: a new strategy for electrochemical immunoassay based on the reversible reaction between dethiobiotin and avidin. *Anal. Chim. Acta.* 2006;557:159–163.
98. Zhou G, Li J, Jiang J, Shen G, Yu R. Chronopotentiometry based on nano-Au labeled aggregate enlargement used for the immunoassay of complement C₃. *Acta Chim. Sin.* 2005;63:2093–2099.
99. Liao K, Huang H. Femtomolar immunoassay based on coupling gold nanoparticle enlargement with square wave stripping voltammetry. *Anal. Chim. Acta.* 2005;538:159–167.
100. Das J, Aziz MA, Yang H. A nanocatalyst-based assay for proteins: DNA-free ultrasensitive electrochemical detection using catalytic reduction of *p*-nitrophenol by gold-nanoparticle labels. *J. Am. Chem. Soc.* 2006;128:16022–16030.
101. Wang J, Proffitt JA, Pugia MJ, Suni II. Au nanoparticle conjugation for impedance and capacitance signal amplification in biosensors. *Anal. Chem.* 2006;78:1769–1778.
102. Wang J. Nanomaterial-based amplified transduction of biomolecular interactions. *Small.* 2005;1:1036–1043.
103. Li M, Lin YC, Su KC, Wang YT, Chang TC, Lin HP. A novel real-time immunoassay utilizing an electro-immunosensing microchip and gold nanoparticles for signal enhancement. *Sens. Actuators B.* 2006;117:451–459.
104. Chen H, Jiang JH, Huang Y, et al. An electrochemical impedance immunosensor with signal amplification based on Au-colloid labeled antibody complex. *Sens. Actuators B.* 2006;117:211–219.

Quantum Dots for the Development of Optical Biosensors Based on Fluorescence

W. RUSS ALGAR and ULRICH J. KRULL

Department of Chemical and Physical Sciences, University of Toronto Mississauga, Mississauga, Ontario, Canada

- 7.1 Introduction
 - 7.1.1 Biosensors and bioprobes
 - 7.1.2 Overview of quantum dots
 - 7.1.3 Comparing quantum dots and organic fluorophores
- 7.2 Quantum dots
 - 7.2.1 Materials
 - 7.2.2 Synthesis
- 7.3 Basic photophysics and quantum confinement
 - 7.3.1 Quantum confinement
 - 7.3.2 Surface effects and passivation
- 7.4 Quantum dot surface chemistry and bioconjugation
 - 7.4.1 Ligand exchange
 - 7.4.2 Silica encapsulation
 - 7.4.3 Polymer coatings
- 7.5 Bioanalytical applications of quantum dots as fluorescent labels
 - 7.5.1 Microarrays
 - 7.5.2 Immunoassays
 - 7.5.3 Fluorescence in-situ hybridization
 - 7.5.4 Aptamers
 - 7.5.5 Quenching
 - 7.5.6 Multiplexed applications of quantum dots
- 7.6 Fluorescence resonance energy transfer and quantum dot biosensing
 - 7.6.1 Maltose-binding protein
 - 7.6.2 Nucleic acids
 - 7.6.3 Proteins, proteases, and immunoassays
- 7.7 Summary

7.1 INTRODUCTION

7.1.1 Biosensors and Bioprobes

A biosensor or bioprobe is built on two principal components: a *biorecognition element* and a *transduction element*. The combination of these two components is intended to create a device or assay that will indicate the presence and amount of a certain target analyte(s) in a sample matrix. The basic biosensor concept is shown in Figure 7.1. The biorecognition elements typically provide a selective binding event, or a selective reaction. Examples of the former include nucleic acids and antibodies, while enzymes are the best example of the latter. The transduction element serves as the interface between the analyte and the biorecognition element by converting the binding event or selective reaction into an electrical signal. This may be through an intermediate step such as the generation of luminescence, which is readily detected and processed electronically. This signal can then be analyzed to determine a quantitative value or a qualitative result of some diagnostic significance. The most popular forms of transduction in optical biosensors are fluorescence and surface plasmon resonance. In this chapter we focus on the use of quantum dots (QDs) in the development of optical biosensors based on fluorescence.

In the discussion of any biosensor, there are a number of figures of merit to consider, including selectivity, speed, sensitivity, the limit of detection, dynamic range, reproducibility, precision, accuracy, and reusability. The relative importance of these figures depends on the target application area. While discussing the application of QDs

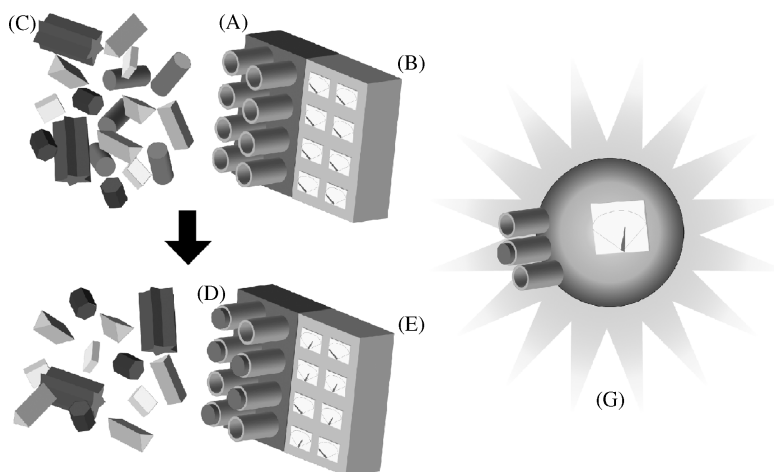


FIGURE 7.1 A biosensor consists of a biorecognition element (A) and transduction element (B), which, in combination, allow a certain analyte to be detected in a complex matrix (C). This usually operates on the basis of a selective interaction (D) and conversion of that binding interaction into a measurable signal (E). QDs are promising for biosensor applications because they act as both transduction elements and interfaces for biorecognition elements (G).

in fluorescence-based biosensing in this chapter, the examples presented will often be evaluated in terms of these criteria. One final distinction will be made, that between a biosensor and a bioprobe. The former is, by definition, reusable, whereas the latter is not. In this chapter it will be seen that QDs can play a role in determining these figures of merit for a biosensor or bioprobe. Furthermore, the use of QDs may be advantageous in one respect and disadvantageous in another. The biosensor field remains of great interest. A challenge is that no single device constructed to date has optimally satisfied the criteria above. QDs have attracted the attention of biosensor researchers because they have the potential to move fluorescence biosensor technology closer to this ultimate goal. QDs can act as both transduction elements and interfaces for bio-recognition elements via conjugation with biomolecules.

7.1.2 Overview of Quantum Dots

QDs, or colloidal semiconductor nanocrystals, have come to the forefront of popular science since the turn of the century and show no signs of receding into a particular niche of research. With perhaps the exception of carbon nanotubes, QDs are the most prolific of contemporary nanomaterials. These nanoparticles are no longer the curious treasures of solid-state physics and materials science, but have matured into bona fide tools that are being used across physics, chemistry, and biology. Interest in QDs ranges from luminescent probes for biomedical imaging [1–7], to luminescent probes for both biosensor [8,9] and chemosensor [10,11] applications, as well as to new materials for lasers and other optoelectronic devices [12,13] or quantum computing [14].

From an optical perspective, QDs are special in that they exhibit size-tunable absorption and luminescence spectra arising from *quantum confinement* effects. Quantum confinement results in an electronic structure for a QD that lies between the bulk and molecular-size scales. They are semiconductor crystals with dimensions on the order of a few nanometers and consisting of 10^3 to 10^4 atoms, depending on their size. To give a sense of scale, the size of a QD is illustrated schematically in Figure 7.2. Traditionally, QDs have been composed of binary systems such as CdS and CdSe. However, primary QDs based on silicon [15,16] have been developed, as have ternary systems such as CdSeTe [17], ZnCdSe [18], or ZnCdS [19,20]. In this chapter we focus on II–VI semiconductors such as CdS, CdSe, and CdTe. This class of QDs has found the most widespread use in bioanalytical applications.

In QDs, it can be argued that the traditional conduction- and valence-band structures used to describe bulk semiconductors can be reduced to two regions of potentially dense, but discrete, electronic states. These states are sometimes referred to as *quantum-confined orbitals*. A bandgap is still considered to exist; however, quantum confinement alters the energetics of the bandgap, and the system takes on “particle-in-a-box” character. The result is a luminescent nanomaterial that has a number of advantages over conventional organic fluorophores, including those such as fluorescein or the cyanine dyes widely used in fluorescence-based biosensor and bioprobe designs.

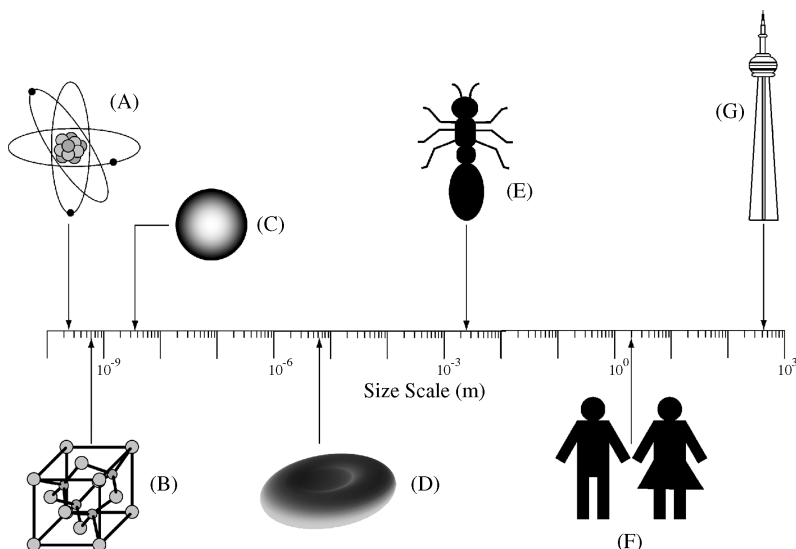


FIGURE 7.2 Comparison of the relative size scales for a variety of objects: (A) a cadmium atom; (B) a zinc blende unit cell; (C) a QD; (D) a red blood cell; (E) an ant; (F) people; (G) the CN Tower in Toronto.

7.1.3 Comparing Quantum Dots and Organic Fluorophores

Fluorescence-based diagnostic technology is widely recognized as being very sensitive and extremely versatile. The versatility and wide applicability of fluorescence results from the relative ease with which multiple colors can be used to perform a multiplexed analysis, the array of experimental methodologies available, and the wealth of information that can be obtained from such experiments. Common methodologies include conventional solution-phase spectrofluorimetry, epifluorescence and confocal imaging, total internal reflection techniques, time-resolved and polarization-based measurements, nonlinear and multiphoton methods, and single-molecule spectroscopy. These techniques may yield information on parameters such as analyte concentration, local environment, dynamics, or intermolecular interactions from measurements such as steady-state intensities, fluorescence lifetimes, anisotropy, resonance energy transfer, or quenching effects. In terms of many of these techniques and observables, QDs are arguably superior to conventional organic fluorophores as reporters and provide much of the same information. It has become apparent that QD-based methods have the potential to further enhance the sensitivity and versatility of fluorescence-based diagnostics.

Although immensely useful, organic fluorophores suffer from a variety of shortcomings, including relatively narrow and weak absorption spectra, broad red-tailed photoluminescence (PL) spectra, high susceptibility to photobleaching,

pH sensitivity, susceptibility to chemical degradation, and short fluorescence lifetimes (typically, nanoseconds). In addition, organic fluorophores are not optimally suited to multiplexed experiments. In a multiplexed experiment, the aim is to excite and observe the PL simultaneously from multiple fluorophores. Given the broad red-tailed PL and relatively small Stokes shift (ca. 10 to 40 nm) of most organic fluorophores, spectral overlap between fluorophores often occurs and results in crosstalk between detection channels. To avoid crosstalk, it is necessary to work with dyes that are spectrally well separated. However, the relatively narrow range over which an organic fluorophore shows strong absorption means that a separate source is required to excite each fluorophore efficiently. In addition, the potentially rapid photobleaching of dyes makes them less than ideal for sensor technology. The result of photobleaching is drift in a single measurement or a loss of signal over many cycles of measurement. Finally, spectrally shifting the absorption and PL spectra of an organic fluorophore strictly requires the synthesis of a new molecule, although series of dyes with related structures can be made to span the visible spectra. For example, the cyanine dyes (Cy2, Cy3, Cy3B, Cy3.5, Cy5, Cy5.5, Cy7) are comprised of closely related compounds.

In contrast to organic fluorophores, QDs exhibit strong broad absorption spectra, narrow and symmetric PL spectra (full width at half maximum ca. 25 to 40 nm), chemical stability, superior resistance to photobleaching, and longer-lived PL (typically tens of nanoseconds) [1,3,4,6]. The peak PL wavelength of QDs is determined by their size, with PL shifting from red to blue with decreasing size. To a first approximation, QDs absorb light at any wavelength shorter than their peak PL wavelength, with a rapidly increasing absorption coefficient at shorter wavelengths. As a consequence, many QDs with different emission wavelengths can be excited simultaneously at a single wavelength in the blue or ultraviolet region of the spectrum, potentially creating a Stokes shift on the order of 100 to 300 nm. The absorption and PL spectra of common organic fluorophores, Cy3 and AlexaFluor 647, are compared in Figure 7.3 with those of commercially available QDs. From the perspective of multiplexing, the unique spectral properties of QDs are highly advantageous. These nanoparticles also offer better or comparable brightness to organic fluorophores, photostability, and low reactivity, all of which are ideal for sensor technology. In addition, the synthetic protocol for preparing QDs with different emission wavelengths is essentially identical, with reaction time generally being the synthetic variable rather than the position and nature of bonds.

Despite all their advantages, QDs have a number of shortcomings. For example, the inorganic nature of QDs renders them inherently insoluble in aqueous media. QDs made from II–VI semiconductors are by far the most common, and their heavy metal components—usually, cadmium or lead—are highly toxic. Considerable effort has been expended in creating water-soluble QDs for biological applications, which include cytometry, immunoassays, hybridization assays, and other bioassays. In addition, QDs are much larger than organic fluorophores in size, with crystal sizes on the order of 2 to 6 nm and surface chemistry that may contribute several more

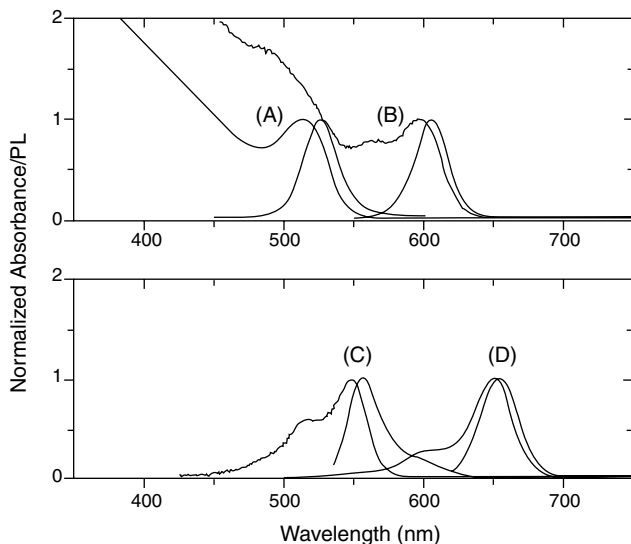


FIGURE 7.3 Comparison between the absorption and PL spectra of (A) 2.1-nm core size CdSe–ZnS QD; (B) 5.2-nm core size CdSe–ZnS QD; (C) Cy3; (D) AlexaFluor 647.

nanometers to their size, leading potentially to hydrodynamic radii on the order of 10–15 nm [21]. A schematic of the sizes of a variety of commonly used luminescent probes and biomolecules relative to a QD is shown in Figure 7.4. Perturbation of the structure or function of biomolecules must be a consideration in biosensor design,

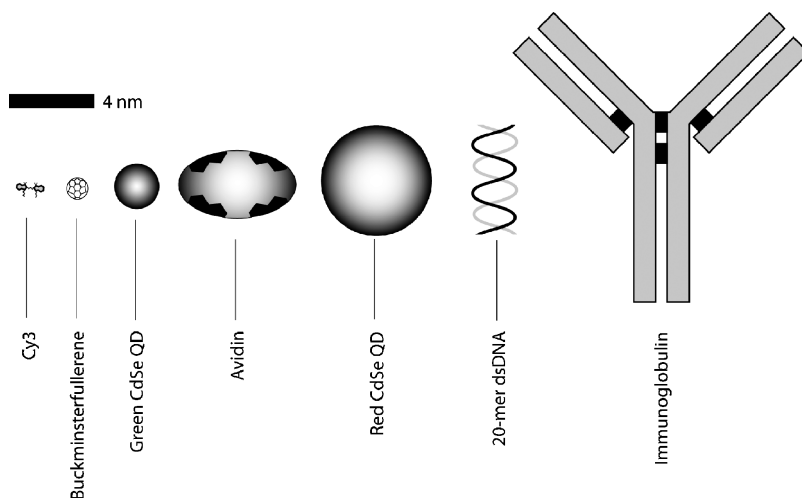


FIGURE 7.4 Comparison of the relative sizes of green- and red-emitting CdSe QDs with a number of molecules relevant to biosensor and bioprobe applications: Cy3, a typical fluorescent label; avidin, which is used to conjugate biotinylated biomolecules; a typical oligonucleotide probe–target hybrid; and an antibody. Buckminsterfullerene is also shown for reference.

particularly since biomolecules such as antibodies, enzymes, and aptamers are dependent on their structure for function. Finally, QDs are known to exhibit blinking under continuous excitation, where their luminescence is observed to turn on and off in time [1,5,22]. Nonetheless, in many applications the advantages of QDs outweigh the disadvantages and justify the time and effort put into overcoming or avoiding these challenges.

7.2 QUANTUM DOTS

7.2.1 Materials

QDs can be classified into two structural types: core nanocrystals and core–shell nanocrystals. The former are less common in practical application, and are composed of a single semiconductor material. The latter are core nanocrystals surrounded by a shell of a few atomic layers of a higher-band-gap semiconductor. Figure 7.5 shows the two structures schematically. As will be described in more detail in Section 7.3.2, the shell greatly improves the PL quantum yield and stability of the core nanocrystal. Regardless of a core or core–shell structure, it is the size of the core nanocrystal which determines the emission wavelength of the QD. However, the wavelength range over which the PL can be tuned is a function of the bandgap energy of the semiconductor material. Thus, different semiconductor cores are used to generate PL in different regions of the spectrum. As shown in Figure 7.6, cadmium sulfide (CdS) is used to generate ultraviolet and blue emission, cadmium selenide (CdSe) is used to span most of the visible spectrum, cadmium telluride (CdTe) is well suited for the red

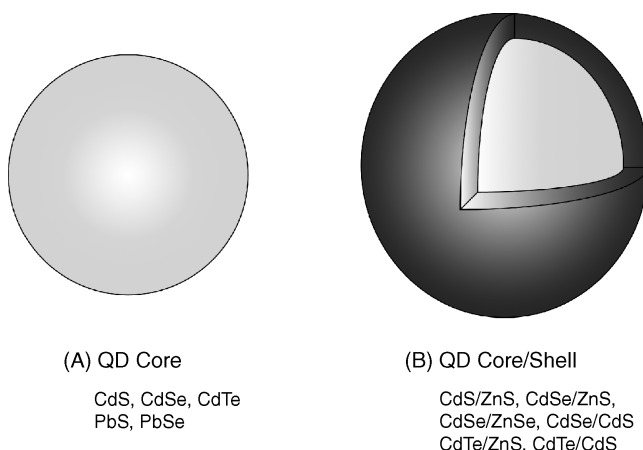


FIGURE 7.5 (A) Core and (B) core–shell structures for QDs. Core–shell structures consist of core nanocrystals surrounded by a thin layer of higher-bandgap material. Some common materials are listed for both structures. In general, the shell structure greatly improves the PL properties of the core.

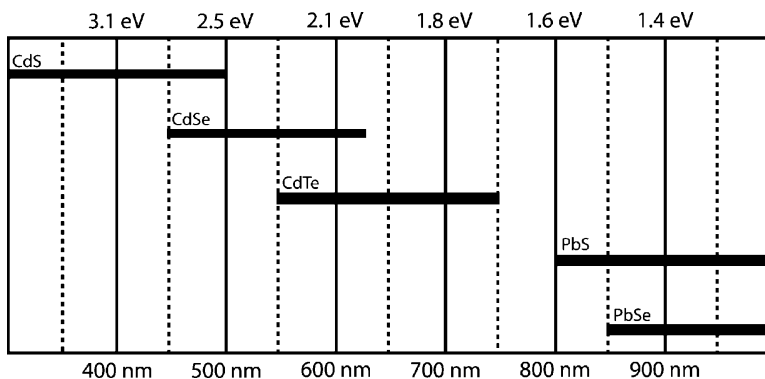


FIGURE 7.6 Approximate size-tunable PL ranges for a variety of QD materials. The wavelength ranges are estimates based on experimental and theoretical results throughout the literature.

and near-infrared region, and lead sulfide (PbS) and lead selenide (PbSe) have been used to create cores that emit in the infrared.

7.2.2 Synthesis

Colloidal QDs are typically synthesized by pyrolysis of organometallic and chalcogen precursors, where rapid nucleation followed by slower and steady growth is desired [23–26]. A typical protocol would involve heating tri-*n*-octylphosphine oxide (TOPO) to a high temperature under an inert gas such as argon or nitrogen, injecting a hot solution containing the precursors to initiate rapid homogeneous nucleation, removing the heat to quickly lower the temperature of the reaction mixture, and letting the crystal growth continue for some time at a lower temperature. For the synthesis of cadmium selenide QDs, dimethyl cadmium (Me_2Cd) and either trioctylphosphine selenide (TOPSe) or bis(trimethylsilyl)selenium [$(\text{TMS})_2\text{Se}$] are typically used as precursors. TOPSe can be prepared by dissolving selenium shot (pellets) in TOP and is preferred due to its greater stability and ease of preparation [26]. For nucleation, the mixture is injected into TOPO at about $>300^\circ\text{C}$, while temperatures in the range 250 to 300°C are typically used for subsequent crystal growth via an Ostwald ripening-type process. Synthesis of cadmium telluride QDs is carried out similarly, using tellurium shot dissolved in TOP (TOPTe) or bis(*tert*-butyldimethylsilyl)tellurium [$(\text{BDMS})_2\text{Te}$] as the chalcogen precursor. However, injection and growth temperatures tend to be lower, around 250°C and 150 to 200°C , respectively. The growth is monitored by measuring absorption spectra of aliquots taken from the reaction mixture at various times. Although organometallic reagents such as Me_2Cd predominate the synthetic literature, their air sensitivity and pyrophoric nature are cause for concern. As a safer alternative, cadmium oxide (CdO) has been shown to be an effective precursor in CdSe and CdTe QD synthesis [27–29]. The role of the organic ligands TOP and TOPO is to coordinate to the Cd centers through the P: and P = O functions,

stabilizing particle growth and preventing aggregation. The ligands also provide a degree of electronic passivation [27]. The TOPO/TOP-capped nanocrystals disperse in nonpolar solvents such as toluene, chloroform, and hexanes.

In many applications, QDs are fabricated as core-shell structures, where, for example, a CdSe or CdTe nanocrystal is enclosed in a few layers of a second semiconductor. Typical shell materials include zinc sulfide for CdSe-ZnS core-shell QDs and cadmium sulfide for CdTe-CdS core-shell QDs. Shell synthesis is carried out analogously to core synthesis, slowly adding a solution of bis(trimethylsilyl)sulfide [(TMS)₂S] and either TOPCd or dimethyl/diethyl zinc (Me₂Zn/Et₂Zn) to the core nanocrystals in TOPO. The temperature for the shell growth is usually in the range 100 to 150°C, although it has been reported that different temperatures are optimal for QDs of different sizes [24].

Although organometallic and chalcogen precursor pyrolysis is the classic and most widely used approach to QD synthesis, a number of other methodologies have been used to prepare QDs for photoelectrochemical applications. Many of these methods employ aqueous solvent and water-soluble metal precursors such as Cd(NO₃)₂, Cd(ClO₄)₂, CdCl₂, ZnCl₂, Zn(ClO₄)₂, Pb(NO₃)₂, or PbCl₂. Chalcogen precursors have included Na₂S or gaseous H₂S. Typically, a solution of the metal precursor is bubbled with nitrogen and titrated with a solution of the chalcogen precursor to produce colloidal solids. Particle growth is arrested at the nanometer scale by the use of ligands such as mercaptoacetic acid (MAA) [30,31] or poly(vinylpyrrolidone) (PVP) [32]. Much like TOPO, these ligands coordinate to the surface of the QDs, rendering them water soluble and stabilizing them against aggregation. A variation on the typical arrested precipitation method makes use of a biphasic mixture to produce QDs [33,34]. In this method, an aqueous solution of the metal precursor is shaken vigorously with a solution of octadecanethiol in petroleum ether. The mixture is then stirred while H₂S is bubbled through the solution. QDs are collected from the organic phase.

Another popular method of producing QDs for electrochemical experiments is through a microemulsion method employing *n*-heptane and bis(2-ethylhexyl)sulfosuccinate (AOT) [35–39]. The water-to-surfactant ratio is used to control the QD size by altering the size of the AOT reverse micelles [37]. The emulsion is divided into two volumes, where the metal precursor, Cd(NO₃)₂, is dissolved in one subvolume and the chalcogen precursor, Na₂S, is dissolved in the other subvolume. Each subvolume is stirred for 1 hour prior to mixing the two together and stirring for another hour. A shell can be grown around the synthesized core nanocrystal by injecting micellar solutions of zinc and sulfur salts alternately [36]. Cysteamine and mercaptoethane sulfonate can then be added as capping agents. The former is useful for bioconjugation, while the latter imparts aqueous solubility.

7.3 BASIC PHOTOPHYSICS AND QUANTUM CONFINEMENT

This section serves as a basic primer to the photophysics of QDs, dealing primarily with quantum confinement and surface effects. Quantum confinement effects yield the

unique optical properties of QDs, while the nature of the QD surface can profoundly affect the optical behavior of QDs. For an extensive treatment of semiconductor QDs and their photophysical properties, the reader is referred to the work of Yoffe [40].

7.3.1 Quantum Confinement

7.3.1.1 Bandgap Energies In a bulk semiconductor, the absorption of light results in the promotion of an electron in the valence band across the bandgap and into the conduction band, creating a loosely bound electron–hole pair or Wannier–Mott exciton [41,42] (Figure 7.7). Each band is centered about atomic energy levels with a width proportional to the magnitude of nearest-neighbor interactions. In semiconductors, the Fermi level essentially lies between the two bands, yielding optical behavior which is dominated by the edges of the bands [43,44]. In a bulk semiconductor, the energy of the bandgap may be relatively small, where, for example, bulk CdSe has a bandgap energy of 1.7 eV [3]. However, shrinking the size of a semiconductor particle down to roughly less than 10^4 atoms results in quantum-confinement effects, which for CdSe can shift the bandgap between 1.9 and 2.8 eV as

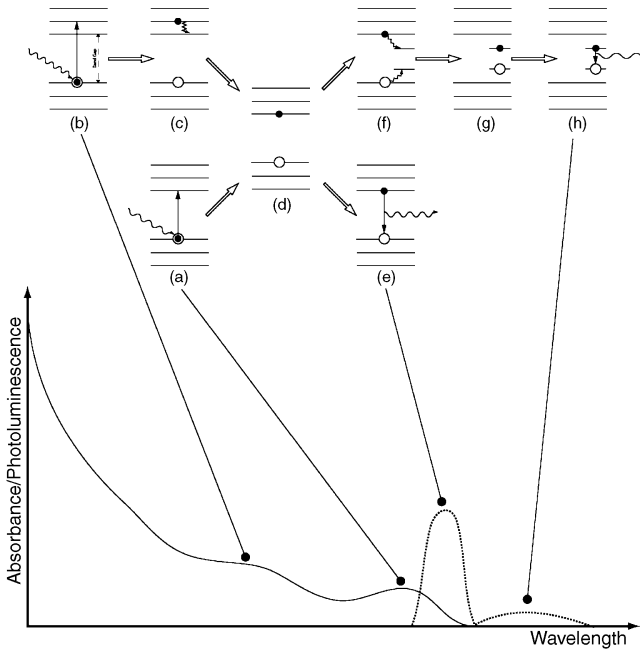


FIGURE 7.7 Absorption of a photon (a, b) promotes an electron across the bandgap to create an exciton. Such transitions yield peaks in the absorption spectrum. Subsequent nonradiative relaxation occurs at the bottom of the conduction band (c). Three processes are possible from (d): (1) Radiative recombination of the exciton (e) to the ground state yield band-edge luminescence; (2) trap states (f) in the bandgap can capture the exciton (g) and lead to bandgap luminescence (h); and (3) nonradiative recombination of the exciton can also occur (not shown).

particle size is decreased from approximately 6 nm to 2 nm [3,24,43]. Similarly, the CdS bandgap can be tuned between 2.5 and 4 eV [44], compared to a bulk bandgap of 2.4 eV [45]. Therefore, a decrease in the size of QDs results in a hypsochromic shift of the absorption and PL spectra by increasing the bandgap energy. Although absorption is significant at photon energies exceeding the bandgap energy, the PL is narrow because emission tends to occur from the bottom of the conduction band and is therefore fixed by the bandgap energy. This is essentially analogous to Kasha's law for molecular fluorescence, where emission is observed from the lowest vibrational level of the first excited singlet state. While QD PL has a natural line width, the major contribution to the full width at half maximum tends to be the size polydispersity of the QDs in the colloidal sample.

Quantum-confinement effects become significant when the nanocrystal dimensions are less than the exciton Bohr radius for the semiconductor. The exciton Bohr radius is analogous to its hydrogenic atom counterpart, and describes the preferred hole–electron separation. In CdS, this distance is roughly 5 to 6 nm [41], and particles of this size represent the onset of the transition from the bulk to quantum-confinement regimes. Exciton Bohr radii in other semiconductor materials tend to be of similar size. One may consider the increasing bandgap with decreasing particle size as the energy cost of confining the exciton to dimensions less than its Bohr radius. However, a more elucidating view is that of the particle in a box, where the exciton is confined by a potential corresponding to the dimensions of the nanocrystal. The energy of a particle confined by a one-dimensional “box” of infinite potential is defined by elementary quantum mechanics as

$$E = \frac{n^2 \hbar^2}{8mL^2} = \frac{k^2 \hbar^2}{2m} \quad (7.1)$$

where n is the quantum number, L is the dimension of the box, and m is the mass of the particle. From this relationship one finds that the spacing between energy levels for the particle in a box increases as the box dimension decreases (Figure 7.8). The same phenomenon is observed with QDs, yielding larger bandgap energy as the dimensions of the QD decrease. Thus, the quantum-confinement effect is a consequence of changes in the density of electronic states.

The particle-in-a-box description of the bandgap energy in QDs was first evaluated by Brus in 1984, considering a Wannier–Mott exciton, an effective mass approximation for the kinetic energy, a hydrogenic Hamiltonian, and particle-in-a-sphere basis wavefunctions [41,45,46]. The oft-cited result is

$$E_{\text{QD}}(R) - E_B = \frac{\hbar^2 \pi^2}{2R^2} \left(\frac{1}{m_e} + \frac{1}{m_h} \right) - 1.786 \frac{e^2}{\epsilon R} - 0.248 E_{\text{Ry}}^* \quad (7.2)$$

where E_B is the bulk semiconductor bandgap energy, E_{QD} is the bandgap energy in a QD of radius R , m_e and m_h are the effective masses of the electron and hole, ϵ is the semiconductor dielectric constant, and E_{Ry}^* is the Rydberg energy for the electron–hole pair.

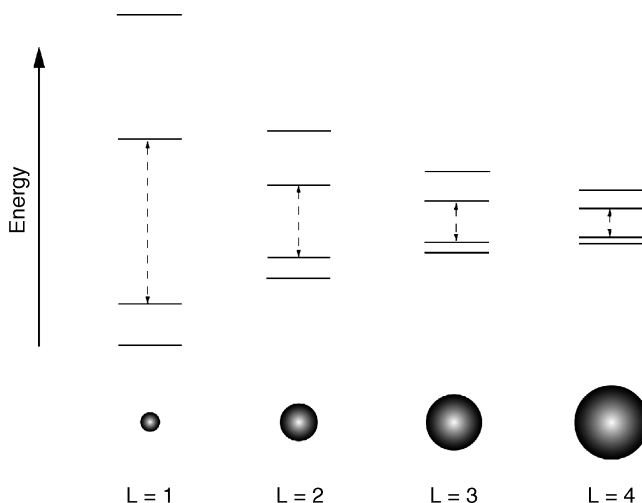


FIGURE 7.8 Energy-level diagrams for a particle-in-a-box model of the change in the density of electronic states and bandgap energy. The bandgap has been modeled by the omission of the intermediate energy level.

The first term in equation (7.2) is readily seen to be the energy corresponding to a particle in a sphere, while the second term is the Coulomb energy between the electron and hole. The electron and hole are loosely bound and thus tend to reside near one another to maximize their coulombic attraction. However, semiconductor dielectric constants are large and screening is significant, resulting in an additional tendency for the electron and hole to reside near the center of the sphere to maximize dielectric stabilization. The spatial correlation is considered in the third term and is generally small compared to the first term, which dominates the overall energy change.

Although the particle-in-a-box model works reasonably well at the upper limit of quantum confinement behavior, it breaks down with QDs of small or even moderate dimensions. This is a result of a breakdown in the effective mass approximation. At smaller dimensions, energy does not scale in proportion to k^2 or, equivalently, in proportion to $1/L^2$ [41,44]. A model that has achieved significant quantitative success is the empirical tight-binding approach, which uses a framework of linear combinations of atomic and molecular orbitals [47,48], but is beyond the scope of this discussion.

7.3.1.2 Oscillator Strength While the particle-in-a-box analogy is sufficient to explain the change in bandgap with crystal size, it does not a priori explain the giant oscillator strength effect observed with QDs. The oscillator strength is a measure of the intensity of an electronic transition (i.e., the magnitude of an optical absorption band). In contrast to QDs which show a few intense transitions, bulk semiconductors do not show a strong exciton absorption band [41,44]. This can be explained by considering the Heisenberg uncertainty principle, $\Delta x \Delta p \geq \hbar/2$, where Δx and Δp represent the uncertainty in a particle's position and momentum, respectively [43,44]. Note that

equation (7.1) also gives the particle-in-a-box energy expression in terms of the particle wave number, k , which from the de Broglie relationship is related to particle momentum as $k = p/\hbar$. Thus, (7.1) also relates the particle energy to its momentum. As the QD decreases in size, the spatial confinement of the exciton wavefunction increases and, according to the uncertainty principle, the uncertainty in the exciton momentum must increase. The energy of the particle in this system is really the superposition of a number of states with different momentum or k [44]. In general, for an optical transition to occur in a lattice, the wavelength of the incident light, λ , must satisfy $K = 2\pi/\lambda$, where K is the vector sum of k -states for the electron and hole. Given the energy–momentum relationship and the increased uncertainty in momentum, it is seen that a series of closely spaced k -states may now satisfy this condition, increasing the probability of a direct transition. Thus, many transitions in a bulk semiconductor are compressed by quantum confinement into a single intense transition in a quantum dot [43,44].

7.3.2 Surface Effects and Passivation

As nanocrystals become smaller, a larger fraction of their constituent atoms are found at the surface. For example, a 5-nm CdS nanocrystal has approximately 15% of its atoms at the surface [41]. In contrast, a 1- μm crystallite would have less than 0.1% of its atoms at the surface. One of the failings of the particle-in-a-box model presented in the preceding section is that it does not consider the surface of the QD. In reality, and in contrast to the ideal box, the surface of a QD is not an infinite potential barrier, and the exciton wavefunction can sample the surrounding medium [41]. Furthermore, the chemical potential at the surface is significantly different from the interior of the QD, due to dangling bonds, reconstructions of the crystal, and possible adsorbates [44,45]. As a consequence, a number of surface states exist that can mix with the interior states, potentially altering the overall energy-level spacing and even introducing states in the energetically forbidden bandgap [43,44]. The defects and imperfections that yield these surface states are widely recognized as traps that confine and promote nonradiative recombination of the electron–hole pair.

The solution to this problem is to enclose the core nanocrystal in an outer shell of semiconductor with a larger bandgap energy. Ideally, this has the effect of confining the exciton to the interior core and preventing exposure to the surrounding medium, thus preventing traps due to surface defects and reactivity from capturing the excited-state energy and providing nonradiative pathways [3,45,49]. The quantum yield is greatly enhanced by capping, potentially approaching an order-of-magnitude improvement [3,25]. The most widespread example of such core–shell structures are CdSe–ZnS quantum dots, although other common capping materials include CdS and ZnSe. As mentioned above, the capping material should be of larger bandgap energy, but also be optically transparent, nonemissive, and structurally related to the core material. By smoothly transitioning growth of the nanocrystal from the core material into the shell material, surface reconstructions of the core are largely avoided and energy levels in the bandgap are eliminated [43,44]. Thus, there is ideally no strain at the surface of the core and only a sudden change in chemical potential [43,44].

7.4 QUANTUM DOT SURFACE CHEMISTRY AND BIOCONJUGATION

In most cases, newly synthesized QDs are soluble in organic solvents and are insoluble in aqueous systems, severely limiting their potential application in biosensors and bioprobes. Therefore, surface modification of QDs is usually required for aqueous solubility and bioconjugation. A variety of strategies have been used; however, amphiphilic or bifunctional molecules are common to all approaches. Ligand exchange, silica coatings, or polymer coatings are the most widely adopted chemistries.

7.4.1 Ligand Exchange

7.4.1.1 Thiol Ligands One of the most widespread approaches to creating water-soluble QDs is ligand exchange with thioalkyl acids such as mercaptoacetic acid (MAA), mercaptopropionic acid (MPA), or mercaptoundecanoic acid (MUA). A number of thiol-based ligands are shown in Figure 7.9. In their thiolate forms, RS^- , these molecules coordinate strongly with the metal ions on the exterior of QDs (e.g., Cd^{2+} , Zn^{2+} , Pb^{2+}), thus exposing the polar and potentially charged carboxylic acid group to the surrounding solution and imparting aqueous solubility. Most procedures for ligand exchange using a thiol-based ligand involve incubating the QDs (usually coated with TOPO ligands) in a solution containing an excess of the thiol ligand of interest. In general, it seems that these preparations are stable over periods ranging from weeks to months. At sufficiently basic pH, the carboxylic acid groups are negatively charged and electrostatic repulsion helps maintain the dispersion of the QDs in aqueous media. However, at acidic pH values or in solutions of high ionic strength, there is a greater tendency for aggregation due to the neutrality of the carboxylic acid groups or decreased Debye length surrounding the QDs, respectively. Our research has shown that more acidic thioalkyl acid ligands yield QDs that are more resistant to aggregation at low pH [50]. For example, mercaptosuccinic acid (MSA)-capped QDs aggregate and precipitate more slowly than MAA-capped QDs. In turn, dihydrolipoic acid (DHLA)-capped QDs are less stable than MAA QDs. The trend correlates with the pK_a of these ligands and the charge density expected on the surface of the QD.

Instability can also be generated by desorption of the thioalkyl acid ligands from the surface of the QD with time. It has been reported that preparations which use bidentate thioalkyl acids such as DHLA increase the shelf life of the preparations to periods ranging from several months to a year [51]. Multidentate ligands have also been created by cross-linking a layer of monodentate ligands. For example, MUA can be cross-linked with lysine or diaminopimelic acid to form a more robust carboxylic acid capping [52].

More rapid desorption of thioalkyl acid ligands can occur at pH values below 5, where it has been reported that the thiolate moiety is converted back to a thiol moiety [53]. Although the process was found to be reversible, there was significant hysteresis in the process.

The pH at which dispersion and redispersion occurred was significantly higher than the pH at which precipitation occurred. The former appears to be solely dependent on

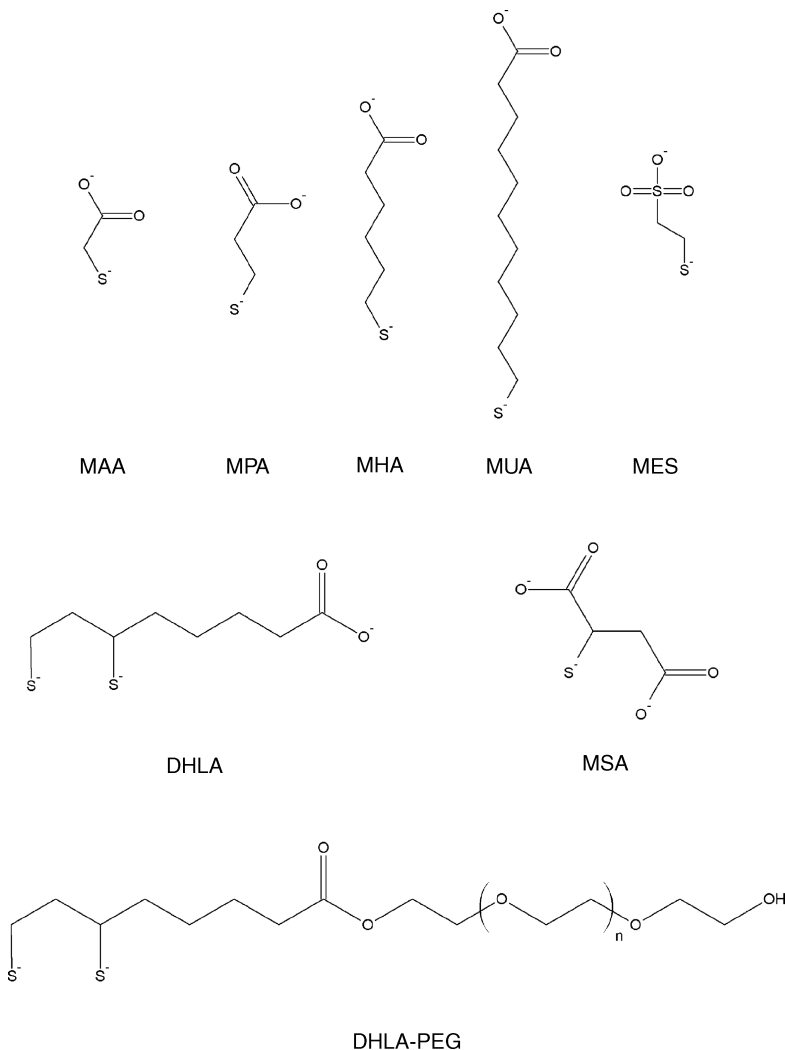


FIGURE 7.9 Commonly used thioalkyl acid ligands for aqueous solubilization of QDs: mercaptoacetic acid (MAA), mercaptopropionic acid (MPA), mercaptohexanoic acid (MHA), mercaptoundecanoic acid (MUA), dihydrolipoic acid (DHLA), and mercaptosuccinic acid (MSA). Other thiol-based ligands can also be used, including mercaptoethane sulfonate (MES) or DHLA appended with poly(ethylene glycol) (PEG).

the pK_a of the thiol ligands, whereas the latter is also dependent on the metal–thiolate interaction. The precipitation pH for MPA QDs showed some size dependence, where smaller QDs precipitated at lower pH values. These values ranged from roughly pH 3.5 for 2-nm QDs to pH 4 for 5-nm QDs. It was also found that charged ligands such as MPA and dimethylaminoethanethiol precipitated at lower pH values than the neutral ligand 3-mercaptopropanol.

Finally, additional instability has been associated with ultraviolet (254 nm) photooxidation of thiol ligands to disulfides and has been studied with CdSe QDs [54]. It was found that the surface of the QD acted as a photocatalyst for the process and was not oxidized itself until the ligands had been fully oxidized. It was also noted that bidentate ligands, which have a strong tendency to form intramolecular disulfides and pack less densely on the surface of the QD, may be less stable than monodentate thiols. Photooxidation can be avoided or minimized by working at longer excitation wavelengths. However, an unavoidable side effect of thioalkyl acid ligand exchange is that it tends to reduce quantum yields relative to QDs capped with TOP/TOPO in the organic phase [9,49,54,55].

In choosing to use thioalkyl acid QD surface chemistry in a biosensor or bioprobe design, it is important to consider the desired lifetime of the sensor and the effect that the gradual desorption of ligands would have on sensor performance or the surrounding matrix. Similarly, the effect of the anticipated pH of the sample matrix on colloidal stability and coordination of the ligands should be considered. Finally, the effect of the excitation wavelength on the ligands must also be taken into account. If brightness is the key factor for the performance of the biosensor or bioprobe, alternative chemistries such as polymers are probably preferable. However, if minimizing QD size is essential, thioalkyl acids could be the best choice.

7.4.1.2 Effects of Ligands on the Physical Chemistry of QDs Thioalkyl acid and other thiol-based ligands are not simply passive surface coatings, but significantly affect the physical properties of the underlying QDs. The effect of ligands on the colloidal stability of QDs has already been discussed. However, ligands also affect properties such as the apparent size of the QD and the luminescence of the QD. The apparent size of a QD can be defined by its hydrodynamic radius, which represents the size of the QD and the added layer(s) of tightly bound solvent that diffuse with the QD as a hypothetical hard sphere. It has been shown that DHLA QDs are 10% larger in aqueous solution than TOPO QDs in organic solvent [56]. Although it is expected that DHLA would have a smaller profile than TOPO as a ligand, the added size is attributed to the strong solvation of the carboxyl groups and many layers of bound water. This phenomenon is not limited to carboxyl groups. QDs with a 2.4-nm radius, capped with DHLA-PEG600 and DHLA-PEG1000, are expected to have geometric radii of 4.8 and 6.1 nm, respectively. The measured hydrodynamic radii were roughly 7 and 8 nm. In general, the hydrodynamic radius is larger than the QD geometric size and increases with increasing QD core size.

We have found that the luminescence properties of CdSe–ZnS QDs are sensitive to the nature of thioalkyl acid capping ligands [50]. For example, the peak PL wavelengths for QDs of the same size varied as 520, 526, and 534 nm for DHLA, MAA, and MSA capping. Progressive bathochromic shifts were also observed with MAA, MPA, mercaptohexanoic acid (MHA), and MUA capping. Each of these capping chemistries also exhibited a bathochromic shift with increasing pH. For QDs originally showing a PL maxima at 512 nm with TOPO capping in organic solvent, PL maxima were observed at 512, 514, 518, and 520 nm, with MAA capping in aqueous solutions at

pH 7.4, 9.5, 12, and 14, respectively. Similar pH-dependent bathochromic shifts were also observed with MPA, MHA, and MUA capping. These observations have tentatively been referred to as ligand chromism, due to the similarity with the solvatochromism of organic fluorophores. In fact, solvatochromic shifts have been observed with TOPO QDs in organic solvent since the optical bandgap energy of QDs shows a weak dependence on the dielectric constant of the surrounding medium [57]. In turn, it is reasonable to expect that altering the nature of the ligands surrounding the QD in a given a solvent would also yield chromic shifts. Our research suggests that there is a correlation between the pK_a or the hole-acceptor ability of the ligands and the degree of bathochromic shift observed. The more acidic a ligand is, or the lower the oxidation potential, the greater the bathochromic shift. However, the problem is surely more complex. The packing of the ligand film should be considered both in terms of the number of ionizable ligands and the ability of the solvent to penetrate the ligand film. In addition, it was found that as the QD size increased, the ligand-chromic effects decreased in magnitude. It can be speculated that this is related to the degree of quantum confinement of the exciton in the CdSe core, by virtue of the core size or the homogeneity of the surrounding ZnS shell.

In addition to ligand-chromic effects, our research has found that changes in quantum yield and lifetime between ligands indicate that the radiative system is not just the QD core, but the QD core-shell and surrounding ligands [50]. Through measurement of the quantum yield and radiative lifetime, it is possible to determine the radiative and nonradiative decay rates for the system. Although both decay rates play a role in determining quantum yield, we found that changes in radiative decay rate were the most important [50]. In some cases, changes in the radiative decay rate had up to a seven- or eightfold larger effect than the nonradiative decay rate. It is well known that avoiding the formation of trap states through effective surface passivation is essential to producing QDs with high quantum yields. As such, it is tacitly assumed that the different quantum yields between surface chemistries are due to different degrees of passivation and thus different nonradiative decay rates. Although this may often be true, it may not always be the case. This is particularly evident between the thioalkyl acid ligands we have studied, which include MAA, MPA, MHA, MUA, MSA, and DHLA.

Our research group has also completed a limited study on capping CdSe-ZnS with mixed films of MAA and hexa(ethylene glycol) (HEG) appended at both ends with DHLA (DHLA-HEG-DHLA) [58]. When the MAA/DHLA-HEG-DHLA ratio was varied from 1 : 0 to 100 : 1, 50 : 1, and 10 : 1, the band edge PL was quenched by 87%, 95%, and 98%, respectively. There was a simultaneous increase in the amount of bandgap PL. The bandgap contribution to the total PL increased from 6% to 15%, 24%, and 58%. The cause of the quenching is not entirely clear. However, we speculate that despite binding to the QD at both termini, the folded HEG retains a great deal of conformational mobility. This may displace and sterically occlude MAA ligands, creating gaps in the surface coverage. Given the favorable solvation of HEG, these sites would be accessible to solvent. The result may be trap states leading to the quenching and bandgap PL observed.

7.4.1.3 Ligand Exchange and Biomolecules Issues such as QD colloidal stability under different solution conditions and the resulting PL properties are clearly important. However, biosensors and bioprobes must also consider the interactions of QDs with biomolecules such as nucleic acids, proteins, and antibodies. The problem is twofold: (1) attachment of the desired biorecognition element to the QD, and (2) avoiding interference from the nonspecific attachment of other biomolecules on the surface of the QD. Figure 7.10 shows a variety of conjugation strategies, many of which are applicable to thiol ligands. The self-assembled thiol ligand coating is a thin chemistry and appears to be both permeable and labile. As such, it is possible to self-assemble thiol-terminated biomolecules on the surface of the QD. For example, nucleic acid–QD conjugates have been created using monodentate [59,60] and bidentate [61] thiol-terminated oligonucleotides and thiol-terminated aptamers [62]. Reduced antibodies also have free thiol groups for binding. Reduced antibodies also have free thiol groups for binding.

Proteins can be engineered to be appended with polyhistidine tails that assemble on the surface of CdSe–ZnS QDs via coordination to metal centers. For example, the binding of proteins appended with five and 11 residue polyhistidine tails can be monitored by following the increase in QD quantum yield [63]. This enhancement of PL results from greater surface passivation as the protein binds and blocks the surface.

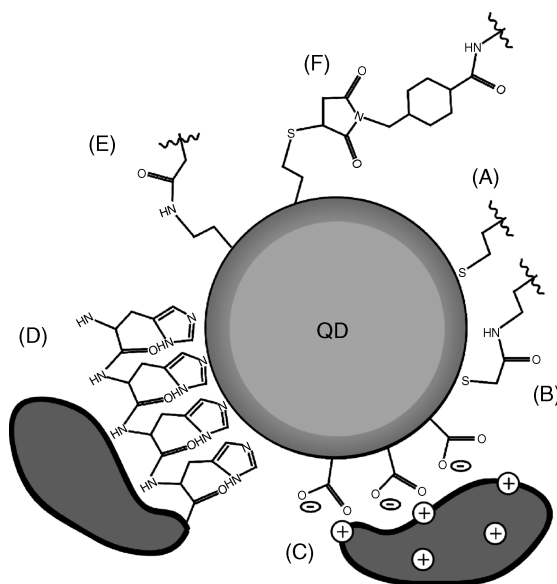


FIGURE 7.10 There are a number of strategies for creating QD bioconjugates: (A) self-assembly of thiol-terminated biomolecules; (B) amide bond formation with thioalkyl acid ligands; (C) electrostatic interaction between a positively charged protein and a negatively charged QD surface; (D) self-assembly of polyhistidine-appended proteins; (E) amide bond formation between a carboxyl-terminated molecule and an amine-terminated QD surface; (F) coupling an amine-terminated molecule to a thiol-terminated QD surface via the cross-linker SMCC. Naturally, other cross-linkers and pairs of functional groups can also be used.

Upon assembly of proteins, the quantum yield of QDs is observed to increase substantially, in the range 50 to 300%, depending on the surface coverage [64,65]. It has also been confirmed experimentally that smaller proteins allow more protein to be conjugated to the QD [63]. Positively charged proteins such as avidin and maltose-binding protein (MBP) can also be assembled on the surface of QDs based on electrostatic self-assembly [63]. Although effective under certain conditions, high ionic strengths and low pH may lead to conjugate instability. Single-molecule fluorescence resonance energy transfer (FRET) experiments have demonstrated that 1 : N QD–protein conjugates (where N is the number of protein molecules per QD) assemble according to a Poisson distribution [66].

Another popular conjugation strategy when employing thioalkyl acid–capped QDs is via amide bond formation. The carboxyl groups on the surface can be activated toward free amine groups with 1-ethyl-3-(3-dimethylaminopropyl)carbodiimide hydrochloride (EDC) or (sulfo-) N -hydroxysuccinimide (NHS). Although the resulting amide bond is quite stable, the strength of linkage is ultimately dependent on the strength of the interaction between the ligand and the surface of the QD. In this sense, the covalent coupling strategy does differ significantly from the self-assembly of thiol-terminated ligands in terms of stability. Although EDC is widely used as a coupling chemistry, it has been known to be problematic when used with thioalkyl acid–capped QDs [9,64], sometimes resulting in a loss of colloidal stability.

Considering the nonspecific attachment of biomolecules, it is clear that any positively charged proteins will have a tendency to assemble on the net negatively charged surface of a thioalkyl acid–capped QD. Other proteins, such as bovine serum albumin (BSA), can also adsorb to the surface of thioalkyl acid–capped QDs despite having a net negative charge. Recently, esterification of DHLA with different short poly(ethylene glycol) (PEG) chains has been reported as a method of creating bidentate ligands that can render QDs soluble in aqueous solutions over a broad pH range and also in certain polar organic solvents [51]. The PEG chains ranged from four to 21 ethylene glycol units, although most experiments were carried out with 12 units (DHLA-PEG600). It is interesting to note that polyhistidine-appended protein was able to bind to a DHLA-PEG600–modified CdSe–ZnS QD surface through a metal affinity interaction. This suggests that the coating did not completely block the surface of the QD, although the protein-binding efficiency increased when the surface chemistry became a mixture of DHLA and DHLA-PEG600. The binding efficiency further increased for a coating that was exclusively DHLA, indicating that greater PEG coverage did provide some hindrance to the assembly of large biomolecules on the QD surface.

We have studied the adsorption of oligonucleotides on MAA-capped QDs using a series of FRET experiments [67]. By fluorescently labeling the oligonucleotide such that the absorption spectrum of the dye overlapped with the PL spectrum of the QD, it was possible to monitor the adsorption of oligonucleotides via FRET-sensitized dye fluorescence. It was found that the adsorption of a mixed-base oligonucleotide (19-mer) showed pH dependence. Comparing results obtained at pH 4.8, 7.4, and 9.5, steady-state adsorption and adsorption kinetics were found to be greatest at pH 4.8.

Both the steady-state adsorption and kinetics of adsorption decreased as the pH was increased.

Adsorption could also be modulated by increasing the amount of formamide in the buffer solution. Formamide is well known to disrupt hydrogen bonding in nucleic acids. The results are suggestive of a hydrogen-bonding interaction between the nucleobases of the oligonucleotide and the carboxyl groups on the surface of the QD. This interaction can be disrupted by formamide and deprotonation of the carboxyl groups as the pH increases. Adsorption was also found to be hindered by conjugating oligonucleotides to the MAA QDs. These conjugated oligonucleotides added more repulsive negative charge to the surface and partially blocked the surface by steric effects. Both factors decrease the tendency for adsorption by unconjugated oligonucleotides. This was further substantiated by the observation that at pH 7.4, where adsorption is favorable, adsorption on MAA-QDs without any conjugated oligonucleotides saturated at slightly more than one oligonucleotide per QD. Hybridization rates were found to mirror the trends in adsorption rates, suggesting a pseudo-solid-state hybridization picture for MAA QD–DNA conjugates. It is likely that the target oligonucleotide first adsorbs on the surface of the QD and subsequently diffuses across the surface to hybridize with the conjugated probe oligonucleotide. Figure 7.11 illustrates the process. This is similar to the hybridization process for solution-phase target oligonucleotides hybridizing at a bulk solid interface with immobilized probe oligonucleotides.

With respect to conjugated oligonucleotides, it was also possible to investigate the conformation of these oligonucleotides qualitatively via FRET [67]. By varying the acceptor dye position between the 3' and 5' termini and varying the length of linker between the QD and oligonucleotide, it was determined that the oligonucleotide adopted a conformation along the surface of the QD. The FRET efficiency between the various permutations of linker length and dye position showed minimal variation, suggesting that the donor–acceptor distance was similar in each case. The best model for this result is that the oligonucleotide lies along the surface of the QD, as shown in Figure 7.11.

The interaction between the MAA QD surface and the oligonucleotide also affects the thermal stability of conjugated dsDNA [67]. Melt curves for dsDNA were compared between bulk solution and QD conjugates. It was found that melt curves obtained with QD–oligonucleotide conjugates were notably sharper than those of their bulk solution counterparts, and had altered melt temperatures. For example, the melt transition for a fully complementary 19-base hybrid was twice as sharp as that obtained in bulk solution. Melt temperatures for perfectly matched, single-base-pair-mismatched, and double-base-pair-mismatched hybrids were generally shifted by 1 to 2°C. When the experimental conditions were altered to reduce adsorption effects, either by increasing the solution pH or by conjugating more oligonucleotides to the QD, the melt curves obtained for QD–oligonucleotide conjugates resembled their bulk solution counterparts much more closely. As the melt temperature is approached, breathing in the duplex structure becomes more significant and the surface of the QD can interact transiently with sections of ssDNA. As shown in Figure 7.11, this interaction provides another driving force for deannealing the dsDNA by “grabbing”

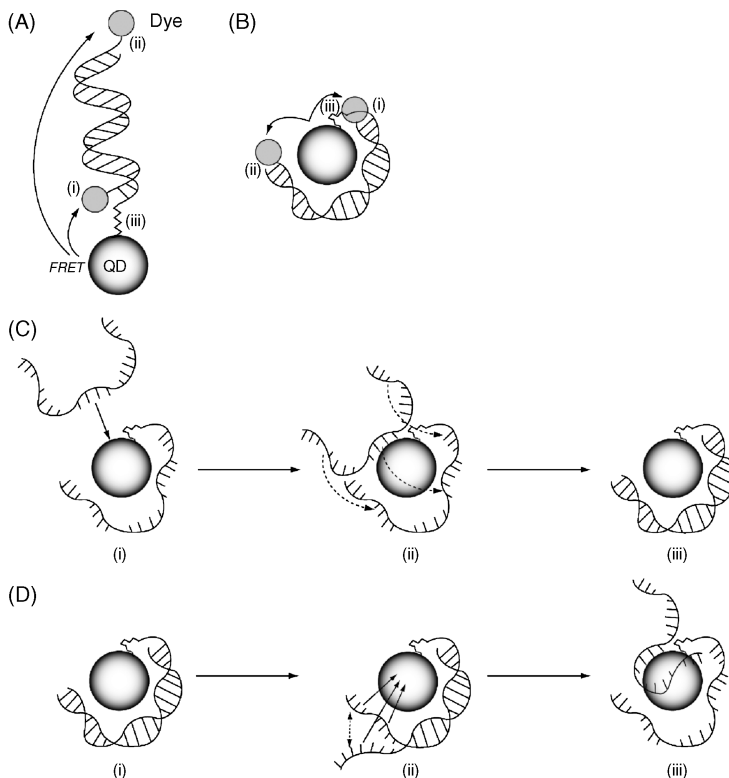


FIGURE 7.11 (A,B) Upright oligonucleotide conformation and a conformation along the surface of the QD, respectively. A FRET experiment can discern between the two conformations by varying the position of the acceptor dye between the two termini (i) and (ii), or by varying the linker length (iii). (C) Pseudo-solid-phase hybridization of oligonucleotides at the surface of a QD. The process is thought to proceed as (i) target adsorption, (ii) diffusion across the surface of the QD to the probe, and (iii) hybridization. (D) Melting process for dsDNA at the surface of a QD. The QD surface interacts with sections of dsDNA (ii) and helps pull the helix apart and onto the surface of the QD (iii).

segments of ssDNA, and results in sharpening of the melt transition by pulling the duplex apart. FRET experiments show that the target oligonucleotide melts onto the surface of the QD and further support this model. It is also interesting to note that polythymine oligonucleotides show very weak interactions with MAA QDs. Melt curves obtained with polyadenine/polythymine–QD conjugates were still sharper than their bulk solution counterparts, but primarily over the second half of the transition. This appears to result from the weak adsorption interaction, with half the duplex and the consequent need for more pronounced breathing from thermal effects.

The thioalkyl acid surface chemistry is advantageous in that it is easily prepared, compact, allows for relatively facile bioconjugation, and can be extended to thiols terminated with other functional groups. It is disadvantageous in that it has limited

stability with respect to pH, ionic strength, and time. Biomolecules also tend to adsorb on the surface of these QDs. Even poly(ethylene glycol) molecules, which are hydrophilic, nontoxic, nonimmunogenic, and nonantigenic, do not prevent adsorption completely. In our experience with mixed films of DHLA-HEG-DHLA and MAA, nonspecific adsorption of oligonucleotides still occurred to some degree [58]. Similarly, DHLA-PEG600 was found to reduce protein-binding efficiency but not to eliminate binding [51]. Obviously, the nonspecific adsorption of biomolecules can affect the selectivity of a biosensor or bioprobe. Nonspecific adsorption can also be to the detriment of the overall biosensor performance if the adsorption blocks the target analyte from interacting with the QD architecture. Similarly, if interactions with the QD affect the behavior of biomolecules, the performance of the sensor may also deviate from the ideal. For example, changes in the melt temperature or melting profile for dsDNA can affect the ability of the biosensor to detect nucleotide polymorphisms. In the context of biosensor or bioprobe development, it is important to weigh the variety of advantages and disadvantages for thioalkyl acid chemistry in the context of the intended application. It may or may not be the case that the thioalkyl acid surface chemistry is the best choice.

7.4.2 Silica Encapsulation

A more robust strategy for preparing water-soluble QDs involves coating the QD with a thin layer of silica grown from organosilane chemistry. Figure 7.12 shows the two most common schemes. One of the first silica-coating strategies to be reported involves displacing the original TOP/TOPO ligands with 3-mercaptopropyltrimethoxysilane (MPS) [68,69]. The MPS molecules coordinate to the surface of the QD via their thiol group and the methoxysilane groups cross-link, forming a siloxane monolayer around the QD. A second layer of organosilane is then cross-linked with the first layer to form a water-soluble silica shell. The surface of the QD is tailored

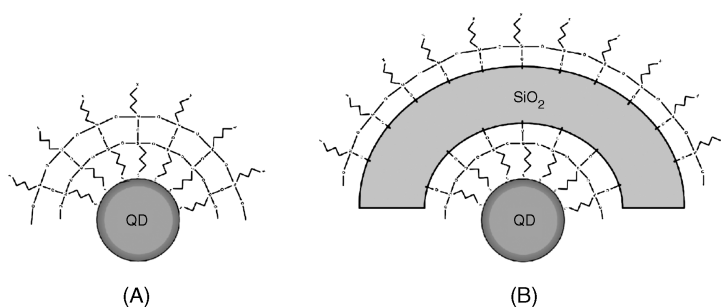


FIGURE 7.12 Silica-coating strategies for QDs. An initial layer of silane coordinates to the surface, typically via thiol (shown) or amine (not shown) groups. This then acts as the nucleation site for (A) the formation of a silane bilayer, where another functional group ($X = \text{SH}, \text{NH}_2, \text{COOH}$, etc.) is exposed to solution; or (B) the formation of multilayered silica via Stöber-like growth and subsequent deposition of a surface layer of silane.

to have amine, thiol, carboxyl, or methyl phosphonate groups by using aminopropyltrimethoxysilane (APTMS), MPS, MPS treated with maleimidopropionic acid, or trihydroxysilylpropyl methylphosphonate [68]. This treatment is not observed to significantly affect the absorption or emission spectra, and quantum yields are 60% or more of those observed in organic solvents with TOP/TOPO ligands. This protocol requires substantially more effort than simple ligand exchange, and special attention must be paid to avoid growing multilayer shells, cross-linking QDs, and aggregation. DNA has been conjugated to these silica-coated QDs, with nonspecific adsorption being observed only under conditions of high salt [69].

A similar approach uses an APTMS layer for initial coordination to the QD surface and cross-linking [70]. A second layer of APTMS is cross-linked to the first layer by hydrolysis and condensation. The synthesis is carried out in a reverse microemulsion. Following the silica-coating process, no change in the QD spectra were observed and the quantum yield decreased by only a few percent. The surface amino groups could be further conjugated.

As an alternative to the bilayer strategy, a thicker layer of silica can be grown on a QD [71]. In this case, CdTe QDs were initially stabilized with MAA. Again, MPS is used to coordinate to the QD surface and cross-link to form a thin initial layer of silica. Silica polymerization is initiated at the QD surface using sodium silicate and a modified Stöber method for growth. A subsequent layer of MPS is added on the surface to provide thiol groups for conjugation. For example, succinimidyl 4-*N*-maleimidomethyl]cyclohexane-1-carboxylate (SMCC) was used to conjugate an immunoglobulin protein or streptavidin maleimide to the QD surface. The coating process was observed to roughly double the size of QDs, resulting in an average shell thickness of 3 nm. It was also observed that the silanization process removed some of the shallow trap states observed previously.

Single QDs can also be encapsulated in silica shells without initial displacement of the coordinating synthesis ligands by a silane precursor [72]. Hydrophobic TOPO capped ligands can be transferred to the aqueous phase by detergent micelles. *N*-Octyltriethoxysilane is then used as a hydrophobic silica precursor. The alkyl chain serves the role of a surface coordinating group by intercalating with the alkyl chains of TOPO. A shell is then grown by adding the amphiphilic triethoxyvinyl silane. The shell thickness is varied by adjusting the amount of this reagent. Finally, the shell is functionalized with a layer of [3-(2-aminoethylamino)-propyl]trimethoxysilane. The available amino groups have subsequently been conjugated to poly(ethylene glycol) NHS esters. The resulting QDs have an 18-nm diameter and 12% size distribution. The full-width-at-half-maximum remained narrow at 30 nm, and the quantum yield observed was 30 to 50% of the value observed for the QDs in organic solvent.

As an alternative to silica encapsulation of single QDs, multiple QDs can be encapsulated in silica nanoparticles 40 to 200 nm in size [73]. QDs are adsorbed on the surface of a preformed amine-modified silica nanoparticle using a mediating layer of poly(vinylpyrrolidone). A silica shell is grown overtop the QD-modified silica nanoparticles by a Stöber growth process using tetraethoxysilane. It is estimated that there are roughly 300 QD per silica particle. A bathochromic shift of 6 nm was

observed in the PL spectra, but the full width at half maximum was unchanged. However, prior to the silica encapsulation, the QD quantum yield was 21%. Following the modification, the quantum yield was reduced to 1%. This was attributed to the creation of trap states by the oxidizing conditions of the Stöber growth process.

Conjugation to silica-coated QDs requires the formation of covalent bonds. As described above, silica-coated QDs can be tailored to have a variety of functional groups. Cross-linkers are available that can react with carboxyl, amine, and thiol groups. These include EDC, NHS, SMCC, and *N*-(γ -maleimidobutyryloxy)succinimide (GMBS). The silica-coating process is clearly a more difficult process than simple ligand exchange. However, the resulting surface chemistry is far more stable. The coating is not labile, meaning that the surface of the QD will not change over time and that conjugated biomolecules are attached by the strength of a covalent bond. There may be concerns over the reproducibility of the silica coatings. This would be particularly true when encapsulating multiple QDs. Given that analytical technologies are pushing single molecule detection, poor reproducibility in the number of QDs that are encapsulated and the quality of the encapsulation would lead to poor precision at low target concentrations. However, in many cases the robustness of the coating and bioconjugation may be a considerable advantage.

7.4.3 Polymer Coatings

Oligomeric phosphines have been developed by cross-linking tris(hydroxy)propylphosphine with diisocyanatohexane to form multidentate phosphines which coordinate to the QD surface [55]. These oligomers are rendered water soluble by further reaction with carboxylic acid or methacrylate-bearing isocyanates. The stability of aqueous QDs prepared with this chemistry exceeds that obtained with ligand exchange using MUA. A similar approach uses an amphiphilic triblock copolymer to encapsulate a QD bearing its original TOP/TOPO ligands [21]. The triblock polymer consists of a hydrophobic polybutylacrylate segment, a hydrophobic polyethylacrylate segment, and a hydrophilic polymethacrylate segment. Hydrophobic octyl side chains are grafted onto the triblock copolymer, and the resulting structure self-assembles around a TOP/TOPO-capped QD. The octyl side chains intercalate with the octyl tails of TOP and TOPO. Similarly, hydrophilic poly(ethylene glycol) (PEG) side chains can be grafted, which help stabilize the encapsulated QDs in aqueous buffer. The photophysical properties of QDs were able to withstand the full pH range and salt concentrations from 0.01 to 1 M. A similar strategy has been used to place hydrophobic side chains randomly onto polyacrylic acid by coupling isopropylamine via DCC [74]. Other amphiphilic polymers that have been used in a similar fashion include poly(maleic anhydride alt-1-tetradecene) (PMAT) [75], hyperbranched polyethylenimine (PEI) [76], and octylamine-modified polyacrylic acid [77]. In the case of the former, the PMAT chains were cross-linked around the QD, and the unreacted anhydride groups were hydrolyzed to produce a negatively charged surface. The hydrodynamic diameter of the QDs increased from 5.7 and 11.6 nm for green and red QDs in chloroform to aqueous diameters of 19.2 and 23.6 nm following PMAT modification. This is larger than would be anticipated strictly on the basis of the polymer structure.

Changes in the overall solvation of the QD are likely to be occurring concurrently with the change in particle size. The hydrodynamic radii of QDs that were stabilized with PEI were ultimately smaller than those that were stabilized with PMAT, but this varied with polymer molecular weight. PEI with a mass of 800 Da yielded PEI QDs with a hydrodynamic diameter of 10.7 nm, while PEI with a mass of 25 kDa yielded PEI QDs with a diameter of 17.5 nm. In contrast to PMAT, it should be noted that the PEI displaces the original ligands. Gradual increases in hydrodynamic diameter have been observed with increases in polymer molecular weight in other systems as well. For example, coatings of poly(*N,N*-dimethylaminethyl methacrylate) (PDMA) with molecular weights of 7, 10, 15, 19, and 29 kDa increased the hydrodynamic radius from 1.9 nm for TOPO-QDs to 2.7, 4.7, 5.2, and 6.3 nm [78]. The quantum yield also increased with the addition of the polymer coatings. Although the PDMA QDs are not soluble in water, further modification converts dimethylamine groups to alkyltrimethylammonium groups for water solubility. In general, the quantum yields of QDs with a polymer coating are substantially greater than those coated by simple ligand exchange. However, it was noted that PEI may promote photooxidation of QDs, although this effect could be reduced by the addition of mercaptoethanol [76]. The general amphiphilic polymer concept is shown in Figure 7.13 with the structures of some amphiphilic polymers.

As an alternative to synthetic polymers, QDs, with their native TOP/TOPO ligands, have been encapsulated in the hydrophobic interior of lipid micelles composed of

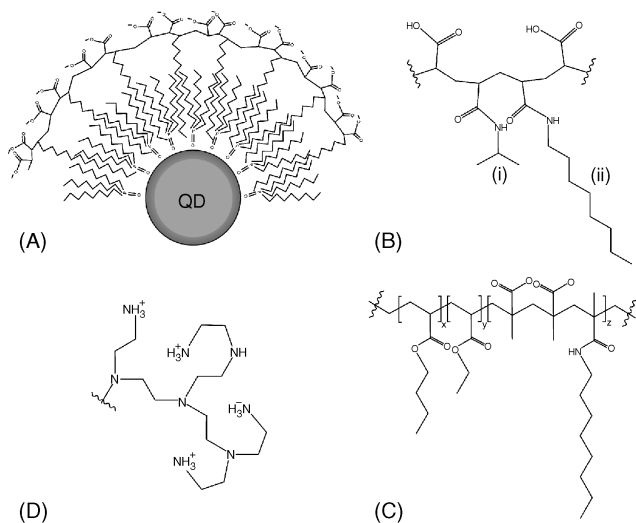


FIGURE 7.13 Amphiphilic polymers for coating QDs. (A) PMAT is shown surrounding a TOPO-capped QD. The hydrophobic tail segments of the PMAT interact with the octyl chains of the TOPO. The charged carboxyl groups along the backbone impart aqueous solubility. (B) Polyacrylate modified with (i) isopropyl amine or (ii) octyl amine and (C) a triblock copolymer can solubilize TOPO-QDs analogously to PMAT. (D) PEI can also be used to solubilize TOPO-QDs in aqueous solution, but displaces the original TOPO ligands.

n-poly(ethylene glycol) phosphatidylethanolamine (PEG-PE) and phosphatidylcholine [79]. The interior of micelles of this nature is estimated to be 3 nm; however, even QDs 4 nm in size were found to be stable for months in aqueous solutions of high salt. It should also be noted that in the case of QDs, significantly less than 3 nm in size, these micelles were capable of encapsulating multiple QDs. The PEG coating has the advantage of being poorly immunogenic, poorly antigenic, and resisting biomolecule adsorption. Replacing some of the PEG-PE with amine-bearing phospholipid allowed conjugation of thiol-modified DNA.

Another approach that has obtained some popularity is to incorporate multiple QDs into a much larger polymer matrix. A common and simple method of doing this is by permeation of QDs into preformed polystyrene microparticles. For example, the procedure can be as simple as adding TOPO QDs and polystyrene microparticles to a doping solution consisting of 60/40 v/v of chloroform and propanol [80] or 95/5 v/v chloroform and butanol [81]. Multiple colors of QD can be incorporated by varying the ratio of the two colors in the doping solution. Carboxyl-modified polystyrene microparticles can be used to allow conjugation of amine-modified oligonucleotides [81]. Commercially available polystyrene microparticles can be modified with chlorosulfonic acid and 6-aminocaproic acid to yield surface carboxyl groups [81]. Incorporation of the QDs is driven by hydrophobic interactions and the porosity of the polystyrene particles as they swell in solvent. Naturally, there is a tendency of the QD to steadily leach out of the polystyrene microparticles when the QD-doped particles are removed from the doping solution and placed in other organic solvents. This can be avoided by coating the surface of the polystyrene microparticle with silica via the hydrolysis of tetraethoxysilane [82]. The thickness of the silica shell is controlled by the coating time. In addition to stabilizing QD loss from the particles, increases in shell thickness were found to yield greater resistance to photobleaching. Conjugation of amine-terminated oligonucleotides was also possible.

QDs can also be polymerized into polymer particles. For example, MPA QDs have been encapsulated in 102-nm-diameter chitosan nanoparticles [83]. Chitosan is a hydrophilic, nontoxic, biocompatible, and biodegradable polymer. The MPA QDs were mixed with chitosan in solution and coupled via EDC. It was found that the quantum yield of the encapsulated QDs was 11.8% larger than those in bulk solution. Alternatively, QDs can be polymerized into polystyrene microspheres [84]. Oligomeric phosphines bearing methacrylate groups are coordinated to the surface of the QD by a ligand exchange process and are largely cross-linked to form a thin polymer coating. The few remaining methyl methacrylate groups are reacted with vinyl groups on styrene during synthesis of the polystyrene microparticles. The result is that the QDs are chemically incorporated. The initial cross-linked poly(methyl methacrylate) coating serves to protect the QDs from quenching by the initiator. The resulting polystyrene beads have an average diameter of 813 nm. This size can be decreased by increasing the amount of oligophosphine ligand, however the size distribution broadens concomitantly.

In the discussion on ligand exchange, it was noted that different thioalkyl acid ligands could cause chromic shifts in the PL maxima of QDs and should be treated as part of the radiative system. It is interesting to note that CdSe-ZnS QDs coated with

calix[*n*]arene carboxylic acids, where $n = 4, 6, \text{ or } 8$, exhibited bathochromic shifts in their PL with increasing calixarene oligomer size [85]. For example, a QD with PL centered at 530 nm exhibited red shifts of 8, 21, and 35 nm. The band edge of the absorption spectrum also shifted to longer wavelengths. Larger QDs exhibited smaller PL shifts, as was observed with thioalkyl acid ligand chromism. Therefore, polymer coatings also have the potential to significantly modify the radiative system associated with QDs.

By virtue of being cross-linked, polymers provide a very stable coating for QDs. Many of the polymer functional groups that impart aqueous solubility can be used for conjugation of biomolecules. Polymers can also be tailored, for example, by the addition of poly(ethylene glycol) chains, to resist the adsorption of biomolecules. QDs coated with polymers typically exhibit high quantum yields, due to the thickness of the coating, which is very effective at protecting the QD from the surrounding matrix. Thus, the principal advantages of polymer coatings are their versatility and stability. However, a potential disadvantage of polymer-coated QDs is their large size, both geometrically and hydrodynamically. This may have the effect of perturbing the system of interest or may preclude a distance-dependent process such as FRET. The coating thickness has a significant effect on the potential sensitivity of a FRET-based assay. Since the process is distance dependent, thicker coatings mean less efficient energy transfer and thus reduced sensitivity. Considering the encapsulation of multiple QDs in larger polymer particles, this presents a significant advantage in terms of sensitivity per label by virtue of the greater brightness. However, it will be shown in Section 7.5 that the primary advantage of this approach is in terms of multiplexing by barcoding. Conversely, the large size of the polymer particles could lower the efficiency of a labeling process compared to single QDs, counteracting any advantages in brightness.

7.5 BIOANALYTICAL APPLICATIONS OF QUANTUM DOTs AS FLUORESCENT LABELS

Given the many advantages of QDs over conventional organic fluorophores, it is no surprise that an area of interest is the replacement of organic fluorophores with QDs in a number of traditional assays. These include microarrays, immunoassays, fluorescence in situ hybridization (FISH), and optical barcoding. The brightness and photostability of QDs are clearly advantageous in terms of sensitivity and reproducibility. The narrow PL spectra and broad absorption spectra increase the versatility of the assay design and the capacity for multiplexing.

7.5.1 Microarrays

With respect to microarray analyses, QDs have been used as luminescent tags in DNA [86], RNA [87], and protein [88] array formats. With respect to the former, it has been possible to resolve single nucleotide polymorphisms on cDNA arrays for

mutation in the human oncogene p53, as well as a multiplexed analysis for hepatitis B and hepatitis C virus, by concurrent use of QDs with peak PL at 566 and 668 nm [86]. Due to the large size of the QD relative organic dyes, it appears that QD densities in microarray spots are less than those achieved with organic dyes, potentially offsetting the advantages of stronger absorption and brighter PL. On a technical note, many commercial microarray readers are designed for Cy3 and Cy5 (or spectral analogs) using 532- and 635-nm laser sources. In addition, although it is easy to match the emission wavelengths of QDs to Cy3 and Cy5, the absorption of QDs decreases steadily moving toward their peak PL wavelengths. In contrast, organic fluorophores show the strongest absorption near their peak PL wavelengths, due to their small Stokes shifts. Thus, as in the case above [86], the apparent sensitivity of the QD array may be less than that observed with organic fluorophores, due to poor excitation efficiency. Such a deficiency is easily remedied with the use of a blue-shifted source and/or red-shifted QDs, where possible. Liang et al. [87] have described a miRNA microarray using biotinylated targets and QD–streptavidin conjugates. The limits of the detection and dynamic range for the microarray were 0.1 fmol and two orders of magnitude, respectively. This compares favorably with a Northern blot analysis, which was found to have a limit of detection of 1.0 fmol and a dynamic range of three orders of magnitude. PEG-modified streptavidin–QD conjugates have been coupled to biotinylated antibodies as luminescent tags for reverse-phase protein microarrays [88]. Sensitivity is particularly important in protein microarrays since, unlike their oligonucleotide analogs, there is no method for amplification of target. The QD tags are sufficiently bright to detect proteins in cellular extract, although the PEG modification of the streptavidin QD conjugates was found to be necessary to limit nonspecific adsorption. Streptavidin QDs have also been used to visualize biotinylated antibodies in a three-dimensional hydrogel matrix containing protein toxins in microarray format [89]. Despite having a molecular volume roughly three times that of IgGs, the QDs were able to diffuse into the gel and effectively label the protein–antibody targets.

7.5.2 Immunoassays

The advantageous properties of QDs have also resulted in increasing use of QD–antibody conjugates in immunoassays. Such conjugates have been prepared from biotinylated antibodies and QD–streptavidin conjugates [90,91] or from direct covalent coupling mediated by EDC and NHS [92]. Applications include the detection of *Salmonella typhimurium* cells from chicken carcass wash water [91] or pathogenic *Escherichia coli* [90] by sandwich assays with QD–antibody conjugates and immunomagnetic separation. Detection limits of 10^3 CFU/mL have been obtained in both cases, the latter of which is two orders of magnitude better than a similar analysis using fluorescein–antibody conjugate. Similar sandwich assays carried out on a glass chip have obtained nanomolar detection levels for human and goat IgG [92]. In this case, the capture antibody was immobilized and a QD-labeled secondary antibody was used as the reporter. Secondary antibodies have been labeled with QDs and used for the detection of sulfamethazine in chicken muscle tissue by way of

a competitive fluorescent immunosorbent assay [93]. A QD-based immunomagnetic assay has also been developed for the simultaneous detection of pathogenic *E. coli* and *Salmonella* [94]. Biotinylated anti-*E. coli* and anti-*Salmonella* were conjugated to streptavidin-coated QDs. Each antibody was associated with a different color of QD. The method achieved a limit of detection of approximately 10^4 CFU/mL with a 2-hour detection time. Streptavidin-modified QDs have also been linked with antibodies for total prostate-specific antigen [95]. This marker is useful in the diagnosis of prostate hyperplasia and cancer. A detection limit of 0.25 ng/mL was obtained, which was well below the 4-ng/mL threshold for cancer. Good selectivity against the possible interferent human chorionic gonadotropin was also achieved. QD-antibody conjugates have also been used in a microfluidics-based immunoassay coupled with FISH using organic fluorophores [96].

Pathak and co-workers completed a study wherein they examined the functional properties of antibodies conjugated to QDs by two different strategies: biotin-streptavidin and covalent bond formation [97]. Antibodies were labeled with four to eight biotin molecules. Quantitative electrophoresis was used to analyze the conjugates and antibodies. It was found that there were 0.60 ± 0.14 functional IgG molecules per QD at a 1 : 1 conjugation ratio, and 1.3 ± 0.35 IgG per QD at a 2 : 1 ratio. Inactive antibodies were suggested as the main cause, and may have had poor orientation on the QD due to the multiple biotin labels. For covalent coupling, antibodies were reduced with DTT to obtain three possible fragments: the heavy chain, the light chain, and heavy-light chain pair. This last fragment is only partially cleaved and is the only functional fragment. The fragments were conjugated to the QDs by SMCC. It was found that there were 0.076 ± 0.014 functional antibodies per QD with the covalent linkage. This is an excellent example of how the conjugation of biomolecules to QDs does not necessarily guarantee their function or availability. This must be considered in the design of biosensors and bioprobes and is a fundamental challenge in the optimization of these assays.

7.5.3 Fluorescence In-Situ Hybridization

Biotinylated DNA has been coupled to QD-streptavidin conjugates for use in FISH, where for example, the HER2 locus in breast cancer cells has been detected using a QD label [98]. This work also found that QDs were twice as bright as Texas Red DNA conjugates and far more stable than both Texas Red and fluorescein with respect to photobleaching [98]. Although both aspects are highly advantageous for FISH, the QD labels were found to blink significantly and showed a slightly different signal distribution than that of organic labels. Texas Red and fluorescein labels appeared at the heterochromatic regions of human metaphase chromosomes 1, 9, and 16, and centromeric regions of other chromosomes; QDs did not label the latter. However, it should be noted that similar effects were observed with fluorescein-streptavidin conjugates under certain conditions, and that this is a function of pH. In addition to streptavidin QDs, MAA QDs conjugated with thiol terminated DNA complementary to plasmid pUC18 have been used to visualize this plasmid in *E. coli* cells via FISH [99].

7.5.4 Aptamers

Aside from antibodies and conventional nucleic acid probes, aptamers can be conjugated to QDs as targeting moieties. For example, a 60-base aptamer has been selected for *Bacillus thuringiensis* (BT) [100]. The aptamer was thiol terminated and coupled covalently to a CdSe–ZnS QD with SMCC. The detection limit of 1000 CFU/mL was sixfold better than a similar assay with a conventional organic fluorophore. Some minimal nonspecific adsorption of the QDs to the cell was observed.

It has been found that DNA aptamers can passivate the surface of near-IR emitting PbS QDs and impart aqueous solubility [101]. Thrombin-binding aptamer (TBA) was incorporated at the time of synthesis, which used a room-temperature, open-air, aqueous method. The TBA QDs were found to be stable over months and exhibited 23% quantum yield. Moreover, the aptamer retained enough of its secondary structure to bind its target selectively. For PbS QDs passivated with TBA, it was found that thrombin binding induced quenching of the QD photoluminescence at 1050 nm. A detection limit of 1 nM was achieved. The QD absorption was bleached significantly by the addition of thrombin, suggesting that the quenching was due to a charge transfer process. Although other proteins were found to adsorb nonspecifically, they did not modulate the PL of the QD and were rapidly displaced by thrombin. A FRET-based bioprobe based on TBA has also been developed and is described in Section 7.6.3.

7.5.5 Quenching

It was noted previously that surface chemistry can affect the quantum yield or PL spectra of QDs. Similarly, adsorbates at the surface of QDs or changes in the nature of the surface can affect the PL properties of a QD. Examples described previously include the adsorption of proteins or conjugation of nucleic acids, which increased the quantum yield of thioalkyl acid capped QDs. If they can be made selective, these interactions can be exploited for biosensor and bioprobe development. In such cases, the QD is acting as a probe rather than simply as a label.

A scheme to detect paraoxon, a toxic agent used in pesticides, has been developed on the basis of QD PL quenching [102]. Positively charged organophosphorous hydrolase (OPH) was self-assembled on the surface of a MAA-capped CdSe–ZnS QD. QD photoluminescence was quenched in the presence of as little as 10^{-8} M paraoxon. Circular dichroism measurements suggested that a conformational change by OPH upon paraoxon binding changed the degree of QD surface passivation, resulting in the quenching observed. It should be noted that the QDs show no response toward paraoxon in the absence of OPH.

Citrate-capped CdSe QDs prepared in aqueous solution have been used to detect, in order of decreasing sensitivity, dopamine, lactic acid, ascorbic acid, and catechol [103]. The selectivity for dopamine was approximately 25 times greater than that for lactic acid. The presence of the species in solution quenches the QD in proportion to the concentration, following a Stern–Volmer type of linear relation. It is believed that the hydroxyl and amine groups of these species act as hole acceptors, preventing radiative recombination of the QD exciton when adsorbed on the surface. Since this

response is not based on a selective binding event, it is not clear how this sensor would perform in a complex matrix containing a variety of reactive hydroxyl and amine groups. Presumably, the selectivity would be low and an analysis would require some sample cleanup or other pretreatment.

A reagentless fiber-optic sensor for immunoglobulin G (IgG) has also been developed on the basis of QD quenching [104]. However, in this case, the quenching interaction does not necessarily occur directly on the surface of the QD, but may be due to more global changes in its local environment. QD-labeled protein A was immobilized via organosilane chemistry and interrogated via an optical fiber. The introduction of IgG and subsequent binding to protein A resulted in IgG concentration-dependent quenching. This approach has the advantage of being a true biosensor, due to the immobilization of the QD and potential for reusability. However, the phenomenon observed may not be generally applicable and thus is of limited practical diagnostic use.

7.5.6 Multiplexed Applications of Quantum Dots

The narrow PL spectra and broad absorption spectra of QDs make them ideal for multiplexed applications. Multiple colors of QD can be excited at a single wavelength toward the blue or ultraviolet end of the spectrum. The narrow PL spectra allow many different colors to fit within a given spectral range, and the symmetry of the PL spectra makes deconvolution straightforward. This is in contrast to the comparatively narrow absorption and broad red-tailed PL of organic fluorophores. Organic fluorophores require multiple excitation sources, fit fewer colors per spectral range or have greater crosstalk for an equal number of colors, and potentially require more complex deconvolution. The use of a single excitation source is preferable to multiple sources for reasons of simplicity, economy, and avoiding problems with poor overlap between the excitation volumes of the two or more laser sources. The photostability of QDs also avoids problems associated with differential photobleaching rates of organic dyes in multiplexed analyses.

An excellent example of multiplexed detection using QDs as labels involves the simultaneous detection of four protein toxins using QDs with PL peaks at 510, 555, 590, and 610 nm via a sandwich immunoassay [105]. The selective chemistry consists of immobilized antitoxin antibodies and secondary antibodies conjugated to QDs. Conjugation was achieved by modifying the QDs with a mixture of maltose-binding protein (MBP) and an adapter protein designed to bind the Fc domain of antibodies. The adapter protein consists of the IgG-binding β_2 domain of streptococcal protein G. This has been modified with a positively charged leucine zipper for self-assembly on the negatively charged surface of DHLA QDs. The toxins of interest were cholera toxin, ricin, Shiga-like toxin 1, and staphylococcal enterotoxin B. Each antitoxin antibody is associated with a certain color of QD. Using ultraviolet excitation and a linear spectral deconvolution algorithm, it was possible to detect all four toxins simultaneously at levels of 30 ng/mL. Some cross-reactivity was observed, although 77 to 95% of the signal observed resulted from the expected QD-antibody conjugate in experiments where a single antibody and toxin were immobilized but were exposed

to a mixture of QD–antibody conjugates. Experiments were also performed with multiple immobilized antibodies and multiple QD–antibody conjugates with a single toxin. It was found that 4 to 17% of the signal observed resulted from cross-reactivity and nonspecific interactions. Cross-reactivity is an issue in multiplexed immunoassays that do not use QDs. Thus, it is not clear that the QDs yield more nonspecific interactions than antibody–fluorophore conjugates, although it remains a possibility. The authors of this study suggest that the immunoassay could be expanded to include six colors of QD and thus six targets. This degree of multiplexing is not possible with the broad spectra of organic fluorophores, and certainly not when considering that a single excitation wavelength was used.

Another approach to multiplexing that benefited from the maturation of colloidal QD technology is optical barcoding. The concept of barcodes is of great interest in analytical chemistry and has been realized by spectral encoding. The idea is that a variety of luminescent species can be grouped in combinations to provide different intensities in different regions of the spectrum. Information is thus stored as a combination of intensity and wavelength, where $N^m - 1$ codes can theoretically be derived from m different colors and N resolvable intensities [106]. QDs are ideal for such applications, due to their narrow symmetric PL spectra and the ability to excite multiple QDs simultaneously with a single source.

In the context of bioassays, one would like to assign a spectral barcode to a certain nucleic acid sequence, antigen, protein, or other target. Since it is not practical to label biomolecules with specific ratios of different colors of QD, the common approach is to incorporate the desired ratio of QDs into microparticles that are on the order of 10^{-1} to $10^1 \mu\text{m}$ in diameter. In this manner, the microparticle matrix protects and carries the QD, maintaining high quantum yields and good stability while facilitating bioconjugation. A typical assay format is to associate a spectral code with a given probe. This could be a certain oligonucleotide sequence or antibody. A binding event can be monitored by using another spectral code as a reporter. Generally, the reporter code is a single color. When individual particles are observed, the probe—and by extension the target—are indicated by the barcode, while a binding event is signaled through the reporter code. The general concept for a hybridization assay is illustrated in Figure 7.14.

A number of materials have been used to fabricate microparticles, including latexes [106–110], chitosan [111], sol–gel composites [112], and polyelectrolyte capsules [113,114]. Polystyrene and other latex microparticles are perhaps the most widely used matrices for organic fluorophores and QDs for barcoding applications. Multicolor QD-encoded microspheres have been applied successfully to hybridization assays. For example, blue–green–red-encoded polystyrene microsphere–oligonucleotide conjugates and single-molecule spectroscopy have been used to conduct simple hybridization assays [110]. Three probe sequences with unique optical codes (1 : 1 : 1, 1 : 2 : 1, 2 : 1 : 1) and “indigo”-labeled targets were found to be successful in identifying the probe–target combination and the presence of complementary target. The target label had to emit a shorter wavelength than the blue QD to allow efficient simultaneous excitation of the reporter label and the three QDs with a single source. Nonspecific adsorption was avoided by passivating the microsphere with bovine

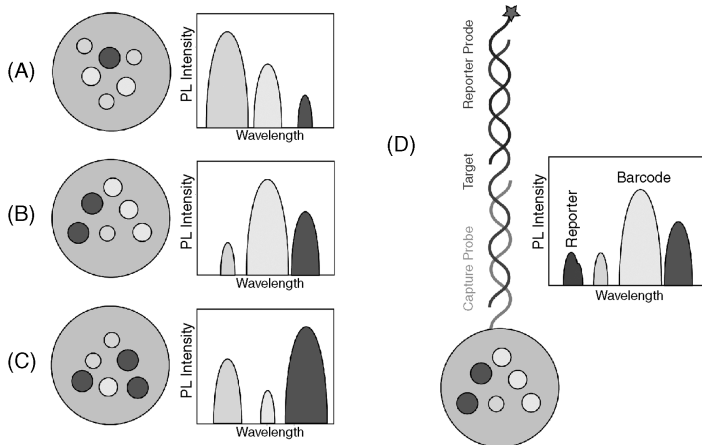


FIGURE 7.14 Spectral encoding is possible using different combinations of green, yellow, and red QDs within microparticles. The green QDs are illustrated as the smallest particles in the illustration; red QDs are the largest. Three different codes and the corresponding spectral signatures are shown in parts (A) to (C). As illustrated in (D), a unique code can be associated with a certain probe. This code, in combination with the reporter probe, can confirm the binding and identity of target by observation of individual microparticles.

serum albumin (BSA). The nonspecific adsorption of any molecule bearing a reporter label will yield a false positive in the analysis. At a more sophisticated level, QD-encoded latex microspheres have been used to discriminate single nucleotide polymorphisms (SNPs) by labeling PCR amplicons of genomic DNA with a three-color scheme [106]. The latex microspheres were coded with combinations of green and yellow QDs (1 : 1, 2 : 1, 1 : 2, 2 : 2) and conjugated with probe oligonucleotides complementary to the amplicon of interest. The PCR primers used to produce the amplicons were labeled with biotin, which was later coupled to streptavidin–Cy5 conjugate. The green and yellow QD spectral signature was indicative of the probe sequence, while the Cy5 signature was indicative of hybridization. The extent of hybridization for a given amplicon was easily measured by flow cytometry.

Genetic analyses can also be done by encoding magnetic beads with different four-color ratios and using coincidence analysis [115]. Magnetic beads incorporating QDs with peak PL wavelengths at 525, 545, 565, and 585 nm were coupled to probe oligonucleotides. Complementary RNA was biotinylated and conjugated to a streptavidin coated red or to infrared emitting QD as a reporter. Hybridization brought the two encoded beads and reporter together for a coincidence analysis. The QD optical code indicated the probe sequence, and the intensity of QD PL reported indicated the amount of cRNA. A limit of detection of 10^6 targets was obtained without T7 amplification, and an LOD of less than 10^4 targets was obtained with one round of T7 amplification. This compares with an LOD of 10^5 for high-density microarrays. The technique has the potential to analyze 455 genes simultaneously, with better speed, sensitivity, and lower sample quantity than those of gene chips.

7.6 FLUORESCENCE RESONANCE ENERGY TRANSFER AND QUANTUM DOT BIOSENSING

A variety of bioprobes have been constructed using a FRET format, including those for maltose [65], oligonucleotides [9,59,60,116,117], proteases [118,119], streptavidin (as a model protein/protein-binding assay) [120,121], and TNT [122].

7.6.1 Maltose-Binding Protein

A number of valuable research contributions to the development of QD-FRET-based bioprobes and biosensors have been made by Medintz, Mattoussi, and co-workers [1,8,51,56,63,65,66,105,119,122–127]. Much of the work has focused on the use QD-MBP conjugates as a model system. These conjugates have been prepared by incorporation of a positively charged leucine-zipper on MBP [64] for electrostatic assembly, or more commonly by incorporating a pentahistidine tag to drive self-assembly by affinity interactions with zinc [65,123,124]. In one study, MBP-QD conjugate was made to function as a probe for maltose, based on the affinity of MBP for this sugar [65]. MBP is also able to bind cyclodextrin, but with less affinity than maltose. As shown in Figure 7.15(D), probe operation was based on displacement of quencher labeled cyclodextrin from the MBP-binding site in the presence of maltose. Bound cyclodextrin quencher reduced QD emission via FRET. However, upon being displaced by maltose, a concentration-dependent recovery of QD fluorescence was observed. In an alternative format, QD PL was quenched by a two-step relay, with energy being transferred from a QD with PL at 530 nm to Cy3-labeled MBP to Cy3.5-labeled cyclodextrin. Such a scheme is of practical value since FRET is strongly distance dependent. Compared with organic dyes, QDs are quite large and are can be made substantially larger by surface chemistries such as proteins and polymers. This potentially limits energy transfer efficiency. The introduction of a relay station keeps transfer efficiencies high. This particular study also highlighted another important consideration in such schemes: There was a tenfold difference in the dissociation constant for MBP between the solution and the surface of the QD. It is always important to consider potential perturbation induced by the presence of QDs, which, because of their larger size, are likely to be more severe than observed with organic fluorophores. Other considerations, such as the organization and orientation of proteins or other biomolecules conjugated to QDs, are equally important. Through a set of FRET-based distance measurements that were equivalent to a triangulation process, it was found that MBP adopted a preferred orientation on the surface of the QD, where its pentahistidine tail was close to the surface and its binding site was exposed to solution [123]. Although MBP clearly retained an orientation that was amenable to its function, there was some apparent perturbation of its function. Surely, this is not limited to MBP, and is more generally applicable to all QD-protein bioconjugates.

The MBP-QD scheme has been redesigned to be reagentless by covalently coupling a Cy3 acceptor dye to an allosterically sensitive site on the protein [125]. Binding of maltose resulted in a conformational change that altered the environment

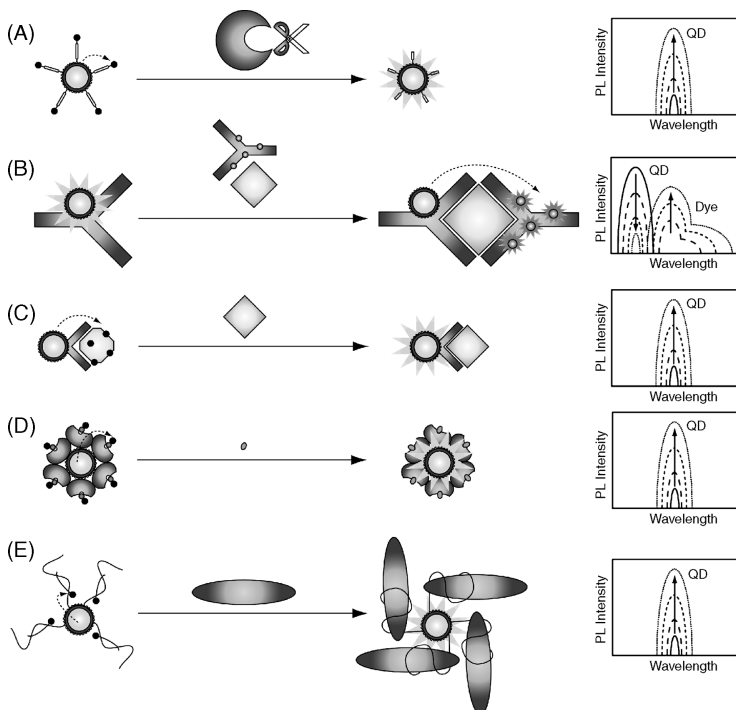


FIGURE 7.15 FRET-based bioprobe strategies: (A) protease detection based on peptide-bound quenchers and QD PL recovery; (B) sandwich immunoassay based on FRET-sensitized acceptor emission; (C) detection of TNT as an analyte by QD PL recovery following the displacement of a quencher-labeled analog from an antibody-binding site; (D) detection of maltose as an analyte by QD PL recovery following the displacement of a quencher-labeled cyclodextrin from the binding site of MBP; (E) detection of thrombin as an analyte by QD PL recovery following the displacement of a quencher-labeled oligonucleotides upon thrombin binding to the secondary structure of the aptamer.

around the dye to the point where the fluorescence emission was quenched. Thus, labeling at the allosteric site performs the same function as the cyclodextrin–quencher described above. However, in contrast to the cyclodextrin–quencher system, where maltose binding increases QD PL, the analytical parameter is the quenching of Cy3 caused by the maltose binding. This maltose concentration–dependent quenching could be used to detect maltose in the range 100 μM to 10 mM. Although this assay could be performed by direct excitation of the Cy3 at the allosteric site on MBP, the FRET relay via the QD reduces photobleaching and provides more versatility in terms of excitation wavelength.

As described previously, the MBP–QD assembly is an effective solution-phase probe for maltose. In this sense the MBP–QD assembly is a bioprobe. However, the assembly has been immobilized on a surface and has been shown to be functional [126,127]. Immobilization is essential to creating a reusable system that can function

as a biosensor. Early studies used Neutravidin-coated glass substrates to immobilize QDs [126]. The QDs were incubated with a mixture of MBP and avidin to create a mixed surface coating by metal affinity and electrostatic-driven self-assembly. Biotinylated MBP or antibodies could then be used to as a bridge between the substrate and the protein-modified QD. The MBP-bridged system was estimated to place the QD 33 nm from the surface, while the antibody-bridged system was estimated to place the QD 40 nm from the surface. A later study immobilized QDs using a rigid rodlike β -strand-based peptide. The peptide, referred to as YEHK_{*m*}, has tyrosine (Y), glutamic acid (E), histidine (H), and lysine (K) residues located at the turns, where *m* is the number of repeats. For immobilization experiments, the C-terminus was modified with a hexahistidine sequence, and the N-terminus was biotinylated. The YEHK protein was captured on a Neutravidin-coated substrate, and the histidine tail was used to capture DHLA QDs. MBP-His₅ could be attached to the YEHK-immobilized QDs and a maltose-binding assay was done with a Cy3 label at the allosteric site. The limit of detection was found to be substantially higher (1 mM) than that of the solution-phase analog, and the dynamic range was smaller. It is thought that steric factors might be a major cause of the reduced performance. Nonetheless, the combination of immobilization of the QD-MBP assembly and labeling at the allosteric site for reagentless operation results in a true biosensor for maltose.

7.6.2 Nucleic Acids

A FRET-based sandwich assay for nucleic acids has been developed on the basis of QD-oligonucleotide conjugates and single-molecule spectroscopy [117]. One biotinylated probe complementary to half the target sequence was bound to a streptavidin-QD conjugate; the second probe was complementary to the remaining half of the target and was fluorescently labeled. When the two probes hybridized with target, the organic acceptor dye and QD were brought in close proximity to one another. FRET was observed between the QD and acceptor dye via single-molecule spectroscopy. The choice of a QD with peak PL at 605 nm and Cy5 as a FRET pair minimizes crosstalk between the two detection channels, albeit at the expense of some reduced spectral overlap. The method of detection is via photon bursts as the sample passes through a diffraction-limited laser detection volume inside a microcapillary. Figure 7.16(B) illustrates the operation of this bioprobe. The bioprobe was found to perform better than molecular beacons, achieving a detection limit of 4.8 fM, compared to 0.48 pM for molecular beacons. The sensors were also combined with an oligonucleotide ligation assay to achieve single-base-pair discrimination in the analysis of Kras point mutations in clinical samples from patients with ovarian serous borderline tumors. Using FRET-sensitized Cy5 photon bursts for detection of ligation products simplified the analysis by avoiding the standard use of gel separations or washing steps to remove unbound probes.

In our lab we have developed an approach for the simultaneous detection of two target nucleic acid sequences based on the use of QDs as energy donors in FRET [9]. Two colors of MAA QDs are conjugated with amine-terminated oligonucleotides via EDC coupling. Upon hybridization with acceptor dye labeled complementary

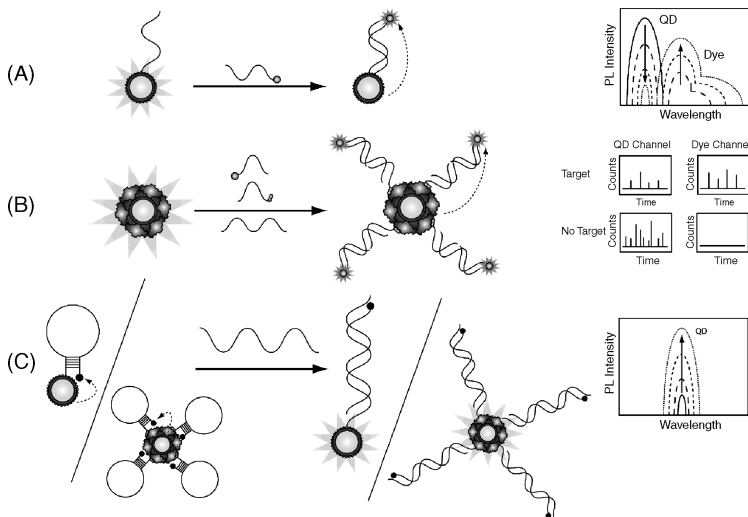


FIGURE 7.16 Bioprobe strategies for nucleic acids based on the use of QDs as energy donors in FRET: (A) signaling of hybridization based on FRET-sensitized acceptor emission and the MAA surface chemistry; (B) signaling of hybridization based on FRET-sensitized acceptor emission in a sandwich format, using single-molecule spectroscopy and streptavidin surface chemistry; (C) molecular beacons based on the recovery of QD PL with the removal of FRET-based quenching upon hybridization, using both the MAA and streptavidin surface chemistries.

material, the proximity between the QD and dye results in FRET sensitized acceptor emission. This is illustrated for a single FRET pair in Figure 7.16(A). A green QD with peak PL at 526 nm was paired with Cy3 as an acceptor and a labeled oligonucleotide sequence diagnostic of spinal muscular atrophy. A red QD with peak PL at 606 nm was paired with Alexa Fluor 647 as an acceptor and a labeled oligonucleotide sequence diagnostic of *E. coli*.

Conjugation of oligonucleotides resulted in an approximate twofold increase in the QD luminescence. Single-color experiments demonstrated that for a $1\ \mu\text{M}$ concentration of green QD probes, the limit of detection was 40 nM. Similarly, for a $0.06\ \mu\text{M}$ concentration of red QD probes, the limit of detection was 12 nM. FRET efficiencies of 52% and 6.7% were observed for the two systems. Due to the broad absorption spectra of QDs, multiplexed analysis is possible using a single excitation wavelength and without the use of discrete sensing elements or single-molecule spectroscopy. Although QD-encoded microbeads offer similar advantages, they require the use of flow cytometry for single-bead spectroscopy. Although simultaneous and independent detection of the two sequences was possible, the signals were found to be reduced compared to single-color experiments. This was due to the nonspecific cross-adsorption of target sequences onto the wrong color QD. In single-color experiments, the steady-state FRET signal was lower for noncomplementary oligonucleotides than for complementary target. Nonetheless, adsorption remained a significant issue.

To alleviate this difficulty, a dye sensitive to dsDNA could be used as an acceptor. Ethidium bromide (EB) is an intercalating dye that undergoes a quantum yield enhancement in the presence of dsDNA. Good selectivity was achieved with this system. It was found that 80% of the signal obtained by the QD–EB system for complementary target in a clean buffer matrix could be obtained in matrices containing a sixfold excess of dA₂₀. Similarly, 100% of the signal could be obtained in matrices containing a 10-fold excess of salmon sperm DNA. The trade-off is a lower limit of detection, due to reduced FRET efficiency and higher background fluorescence from EB.

Another strategy for the detection of nucleic acids has been the use of QDs in a molecular beacon (MB) format, with either an organic quencher such as DABCYL [116] or, conceivably, gold nanoparticles, which have been shown to quench QDs [118]. The MB concept is shown in Figure 7.16(C). In the case of the DABCYL–QD MB, MAA–QDs were coupled with 5' amine–modified and 3' DABCYL–modified hairpins via EDC. In the presence of complementary target, the PL intensity increased sixfold. A minimal increase was observed for noncomplementary target. Although roughly 10-fold changes in fluorescence intensity are typical for organic dye MBs, the QD MB showed no decrease in PL over 10 minutes of continuous illumination, whereas a 6-FAM MB showed a 15% decrease. In some applications the greater photostability may be more important than the lower sensitivity. Molecular beacons have also been developed using streptavidin–QD conjugates [128]. Three colors of QD—with peak PL at 515, 565, and 605 nm—were coupled with Black Hole Quencher 2 (BHQ2) as molecular beacons. The number of hairpins per QD was estimated as 12 to 15, yielding FRET efficiencies in the range 35 to 61%. Upon target binding, roughly 80% increases in QD PL were observed. Some single-nucleotide polymorphism discrimination was achieved.

7.6.3 Proteins, Proteases, and Immunoassays

Aptamer chemistry has been used for the development of FRET-based assays for the detection of protein. For example, thrombin-binding aptamer (TBA) has been conjugated to QDs for the analysis of thrombin [62]. In this arrangement, the aptamer probe is initially bound to a short complementary sequence labeled with an Eclipse quencher dye. However, in the presence of thrombin, the short sequence is displaced in favor of aptamer–thrombin binding, yielding an increase in QD emission. This is illustrated in Figure 7.15(E). In this system, the QD diameter is estimated to be 15 nm and the quencher dye is estimated to be 7.5 nm from the QD core. Oligonucleotides synthesized with one and two quencher moieties yielded 75% and 95% quenching, respectively. Upon addition of thrombin, a 19-fold increase in PL intensity was observed. This compares with the 12-fold increase observed with the organic dye analog of this system.

A protease-sensitive QD–FRET construct has been developed to operate on a similar principle [118]. The peptide sequence targeted by the protease of interest is

labeled with a gold nanoparticle and linked to the surface of the QD. In this case, the target protease is collagenase and the peptide sequence was collagenase degradable. The QD was modified with carboxyl groups and 750 Da PEG. The gold NP/QD ratio was 6:1, and 71% quenching was observed. After incubating for 47 hours in the presence of 0.2 mg/mL collagenase, a 51% luminescence increase was observed. A FRET-based protease bioprobe has also been designed on a DHLA QD platform using an organic dark quencher, QXL-520 [119]. Conjugated peptides were designed to have a hexahistidine sequence at the N-terminus of the sequence, a rigid helical region separating the hexahistidine residues from the protease recognition and cleavage site, and a C-terminal cysteine thiol for dye attachment. The peptide maintained the quencher in close proximity to the QD, resulting in QD PL quenching via FRET. The target enzymes were caspase-1, thrombin, collagenase, and chymotrypsin. In the presence of the target protease, the peptide sequence was cleaved. The dark quencher was no longer bound to the QD and FRET ceased, resulting in restoration of the QD PL. To avoid steric complications, 8 to 10 peptides were used per QD. Proteolytic assays for each enzyme and a thrombin inhibition assay for thrombin inhibitor were done. Although it was found that the Michaelis constant for caspase was 50% lower than reported in the literature, Michaelis constants for collagenase, chymotrypsin, and thrombin were in reasonable agreement. Again, it is apparent that much like at bulk interfaces, interactions between the enzymes and the surface of QDs have the potential to perturb their structure and function. Figure 7.15(A) shows the general concept of the protease–QD–FRET assay.

An immunoassay developed for the detection of TNT also uses the idea of FRET-mediated PL recovery of a QD [122]. Antibodies toward TNT are appended with a histidine tag and self-assembled on the surface of a CdSe–ZnS QD. A quencher-labeled TNT analog is introduced and occupies the antibody-binding site, quenching the QD via FRET. As shown in Figure 7.15(C), the addition of TNT displaces the analog, resulting in a concentration-dependent increase in QD PL. This probe was tested against soil sample extracts and found to yield the same trend as an HPLC analysis, but somewhat lower absolute values for the quantity of TNT. The lowest detectable level of TNT was 20 ng/mL. The system showed a largely nonlinear response but was loglinear between 0.3 and 10 $\mu\text{g/mL}$. Fourfold-smaller signals were observed for the TNT analogs tetryl, 2A, and 4,6-DNT, and negligible signals were observed for 2,6-DNT.

A series of homogeneous FRET-based binding assays have been developed for biotin, fluorescein, and cortisol [129]. Amine-modified QDs were conjugated to these haptens via EDC and NHS. Biotin binding could be detected via AlexaFluor dye-labeled streptavidin or AlexaFluor-labeled monoclonal antibiotin antibody. The QD–dye proximity induced by binding yielded FRET-sensitized AlexaFluor emission. Rabbit anti-fluorescein and monoclonal anticortisol antibody were also labeled with AlexaFluor dyes. The free haptens could be detected with competitive binding assays, where fixed amounts of QD–hapten conjugates and AlexaFluor-labeled antibodies were mixed with variable amounts of free hapten. Detection limits of 25 nM for free fluorescein and 2 nM for free cortisol were obtained. As shown

in Figure 7.15(B), FRET-based fluoroimmunoassays have also been developed in sandwich format using AlexaFluor-labeled antibodies [130]. A QD with peak PL at 565 nm was conjugated to the hinge of a monoclonal antibody for estrogen receptor β . A polyclonal antibody was labeled with AlexaFluor 568 or 633 to complete the sandwich. The proximity induced by the binding results in FRET sensitized AlexaFluor fluorescence. FRET efficiencies of 30% and 20% were observed for the two dyes. A dynamic range of 0.05 to 50 nM was achieved.

7.7 SUMMARY

QDs have a number of unique optical properties that are advantageous for biosensors and bioprobes based on fluorescence. Foremost among these are their size-tunable absorption and PL spectra, as well as their good photostability. The absorption spectra are broad and the PL spectra are narrow and symmetric, making QDs particularly well suited for multiplexing applications. In general, the same synthetic protocol for QD production can be used to produce a full spectrum of QD colors, further increasing their versatility. Most of the optical properties of QDs arise from quantum confinement effects, which occur when the dimensions of the semiconductor nanocrystals are reduced below the preferred separation of an exciton in that material.

QDs are especially interesting in that they can act as both transduction elements and interfaces for biorecognition elements. A variety of chemistries are available for aqueous solubilization of QDs, including ligand exchange, silica coatings, and polymer coatings. These chemistries also allow for conjugation of biomolecules such as proteins, antibodies, and nucleic acids. It is important to realize that the QD and associated surface chemistry are not necessarily passive. While both can potentially perturb the structure and function of conjugated biomolecules, the latter can also affect the physical and optical properties of the QD itself. Nonetheless, QDs have been used successfully in the development of biosensors and bioprobes based on fluorescence. Applications include the use of QDs as labels for microarrays, immunoassays, FISH, and spectral barcode-based multiplexing. A large number of FRET-based strategies have also been developed for the detection of nucleic acid, proteins, haptens, and other small molecules. Although research in this area is expanding rapidly, much remains to be done. The majority of work to date has been in the area of single-use bioprobes. Issues such as the immobilization, reusability, and long-term stability of QD-biomolecule architectures must be addressed to create true biosensors. Undoubtedly, the future of QDs in this area is promising.

Acknowledgments

We are grateful to the Natural Sciences and Engineering Research Council of Canada (NSERC) for financial support of our research. W.R.A. is also grateful to NSERC for provision of a graduate fellowship.

REFERENCES

1. Medintz IL, Uyeda HT, Goldman ER, Mattoussi H. Quantum dot bioconjugates for imaging, labelling and sensing. *Nat. Mater.* 2005;4:435–446.
2. Gao X, Yang L, Petros JA, Marshall FF, Simons JW, Nie S. In vivo molecular and cellular imaging with quantum dots. *Curr. Opin. Biotechnol.* 2005;16:63–72.
3. Smith AM, Gao X, Nie S. Quantum dot nanocrystals for in vivo molecular and cellular imaging. *Photochem. Photobiol.* 2004;80:377–385.
4. Parak WJ, Pellegrino T, Plank C. Labelling of cells with quantum dots. *Nanotechnology.* 2005;16:R9–R25.
5. Pinaud F, Michalet X, Bentolila LA, et al. Advances in fluorescence imaging with quantum dot bio-probes. *Biomaterials.* 2006;27:1679–1687.
6. Bruchez M, Morronne M, Gin P, Weiss S, Alivisatos AP. Semiconductor nanocrystals as fluorescent biological labels. *Science.* 1998;281:2013–2016.
7. Chan WCW, Nie S. Quantum dot bioconjugates for ultrasensitive nonisotopic detection. *Science.* 1998;281:2016–2018.
8. Medintz IL, Clapp AR, Mattoussi H, Goldman ER, Fisher B, Mauro JM. Self-assembled nanoscale biosensors based on quantum dot FRET donors. *Nat. Mater.* 2003;2:630–638.
9. Algar WR, Krull UJ. Towards multi-colour strategies for the detection of oligonucleotide hybridization using quantum dots as energy donors in fluorescence resonance energy transfer (FRET). *Anal. Chim. Acta.* 2007;581:193–201.
10. Jin WJ, Fernandez-Arguelles MT, Costa-Fernandez JM, Pereiro R, Sanz-Medel A. Photoactivated luminescent CdSe quantum dots as sensitive cyanide probes in aqueous solutions. *Chem. Commun.* 2005;883–885.
11. Chen Y, Rosenzweig Z. Luminescent CdS quantum dots as selective ion probes. *Anal. Chem.* 2002;74:5132–5138.
12. Bimberg D, Ledentsov N. Quantum dots: lasers and amplifiers. *J. Phys. Condensed Matter.* 2003;15:R1063–R1076.
13. Bhattacharya P, Ghosh S, Stiff-Roberts AD. Quantum dot opto-electronic devices. *Annu. Rev. Mater. Res.* 2004;34:1–40.
14. Goldhaber-Gordon D, Montemerlo MS, Love JC, Opiteck GJ, Ellenbogen JC. Overview of nanoelectronic devices. *Proc. IEEE.* 1997;85:521–540.
15. Pettigrew KA, Liu Q, Power PP, Kauzlarich SM. Solution synthesis of alkyl- and alkyl/alkoxy-capped silicon nanoparticles via oxidation of Mg₂Si. *Chem. Mater.* 2003;15:4005–4011.
16. Warner JH, Hoshino A, Yamamoto AK, Tilley RD. Water-soluble photoluminescent silicon quantum dots. *Angew. Chem. Int. Ed.* 2005;44:4550–4554.
17. Bailey RE, Nie S. Alloyed semiconductor quantum dots: tuning the optical properties without changing particle size. *J. Am. Chem. Soc.* 2003;125:7100–7106.
18. Lee H, Holloway PH, Yang H, Hardison L, Kleiman VD. Synthesis and characterization of colloidal ternary ZnCdSe semiconductor nanorods. *J. Chem. Phys.* 2006;125:164711.
19. Wang W, Germanenko I, El-Shall MS. Room-temperature synthesis and characterization of nanocrystalline CdS, ZnS, and Cd_xZn_{1-x}S. *Chem. Mater.* 2002;14:3028–3033.
20. Li Y, Ye M, Yang C, Li X, Li Y. Composition- and shape-controlled synthesis and optical properties of Zn_xCd_{1-x}S alloyed nanocrystals. *Adv. Funct. Mater.* 2005;15:433–441.

21. Gao X, Cui Y, Levenson RM, Chung LWK, Nie S. In vivo cancer targeting and imaging with semiconductor quantum dots. *Nat. Biotechnol.* 2004;22:969–976.
22. Hohng S, Ha T. Single-molecule quantum-dot fluorescence resonance energy transfer. *ChemPhysChem.* 2005;6:956–960.
23. Warburton RJ. Self-assembled semiconductor quantum dots. *Contemp. Phys.* 2002;43:351–364.
24. Dabbousi BO, Rodriguez-Viejo J, Mikulec FV, et al. *J. Phys. Chem. B.* 1997;101:9463–9475.
25. Hines MA, Guyot-Sionnest P. Synthesis and characterization of strongly luminescing ZnS-capped CdSe nanocrystals. *J. Phys. Chem.* 1996;100:468–471.
26. Murray CB, Norris DJ, Bawendi MG. Synthesis and characterization of nearly monodisperse CdE (E = S, Se, Te) semiconductor nanocrystallites. *J. Am. Chem. Soc.* 1993;115:8706–8715.
27. Yu K, Singh S, Patrito N, Chu V. Effect of reaction media on the growth and photoluminescence of colloidal CdSe nanocrystals. *Langmuir.* 2004;20:11161–11168.
28. Yu K, Zaman B, Singh S, Wang D, Ripmeester JA. The effect of dispersion media on photoluminescence of colloidal CdSe nanocrystals synthesized from TOP. *Chem. Mater.* 2005;17:2552–2561.
29. Yu K, Zaman B, Romanova S, Wang D, Ripmeester JA. Sequential synthesis of type II colloidal CdTe/CdSe core-shell nanocrystals. *Small.* 2005;1:332–338.
30. Xu Y, Cai H, He PG, Fang YZ. Probing DNA hybridization by impedance measurement based on CdS–oligonucleotide nanoconjugates. *Electroanalysis.* 2004;16:150–155.
31. Zhu N, Zhang A, Wang A, He P, Fang Y. Lead sulfide nanoparticle as oligonucleotides labels for electrochemical stripping detection of DNA hybridization. *Electroanalysis.* 2005;15:577–582.
32. Liu M, Shi G, Zhang L, Cheng Y, Jin L. Quantum dots modified electrode and its application in electroanalysis of hemoglobin. *Electrochem. Commun.* 2006;8:305–310.
33. Kuma A, Mandale AB, Sastry M. Phase transfer of aqueous CdS nanoparticles by coordination with octadecanethiol molecules present in nonpolar organic solvents. *Langmuir.* 2000;16:9299–9302.
34. Wang J, Liu G, Rivas G. Encoded beads for electrochemical identification. *Anal. Chem.* 2003;75:4667–4671.
35. Wang J, Liu G, Polsky R, Merkoci A. Electrochemical stripping detection of DNA hybridization based on cadmium sulfide nanoparticle tags. *Electrochem. Commun.* 2002;4:722–726.
36. Kortan AR, Hull R, Opila RL, et al. *J. Am. Chem. Soc.* 1990;112:1327–1332.
37. Steigerwald ML, Alivisatos AP, Gibson JM, et al. Surface derivatization and isolation of semiconductor cluster molecules. *J. Am. Chem. Soc.* 1988;110:3046–3050.
38. Granot E, Patolsky F, Willner I. Electrochemical assembly of a CdS semiconductor nanoparticle monolayer on surfaces: structural properties and photoelectrochemical applications. *J. Phys. Chem. B.* 2004;108:5875–5881.
39. Willner I, Patolsky F, Wasserman J. Photoelectrochemistry with controlled DNA–cross-linked CdS nanoparticle arrays. *Angew. Chem. Int. Ed.* 2001;40:1861–1864.
40. Yoffe AD. Semiconductor quantum dots and related systems: electronic, optical, luminescence and related properties of low dimensional systems. *Adv. Phys.* 2001;50:1–208.

41. Wang Y, Herron N. Nanometer-sized semiconductor clusters: materials synthesis, quantum size effects, and photophysical properties. *J. Phys. Chem.* 1991;95:525–532.
42. Mizel A, Cohen ML. Electronic energy levels in semiconductor nanocrystals: a Wannier function approach. *Phys. Rev. B.* 1997;56:6736–6741.
43. Alivisatos AP. Semiconductor clusters, nanocrystals, and quantum dots. *Science.* 1996;271:933–937.
44. Alivisatos AP. Perspectives on the physical chemistry of semiconductor nanocrystals. *J. Phys. Chem.* 1996;100:13226–13239.
45. Murphy CJ, Coffey JL. Quantum dots: a primer. *Appl. Spectrosc.* 2002;56:16A–27A.
46. Brus LE. Electron–electron and electron–hole interactions in small semiconductor crystallites: the size dependence of the lowest excited electronic state. *J. Chem. Phys.* 1984;80:4403–4409.
47. Sapra S, Shanthi N, Sarma DD. Realistic tight-binding model for the electronic structure of II–VI semiconductors. *Phys. Rev. B.* 2002;66:205202.
48. Sapra S, Sarma DD. Evolution of the electronic structure with size in II–VI semiconductor nanocrystals. *Phys. Rev. B.* 2004;69:205304.
49. Kloepfer JA, Bradforth SE, Nadeau JL. Photophysical properties of biologically compatible CdSe quantum dot structures. *J. Phys. Chem. B.* 2005;109:9996–10003.
50. Algar WR, Krull UJ. Luminescence and stability of aqueous thioalkyl acid capped CdSe/ZnS quantum dots correlated with ligand ionization. *ChemPhysChem.* 2007;8:561–568.
51. Uyeda HT, Medintz IL, Jaiswal JK, Simon SM, Mattoussi H. Synthesis of compact multidentate ligands to prepare stable hydrophilic quantum dot fluorophores. *J. Am. Chem. Soc.* 2005;127:3870–3878.
52. Jiang W, Mardiyani S, Fischer H, Chan WCW. Design and characterization of lysine cross-linked mercapto-acid biocompatible quantum dots. *Chem. Mater.* 2006;18:872–878.
53. Aldana J, Lavelle N, Wang Y, Peng X. Size-dependent dissociation pH of thiolate ligands from cadmium chalcogenide nanocrystals. *J. Am. Chem. Soc.* 2005;127:2496–2504.
54. Aldana J, Wang YA, Peng X. Photochemical instability of CdSe nanocrystals coated by hydrophilic thiols. *J. Am. Chem. Soc.* 2001;123:8844–8850.
55. Kim S, Bawendi MG. Oligomeric ligands for luminescent and stable nanocrystal quantum dots. *J. Am. Chem. Soc.* 2003;125:14652–14653.
56. Pons T, Uyeda HT, Medintz IL, Mattoussi H. Hydrodynamic dimensions, electrophoretic mobility, and stability of hydrophilic quantum dots. *J. Phys. Chem. B.* 2006;110:20308–20316.
57. Leatherdale CA, Bawendi MG. Observation of solvatochromism in CdSe colloidal quantum dots. *Phys. Rev. B.* 2001;63:165315.
58. Algar WR, Zhou Y, Zeng J, Krull UJ. Towards quantum dot and FRET-based optical DNA biosensor technology: surface chemistry and photoluminescence of CdSe/ZnS and Si quantum dots. *Proc. SPIE.* 2007;67960Q:1–12.
59. Gill R, Willner I, Shweky I, Banin U. Fluorescence resonance energy transfer in CdSe/ZnS-DNA conjugates: probing hybridization and DNA cleavage. *J. Phys. Chem. B.* 2005;109:23715–23719.

60. Zhou D, Piper JD, Abell C, Klenerman D, Kang DJ, Ying L. Fluorescence resonance energy transfer between a quantum dot donor and a dye acceptor attached to DNA. *Chem. Commun.* 2005;4807–4809.
61. Gill R, Patolsky F, Katz E, Willner I. Electrochemical control of the photocurrent direction in intercalated DNA/CdS nanoparticle systems. *Angew Chem. Int. Ed.* 2005;44:4554–4557.
62. Levy M, Carter SF, Ellington AD. Quantum-dot aptamer beacons for the detection of proteins. *ChemBioChem.* 2005;6:2163–2166.
63. Goldman ER, Medintz IL, Hayhurst A, et al. Self-assembled luminescent CdSe–ZnS quantum dot bioconjugates prepared using engineered polyhistidine terminated proteins. *Anal. Chim. Acta.* 2005;534:63–67.
64. Mattoussi H, Kuno MK, Goldman ER, et al. Self-assembly of CdSe–ZnS quantum dot bioconjugates using an engineered recombinant protein. *J. Am. Chem. Soc.* 2000;122:12142–12150.
65. Medintz IL, Clapp AR, Mattoussi H, Goldman ER, Fisher B, Mauro JM. Self-assembled nanoscale biosensors based on quantum dot FRET donors. *Nat. Mater.* 2003;2:630–638.
66. Pons T, Medintz IL, Wang X, English DS, Mattoussi H. Solution-phase single quantum dot fluorescence resonance energy transfer. *J. Am. Chem. Soc.* 2006;128:15324–15331.
67. Algar WR, Krull UJ. Adsorption and hybridization of oligonucleotides on mercaptoacetic acid-capped CdSe/ZnS quantum dots and quantum dot–oligonucleotide conjugates. *Langmuir.* 2006;22:11346–11352.
68. Gerion D, Pinaud F, Williams SC, et al. Synthesis and properties of biocompatible water-soluble silica-coated CdSe/ZnS semiconductor quantum dots. *J. Phys. Chem. B.* 2001;105:8861–8871.
69. Parak WJ, Gerion D, Zanchet D, et al. Conjugation of DNA to silanized colloidal semiconductor nanocrystalline quantum dots. *Chem. Mater.* 2002;14:2113–2119.
70. Selvan ST, Patra PK, Ang CY, Ying JY. Synthesis of silica-coated semiconductor and magnetic quantum dots and their use in the imaging of live cells. *Angew. Chem. Int. Ed.* 2007;46:2448–2452.
71. Wolcott A, Gerion D, Visconte M, et al. Silica-coated CdTe quantum dots functionalized with thiols for bioconjugation to IgG proteins. *J. Phys. Chem. B.* 2006;110:5779–5789.
72. Bakalova R, Zhelev Z, Aoki I, Ohba H, Imai Y, Kanno I. Silica-shelled single quantum dot micelles as imaging probes with dual or multimodality. *Anal. Chem.* 2006;78:5925–5932.
73. Graf C, Dembski S, Hofmann A, Ruhl E. A general method for the controlled embedding of nanoparticles in silica colloids. *Langmuir.* 2006;22:5604–5610.
74. Luccardini C, Tribet C, Vial F, Marchi-Artzner V, Dahan M. Size, charge, and interactions with giant lipid vesicles of quantum dots coated with an amphiphilic macromolecule. *Langmuir.* 2006;22:2006.
75. Pellegrino T, Manna L, Kudera S, et al. Hydrophobic nanocrystals coated with an amphiphilic polymer shell: a general route to water soluble nanocrystals. *Nano Lett.* 2005;4:703–707.
76. Nann T. Phase-transfer of CdSe–ZnS quantum dots using amphiphilic hyperbranched polyethylenimine. *Chem. Commun.* 2005;1735–1736.
77. Wu X, Liu H, Liu J, et al. Immunofluorescent labeling of cancer marker Her2 and other cellular targets with semiconductor quantum dots. *Nat. Biotechnol.* 2003;21:41–46.

78. Wang M, Oh JK, Dykstra TE, Lou X, Scholes GD, Winnik MA. Surface modification of CdSe and CdSe/ZnS semiconductor nanocrystals with poly(*N,N*-dimethylaminoethyl methacrylate). *Macromolecules*. 2006;39:3664–3672.
79. Dubertret B, Skourides P, Norris DJ, Noireaux V, Brivanlou AH, Libchaber A. In vivo imaging of quantum dots encapsulated in phospholipid micelles. *Science*. 2002;298:1759–1762.
80. Wang HQ, Huang ZL, Liu TC, et al. A feasible and quantitative encoding method for microbeads with multicolor quantum dots. *J. Fluoresc*. 2007;17:133–138.
81. Cao YC, Liu TC, Hua XF, et al. Quantum dot optical encoded polystyrene beads for DNA detection. *J. Biomed. Opt*. 2006;11:054025.
82. Cao YC, Huang ZL, Liu TC, et al. Preparation of silica encapsulated quantum dot encoded beads for multiplex assay and its properties. *Anal. Biochem*. 2006;351:193–200.
83. Nie Q, Tan WB, Zhang Y. Synthesis and characterization of monodisperse chitosan nanoparticles with embedded quantum dots. *Nanotechnology*. 2006;17:140–144.
84. Sheng W, Kim S, Lee J, Kim SW, Jensen K, Bawendi MG. In-situ encapsulation of quantum dots into polymer microspheres. *Langmuir*. 2006;22:3782–3790.
85. Jin T, Fujii F, Yamada E, Nodaska Y, Kinjo M. Control of the optical properties of quantum dots by surface coating with calix[*n*]arene carboxylic acids. *J. Am. Chem. Soc*. 2006;128:9288–9289.
86. Gerion D, Chen F, Kannan B, et al. Room-temperature single-nucleotide polymorphism and multiallele DNA detection using fluorescent nanocrystals and microarrays. *Anal. Chem*. 2003;75:4766–4772.
87. Liang RQ, Lei W, Li Y, et al. An oligonucleotide microarray for microRNA expression analysis based on labeling RNA with quantum dots and nanogold probe. *Nucleic Acids Res*. 2005;33:e17.
88. Geho D, Lahar N, Gurnani P, et al. Pegylated, streptavidin-conjugated quantum dots are effective detection elements for reverse-phase protein microarrays. *Bioconj. Chem*. 2005;16:559–566.
89. Goldman ER, O'Shaughnessy TJ, Soto CM, et al. Detection of proteins cross-linked within galactoside polyacrylate-based hydrogels by means of a quantum dot fluororeagent. *Anal. Bioanal. Chem*. 2004;380:880–886.
90. Su XL, Li Y. Quantum dot biolabeling coupled with immunomagnetic separation for detection of *Escherichia coli* O157:H7. *Anal. Chem*. 2004;76:4806–4810.
91. Yang L, Li Y. Quantum dots as fluorescent labels for quantitative detection of *Salmonella typhimurium* in chicken carcass wash water. *J. Food Prot*. 2005;68:1241–1245.
92. Sun B, Xie W, Yi G, Chen D, Zhou Y, Cheng J. Microminiaturized immunoassays using quantum dots as fluorescent label by laser confocal scanning fluorescence detection. *J. Immunol. Methods*. 2001;249:85–89.
93. Ding S, Chen J, Jiang H, et al. Application of quantum dot–antibody conjugates for detection of sulfmethazine residue in chicken muscle tissue. *J. Agric. Food Chem*. 2006;54:6139–6142.
94. Yang L, Li Y. Simultaneous detection of *Escherichia coli* O157:H7 and *Salmonella typhimurium* using quantum dots as fluorescence labels. *Analyst*. 2006;131:394–401.
95. Kerman K, Endo T, Tsukamoto M, Chikae M, Takamura Y, Tamiya E. Quantum dot–based immunosensor for the detection of prostate-specific antigen using fluorescence microscopy. *Talanta*. 2007;71:1494–1499.

96. Zhang Q, Zhu L, Feng H, Ang S, Chau FS, Liu WT. Microbial detection in microfluidic devices through dual staining of quantum dots–labeled immunoassay and RNA hybridization. *Anal. Chim. Acta.* 2006;556:171–177.
97. Pathak S, Davidson MC, Silva GA. Characterization of the functional binding properties of antibody conjugated quantum dots. *Nano Lett.* 2007;7:1839–1845.
98. Xiao Y, Barker PE. Semiconductor nanocrystal probes for human metaphase chromosomes. *Nucleic Acids Res.* 2004;32:e28.
99. Wu SM, Zhao X, Zhang ZL, et al. Quantum-dot-labeled DNA probes for fluorescence in situ hybridization (FISH) in the microorganism *Escherichia coli*. *ChemPhysChem.* 2006;7:1062–1067.
100. Ikanovic M, Rudzinski WE, Bruno JG, et al. Fluorescence assay based on aptamer–quantum dot binding to *Bacillus thuringiensis* spores. *J. Fluoresc.* 2007;17: 193–199.
101. Choi JH, Chen KH, Strano MS. Aptamer-capped nanocrystal quantum dots: a new method for label-free protein detection. *J Am. Chem. Soc.* 2006;128:15584–15585.
102. Ji X, Zheng J, Xu J, Rastogi VK, Chen TC, DeFrank JJ, Leblanc RM. (CdSe)ZnS quantum dots and organophosphorus hydrolase bioconjugate as biosensors for detection of paraoxon. *J. Phys. Chem. B.* 2005;109:3793–3799.
103. Ma Y, Yang C, Li N, Yang X. A sensitive method for the detection of catecholamine based on fluorescence quenching of CdSe nanocrystals. *Talanta.* 2005;76:979–983.
104. Aoyagi S, Kudo M. Development of fluorescence change-based, reagent-less optic immunosensor. *Biosens. Bioelectron.* 2005;20:1680–1684.
105. Goldman ER, Clapp AR, Anderson GP, et al. Multiplexed toxin analysis using four colors of quantum dot fluororeagents. *Anal. Chem.* 2004;76:684–688.
106. Xu H, Sha MY, Wong EY, et al. Multiplexed SNP genotyping using the Qbead™ system: a quantum dot-encoded microsphere-based assay. *Nucleic Acids Res.* 2003;31:e43.
107. Yang X, Zhang Y. Encapsulation of quantum nanodots in polystyrene and silica micro-/nanoparticles. *Langmuir.* 2004;20:6071–6073.
108. Gao X, Nie S. Quantum dot-encoded mesoporous beads with high brightness and uniformity: rapid readout using flow cytometry. *Anal. Chem.* 2004;76:2406–2410.
109. Stsiapura V, Sukhanova A, Artemyev M, et al. Functionalized nanocrystal-tagged fluorescent polymer beads: synthesis, physicochemical characterization, and immunolabeling application. *Anal. Biochem.* 2004;334:257–265.
110. Han M, Gao X, Su JZ, Nie S. Quantum-dot-tagged microbeads for multiplexed optical coding of biomolecules. *Nat. Biotechnol.* 2001;19:631–635.
111. Nie Q, Tan WB, Zhang Y. Synthesis of monodisperse chitosan nanoparticles with embedded quantum dots. *Nanotechnology.* 2006;17:140–144.
112. Mokari T, Sertchook H, Aharoni A, Ebenstein Y, Avnir D, Banin U. Nano-Micro: general method for entrapment of nanocrystals in sol–gel-derived composite hydrophobic silica spheres. *Chem. Mater.* 2005;17:258–263.
113. Gaponik N, Radtchenko IL, Sukhorukov GB, Weller H, Rogach AL. Toward encoding combinatorial libraries: charge-driven microencapsulation of semiconductor nanocrystals luminescing in the visible and near IR. *Adv. Mater.* 2002;14: 879–882.
114. Wang D, Rogach AL, Caruso F. Semiconductor quantum dot–labeled microsphere bioconjugates prepared by stepwise self-assembly. *Nano Lett.* 2002;2:857–861.

115. Eastman PS, Ruan W, Doctolero M, et al. Qdot nanobarcode for multiplexed gene expression analysis. *Nano Lett.* 2006;6:1059–1064.
116. Kim JH, Morikis D, Ozkan M. Adaptation of inorganic quantum dots for stable molecular beacons. *Sens. Actuators B.* 2004;102:315–319.
117. Zhang CY, Yeh HC, Kuroki MT, Wang TH. Single-quantum-dot-based DNA nanosensor. *Nat. Mater.* 2005;4:826–831.
118. Chang E, Miller JS, Sun J, et al. Protease-activated quantum dot probes. *Biochem. Biophys. Res. Commun.* 2005;334:1317–1321.
119. Medintz IL, Clapp AR, Brunel FM, et al. Proteolytic activity monitored by fluorescence resonance energy transfer through quantum-dot-peptide conjugates. *Nat. Mater.* 2006;5:581–589.
120. Willard DM, Carillo LL, Jung J, Orden AV. CdSe-ZnS quantum dots as resonance energy transfer donors in a model protein-protein binding assay. *Nano Lett.* 2001;1:469–474.
121. Nagasaki Y, Ishii T, Sunaga Y, Watanabe Y, Otsuka H, Kataoka K. Novel molecular recognition via fluorescent resonance energy transfer using a biotin-PEG/polyamine stabilized CdS quantum dot. *Langmuir.* 2004;20:6396–6400.
122. Goldman ER, Medintz IL, Whitley JL, et al. A hybrid quantum dot-antibody fragment fluorescence resonance energy transfer-based TNT sensor. *J. Am. Chem. Soc.* 2005;127:6744–6751.
123. Medintz IL, Konnert JH, Clapp AR, et al. A fluorescence resonance energy transfer-derived structure of a quantum dot-protein bioconjugate nanoassembly. *Proc. Nat. Acad. Sci. USA.* 2004;101:9612–9617.
124. Medintz IL, Trammell SA, Mattoussi H, Mauro JM. Reversible modulation of quantum dot photoluminescence using a protein-bound photochromic fluorescence resonance energy transfer acceptor. *J. Am. Chem. Soc.* 2004;126:30–31.
125. Medintz IL, Clapp AR, Melinger JS, Deschamps JR, Mattoussi H. A reagentless biosensing assembly based on quantum dot-donor Forster resonance energy transfer. *Adv. Mater.* 2005;17:2450–2455.
126. Sapsford KE, Medintz IL, Golden JP, Deschamps JR, Uyeda HT, Mattoussi H. Surface-immobilized self-assembled protein-based quantum dot nanoassemblies. *Langmuir.* 2004;20:7720–7728.
127. Medintz IL, Sapsford KE, Clapp AR, et al. Designer variable repeat length polypeptides as scaffolds for surface immobilization of quantum dots. *J. Phys. Chem. B.* 2006;110:10683–10690.
128. Kim JH, Chaudhary S, Ozkan M. Multicolour hybrid nanoprobe of molecular beacon conjugated quantum dots: FRET and gel electrophoresis assisted target DNA detection. *Nanotechnology.* 2007;18:195105.
129. Nikiforov TT, Beechem JM. Development of homogeneous binding assays based on fluorescence resonance energy transfer between quantum dots and AlexaFluor fluorophores. *Anal. Biochem.* 2006;357:68–76.
130. Wei Q, Lee M, Yu X, et al. Development of an open sandwich fluoroimmunoassay based on fluorescence resonance energy transfer. *Anal. Biochem.* 2006;358:31–37.

Nanoparticle-Based Delivery and Biosensing Systems: An Example

ALMUDENA MUÑOZ JAVIER and PABLO DEL PINO

Fachbereich Physik, Philipps Universität Marburg, Marburg, Germany

STEFAN KUDERA

Department of New Materials and Biosystems, Max Planck Institute for Metals Research, and Department of Biophysical Chemistry, University of Heidelberg, Stuttgart, Germany

WOLFGANG J. PARAK

Fachbereich Physik, Philipps Universität Marburg, Marburg, Germany

- 8.1 Introduction
- 8.2 Functional colloidal nanoparticles
 - 8.2.1 Short overview of colloidal nanoparticle properties
 - 8.2.2 Synthesis of colloidal nanoparticles
 - 8.2.3 Surface modification
 - 8.2.4 Biocompatibility
- 8.3 Polyelectrolyte capsules as a functional carrier system
- 8.4 Uptake of capsules by cells
 - 8.4.1 Uptake mechanism
 - 8.4.2 Capsule deformation during uptake
 - 8.4.3 Toxicity of capsules
- 8.5 Delivery and sensing with polyelectrolyte capsules
 - 8.5.1 Multifunctional polyelectrolyte capsules as smart delivery vehicles
 - 8.5.2 Multifunctional polyelectrolyte capsules as local sensors
- 8.6 Conclusions

8.1 INTRODUCTION

Richard Feynman, one of the most important visionary pioneer physicists, captured the conceptual importance of nanotechnology with his famous statement

“there is plenty of room at the bottom” in a speech in 1959. His guiding idea was to manipulate individual atoms and molecules in a bottom-up approach to create new materials, designed at the nanometer scale. In light of the ongoing dispute between different areas and disciplines of research (i.e., what is and what is not nanotechnology), we prefer to provide one example and explain its concepts rather than giving a broad overview that would necessitate a definition of nanotechnology.

For decades, clusters of inorganic atoms and molecules in both gas and aqueous phases have attracted researchers [1,2]. Science within this discipline has developed rapidly, culminating in the present-day capability to synthesize crystalline clusters and nanoparticles comprising hundreds to thousands of atoms. The dimensions of such clusters are within the range of a few nanometers. Since in this section we describe water-based delivery and sensing systems, we focus on colloidal clusters or particles. Nanoparticles can be synthesized from a broad variety of materials, where each constituent can lead to characteristic properties [3]. For example, semiconductor nanoparticles such as CdSe are fluorescent, and some metals, metaloxides, and metal alloys, such as Co, Fe₂O₃, and FePt, exhibit magnetic properties.

From the point of basic research, nanoparticles are interesting, since in several cases their properties differ from those of equivalent materials in bulk form [3]. Nanoparticles exhibit properties that are intermediate between those of the bulk material and the corresponding atomic or molecular systems. Obviously, for bulk materials the percentage of atoms at the surface is negligible relative to the overall number of atoms within the material. In contrast, for nanoparticles the number of atoms on the surface is a significant fraction of the overall number of atoms. This fact largely influences the (chemical) surface properties of nanoparticles. In particular, in the field of catalysis, the enhanced surface-to-volume ratio is beneficial. Less obvious are the important physical effects related to the small size of nanoparticles, such as quantum confinement in semiconductor nanoparticles [3], surface plasmon resonance in some metallic nanoparticles [4,5], or superparamagnetism in magnetic nanoparticles [6]. Studying the differences between bulk and nanoparticle materials therefore leads to a more profound understanding of materials.

From a practical point of view, the functional properties of inorganic nanoparticles are interesting for several reasons. First, due to their small size, new properties arise. In addition, inorganic nanoparticles are generally more stable than organic molecules with equivalent functionality. In this section we describe three different types of nanoparticles with distinct functionalities.

Semiconductor nanoparticles are fluorescent, their fluorescence color depending on the quantum confinement effect on their size, so that its fluorescence is always blue-shifted with respect to the fluorescence of the bulk material [7]. In this way, the color of fluorescence can be tuned by the size of the particles, and particles from the same material (but of different size) can generate different colors of light. By selecting materials whose bulk semiconductor bandgap is in the infrared spectrum, nanoparticles comprised of these materials can be generated that cover virtually all

positions of the entire visible spectrum. For example, whereas 5-nm CdSe nanoparticles emit in the red, approx. 2-nm CdSe nanoparticles emit in the green. Compared to organic fluorophores, the emission bands are generally narrower and there is less photobleaching. Semiconductor nanoparticles therefore exhibit special properties due to their small size, and most important, the size dependence of the bandgap, and in several characteristics they are more stable than organic fluorophores. In this way, semiconductor nanoparticles can be seen as small and stable fluorescent light sources that could be used for all types of labeling purposes. Magnetic nanoparticles, on the other hand, can be single-crystalline particles that comprise only a single magnetic domain. Compared to organic magnets, higher magnetic moments can be achieved. Due to their inorganic nature, nanoparticles are also mechanically more stable.

Several noble metals, such as gold and silver, can be optically excited so that the free electrons gain kinetic energy. At a certain resonance frequency, even collective oscillation of the electrons in the external electromagnetic field can be excited. Such electrons are called *surface plasmons*. Eventually, the kinetic energy of the electrons is transferred to the lattice and the metal particles get heated. As the heat of the particles is finally transferred to the surrounding environment, each metal nanoparticle can be seen as an optically triggered nanooven [8,9]. In this way we can have a nanoparticle tool kit comprising fluorescent, magnetic, and heatable particles. Because each particle possesses controllable and defined properties, this pool of particles can be regarded as functional building blocks. The big conceptual advantage of nanobiotechnology is that it not only allows for generating the individual building blocks, but also allows for linking different building blocks together in a defined and tailored way. As glue linking the different (in this case, inorganic) building blocks, organic molecules can be used [10]. Organic molecules—in particular, many biological molecules—can undergo defined reactions that are compatible with biological environments. A strategy for linking two particles would involve the attachment of a ligand molecule to one of the particles and the corresponding receptor molecule to the other particle. The key lock mechanism of biological receptor ligand pairs would result in defined linkage of both particles.

Although such approaches have been demonstrated in the literature, they are still limited by their complexity [11,12]. For this reason, an alternative, less well-controllable but more robust approach is described in this section. As colloidal nanoparticles used as functional building blocks are typically electrically charged, controlled particle assemblies can also be mediated by electrostatic attraction. In this section, polyelectrolyte capsules resembling table tennis balls of only micrometer diameter are described. The walls of these capsules consist of layers of oppositely charged polymers and are thus held together solely by electrostatic forces. Similarly, charged colloidal nanoparticles can therefore be integrated in the walls by electrostatic attraction. Since the capsules are hollow, their cavity can be loaded with specific cargo. In this way, nanoparticle-modified capsules are an example for a nanotechnological carrier system. Functionality is provided by inorganic nanoparticles in the walls of the

capsules; the capsule walls are the organic glue holding the assembly together, and the capsule cavity is available to carry cargo molecules.

In this section we discuss two concepts for nanoparticle-modified capsule carriers. For delivery applications, the cargo desired is loaded into the capsule cavity. The walls of the capsules can be modified with fluorescent, magnetic, and heatable colloidal nanoparticles. By applying an external magnetic field gradient, the capsules with magnetic nanoparticles in their walls can be directed toward the designated area where the cargo is to be released. Due to the fluorescent particles in the capsule walls, this transportation process can be monitored using fluorescence microscopy. At the target location designated, the heatable nanoparticles in the capsule wall can be heated with a light pointer, whereby the heat causes rupture of the capsule wall and subsequent release of the cargo molecules from the capsule cavity. In this way, the nanoparticles in the capsule wall can be used to direct, observe, and open the carrier remotely, resulting in release of the cargo. For sensing applications, on the other hand, the active sensing element can be loaded into the capsule's cavity. Again, magnetic nanoparticles in the capsule walls could be used to direct the sensor capsules to the designated location, and fluorescent particles can be used for observing the capsules. It is important to point out that these two applications should be viewed merely as examples. They are far from covering the complete spectrum of nanotechnologically generated delivery and sensing systems, and many alternative systems have been published [13,14]. These two examples are intended as a demonstration of what is conceptually possible using nanotechnology: the generation of defined functional building blocks and their tailored linkage to a multifunctional assembly on the nanometer scale.

The synthesis and properties of inorganic nanoparticles, which serve as functional building blocks, are described in Section 8.2. In Section 8.3 we give a short overview of how these nanoparticles can be linked easily to multifunctional assemblies by embedding them in the shell of polyelectrolyte capsules. For cellular applications, transport of these multifunctional capsules into cells is required. In Section 8.4 we describe how capsules are incorporated spontaneously by many cell lines. Finally, in Section 8.5, capsule-based delivery and sensing applications are demonstrated.

8.2 FUNCTIONAL COLLOIDAL NANOPARTICLES

8.2.1 Short Overview of Colloidal Nanoparticle Properties

The most intriguing example of the particular properties of colloidal nanoparticles is the fluorescence of semiconductor nanoparticles. By varying only their size, one can tune the color of the emitted light over a considerable range. ZnSe nanoparticles fluoresce in the near-ultraviolet (UV) range [15], CdS nanoparticles span the range from near UV to green [16], CdSe covers almost the entire visible spectrum [16], CdTe nanoparticles fluoresce somewhere between red and near infrared [16], and with PbS,

PbSe, or PbTe, emission wavelengths of up to 2400 nm can be attained [17,18]. One can reach a qualitative understanding for this dependence by considering the electron–hole pair that is generated upon light excitation, called the *exciton*, as an object that is confined to the volume of the nanoparticle. Due to the quantum mechanic confinement energy, exciton energy and nanoparticle size exhibit an inverse relationship. Upon (radiative) recombination of the electron–hole pair, fluorescent light is emitted. Consequently, the wavelength of fluorescence is shorter the smaller the nanoparticle [7]. In a more refined model, nanoparticles are regarded as an intermediate state between simple molecules and bulk material.

The quantum mechanic description of the levels in a molecule is given by the linear combination of the atomic orbitals [19]. In the framework of this description, upon the addition of individual atoms to the molecule, energy bands are formed as an aggregation of many closely spaced energy states, and the energetic distance between the bands decreases with increasing number of atoms in the molecule (i.e., with its size) [7]. The presence of these bands represents one of the major differences between the fluorescent nanoparticles and organic fluorophores. The absorption spectrum of organic fluorophores roughly resembles their fluorescence spectrum. It is shifted only slightly toward higher energies. The absorption spectrum of semiconductor nanoparticles, in turn, shows a sharp onset at energies slightly above the fluorescence line and then spans the entire spectral range toward UV. In Figure 8.1, a comparison between the optical properties of organic fluorophores and of semiconductor nanoparticles is shown. The fact that all the samples of semiconductor nanoparticles shown in this example absorb light at low wavelengths below about 500 nm can be exploited for the simultaneous excitation of these samples. In contrast, for the simultaneous excitation of the various fluorophores, different light sources are necessary because each organic fluorophore can be excited only in a relatively narrow spectral range [20].

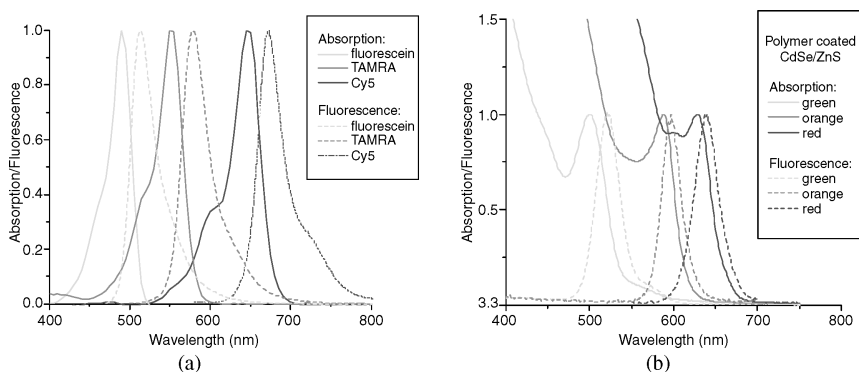


FIGURE 8.1 Comparison of the fluorescence properties of semiconductor nanoparticles and organic fluorophores: (a) absorption and fluorescence spectra of organic fluorophores; (b) absorption and fluorescence spectra of semiconductor nanoparticles. All the nanoparticles shown here have considerable absorption in the UV spectral range. (From ref. 21, with permission.)

Noble-metal nanoparticles show interesting optical features that are dominated by a free electron plasmon that can be excited by electromagnetic fields. Due to the plasmon mode, the particles scatter light and show strong absorbance. The major part of the absorbed energy is dispersed into heat [8,9]. When employing anisotropically grown metal nanoparticles, called nanorods, the resonance frequency can be tuned over a wide range by the aspect ratio and also by the dielectric constant of the surrounding medium [22]. In this way, noble metal nanoparticles can be considered as nanoovens, which convert light energy into heat.

Magnetic nanoparticles can be synthesized from a wide variety of materials, such as metals, metal alloys, or metal oxides [23–26]. Also, for these particles in the nanometer regime, the properties differ greatly from the properties of the corresponding bulk material. This accounts for the saturation magnetization, the coercive field, or the Verwey transition [27]. With the help of an external magnetic field gradient, magnetic nanoparticles can be transported to defined spots [28]. Additionally, magnetic nanoparticles also offer the possibility of generating heat by an effect termed *hyperthermia* [29,30]. When an alternating magnetic high-frequency field is applied to the nanoparticles, the hysteresis of their magnetization can be exploited to generate heat, as sketched in Figure 8.2.

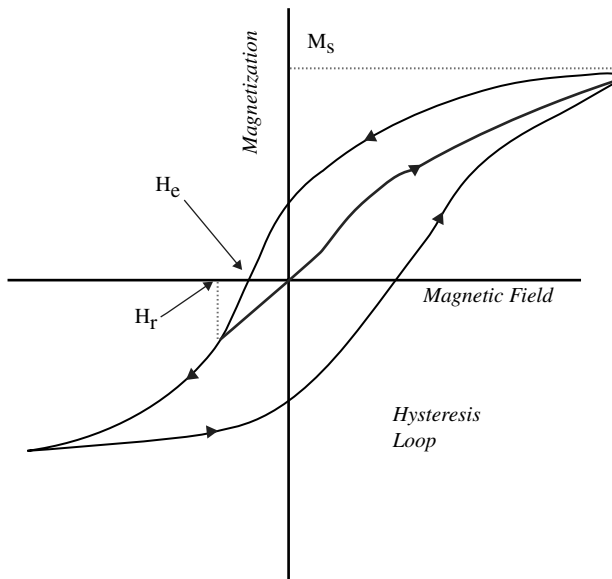


FIGURE 8.2 Hysteresis loop of a magnetic material. The heat released in one cycle of the magnetization is proportional to the area circumscribed by the loop. This area is generally rather small, yet with several cycles, a considerable amount of heat can be extracted. M_s is the saturation magnetization and represents the highest induced magnetic moment that can be obtained in a magnetic field. H_c , the coercivity, represents the intensity of the magnetic field needed to reduce the magnetization of a magnetic material to zero after it has reached saturation. H_r , the coercivity of remanence, represents the reverse field which, when applied and then removed, reduces the saturation remanence to zero. It is always larger than the coercive force.

8.2.2 Synthesis of Colloidal Nanoparticles

The synthesis of colloidal nanoparticles can be carried out under a variety of conditions [24]. In this section we focus on the preparation in organic solvents. This surrounding is advantageous because it offers a greater ease for the fine adjustment of the critical parameters of the particles, such as size and crystalline structure [31,32]. Furthermore, for particles prepared in organic solution, a variety of methods exist to transfer the particles into aqueous solution, a topic presented in the following section. In this section we only briefly outline the principle of the growth of nanoparticles. For the precise synthetic procedures, we refer readers to recent review articles on that subject [24,25,33] and the original literature referred to therein.

In a general synthesis scheme, an appropriate solvent is heated to the temperature of the reaction, which is usually in the range 200 to 300° C. Then the molecular constituents of the nanoparticles to be grown are injected rapidly into this hot solution. The heat decomposes these precursors and frees the atoms, which can then be incorporated into a growing crystal. The role of the solvent is twofold. First, it serves to disperse the reactants and the product. This is not negligible, as the growth depends on parameters such as the concentration of the reactants and their diffusion constants. Furthermore, the solvent needs to resist the high temperature employed in the synthesis. Some of the most frequently used solvents are TOPO (tri-*n*-octylphosphine oxide)[16], diphenyl ether [34], octyl ether [35], or *o*-dichlorobenzene [36]. A second purpose of the solvent is to serve as a stabilizing agent. In this role, they stabilize the nanoparticles through steric repulsion; they also control the growth rate. The solvent molecules dynamically attach themselves to, and detach themselves from, the nanoparticle, so that they statistically free sites on the nanoparticles where new atoms could be deposited. Especially when referring to this second role, the molecules are termed *surfactants*.

In a more detailed description of the growth process, one can introduce a critical size that characterizes the state of the reaction solution [37,38]. The value of the critical size depends on parameters such as temperature, concentration of the atomic species, and chemical potential. Particles larger than the critical size experience a positive growth rate, particles smaller than this size show a negative growth rate, and thus they melt. Interestingly, the growth rate shows a maximum for particles with a diameter of twice the critical size. This behavior is actually of great help for the production of monodisperse samples. If the size distribution of the nanoparticles at one stage of the growth is such that all particles are larger than twice the critical size, the smallest particles grow the fastest (Figure 8.3). Therefore, the size distribution will narrow and the system is said to be in the *focusing regime*. During synthesis the critical size is actually not stable. The consumption of the atomic species especially leads to a rise in the critical size. When the size distribution is now situated such that it comprises particle sizes with the overall maximum in growth rate, the smallest particles will no longer be the fastest growing. This results in an effective broadening of the size distribution the (*broadening regime*). Ultimately, when the critical size is situated within the size distribution of the sample, the smallest particles will even disappear to

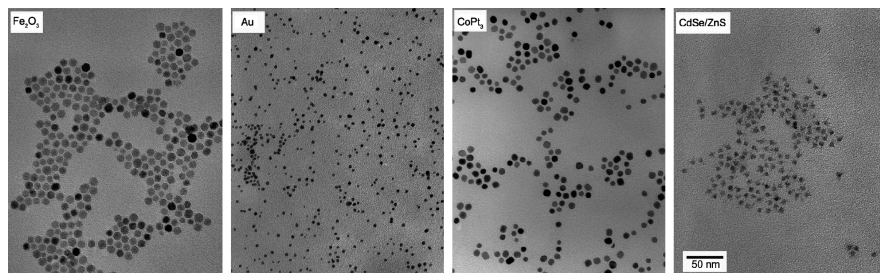


FIGURE 8.3 Transmission electron microscopy (TEM) images of nanoparticles of various materials (from left to right: Fe_2O_3 , Au, CoPt_3 , CdSe/ZnS). Each of the dots corresponds to one individual nanoparticle. The scale bar is 50 nm. (From ref. 39, with permission.)

free their constituents, which will be incorporated into the largest particles. This growth regime is termed *Ostwald ripening*. Generally, it is desirable to keep the system in the focusing regime. The most efficient way to do so is to maintain the a high concentration of free atoms in the growth solution [16]. This helps to maintain the critical size at a low value and thus allows us to obtain samples with narrow size distributions.

8.2.3 Surface Modification

After the synthesis in organic solvents, the nanoparticles are covered with a layer of surfactants which render them hydrophobic. In that state, the particles are of no use for applications in aqueous surrounding. There are different methods for the transfer of the nanoparticles into an aqueous surrounding [40]. In general, these methods rely on the design of the nanoparticles, as composed of an inorganic core and an organic shell. The inorganic core determines the physical properties, such as fluorescence or magnetization; the organic shell influences primarily chemical interaction with the surroundings. In a phase transfer, the organic layer of surfactants is either completely exchanged or is manipulated in such a way as to stabilize the surfactants and introduce additional functional groups that render the particles soluble in different media. In the following, we present three major techniques for this phase transfer (see Figure 8.4).

1. *Ligand exchange*. In this approach, the surfactant is simply exchanged. The original surfactant is exchanged with another surfactant of choice simply by exposing the sample to an excess of the new surfactant. The gentle application of heat facilitates the process. For a successful exchange, one has to choose carefully both the original and the new surfactant. The new surfactant should have a higher affinity for the nanoparticles than the original. Of course, it should also provide the new, desired functionality. As an example, the transfer of CdSe nanoparticles from the organic to the aqueous phase can be accomplished with a surfactant that binds to the nanoparticle

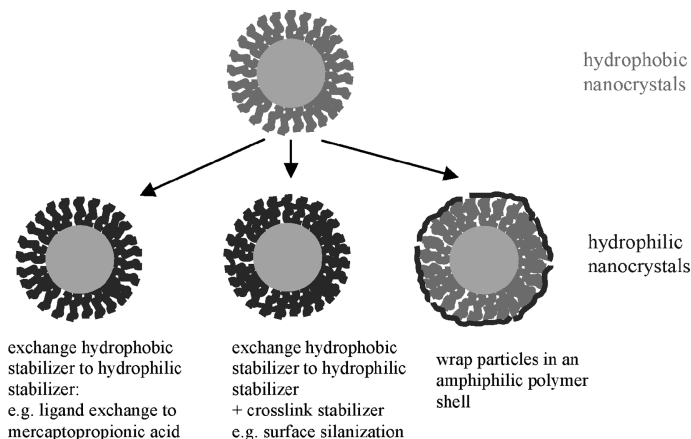


FIGURE 8.4 Three ways to transfer nanoparticles to aqueous solution. (Adapted from ref. 44, with permission.)

with a thiol group and carries a carboxylic group on the opposing end (e.g., mercaptopropionic acid) [41].

2. *Polymer coating.* This approach leaves the layer of surfactants on the nanoparticles untouched and adds only a second amphiphilic shell. This shell consists of a comblike polymer with alkyl chains and hydrophilic groups attached to the backbone [39]. The alkyl chains have a length similar to that of the surfactants. When exposed to the nanoparticles, the alkyl chains intercalate with the alkyl chains of the surfactant layer, and the hydrophilic groups point outward. The polymer can be cross-linked to form a closed shell around the particles for higher stability.

3. *Silanization.* Silanization combines the two approaches described above. It involves a ligand exchange and subsequent cross-linking of the new surfactant [42,43]. In the first step, the ligand is exchanged against mercaptopropyltrimethoxysilane. Again, the mercapto group serves as an anchor on the nanoparticle. In the second step the trimethoxysilane groups can be cross-linked with other silanes through siloxane bonds. Other functional groups can be incorporated into the shell during this step.

The most flexible method among those described above is polymer coating. It does not rely on specific interactions with the nanoparticles. Polymer coating only requires a hydrophobic shell surrounding the nanoparticle. In contrast, the other two methods rely on the binding of some molecule on the nanoparticle. The nature of the appropriate molecule for this binding can vary significantly from material to material. Therefore, these methods must be optimized for any new material. Both silanization and polymer coating offer a simple method of incorporating functional molecules into the organic shells of nanoparticles.

8.2.4 Biocompatibility

Nanoparticles are also attractive candidates for future clinical applications, due to their wide variety of properties, as discussed in Section 8.5. However, for any clinical application, the biocompatibility of the material is crucial. There are at least four different pathways by which nanoparticles might induce severe damage to living cells:

1. If nanoparticles are composed of toxic material, they might release toxic ions and thus poison the cell [45,46].
2. In some cases, biological material reacts very specifically to single properties of nanoparticles. For example, specific gold clusters, Au₅₅, can interact in a unique manner with DNA, thereby exerting a strong influence on the functionality of a cell [47].
3. There may be a nonspecific, negative effect on the cells. Nanoparticles can stick to the cell membrane, or they can be uptaken and stored in intracellular compartments [48,49]. Both effects lead potentially to damage of the cell.
4. Also, the shape of the nanoparticles plays a role in their toxicity. It has been reported that carbon nanotubes can impale cells like needles [50].

Some of these pathways can be avoided (e.g., pathways 2 and 4); the others must be suppressed by other means. Surface modification of initially toxic materials can sometimes reduce their toxicity. Silanization shows especially good results in this respect. Also, the choice of material is crucial. Obviously, one should prefer nontoxic material. But if there is no choice but to use the toxic material, an inorganic shell of an already less toxic material reduces the toxicity of the nanoparticles. For instance, core-shell particles of CdSe-ZnS are significantly less toxic than are bare CdSe particles [46].

In this section the synthesis and properties of inorganic nanoparticles have been described. In the next section the glue that holds these particles together in functional assemblies is discussed.

8.3 POLYELECTROLYTE CAPSULES AS A FUNCTIONAL CARRIER SYSTEM

The method to synthesize polyelectrolyte polymer capsules is based on layer-by-layer (LBL) adsorption [51] of oppositely charged polyelectrolyte polymers on colloidal templates, followed by core dissolution [52]. Figure 8.5 is a sketch of the general process that is used for the assembly of capsules. The basic idea is simple. First, a highly charged polymer (polyelectrolyte) is added to the oppositely charged template core. Due to coulombic attraction, this polymer will wrap itself around the template core. The overall charge of the polymer-coated core now assumes the polarity of the added polymer's charge. After the unbound polymer is removed, a second polymer with a charge opposite that of the first polymer is added. Again, the new polymer will

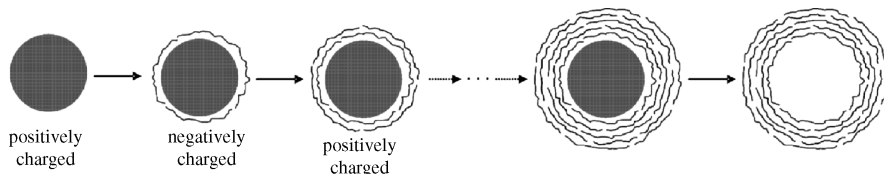


FIGURE 8.5 Capsule assembly. Negatively charged polymer is added to a positively charged template core. The resulting particle is then negatively charged, and after removal of unbound polymer, positively charged polymer is added. This layer-by-layer addition of oppositely charged layers of polymer continues until the multilayer wall has the desired thickness. After removal of the template core by dissolution, a hollow capsule remains. The capsules are not drawn to scale. The thickness of the walls is in the nanometer range, whereas the diameter of the capsules is in the micrometer range. The assembly could be started with negatively charged template cores in the same fashion.

stick to the polymer-coated core due to coulombic attraction. This process is repeated by subsequent addition of oppositely charged polymers, resulting in the addition of layer upon layer of polymer. In the end the template core is dissolved, yielding a hollow capsule whose walls are composed of the polymer multilayer. Thus, polyelectrolyte capsules can be visualized as shells of onions, where each layer is made of alternating layers of negative and positive polyelectrolyte polymers. The capsule wall is typically a few nanometers thick, whereas the capsule diameter can vary from tens of nanometers to several micrometers. The capsule's outermost layer determines the capsule's overall charge. In this way, polyelectrolyte polymer capsules can be positively or negatively charged.

The initial core used in the layer-by-layer synthesis method can be made out of different materials, such as calcium carbonate, polyester, or melamine formaldehyde latex particles [52]. Different positively and negatively charged polyelectrolyte polymers can be used for the core coating [53]. Polyelectrolyte polymers are simple polymers decorated with charges. They consist of long chains of molecules with ionizable groups that dissociate in water, leaving behind a charged chain. Depending on the ionizable groups, negative or positive charged chains can be obtained. Since the entire capsule is held together in first order by coulombic attraction, a huge variety of polyelectrolyte polymers can be used for building the capsule walls. Besides the natural requirement of sufficient charge distributed along the polymer molecule, the length (i.e., the molecular weight) of the polymer molecules is important and has to be adjusted, depending on the diameter of the capsules.

By adding charged particles during the layer-by-layer assembly of the capsules (e.g., negatively charged particles to a positively charged polymer layer) it is also possible to embed particles in the capsule walls (Figure 8.6). Once again, the particles are stuck to the polymer layers solely by electrostatic attraction, and virtually any charged functional nanoparticle of appropriate size can be embedded in the capsule walls (Figure 8.7). Typically, after the addition of nanoparticles, more subsequent layers of polymers are added so that the particles are between inner layers of the

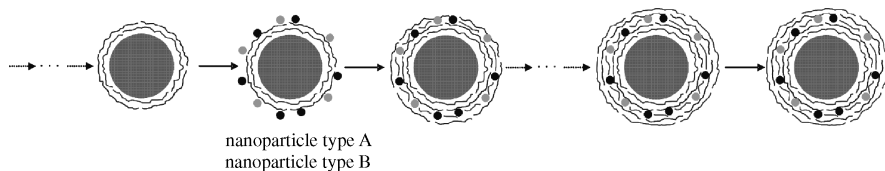


FIGURE 8.6 Embedding nanoparticles into the walls of capsules. Negatively charged nanoparticles (which can be a mixture of different types) can be added during the assembly process of the capsule walls when the outer capsule layer is positively charged. The capsules are not drawn to scale. The thickness of the walls and the diameter of the nanoparticles are in the nanometer range, whereas the diameter of the capsules is in the micrometer range.

capsules. In a similar fashion, charged molecules can also be added to the outer layers of the capsules: for example, to act as ligands for molecular recognition.

After the deposition of polymer layers is completed and the dissolution of the template core, cargo molecules can be loaded into the capsules by changing the permeability of the capsule walls [54]. For example, swelling of the polymer network can be achieved by lowering the pH or by exposure to ethanol. In this state, cargo molecules can diffuse into and out of the capsules. After increasing the pH back to original levels or removal of ethanol by washing with water the polymer network of the capsule walls shrinks, and the cargo molecules remain captured inside the capsules. Alternatively, a second method of loading cargo molecules in the capsule cavity has

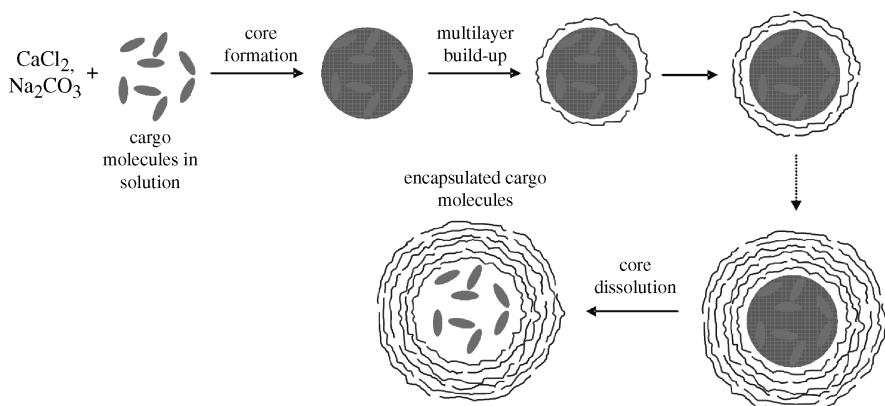


FIGURE 8.7 Encapsulation process. Spherical calcium carbonate microparticles comprising the cargo molecules were fabricated by precipitation from supersaturated CaCl_2 and Na_2CO_3 solution in the presence of the cargo molecules (co-precipitation-method). After the layer-by-layer self-assembly of oppositely charged polymer layers, the CaCO_3 was extracted by EDTA treatment, resulting in hollow polyelectrolyte capsules. This image includes three double layers of negatively charged polymer (red) and positively charged polymer (blue). The capsules are not drawn to scale. The thickness of the walls is in the nanometer range, whereas the diameter of the capsules is in the micrometer range.

recently been developed. This method consists of synthesizing co-precipitates of the cargo molecules with calcium carbonate. The particles are then used as a template core for assembly of the capsule walls. In the final step, the calcium carbonate core is dissolved with EDTA, leaving the cargo molecules inside the capsule cavity [55].

By means of the methods presented, different types of nanoparticles and biological molecules can be embedded in the capsule walls, and cargo molecules can also be loaded in the cavity of the capsules. These added molecules and particles confer different functionalities to the capsules [56]. Depending on the type of polyelectrolyte polymers that are employed for the wall synthesis, on the type of embedded nanoparticles in the capsule walls, and on the type of ligand molecules present on the capsule surface, the capsule will possess certain release, permeability, and adhesion properties [53,57]. Returning to the motivation discussed in Section 8.1, the nanoparticles provide the functionality, and the polymer is the glue used to assemble them. As on first order, the only force holding the assembly together is coulombic attraction, and a huge variety of particles and molecules can be integrated in the walls of the capsules. In this way, the capsules can be custom-made for the designated application. Similar ideas have also led to other types of microcontainers, which are based on alternative materials such as liposomes [58]; micelles [59], or gel matrixes [60,61].

8.4 UPTAKE OF CAPSULES BY CELLS

8.4.1 Uptake Mechanism

Endocytosis is the process by which animal cells internalize substances such as particulate material (such as cellular debris and microorganisms), macromolecules (such as proteins and complex sugars), and low-molecular-mass molecules (such as vitamins and simple sugars) (Figure 8.8). Two main types of endocytosis are distinguished on the basis of the size of the endocytic vesicles that are formed during this process. *Phagocytosis* (“cellular eating”) involves the uptake of large particles and *pinocytosis* (“cellular drinking”) involves the ingestion of fluid and solutes via small vesicles. Phagocytosis is typically restricted to specialized mammalian cells such as macrophages or dendritic cells, whereas pinocytosis occurs in all cells by at least four basic mechanisms: macropinocytosis, clathrin-mediated endocytosis, caveolae-mediated endocytosis, and clathrin- and caveolae-independent endocytosis [62]. During macropinocytosis, the capsule internalization begins with the invagination of plasma membrane and the capsule, followed by the conversion of this membrane into a closed vesicle called an *endosome* (or *endosomal vesicle*). The endosomes often fuse with lysosomes that contain many different hydrolytic enzymes for intracellular ingestion. Unfortunately, particle uptake cannot always be classified straightforwardly according to the standard pathways described in textbooks.

Strictly speaking, the detailed uptake mechanism of polyelectrolyte capsules by cells remains unclear. On the other hand, it is a fact that capsules are ingested spontaneously by a huge variety of cells [63]. The transport mechanism of the capsules

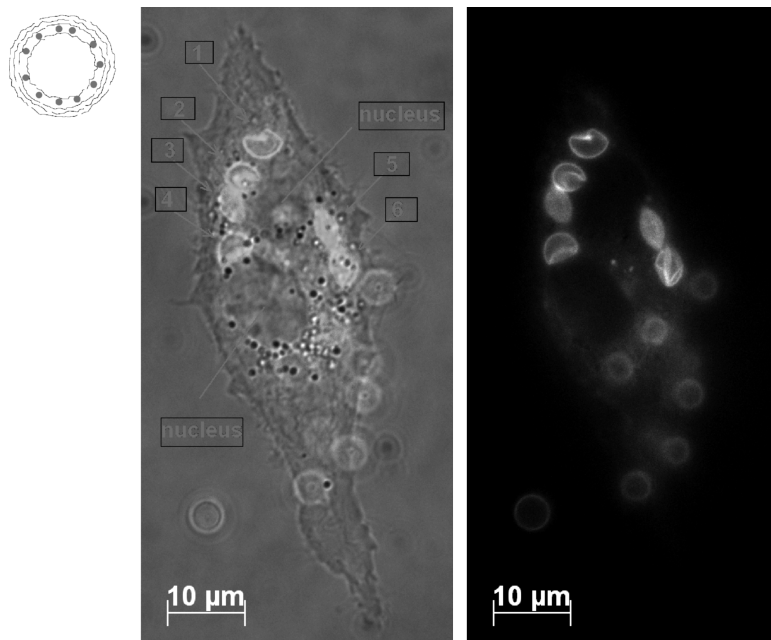


FIGURE 8.8 A cell has incorporated six capsules, and additional capsules adhere to the outer cell membrane. Fluorescent semiconductor nanoparticles had been embedded in the walls of the capsules. The left image shows an overlay of phasecontrast and fluorescence, the right image, fluorescence, along. (From ref. 56, with permission.)

across the cell membrane remains subject to further studies, and the final location of the capsules inside the cells is also not known precisely, even though co-localization attempts have been reported [63]. However, there is significant evidence that capsules, having been ingested by cells, are stored in endosomal, lysosomal, or phagosomal compartments.

Although the detailed uptake process and the localization of polyelectrolyte capsules after uptake remain unclear, important parameters that influence the uptake process have been investigated. As mentioned in Section 8.3, the outer shell (surface) of polyelectrolyte polymer capsules can be either negatively or positively charged, depending on the charge of the last layer. Cell membranes have a negative net charge, although positively charged domains do exist [64,65]. It is therefore reasonable to think that adhesion and, correspondingly, the uptake of polyelectrolyte capsules should depend on the capsule charge. Therefore, the adherent rate for positive polyelectrolyte capsules should be higher than for negative polyelectrolyte capsules. Since particle uptake is preceded by adhesion to the cell membrane, there should also be a correlation between the adhesion and the uptake rate, and hence the uptake rate for positive polyelectrolyte capsules should also be higher than for negative capsules. Indeed, this correlation could be demonstrated experimentally, although the charge effect became less pronounced with longer incubation times [66]. Proteins from the

cell medium can adsorb to the capsule surface and thus smear out the preexisting difference in the surface charge of the capsules [67]. Covering the capsule surface with poly(ethylene glycol) (PEG), on the other hand, effectively reduces capsule uptake.

8.4.2 Capsule Deformation During Uptake

A major requirement for the concept of using polyelectrolyte polymer capsules as multifunctional carrier system is that the cargo material within the container is protected against any possible undesirable external interaction until it is released in a controlled way. During the uptake of capsules by cells, it is frequently observed that many capsules are deformed upon the incorporation process. This effect could lead to an undesirable release of the material, making further applications unviable [68]. It is therefore crucial to determine whether capsule deformation could lead to an unwanted release of cargo material. To investigate whether material release upon deformation had taken place, experiments at a single cell level were performed [63]. For these experiments, capsules were loaded with different fluorescent-labeled polymers within both their cavity and in their wall (Figure 8.9). The fluorescent polymers inside the cavity were used as model cargo, whereas the differently colored fluorophores in the capsule walls were used to label the walls. After capsule uptake, co-localization of the cargo and the capsule walls was recorded using fluorescence microscopy. Data indicate that the cargo polymers remain within the capsule cavity after capsule deformation, although a quantitative study is still missing. At any rate, these experiments demonstrate that capsules with cargo in their cavity are ingested by cells without uncontrolled release of the cargo [63].

8.4.3 Toxicity of Capsules

As demonstrated in Section 8.3, a number of functionalities can be achieved by loading different types of nanoparticles, such as semiconductor, magnetic, or metallic

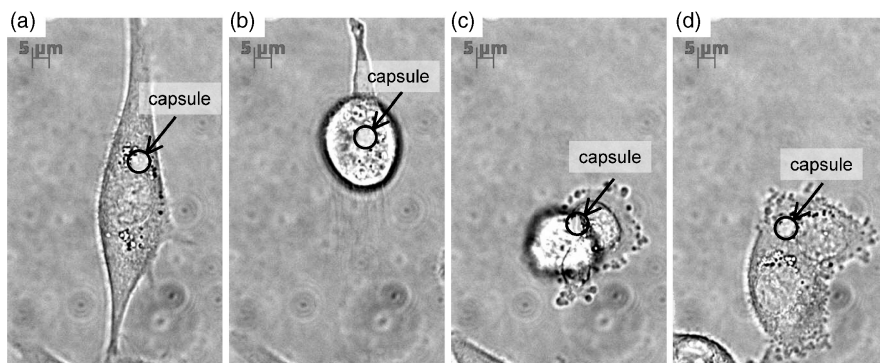


FIGURE 8.9 A cell that has incorporated one capsule (whose walls had been modified with fluorescent nanoparticles) is shown in the process of cell division. After division the capsule is passed to one of the daughter cells. (From ref. 66, with permission.)

nanoparticles, into the walls of polyelectrolyte capsules. In Section 8.4.1 we described the fact that polyelectrolyte capsules are taken up by a large variety of cell lines. As in future steps, polyelectrolyte capsules could also be introduced into animals or humans for clinical applications, such as drug delivery or hyperthermia, but first their biocompatibility must be tested. Detailed studies of capsules with cytotoxic effects that might impair cells and tissue are therefore paramount. Toxicity might originate from two different sources, from the actual polyelectrolyte capsules and from the nanoparticles embedded in the capsule walls.

Since capsules can be assembled out of most polyelectrolytes, it should also be possible to compose capsules out of biocompatible materials [69]. However, state-of-the-art capsules have been demonstrated to cause inflammation after injection into animal tissue [70]. Even more important, the biocompatibility of the nanoparticles loaded in the capsule must be analyzed. Using the delivery application described in Section 8.5, capsules must be modified with magnetic, metallic, and semiconductor nanoparticles. In the case of magnetic nanoparticles, iron oxides have been proven to be relatively biocompatible [71]. This is because they can be degraded into iron and oxygen, both of which are compounds of our metabolism. As for metallic nanoparticles, Au nanoparticles are inert and are also claimed to be relatively harmless to cells [72]. On the other hand, the commonly used fluorescent II–VI semiconductor nanoparticles (e.g., CdSe–ZnS) are clearly cytotoxic, as they release toxic cadmium ions upon corrosion [45,46]. Consequently, capsules that contain fluorescent II–VI nanoparticles in their walls are also cytotoxic [73]. Still the remaining toxicity forbids any use of these multifunctional capsules in human beings. Further reduced toxicity can be expected from new generations of materials. Independent of medical–clinical applications, capsules can well be used for experiments with cell lines without any signs of acute cytotoxicity.

8.5 DELIVERY AND SENSING WITH POLYELECTROLYTE CAPSULES

8.5.1 Multifunctional Polyelectrolyte Capsules as Smart Delivery Vehicles

One of the most promising applications of nanotechnology is in the field of medicine. Areas such as cancer pathology need innovative techniques and methods to improve the diagnostics and develop a cure for this deadly disease. For cancer therapy, novel drug delivery methods are required to increase the therapeutic efficacy of chemotherapeutic agents. One of the directions contributing to the improvement of cancer therapies within the field of nanomedicine is the creation of nanostructures, which have the potential to enhance drug bioability and enable precision drug targeting. Several drug carrier systems are currently under development [13]. Currently, most (chemical/drug-based) cancer therapies are not sufficiently effective and show many side effects that can diminish the patient's quality of life. In some tumors it is difficult to reach the desired physiological target with most of the drugs available. Furthermore, it is still impossible to localize chemotherapeutic agents specifically in the pathological cells. This fact calls attention to the problem that healthy cells are affected as well [74]. There is currently no pharmaceutical treatment available that can be applied locally,

into the tumor, and in a controlled way, thereby shielding healthy cells from drug interaction. A new method to release the chemotherapeutic agents in a locally, temporally, and quantitatively controlled manner is urgently needed.

Although it must be stated clearly that so far, nanotechnology has not yet resulted in any breakthroughs in cancer therapy, there is still hope and great potential. In this section, the possible uses of polyelectrolyte capsules toward this end will be discussed. With this goal in mind, the conceptual possibilities relating to the contribution of nanotechnology will also be stressed, even though polymer capsules are still far away from being used in any medical cure. As mentioned in the introduction, the clear advantage of nanotechnology is the ability to create new materials in a controlled way on the nanometer scale. In particular, building blocks of different functionality can be linked. Regarding cancer therapy, it would be desirable to combine different methods of targeting, as multiple targeting steps in combination should make targeting increasingly specific. Nowadays, a huge variety of anticancer drugs is based on molecular recognition via receptor–ligand pairs. It was also shown recently that it is possible to direct drugs bound to magnetic particles close to tumors using magnetic field gradients [75,76]. These are two examples of different strategies for targeting which are already in use. Nanobiotechnology could link both strategies into one carrier system, a topic explained below using polyelectrolyte capsules as an example.

The main idea of drug delivery using polyelectrolyte capsules is schematized in Figure 8.10. Polyelectrolyte capsules can be loaded with magnetic, fluorescent, and

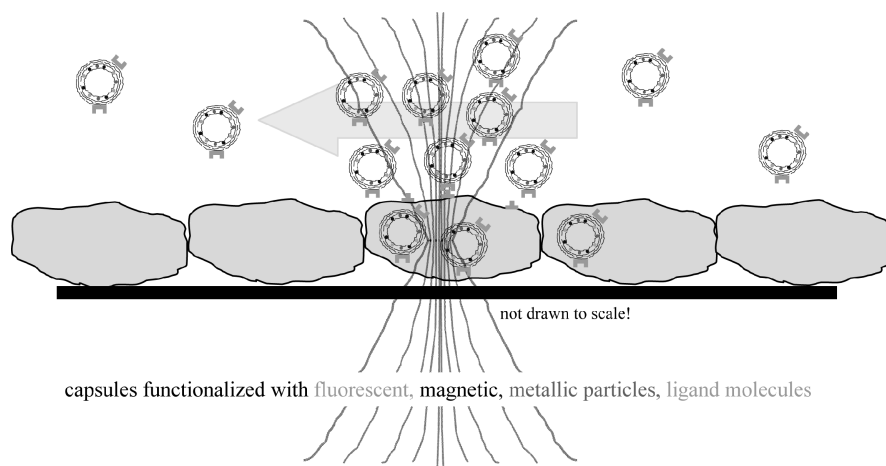


FIGURE 8.10 Concept and vision of drug delivery using multifunctional polyelectrolyte capsules. Due to the magnetic particles in their walls, capsules can be focused with a magnetic field gradient to the target tissue. (Note: This does not work on the level of single cells.) The capsules can be monitored using fluorescence microscopy (preferentially in the IR), due to the fluorescent nanoparticles in the capsule walls. Capsules are incorporated selectively by tumor cells through recognition of their ligands by tumor-specific receptors. Inside the cells, capsules can be illuminated with a light pointer. Metal particles in the capsule wall absorb the light and get heated, which results in a rupture and melting of the capsule wall, thus releasing into the cytosol a chemotherapeutic agent inside the capsule cavity.

metallic nanoparticles in their walls, ligand molecules can be attached to their surface, and chemotherapeutic agents can be loaded into the capsule cavity [56]. Loading the polyelectrolyte capsule with these different types of inorganic nanoparticles would provide different functionalities to the capsules, whereas the polymer molecules would act as glue to hold the assembly together. Due to the magnetic particles in their walls, the polyelectrolyte capsules could be directed to the desired position by using a magnetic field gradient. Focusing of magnetic particles in magnetic gradients has already been demonstrated successfully in experiments on animals, in particular in tumors close to the skin [76–78]. Near-target uptake of the capsules by the cancerous cells would be mediated by interaction of the ligands on the capsule surface with receptor molecules that are expressed on the membrane of cancer cells but not of healthy cells. After incorporation by cells, the chemotherapeutic agent had to be released in a controlled way. This could be done, for example, by loading metal nanoparticles in the walls of the capsules and by illuminating them with a light pointer. Light absorption promotes local heating of the metal nanoparticles. Heat would rupture the capsule walls, and thus the chemotherapeutic agents would finally be released. The entire uptake and transport process could be visualized by (infrared) fluorescent nanoparticles loaded in the capsule walls. In this way, three different targeting mechanisms would be involved: trapping of the capsules in the surrounding of the tumor with magnetic field gradients, enhanced receptor-mediated uptake of the capsules by tumor cells, and local release of the chemotherapeutic agent due to illumination with a light pointer. Although it must again be stressed that the concept described heretofore is in its infancy and far from any clinical application, there have been important proofs of concepts of the individual components on the level of cell cultures, as we demonstrate in the following section.

As we have seen in Section 8.3, polyelectrolyte capsules can be synthesized with different particles in their walls, and it is also possible to load macromolecules inside the cavity. From the point of preparation, the basic requirements needed for the delivery system introduced earlier can be fulfilled. In Section 8.4 it has been demonstrated that capsules are also incorporated by cells, an essential presupposition for the delivery system. On this basis, the concepts of magnetic drug targeting and the remote release of the molecules in the capsule cavity by light-induced heating could be demonstrated.

Zebli et al. have demonstrated that polyelectrolyte capsules can be targeted to tumor cells by using a magnetic field gradient [79]. Capsules with magnetic and fluorescent nanoparticles incorporated into their walls were added to the medium flowing above a layer of cultured cells. At one position of the layer, a small magnet was fixed. Since capsules were labeled with fluorescent particles, they could be conveniently observed with fluorescence microscopy. Indeed, due to the magnetic field gradient present at the edges of the magnet, an enrichment of capsules close to the magnet was found, whereas almost no capsules were found in regions far away from the magnet. In this way, the concept of magnetic drug targeting, which has been introduced by several groups, can also be used with polyelectrolyte capsules. It has to

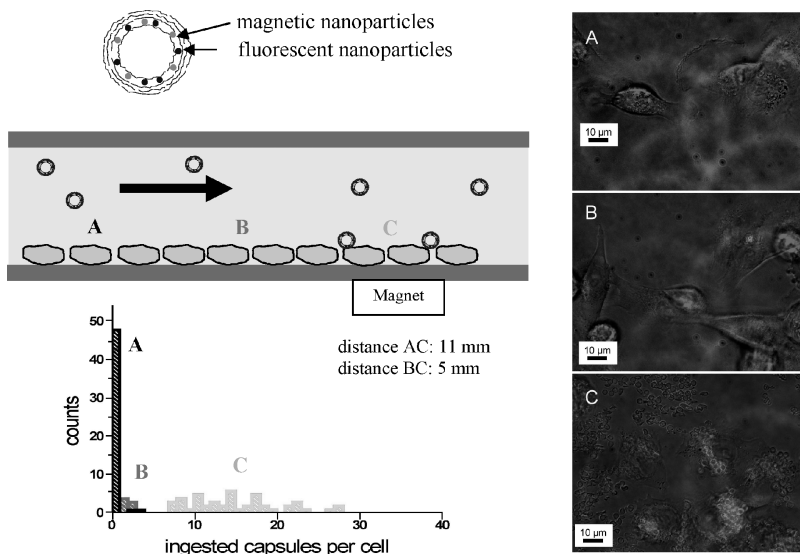


FIGURE 8.11 Capsules have been loaded with magnetic nanoparticles and fluorescent nanoparticles. These capsules were added to a medium with which cells cultured in a flow channel were continuously perfused. A small magnet was placed at position C of the channel. Fluorescence microscopy images demonstrate that there is an accumulation of capsules close to the magnet (region C), but that there are only a few capsules located in regions farther away from the magnet (A, B). Not all the capsules shown in the fluorescence microscopy images are actually inside the cells; a huge fraction adhere only to the outer cell membrane. However, by counting the number of capsules that have been incorporated by each cell and plotting the data as a histogram, it can also be shown that the number of capsules uptaken by each cell is highest at regions close to the magnet (C). (Adapted from ref. 79, with permission.)

be pointed out that the magnetic field gradient does not cause a higher uptake rate of capsules by cells. The magnetic field gradient causes an accumulation of capsules. Therefore, not all of the capsules shown in Figure 8.11 have actually been incorporated by the cells. However, due to a higher local concentration of capsules close to the magnet cells, this area can incorporate more capsules than cells at areas where few capsules are present.

It has already been proven by the Sukhorukov group that by using an appropriate laser, polyelectrolyte capsules loaded with metallic nanoparticles in their wall can be disrupted [56,80]. Metallic nanoparticles serve as absorption centers for the energy supplied by the laser beam (Figure 8.12). These absorption centers cause local heating that can disrupt the local polymer matrix and allow the encapsulated material to exit the capsule.

This technique could also be demonstrated on a single-cell level [81]. For this purpose, the walls of the polyelectrolyte capsules were loaded with Au nanoparticles that acted as heating centers for the capsule opening and with dye-labeled polymers in

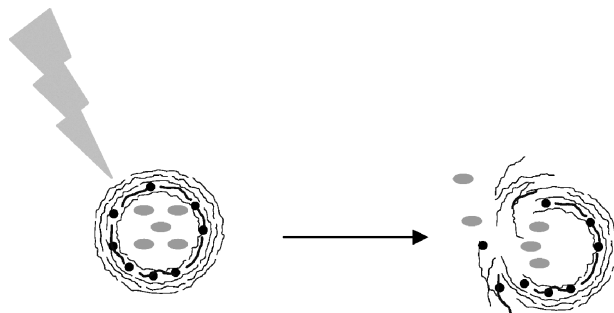


FIGURE 8.12 Laser-controlled opening of individual capsules by local heating mediated by Au nanoparticles. The capsule wall is modified with metal nanoparticles, and a macromolecule is loaded inside the capsule cavity. Upon illumination the Au nanoparticles are heated, causing the polymer capsule to rupture, releasing the macromolecules. This experiment works at the single-capsule level.

their cavity as a model for a drug. The release of the polymer from the capsule cavity upon illumination is shown in Figure 8.13. This work demonstrates that it is possible to release encapsulated materials selectively (in this case, a fluorescence-labeled polymer) inside tumor cell lines by applying a laser beam to excite the metal nanoparticles in the walls of polyelectrolyte capsules [68]. To avoid any possible additional cellular

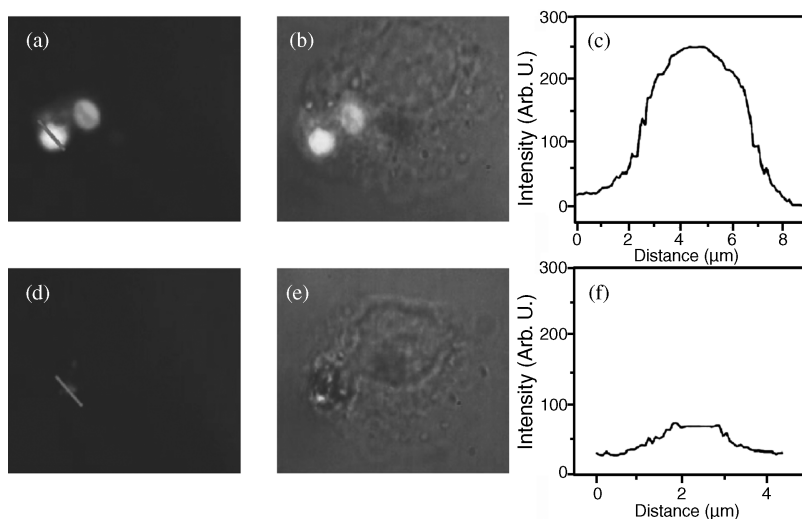


FIGURE 8.13 Polymer capsules have been modified with metal nanoparticles in their walls and with a fluorescent polymer as a model drug in their cavity. In the upper row, a cell that has ingested two such capsules is shown [fluorescence image, overlay of phase contrast and fluorescence image; fluorescence intensity profile along the line marked in (a)]. After illumination of the capsules with a light pointer, the capsule walls opened, and as can be seen in the lower row, the fluorescent polymer has been released from the capsule cavity. (Adapted from ref. 81, with permission.)

damage from laser irradiation, the wavelength of the laser was chosen in the biologically “friendly” window: namely, the near-infrared part of the spectrum. Cytotoxic effects due to capsule opening and local increase of cellular temperature are currently being addressed, but data suggest that lasers can be operated with optimized power to open capsules without damaging the cells.

Putting both experiments together, it should be possible to direct capsules to the target location by means of metallic particles embedded in their walls and magnetic field gradients. As stated earlier, capsules are ingested spontaneously. By putting metal nanoparticles in the walls of the capsules, the capsules can be opened selectively via illumination with a light pointer, which leads to a release of the contents of the capsule cavity into the cytosol. Although the state of the art of this drug delivery system is still very much in the experimental phase, the combination of different targeting strategies within one carrier system could nevertheless be clearly proven.

8.5.2 Multifunctional Polyelectrolyte Capsules as Local Sensors

Measuring analyte concentration in small volumes is a very interesting task for many applications. In cell biology, for instance, it would be very interesting to be able to measure the concentration of different analytes within the cell (e.g., pH, Ca^{2+} , K^+) since these analytes play a role in many cellular processes [82]. In diagnostics, the analyte concentrations of samples must be measured routinely. Sometimes these samples are only available in small quantities, and it is therefore necessary to waste as little sample as possible. A broad variety of organic fluorophores has already been developed in order to measure analyte concentrations. Due to their small size, organic fluorophores can also be used to measure analyte concentrations inside the cell [83]. However, some fluorophores have been demonstrated to react with cellular organelles and fluids, which could lead to cytotoxic effects and to dye degradation.

Polyelectrolyte polymer capsules with embedded ion-sensitive fluorescence dyes have been proposed as a possible concept to circumvent the problems mentioned above [55]. As a proof of principle for this new system, a fluorimetric pH sensor named Snarf-1 was loaded into the cavity of polyelectrolyte capsules. Snarf-1 is an organic fluorophore whose fluorescence color depends on the pH of the surrounding medium [84]. At acidic pH, its protonated form emits at 580 nm (green color) whereas at alkaline pH, its deprotonated form emits at 640 nm (red color) (Figure 8.14). The respective fluorescence intensities at 580 and 640 nm are related to the pH of the local environment in such a way that the 580-nm intensity decreases with increasing pH values. Analogously, the 640-nm intensity increases with increasing pH. The pH of the environment can therefore be determined by measuring the ratio of the two fluorescence intensities (green and red).

Snarf-loaded capsules have been used to measure the pH inside endosomal, lysosomal, and phagosomal structures inside living cells. In Section 8.4 it had been described that after incorporation by cells, capsules are stored in endosomal, lysosomal, and phagosomal compartments. Since these compartments typically have acidic environments [85], Snarf capsules will fluoresce green. The pH of the cell culture medium, on the other hand, is slightly alkaline, and thus capsules outside cells

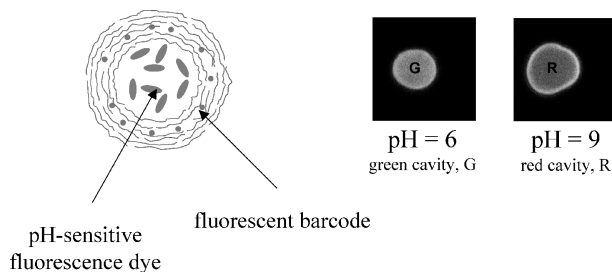


FIGURE 8.14 Polyelectrolyte capsules have been modified with fluorescent nanoparticles in their walls, which act as a barcode for their identification. The cavity of the capsules has been loaded with a pH-sensitive dye (attached to a polymer, so that the dye cannot diffuse outside the capsule cavity). The wall of the capsules appears fluorescent, due to the nanoparticle labeling. The fluorescence of the cavity of the capsules depends on the pH value. The capsule cavity fluoresces green (G) in the case of acidic pH, and red (R) in the case of alkaline pH. (Adapted from ref. 55, with permission.)

should fluoresce red. Figure 8.15 shows two images from a movie in which polyelectrolyte capsules were taken up by cells. The color of the capsules changes from red to green when they are incorporated by cells [55].

We stress the conceptual value of this study, which must be seen as a proof of principle for a new system for analyte detection. The first advantage is that embedding analyte-sensitive fluorescent dyes in capsules involves high local dye concentration in a very small volume (Figure 8.16). In this way, the sensitivity of the dye is enhanced. In addition, the cytotoxicity effects of the dye in cells should be reduced. Also, the dye would be protected against any possible interaction with cellular organelles and would be protected against degradation by the cell. In this way, long-term measurements should be possible.

Another very important advantage of these microcontainers is the fact that they can also be labeled by putting fluorescent nanoparticles or organic fluorophores in the

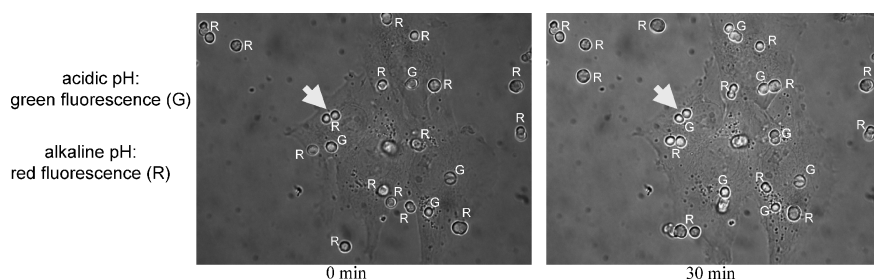


FIGURE 8.15 SNARF-1-dextran-loaded microcapsules were added to the medium of MDA-MB-435S breast cancer cells that were cultured on glass substrates. Capsules in the alkaline cell medium retain their overall red (R) fluorescence. Capsules that are incorporated in acidic endosomal-lysosomal-phagosomal compartments inside cells show green (G) fluorescence. More capsules are ingested by cells and thus change their color of fluorescence from red to green (see the arrow) upon prolonged incubation times. (Adapted from ref. 55, with permission.)

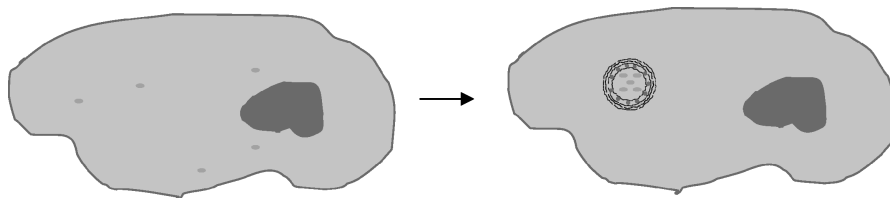


FIGURE 8.16 Comparison of the situation when N dye molecules have been directly injected to the cytoplasm of a cell to the situation when the N dye molecules are inside the cavity of a capsule that has been incorporated by a cell. Encapsulation of the dye in capsules allows for (1) a high local dye concentration and thus high fluorescence intensities, (2) protecting the cell from cytotoxic damage due to the dye, and (3) preventing degradation of the dye by the cell. Whereas dye molecules can be injected directly into the cytosol of cells, ingested capsules are located in endosomal–lysosomal–phagosomal compartments, and it is still a future challenge to release capsules to the cytosol.

capsule wall. In this way, each individual capsule could have a name that would correspond to one fluorescent barcode. Capsules with different names could be loaded inside their cavities with dyes that are sensitive to different analytes. In this way, one could measure different analyte concentrations by introducing different capsules, each loaded in its cavity with a different analyte-sensitive dye and with a different fluorescent barcode in its wall (Figure 8.17).

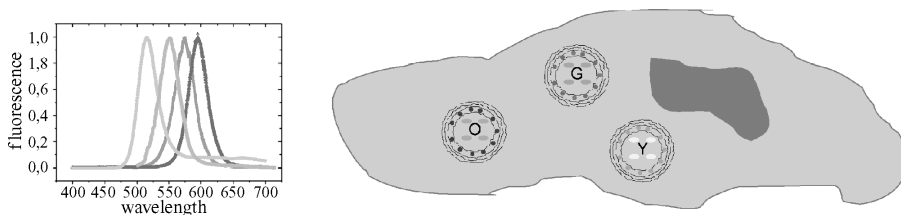


FIGURE 8.17 In case different ions (e.g., Na^+ , K^+ , H^+) should be detected in parallel, one could use different ion-sensitive fluorophores: for example, one that emits in the green (G) fluorophore for sodium, one that emits in yellow (Y) for potassium, and one that emits in orange (O) for pH. Even if ion-sensitive fluorophores with this color of emission existed, spectral overlap of the fluorescence of the various fluorophores would still be a problem, particularly when several fluorophores are used in parallel. Capsules can carry fluorescence molecules at two distinct positions. In this way, the cavity can be loaded with the ion-sensitive dye, and the wall can be labeled with fluorescent molecules or nanoparticles as spectral barcode. By identifying individual capsules with their barcode, the problem of spectral overlap could be circumnavigated. The fluorescence in the cavity of the capsules would correspond to the concentration of the ions, and the barcode in the capsule walls would indicate the respective ion sensitivity of the capsule. This would allow for multiplexed measurements of different ion concentrations.

8.6 CONCLUSIONS

Due to their small size, nanoparticles present interesting and promising properties for a number of applications. These new particles are still under investigation, and because they are relatively new, many parameters in their synthesis, characterization, and properties have yet to be investigated. While such inorganic nanoparticles can be considered as building blocks with tailored functionality, (biological) macromolecules can be used to assemble them into larger multifunctional units. Nanoparticle-modified polyelectrolyte capsules have been demonstrated to be such a multifunctional unit.

Since polyelectrolyte polymer capsules are relatively new systems, there are still many parameters that have to be adjusted. Polyelectrolyte capsules can be taken up and stored by the cells. However, little is known about specific pathways of capsule uptake and the localization of capsules within a cell. To use polyelectrolyte capsules for in vivo applications such as drug delivery, these missing details must be ascertained. Analogously to nanoparticles, similar cytotoxic effects of polyelectrolyte capsules must be taken into consideration. For drug delivery applications, many parameters still have to be controlled. For instance, it is necessary to trace where the drugs are located inside cells after capsule opening. Cytotoxicity effects due to capsule opening and local heating in the cell must also be investigated. Once all these parameter are finely controlled, real drug delivery could be addressed by loading polyelectrolyte capsules with such drugs as the lethal doxorubicin to study cytotoxic effects on cells. In addition, a complete performance of the drug delivery system (capsule targeting plus drug release) must be achieved.

Acknowledgments

The experimental results presented in this chapter are based on capsule systems that have been prepared by Prof. Gleb Sukhorukov's group: Dr. Oliver Kreft, Dr. Andrei Skirtach, and Matthieu Bedard. The authors are grateful to Dr. Pilar Rivera Gil for careful proofreading of the manuscript and valuable discussions. The authors are also grateful to Eric S. Anderson for editing the manuscript. This publication was supported by the DFG, EU-STREP SA-NANO, and the Max Planck Society.

REFERENCES

1. Alivisatos A, et al. Electronic states of semiconductor clusters: homogeneous and inhomogeneous broadening of the optical spectrum. *J. Chem. Phys.* 1988;89:4001–4011.
2. Schmidt G, et al. Large transition metal clusters: VI. Ligand exchange reactions on $\text{Au}_{55}(\text{PPh}_3)_{12}\text{Cl}_6$ —the formation of a water soluble Au_{55} cluster. *Polyhedron.* 1988;7: 605–608.
3. Schmid G, ed. *Nanoparticles: From Theory to Application.* Wiley-VCH; Weinheim, Germany, 2004.

4. Eustis S, El-Sayed MA. Why gold nanoparticles are more precious than pretty gold: noble metal surface plasmon resonance and its enhancement of the radiative and non-radiative properties of nanocrystals of different shapes. *Chem. Soc. Rev.* 2006;35:209–217.
5. Link S, El-Sayed MA. Spectral properties and relaxation dynamics of surface plasmon electronic oscillations in gold and silver nanodots and nanorods. *J. Phys. Chem. B.* 1999;103:8410–8426.
6. Huber DL. Synthesis, properties, and applications of iron nanoparticles. *Small.* 2005;1(5):482–501.
7. Parak WJ, et al. Quantum dots. In Schmid G, ed. *Nanoparticles: From Theory to Application.* Wiley-VCH; Weinheim, Germany, 2004, pp. 4–49.
8. Govorov AO, et al. Gold nanoparticle ensembles as heaters and actuators: melting and collective plasmon resonances. *Nanoscale Res. Lett.* 2006;1(1):84–90.
9. Govorov AO, Richardson HH. Generating heat with metal nanoparticles. *Nano Today.* 2007;2(1):30–38.
10. Alivisatos AP, et al. Organization of ‘nanocrystal molecules’ using DNA. *Nature.* 1996;382(15 August):609–611.
11. Zanchet D, et al. Electrophoretic and structural studies of DNA-directed Au nanoparticle groupings. *J. Phys. Chem. B.* 2002;106(45):11758–11763.
12. Mirkin CA, et al. A DNA-based method for rationally assembling nanoparticles into macroscopic materials. *Nature.* 1996;382:607–609.
13. Hughes GA. Nanostructure-mediated drug delivery. *Nanomed.: Nanotechnol., Biol. Med.* 2005;1(1):22–30.
14. Buck SM, et al. Nanoscale probes encapsulated by biologically localized embedding (PEBBLEs) for ion sensing and imaging in live cells. *Talanta.* 2004;63(1):41–59.
15. Hines MA, Guyot-Sionnest P. Bright UV-blue luminescent colloidal ZnSe nanocrystals. *J. Phys. Chem. B.* 1998;102(19):3655–3657.
16. Murray CB, Norris DJ, Bawendi MG. Synthesis and characterization of nearly monodisperse CdE (E = S, Se, Te) semiconductor nanocrystallites. *J. Am. Chem. Soc.* 1993;115:8706–8715.
17. Du H, et al. Optical properties of colloidal PbSe nanocrystals. *Nano Lett.* 2002;2(11):1321–1324.
18. Murphy JE, et al. PbTe colloidal nanocrystals: synthesis, characterization, and multiple exciton generation. *J. Am. Chem. Soc.* 2006;128(10):3241–3247.
19. Ashcroft NW, Mermin ND. *Solid State Physics.* W.B. Saunders, Philadelphia; 1976.
20. Medintz IL, et al. Quantum dot bioconjugates for imaging, labelling and sensing. *Nat. Mater.* 2005;4(6):635–446.
21. Parak WJ, Pellegrino T, Plank C. Labelling of cells with quantum dots. *Nanotechnology.* 2005;16:R5–R25.
22. Perez-Juste J, et al. Gold nanorods: synthesis, characterization and applications. *Coord. Chem. Rev.* 2005;249:1870–1901.
23. Hyeon T. Chemical synthesis of magnetic nanoparticles. *Chem. Commun.* 2003;8: 927–934.
24. Masala O, Seshadri R. Synthesis routes for large volumes of nanoparticles. *Annu. Rev. Mater. Res.* 2004;34:41–81.

25. Lin XM, Samia ACS. Synthesis, assembly and physical properties of magnetic nanoparticles. *J. Magn. Magn. Mater.* 2006;305(1):100–109.
26. Wilcoxon JP, Abrams BL. Synthesis, structure and properties of metal nanoclusters. *Chem. Soc. Rev.* 2006;35:1162–1194.
27. Goya GF, Berquó TS, Fonseca FC. Static and dynamic magnetic properties of spherical magnetite nanoparticles. *J. Appl. Phys.* 2003;95(5):3520–3528.
28. Alexiou C, et al. Targeting cancer cells: magnetic nanoparticles as drug carriers. *Eur. Biophys. J.* 2006;35:446–450.
29. Kawai N, Ito A, Nakahara Y, et al. Anticancer effect of hyperthermia on prostate cancer mediated by magnetite cationic liposomes and immune-response induction in transplanted syngeneic rats. *Prostate.* 2005;64(4):373–381.
30. Mornet S, et al. Magnetic nanoparticle design for medical diagnosis and therapy. *J. Mater. Chem.* 2004;14(14):2161–2175.
31. Yeh CY, et al. Zinc-blende–wurtzite polytypism in semiconductors. *Phys. Rev. B.* 1992;46:10086–10097.
32. Yu WW, Wang YA, Peng X. Formation and stability of size-, shape-, and structure-controlled CdTe nanocrystals: ligand effects on monomers and nanocrystals. *Chem. Mater.* 2003;15:4300–4308.
33. Cozzoli PD, Pellegrino T, Manna L. Synthesis, properties and perspectives of hybrid nanocrystal structures. *Chem. Soc. Rev.* 2006;35(11):1195–1208.
34. Wehrenberg BL, Wang CJ, Guyot-Sionnest P. Interband and intraband optical studies of PbSe colloidal quantum dots. *J. Phys. Chem. B.* 2002;106(41):10634–10640.
35. Hyeon T, et al. Synthesis of highly crystalline and monodisperse maghemite nanocrystallites without a size-selection process. *J. Am. Chem. Soc.* 2001;123(51):12798–12801.
36. Cheon J, et al. Shape evolution of single-crystalline iron oxide nanocrystals. *J. Am. Chem. Soc.* 2004;126(7):1950–1951.
37. Sugimoto T. Preparation of monodispersed colloidal particles. *Adv. Colloid Interface Sci.* 1987;28:65.
38. Peng X, Wickham J, Alivisatos AP. Kinetics of II–VI and III–V colloidal semiconductor nanocrystal growth: “focusing” of size distributions. *J. Am. Chem. Soc.* 1998;120(21):5343–5344.
39. Pellegrino T, et al. Hydrophobic nanocrystals coated with an amphiphilic polymer shell: a general route to water soluble nanocrystals. *Nano Lett.* 2004;4(4):703–707.
40. Smith AM, et al. A systematic examination of surface coatings on the optical and chemical properties of semiconductor quantum dots. *Phys. Chem. Chem. Phys.* 2006;8:3895–3903.
41. Aldana J, Wang YA, Peng X. Photochemical instability of CdSe nanocrystals coated by hydrophilic thiols. *J. Am. Chem. Soc.* 2001;123(36):8844–8850.
42. Liz-Marzán LM, Giersig M, Mulvaney P. Synthesis of nanosized gold–silica core–shell particles. *Langmuir.* 1996;12(18):4329–4335.
43. Gerion D, et al. Synthesis and properties of biocompatible water-soluble silica-coated CdSe/ZnS semiconductor quantum dots. *J. Phys. Chem. B.* 2001;105(37):8861–8871
44. Pellegrino T, et al. On the development of colloidal nanoparticles towards multifunctional structures and their possible use for biological applications. *Small.* 2005;1(1):48–63.

45. Derfus AM, Chan WCW, Bhatia SN. Probing the cytotoxicity of semiconductor quantum dots. *Nano Lett.* 2004;4(1):11–18.
46. Kirchner C, et al. Cytotoxicity of colloidal CdSe and CdSe/ZnS nanoparticles. *Nano Lett.* 2005;5(2):331–338.
47. Tsoli M, et al. Cellular uptake and toxicity of Au₅₅ clusters. *Small.* 2005;1(8–9):841–844.
48. Parak WJ, et al. Cell motility and metastatic potential studies based on quantum dot imaging of phagokinetic tracks. *Adv. Mater.* 2002;14(12):882–885.
49. Kloepfer JA, et al. Quantum dots as strain- and metabolism-specific microbiological labels. *Appl. Environ. Microbiol.* 2003;69(7):4205–4213.
50. Warheit DB, et al. Comparative pulmonary toxicity assessment of single-wall carbon nanotubes in rats. *Toxicol. Sci.* 2004;77:117–125.
51. Decher G. Fuzzy nanoassemblies: toward layered polymeric multicomposites. *Science.* 1997;277:1232–1237.
52. Sukhorukov GB, et al. Stepwise polyelectrolyte assembly on particle surfaces: a novel approach to colloid design. *Polym. Adv. Technol.* 1998;9(10–11):759–767.
53. Peyratout CS, Dähne L. Tailor-made polyelectrolyte microcapsules: from multilayers to smart containers. *Angew. Chem.-Int. Ed.* 2004;43:3762–3783.
54. Mauser T, Dejugnat C, Sukhorukov GB. Reversible pH-dependent properties of multilayer microcapsules made of weak polyelectrolytes. *Macromol. Rapid Commun.* 2004;25(20):1781–1785.
55. Kreft O, et al. Polymer microcapsules as mobile local pH-sensors. *J. Mater. Chem.* 2007;17:4471–4476.
56. Sukhorukov GB, et al. Nanoengineered polymer capsules: tools for detection, controlled delivery and site specific manipulation. *Small.* 2005;1(2):194–200.
57. De Geest BG, et al. Release mechanisms for polyelectrolyte capsules. *Chem. Soc. Rev.* 2007;36:636–649.
58. Ruysschaert T, et al. Liposome-based nanocapsules. *IEEE Trans. Nanobiosci.* 2005;3(1):49–55.
59. Kwona GS, Okano T. Polymeric micelles as new drug carriers. *Adv. Drug Deliv. Rev.* 1996;21(2):107–116.
60. Buck SM, et al. Optochemical nanosensor PEBBLES: photonic explorers for bioanalysis with biologically localized embedding. *Curr. Opin. Chem. Biol.* 2004;8:540–546.
61. Nowak AP, et al. Rapidly recovering hydrogel scaffolds from self-assembling diblock copolypeptide amphiphiles. *Nature.* 2002;417(23 May):424–428.
62. Conner SD, Schmid SL. Regulated portals of entry into the cell. *Nature.* 2003;422:37–41.
63. Muñoz-Javier A, et al. Uptake of colloidal polyelectrolyte multilayer capsules by living cells. 2007; in preparation.
64. Mehrishi JN. Molecular aspects of the mammalian cell surface. *Prog. Biophys. Mol. Biol.* 1972;25:1–70.
65. Ghitescu L, Fixman A. Surface charge distribution on the endothelial cell of liver sinusoids. *J. Cell Biol.* 1984;99:639–647.
66. Muñoz-Javier A. et al. Combined atomic force microscopy and optical microscopy measurements as a method to investigate particle uptake by cells. *Small.* 2006;2(3):394–400.

67. Ai H, et al. Interactions between self-assembled polyelectrolyte shells and tumor cells. *J. Biomed. Mater. Res. A*. 2005;73A(3):303–312.
68. Muñoz-Javier A, et al. Uptake of colloidal polyelectrolyte coated particles and polyelectrolyte multilayer capsules by living cells. *Adv. Mater.* 2008;20(22):4281–4287.
69. de Geest BG, et al. Intracellularly degradable polyelectrolyte microcapsules. *Adv. Mater.* 2006;18:1005–1009.
70. De Koker S, et al. In vivo cellular uptake, degradation, and biocompatibility of polyelectrolyte microcapsules. *Adv. Funct. Mater.* 2007;17(18):3754–3763.
71. Weissleder R, et al. Superparamagnetic iron oxide: pharmacokinetics and toxicity. *Am. J. Roentgenol.* 1989;152:167–173.
72. Shukla R, et al. Biocompatibility of gold nanoparticles and their endocytotic fate inside the cellular compartment: a microscopic overview. *Langmuir.* 2005;21:10644–10654.
73. Kirchner C, et al. Cytotoxicity of nanoparticle-loaded polymer capsules. *Talanta.* 2005;67:486–491.
74. Cortez C, et al. Targeting and uptake of multilayered particles to colorectal cancer cells. *Adv. Mater.* 2006;18(15):1998–2003.
75. Alexiou C, et al. In vitro and in vivo investigations of targeted chemotherapy with magnetic nanoparticles. *J. Magn. Magn. Mater.* 2005;293:389–393.
76. Alexiou C, et al. Magnetic drug targeting: biodistribution of the magnetic carrier and the chemotherapeutic agent mitoxantrone after locoregional cancer treatment. *J. Drug Targeting.* 2003;11(3):139–149.
77. Häfeli UO. Magnetically modulated therapeutic systems. *Int. J. Pharm.* 2004;277:19–24.
78. Alexiou C, et al. Locoregional cancer treatment with magnetic drug targeting. *Cancer Res.* 2000;60(23):6641–6648.
79. Zebli B, et al. Magnetic targeting and cellular uptake of polymer microcapsules simultaneously functionalized with magnetic and luminescent nanocrystals. *Langmuir.* 2005;21:4262–4265.
80. Skirtach AG, et al. The role of metal nanoparticles in remote release of encapsulated materials. *Nano Lett.* 2005;5(7):1371–1377.
81. Skirtach AG, et al. Laser-induced release of encapsulated materials inside living cells. *Angew. Chem. Int. Ed.* 2006;45:4612–4617.
82. Sheldon C, Cheng YM, Church J. Concurrent measurements of the free cytosolic concentrations of H⁺ and Na⁺ ions with fluorescent indicators. *Pflügers Arch. Eur. J. Physio.* 2004;449(3):307–318.
83. Altan BN, et al. Defective acidification in human breast tumor cells and implications for chemotherapy. *J. Exp. Med.* 1998;187(10):1583–1598.
84. Haugland RP. *Handbook of Fluorescent Probes and Research Biochemicals*. Molecular Probes, Eugene, OR, 2004.
85. Tycko B, Maxfield FR. Rapid acidification of endocytic vesicles containing α_2 -macroglobulin. *Cell.* 1982;28(3):433–681.

Luminescent Quantum Dot FRET-Based Probes in Cellular and Biological Assays

LIFANG SHI, NITSA ROSENZWEIG, and ZEEV ROSENZWEIG

Department of Chemistry and the Advanced Materials Research Institute,
University of New Orleans, New Orleans, Louisiana

- 9.1 Introduction
- 9.2 Luminescent quantum dots
- 9.3 Fluorescence resonance energy transfer
- 9.4 Quantum dot FRET-based protease probes
- 9.5 Summary and conclusions

9.1 INTRODUCTION

In this chapter we describe the development of luminescent quantum dot-based bioanalytical probes for the analysis of target analytes in biological samples. The newly developed quantum dots respond to changes in biological systems by changing their luminescence properties. More specifically, we focus on studies carried out in our laboratory toward the development of quantum dot fluorescence resonance energy transfer (FRET)-based protease sensors for real-time monitoring of proteolytic activity as a mean to discriminate between normal and cancerous cells. These studies are a part of a large effort by the research community to develop sensors with high sensitivity and high specificity for cancer research [1]. To date, fluorescence methods based on the use of molecular fluorophores have been the most common methods of detecting biomolecules. Many of these molecular fluorophores suffer from serious chemical and photophysical limitations, such as broad emission spectra, low

photobleaching thresholds, and poor chemical stability. The field of optical imaging was recently advanced by the development of nanoparticle-based agents such as luminescent quantum dots that exhibit higher photostability and more desirable photophysical properties. The development of water-soluble and biocompatible quantum dots was first reported in 1998 [2,3]. Since then, luminescent quantum dots have emerged as new and promising components in fluorescence sensors for cancer detection [4]. The quantum dot FRET-based probes that have been developed in our laboratory are prepared by linking molecular fluorophores to the surface of CdSe–ZnS luminescent quantum dots. Their analyte response is based on FRET interactions between the quantum dots and molecular acceptors and on the attenuation of these interactions in the presence of target analytes. In the following sections we briefly review recent developments in the field of quantum dots and the phenomenon of FRET to enable better understanding of the working principle and analytical utility of quantum dot FRET-based nanosensors.

9.2 LUMINESCENT QUANTUM DOTS

Quantum dots are semiconductor nanoparticles 1 to 10 nm in diameter. These luminescent nanocrystals are composed of atoms from the II–VI (CdS, CdSe, CdTe, ZnO, ZnSe), III–V (InP, InAs, GaN, GaP, GaAs), and IV–VI (PbS, PbSe, PbTe) groups of the periodic table. Quantum dots are spherical, crystalline particles of a given material consisting of hundreds to thousands of atoms. Their diameter is smaller than the Bohr radius of electron–hole pairs (excitons). When the size of a semiconductor particle is small enough to approach the size of the material exciton Bohr radius, the electron energy levels are no longer treated as a continuum but, instead, are treated as discrete, a condition defined as *quantum confinement*. Quantum confinement leads to increased stress on an exciton, which results in increased energy of the photon emitted. The smaller the quantum dots, the higher the energy required to form the exciton. The behavior of the excited electron can be described by a simple particle-in-a-box model [5]. The quantum confinement increases the probability of overlap between the electron and hole, which increases the rate of radiative recombination. This results in quantum dots with unique optical and electronic properties [6–10].

CdX quantum dots (X = S, Se, Te) have attracted great interest, due to their emission in the ultraviolet–visible–near infrared range of the electromagnetic spectrum. These quantum dots have several optical characteristics which distinguish them from conventional organic fluorophores. These include size-dependent luminescence [2,11], in which the light wavelength emitted is determined by the energy bandgap between the valence and conduction bands of the quantum dots. As the size of the quantum dots decreases, the energy bandgap increases. Since the energy bandgap of the quantum dots is size dependent, the emission color of the quantum dots is also size dependent [12,13]. Luminescent quantum dots have a much wider absorption spectrum than that of molecular fluorophores. This enables excitation of quantum dots using a wide range of wavelengths. It also enables the excitation of quantum dots of

different sizes by a single wavelength, which makes them suitable for multiplexing or simultaneous detection of quantum dots of different emission colors (8). Additionally, the molar extinction coefficients of quantum dots are larger than those of organic dyes [14,15]. Quantum dots have symmetric and narrow emission spectra without a red tail. This reduces crosstalk between emission signals of quantum dots of different emission colors [16]. The long fluorescence lifetime of quantum dots is also an advantage since it enables their use in time-gated detection to separate their signal from that of shorter-lifetime species: for example, the autofluorescence of cells [17,18]. Finally, a major advantage of quantum dots is their high photostability and chemical stability compared to molecular fluorophores, which enables their use in imaging applications that require long exposure times [19–25].

The size and shape of quantum dots are controlled by altering the duration, temperature, and ligand molecules used in their synthesis. To date, quantum dots such as CdSe, CdS, and CdTe have been synthesized in various media, including aqueous solution [26,27], reverse micelles [28], polymer films [29,30], sol-gel systems [31], and trioctylphosphine oxide (TOPO)/trioctylphosphine (TOP) [11,32–34]. High-quality quantum dots have been achieved by pyrolysis of organometallic precursors in TOP–TOPO media, first reported by Murray in 1993 [11]. The synthesis is carried out by injecting dimethylcadmium [$\text{Cd}(\text{CH}_3)_2$] and sulfur, selenium, or tellurium dissolved in TOP solution to hot TOPO media. However, dimethylcadmium is very toxic, pyrophoric, unstable, and expensive. The synthesis procedure was later refined by Peng and co-workers, who replaced the toxic cadmium precursor $\text{Cd}(\text{CH}_3)_2$, with CdO , $\text{Cd}(\text{Ac})_2$, and CdCO_3 , which led to a more user-friendly green synthesis [32–34]. Confining the electrons to the bulk of luminescent quantum dots is imperative to their bright luminescence. The excited electron or hole could be trapped by surface defects such as vacancies, local lattice mismatches, dangling bonds, and adsorbates at the surfaces. These lead to nonradiative recombination and to low emission quantum yield (5). Additionally, the uncapped quantum dots are so reactive that they readily undergo photochemical degradation. To decrease the effect of surface defects and to protect surface atoms from oxidation and other chemical reactions, an additional thin layer made of a higher-energy bandgap semiconductor material (e.g., ZnS) is grown on the surface of the quantum dots [35–39]. This process, often described in the literature as surface passivation, increases the emission quantum yield, improves chemical stability and photostability, and reduces the toxicity by preventing leakage of Cd or Se to the surrounding environment. Due to the availability of precursors and the simplicity of crystallization, CdSe–ZnS core–shell quantum dots have been widely used in biological applications.

High-quality quantum dots that are synthesized in organic solvents are not water soluble, are not biocompatible, and do not have the functional groups required for bioconjugation. To facilitate their application in aqueous biological systems, the hydrophobic TOPO molecules that serve as capping ligands of luminescent quantum dots must be replaced by bifunctional hydrophilic capping ligands or coated with amphiphilic protective layer to impart water solubility and potential bioconjugation sites. Various methods of quantum dot surface functionalization to facilitate their water solubility, stability in aqueous systems, and biocompatibility have been

developed in recent years. These solubilization strategies can be divided into three categories.

1. Ligand exchange is a process involving the replacement of hydrophobic ligands with bifunctional ligands in which one end binds to the quantum dot surface and an opposing end imparts water solubility via hydrophilic groups. Thiols ($-SH$) are often used to bind the capping ligand to a quantum dot ZnS surface. The TOPO ligands are often exchanged with thiol-functionalized compounds such as mercaptoacetic acid (MAA) [3], dihydrolipoic acid (DHLA) [40], dithiothreitol (DTT) [41], and dendrons [42]. In our laboratory we found that the amino acid cysteine is also an effective capping ligand to create hydrophilic quantum dots [43]. Pinaud and co-workers reported that cysteine-containing peptides can also be used as effective capping ligands to facilitate the water solubility of quantum dots [44]. Since the bond between thiol and ZnS is not particularly strong, the ligands often fall off the surface, which leads aggregation of the quantum dots [45]. In addition, the ligand exchange process often disturbs the chemical and physical state of the surface atoms of quantum dots and reduces their emission quantum yield [46].
2. Silica encapsulation involves the growth of a silica layer on the surface of quantum dots. Functional organosilane molecules are incorporated into the shell to provide surface functionalities for bioconjugation [2,47–50]. The silica-coated quantum dots are extremely stable because the silica layer is highly cross-linked. However, the method is very laborious and the silica layer may be hydrolyzed [51].
3. Another approach is to coat quantum dots with an amphiphilic polymer or phospholipids, which interleave with the hydrophobic TOPO ligands through hydrophobic attraction and provide a hydrophilic exterior to ensure aqueous solubility [25,52–54]. This process maintains the native ligands (TOPO) on the surface of quantum dots. This retains the high-emission quantum yield of quantum dots and protects the quantum dot surface from deterioration in biological solution. However, the final size of quantum dots is large, which could limit many biological applications [51].

Despite these limitations, water-soluble quantum dots have been widely used in protein assays [55–59] and in DNA and RNA hybridization assays [60–64]. They have also been used as labels in *in vitro* imaging of cells and tissues [25,65–68] and in *in vivo* imaging applications in whole animals [69–73]. As mentioned previously, the focus of our work is the development of quantum dot FRET-based probes for biological applications. A brief description of FRET leading to our results in this area is given next.

9.3 FLUORESCENCE RESONANCE ENERGY TRANSFER

Fluorescence resonance energy transfer involves nonradiative energy transfer from an excited donor to an acceptor via through-space dipole–dipole interaction [74–76].

Molecular FRET donor–acceptor pairs satisfy the following conditions: (1) spectral overlap between the absorption spectrum of the acceptor and the fluorescence emission spectrum of the donor, and (2) the fact that the donor and acceptor molecules must be in close proximity (typically, 10 to 100 Å). The rate of energy transfer depends on the extent of spectral overlap between the emission spectrum of the donor and the absorption spectrum of the acceptor, the relative orientation of donor–acceptor transition dipoles, and the distance between the donor and acceptor. The rate of energy transfer is given by

$$k_t = \tau_D^{-1} \left(\frac{R_0}{R} \right)^6 \quad (9.1)$$

where τ_D is the measured lifetime of the donor in the absence of the acceptor, and R_0 is the critical radius of the transfer or the Forster distance, which is the distance at which the energy transfer efficiency is 50%. R_0 depends on the spectral characteristics of the donor–acceptor pair and is expressed as

$$R_0 = \left(\frac{3000}{4\pi N |A|_{1/2}} \right)^{1/3} \quad (9.2)$$

where N is Avogadro's number and $|A|_{1/2}$ is the concentration of the acceptor at which the energy transfer efficiency E is 50%. For a donor and acceptor pair that is covalently bound, E is expressed as

$$E = \frac{R_0^6}{R_0^6 + R^6} \quad (9.3)$$

The FRET efficiency can be measured experimentally by monitoring changes in the donor or/and acceptor fluorescence intensities, or changes in the fluorescent lifetimes of fluorophores. As a result, the fluorescence intensity and lifetime of donor decrease while the acceptor fluorescence is sensitized and its lifetime is longer.

Molecular fluorophores have been used widely as donors and acceptors in FRET-based assays and sensors. However, they have several limitations as FRET agents [51,77,78]. These include narrow and overlapping absorption spectra, which make it difficult to avoid direct excitation of the acceptor; and a broad emission spectrum of the donor with long red tailing, which often overlaps with the emission spectrum of the acceptor and results in spectral crosstalk. In addition, molecular fluorophores have low photobleaching thresholds, which prevent real-time monitoring of FRET signals over long durations under conditions of continuous exposure.

Quantum dots have been investigated as FRET donors, as alternatives to traditional molecular fluorophores because of their high photostability and their unique spectral properties [52,77,79]. In 1996, Kagan and co-workers first reported energy transfer between quantum dots [80,81]. In 2001, several research groups reported FRET between quantum dots and molecular fluorophores and quenchers [82–84]. For example, Willard et al. developed quantum dots as a FRET donor in a protein–protein

binding assay [82]. In 2003, Medinta et al. reported the development of quantum dot FRET-based biosensors for maltose, which was realized by coating CdSe–ZnS quantum dots capped with DHLA with maltose-binding protein (MBP) molecules [85]. The FRET assay was based on competitive interactions between maltose and molecular quenchers on the MBP-binding site. Maltose molecules displaced the molecular quenchers from the MBP-binding sites, which resulted in a maltose concentration–dependent increase in the emission of MBP-coated quantum dots. Similar quantum dot FRET-based sensors were developed for TNT [86], toxins [87], β -lactamase [88], collagenase [89], DNA [64], RNA [90], and proteins [91]. In all of these probes, the quantum dots were used as donors while the organic fluorophores served as fluorescent acceptors. The FRET mechanism allows the quantum dots to respond to environmental changes while avoiding direct chemical interaction with the quantum dots that could negatively affect their photophysical properties and decrease their brightness.

9.4 QUANTUM DOT FRET-BASED PROTEASE PROBES

Recent studies in our laboratory focused on the development of quantum dot FRET-based protease probes [92,93]. The working principle of these probes is illustrated in Figure 9.1. Luminescent quantum dots that are coated with unlabeled RGDC peptide molecules emit green light. When capped with rhodamine-labeled RGDC molecules, the emission color turns orange, due to FRET interactions between the quantum dots and rhodamine molecules. The RGDC peptide molecules are cleaved by proteolytic enzymes to release the ehodamine molecules from the surface. This, in turn, restores the green emission of the quantum dots. To prepare quantum dot FRET-based probes, TOPO-capped CdSe–ZnS quantum dots were first synthesized following a method developed by Peng and others with slight modifications [32,94]. A ligand exchange reaction was then used to replace the TOPO ligands with RGDC peptide molecules, some labeled with rhodamine and some unlabeled. The reaction was carried out in a mixture of pyridine and dimethyl sulfoxide (DMSO) following a method developed by Pinaud and co-workers [44]. Unbound peptide molecules were removed by spin dialysis. The ratio between rhodamine-labeled RGDC and unlabeled RGDC peptide

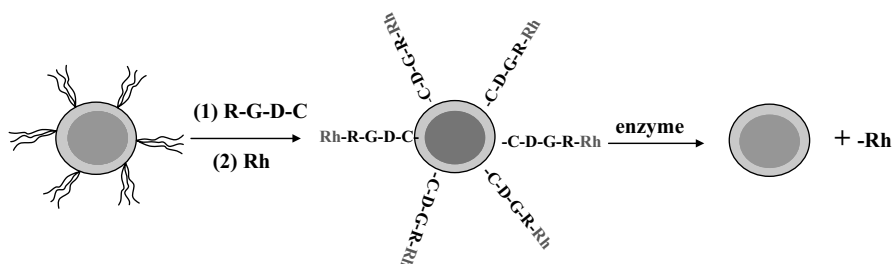


FIGURE 9.1 Quantum dot FRET-based protease sensor. Green and orange emitting quantum dots are shown in light and dark gray, respectively.

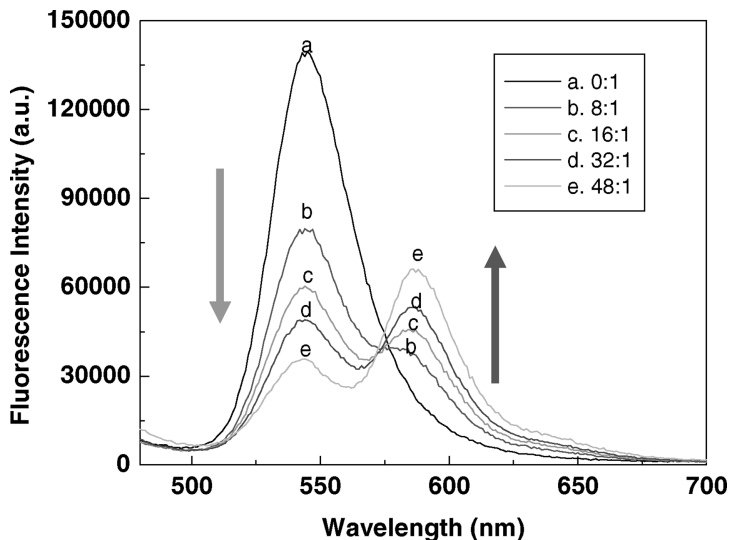


FIGURE 9.2 (a) Emission spectra of rhodamine-labeled peptide-coated quantum dots at increasing ratio between rhodamine-labeled RGDC peptide and unlabeled RGDC peptide molecules: curve a, 0:1; curve b, 8:1; curve c, 16:1; curve d, 32:1; curve e, 50:1.

molecules was varied to maximize the FRET signal between the quantum dots and attached rhodamine molecules. Figure 9.2 shows the emission spectra of rhodamine-labeled peptide coated at increasing rhodamine-labeled RGDC concentration. When excited at 445 nm, the emission peak of the quantum dots at 545 nm decreased with increasing rhodamine concentration. The emission peak of rhodamine at 590 nm also increased progressively with increasing rhodamine-labeled RGDC concentration. These observations indicated the occurrence of FRET between the quantum dots and the rhodamine molecules. Digital fluorescence microscopic images were used to provide additional visual evidence of FRET between the quantum dots and rhodamine molecules. The emission color of unlabeled peptide-coated quantum dots was green. The emission color turned yellow–orange when the unlabeled RGDC peptide molecules were replaced with rhodamine-labeled RGDC molecules. This emission color change from green to orange also indicated the occurrence of FRET between quantum dots and bound rhodamine molecule.

The quantum dot FRET-based probes were first used to determine the activity of the proteolytic enzyme trypsin, which cleaves peptides and proteins at the carboxyl end of lysine (K) and arginine (R). Figure 9.3(a) shows the temporal dependence of the F_d/F_a ratio at increasing trypsin concentrations, ranging from 0 to 500 $\mu\text{g}/\text{mL}$. F_d/F_a is a direct measure of the FRET efficiency between the quantum dots and molecular acceptors. High F_d/F_a values indicate low FRET efficiency. F_d/F_a was normalized to $(F_d/F_a)_0$, which is the value of F_d/F_a prior to the addition of trypsin to the quantum dot solutions. It can be seen that F_d/F_a increased faster at higher trypsin concentrations. For example, at 250 $\mu\text{g}/\text{mL}$ trypsin, the enzymatic reaction was completed in less than

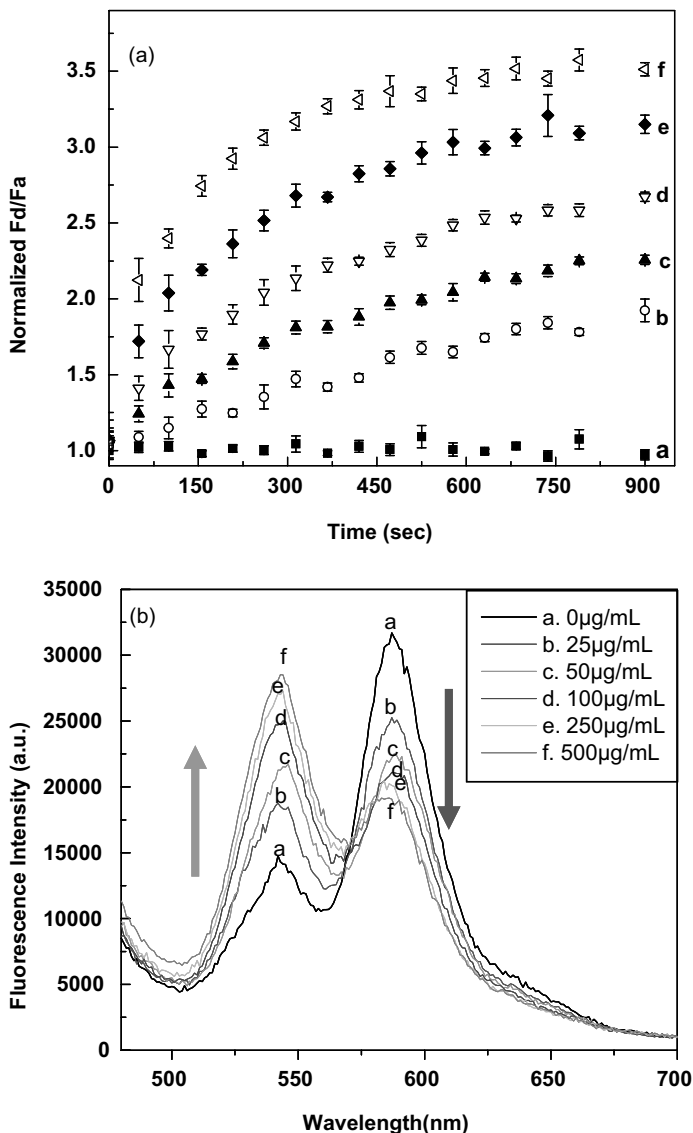


FIGURE 9.3 (a) Temporal dependence of the rhodamine-labeled peptide-coated quantum dots at increasing trypsin concentration: curve a, 0 $\mu\text{g/mL}$; curve b, 25 $\mu\text{g/mL}$; curve c, 50 $\mu\text{g/mL}$; curve d, 100 $\mu\text{g/mL}$; curve e, 250 $\mu\text{g/mL}$; curve f, 500 $\mu\text{g/mL}$. The ratio F_d/F_a was normalized to $(F_d/F_a)_0$, which is the ratio F_d/F_a prior to adding trypsin to the quantum dot probe solutions. (b) Emission spectra of the quantum dot FRET-based probes at increasing trypsin concentration: curve a, 0 $\mu\text{g/mL}$; curve b, 25 $\mu\text{g/mL}$; curve c, 50 $\mu\text{g/mL}$; curve d, 100 $\mu\text{g/mL}$; curve e, 250 $\mu\text{g/mL}$; curve f, 500 $\mu\text{g/mL}$. ($\lambda_{\text{ex}} = 445 \text{ nm}$.)

15 minutes. The short assay time is a significant advantage over previously reported quantum dot FRET-based probes, in which longer reaction times were reported [89]. The quantum dot FRET-based probes were also used successfully to determine the activity of collagenase, another proteolytic enzyme from the family of extracellular matrix metalloproteinases (MMP). Following a demonstration of the ability of quantum dot FRET-based probes to monitor the activity of collagenase in solution, we employed the same probes to measure the activity of MMPs in cell cultures. Quantum dot FRET-based probes were embedded in the extracellular matrix of normal and cancerous breast cells. Images of quantum dot FRET-based probes in normal and cancerous breast cell cultures were taken at $t=0$ and $t=15$ minutes following addition of the quantum dot-based probes to the cultures. The emission color of the orange emitting quantum dots did not change when incubated with normal breast cells. On the other hand, a clear change of emission color from orange to green was observed when the quantum dot FRET-based probes were incubated with breast cancer cells, which is attributed to the overexpression of MMPs in breast cancer cells. Similar to soluble collagenase, the MMPs cleave the peptide molecules and release the rhodamine molecules from the quantum dots. This results in rapid FRET signal changes and in an emission color change in the quantum dots. These newly developed cellular assays provide valuable tools in the quest of the research community to develop new and improved methods for cancer detection and monitoring.

9.5 SUMMARY AND CONCLUSIONS

In this chapter we describe the development of quantum dot FRET-based sensors with a particular focus on protease activity probes. The quantum dot FRET-based sensors are based on FRET interactions between quantum dots, which serve as donors, and molecular fluorophores, which are attached to the quantum dot surface and serve as fluorescent acceptors. This unique geometry has enabled the use of quantum dots for the first time in nanosensing applications. It must, however, be noted that FRET interactions between quantum dots and fluorescent acceptor molecules are not fully understood and need to be studied in greater detail. Unlike in FRET interactions between molecular donors and acceptors, the distance between quantum dots and molecular acceptors is not well defined. Our studies show that the FRET efficiency is high even when a short tetrapeptide links the quantum dots and the acceptor molecules. It is possible that the accumulative interaction between single quantum dots and multiple acceptor molecules compensates for the low FRET efficiency between quantum dots and individual acceptor molecules when these are bound through a short linker. It should also be noted that the Forrester theory commonly used to describe energy transfer between molecular donor and acceptor molecules was never tested in heterogeneous systems consisting of luminescent nanoparticles as donors and fluorescent molecules as acceptors. The heterogeneity in quantum dot size can affect the precision of single-molecule FRET measurements.

In broader terms it is clear that quantum dots have considerable advantages over molecular fluorophores. However, quantum dots have their limitations in

biological applications. Surface modification of quantum dots to realize aqueous solubility and the presence of functional groups suitable for bioconjugation often decrease the emission quantum yield of quantum dots. Also, quantum dots have limited pH stability and tend to aggregate in biological media. Although it is possible to attach a number of biomolecules to a single quantum dot, it is difficult to quantify the actual number of biomolecules on the quantum dot surface. This requires the development of a new generation of instrumentation with the capability to interrogate the surface of nanoparticles to quantify molecular surface coverages at the single particle level. Perhaps the biggest concern associated with large-scale use of luminescent quantum dots is their cytotoxicity. It is difficult to envision widespread use of cadmium-based quantum dots given their toxicity properties. Nevertheless, given the superb photophysical properties of luminescent quantum dots, it is likely that research will continue to minimize, if not eliminate, their toxicity and increase their stability in biological systems and biocompatibility while maintaining their unique photophysical properties intact.

Acknowledgments

Studies described in this chapter were supported by National Science Foundation award CHE-0717526 and Department of Defense/DARPA award HR0011-07-01-0032.

REFERENCES

1. Murcia MJ, Naumann CA. Biofunctionalization of fluorescent nanoparticles. In Kumar CSSR, ed. *Biofunctionalization of Nanomaterials*. 2005; pp. 1–38.
2. Bruchez M, Moronne M, Gin P, Weiss S, Alivisatos AP. Semiconductor nanocrystals as fluorescent biological labels. *Science*. 1998; 281:2013–2016.
3. Chan WCW, Nie SM. Quantum dot bioconjugates for ultrasensitive nonisotopic detection. *Science*. 1998; 281:2016–2018.
4. Willard DM, Mutschler T, Yu M, Jung J, Van Orden A. Directing energy flow through quantum dots: towards nanoscale sensing. *Anal. Bioanal. Chem*. 2006; 384:564–571.
5. Murphy CJ. Optical sensing with quantum dots. *Anal. Chem*. 2002; 74(19): 520A–526A.
6. Alivisatos AP. Semiconductor clusters, nanocrystals, and quantum dots. *Science*. 1996; 271 (5251):933–937.
7. Efros AL, Rosen MM. The electronic structure of semiconductor nanocrystals. *Annu. Rev. Mater. Sci*. 2000; 30:475–521.
8. Chan WCW, Maxwell DJ, Gao X, Bailey RE, Han M, Nie S. Luminescent quantum dots for multiplexed biological detection and imaging. *Curr. Opin. Biotechnol*. 2002; 13:40–46.
9. Gao XH, Yang L, Petrosos JA, Marshall FF, Simons JW, Nie SM. In vivo molecular and cellular imaging with quantum dots. *Curr. Opin. Biotechnol*. 2005; 16:63–72.

10. Michalet FX, Pinaud F, Bentolila LA, et al. Quantum dots for live cells, in vivo imaging, and diagnostics. *Science*. 2005; 307:538–544.
11. Murray CB, Norris DJ, Bawendi MG. Synthesis and characterization of nearly monodisperse CdE (E = sulfur, selenium, tellurium) semiconductor nanocrystallites. *J. Am. Chem. Soc.* 1993; 115:8706–8715.
12. Alivisatos AP. Perspectives on the physical chemistry of semiconductor nanocrystals. *J. Phys. Chem.* 1996; 100:13226–13239.
13. Easley RE, Smith AM, Nie SM. Quantum dots in biology and medicine. *Physica E*. 2004; 25:1–12.
14. Striolo A, Ward J, Prausnitz JM, et al. Molecular weight, osmotic second virial coefficient, and extinction coefficient of colloidal CdSe nanocrystals. *J. Phys. Chem. B*. 2002; 106:5500–5505.
15. Leatherdale CA, Woo WK, Mikulec FV, Bawendi MG. On the absorption cross section of CdSe nanocrystal quantum dots. *J. Phys. Chem. B*. 2002; 106:7619–7622.
16. Parak WJ, Pellogrino T, Plank C. Labeling of cells with quantum dots. *Nanotechnology*. 2005; 16:R9–R25.
17. Dahan M, Laurence T, Pinaud F, Chemla DS, Alivisatos AP. Time-gated biological imaging using colloidal quantum dots. *Opt. Lett.* 2001; 26:825–827.
18. Hohng S, Ha T. Near-complete suppression of quantum dot blinking in ambient conditions. *J. Am. Chem. Soc.* 2004; 126:1324–1325.
19. Michalet X, Pinaud F, Lacoste TD, Dahan M, Bruchez M. Properties of fluorescent semiconductor nanocrystals and their application to biological labeling. *Single Mol.* 2001; 2:261–276.
20. Wu X, Liu H, Liu J, Haley KN, Treadway JA. Immunofluorescent labeling of cancer marker Her2 and other cellular targets with semiconductor quantum dots. *Nat. Biotechnol.* 2003; 21:41–46.
21. Xiao Y, Barker PE. Semiconductor nanocrystal probes for human metaphase chromosomes. *Nucleic Acids Res.* 2004; 32:e28.
22. Ness JM, Akhtar RS, Latham CB, Roth KA. Combined tyramide signal amplification and quantum dots for sensitive and photostable immunofluorescence. *J. Histochem. Cytochem.* 2003; 51:981–987.
23. Jaiswal JK, Mattoussi H, Mauro JM, Simon SM. Long-term multiple color imaging of live cells using quantum dot bioconjugates. *Nat. Biotechnol.* 2003; 21:47–51.
24. Hanaki K, Momo A, Oku T, Komoto A, Maenosono S. Semiconductor quantum dot/albumin complex is a long-life and highly photostable endosome marker. *Biochem. Biophys. Res. Commun.* 2003; 302:496–501.
25. Dubertret B, Skourides P, Norris DJ, Noireaux V, Brivanlou AH, Libchaber A. In vivo imaging of quantum dots encapsulated in phospholipid micelles. *Science*. 2002; 298:1759–1762.
26. Gaponik N, Talapin DV, Rogach AL, Eychmuller A, Weller H. Efficient phase transfer of luminescent thiol-capped nanocrystals: from water to nonpolar organic solvents. *Nano Lett.* 2002; 2(8):803–806.
27. Ni T, Nagesha DK, Robles J, Materer NF, Mussig S, Kotov NA. CdS nanoparticles modified to chalcogen sites: new supramolecular complexes, butterfly bridging, and related optical effects. *J. Am. Chem. Soc.* 2002; 124(15):3980–3992.

28. Hirai T, Watanabe T, Komasa I. Preparation of semiconductor nanoparticle–polyurea composites using reverse micellar systems via an in situ diisocyanate polymerization. *J. Phys. Chem. B.* 1999; 103(46):10120–10126.
29. Farmer SC, Patten TE. Photoluminescent polymer/quantum dot composite nanoparticles. *Chem. Mater.* 2001; 13(11):3920–3296.
30. Mansur HS, Vasconcelos WL, Grieser F, Caruso F. Photoelectrochemical behavior of CdS “Q-state” semiconductor particles in 10,12-nonacosadiynoic acid polymer Langmuir–Blodgett films. *J. Mater. Sci.* 1999; 34(21):5285–5291.
31. Zelner M, Minti H, Reisfeld R, Cohen H, Tenne R. Preparation and characterization of CdS films synthesized in situ in zirconia sol–gel matrix. *Chem. Mater.* 1997; 9(11):2541–2543.
32. Peng ZA, Peng X. Formation of high-quality CdTe, CdSe, and CdS nanocrystals using CdO as precursor. *J. Am. Chem. Soc.* 2001; 123(1):183–184.
33. Peng ZA, Peng X. Mechanisms of the shape evolution of CdSe nanocrystals. *J. Am. Chem. Soc.* 2001; 123(7):1389–1395.
34. Yu WW, Qu L, Guo W, Peng X. Experimental determination of the extinction coefficient of CdTe, CdSe, and CdS nanocrystals. *Chem. Mater.* 2003; 15(14):2854–2860.
35. Hines MA, Guyot-Sionnest P. Synthesis and characterization of strongly luminescing ZnS-capped CdSe nanocrystals. *J. Phys. Chem.* 1996; 100:468–471.
36. Dabbousi BO, Rodriguez-Viejo J, Mikulec FV, et al. (CdSe)ZnS core–shell quantum dots: synthesis and characterization of a size series of highly luminescent nanocrystallites. *J. Phys. Chem. B.* 1997; 101:9463–9475.
37. Li JJ, Wang YA, Guo W, et al. Large-scale synthesis of nearly monodisperse CdSe/CdS core/shell nanocrystals using air-stable reagents via successive ion layer adsorption and reaction. *J. Am. Chem. Soc.* 2003; 125:12567–12575.
38. Mekis I, Talapin DV, Kornowski A, Haase M, Weller H. One-pot synthesis of highly luminescent CdSe/CdS core-shell nanocrystals via organometallic and “Greener” chemical approaches. *J. Phys. Chem. B.* 2003; 107:7454–7464.
39. Malik MA, O’Brien P, Revaprasadu N. A simple route to the synthesis of core/shell nanoparticles of chalcogenides. *Chem. Mater.* 2002; 14:2004–2010.
40. Mattoussi H, Mauro JM, Goldman ER, et al. Self-assembly of CdSe–ZnS quantum dot bioconjugates using an engineered recombinant protein. *J. Am. Chem. Soc.* 2000; 122:12142–12150.
41. Pathak S, Choi SK, Arnheim N, Thompson ME. Hydroxylated quantum dots as luminescent probes for in situ hybridization. *J. Am. Chem. Soc.* 2001; 123:4103–4104.
42. Guo W, Li JJ, Wang YA, Peng X. Conjugation chemistry and bioapplications of semiconductor box nanocrystals prepared via dendrimer bridging. *Chem. Mater.* 2003; 15:3125–3133.
43. Chen Y, Rosenzweig Z. Luminescent CdS quantum dots as selective ion probes. *Anal. Chem.* 2002; 74(19):5132–5138.
44. Pinaud F, King D, Moore HP, Weiss S. Bioactivation and cell targeting of semiconductor CdSe/ZnS nanocrystals with phytochelatin-related peptides. *J. Am. Chem. Soc.* 2004; 126:6115–6123.
45. Aldana J, Wang YA, Peng S. Photochemical instability of CdSe nanocrystals coated by hydrophilic thiols. *J. Am. Chem. Soc.* 2001; 123:8844–8850.

46. Yu WW, Chang E, Drezek R, Colvin VL. Water-soluble quantum dots for biomedical applications. *Biochem. Biophys. Res. Commun.* 2006; 348:781–786.
47. Mulvaney P, Liz-Marzan LM, Giersig M, Ung T. Silica encapsulation of quantum dots and metal cluster. *J. Mater. Chem.* 2000; 10:1259–1270.
48. Gerion D, Pinaud F, Williams SC, et al. Synthesis and properties of biocompatible water-soluble silica-coated CdSe/ZnS semiconductor quantum dots. *J. Phys. Chem. B.* 2001; 105:8861–8871.
49. Nann T, Mulvaney P. Single quantum dots in spherical silica particles. *Angew. Chem. Int. Ed.* 2004; 43:5393–5396.
50. Rogach AL, Nagesha D, Ostrander JW, Giersig M, Kotov NA. “Raisin bun”-type composite spheres of silica and semiconductor nanocrystals. *Chem. Mater.* 2000; 12:2676–2685.
51. Alivisatos AP, Gu WW, Larabell C. Quantum dots as cellular probes. *Annu. Rev. Biomed. Eng.* 2005; 7:55–76.
52. Gao X, Cui Y, Levenson RM, Chung LW, Nie S. In vivo cancer targeting and imaging with semiconductor quantum dots. *Nat. Biotechnol.* 2004; 22:969–976.
53. Pellegrino T, Manna L, Kudera S, et al. Hydrophobic nanocrystals coated with an amphiphilic polymer shell: a general route to water soluble nanocrystals. *Nano. Lett.* 2004; 4:703–707.
54. Fan H, Leve EW, Scullin C, et al. Surfactant-assisted synthesis of water-soluble and biocompatible semiconductor quantum dot micelles. *Nano. Lett.* 2005; 5:645–648.
55. Goldman ER, Balighian ED, Mattoussi H, et al. Avidin: a natural bridge for quantum dot–antibody conjugates. *J. Am. Chem. Soc.* 2002; 124(22):6378–6382.
56. Lingerfelt BM, Mattoussi H, Goldman ER, Mauro JM, Anderson GP. Preparation of quantum dot–biotin conjugates and their use in immunochromatography assays. *Anal. Chem.* 2003; 75(16):4043–4049.
57. Aoyagi S, Kudo M. Development of fluorescence change-based, reagent-less optic immunosensor. *Biosens. Bioelectron.* 2005; 15; 20(8):1680–1684.
58. Ravindran S, Kim S, Martin R, Lord EM, Ozkan CS. Quantum dots as bio-labels for the localization of a small plant adhesion protein. *Nanotechnology.* 2005; 16(1):1–4.
59. Zhang Y, So M-K, Loening AM, Yao H, Gambhir SS, Rao J. HaloTag protein-mediated site-specific conjugation of bioluminescent proteins to quantum dots. *Angew. Chem. Int. Ed.* 2006; 45(30):4936–4940.
60. Tholouli E, Hoyland JA, Di Vizio D, et al. Imaging of multiple mRNA targets using quantum dot based in situ hybridization and spectral deconvolution in clinical biopsies. *Biochem. Biophys. Res. Commun.* 2006; 348(2):628–636.
61. Srinivasan C, Lee J, Papadimitrakopoulos F, Silbart LK, Zhao M, Burgess DJ. Labeling and intracellular tracking of functionally active plasmid DNA with semiconductor quantum dots. *Mol. Ther.* 2006; 14(2):192–201.
62. Crut A, Geron-Landre B, Bonnet I, Bonneau S, Desbiolles P, Escude C. Detection of single DNA molecules by multicolor quantum-dot end-labeling. *Nucleic Acids Res.* 2005; 33(11): e98/1–e98/9.
63. Gill R, Willner I, Shweky I, Banin U. Fluorescence resonance energy transfer in CdSe/ZnS-DNA conjugates: probing hybridization and DNA cleavage. *J. Phys. Chem. B.* 2005; 109:23715–23719.
64. Zhang CY, Yeh HC, Kuroki MT, Wang TH. Single-quantum-dot-based DNA nanosensor. *Nat. Mater.* 2005; 4:826–831.

65. Wu X, Liu H, Liu J, et al. Immunofluorescent labeling of cancer marker Her2 and other cellular targets with semiconductor quantum dots. *Nat. Biotechnol.* 2003; 21(1):41–46.
66. Fu A, Gu W, Larabell C, Alivisatos AP. Semiconductor nanocrystals for biological imaging. *Curr. Opin. Neurobiol.* 2005; 15(5):568–575.
67. Smith AM, Dave S, Nie S, True L, Gao X. Multicolor quantum dots for molecular diagnostics of cancer. *Expert Rev. Mol. Diagn.* 2006; 6(2):231–244.
68. Weng J, Song X, Li L, et al. Highly luminescent CdTe quantum dots prepared in aqueous phase as an alternative fluorescent probe for cell imaging. *Talanta.* 2006; 70(2):397–402.
69. Akerman ME, Chan WCW, Laakkonen P, Bhatia SN, Ruoslahti E. Nanocrystal targeting in vivo. *Proc. Natl. Acad. Sci. USA.* 2002; 99:12617–12621.
70. Larson DR, Zipfel WR, Williams RM, et al. Water-soluble quantum dots for multiphoton. Fluorescence imaging in vivo. *Science.* 2003; 300(5624):1434–1437.
71. Hoshino A, Hanaki K, Suzuki K, Yamamoto K. Applications of T-lymphoma labeled with fluorescent quantum dots to cell tracing markers in mouse body. *Biochem. Biophys. Res. Commun.* 2004; 314(1):46–53.
72. So M-K, Xu C, Loening AM, Gambhir SS, Rao J. Self-illuminating quantum dot conjugates for in vivo imaging. *Nat. Biotechnol.* 2006; 24(3):339–343.
73. Cai W, Shin D-W, Chen K, et al. Peptide-labeled near-infrared quantum dots for imaging tumor vasculature in living subjects. *Nano Lett.* 2006; 6(4):669–676.
74. Lakowicz JR. *Principles of Fluorescence Spectroscopy*. Plenum Press, New York, 1999;.
75. Vekshin N. *Energy Transfer in Macromolecules*. SPIE Press, Bellingham, WA, 1997;.
76. Van Der Meer BW, Coker G, Chen S-YS. *Resonance Energy Transfer: Theory and Data*. VCH, New York, 1994;.
77. Clapp AR, Medintz IL, Mattoussi H. Förster resonance energy transfer investigations using quantum-dot fluorophores. *ChemPhysChem.* 2006; 7:47–57.
78. Clapp AR, Medintz IL, Mauro JM, Fisher BR, Bawendi MG, Mattoussi H. Fluorescence resonance energy transfer between quantum dot donors and dye-labeled protein acceptors. *J. Am. Chem. Soc.* 2004; 126(1):301–310.
79. Willard DM, Van Orden A. Quantum dots: resonant energy-transfer sensor. *Nat. Mater.* 2003; 2(9):575–576.
80. Kagan CR, Murra CB, Bawendi MG. Long-range resonance transfer of electronic excitations in close-packed CdSe quantum-dot solids. *Phys. Rev. B.* 1996; 54:8633–8643.
81. Kagan CR, Murray CB, Nirmal M, Bawendi MG. Electronic energy transfer in CdSe quantum dot solids. *Phys. Rev. Lett.* 1996; 76:1517–1520.
82. Willard DM, Carillo LL, Jung J, Orden AV. CdSe–ZnS Quantum dots as resonance energy transfer donors in a model protein-protein binding assay. *Nano Lett.* 2001; 1:469–474.
83. Finlayson CE, Ginger DS, Greenham NC. Enhanced forster energy transfer in organic/inorganic bilayer optical microcavities. *Chem. Phys. Lett.* 2001; 338:83–87.
84. Mamedova NN, Kotov NA, Rogach AL, Studer J. Albumin–CdTe nanoparticle bioconjugates: preparation, structure, and interunit energy transfer with antenna effect. *Nano Lett.* 2001; 1:281–286.
85. Medintz IL, Clapp AR, Matoussi H, Goldman ER, Fisher B, Mauro JM. Self-assembled nanoscale biosensors based on quantum dot FRET donors. *Nat. Mater.* 2003; 2:630–638.
86. Goldman ER, Medintz IL, Whitley JL. A hybrid quantum dot-antibody fragment fluorescence resonance energy transfer-based TNT sensor. *J. Am. Chem. Soc.* 2005; 127:6744–6751.

87. Goldman ER, Clapp AR, Anderson GP, et al. Multiplexed toxin analysis using four colors of quantum dot fluororeagents. *Anal. Chem.* 2004; 76(3):684–688.
88. Xu C, Xing B, Rao J. A self-assembled quantum dot probe for detecting beta-lactamase activity. *Biochem. Biophys. Res. Commun.* 2006; 344:931–935.
89. Chang E, Miller JS, Sun J, et al. Protease-activated quantum dot probes. *Biochem. Biophys. Res. Commun.* 2005; 334:1317–1321.
90. Bakalova R, Zhelev Z, Ohba D, Baba Y. Quantum dot-conjugated hybridization probes for preliminary screening of siRNA sequences. *J. Am. Chem. Soc.* 2005; 127:11328–11335.
91. Medintz IL, Konnerth JH, Clapp AR. A fluorescence resonance energy transfer-derived structure of a quantum dot–protein bioconjugate nanoassembly. *Proc. Natl. Acad. Sci. USA.* 2004; 101:9612–9617.
92. Shi L, De Pauli V, Rosenzweig N, Rosenzweig Z. Synthesis and application of quantum dots FRET-based protease sensors. *J. Am. Chem. Soc.* 2006; 128:10378–10379.
93. Shi L, Rosenzweig N, Rosenzweig Z. Luminescent quantum dots fluorescence resonance energy transfer-based probes for enzymatic activity and enzyme inhibitors. *Anal. Chem.* 2007; 79(1):208–214.
94. Wang D, He J, Rosenzweig N, Rosenzweig Z. Superparamagnetic Fe₂O₃ beads–CdSe/ZnS quantum dots core–shell nanocomposite particles for cell separation. *Nano Lett.* 2004; 4(3):409–413.

Quantum Dot–Polymer Bead Composites for Biological Sensing Applications

JONATHAN M. BEHRENDT and ANDREW J. SUTHERLAND

Department of Chemical Engineering and Applied Chemistry, Aston University, Birmingham, United Kingdom

- 10.1 Introduction
- 10.2 Quantum dot–composite construction
 - 10.2.1 Polymer coating of individual QD surfaces
 - 10.2.2 Encapsulation of multiple QDs within micelles or microcapsules
 - 10.2.3 QD immobilization by doping into polystyrene microspheres
 - 10.2.4 Layer-by-layer deposition of QDs onto polymer particles
 - 10.2.5 In situ encapsulation of QDs in polymer particles
 - 10.2.6 Silica encapsulation of QDs
- 10.3 Applications of QD composites
 - 10.3.1 Introduction
 - 10.3.2 Characterization
 - 10.3.3 Discrete QD–polymer composites
 - 10.3.4 Polymer beads that contain a plurality of QDs
- 10.4 Future directions

10.1 INTRODUCTION

Quantum dots (QDs) are tiny, discrete particles of nanocrystalline material comprised of one or more inorganic semiconductors. As a result of their small size, they possess unique optical properties which result from quantum confinement of their conduction band electrons. Consequently, quantum dots display broadband excitation and

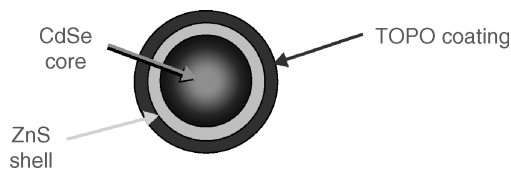


FIGURE 10.1 Typical core–shell QD.

relatively narrow emission profiles which are intrinsically size dependent. QD diameters are typically in the range 1 to 12 nm, with emissions shifting to higher wavelengths with increasing size [1]. Typically, CdSe-based QDs with diameters of 2 to 6 nm emit in the visible spectrum. To maintain these unique optical properties, it is imperative that individual quantum dots remain as discrete entities. This is achieved by coating the QDs in additional layers of inorganic and/or organic materials. The QDs may either be directly coated in an organic ligand such as trioctylphosphine oxide (TOPO, core particles), or the QD may first be coated in one or more shells of an inorganic passivating layer (core–shell particles) such as zinc sulfide (Figure 10.1). Passivating layer(s) are employed to confer improved optical properties and greater stability of the QDs. Advances in QD synthesis, coating technologies, and functionalization have provided materials with a number of advantages over conventional fluorophores for use as biological probes (see Table 10.1) [2].

Two seminal reports in *Science*, by Bruchez et al. [3] and Chan and Nie [4], described the first examples of using QDs as biological probes and provided compelling evidence of the importance of these materials in biological applications. Primarily as a result of these two articles, great effort has been directed at developing methods for exploiting QDs in the biological arena. Although QDs are also attracting significant interest in the areas of electronics (e.g., displays, solar cells, solar cell concentrators, LEDs) and security (e.g., authentication tagging, tracking), these areas do not fall within the scope of this chapter, in which we focus solely on biological sensing applications. Moreover, the utility of simple QD-based probes is not dealt with

TABLE 10.1 Comparison of the Properties of Conventional Fluors and QDs

	Property	Fluorescent Probe	Quantum Dot Probe
1	Broadband excitation	No	Yes
2	Narrow bandwidth emission	No	Yes
3	Emit light of high intensity	Moderate	Yes
4	Available in many colours	Yes	Yes
5	Readily attachable to analytes	Yes	Moderate
6	Resistant to quenching	No	Yes
7	Photochemically stable	No	Yes
8	Cheap and readily available	Yes	No

Source: From ref. 2, with permission from Elsevier.

here (although we direct the interested reader to a number of comprehensive reviews in this area) [5], as we seek to focus on biologically compatible QD-polymer composites. The chapter is divided roughly into two sections. In the first we outline various methods employed to synthesize QD-polymer composites. Here the construction of polymer composites that contain both individual QDs and a plurality of QDs is discussed. Potential problems with each method, such as ligand exchange and reduction in quantum yield, are highlighted and the optimal methods currently available are identified. The second section is concerned with applications of these QD-containing materials. Following a short discussion of QD-polymer composite characterization, in the majority of the second section we focus on reviewing a number of successfully developed quantum dot-polymer composites that have been reported recently, and these exemplars are evaluated from a strengths and weaknesses perspective. In the final part of the chapter we focus on potential future directions in the areas covered.

10.2 QUANTUM DOT-COMPOSITE CONSTRUCTION

10.2.1 Polymer Coating of Individual QD Surfaces

For a number of applications, particularly in biological targeting and imaging studies, it has been desirable to coat individual QDs with polymers in order to confer useful properties while maintaining a relatively small hydrodynamic volume. Amphiphilic polymers are ideal for this purpose, as their hydrophobic component can be used to bind them to the surface of similarly hydrophobic QDs (e.g., TOPO coated), while their hydrophilic component can render the resulting composite materials water soluble. When coating QDs with amphiphilic polymers, care must be taken, as in addition to discrete QD-polymer composites, micelles and vesicles can be formed. In an early study by Wu et al., octylamine-modified acrylic acid was used to coat organic-soluble Cd-ZnS QDs, forming water-soluble nanoparticles [6]. The surface was further cross-linked by EDC-mediated coupling to lysine prior to conjugation to various biomolecules via the carboxyl groups on the polymer backbone. It has also been demonstrated that following conjugation with biomolecules (e.g., Tuftsin) and PEG chains, such QD-polymer composites display long-term colloidal stability in aqueous PBS buffer solutions [7]. Yu et al. describe the solubilization of hydrophobic ligand-coated CdSe-CdS and CdSe-ZnS QDs using amphiphilic block copolymers constructed by reacting poly(maleic anhydride-alt-1-octadecene) with amino- and hydroxyl-terminated PEGs [8]. Photoluminescent (PL) properties of the QDs were unaffected by this coating process, and cryogenic-transmission electron microscopy (TEM) images of the QD-polymer composites in water show clearly that they are discrete entities (Figure 10.2). Moreover, the size, shape, and PL properties of the polymer-encapsulated QDs are the same as those before exposure to the amphiphilic block co-polymer. As well as conferring water solubility, PEG groups were incorporated into the polymer to give improved biocompatibility, and free carboxylic acid groups on the polymer surface provided sites for further functionalization.

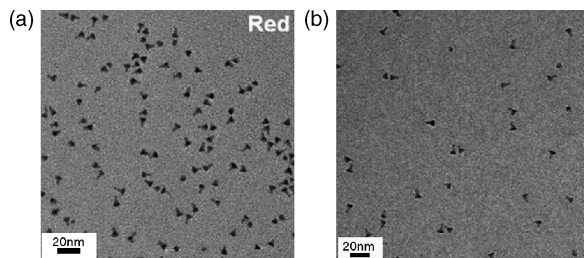


FIGURE 10.2 (a) TEM photograph, obtained from an evaporated chloroform solution, showing CdSe–CdS QDs of dimensions 5.8×8.4 nm; (b) cryogenic TEM photograph clearly showing well-dispersed water-soluble discrete QD–polymer composites in water. (From ref. 8, with permission. Copyright © 2007 American Chemical Society.)

In a similar study, Gao and co-workers [9] used hydrophobic interactions to encapsulate TOPO-coated QDs with an ABC triblock co-polymer comprised of poly(butyl acrylate), poly(ethyl acrylate), and poly(methacrylic acid) segments. In this example, some of the poly(methacrylic acid) moieties were converted into amides with pendent C-8 alkyl chains to enable hydrophobic association of the triblock copolymer with the alkyl chains of the TOPO ligands surrounding the QDs. Subsequent polymer encapsulation of the QDs was found to occur spontaneously and resulted in highly stable discrete QD–polymer composites. As with diblock copolymer encapsulation, no deleterious effects on emission properties and quantum yields were observed.

Branched polymers have also been used to coat the surface of QDs and confer water solubility. A straightforward example of this is the exchange of the native ligands of hydrophobic CdSe–ZnS QDs with hyperbranched poly(ethylenimine) (PEI), which promotes phase transfer from organic solvents into water [10]. Low-molecular-weight PEI (800 Da) afforded QDs with a hydrodynamic volume of 10.7 ± 1.4 nm, and this value increased to 17.5 ± 2.5 nm with high-molecular-weight PEI (25 kDa). In this example, PEI is attached to the QD surface through the numerous amine functionalities within the polymer backbone, all of which can act as ligands. This will invariably give a non-region-specific attachment and could lead to multiple QDs being immobilized by the same PEI molecule. In another example, polyamidoamine (PAMAM) dendrimers, which also contain many amines throughout their structures, were partially thiolated by reaction with the *N*-hydroxysuccinimide ester of 3-mercaptopropionic acid [11]. The addition of a small number of thiol groups relative to amines was shown to give improved binding efficiency over unmodified PAMAM dendrimers when ligand exchange reactions were carried out with TOPO-coated CdSe nanoparticles in order to provide water-soluble QDs. The degree of specificity for the thiol groups when the dendrimer binds to the QD surface was not elucidated in this study.

In order to reduce the tendency of QD–polyamine composites to aggregate and precipitate in biological buffers, as well as to reduce cytotoxicity for intracellular studies, Duan and Nie have coated QDs with branched PEIs that were first modified by attaching PEG chains via succinimide coupling [12]. TEM imaging of the composite

particles also indicated that they consisted primarily of single QDs, and in optical imaging studies they displayed the on-off blinking behavior that is characteristic for single dots spread on a glass surface. In an alternative approach, Nikolic et al. [13] have grafted PEG chains to both branched PEIs and linear diethylenetriamine (DETA) by use of a diisocyanate spacer, and the comparative properties of QDs coated with these polymers have been studied. They report that the best quantum efficiencies for CdSe–CdS nanoparticles were observed when using relatively low-molecular-weight poly(ethylene oxide) (PEO, MW = 2000 g/mol) modified with linear DETA, which they attributed to a higher grafting density than that of the branched PEI co-polymers. A reduction in quantum yield was also observed for higher-molecular-weight PEOs, which was again thought to be due to a lower grafting density. Despite the superior quantum yield observed for QDs coated with PEO–DETA, TEM images revealed that these nanocomposites had a tendency to form wormlike aggregates [Figure 10.3(c) and (d)], unlike those coated with PEO–PEI, which were observed to be single, well-separated entities [Figure 10.3 (a) and (b)].

CdSe/ZnS QDs have been encapsulated within phospholipid micelles composed of *n*-poly(ethylene glycol) phosphatidylethanolamine and phosphatidylcholine. [14]. These QD-containing micelles displayed highly uniform size and shape, and their outer layer of PEG provided enhanced colloidal stability in water and biocompatibility. When QDs above 4 nm were modified in this way, the majority of the micelles

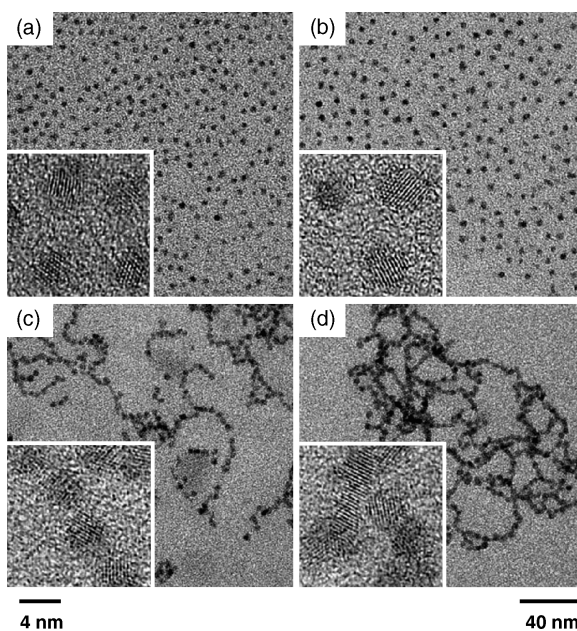


FIGURE 10.3 TEM images of CdSe–CdS QDs coated with (a) PEO2000-PEI, (b) PEO5000-PEI, (c) PEO2000-DETA, and (d) PEO5000-DETA. (From ref. 13, with permission. Copyright ©2006 Wiley-VCH Verlag GmbH & Co. KGaA.)

formed were reported to contain individual QDs, whereas those below 4 nm in diameter formed micelles containing multiple QDs.

10.2.2 Encapsulation of Multiple QDs Within Micelles or Microcapsules

To protect QDs from quenching or surface degradation, as well as to enhance the biocompatibility of these intrinsically hydrophobic nanoparticles, it is desirable that they be immobilized within the core of polymeric particles. Where single QDs are polymer coated, as described in Section 10.2.1, this will invariably be the case; however, where the formation of larger composites containing multiple QDs is desired, localization of the nanocrystals within the core is more complicated. It is also important that the QDs remain spatially separated from one another to avoid self-quenching. Block co-polymers containing both a polystyrene and a poly(acrylic acid) component have been used in the formation of QD compound micelles (QDCMs) containing multiple nanoparticles [15]. Self-assembly of these QDCMs was induced by the dropwise addition of water to DMF solutions containing block copolymer-stabilized QDs and the amphiphilic polymer. The block co-polymer chains around the individual QDs separates them spatially within the core of the micelle. Kinetic control over the micelle size was achieved by varying either the initial polymer concentration or the rate of addition of water, affording QDCMs in the approximate range 50 to 200 nm.

Charge-driven encapsulation of QDs into preformed microcapsules with a charged core has been explored by Gaponik et al. (Figure 10.4) [16]. The microcapsules were built up around melamine formamide microspheres by deposition of alternating layers

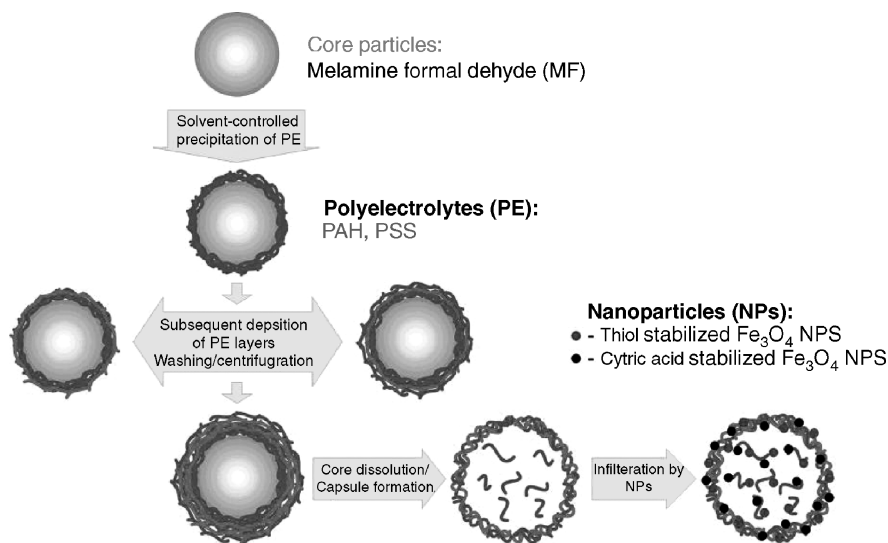


FIGURE 10.4 Formation of polyelectrolyte microcapsules and charge-driven encapsulation of nanoparticles. (From ref. 16b, with permission. Copyright © 2004 American Chemical Society.)

of polycation [poly(allylamine hydrochloride)] or polyanion [sodium poly(styrene sulfonate)]; see Figure 10.4. The core melamine particles were then etched out by treatment with 0.1 M HCl and the inner electrolyte shell, composed of a complex of citrate ions and either polyanion or polycation, was destroyed by treatment with 2 M NaCl and then basic medium (ca. pH 10), to give a charged liquid center. Water-soluble thiol-capped CdTe QDs with a negative charge were dragged into microcapsules with a positively charged center by electrostatic forces, and positively charged nanocrystals were similarly encapsulated by microcapsules with a negatively charged center. Furthermore, microcapsules could be tagged with multiple QDs of different sizes (and therefore emission spectra), giving rise to encoding strategies for combinatorial libraries, or tagged simultaneously with QDs and Fe₃O₄ nanoparticles to give fluorescent microcapsules with magnetic properties.

10.2.3 QD Immobilization by Doping into Polystyrene Microspheres

Perhaps the most straightforward method of immobilizing QDs into polymer particles is by doping polystyrene microspheres with solutions of the QDs in an appropriate solvent to allow penetration of the nanoparticles into the polymer core. This method often relies upon hydrophobic interactions between the QD ligand (commonly, TOPO) and the polymer surface, preventing QDs from leaching out of the polymer particle. Furthermore, the polymer matrix is able to keep the immobilized QDs spatially separated, thus maintaining their optical properties and avoiding self-quenching. This technique was first reported by Nie and co-workers [17] and is still widely used to provide rapid access to QD-polymer conjugates. In this seminal report, the polymer particles utilized in QD immobilization were synthesized by emulsion polymerization of styrene with DVB as a cross-linker and acrylic acid as a functional co-monomer. By controlling the amount of poly(vinylpyrrolidone) (PVP) stabilizer used in such reactions, particles with diameters in the range 0.1 to 5.0 μm were synthesized. The embedding process was carried out by doping the polymer particles with QDs in a solvent mixture of chloroform/propanol (5 : 95) for about 30 minutes at room temperature. The immobilized QDs were further protected by polymerization of 3-mercaptoptrimethoxysilane within the pores of the polymer particles. They also demonstrated that the narrow emission profiles of QDs allowed for the synthesis of polymer particles with unique and identifiable optical codes by doping of multiple QDs of different colors, the applications of which are discussed further in Section 10.3.4.4. They suggested that this must be carried out in a sequential manner, with QDs being loaded in order of decreasing size, although later reports have shown that solutions containing multiple QDs in the desired molar or fluorescent ratio can be used to dope polymer particles directly [18]. Several years after reporting the immobilization of QDs onto nonporous microspheres, Gao and Nie suggested that vast improvements could be made to the technique by use of macroporous polystyrene particles (Figure 10.5) [19]. The combined effect of a greater surface area and more extensive diffusion of NPs through the porous network afforded QD-polystyrene particles that were around 1000 times brighter than nonporous particles of similar size and chemical composition. Incorporation of the QDs into the macroporous

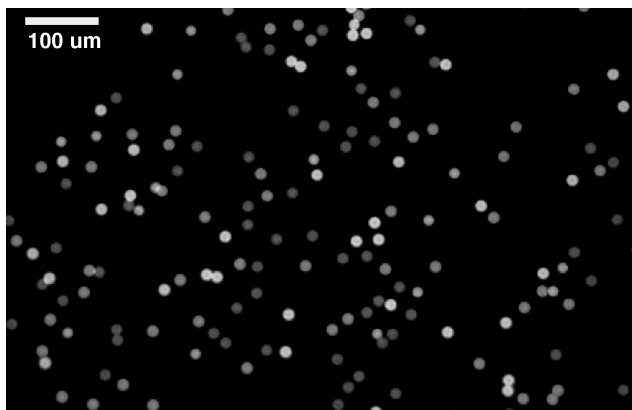


FIGURE 10.5 Grayscale fluorescence images of mesoporous polystyrene beads doped with different-sized QDs. (Reproduced in part from ref. 19, with permission. Copyright © 2004 American Chemical Society.)

polystyrene particles was shown to be very rapid, with only 0.1% of QDs left in solution after 10 minutes, and TEM images revealed that QDs were incorporated uniformly throughout the sample. It was reported that no leakage of the QDs was observed in water or polar solvents. However, it is highly likely that leaching would occur in nonpolar solvents such as chloroform and toluene, which are known to readily solubilize hydrophobic QDs [20].

Polymer spheres, synthesized by surfactant-free emulsion polymerization of styrene and acrylamide, have also been used to encapsulate NPs in a weakly polar organic solvent mixture (chloroform/butanol, 5 : 95). SEM analysis of the polymer particles indicated a mesoporous surface with hydrophobic cavities in which both QDs and nano- γ - Fe_2O_3 particles were trapped simultaneously [21]. Gao and Nie report that in the case of nonporous beads, QDs can only penetrate to 10 to 20 nm below the surface [19]. However, Bradley et al. have since shown that this is not true in all cases and that with lightly DVB cross-linked (1 to 5 wt%) polystyrene microgels the extent of QD penetration is directly related to the degree of swelling of the polymer particle [22]. Furthermore, in the case of 1% cross-linked particles, doping in a suitable swelling solvent (e.g., chloroform) allowed the QDs to become evenly distributed throughout the microgel. A number of QD immobilization strategies, including Gao and Nie's early report, discussed above, have utilized carboxyl-grafted polystyrene particles [17,23]. Carboxyl functionalities have been selected largely to provide points of attachment of biomolecules following immobilization. Although it has never been suggested explicitly in the literature, it is also possible that these carboxyl groups are able to interact with the QD surface to provide a more stable attachment. Where Li et al. transferred aqueous CdTe nanoparticles into chloroform using a cationic surfactant and then doped acrylic acid-containing polystyrene microspheres with this solution, they reported that QDs seemed "cemented" into the polymer microspheres, with no need for a polymer or silica shell [23b]. As well as having applications in the formation of QD-polymer conjugates with sites for

subsequent attachment of biomolecules, QD doping has been shown to be compatible with preconjugated oligonucleotide-polystyrene microspheres [24]. However, although having the advantage that QDs are not subjected to potentially damaging chemical reagents post-immobilization, this approach is unlikely to be applicable for more complex biomolecules (e.g., proteins), which are not likely to be stable in the organic solvents required to swell microspheres for QD doping.

Stsaipura et al. have highlighted a disadvantage of immobilizing QDs by the type of doping strategies discussed above, which could potentially limit the usefulness of the technique [25]. They report that QDs that are only partially embedded close to the microsphere surface are far more like unmodified QDs than are those that are truly encased in the polymer matrix. As such, hydrophobic interactions between surface QDs in different beads can cause aggregation of the microsphere population in water. They also suggest that such interactions can lead to self-quenching of the PL of QD-polymer conjugates, due to the surface QDs being brought into close proximity. Addition of 1% (w/w) bovine serum albumin (BSA), which is known to block hydrophobic interactions, to a suspension of agglomerated QD microspheres was shown to cause a substantial increase (> 25%) in the PL intensity. However, considering that surface QDs make up relatively little of the overall population in QD-polymer conjugates of this type, it seems unlikely that the extent of this effect can be attributed solely to self-quenching. A PL increase of this magnitude is more likely to be due to the substantial increase in surface area of the freely suspended microspheres compared to the previously agglomerated mass of microspheres, allowing light to travel more freely throughout the sample. Cao et al. [26] have reported the formation of silica shells around pre-doped QD-carboxyl-polystyrene microspheres to provide increased protection to any QDs near the surface and to circumvent any possibility of QD leakage. They report that this inorganic shell has the advantages of being chemically inert, optically transparent, and able to protect the immobilized QDs from chemical and biochemical reagents. This last claim is possibly suspect, as they carry out subsequent modifications of the carboxyl groups, demonstrating that chemical reagents and biomolecules are indeed able to diffuse through the silica shell.

10.2.4 Layer-by-Layer Deposition of QDs onto Polymer Particles

A commonly used alternative to trapping QDs within the matrix of polymer particles is simply to coat QDs in one or more layers around the surface of the polymer. This approach generally utilizes polyelectrolytes to create charged surfaces which hold the QDs in place by electrostatic interactions. To facilitate this type of interaction, the QDs themselves must, of course, also carry a surface charge, and this is achieved through selecting an appropriate ligand. Bifunctional ligands such as thioglycolic acid [27], mercaptopropanoic acid [28], and DL-cysteine [29] have all been used to give QDs a negative surface charge through their carboxyl groups (COO^-), while being anchored to the QD surface through their sulfhydryl groups. These ligands also confer water solubility on the particles, and reactions of this nature are generally carried out in an aqueous environment (note that unlike with the doping strategies discussed previously, swelling of the polymer particles is not necessary). The more straightforward

approach to this type of QD–polymer composite assembly is to coat polymer particles with alternating positively charged [e.g., poly(allylamine hydrochloride) (PAH)] and negatively charged [e.g., poly(styrene sulfonate)] polyelectrolyte layers, terminating with a positively charged layer prior to adsorbing the negatively charged QDs onto the accessible surfaces of the particles [30]. Particles synthesized by this approach were observed to have uniformly intense PL emissions, and there was no agglomeration of the particles despite the close proximity of the QDs to the particles' surfaces, presumably due to charge repulsion between the beads. It could be argued that this is not a true layer-by-layer deposition, as the QDs are incorporated only after formation of the polyelectrolyte layers.

By extension of this strategy, it has been demonstrated that multiple layers of QDs can be assembled. An example of this was reported by Wang et al. [27]. Following the deposition of a primer three-layer polyelectrolyte film [PAH/poly(sodium 4-styrenesulfonate) (PSS)/PAH] onto polystyrene spheres and adsorption of negatively charged CdTe QDs, repeated iterations of polyelectrolyte deposition and NP adsorption were carried out before finally capping with anti-immunoglobulin G. This approach has the advantage that the QD loading and structure of the composite materials is determined by the number of NP adsorption cycles. To add further robustness to the electrostatic immobilisation, Sukhanova et al. [29] coated QD–polymer composites formed by layer-by-layer assembly with two additional layers of dense polyelectrolyte to avoid any leakage of the NPs during further surface modification (e.g., coating with recombinant DNA). Multicolor quantum dot–encoded beads can also be synthesized by this procedure, simply by adding different-sized QDs to the various layers, as desired [28].

As an interesting counterpoint to charge-driven deposition of QD layers, Wang et al. have developed a method for immobilizing CdSe/ZnS QDs onto polymer-coated Fe₂O₃ nanoparticles modified with dimercaptosuccinic acid [31]. This approach is driven by the stable bonds formed between thiol groups and the metallic surface of QDs, and as a result can be achieved using uncharged QDs. Again, the composite particles formed were readily dispersed in aqueous solution without particle aggregation.

10.2.5 In Situ Encapsulation of QDs in Polymer Particles

Direct in situ encapsulation of QDs into polymer particles has attracted the attention of a number of research groups in recent years, bringing with it the promise of a “one-pot” strategy for the synthesis of uniform, spherical polymer conjugates containing multiple QDs. However, in practice this approach is far from straightforward, with several obstacles that need to be overcome before this method can become universally applicable. Perhaps the greatest challenge faced is the chemical instability of QDs in the presence of the radical initiators often used in polymerization reactions.

As part of a strategy toward the encapsulation of CdTe QDs by emulsion polymerization, Yang et al. have carried out a comparative study on the effect of commonly used free-radical initiators on the optical properties of QDs [32]. Of the initiators tested, they found that oxidants such as benzoyl peroxide, K₂S₂O₈, and H₂O₂ had the most

deleterious effect on the QD fluorescence, due to their ability to strongly oxidize the QD surface. They found that of all the radical initiators tested, fluorescence was preserved only when azo-containing compounds such as azoisobutyronitrile (AIBN) were employed. It should be noted, however, that QDs are by no means immune to degradation by radicals generated from azo initiators [33]. It is therefore reasonable to infer that successful formation of QD-polymer composites is somewhat reliant on rapid polymer formation, thus coating the QDs and protecting them from the harmful effect of radicals. Polymerizable ligands [33,34] or preformed polymeric shells with ligand sites [35] can also be used to help protect QDs from oxidative degradation.

The three major methods for synthesizing uniform polymer particles are emulsion, suspension, and dispersion polymerization reactions, and unsurprisingly, the scope of all three techniques for encapsulating QDs has been explored. Of these methods, in situ encapsulation of QDs by particles formed during emulsion polymerization has received the most attention and provides access to fluorescent-tagged submicrometer polymer beads suitable, for example, for intracellular delivery and labeling of subcellular biomolecules [36]. When using TOPO-coated CdSe-ZnS QDs, it has been shown that batch emulsion polymerization reaction conditions are not suitable for the formation of QD-polymer conjugates, instead resulting in the formation of a white nonfluorescent latex and deposition of a pink residue on the inner wall of the reaction vessel [37]. The failure of this approach was attributed to the inability of the hydrophobic QDs to be transported through the aqueous phase from the solvent reservoir to the growing polymer particles. QDs coated with cysteine acrylamide have been shown to be more compatible with this bulk approach, presumably due to the increased aqueous compatibility afforded by free carboxyl groups on the QD surfaces. However, nontrapped CdSe-CdS particles were still observed following polymerization [38]. Synthesis of the desired materials can instead be achieved using a microemulsion technique [32,37,39]. This involves the formation of tiny monomer droplets by ultrasonication of the monomer-water-emulsifier mixture prior to polymerization. As the QDs are located within these monomer droplets at the beginning of the polymerization reaction, transport through the aqueous phase is no longer necessary. Where TOPO-coated QDs have been encapsulated by microemulsion polymerization, an observed phase separation between the QDs and the growing polystyrene chains caused the QDs to accumulate, largely in the outer layers of the polymer particle [37]. Furthermore, ligand exchange of TOPO with 4-mercapto-vinylbenzene, theoretically a polymerizable ligand, failed to remedy this problem. Phase separation was also observed with hexadecylamine-coated QDs, and it was suggested that the interaction between the alkyl chains of this ligand and the SDS surfactant employed in the polymerization reaction could be a driving force in the QDs being drawn to the particle's surface [39b]. Conversely, where the polymerizable phase transfer agent didecyl-*p*-vinylbenzylmethylammonium chloride (DVMAC) was used to coat aqueous CdTe QDs, they were shown to be uniformly incorporated into polystyrene particles by use of a similar microemulsion procedure, as evidenced by cross-sectional TEM imaging (Figure 10.6)[32,39c].

To demonstrate that QDs were indeed covalently incorporated into the polymer backbone through the polymerizable ligand, QD-polymer beads were made following

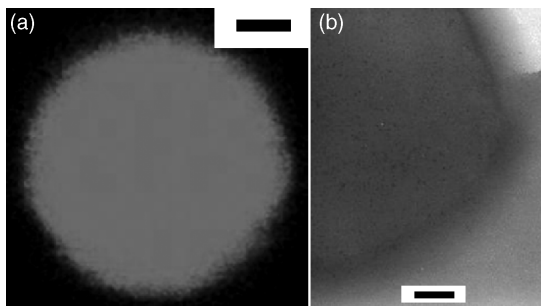


FIGURE 10.6 Confocal fluorescence image (a) and cross-sectional TEM image (b) of a CdTe–polystyrene bead, demonstrating uniform incorporation of QDs. In each case the scale bar is 100 nm. (From ref. 39c, with permission from the Royal Society of Chemistry.)

the same recipe, using QDs coated in the nonpolymerizable surfactant didecyl-*p*-ethylbenzylmethylammonium chloride (DEMAC) rather than DVMAC [32]. Following 24 hours dispersed in toluene, beads prepared using DVMAC retained nearly all of their QDs, whereas those prepared using DEMAC-coated QDs lost 70% of their NPs under these conditions. QDs coated with a silica shell prepared using methacryloxypropyltrimethoxysilane to provide polymerizable surface functionalities have also been encapsulated successfully into polymer nanoparticles by a microemulsion polymerization reaction using a monomer mixture of *n*-butyl methacrylate and styrene, although a study of the arrangement of QDs within these particles has not been reported [40]. The scope of such reactions is extended further by the use of functional co-monomers, providing access to QD–polymer particles with sites for further chemical modification or conjugation of biomolecules (e.g., carboxyl functionalities have been incorporated through use of methacrylic acid as co-monomer, and these particles were also highly cross-linked with DVB) [39a].

Suspension polymerization reactions have also been used for the *in situ* encapsulation of hydrophobic QDs, providing access to fluorescent polymer spheres with much larger diameters (ca. 2 to 500 μm) [41]. It has been shown that ZnS shelling is essential for preserving the QD fluorescence in standard suspension polymerization reaction conditions, with ultramicroscopic analysis showing that nonshelled particles were aggregated within the resulting composite materials [22]. Where CdSe–ZnS (core–shell) QDs were incorporated into 1 wt% DVB cross-linked polymer microspheres under the same conditions, fluorescent materials were produced successfully, although confocal microscopy revealed that phase separation had again caused the majority of QDs to be located in the outermost region of the polymer particles. Furthermore, swelling of these microspheres in 60 vol% chloroform caused the QDs to be redistributed throughout the entire polymer particle. Unfortunately, this paper does not clarify which ligand was used to coat the core–shell QDs used, although the nonshelled QDs used in these studies were coated with TOPO or hexadecylamine, and the use of such ligands would be consistent with phase separation observed in the microemulsion procedures discussed above.

Several polymerizable phosphine ligands (Figure 10.7) have been synthesized in an attempt to facilitate uniform covalent incorporation of QDs into polystyrene microbeads

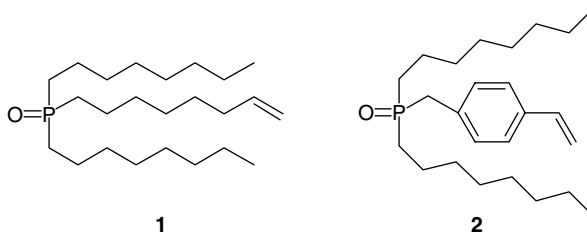


FIGURE 10.7 Polymerizable phosphine ligands used for the covalent incorporation of QDs into polystyrene microspheres. (From ref. 34, with permission from the Royal Society of Chemistry.)

(100 nm to 500 μm in diameter) via suspension polymerization [34]. Microanalysis of the resulting composite materials suggested that there was very low incorporation of QDs coated with ligand 1, in Figure 10.7, while microanalysis of composite beads formed with ligand 2 revealed that QDs remained fairly constant even after prolonged Soxhlet extraction with chloroform. This provided evidence of covalent QD incorporation into the polymer backbone via the styrenic group of this ligand. The same research group went on to synthesise DVB cross-linked QD-polymer microspheres by this in situ suspension polymerization method using oleic acid-capped QDs [41]. Here, laser cross-sectional confocal imaging indicated that there was uniform incorporation of the QDs throughout the polymer particles and that phase separation was not observed (Figure 10.8).

Whereas dispersion polymerization reactions have been widely utilized in the formation of polymeric nanospheres and microspheres with very uniform size distributions, a comprehensive search of the background literature draws only one example of in situ encapsulation of QDs by this method [35a]. Here, QDs were coated with an oligomeric phosphine ligand, 6, the synthesis of which had been described by the same research group in a previous paper [42]. Briefly, a monomeric phosphine 3 is reacted with diisocyanate 4 and the resulting oligomer, 5, is further

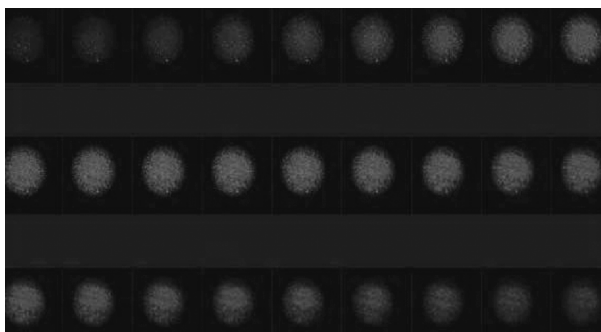


FIGURE 10.8 Confocal laser cross-sectional images through a polystyrene microsphere embedded with CdS QDs, showing uniform QD incorporation throughout the polymer matrix of the bead. (From ref. 41, with permission from the Royal Society of Chemistry.)

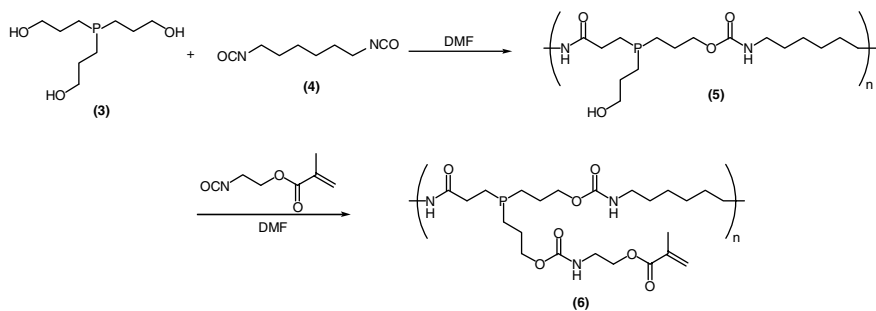


FIGURE 10.9 Synthesis of oligomeric phosphine ligand 6 used to coat QDs prior to in situ encapsulation by a dispersion polymerization reaction. (Adapted from ref. 42, with permission. Copyright © 2003 American Chemical Society.)

functionalized with polymerizable methacrylate groups through further isocyanate coupling (Figure 10.9). CdSe–CdS–ZnS QDs were synthesized in TOPO, which was subsequently exchanged with 6 prior to heating to 60°C in ethanol in order to cross-link the methacrylate groups and thus form a polymeric shell around the QDs. The utility of the oligomeric phosphine ligand was threefold: conferring QDs with solubility in the ethanol media commonly used for dispersion polymerization reactions, providing protection from fluorescence quenching by AIBN radicals, and providing sites for covalent incorporation of QDs into the polymer backbone through any unreacted methacrylate groups remaining following the cross-linking procedure. At lower QD–phosphine concentrations (4 wt% relative to styrene), QDs were incorporated uniformly into relatively monodisperse polystyrene spheres with an average diameter of about 1 μm by a PVP-stabilized dispersion polymerization reaction in ethanol. However, incremental increases in the QD concentration led to mounting disruption of the sensitive nucleation period associated with dispersion polymerization reactions and resulted in decreasing particle diameter, increased polydispersity, degradation of surface morphology, and loss of spherical character. Self-polymerization of QDs, leading to localized areas with many QDs, also became more of an issue at higher concentrations.

In the vast majority of examples of in situ encapsulation of QDs reported in the literature, the polymer particles formed are composed primarily of polystyrene. The examples discussed above highlight the versatility of this polymer, affording QD–polymer composites with a relatively chemically inert backbone and further diversity can be achieved by the addition of functional co-monomers. Although it is clearly a useful polymer in such encapsulation processes, the almost exclusive use of polystyrene in this area can probably be ascribed largely to its dominance in the formation of polymer particles in general, with many research papers devoted to the synthesis of uniform polystyrene spheres from nano to macro scale. A few examples of in situ encapsulation utilizing alternative polymers have been reported, however. Of particular note is the encapsulation of CdS nanoparticles in an acrylic acid (AA)–based polymer shell [43], as the resulting QD–polymer particles demonstrate markedly different properties from the examples described elsewhere in this section. The

experimental procedure utilized was as follows. Following preparation of the CdS nanoparticles, acrylic acid and potassium persulfate initiator were added and the polymerization reaction was carried out under ultrasonic irradiation. The average diameter of the particles formed was only 9 nm larger than the diameter of the unmodified CdS nanoparticles, suggesting that this method results in the encapsulation of single QDs within discrete polymer particles. Furthermore, the multitude of carboxyl groups on the surface of the composite nanoparticles rendered them water soluble as well as providing colloidal stability in aqueous solutions and sites for biomolecule attachment. TEM images suggest that the QD-acrylic acid nanoparticles are perhaps not as uniform in size and shape as some of the composites particles formed by ligand exchange on the QD surface by preformed polymeric ligands, discussed in Section 10.2.4, but the useful properties of these composite materials warrant further investigation and hopefully, optimization of the approach.

Yin et al. have reported the synthesis of QD-polyisoprene nanocomposites via an emulsification and solvent evaporation technique [44]. CdSe-ZnS QDs were dissolved along with polyisoprene in a compatible solvent, and this mixture was emulsified into an aqueous surfactant solution prior to evaporation of the polymer solvent. In an extension of this method, AIBN and acrylic acid were added to the QD-polymer solution, which was then similarly emulsified and heated to 70°C for 6 hours to form a cross-linked latex. It was shown that the size of the relatively monodisperse particles formed could be controlled by adjusting the homogenizing speed, providing access to nanocomposites from 200 to 500 nm. The resulting QD-isoprene composites displayed colloidal stability in water as well as enhanced long-term fluorescence, and modification of the surface with carboxyl groups provided sites for bioconjugation.

10.2.6 Silica Encapsulation of QDs

Although in this chapter we focus on the coating and functionalization of QDs with synthetic organic polymers such as polystyrene, it would be remiss not to include a brief discussion of the many examples of silica shelling of QDs in the literature. In some respects, these inorganic glassy polymer shells can offer advantages over the strategies discussed thus far. The majority of the literature in this area focuses on the encapsulation of single QDs within discrete silica shells, grown in situ around the nanoparticles by a modification of the Stöber process. The wide variety of functionalized silane co-monomers that are readily available lends a fair degree of scope to such reactions. The initial consideration is how to anchor the shell to the QD surface in a robust fashion. Here, the most straightforward approach is to use a silane co-monomer with a hydrophobic tail (e.g., *n*-octyltriethoxysilane), which is able to interact with hydrophobic chains in the QD surface ligands (e.g., TOPO) [45]. Other research groups have utilized ligand exchange of the parent QD ligand with a functionalized silane [e.g., mercaptopropyltris(methoxy)silane (MPS)] to provide a more robust attachment as well as improved compatibility with the polar solvents often used in such reactions [46]. The classical Stöber process [47] is the alkaline hydrolysis and polycondensation of tetraethylorthosilicate (TEOS) in ethanol, but this

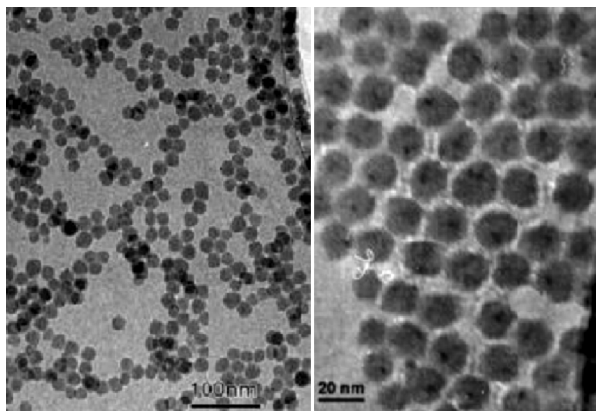


FIGURE 10.10 TEM images of single QDs encapsulated in silica shells. (Reproduced in part from ref. 45b, with permission. Copyright © 2006 American Chemical Society.)

alone would not give conjugate materials with useful properties such as water solubility and sites for further functionalization. To confer water solubility, alternative silanes with hydrophilic groups, such as (trihydroxysilyl)propylmethylphosphonate [46] or 2-[methoxy(polyethyleneoxy)propyl]trimethoxysilane (PEOS) [40], have been used. These silane monomers can be used in conjunction with co-monomers such as aminopropyltris(methoxy)silane and MPS, which provide sites for biomolecule conjugation [46], or methacryloxypropyltrimethoxysilane, which forms a silica shell with polymerizable end groups [40]. Under optimal conditions, relatively monodisperse silica spheres can be formed, the majority of which contain only single QDs (Figure 10.10). QD–silica conjugates have also been shown to retain the narrow characteristic emission spectrum of unmodified QDs in chloroform, albeit with some loss of PL [45b]; however, the shelling process is often relatively complex, requiring multiple steps. Also, when these reactions are carried out in alcoholic media, high dilution is required to avoid aggregation of the silica particles formed.

A more straightforward strategy recently reported by Zhu et al. [40] facilitates the formation of silica-shelled QDs at relatively high concentration (up to 10^{-4} M) in toluene without aggregation. This is a two-step process, with shell formation initiated by addition of MPS and another functionalized trialkoxysilane (e.g., PEOS, to QDs in toluene and heating to 100°C for 12 hours, followed by the addition of a functionalized mono- or dialkoxysilane to terminate shell growth by blocking the active silanols and heating for a further 12 hours. A diverse range of functionalized silanes were incorporated into the silica shell under these conditions, and the shelled QDs retained their characteristic emission profiles without much loss of quantum yield (and the quantum yield was, in fact, shown to increase where PEOS was incorporated into the shell). The homogeneous reaction conditions also lead to high conversion yields ($>90\%$).

The synthesis of larger silica spheres containing multiple QDs has also been explored by a number of research groups. In an early report, treatment of QDs with MPS in ethanol, followed by addition of sodium silicate, 4-hour ultraviolet–visible light treatment, and further ripening for 5 days was shown to form a “raisin-bun” type

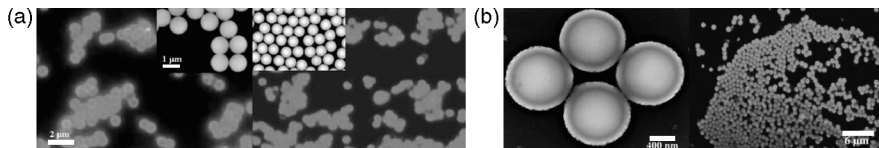


FIGURE 10.11 (a) 954-nm ($\pm 2.7\%$) and 609-nm ($\pm 2.5\%$)-diameter silica microspheres which emit at 625 and 531 nm, respectively; (b) TEM and fluorescent microscope images of titania-coated silica microspheres showing outer, QD-containing shell about 60 nm thick. (From ref. 49, with permission. Copyright © 2004 Wiley-VCH Verlag GmbH & Co. KGaA.)

of composite 40 to 80 nm in size containing a number of spatially separated QDs [48]. However, this procedure led to a significant broadening in the emission spectrum and for CdTe and CdSe–CdS nanoparticles a strong decrease in luminescence intensity following silicate addition. Gao and Nie have circumvented this degradation of optical properties by doping solutions of QDs into preformed mesoporous silica beads (5 μm in diameter) [20]. Silica spheres with a pore size of 32 nm were rapidly saturated with QDs (<5 minutes), and significantly, the resulting composite materials were 50 to 100 times brighter than their QD-tagged polystyrene latexes, the synthesis of which is described in Section 10.2.3. By doping with different ratios of just two colors of QDs, 30 distinguishable barcodes were used to tag these silica beads. However, as QDs were held in place only by hydrophobic interactions between QD TOPO ligands and hydrocarbon chains coated onto the pore surface, QDs were able to leach out in nonpolar organic solvents. Chan et al. have reported perhaps the most elegant formation of silica microspheres containing multiple QDs thus far, utilizing a core–shelling strategy [49]. Preformed silica microspheres are coated using TEOS in the presence of QDs capped with 5-amino-1-pentanol and APS via the Stöber process, giving a thin, fluorescent shell around the core particles. As shown in Figure 10.11, these core–shell particles are spherical, with very smooth surface morphology and very narrow size distributions. Furthermore, the immobilized QDs retained an almost identical emission profile of their unmodified counterparts, suggesting that individual QDs are separated spatially within the shell, and the QD–silica conjugates formed had quantum yields as high as 13%.

10.3 APPLICATIONS OF QD COMPOSITES

10.3.1 Introduction

To enable their utility in biological applications, the organic ligand layer that surrounds QDs following their production must either be directly biologically compatible or else, far more commonly, be converted into a biologically compatible form postproduction. There are many examples of applications of QDs that have been rendered biologically compatible via a ligand-exchange process employing small molecules. As outlined at the start of the chapter, these systems lie outside the scope of

this chapter. Accordingly, in the following section we deal solely with QDs that have been rendered biologically compatible through coating/incorporation with/into one or more polymers. To achieve this, there are two main approaches, and thus the following discussion on applications has been broken down into two sections, dealing with discrete QD-polymer composites (i.e., systems in which individual QDs have been incorporated into a polymer composite) and QD-polymer composites that contain a plurality of QDs.

10.3.2 Characterization

When using discrete QD-polymer composites and micelle-encapsulated QDs in biological applications, one important aspect is to determine how big the solvated composite actually is (i.e., its hydrodynamic radius, which may differ significantly from its geometric radius) and how charged it is i.e., its zeta potential and how many biomolecules are attached to it). This type of quantification is not so relevant to larger composites such as polymeric microspheres, as these generally have very similar geometric and hydrodynamic sizes in aqueous media, and this property may be assessed readily, for example, by microscopy. Similarly, the number of charges or biomolecules on a bead relates directly to its loading level, a parameter that may be assessed readily using routine analytical methods such as the Fmoc release assay [50].

In a recent publication, Pons and co-workers [51] describe a study aimed at establishing the hydrodynamic radii and zeta potentials of a series of discrete QDs and discrete QD-polymer composites. Hydrodynamic radii were determined using dynamic light scattering (DLS). This method is preferred as it enables a larger sample size to be evaluated compared with atomic force microscopy (AFM), and DLS does not suffer from the inherent drawbacks associated with the use of fluorescence correlation spectroscopy (FCS) (e.g., saturation intensity, bleaching, QD blinking). The values of the hydrodynamic radii of various QD-containing species were obtained by DLS and compared with the corresponding geometric radii, established, for example, by transmission electron microscopy (TEM). In all the examples studied, the radius sizes obtained by DLS were found to be between about 2.7 and 4 times bigger than the corresponding geometric radii, depending on the nature of the outer organic layer. For example, in going from an outer layer of dihydrolipoic acid (DHLA), to DHLA conjugated to PEG₆₀₀, to DHLA-conjugated to PEG₁₀₀₀, the hydrodynamic radius/geometric radius increased from about 2.7 to about 2.9 to about 3. They also analyzed the QD-containing species by agarose gel electrophoresis (AGE) and found that this method gave good sizing information but reported the data to be more prone to error than data obtained using the DLS method, for example, DLS is more sensitive for detecting aggregates. In terms of measuring zeta potentials, they found that values derived from AGE compared very favorably with those obtained using laser Doppler velocimetry. In a similar study, size exclusion chromatography (SEC) was compared with AGE, FCS, and TEM [52]. AGE was reported to be far more sensitive than SEC for separating discrete QD species, with no, one, two, three, etc. PEG chains attached to them. When using just SEC, the measured dimensions are reported to be more accurate for smaller samples than for larger ones, due to the lack of availability of appropriately sized standards for the larger composites (> 20 nm radii). The authors of

this study conclude that when using any technique, the trends observed within a series (e.g., the discrete QD–composite size increases as the size of PEG grafts increases) are correct, but in comparing values obtained using different techniques, care must be exercised. Each technique depends on different physical principles and thus is highly composite-type depend, so the values should always be treated cautiously and control samples should always be included in the measurements.

AGE can also be applied to study or estimate the number of molecules or particles attached to nanoparticles. For example, in a study involving QDs coated with Au nanoparticles, AGE, followed by band excision, provided samples for analysis by TEM, which showed the presence of QD–Au particles with composition ratios of 1:1 to 1:4 [53]. Similarly, AGE enabled the number of PEG chains conjugated to individual QDs and Au nanoparticles to be established and also the number of maltose-binding protein molecules attached to the surface of DHLA-coated QDs [54]. The method should be readily adaptable to discrete QD–polymer composites, but to our knowledge this has not yet been reported. An alternative to AGE for determining the number of conjugated biomolecules on the surface of nanoparticles has recently been reported and centers on a double-labeling approach. Specifically, the biomolecule is tagged with a fluorescent dye molecule prior to attachment to amino-functionalized silica-coated nanoparticles. Attachment is covalent and is achieved using a bifunctionalized linker, two succinimidyl groups or one succinimidyl group and one maleimido group, to link amino groups on the silica shell to amino or sulfhydryl groups on the protein, respectively. Once the doubly labeled nanoparticle–bioconjugate has been constructed, quantification of the number of immobilized proteins is achieved simply by monitoring the sequential photobleaching of the organic dye molecules attached to an individual nanoparticle. Although this approach has yet to be applied to QDs, it should be readily transferable to the study of this class of nanoparticle. The principal drawback of the approach is that it appears to be relatively timeconsuming compared with an approach such as AGE, and requires ready access to very expensive microscopy equipment compared with the equipment required for AGE [55].

10.3.3 Discrete QD–Polymer Composites

As outlined earlier, individual QDs may be coated with a single polymer layer in a number of ways, which include (1) synthesis or encapsulation of the QDs within preformed micelles [14,15], (2) direct ligand exchange by a polymer [56], (3) interaction of the QD ligand layer with a polymer (e.g., by hydrophobic interaction) [8] or (4) growth of a polymer shell from the surface of the ligand-coated QD: for example, by encasing the QD in a silica layer [45,46]. Examples of applications of discrete QD–polymer composites constructed in these ways are described in more detail below.

10.3.3.1 *In Vitro Applications*

Discrete QDs in Micelles Although not formally comprising a polymer coating, micelles composed of a mixture of amino-terminated PEG-phosphatidylethanolamine and phosphatidylcholine have been used to encapsulate QDs [14]. The micelles were of

the appropriate size to encapsulate just one QD per micelle, and the authors report that very few micelles contained more than one QD. Thiol-modified DNA was attached to the amino residues on the outsides of the micelles using the heterobifunctional linker sulfosuccinimidyl 4-(*N*-maleimidomethyl)cyclohexane-1-carboxylate. Incubation of the resulting QD–micellar composites with agarose beads bearing DNA sequences resulted in hybridization only when the beads bore complementary oligonucleotides.

Discrete QDs Coated in Amphiphilic Polymers The discrete QD–polymer composites formed using amphiphilic block co-polymers, as described by Yu et al. [8] (see Section 10.2.1) were sized by DLS and SEC and found to have hydrodynamic radii of between 15 and 21 nm (SEC) and 12 to 23 nm (DLS), depending on the molecular weight of PEG used to render the probes water soluble (PEG₇₅₀ was the smallest PEG used and PEG₁₉₃₀₀ the largest). These QD-based probes were found to be taken up by the human breast cancer cell line SK-BR-3, presumably by endocytosis as the authors suggest, and clearly stained the inside of the cells [Figure 10.12(a)]. The pendent carboxylic acid residues on the polymer coating enabled covalent attachment of anti-Her2 antibodies to the accessible surfaces of the QD–polymer particles using an EDC-mediated coupling procedure. Her-2 is a member of the transmembrane tyrosine kinase receptor protein family and is a biomarker of breast cancer, and these bioconjugated QDs were found to act as efficient labels of the cell membranes of the same human breast cancer cell line [Figure 10.12(b)][57]. These two tagging approaches enabled both the interior and the membranes of the cancer cells to be labeled selectively with discrete QD–polymer composites (Figure 10.12).

The study by Yu et al. builds on the beautiful pioneering work of Wu and co-workers, who similarly stained Her2-presenting cancer cells with QD–polymer composites [6]. In their approach, amphiphilic polymer-coated QDs were covalently coupled to goat antimouse IgG using EDC, and these discrete QD–polymer composite probes were used subsequently to label SK-BR-3 human breast cancer cells, which had first been incubated with a monoclonal mouse anti-Her2 antibody. They also described an alternative approach in which the same cancer cell line was labeled by sequential

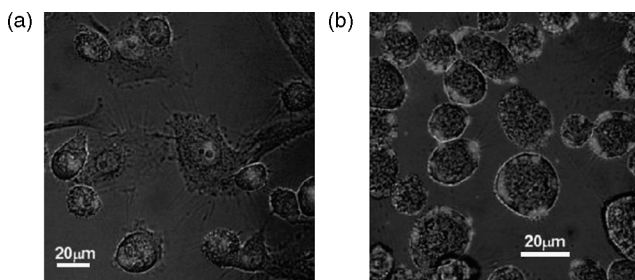


FIGURE 10.12 (a) SK-BR-3 human breast cells with internalized QD–polymer composites; (b) SK-BR-3 human breast cells whose membranes have been targeted, via the Her2 receptor, with discrete QD–polymer composite–anti-Her2 bioconjugates. In both (a) and (b) the QDs were excited at 458 nm and visualized by confocal microscopy. (From ref. 8, with permission. Copyright © 2007 American Chemical Society.)

incubation with humanized anti-Her2 antibodies, biotinylated goat anti-human IgG, and finally, amphiphilic polymer-coated QDs which had been coupled covalently to streptavidin. Variations on these two approaches were also shown to be effective for labeling actin and microtubule fibers in the cytoplasm and nuclear antigens in the nuclei of cells. The original study by Wu et al. was most timely, but the recent active targeting approach by the Yu et al. approach represents a significant improvement in that it is more direct, as it negates the need for preincubation of the cells with one or more monoclonal antibodies.

Other examples in which amphiphilic polymers have been used for in vitro imaging applications include Li and co-workers [7], who attached the tetrapeptide tuftsin covalently via a bis(aminopropyl PEG) linker to an amphiphilic polymer composed of modified poly(acrylic acid) which had been used to encapsulate hexadecylamine-coated QDs (see Section 10.2.1). DLS was used to size the QD–polymer composites prior to tuftsin addition, which had an average hydrodynamic radius of 9 nm, with the inorganic core having a radius of 3 nm as determined by TEM. Tuftsin is a tetrapeptide that binds to receptors on the surface of macrophages and lymphocytes. As expected, the tuftsin-bearing water-soluble discrete QD–polymer composites were able to label both of these types of cells, obtained from mice, in subsequent in vitro studies.

Discrete QDs Coated in Polymers Generated in Situ Discrete QD–polymer composites whose polymer coating was constructed by carrying out an in situ polymerization reaction involving acrylic acid (see Section 10.2.5) have been used to quantify a number of biologically relevant proteins in real human serum samples using the technique of resonance light scattering (RLS) [43b]. Calibration curves for the resonance light scattering observed were constructed when the QD probes were incubated with a single protein or serum at different concentrations. Three proteins—IgG, bovine serum albumin (BSA), and human serum albumin (hSA)—and a standard human serum composed of 40 different serum samples were used in this calibration work. In addition, the effects of pH, temperature, and other agents commonly found in serum were assessed for their effects on the RLS measurements. Finally, to benchmark the method, three individual human serum samples were assessed for total protein content using this RLS method. The values obtained had excellent agreement with values arrived at using the more conventional Bradford assay [58].

10.3.3.2 In Vivo Imaging Applications The number of examples of using QD–polymer composites for in vivo imaging applications is still very small. With ongoing developments in QD technology such as the construction of nontoxic QDs and QDs that emit in the near-infrared (NIR), tissue is relatively transparent to emissions in this wavelength, it is highly likely that this situation will change rapidly in the coming years. The QD-containing micelles described by Dubertret and co-workers [14] were sufficiently stable to be used in in vivo studies. The QD-containing micelles were injected into the cells of an early *Xenopus* embryo and found to have very little toxicity and moreover, were passed to successive generations of daughter cells formed from the cells injected initially. Compared with more conventional fluorophores, a time-course study under continuous photoexcitation provided a really

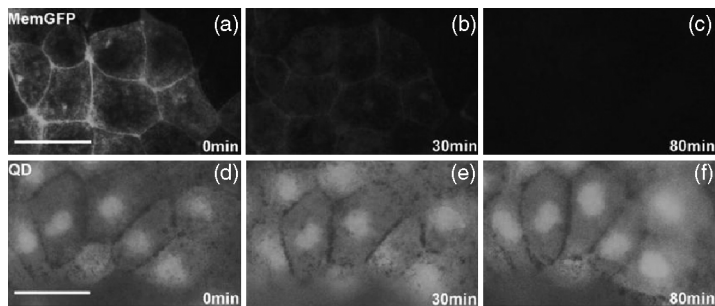


FIGURE 10.13 Resistance of micelle-encapsulated QDs to photobleaching compared with GFP. The images were obtained after continuous irradiation at 450 nm for the times shown. (A–C) Consecutive images of membrane-GFP expressed in *Xenopus* cells; (D–F) consecutive images of *Xenopus* cells into which micelle-encapsulated QDs have been injected. (From ref. 14, with permission.)

nice demonstration of the benefit of using QDs as imaging agents. Even after 80 minutes of continuous illumination at 450 nm, the QDs showed no evidence of photobleaching. Conversely, a sample of cells labeled with green fluorescent protein (GFP) was photobleached completely after the same degree of exposure (Figure 10.13).

Encapsulation of QDs in amphiphilic polymers has also been reported to confer additional stabilization of the encapsulated QDs. For example, Gao and co-workers [9] reported that an amphiphilic ABC tri-block copolymer layer comprised of poly(butyl acrylate), poly(ethyl acrylate), and poly(methacrylic acid) afforded additional protection to QDs against hydrolysis and exposure to enzymes even under *in vivo* conditions. To increase circulation time and improve biocompatibility (i.e., to render them more suited for use in an *in vivo* study), some of the remaining carboxylic acid residues on the triblock copolymer, within the poly(methacrylic acid) segments (some carboxylic acid residues had been used to attach hydrophobic chains to enable QD encapsulation; see Section 10.2.1), were PEGylated with PEG₅₀₀₀ while others were coupled, using EDC, to antibodies raised against a prostate-specific membrane antigen (PSMA). The resulting antibody-coated PEGylated discrete QD–polymer composites were sized by DLS and found to have ligand-dependent hydrodynamic radii of 10 to 15 nm comprising a 2.5-nm QD radii, 1-nm TOPO layer, 2-nm polymer layer, and a 4–5 nm PEG–antibody layer. The authors used these dimensions in estimating that each QD was surrounded by about 200 TOPO molecules, four or five tri-block copolymers, five or six PEG molecules, and five or six antibody molecules. These bioconjugated QD composites were then employed as tumor-targeting agents in mice with and without tumor xenografts. Upon injection the antibody-labeled QD–polymer composites were localized in the tumor sites of the mice with the tumor xenografts (i.e., active targeting had occurred). No such specific localization of the probes was observed in the control group of mice (no tumors). As a control experiment, dosing with just PEGylated discrete QD–polymer composites (no antibodies) resulted in passive targeting of the tumors but only upon dosing with much higher levels of the

QD-based probes. Passive targeting of tumors by particles and macromolecules is a well-known phenomenon and arises as a result of the leaky vasculature of the tumor coupled with poor clearance of such particles from the tumor site. The authors also compared the QD-based probes with green fluorescent protein (GFP)-based probes. They found that in vivo tumor imaging was more effective with the QD-based probes, despite the fact that in vitro cell cultures, both probes were equally visible.

In a similar study Cai and co-workers [59] coupled amino-terminated PEG-coated discrete 705-nm QD composites to a thiolated tripeptide, arginine-glycine-aspartic acid (RGD), via heterobifunctional (succinimide/maleimide) linker chemistry. RGD is a sequence that is bound by integrin $\alpha_v\beta_3$, a receptor vital for tumor angiogenesis. These RGD-tagged discrete QD PEG composites (*ca.* 30 RGD molecules per QD) were injected into tumor-bearing mice. It was found that the tumor site was targeted highly selectively relative to non-RGD-bearing control samples of discrete QD polymer composites, and after just 20 minutes, tumors could be visualized by fluorescent imaging. The authors reason that it was the tumor vasculature that became fluorescent, as the QD composite materials were too large to extravasate significantly, and integrin $\alpha_v\beta_3$ levels are significantly higher than normal in virtually all tumor vasculature. This conclusion correlated well with preliminary in vitro and ex vivo findings reported in the same paper.

In some very elegant studies, again evaluating QD-polymer composites for their utility in imaging-guided surgery, collaborators at the Beth Israel Deaconess Imaging Center and the Brigham Women's Hospital, evaluated discrete QD-polymer composites as imaging agents for use in sentinel lymph node (SLN) mapping during oncologic surgery[60]. Real-time mapping of SLNs is vital for effective removal of all metastatic cells during a surgical procedure to remove a tumor. In the latest exemplar paper[60a], discrete QD-polymer composites, comprising QDs coated with a stable oligomeric phosphine coating [60b,61] (see Section 10.2.5) and two comparator organic fluorophore mapping agents were all highly negatively charged. Whereas the two organic fluorophore mapping agents were found by SEC to have hydrodynamic radii of 7.3 and 7.4 nm, respectively, irrespective of environment (PBS or serum), the QD-polymer composites were found to increase significantly in size on moving from PBS (15 nm) to serum (20 nm). Moreover, in serum, a broader size distribution was observed and some very high-molecular-weight species were observed. Thus, despite the advantages for this application conferred by using QDs in preference to organic fluorophores (brightness and excellent resistance to photobleaching), the QD-polymer composites were found to have serious shortcomings for mapping smaller SLNs and SLN branches. Indeed, the authors state that in contrast to the situation when organic fluorophores were employed, SLN branches were never observed when discrete anionic QD-polymer composites were used as imaging agents. This is a very serious problem, as incomplete SLN imaging during surgery will probably result in incomplete excision of smaller SLNs and partial SLN systems, which in turn could mean that some cancerous cells will be left behind during surgery. Consequently, although this is a very thorough and interesting study, it would appear that organic fluorophores are currently far better suited as imaging agents for the specific application of SLN mapping.

10.3.3.3 FRET-Based Applications In 1996, Kagan et al. first demonstrated that QDs could undergo fluorescence (or Förster) resonant energy transfer (FRET) [62]. Since this original finding, Clapp, Matoussi, and others demonstrated in a series of very elegant papers that it is possible to exploit the FRET capabilities of QDs in the biological arena [63]. In addition to this group, a number of others have developed FRET-based QD-containing systems, and these are included in a recent review of QDs used in bioanalytical and biolabeling applications [64]. The following is a brief description of the approach adopted by Clapp et al. [63b]. QDs of a size that gave rise to an emission maximum at 555 nm were labeled, by simple ligand displacement, with approximately 15 copies of a histidine tag-terminated maltose-binding protein, which in turn had been labeled with the organic fluorophore Cy3. Subsequent excitation at 430 nm of the QDs resulted in an efficient FRET transfer to the Cy3 molecules attached to the periphery of each QD and subsequent emission at 570 nm (consistent with that expected for Cy3). The greater the number of protein molecules attached to the surface of the QDs, the greater the extent of the FRET observed.

Unfortunately, extending this type of methodology to discrete QD-polymer composite systems is inherently problematic, due to the thickness of any polymeric layer surrounding the QD. FRET is very much a distance-dependent phenomenon, and fluorophore-dependent efficient energy transfer of this type is simply not possible over distances much longer than 100 Å (i.e., R_0 , the Förster radius, is \leq ca. 100 Å; in the QD FRET example discussed above, $R_0 = 56.5$ Å) [65]. One approach that attempts to circumvent the “distance problem” is described in a recent publication by Fernández-Argüelles and co-workers [66]. Here discrete amphiphilic polymer-coated QDs were constructed using conventional methods, as outlined in Section 10.2.1, with the amphiphilic polymer incorporating multiple copies of an acceptor fluorophore. Excitation of the QDs results in FRET, and emission from the acceptor fluorophores is observed. Unfortunately, no applications of this system are given. The research is clearly at a very early stage, but the authors suggest that ligand binding on the surface of such discrete QD-polymer composites should result in modulation of the acceptor fluorophore’s quantum efficiency and conclude that in the future, sensor systems of this type should be useful in monitoring cellular traffic.

10.3.4 Polymer Beads That Contain a Plurality of QDs

10.3.4.1 In Vitro Applications Perhaps unsurprisingly, there are only a few examples where beads containing a plurality of QDs have been used solely as labeling probes; the vast majority of applications of QD-containing beads have been focused on developing optical coding systems. However, an early example of a nonencoding application of QD-containing beads was reported by Wang, et al. [27], who used a layer-by-layer approach (see Section 10.2.4) to label a batch of polystyrene beads with QDs. Subsequent to QD labeling, a further simple adsorption process was used to coat the beads with a final outer layer of anti-IgG, antibodies raised against immunoglobulin G (IgG). Subsequent incubation of the anti-IgG-coated beads with IgG resulted in bead agglutination as a result of anti-IgG/IgG-binding interactions. This report

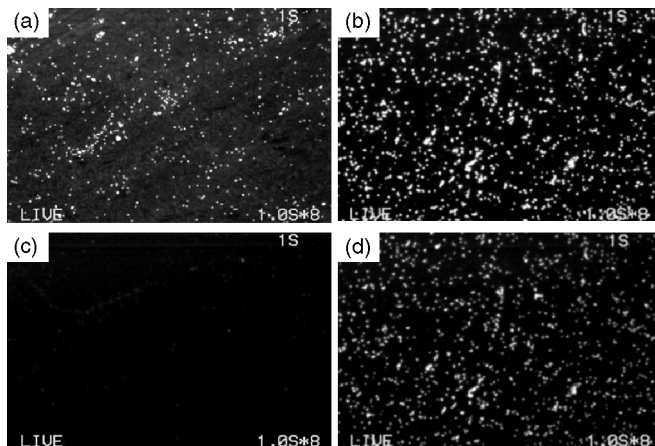


FIGURE 10.14 Time dependence of the fluorescence intensity of dye-labeled beads (a,c) and QD-labeled beads (b,d) upon continuous illumination with a high-pressure mercury light for 0 minutes (a,b) and 20 minutes (c,d), respectively. (From ref. 25, with permission from Elsevier.)

demonstrated that the anti-IgG remained biologically active despite being coated onto the accessible surfaces of the PS beads that incorporated QDs.

This early report was expanded on by Stsaipura and co-workers [25], who labeled a batch of beads by doping with QDs prior to covalently attaching anti-mouse goat immunoglobulins to their accessible surfaces using an EDC-mediated coupling procedure. Beads produced in this manner were compared with conventional fluorescent dye-labeled beads and found overall to give comparable fluorescent signals. (The quantum yield calculated for a single QD-labeled bead was shown to be 38 times lower than for a dye-labeled bead, but this was countered by the far-higher molar extinction coefficients of the QDs used compared with the extinction coefficient of the fluorescent dye.) However, the QD-doped beads possessed far greater photostability to continuous photoexcitation than that of the dye-labeled beads, which were entirely photobleached after just 20 minutes (see Figure 10.14).

In addition to assessing the photochemical properties of the QD-doped beads, they were assessed for their utility in immunolabeling of cancer cells. Specifically, multi-drug-resistant MCF7r breast adenocarcinoma cancer cells, which overexpress the *p*-glycoprotein transmembrane transporter protein (*p*-gp), were incubated with primary murine anti-*p*-gp antibodies. Subsequent incubation with the secondary anti-mouse goat antibody-coated QD-containing beads resulted in the cancer cells being labeled with the fluorescent beads. Cells labeled in this way were easily discernible from cells studied in two parallel control experiments: (1) an identical assay procedure without the addition of the primary anti-*p*-gp antibodies and (2) an identical assay procedure employing cancer cells that only weakly express *p*-gp. A further strength of this approach is its sensitivity; indeed, the authors claim that it should enable the detection of just a single antigen. Conversely, the main weakness of the procedure was that the doping process used to label the beads led to there being a considerable number of QDs

at or near the surface of the beads, which in turn led to aggregation and embedded QD degradation. The authors circumvented this problem partially by blocking the beads with bovine serum albumin (BSA).

Applications exploiting polymeric beads that both incorporate a plurality of QDs and particles that make the bead magnetic are more plentiful. One of the earliest, if not the earliest, example of materials of this type are the QD-covered polymer-coated γ -Fe₂O₃ nanoparticles reported by Wang et al. [31] in 2004 (see Section 4.2.4). The surfaces of these novel composite materials were reacted with mercaptoacetic acid to render them highly water soluble prior to coupling them to mouse anticycline E antibodies, using *N*-(3-dimethylaminopropyl)-*N'*-ethylcarbodiimide hydrochloride (EDAC), and incubating them with MCF-7 breast cancer cells. It then proved possible to pull the resulting magnetic QD–composite-labeled cells to a magnet, allowing their facile separation/isolation and imaging by fluorescence imaging microscopy. The authors conclude by stating that in preliminary studies it had proved possible to be able to separate and detect one cancer cell from within 10,000 red blood cells in a serum sample. A similar but non-antibody-based approach for cell targeting was reported a year later by Xie and co-workers [21]. Bifunctional nanospheres were constructed by trapping QDs and nano- γ -Fe₂O₃ particles simultaneously inside styrene–acrylamide polymer spheres (see Section 10.2.3), and these particles were then coated with folic acid and subsequently incubated with both HeLa and MCF-7 cancer cells. In each case it was possible to observe QD fluorescence on the cells' surfaces, indicating folic acid–mediated targeting of the cells via their folic acid receptors, receptors that are vastly overexpressed in many tumors. Unfortunately, no cell separation procedures exploiting the magnetic properties of the beads were reported in this example.

A second early example of magnetic QD-containing beads was reported by Mulvaney, et al. [67] who employed a conventional QD doping procedure (see Section 10.2.3) to label commercial 0.8- μ m magnetic beads with about 70,000 QDs per bead. Although no application of these QD-containing beads was described, it is interesting to note that when rhodamine-containing beads produced in an identical fashion were employed in a surface-immobilized immunoassay procedure, both the sensitivity and selectivity of the assay were improved by using a magnet to remove unbound and non-specifically bound dye-labeled beads. In another early example of magnetic QD-containing beads, Gaponik et al. [16b] showed that it was possible to align their QDs and Fe₃O₄ nanoparticle-containing capsules (see Section 10.2.2) into larger linear aggregated structures simply by exposing a solution of the capsules to a magnetic field. Although no biological applications were described in this paper, the authors speculate that the ability to manipulate the capsules magnetically will enable them to be employed in directed capsule-mediated drug delivery in the future, possibly to target specific parts of tissue and organs. This speculation has been consolidated further by a more recent example of an imaging application of magnetic QD-containing beads. Guo et al. [68] described the generation of cross-linked poly(*N*-isopropylacrylamide) (PNIPAM)-coated QD/Fe₃O₄-containing silica particles. Incubation of these luminescent/magnetic microspheres (ca. 150 nm in diameter, with a ca. 20-nm PNIPAM shell) with Chinese hamster ovary (CHO) cells resulted in them being internalized by the cells by what the authors suggest is an unknown endocytosis

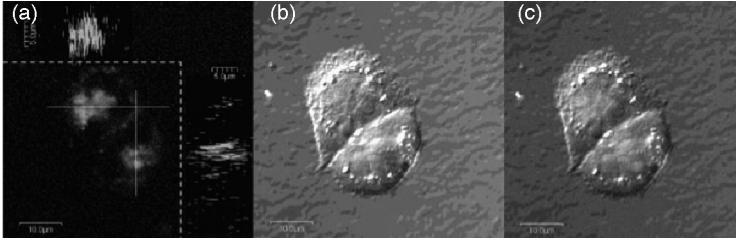


FIGURE 10.15 Confocal microscopic images of two CHO cells incubated with PNIPAM-coated QD/Fe₃O₄-containing silica particles; (a) PL images in the x–y (main), y–z (left), and x–z (top) planes; (b) differential interference contrast (DIC) image; (c) superimposition of images (a) main panel and (b). (From ref. 68, with permission. Copyright © 2006 American Chemical Society.)

process. However, once internalized, there was evidence of intracellular aggregation and protein adsorption (see Figure 10.15). Like Gaponik et al. [16b], the authors concluded that in the future these types of capsule may prove useful in drug delivery applications.

10.3.4.2 In Vivo Imaging Applications The Bawendi and Jain groups have pioneered the use of sub-micrometer-diameter silica spheres coated with a QD-containing silica or titania layer (see Section 10.2.6) for in vivo imaging applications [49,69]. In a typical example, beads produced in this manner contained ≈ 1200 QDs per bead and had quantum yields as high as 13%. In the first example of an application of these doped materials [49], two differently sized sets of monodisperse QD-containing spheres (500 and 100 nm in diameter) were PEGylated to increase their circulation time, and subsequently, were injected directly into the carotid artery of a mouse. The beads were imaged flowing through the blood vessels in the brain of the mouse using multiphoton microscopy via a cranial window: a glass-covered cutaway section in the mouse's skull. As Figure 10.16 demonstrates, using this approach it was possible to see clearly both sets of QD-labeled microspheres flowing through the blood vessels. The authors conclude that the ability to image differently sized sets of QD-labeled spheres simultaneously in this manner will enable processes such as endocytosis of differently sized particles, vital for developing particulate drug delivery systems, to be studied in vivo and in real time.

This fantastic proof-of-concept imaging work was then extended in a cancer-based study [69]. The same QD-encoded silica spheres were employed, again in an in vivo mouse model in conjunction with multiphoton microscopy, to enable (1) the precise imaging of a tumor's vasculature by differentiating clearly between tumor blood vessels and perivascular cells (cells that comprise part of the cell wall of healthy blood vessels which are absent or abnormal in tumor blood vessels) and matrix, as the QD-labeled silica particles were too big to leak from the blood vessels; (2) the assessment of how differently sized particles entered a tumor; and (3) a study of how tumor vasculature develops by establishing how bone marrow cells, ex-vivo labeled with TAT-bearing QD-containing spheres, were incorporated into a tumor's blood vessels. Both of these ground-breaking

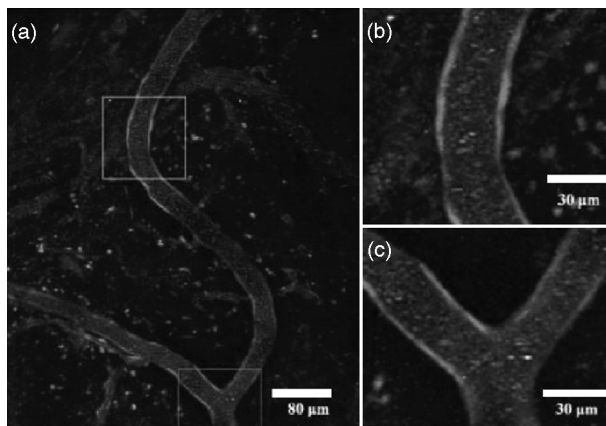


FIGURE 10.16 (a) Multiphoton microscopy image of a blood vessel in the brain of a mouse, showing two different types of QD-containing microspheres flowing through the vessel. The blood vessel walls appear light gray, as they are lined with GFP-expressing epithelial cells. (b,c) Expansions of selected regions within (a). (From ref 49 with permission. Copyright © 2004 Wiley-VCH Verlag GmbH & Co. KGaA.)

studies exploited multiplexing, and this is really only possible using QDs, since it relies on both broadband excitation and extremely bright and narrow emission profiles.

Despite the advantages alluded to at the beginning of Section 10.3.3.2, the principal weakness in using QDs for *in vivo* imaging is, as the authors of the second study pointed out correctly, the toxicity of the QD-containing probes. In the second study, no side effects in the mice were observed for up to one month after administering the QD-based probes, but until more compelling evidence of the long-term safety of QD-containing agents is provided, their use for *in vivo* imaging in humans will be precluded.

10.3.4.3 FRET-Based Applications As outlined in Section 10.3.3.3, FRET is highly dependent on the distance between donor and acceptor fluorophores, and thus even for discrete QD–polymer composites, the number of FRET-based examples is relatively small. In terms of FRET-based applications involving QD–polymer composites, the donor–acceptor distance is even more problematic. This caveat notwithstanding, Müller et al. describe the application of QD-containing polystyrene beads in FRET-scanning near-field optical microscopy (SNOM) [30]. CdTe QD-containing polystyrene beads (ca. 300 nm in diameter) were constructed via the layer-by-layer deposition method (see Section 10.2.4). A single bead of this type was then attached to a SNOM tip and the resulting construct used to probe the interaction of the bead with a thin film of AlexaFluor 633. Although such an approach is still very much in its infancy, and no biological application has yet been provided, this type of sensor, or indeed one based around an AFM tip [70] could eventually enable a study of the controlled interaction between nanocrystals and single molecules of biological relevance.

In a more directly biologically relevant example, Sukhanova and co-workers [29] have reported a QD-containing bead-based FRET assay in combination with FACS to detect anti-topoI antibodies, disease-marker antibodies associated with the disease

systemic sclerosis. Specifically, batches of encoded beads were produced by the incorporation of QDs into the outer regions of layer-by-layer coated melamine beads (see Section 10.2.4). Each batch of beads was encoded with QDs that emitted a different color. A known antigen of antitopoI antibodies, a 68-kDa recombinant fragment of human DNA-topoisomerase I (topoI) was bound to one batch of encoded beads by nonspecific absorption. The beads were then incubated with human serum samples either from patients with scleroderma or from healthy donors, as a negative control. Binding of antitopoI antibodies to the bead-immobilized topoI fragment was detected in a two-stage process: (1) addition of a fluorescently labeled secondary antibody which bound to the antitopoI antibodies, and (2) photo-excitation of the QDs within the beads, which resulted in a FRET emission from the fluorescent probe attached to the secondary antibodies. In a similar way, by attaching the Sm antigen to another batch of encoded beads, it was possible to detect antibodies from human serum samples for this second target. In each case, the FRET-based proximity assay exploited the fact that the QDs could be excited at a wavelength distinct from the excitation wavelength of the fluorescent tag attached to the secondary antibodies. The authors were also able to demonstrate that it was possible to pass the beads through a FACS and sort, with excellent accuracy, the beads, which gave a positive assay response. Moreover, in single-bead imaging studies, the authors demonstrated that this FRET-based approach was extremely sensitive—just 30 dye-labeled antibodies binding to one region of a single bead could be detected readily. Finally, the authors were able to demonstrate a multiplexed assay whereby both antibody targets, in human serum samples, were screened for with FACS enabling their facile separation and detection.

As an alternative to FRET-based sensors, ion-selective nano-optodes that incorporate QDs have been reported recently. In this approach, QDs were coated sequentially (see Section 10.2.4) with an ion-selective polymer layer and an outer biocompatible PEG-lipid layer and shown to be capable of acting as ion-selective sodium sensors [71]. Although the idealized sensor is based on a single discrete encapsulated QD [see Figure 10.17(a)], the method used to generate the particulate sensors and the

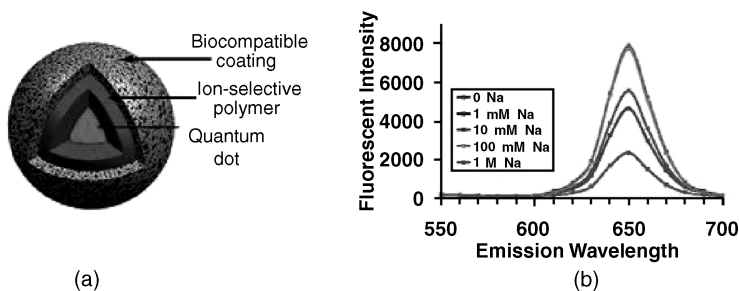


FIGURE 10.17 (a) Ion-selective QD-polymer composite sensor. In reality, these are likely to contain more than one QD per particle. (b) Experimentally observed spectral response of ion-selective QD-polymer composite sensor to increasing concentrations of sodium. Data used to plot the graphs were obtained from a plurality of sensor particles immobilized within thin films. (Reproduced in part from ref. 71, with permission. Copyright © 2007 American Chemical Society.)

size of these particles (103 ± 2 nm) means that in reality each sensing particle contains more than one QD. The ion-selective polymer layer was composed of high-molecular-weight poly(vinyl chloride), a sodium ionophore, and a chromoionophore. A size of QD was chosen carefully so that its emission was absorbed by the chromoionophore within the ion-selective polymer layer. Sodium sensing was achieved by sodium ions entering the polymer matrix, interacting with the ionophore, resulting in the QD absorbance of the chromoionophore becoming less with increasing levels of sodium ion concentration. Thus, increasing sodium ion levels results in increasing amounts of observable QD fluorescence [see Figure 10.17(b)]. These particulate sensors were shown to be biocompatible by incubating them with HEK 293 cells: a procedure which, even after 2 days, was shown to have no deleterious effects on the cells (in terms of viability, apoptosis, and necrosis) relative to control samples.

10.3.4.4 Optical Encoding Applications A particularly attractive application of QDs, which exploits their unique photochemical properties to the full, is encoding. Examples of very limited QD encoding in the form of multiplexing assays are relatively common. Indeed, one [3] of the two original papers in which QD labeling of biological molecules was first reported [3,4] centered on a study in which actin filaments within 3T3 mouse fibroblast cells were stained green while their nuclei were stained red, in both instances using QDs as labels. However, multiplexing assays typically utilize only a very small number of codes. Encoding applications such as coding proteins for drug screening, gene expression studies, and clinical diagnostics require far greater numbers of codes to be readily available, and realistically this is only likely to be possible using a plurality of QDs incorporated into larger structures such as polymeric beads. The first steps toward this goal were reported in 2001 by Han and co-workers [17], who reported the first example of QD-encoded polymer beads. Different but precisely controlled amounts, predetermined empirically, of differently colored QDs were incorporated into polymer microbeads by doping (see Section 10.2.3). Doping, typically between 640 and 50,000 QDs per bead, produced beads with fluorescent emission profiles which were slightly narrower than those obtained from the corresponding doping solutions, but the maxima of emission and relative intensity of emissions remained unchanged upon doping (i.e., there was no evidence of FRET upon doping). In a proof-of-concept study, the authors used a three-color code with two different intensity levels (1 or 2) to generate beads with three different codes (1:1:1, 2:1:1, 1:2:1). These beads were first coupled covalently to streptavidin and then to three different biotinylated ssDNA probes, and each bead type was incubated with three different fluorescently labeled target oligonucleotide sequences. The fluorophore in each case was Cascade Blue, as it gave a signal remote from those of the encoding QDs. In this way it proved possible to detect hybridization between probe and target at the same time as decoding the QD code, a procedure that exploited the broadband excitation characteristics of the coding QDs. The authors demonstrated that beads with up to 10 different intensity levels could be differentiated from one another using a one-color QD and extended this finding to predict that this type of approach could generate a realistic encoding strategy with up to 1 million codes (six colors at 10 intensity levels). This paper constituted a compelling starting point for QD-based

encoding, but one of the weaknesses of the work was the intensity of the coding signal, which may be why only a very small number of encoded types of microsphere were actually utilized in the study.

Silica-based beads similarly doped with QDs were shown by Gao and Nie to be 50 to 100 times brighter [20]. The authors also demonstrated that it was possible to generate up to 1000 discernible codes with just three colors of QD, but unfortunately, no descriptions of real applications of these materials were given. One possible reason for the lack of real applications is that the beads were not monodisperse enough to enable direct bead-to-bead comparisons to be made. For example, fluorescence intensities were shown to vary significantly from one bead to another of the same bead type, in some cases by as much as by 50%. Significant bead-to-bead variations like this could at best severely hamper, and at worst preclude, optical decoding.

Gao and Nie subsequently rectified this dispersity problem in an extremely elegant manner by returning to QD-doped polystyrene beads [19]. Here, virtually monodisperse mesoporous polystyrene-based beads were doped with QDs to generate composite materials that had extremely bright emission characteristics coupled with very good reproducibility of emission from one bead to another. In fact, the bead-to-bead reproducibility of these materials was so good that it proved possible to sort them, on the basis of QD emission, using a standard flow cytometer at a sort rate of up to 1000 beads per second. The ability to combine QD encoding with flow cytometry in this manner is extremely attractive, as it combines both high-speed sorting and deciphering with unique optical signatures that are both photochemically robust and have intense emissions. The only weakness with the materials described in this excellent paper is that the QDs are only immobilized within the mesopores of the beads by hydrophobic interactions. The encoded materials may thus be used only in aqueous and highly polar protic solvents such as ethanol. Exposure to the majority of organic solvents would simply result in leaching of the QDs from within the pores of the beads into the surrounding solvent, rendering the beads entirely useless in subsequent coding and decoding applications.

Since the original QD-based encoding paper of Han et al. [17], a number of other examples describing applications of QD encoding of beads have been reported [18,23a,24,26,28,36]. Of special recent note is an example whereby encoding has been coupled with flow cytometry [72]; two examples where QD-encoded beads have been used in lab-on-a-chip-type applications [73,74], one of which involves the use of a spinning disk format [73] and the other a microfluidic chip format [74]; and a fourth example where magnetic beads have been encoded with QDs and used to analyze gene expression [75]. In the first of these four examples, carboxylic acid-functionalized polystyrene beads were encoded by doping with controlled amounts of QDs (see Section 10.2.3) [72]. Three separately encoded batches of beads were attached to three different ssDNA oligonucleotides, and a mixture of these three bead types was subsequently incubated with a FITC-labeled target ssDNA oligonucleotide that was complementary to only one of the three bead-immobilized ssDNA oligonucleotides. The beads were removed from the hybridization reaction, washed to remove non-specifically bound ssDNA target, and subjected to a fluorescence-based assay procedure using the “homemade” FACS-like setup shown schematically in Figure 10.18. In this manner it was possible to assay the collection of beads and

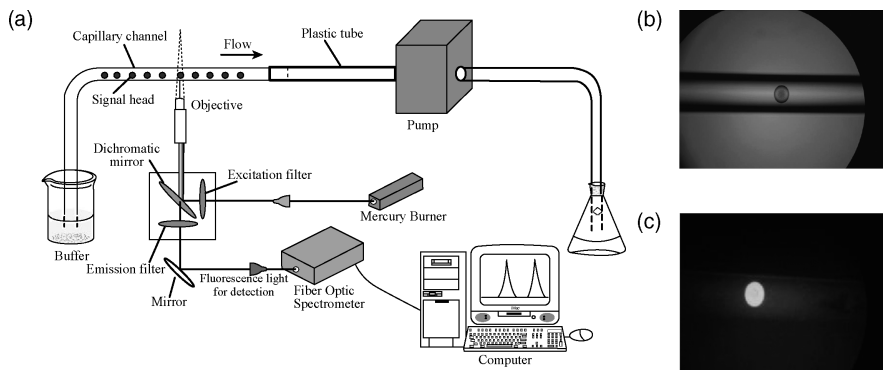


FIGURE 10.18 (a) Homemade flow cytometer setup for screening QD-containing beads; (b) transparent and (c) fluorescent images of a bead flowing through the home made flow cytometer. (From ref. 72, with permission from Elsevier.)

identify, on the basis of FITC fluorescence emission, the beads where hybridization had occurred. Moreover, the QD fluorescence emission from those beads was both distinct from, and generated concomitantly with, the FITC emission. Thus, the QD-based emission enabled the sequence of the ssDNA oligonucleotide attached to an active bead to be determined at the same time as the bead was identified as “active.” This flow cytometric assay, which enables beads to be interrogated at a speed of up to 76 beads per second, is a real strength of the paper. The homemade setup, which although it does not have sorting capability, enables on-bead assays to be conducted, should (1) enable many research groups to have in-house access to FACS-like capability at a very reasonable cost, and (2) be more versatile for analyzing multiple QD-colored beads than using commercial FACS machines, as it does not have a relatively limited number of color channels but instead, relies on a simple photoluminescent probe of the sort that many groups use routinely to assess the properties of QD-containing materials.

In the first of two recent examples where encoded beads have been employed in a lab-on-a-chip application, QD-encoded beads, generated by doping about 150- μm polystyrene beads (see Section 10.2.3) were employed [73]. Three different colors of QD were used to make just three types of coded bead, one for each color of QD employed. No color combinations were evaluated in this study. The three batches of encoded beads were then functionalized separately with one of three different primary antibodies before being mixed together and loaded into an inlet reservoir on the surface of a compact disk. The reservoir also contained buffer and an antigen for one of three primary antibodies attached to the encoded beads. Subsequently, a fluorescently labeled secondary antibody that targets one of the antigens was added to the reservoir. After an appropriate incubation time, spinning the disk resulted in the beads in the inlet reservoir flowing, by centrifugal microfluidics, into a detection chamber designed so that as the beads enter it, they are forced into a closely packed monolayer arrangement. The beads within the detection chamber were then illuminated with an LED light source via a long-pass filter which excited the QD codes, and the entrapped monolayer

of beads was imaged, in just a few seconds, using a color CCD camera. A second image was then recorded, again using the same illumination source and a CCD camera, but this time an alternative bandpass filter enabled the fluorescent label on the secondary antibody to be detected without interference from the QD-based emissions. Combining the two images enable active beads to be identified and simultaneously decoded in a process that takes just a few tens of seconds. The assay format was applied to the detection of antibodies for tetanus and hepatitis A in human serum samples, and the presence of antibodies at levels consistent with those affording long-term immunity against both diseases following vaccination were identified successfully. This application is a very nice example of using QD-encoded beads in a passive microstructured CD-based microfluidic system. The authors state that the CDs, the only disposable element of the setup, are ideally placed to be replicated by standard hot embossing or injection molding at low cost and in very high numbers.

The second example of an application of QD-encoded beads in a microfluidic assay system again focuses on detecting disease marker antibodies in human serum samples [74]. Three different batches of 5- μm QD-encoded beads were generated using the doping method pioneered by Han et al. (see Section 10.2.3). A different antigen was then attached to each batch of QD-encoded beads covalently using EDC. The specific antigens employed in this study were hepatitis B surface antigen, hepatitis C virus nonstructural protein 4, and HIV glycoprotein 41. The antigen-labeled QD-encoded beads were then incubated with human serum samples that had been spiked with one or more of the appropriate antibodies for each antigen. Subsequent to this initial incubation process with the primary disease marker antibodies, a secondary fluorescently labeled antibody ($\lambda_{\text{em}} \approx 520 \text{ nm}$) was added. The QD-encoded beads reacted with this secondary antibody only if there had been a successful antigen–primary antibody interaction. Each serum sample prepared in this manner was added into a disposable poly(dimethylsiloxane) (PDMS) microfluidic chip [see Figure 10.19(a)], and the QD-encoded beads were passed along the chip, by electrokinetically driven microfluidics, to a detection region. As each bead entered the detection region, laser excitation enabled beads bound to antibodies to be detected via a three-color photodiode detector–based system. A representation of some of the data obtained is shown in Figure 10.19(b). When multiplexing was used to assay more

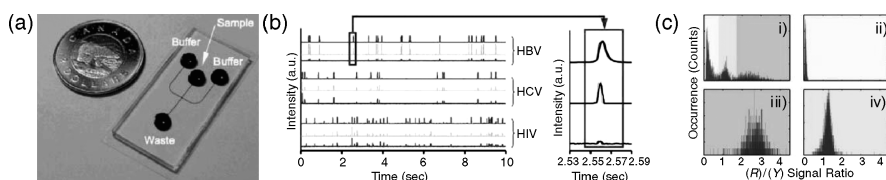


FIGURE 10.19 (a) Layout of the microfluidic chip used in this study in which the channels (100 μm wide by 15 μm high) have been highlighted with a dye to make them easily visible. The detection region is at the intersect of all three inlet channels. (b) Photodetector data generated for QD-encoded beads flowing through the detector region over a period of 10 seconds. (c) Multiplexing data showing the red/yellow signal ratios which enable the QD-based code to be deciphered for (i) hepatitis B, HIV, and hepatitis C; (ii) hepatitis B only; (iii) HIV only; and (iv) hepatitis C only. (Reproduced in part from ref. 74, with permission. Copyright © 2007 American Chemical Society.)

than one antibody type at a time, the yellow channel provided evidence of a bead bound to an antibody, while the red/green channel ratio enabled the QD code to be deciphered thus identifying the specific antibody–antigen interaction on a particular active bead [see Figure 10.19(c)]. Using this approach, it proved possible to detect the presence of just two or all three antibodies in different serum samples. Two of the strengths of this approach are its elegant simplicity and the fact that in the relatively near term, it should be possible to transfer all of the technology to a setup consisting of disposable chips coupled with a compact controller/reader for at-point-of-treatment use. One potential problem is the time taken and the skills required to conduct the off-chip aspects of the assay. The authors report that the time taken in going from antigen-coated QD-encoded beads to a readout is about 1 hour, and part of this process involves the biorecognition process, which currently is nontrivial to conduct. Perhaps the time scale could be shortened considerably and the process made more facile to conduct if the biorecognition events could also be carried out in the microfluidic chip. Moreover, it will probably prove possible to improve the already very creditable 70 beads per minute barcode deciphering rate.

The last of the four examples of applications involving the use of QD-encoded beads is something of a tour de force and provides a great example of just what can be achieved using QD encoding [75]. Different combinations of four differently colored QDs (525, 545, 565, and 585 nm), each at one of 12 intensity (I) levels, were mixed with a polymer, and the outer surfaces of 8- μm magnetic beads were coated with this polymer mixture. A very clever uniform coding strategy was adopted in which each bead was encoded with a combination of QDs that gave rise to an equal-intensity emission. Specifically, intensity levels for each color of QD were chosen so that for each bead type, $I_{525\text{ nm}} + I_{545\text{ nm}} + I_{565\text{ nm}} + I_{585\text{ nm}} = I_{\text{max}}$. Using this normalized coding strategy, a total of up to 455 differently coded batches of beads, called Qbeads by the authors, could be generated [see Figure 10.20(a)]. While this means that the total number of potential codes was not maximized, each code gave out exactly the same total amount of light. This normalized coding strategy circumvented problems of weaker emitting beads encountered in other strategies, such as the original report by Han et al. [17]. Here some beads had barcodes (e.g., QD intensity levels 1:1:1) that gave out much less light than others (e.g., QD intensity levels 10:10:10), which in turn resulted in markedly different degrees of signal-to-noise ratios, which could be problematic when decoding the beads.

Different gene-specific oligonucleotide probes were then attached to each differently coded batch of Qbeads [see Figure 10.20(b)]. These bead-encoded probe sequences were then mixed together and incubated with biotinylated cRNA. Complementarity between probe sequence and cRNA resulted in successful hybridisation, and this was evidenced by subsequent incubation with streptavidin-labeled with QD_{655 nm} (or QD_{705 nm} or QD_{800 nm}). Beads were labeled with QD_{655 nm} (or QD_{705 nm} or QD_{800 nm}) only in cases where successful probe–cRNA hybridization had occurred. The degree of gene expression affected the amount of cRNA available for hybridization, which in turn could be quantified directly simply by measuring the intensity of the QD_{655 nm} emission. The magnetic properties of the beads enabled facile separation of unbound materials prior to interrogating the fluorescent emission profiles (by excitation at 405 nm) of the beads to enable both gene identification and quantification [see Figure 10.20(c)].

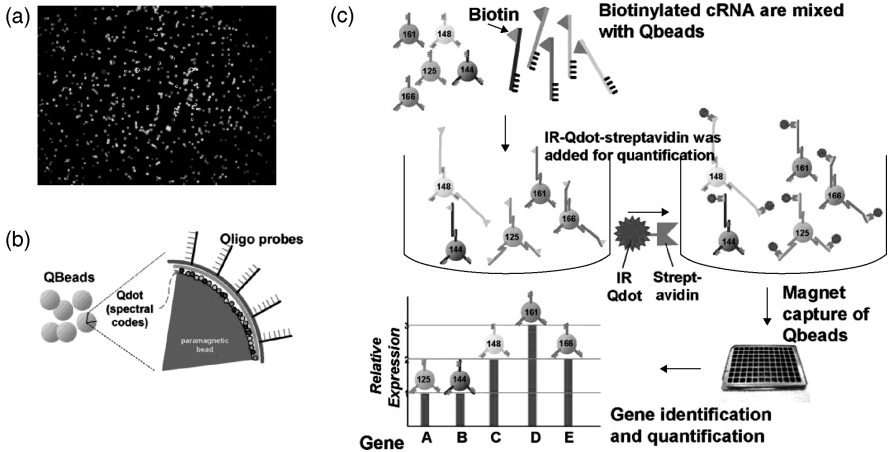


FIGURE 10.20 (a) Pseudocolored image of a collection of differently encoded Qbeads; (b) schematic representation of a cut through section of a Qbead functionalized with a gene-specific oligonucleotide probe; (c) schematic representation of the sequential processes of hybridization, streptavidin labeling, and gene expression analysis. (Reproduced in part from ref. 75, with permission. Copyright © 2006 American Chemical Society.)

The Qbead platform was then benchmarked and found to be sufficiently sensitive to detect just 10^6 target molecules. Moreover, assay sensitivity could be improved further, to 10^4 or more target molecules, by employing a single round of T7-mediated amplification of the target genes. The authors report that this value compares favorably with that of high-density microarray platforms (10^5 target molecules) and methods employing quantitative PCR (qPCR) (10^3 to 10^4 target molecules). In terms of dynamic range, the Qbead platform (3.5 logs) fared better than did most microarray-based assays (2 to 3 logs) but not as well as qPCR (6 logs). The Qbead methodology was then used to probe the expression levels of 92 selected housekeeping genes involved with transforming growth factor- β_1 , which causes changes in transcription in human bone marrow mesenchymal stem cells. This study enabled a direct comparison to be made between the Qbead and Affymetrix Human U133A2.0 GeneChip platforms for the analysis of gene expression. The authors were able to show good correlation between the two platforms, both of which produced highly reproducible results. Moreover, the authors reported that the Qbead platform was faster, in terms of hybridization, and more sensitive than the Affymetrix GeneChip platform, enabling analyses to be made with much less RNA (100 ng vs. 2 μ g of total RNA, when T7 amplification was employed in both instances).

10.4 FUTURE DIRECTIONS

In this chapter we hope that we have been able to convey the excitement of those who work with QD-containing polymer systems for biosensing applications. We have attempted to illustrate the breadth of this vibrant area with pertinent examples. In terms

of the future development of this field, any system that incorporates QDs is fundamentally reliant on QD quality and stability. The quality of QDs currently being incorporated into polymers is for the most part very good. In the examples we have highlighted, some QDs have been made in-house, and in other instances they have been bought in. Good-quality QDs are now becoming commercially available at increasingly attractive prices; for example, Sigma-Aldrich has recently started selling Lumidots, QDs manufactured by Nanoco Technologies Ltd., in 10- and 50-mg batches for as little as \$6 per milligram, which will enable their evaluation in more laboratories and also in larger-scale polymer systems. In the future the price of QDs is likely to decrease, and there is also likely to be an increase in quality and in batch-to-batch reproducibility as commercial suppliers address both of these key parameters.

The stability of QDs is very dependent on the outer layers surrounding them, especially the outermost organic layer. Moreover, the outer ligand layer is also vital in controlling the solubility and reactivity of the QDs. This is still an area that is very active in terms of research, and new ligand coating strategies are being reported all the time. Similarly, it is to be hoped that more comparator papers, such as the systematic study by Smith et al. [76] in which ligands were evaluated for a range of applications, will be published. This will aid investigators to select the most appropriate ligand and/or QD “incorporation” strategy for a given purpose. It would be an excellent idea for a study to evaluate QD stability upon exposure to a number of different sets of reaction conditions, particularly those used to couple biological molecules on to the outer surfaces of QDs and solvent-accessible regions of QD-containing polymers. It would also be most useful if reagents and conditions of a number of polymerization reactions were evaluated similarly. For example, it is well known that radical initiators such as AIBN can have a dramatic impact on the quantum yields of QDs. Similarly, a methodical study centered on the comparative strengths of ligand-QD surface interactions would be invaluable, particularly for those examples where this forms the basis of the QD-polymer conjugation strategy.

Another important aspect of using QDs is their toxicity when ions such as Cd^{2+} are released from their surfaces. Although QDs have been widely used in *in vitro* imaging and assays and similarly in *in vivo* animal studies, their use in humans will not occur until QD toxicity can be reduced significantly or until nontoxic QDs [77] become more widely available. Polymer coating and encapsulation strategies are likely to play a key role in reducing QD toxicity in a manner similar to the way in which they have been employed to reduce the toxicity of MRI contrast agents such as iron nanoparticles [78]. Metabolism and clearance studies will also play a key role in developing human-compatible QD-polymer composite probes for imaging, delivery, and therapeutic applications.

In terms of polymer composites that contain multiple QDs, Sheng et al. [35a] have recently highlighted the failings in current strategies for QD incorporation into polymer beads. Specifically, they called for more detailed analysis of composite materials to be made and the need for robust strategies that enable greater amounts of QDs to be incorporated into polymeric matrices. We echo this view, especially as we consider one of the earliest reports, that of Han et al., who doped into carboxylic acid-functionalized polystyrene beads and subsequently silica coated the surfaces of the immobilized QDs

of beads, to be the most effective strategy to date. Moreover, we think that the incorporation of QDs into polymer matrices by radical polymerization reactions are less likely to find general application in the future, due to the inherent incompatibility between QDs and the relatively aggressive (to QDs) reaction conditions employed in free-radical-mediated processes. The capricious nature of these free-radical-mediated processes in terms of QD degradation means that there is likely to be significant batch-to-batch variability in terms of resulting PL emissions, quantum yields, and so on. Consequently, we think that the majority of polymer composites that contain a plurality of QDs for encoding applications will be generated by doping methods. It is likely that new polymer matrices and oligomeric ligands, for example, like those reported recently [35a,40], will be developed that will enable more robust immobilization strategies of QDs into polymer beads, helping to prevent leaching, aggregation, and QD degradation processes occurring during subsequent application.

REFERENCES

1. Murray CB, Kagan CR, Bawendi MG. Synthesis and characterization of monodisperse nanocrystals and close-packed nanocrystal assemblies. *Annu. Rev. Mater. Sci.* 2000;30:545–610.
2. Sutherland AJ. Quantum dots as luminescent probes in biological systems. *Curr. Opin. Solid State Mater.* 2002;6:365–370.
3. Bruchez M, Jr., Moronne M, Gin P, Weiss S, Alivisatos AP. Semiconductor nanocrystals as fluorescent biological labels. *Science.* 1998;281:2013–2016.
4. Chan WCW, Nie S. Quantum dot bioconjugates for ultrasensitive nonisotopic detection. *Science.* 1998;281:2016–2018.
5. (a) Somers RC, Bawendi MG, Nocera DG. CdSe nanocrystal based chem-/bio-sensors. *Chem. Soc. Rev.* 2007;36:579–591. (b) Bailey RE, Smith AM, Nie S. Quantum dots in biology and medicine. *Physica E.* 2004;25:112. (c) Li ZB, Cai W, Chen XY. Semiconductor quantum dots for in vivo imaging. *J. Nanosci. Nanotechnol.* 2007;7:2567–2581. (d) Rosenthal SJ, McBride J, Pennycook SJ, Feldman LC. Synthesis, surface studies, composition and structural characterization of CdSe, core/shell and biologically active nanocrystals. *Surf. Sci. Rep.* 2007;62:111–157. (e) Raymo FM, Yildiz I. Luminescent chemosensors based on semiconductor quantum dots, *Phys. Chem. Chem. Phys.* 2007;9:2036–2043.
6. Wu X, Liu H, Liu J, et al. Immunofluorescent labeling of cancer marker Her2 and other cellular targets with semiconductor quantum dots. *Nat. Biotechnol.* 2003;21:41–46.
7. Li Y, Feng J, Daniels S, Pickett NL, O'Brien P. A highly luminescent ZnS/CdSe/ZnS nanocrystals–tetrapeptide biolabeling agent. *J. Nanosci. Nanotechnol.* 2007;7:2301–2308.
8. Yu WW, Chang E, Falkner JC, et al. Forming biocompatible and nonaggregated nanocrystals in water using amphiphilic polymers. *J. Am. Chem. Soc.* 2007;129:2871–2879.
9. Gao X, Cui Y, Levenson RM, Chung LWK, Nie S. In vivo cancer targeting and imaging with semiconductor quantum dots. *Nat. Biotechnol.* 2004;22:969–976.
10. Nann T. Phase-transfer of CdSe–ZnS quantum dots using amphiphilic hyperbranched polyethylenimine. *Chem. Commun.* 2005;13:1735–1736.

11. Wisher AC, Bronstein I, Chechik V. Thiolated PAMAM dendrimer-coated CdSe/ZnSe nanoparticles as protein transfection agents. *Chem. Commun.* 2006;15:1637–1639.
12. Duan H, Nie S. Cell-penetrating quantum dots based on multivalent and endosome-disrupting surface coatings. *J. Am. Chem. Soc.* 2007;129:3333–3338.
13. Nikolic MS, Krack M, Aleksandrovic V, Kornowski A, Förster S, Weller H. Tailor-made ligands for biocompatible nanoparticles. *Angew. Chem. Int. Ed.* 2006;45:6577–6580.
14. Dubertret B, Skorides P, Norris DJ, Noireaux V, Brivanlou AH, Libchaber A. In vivo imaging of quantum dots encapsulated in phospholipid micelles. *Science.* 2002;298:1759–1762.
15. Yusuf H, Kim W-G, Lee DH, Guo Y, Moffitt MG. Size control of mesoscale aqueous assemblies of quantum dots and block copolymers. *Langmuir.* 2007;23:868–878.
16. (a) Gaponik N, Radtchenko IL, Sukhorukov GB, Weller H, Rogach AL. Toward encoding combinatorial libraries: charge-driven microencapsulation of semiconductor nanocrystals luminescing in the visible and near IR. *Adv. Mater.* 2002;14:879–882. (b) Gaponik N, Radtchenko IL, Sukhorukov GB, Rogach AL. Luminescent polymer microcapsules addressable by a magnetic field. *Langmuir.* 2004;20:1449–1452. (c) Zebli B, Susha AS, Sukhorukov GB, Rogach AL, Parak WJ. Magnetic targeting and cellular uptake of polymer microcapsules simultaneously functionalized with magnetic and luminescent nanocrystals. *Langmuir.* 2005;21:4262–4265.
17. Han M, Gao X, Su JZ, Nie S. Quantum-dot-tagged microbeads for multiplexed optical coding of biomolecules. *Nat. Biotechnol.* 2001;19:631–635.
18. Wang H-Q, Huang Z-L, Liu T-C, et al. A feasible and quantitative encoding method for microbeads with multicolor quantum dots. *J. Fluoresc.* 2007;17:133–138.
19. Gao X, Nie S. Quantum dot-encoded mesoporous beads with high brightness and uniformity: rapid readout using flow cytometry. *Anal. Chem.* 2004;76:2406–2410.
20. Gao X, Nie SJ. Doping mesoporous materials with multicolor quantum dots. *J. Phys. Chem. B.* 2003;107:11575–11578.
21. Xie H-Y, Zuo C, Liu Y, et al. Cell-targeting multifunctional nanospheres with both fluorescence and magnetism. *Small.* 2005;1:506–509.
22. Bradley M, Bruno N, Vincent B. Distribution of CdSe quantum dots within swollen polystyrene microgel particles using confocal microscopy. *Langmuir.* 2005;21:2750–2753.
23. (a) Gao X, Chan WCW, Nie S. Quantum-dot nanocrystals for ultrasensitive biological labeling and multicolor optical encoding. *J. Biomed. Opt.* 2002;7:532–537. (b) Li M, Zhang H, Zhang J, Wang C, Han K, Yang B. Easy preparation and characterization of highly fluorescent polymer composite microspheres from aqueous CdTe nanocrystals. *J. Colloid Interface Sci.* 2006;300:564–568.
24. Xu H, Sha MY, Wong EY, et al. Multiplexed SNP genotyping using the Qbead (TM) system: a quantum dot-encoded microsphere-based assay. *Nucleic Acids Res.* 2003;31:e43.
25. Stsaipura V, Sukhanova A, Artemyev M, et al. Functionalized nanocrystal-tagged fluorescent polymer beads: synthesis, physicochemical characterization, and immunolabeling application. *Anal. Biochem.* 2004;334:257–265.
26. Cao Y-C, Huang Z-L, Liu T-C, et al. Preparation of silica encapsulated quantum dot encoded beads for multiplex assay and its properties. *Anal. Biochem.* 2006;351:193–200.
27. Wang D, Rogach AL, Caruso F. Semiconductor quantum dot-labeled microsphere bioconjugates prepared by stepwise self-assembly. *Nano Lett.* 2002;2:857.

28. Ma Q, Wang X, Li Y, Shi Y, Su X. Multicolor quantum dot-encoded microspheres for the detection of biomolecules. *Talanta*. 2007;72:1446–1452.
29. Sukhanova A, Susha AS, Bek A, et al. *Nano Lett.* 2007;7:2322–2327.
30. Müller F, Götzinger S, Gaponik N, Weller H, Mlynek J, Benson O, *J. Phys. Chem. B*. 2004;108:14527–14534.
31. Wang D, He J, Rosenzweig N, Rosenzweig Z. Superparamagnetic Fe₂O₃ beads–CdSe/ZnS quantum dots core–shell nanocomposite particles for cell separation. *Nano Lett.* 2004;4:409–413.
32. Yang Y, Wen Z, Dong Y, Gao M. Incorporating CdTe nanocrystals into polystyrene microspheres: towards robust fluorescent beads. *Small*. 2006;2:898–901.
33. Sill K, Emrick T. Nitroxide-mediated radical polymerization from CdSe nanoparticles. *Chem. Mater.* 2004;16:1240–1243.
34. O'Brien P, Cummins SS, Darcy D, et al. Quantum dot-labelled polymer beads by suspension polymerisation. *Chem. Commun.* 2003;20:2532–2533.
35. (a) Sheng W, Kim S, Lee J, Kim S-W, Jensen K, Bawendi MG. In-situ encapsulation of quantum dots into polymer microspheres. *Langmuir*. 2006;22:3782–3790. (b) Zhu M-Q, Chang E, Sun J, Drezek RZ. Surface modification and functionalization of semiconductor quantum dots through reactive coating of silanes in toluene. *J. Mater. Chem.* 2007;17:800–805.
36. Zhang Y, Huang NJ. Intracellular uptake of CdSe–ZnS/polystyrene nanobeads. *Biomed. Mater. Res. B*. 2006;76B:161–168.
37. Joumaa N, Lansalot M, Théretz A, Elaissari A. Synthesis of quantum dot-tagged submicrometer polystyrene particles by miniemulsion polymerization. *Langmuir*. 2006; 22:1810–1816.
38. Sherman RL, Jr, Ford WY. Semiconductor nanoparticle/polystyrene latex composite materials. *Langmuir*. 2005;21:5218–5222.
39. (a) Yang X, Zhang Y. Encapsulation of quantum nanodots in polystyrene and silica micro-/nanoparticles. *Langmuir*. 2004;20:6071–6073. (b) Fleischhaker F, Zentel R. Photonic crystals from core–shell colloids with incorporated highly fluorescent quantum dots. *Chem. Mater.* 2005;17:1346–1351 (c) Yang Y, Tu C, Gao M. A general approach for encapsulating aqueous colloidal particles into polymeric microbeads. *J. Mater. Chem.* 2007;17:2930–2935.
40. Zhu M-Q, Chang E, Sun J, Drezek RA. Surface modification and functionalization of semiconductor quantum dots through reactive coating of silanes in toluene. *J. Mater. Chem.* 2007;17:800–805.
41. Li Y, Lui CY, Pickett N, et al. Synthesis and characterization of CdS quantum dots in polystyrene microbeads. *J. Mater. Chem.* 2005;15:1238–1243.
42. Kim S, Bawendi MG. Oligomeric ligands for luminescent and stable nanocrystal quantum dots. *J. Am. Chem. Soc.* 2003;125:14652–14653.
43. (a) Wang L, Chen H, Wang L, et al. Preparation and application of a novel composite nanoparticle as a protein fluorescence probe. *Anal. Lett.* 2004;37:213–223. (b) Chen H, Xu F, Hong S, Wang L. Quantitative determination of proteins at nanogram levels by the resonance light-scattering technique with composite nanoparticles of CdS/PAA. *Spectrochim. Acta A*. 2006;65:428–432.
44. Yin W, Liu H, Yates MZ, et al. Fluorescent quantum dot–polymer nanocomposite particles by emulsification/solvent evaporation. *Chem. Mater.* 2007;19:2930–2936.
45. (a) Zhelev Z, Onbah H, Bakalova R. Single quantum dot–micelles coated with silica shell as potentially non-cytotoxic fluorescent cell tracers. *J. Am. Chem. Soc.* 2006; 128:6324–6325.

- (b) Bakalov R, Zhelev Z, Aoki I, Ohba H, Imai Y, Kanno I, Silica-shelled single quantum dot micelles as imaging probes with dual or multimodality *Anal. Chem.* 2006;78:5925–5932.
46. Gerion D, Pinaud F, Williams SC, et al. Synthesis and properties of biocompatible water-soluble silica-coated CdSe/ZnS semiconductor quantum dots. *J. Phys. Chem. B* 2001;105:8861–8871.
47. Stöber W, Fink A, Bohn E. Controlled growth of monodisperse silica spheres in the micron size range. *J. Colloid Interface Sci.* 1968;26:62.
48. Rogach AL, Nagesha D, Ostrander JW, Giersig M, Kotov NA. “Raisin bun”-type composite spheres of silica and semiconductor nanocrystals. *Chem. Mater.* 2000;12:2676–2685.
49. Chan Y, Zimmer JP, Stroh M, Steckel JS, Jain RK, Bawendi MG. Incorporation of luminescent nanocrystals into monodisperse core-shell silica microspheres. *Adv. Mater.* 2004;16:2092–2097.
50. Gude M, Ryf J, White PD. An accurate method for the quantitation of Fmoc-derivatized solid phase supports. *Lett. Pept. Sci.* 2002;9:203–206.
51. Pons T, Uyeda HT, Medintz IL, Mattoussi H. Designer variable repeat length polypeptides as scaffolds for surface immobilization of quantum dots. *J. Phys. Chem. B* 2006;110:20308–20316.
52. Sperling RA, Liedl T, Duhr S, et al. Size determination of (Bio)conjugated water-soluble colloidal nanoparticles: a comparison of different techniques. *J. Phys. Chem. C.* 2007;111:11552–11559.
53. Fu A, Micheel CM, Cha J, Chang H, Yang H, Alivisatos AP. Discrete nanostructures of quantum dots/Au with DNA. *J. Am. Chem. Soc.* 2004;126:10832–10833.
54. Sperling RA, Pellegrino T, Li JK, Chang WH, Parak WJ. Electrophoretic separation of nanoparticles with a discrete number of functional groups. *Adv. Funct. Mater.* 2006;16:943–948.
55. Casanova D, Giaume D, Moreau M, et al. Counting the number of proteins coupled to single nanoparticles. *J. Am. Chem. Soc.* 2007;129:12592–12593.
56. Wang M, Felorzabih N, Guerin G, Haley JC, Scholes GD, Winnik MA. Water-soluble CdSe quantum dots passivated by a multidentate diblock copolymer. *Macromolecules.* 2007;40:6377–6384.
57. Ross JS, Fletcher JA, Linette GP, et al. The *HER-2/neu* gene and protein in breast cancer 2003: biomarker and target of therapy. *Oncologist.* 2003;8:307–325.
58. Li YX, Zhao DH, Zhu CQ, Wang L, Xu JG. Determination of proteins at nanogram levels by their quenching effect on the chemiluminescence reaction between luminol and hydrogen peroxide with manganese-tetrasulfonatophthalocyanine as a new catalyst. *Anal. Bioanal. Chem.* 2002;374:395–398.
59. Cai W, Shin D-W, Chen K, et al. Peptide-labeled near-infrared quantum dots for imaging tumor vasculature in living subjects. *Nano Lett.* 2006;6:669–676.
60. (a) Tanaka E, Choi HS, Fujii H, Bawendi MG, Frangioni JV. Image-guided oncologic surgery using invisible light: completed pre-clinical development for sentinel lymph node mapping *Ann. Surg. Oncol.* 2006;13:1671–1681. (b) Kim S, Lim YT, Soltesz EG. Near-infrared fluorescent type II quantum dots for sentinel lymph node mapping. *Nat. Biotechnol.* 2004;22:93–97.

61. Kim SW, Kim S, Tracey JB, Jasanoff A, Bawendi MG. Phosphine oxide polymer for water-soluble nanoparticles. *J. Am. Chem. Soc.* 2005;127:4556–4557.
62. Kagan CR, Murray CB, Nirmal M, Bawendi MG. Electronic energy transfer in CdSe quantum dot solids. *Phys. Rev. Lett.* 1996;76:1517–1520.
63. (a) Clapp AR, Pons T, Medintz IL. Two-photon excitation of quantum-dot-based fluorescence resonance energy transfer and its applications. *Adv. Mater.* 2007;19:1921–1926. (b) Clapp AR, Medintz IL, Mauro JM, Fisher BR, Bawendi MG, Mattoussi H. Fluorescence resonance energy transfer between quantum dot donors and dye-labeled protein acceptors. *J. Am. Chem. Soc.* 2004;126:301–310. (c) Medintz IL, Clapp AR, Mattoussi H, Goldman ER, Mauro JM. *Nat. Mater.* 2003;2:630–638.
64. Lin C-AJ, Liedl T, Sperling RA, et al. Bioanalytics and biolabeling with semiconductor nanoparticles (quantum dots). *J. Mater. Chem.* 2007;17:1343–1346.
65. Hillisch A, Lorenz M, Diekmann S. Recent advances in FRET: distance determination in protein–DNA complexes. *Curr. Opin. Struct. Biol.* 2001;11:201–207.
66. Fernández-Argüelles MT, Yakovlev A, Sperling RA, et al. Synthesis and characterization of polymer-coated quantum dots with integrated acceptor dyes as FRET-based nanoprobe. *Nano Lett.* 2007;7:2613–2617.
67. Mulvaney SP, Mattoussi H, Whitman LJ. Incorporating fluorescent dyes and quantum dots into magnetic microbeads for immunoassays. *BioTechniques.* 2004;36:602–609.
68. Guo J, Yang W, Wang C, He J, Chen JY. Poly(*N*-isopropylacrylamide)-coated luminescent/magnetic silica microspheres: preparation, characterization, and biomedical applications. *Chem. Mater.* 2006;18:5554–5562.
69. Stroh M, Zimmer JP, Duda DG, et al. Quantum dots spectrally distinguish multiple species within the tumor milieu in vivo. *Nat. Med.* 2005;11:678–682.
70. Ebenstein Y, Mokari T, Banin U. Quantum-dot-functionalized scanning probes for fluorescence-energy-transfer-based microscopy. *J. Phys. Chem. B.* 2004;108:93–99.
71. Dubach JM, Harjes DI, Clark HA. Ion-selective nano-optodes incorporating quantum dots. *J. Am. Chem. Soc.* 2007;129:8418–8419.
72. Wang H-Q, Liu T-C, Cao Y-C, et al. A flow cytometric assay technology based on quantum dots-encoded beads. *Anal. Chim. Acta.* 2006;580:18–23.
73. Riegger L, Grumann M, Nann T, Riegler J, et al. Read-out concepts for multiplexed bead-based fluorescence immunoassays on centrifugal microfluidic platforms. *Sens. Actuators A.* 2006;126:455–462.
74. Klostranec JM, Xiang Q, Farcas GA, et al. Convergence of quantum dot barcodes with microfluidics and signal processing for multiplexed high-throughput infectious disease diagnostics. *Nano Lett.* 2007;7:2812–2818.
75. Eastman PS, Ruan W, Doctolero M, et al. Qdot nanobarcode for multiplexed gene expression analysis. *Nano Lett.* 2006;6:1059–1064.
76. Smith AM, Duan H, Rhyner MN, Ruan G, Nie S. A systematic examination of surface coatings on the optical and chemical properties of semiconductor quantum dots. *Phys. Chem. Chem. Phys.* 2006;8:3895–3903.
77. See, for example, Thakar R, Chen Y, Snee PT. Efficient emission from core/(doped) shell nanoparticles: Applications for chemical sensing. *Nano Lett.* 2007;7:3429–3432.
78. Kim J-H, Park K, Nam HY, Lee S, Kim K, Kwon IC. Polymers for bioimaging. *Prog. Polym. Sci.* 2007;32:1031–1053.

Quantum Dot Applications in Biomolecule Assays

YING XU, PINGANG HE, and YUZHI FANG

Department of Chemistry, East China Normal University, Shanghai, China

- 11.1 Introduction to QDs and their applications
- 11.2 Preparation of QDs for conjugation with biomolecules and cells
 - 11.2.1 Particle synthesis methods
 - 11.2.2 Particle surface modification and bioconjugation
 - 11.2.3 Signal detectors in QD-based biotechnologies
 - 11.2.4 Other QD synthesis developments
- 11.3 Special optoelectronic properties in the bioemployment of QDs
 - 11.3.1 Introduction to traditional fluorescent reagents
 - 11.3.2 Use of QDs in bioemployment
- 11.4 Employment of QDs as biosensing indicators

11.1 INTRODUCTION TO QDs AND THEIR APPLICATIONS

Our introduction to quantum dots (QDs) begins with a brief description of nanosciences and nanomaterials. There is no doubt that nanomaterial research has been the most important and challenging during the last two decades. Nanoscience technology consists of nanophysics, nanochemistry, nanobiology, nanoelectronics, nanomechanics, nanomachining, and nanomaterials, focusing on the materials and technologies developed in the mesoscopy-scale range, which is between the classical macroscopic size and the molecular/atomic microscopic size. The novel materials can be divided into three classes: (1) nanoparticles and atom clusters as zero-dimensional (0D) nanomaterials, with a particle diameter below 100 nm; (2) nanotubes, nanowires, and nanocables as 1D nanomaterials, with a tube width below

100 nm; and (3) nanofilms and superlattice as 2D nanomaterials, with a layer thickness on the nanoscale. Nanomaterials consist of different classes of materials, including elemental and composite; conductor, semiconductor, and insulator; and metal, ceramic, and polymer. When materials decrease in size from traditional bulky macroscopic sizes into micro- and then nanometer scales, they display novel chemical and physical properties, distinguishing them from or even making them superior to the common bulky materials (e.g., increased conductivity, strength, and toughness; superplasticity; superparamagnetic–paramagnetic characteristics). These unique size- and shape-dependent properties make them perfect materials for engineering, electronic, biological, and chemical research, opening a new era for science and technology. Chemists are synthesizing novel nanomaterials with controllable chemical and physical properties. A good sample is the noble metal nanoparticles of Pt as superior catalysts for chemical reactions; physical scientists are studying these interesting and special properties and providing the mechanics; biologists are finding bioapplications for the biocompatible nanomaterials, such as magnetic nanoparticles serving as the new generation of nuclear magnetic resonance contrast reagents, and these particles are also the tools need to capture and enrich biosamples; noble-metal nanoparticles, especially gold nanoparticles, are the commonly used biosensor labels; polymer particles are the carriers of medicine used to target tumor cells; and electronic scientists are building very small electronic devices using semiconductor and conductor nanoparticles, eliminating the problems associated with the finite size of traditional materials.

A quantum dot is a very tiny particle of nanocrystal composed of the semiconductor materials of transition metal [1]. Generally, they are the elements from groups IIA and VIA (MgS, MgSe, MgTe, CaS, CaSe, CaTe, SrS, SrSe, SrTe, BaS, BaSe, BaTe), IIB and VIA (ZnS, ZnSe, ZnTe, CdS, CdSe, CdTe, HgS, HgSe) and groups IIIA and VA (GaAs, InGaAs, InP, InAs). The semiconductor nanocrystals are usually in the diameter range 2 to 10 nm, structured in quasi-0D. Within this size range, QDs confine their electrons to discrete energy levels, which are similar to the energy levels in atoms. These special nanoparticles can absorb and then emit light, and in general when illuminated with invisible ultraviolet light, they fluoresce visible light [2]. The wavelength range for the various semiconductor material prepared QDs have been reviewed by Vashist et al. [3]. The light wavelength for QD adsorption and emission are controlled primarily by particle size, and when the size is decreased, the quantum size effect causes a blue shift in the excitation and emission light in QDs [4]. For example, CdSe nanocrystals about 2 nm in diameter are green, whereas 5-nm nanocrystals display red.

The quantum confinement effect causes QDs to have unique optical and electronic properties, and beginning in the 1970s, made them a promising optoelectronic material, developed as QD lasers, LEDs, amplifiers, storage devices, infrared detectors, quantum computing, and ultrahighly efficient solar cells. For example, QDs are considered the next-generation solar cells, having much higher energy transform efficiency than that of traditional solar cells. As today's traditional silicon photovoltaic cells (i.e., the current P-N junction solar cells) create only one electron per photon,

traditional solar technology can only reach a maximum theoretical efficiency (MTE) of about 31%. Comparatively, QDs can allow a single photon to create three electrons, thus increasing the MTE to 66%. Additionally, QD solar cell technology decreases the cost to produce cells compared with that to produce silicon solar cells, as they can be prepared through simple chemical reactions. Therefore, QDs have the advantage of being more efficient, cleaner, and cheaper solar cell materials.

Although QDs had already been prepared in the laboratory in the 1950s, they did not attract much attention, and today they are considered an attractive nanomaterial for bioemployment. By the end of 1980s, the development of mature molecular beam epitaxy technology made it possible to prepare QDs in different material systems, thus stimulating QD research and increasing interest in QD synthesis and applications. In 1998, two research groups published important findings about QDs in *Science*, opening the way for QD-involved biological technologies [5,6]. Bruchez et al. and Chen and Nie described approaches to offer water solubility and biocompatibility to QDs. Since then, QD bioscience has become a hot research area. Today, deeper studies on QD solubility, biocompatibility, and toxicity dramatically push the development of QD-based biotechnologies. In the book *Quantum Dots* [8], the increase in number of publications on QDs annually is given from 1985, when Ekimov et al. [7] suggested that quantum size effects determined the colors of CdS and CdSe dots, to the year 2000. The *Nanotech News* of the National Cancer Institute (nano.cancer.gov/index.asp) reported that there were about 1200 papers published on QD use in biomedical research from 1987 to the middle of 2005, and over 700 were published after 2000. Up to now, they have proved themselves to be novel and promising imaging toolkits, comparable, even superior, to other biological technologies. Today, most studies of QDs in biology focus on QDs complementing the traditional chemical organic fluorophores and biological fluorescent proteins, developing QD fluorescent probing technologies for “coloring” cells tissues and whole bodies in vitro and in vivo [9]. For example, for tumor cells investigations, QDs are encapsulated into amphiphilic polymers and attached to ligands to work against special tumor cell. After the QDs find the target cells, scientists can image the tumor cells and then study the cell processes using light to excite the QDs. Once internalized by the cells, QDs can be distributed to vesicles throughout the cytoplasm, displaying intense and stable fluorescence for a long time under complex biological conditions. Also, QD-based biotechnologies can detect other diseased tissues, provide the treatment, and report or diagnostic progress. As the new biological imaging tools, QDs have the advantages of higher imaging depth and longer stability. Due to the high brightness and long lifetime, even a single dot can be investigated and tracked using special spectrum techniques. Cells and tissues labeled with QDs can be reanalyzed with a similar level of fluorescence intensity. Moreover, as reported by Invitrogen, their Qdot can be passed to at least six generations of daughter cells without transfer to adjacent cells or effect on cell proliferation or cellular enzyme bioactivity. A QD-based drug delivery technique has also been developed. For cancer treatment, the drugs are first combined with QDs, and then peptides or antibodies are modified onto the QDs. QDs so prepared

can attach to target cells and release drugs to treat these cells when exposed to laser light heating. Such a drug transfer method increases drug efficiency to target cells and decreases damage to normal cells. Many QD-based in vivo experiments carried out with live animals have targeted liver, bone marrow, lymph, lung, blood vessels, and other areas. These studies offer the possibility of QD studies in humans.

Many books and review articles have discussed QDs comprehensively, including their novel physical and optical characteristics, and their promising technologies and applications. Recent review articles cover QD use in the following areas:

1. Special properties of QDs and their electronic applications. The article “Molecular aspects of electron correlation in quantum dots” reviews theories of electron correlation in QDs, with emphasis placed on the physics of QDs in strong magnetic fields [10]. In “Review on recent development of quantum dots: from optoelectronic devices to novel biosensing applications,” the authors covered potential applications of speedy and tunable light-emitting sources based on QD lasers, and addressed the physical properties of QD photodetectors [11].
2. Bioconjugation technologies for QDs. The review entitled “Quantum dot bioconjugates for imaging, labeling and sensing” focuses on methods conjugating biomolecules to QDs in QD-based imaging, labeling, and sensing biological applications, also outlining the limitations of the techniques on reproducible and robust conjugates between QDs and biomolecules [12].
3. QDs used in bioapplications. The review “Labeling of cells with quantum dots” gives an overview on QD employment in cell biology, focusing on labeling cellular structures and receptors with QDs, incorporation of QDs with live cells, tracking the path and fate of individual cells using QD labels, and the employment of QDs as contrast agents [13]. In “Quantum dots as cellular probes,” the advances of QDs are summarized in terms of the new generation of fluorescent probes used at the cellular level, including immunolabeling, cell tracking, in situ hybridization, fluorescence resonance energy transfer, in vivo imaging, and related technologies, as well as their limitations and potential future use [14]. The book *Nanobiotechnology Protocols* also summarizes and describes experiments for the application of QDs in biology [15].
4. Cancer treatment using QDs. “Review of quantum dot technologies for cancer detection and treatment” discusses advances in QD technology for the diagnosis of cancer, including QD-peptide conjugates to target tumor cells, QD-based drug delivery to target cancer, and QDs for multiplexed analysis [3]. It also outlines some early success in the detection and treatment of breast cancer.
5. QD safety for bioemployment. In the review “A toxicologic review of quantum dots: toxicity depends on physicochemical and environmental factors” factors influencing QD toxicity are discussed. The authors call for research toward a better understanding of QD toxicity mechanisms now, to avoid future pitfalls [16].

11.2 PREPARATION OF QDs FOR CONJUGATION WITH BIOMOLECULES AND CELLS

11.2.1 Particle Synthesis Methods

The sizes and shapes of QDs can be controlled precisely by particle synthesis conditions, including reaction time, synthesis temperature, and ligand reagents for stabilizing freshly prepared particles. On the other hand, their sizes dominate the physical and chemical properties of these nanoparticles. Until now, a variety of synthesis methods have been developed for preparing QDs that have the tunable sizes, shapes, and properties desired. Colloidal synthesis is the most commonly used and cheapest method for mass production of QDs. Most commonly, QDs are synthesized in organic solvents (e.g., toluene, chloroform) through chemistry reactions that result in surfactant-coated nanoparticles. The polar surfactant headgroups are attached to an inorganic particle surface whose hydrophobic chain protrudes into organic solvents. QDs so prepared are well dispersed in organic solvents and not soluble in aqueous media. Recently, newer, direct methods for the synthesis of intrinsic water-soluble QDs have been developed, using inorganic solvents and reagents [17,18]. Additionally, nanofabrication techniques developed recently, such as x-ray nanolithography, electron-beam lithography, and nanoprinting, have been employed to create QDs.

During nanoparticle synthesis, core-shell structure is widely used for particle surface modification and stabilization. One example is that of magnetic particles. Iron nanoparticles have a strong magnetic force and are considered promising novel superparamagnetic materials. However, they are sensitive to air conditions, and because they are very readily oxidized, they quickly lose their special magnetic characteristics. One efficient way to stabilize magnetic particles is to wrap them in a layer of gold, forming an iron core-gold shell structure. Gold is more stable than iron in air and aqueous conditions. Although some studies suggest that a gold shell could not absolutely keep air from contacting the inner iron atoms, it has been agreed that the gold shell structure can stabilize magnetic particles for several weeks at least. Gold shells are also used to provide stability to other metal particles, such as copper. As in the QD case, the lattice imperfection and impurity of the metals would decrease the quantum yield, due to the unpassivated surface sites, which also cause the nonradiative recombination and photodegradable sites to suppress efficient luminescence and promote photodegradation. For example, the quantum yield of QDs capped with long-chain organic surfactants was only 10% [19,20]. Therefore, a special shell should be used to coat the particles to stabilize the inner core, decreasing the photodamage and enhancing the quantum yield and brightness [21–23]. Crystalline semiconductor shells are made from more stable materials with higher bandgaps, and the central nanocrystal core determines the final fluorescence color of the particles. Until now, many core-shell structured QDs have been synthesized, such as $\text{Ag}_2\text{S}-\text{CdS}$, $\text{Cd}(\text{OH})_2-\text{CdS}$, $\text{ZnS}-\text{CdS}$, $\text{HgS}-\text{CdS}$, $\text{PbS}-\text{CdS}$, $\text{CdSe}-\text{ZnS}$, $\text{CdSe}-\text{ZnSe}$, and $\text{CdS}-\text{HgS}-\text{CdS}$ [24–31]. It has been reported that the shell structure could increase the quantum yield to 50 to 70%. ZnS-capped CdSe

nanocrystals exhibited an enhanced quantum yield of 50%, which was stable for months [32]. The quantum yield of CdS-capped CdSe QDs was 100% [33]. ZnSe–ZnS QDs showed a 2000% enhanced quantum yield compared to bare ZnSe nanocrystals [34].

11.2.2 Particle Surface Modification and Bioconjugation

Actually, a succession of complex surface modification steps should be carried out for QDs before their use in biotechnologies. These steps include core–shell structure formation to stabilize particle fluorescence, then multilayer modification to assure particle water solubility, and finally, the biomolecule conjugation to site bimolecular probes. Such prepared QDs can then be used to target DNA, proteins, both living and fixed cells, and tissues.

For their biological and medical applications, QDs should be hydrophilic either by replacing the surfactant with hydrophilic reagents or by coating the particles with additional amphipathic polymers. In the first case, the hydrophilic reagents replace the hydrophobic surfactant via binding their functional groups to QDs and leaving their hydrophilic groups at the other end, causing the QDs to become water soluble. Thiol groups (–SH) are generally used to react with the nanocrystal surfaces [23,35–42]. However, it has been found that bonds based on –SH are not strong enough for long-term stability [43,44], resulting in particle aggregation. In the second case, the hydrophobic side of amphipathic polymers can react with the surfactants on QDs, resulting in particles wrapped into polymer layers, with the hydrophilic side of the polymer making the particles water soluble [45–48] [e.g., poly(ethylene glycol)] [49]. Phospholipid micelle encapsulation can also make QDs water soluble [50]. If the surface ligand molecules carry electric charges, the QDs are stabilized by repulsive electrostatic force. Alternatively, these semiconductor particles are stabilized by the steric repulsion forces from uncharged polymer materials. The optical properties of the QDs so prepared are determined by the size of the inner nanocrystal core, and their surface chemistry is defined by the outside coating materials. Therefore, QDs of different colors could have identical surface properties for the bioconjugation procedure. Comparatively, different-colored organic dye fluorophores are mostly different molecules that have varied surface properties, which should result in different cross-link reactions to couple biomolecules onto those dyes, increasing the experimental complexity and cost.

The surface functionalization of QDs increases the particle water solubility and biocompatibility; however, some studies found that it also reduces the particle quantum yield in aqueous media compared with the original particles bearing a hydrophobic layer in organic solvents [51,52], because the surface modification changes the charges on QD surfaces. Other studies found that protein functionalizations could retain the QDs quantum yield, offer a long fluorescence time, and serve as a bridge to linking other biomolecules via their functional groups. Although the surface modifications sometimes decrease the quantum yield, the particles retain their basic superior optical properties (i.e. narrow and symmetric spectra, broad adsorption,

reduced photobleaching, and long lighting life), making them suitable for biological experiments [52].

The last layers for QDs used for biological purposes are the functionalized antibodies and other biomolecules which have complementary sequences against target biomolecules, such as special antibodies to the marker proteins on a tumor cell surface. Due to their small size, QDs have a higher surface-to-volume ratio in attaching various biomolecules, thus making QDs more complex multifunctional structures. For example, a 5-nm-diameter CdS has around 15% of its atoms on the surface [53], and about 160 serotonin molecules can link onto one dot [54]. Various strategies for conjugating biomolecules onto QDs have been developed, which can be classed as covalent and noncovalent methods: cross-linking via special chemical reactions, and adsorption by electrostatic force between charged biomolecules and QDs. The chemical groups used most often on QDs are $-\text{COOH}$, $-\text{NH}_2$, and $-\text{SH}$. Generally, proteins contain primary amines and thus can react with carboxyl group-derivatized QDs in the presence of EDC-NHS without chemical modification of the proteins [38,50,55,56]. Thiol-containing biomolecules can be coupled to the amine group-derivatized QDs using SMCC [56–58]. SMCC can activate amine groups to reactive maleimide groups [5,59]. However, the free sulfhydryl groups are unstable in the presence of oxygen, and additionally, are not very common in native biomolecules. As proteins usually have positively charged domains, they can also bind electrostatically to negatively charged QDs [60]. In addition to these strategies, streptavidin-biotin binding bridges are widely used to bind biotinylated biomolecules onto streptavidin-coated QDs [41,45,61,62]. As the reaction of avidin-streptavidin with biotin is special and their combination force is strong, streptavidin-coated QDs can readily be modified with biotinylated biomolecules. Additionally, streptavidin-coated QDs are available commercially, and biomolecules usually possess biotins or it is easy to synthesize this moiety onto the biomolecules.

Biomolecules attached to QDs should retain their special biofunctions, including their target recognition ability, as well as special effects and actions, such as their catalysis effect and their ability to block ion channels. It was found that in many cases, the conjugation of biomolecules onto QDs did not influence their biological functions or change their binding ability to specific receptors. For example, QD conjugation to transferring proteins did not affect the protein function [37], and the binding of QDs onto membrane-bound receptors did not affect the receptor diffusion behavior through membranes [63]. However, some reports suggest that QDs induce a steric hindrance effect and thus influence the biological functions of biomolecules. For example, the QD attachment influenced the binding affinity of neurotransmitter serotonin to serotonin-transporter proteins [57].

Consequently, these surface modifications increase QD size from several nanometers to larger sizes, sometimes within the protein size range (atoms, 0.05 to 0.5 nm; dye molecules, 0.5 to 10 nm; fluorescence proteins, 10 to 20 nm; viruses, 20 to 400 nm; bacteria, 500 nm to 10 μm ; animal cells, 10 to 100 μm), but no obvious influence has been found on their bioapplications for cell labeling, tissue modification, and

cell transfer, for example. This result is attributed to the fact that the semiconductor nanocrystal core controls the photonic property of the entire particle, and the outside modification multilayers for biomolecular conjugation determine the particle surface chemistry, which would not obviously influence the fluorescence emitted from the inner core.

11.2.3 Signal Detectors in QD-Based Biotechnologies

Biotechnologies involving QD fluorophores are fabricated by readout of the fluorescence intensity of the photonic signal excited from QDs. Deep tissue imaging requires the use of far- and near-infrared light to avoid blood and water absorption [64,65]. Many special instruments have been developed to detect QD optical signals for observing and tracking QDs, such as confocal microscopy [66], total internal reflection microscopy [67,68], epifluorescence microscopy [61,69], and flow cytometry. The laser scanning confocal microscope came into use during the 1980s. This technology has an advantage over traditional luminescence-detecting instruments in its ability to produce images in three dimensions and thus has been used widely in life science research, lithographic microfabrication, and so on. Especially when using two-photon laser scanning fluorescence microscopy, much higher intrinsic three dimensional spatial resolution would be obtained. Additionally, two-photon laser scanning fluorescence microscopy uses the light at long wavelengths to excite samples and therefore decreases the background signal caused by cellular autofluorescence of biosamples, increasing the signal-to-noise ratios [35,70–72].

11.2.4 Other QD Synthesis Developments

New compositions offer QDs with many novel and interesting properties as well as with improved special photophysical properties which can help extend traditional applications and also open up new applications of QDs. For example, manganese-doped CdSe nanocrystal colloids have been synthesized which are sensitive to electric and magnetic fields [73]. Due to their anisotropic shape, asymmetric nanorods can emit fluorescence light that is polarized, and therefore they can detect the orientation of their labeled structures [74]. By synthesizing ternary alloyed QDs, Nie's group found that in addition to particle size, the composition and structure can also tune the QDs optical and electronic properties [75].

11.3 SPECIAL OPTOELECTRONIC PROPERTIES IN THE BIOEMPLOYMENT OF QDs

As described above, QDs are single semiconductor fluorescent crystals whose size is generally controlled at several nanometers. Due to the fact that such sizes are

comparable to the de Broglie wavelength, these particles change their energy states in a way similar to atoms and they are called “artificial atoms.” When QDs are exposed to light or voltage with enough energy, the electrons on ground states will be excited to higher states, and the behavior of these activated electrons will drop back to that of ground states (i.e., recombination would emit special colored fluorescence). Quantum confinement effects begin to dominate the physical and chemical properties, resulting in dramatically changed magnetic, photo, thermal, electronic, and other chemophysical properties [4,76–78]. Consequently, the emission wavelength of QDs is dependent on their sizes [79–82].

11.3.1 Introduction to Traditional Fluorescent Reagents

An ideal fluorescence labeling reagent should be very stable and bright, having water solubility and very low toxicity, especially in the biotechnologies. Herein are the comparisons and discussions of QDs with other labeling technologies. The earlier labeling tools include isotopes, enzymes, dyes, and electrochemistry-induced luminescent reagents. As isotopes are very harmful, they are not generally used today. Enzymes have the advantage of enlarging signal by their special catalysis effects; however, they are sensitive to conditions, lose bioactivity easily, and consequent, need special storing conditions of temperature and buffer solutions to retain the activity. The electrochemistry-induced luminescence is usually irreversible and has poorer reproducibility. The advantages as well as the disadvantages of dyes are described below.

Up to now, organic dyes are still the fluorophores most used to “color” biomolecules and cells for imaging, tracking, and sensing, and these fluorescent targets can then be read out by using special luminescence detectors. In cell biology studies, the dyes “light” cells by conjugation onto the cell surface as well as the parts inside cells, and scientists can then investigate the structures and functions of cells *in vitro* and also *in vivo*. Tracking cells is also based on such dye-based fluorescence labeling. In biosensing technologies, fluorescent dyes are the current labeling reagents for indicating the biomolecules of interest. Although they are considered to be the standard fluorophore indicators, organic dyes still have encountered shortcomings during their employment in biological technologies. The principal limitations are their unstable lighting, narrow excitation wavelength window, and unsymmetric emission spectra. First, organic dye fluorophores are very sensitive to local environments. As a consequence of the thermal fluctuation of the solvents, dye fluorophores sometimes are transferred reversibly to the states in which they can no longer fluoresce, and the fluorescence of a single dye molecule goes “on” and “off” statistically, called *blinking* [83,84]. Dye has very obvious and frequent blinking, which is difficult to solve. Although single quantum dot also has blinking, suitable surface modification, such as fabricating the core–shell structure, could efficiently improve its photo stability and decrease the blinking phenomenon. On optical excitation, in addition to fluorescence emission, organic dyes would undergo some irreversible light-induced reactions, such as photooxidations. Consequently, these molecules are no longer

fluorescent, which is known as *photobleaching* [85]. It is a photochemical destruction procedure for fluorophores. Photobleaching limits the observation time during use of a long-time light exposition, such as for cell tracking. Several approaches can decrease the loss of photo activity caused by photobleaching, including using a reduced intensity of light emission, decreasing the timespan of the light exposure, increasing the fluorophore concentrations, and using the more stable fluorophores, such as QDs. QDs have stable light emission even in intense illumination conditions such as using a confocal microscope and flow cytometer. Another restriction for using organic fluorophores is their low quantum yield. Quantum yield is one measure for judging the brightness of a fluorophore molecule and the efficiency of the light absorbed. It is defined by the ratio of the number of photons emitted to those absorbed. Some fluorescent dyes have very high quantum yields, even as high as 100%. However, the surface conjugation of biomolecules onto dyes would decrease their quantum yields significantly.

Beside these traditional fluorescent tools, fluorescence labeling reagents called *fluorescent proteins* have also been developed around the 1990s and received much attention. Those most used are the green fluorescent proteins (i.e., GFP with its derivatives). GFP was first isolated from the jellyfish *Aequorea victoria*, and this type of natural protein can produce green fluorescence with an emission peak at 509 nm and an adsorption peak at 395 nm. After derivation, fluorescent proteins could give red, yellow, blue, or other colored light. There are several advantages to using GFP in bioimaging. First, their photo and chemical properties are stable, and these proteins can fluoresce even after being exposed for a long time at pH 7 to 12. Additionally, they can retain their structures and properties under conditions of high temperature 70°C, high salt strength, in organic solutions, and so on. Furthermore, these natural proteins have no toxicity and thus are biocompatible without obvious decomposition by protein enzymes. Recently, they have been expressed successfully in microbes, plants, and animals and in all types of cells and cell components. The fourth advantage is that these proteins are small in size and of molecular weight 27 to 30 kDa, and therefore they can readily cooperate with other proteins without obviously changing the host proteins' structures and functions. Finally, their alteration is easily carried out by gene mutation, producing new proteins with different colors and fluorescence intensity. Therefore, these special proteins, called *reporter genes*, are also employed to report genes, image cells, orient proteins and so on. However, they have also encountered limitations. One is that their fluorescence intensity is not linearly varied with their amounts, which limits the quantization analysis. Second, their characteristic adsorption and excitation wavelengths range from 400 to 650 nm. The fur, skin, food, proteins, and so on, in the biosamples will all produce autofluorescence in this wavelength window, which produces background fluorescence and influences the signal measurement. The haemoglobin, especially would adsorb the light below 600 nm. Third, the transformation of GFP to its active structure for fluorescence emission is very slowly influencing the detection speed. Additionally, using higher-energy light as an excitation source, such as ultraviolet exposition, these proteins will carry out photobleaching. Finally, these proteins have only a few colors, limiting their use in multicolor analysis and coding technology.

11.3.2 Use of QDs in Bioemployment

Comparatively, QDs exhibit unique optical and electronic properties, which make them more suitable than dyes for labeling, imaging, encoding, and for use as electrophoto materials, and guarantee them to be a promising alternative to conventional organic dyes in a variety of biotechnologies. These special properties are the broad excitation and symmetric emission spectra, the high chemical and photo stability, and the wide-ranging bioconjugation approaches, dissolving the limitations of dyes and other fluorescent reagents in biotechnologies. First, QDs have a much broader absorbance wavelength window, and they can adsorb all the lights at the wavelength window shorter than their emission wavelengths (i.e., about 10 nm). Additionally, QDs have larger extinction coefficients than dyes, so absorb light more efficiently [48,50]. The extinction coefficients of common dyes and QDs are provided in the review of Vashist et al. [3]. Therefore, the same QDs can be excited by varied wavelengths; on the other hand, different QDs can be excited simultaneously using one wavelength. The emission spectra of QDs are size-tunable (i.e., the particle size controls its emission spectra). Therefore, it can readily vary the QDs' fluorescence by varying their size and still retain the same compositions and surface chemistries as those obtained using the bioconjugation approach. However, as described above, the conjugation methods for different dye molecules are different, which increases the cost and complexity of the biolabeling operations. Furthermore, compared with dyes displaying mostly broader asymmetric emission spectra and having obvious tails, QDs have much narrower symmetric emission spectra in a Gaussian shape and a full width at half maximum of less than 40 nm. Additionally, QDs have a larger Stock shift and the wavelength difference between maximum absorbance and emission is usually hundreds of nanometers. Consequently, overlapping of the emission spectrum during the use of various dyes can be solved by using different QDs or even the same QDs in varied sizes. As the QDs emit light in very specific Gaussian distributions, they can more accurately reflect the colors to human eyes, and therefore they are also of value for display development. All these special properties allow simultaneous excitation by using one exciting wavelength and then detecting the emission signal at different wavelengths for individual QDs [45,86–90]. QD-based multicolor measurements reduce the excitation time and cost significantly, and simplify the measurement procedure. By contrast, traditional dyes absorb light primarily during a narrow wavelength window, which is close to their emission lights, around 15 to 30 nm. Therefore, simultaneous multicolored measurements are carried out by using different dyes, and different excitation wavelengths should be used to excite every dye efficiently. In addition, to reduce the scatter and autofluorescence induced by the close excitation and emission wavelengths, special optical filters should be used. These additional treatments and procedures also increase the multianalysis cost. QD-based multibioassay research has accelerated spectral coding research, and QD-encoded beads have become a promising tool for high-throughput screening. QD encoding is a biotechnology that utilizes polymer beads to carry a varied number of the different fluorescent QDs as encoding labels. As one combination of

QDs will give one combination of fluorescence color, this encoding method shows its powerful ability especially for medical diagnostics, gene expression studies, and DNA/protein biochip technologies [89–93]. Living cells can also be encoded by using the QDs in different colors [65]. Typically, dyes have a fluorescence lifetime around several nanoseconds, which is very close to the lifetime of autofluorescence. QDs, however, could keep their bright fluorescence for a much longer time: to about tens or even hundreds of nanoseconds [78,94]. This long fluorescence time could efficiently decrease the autofluorescence interruption by recording the signal after the autofluorescence decay. Another advantage of QDs over dyes is that QDs, especially QDs structured at core–shell formations have chemical and photo stability without suffering significant chemical degradation and photodegradation. The ability to anti-photobleach is 50 to 100 times greater for QDs than for dyes [76,90,95–97]. Finally, QDs have vast conjugation strategies for biomolecule attachments, and these approaches, as described above, are relatively simple. After the right surface modification, QDs change into biocompatible with less toxicity, to live cells. However, dyes generally have higher toxicity, and many of them are carcinogenic.

Also, there are two shortcomings to the use of QD-based biotechnologies, which should be solved for their further development, especially use in humans. One drawback is the irregular blinking. It has found that the single dot also has blinking, which can be attributed to Auger ionization [65,98–102] and limits its application for single-particle tracking. The other drawback is the QD potential toxicity for live cells. Cell cytotoxicity and potential interference studies have been discussed for QD presence in live cells, and the results showed that there are no obvious effects on cell viability, morphology, function, and development from several hours to several days and even weeks [48,49,56,63,71,72,88]. For example, the micelle-encapsulated QDs injected into the frog embryo did not affect its development [50]. However, if using a higher concentration of QDs or exposing the QDs to ultraviolet light for a long time, the QDs would be dissolved [37,50,103]. It is suggested that the toxic effect of QDs on cells can be neglected when QDs are at moderate concentrations and with an appropriate encapsulation shell, especially coated with protein or polymer shells. Therefore, works should be carried out to modify QDs with a safe protective reagent such as polymer coating making them biocompatible [48]. The core–shell structure of QDs should be studied carefully to improve particle stability, avoiding ion release from particles. Additionally, the safe employment of QDs based on their components, structures, shapes, and synthesis protocols should be investigated as one important part of QD studies, especially for experiments carried out *in vivo*.

11.4 EMPLOYMENT OF QDs AS BIOSENSING INDICATORS

Among different biosensing techniques, optical transducing methods have the advantage of high sensitivity, and the used traditionally optical indicators are

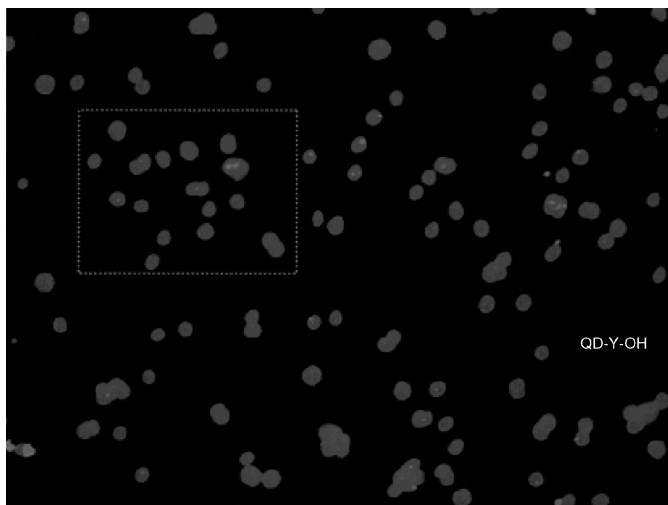


FIGURE 11.1 Fluorescence micrograph of in situ hybridization of red quantum ($\lambda_{\text{max}} = 609 \text{ nm}$, full width at half maximum = 38 nm) dot probe(s) for the Y chromosome in human sperm cells. (From ref. 49, with permission. Copyright © 2001 American Chemical Society.)

fluorescent dye molecules. However, the need for sophisticated, high-cost equipment, insufficient photostability, and the fact that one biomolecule can only be labeled with one or a few fluorophores, which results in a lack of signal amplification, also become shortcomings for developing this fluorescence biosensing technology. As described above, semiconductor QDs possess strong and photostable fluorescence signals [104], and consequently attract the attention from biosensing research fields [90,105]. Recently, Pathak et al. used hydroxylated CdSe–ZnS quantum dots as luminescent probes to analyze in situ DNA hybridization (Figure 11.1) [49]. Their experiments give a strong positive result of about 41% compared to the theoretical 50%. Other optical techniques have been employed in QD-based biosensors such as photoelectrochemical detection [106,107]. As shown in Figure 11.2, the dsDNA-linked CdS arrays on electrode can generate photocurrents upon the irradiation of CdS, and $[\text{Ru}(\text{NH}_3)_6]^{3+}$ on the dsDNA strands provided the electronic tunneling routes, thus enhancing the photocurrent signals.

In addition to optical detection, the QD labels can also be measured using electrochemical techniques in electrochemical biosensors, especially for the CdS and PbS [108]. Traditionally, QDs linked to the target hybrid would undergo acid treatment to dissolve into metal ions for electrochemical measurements. Because one dot possesses a large number of metal atoms e.g., there are about 1500 atoms in one 4-nm-diameter CdS, the detection limit has thus been improved significantly if electrochemically quantifying the dissolved metal ions in those QD-based biosensors. For example, the biotinylated DNA target were first linked onto streptavidin-coated magnetic beads and then hybridized with CdS-labeled DNA

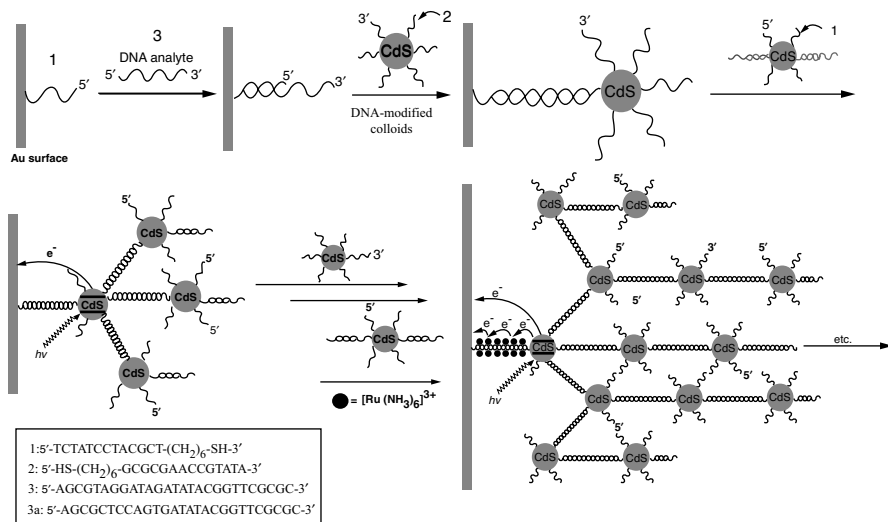


FIGURE 11.2 Organization of oligonucleotide–DNA-cross-linked arrays of CdS nanoparticles and the photoelectrochemical response of the nanoarchitectures. (From ref. 106, with permission. Copyright © 2001 Wiley-VCH Verlag GmbH & Co. KGaA.)

probe; finally, the CdS tags were dissolved into binary cadmium ions for electrochemical stripping detection [109]. Our group has also fabricated such sensitive electrochemical DNA biosensors by using CdS, PbS, and ZnS QDs [110–112]. In these DNA biosensors, as shown in Figure 11.3, the

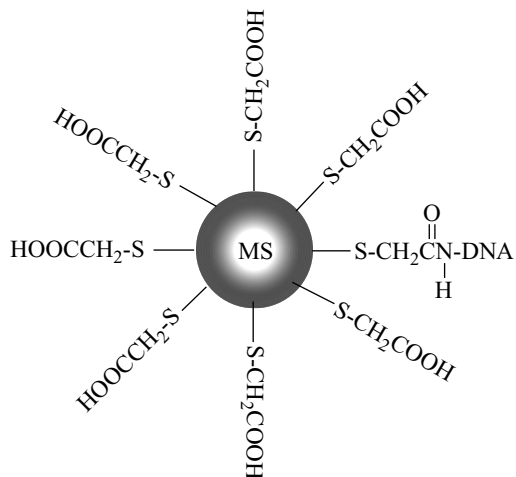


FIGURE 11.3 PbS and CdS nanoparticles conjugated to ssDNA probe by cross-linking reaction (MS = PbS, CdS, and ZnS).

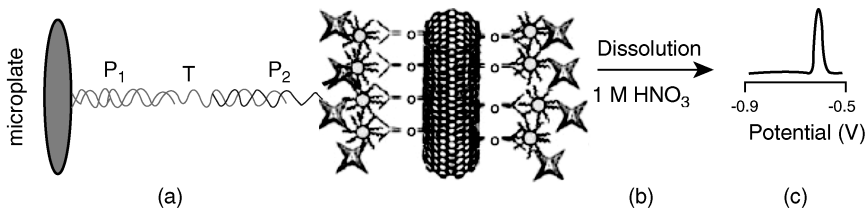


FIGURE 11.4 Analytical protocol: (a) dual hybridization event of the sandwich hybridization assay, leading to capturing the CdS-loaded CNT tags into the microwell; (b) dissolution of the CdS tracer; (c) stripping voltammetric detection of cadmium ions at a mercury-coated glassy carbon electrode. P₁, DNA probe 1; T, DNA target; P₂, DNA probe 2. (From ref. 115, with permission. Copyright © 2003 Elsevier.)

water-soluble QDs synthesized with carboxyl groups [113,114] were attached onto a NH₂-ssDNA probe in the presence of EDC. After hybridization, these QD tags were dissolved in concentrated HNO₃ and the Pb²⁺, Cd²⁺, or Zn²⁺ ions dissolved were determined by anodic stripping voltammetry. Wang's group recently employed carbon nanotubes to attach QDs further amplifying the hybridization signal [115]. As shown in Figure 11.4, a larger number of octadecanethiol-capped CdS nanoparticles can be attached to acetone-activated single-walled carbon nanotubes via hydrophobic force, and the entire CNTs–CdS complex was then used as a powerful hybridization indicator. After hybridization in a sandwich manner, the CdS nanoparticles were dissolved into Cd²⁺ and measured by stripping voltammetry. As one CNT can carry 500 CdS particles, the detection limit has been improved significantly compared with the single CdS nanoparticle labeling technique.

By labeling different QDs tags, multitarget biomolecules can be analysed simultaneously using one single electrochemical scan. For example, Wang et al. reported the simultaneous detection of three *BRCA1* breast-cancer gene sequences by using Zds, CdS, and PbS QDs [116]. They also displayed the simultaneous detection of four different proteins (i.e., IgG, BSA, microglobulin, and CRP) by using the QDs of ZnS-anti-microglobulin, CdS-anti-IgG, PbS-anti-BSA, and CuS-polyclonal anti-CRP [117]. The key point for this method, as shown in Figure 11.5, is that these QD tags should possess diverse electrochemical potentials, and therefore their electrochemical signals would not overlap with each other. QDs also have been employed in single-nucleotide polymorphism (SNPs) identification using electrochemical measurements [118]. The group coded individual SNPs by base pairing each mutation with different quantum dot–mononucleotide conjugates, yielding a distinct electronic fingerprint.

With their dramatic development in the past 10 years, QDs have been involved in all aspects of biology; now they are the novel imaging tools for different types of biotechnologies and the powerful indicators used in various biosensing technologies. Safety research and mass production are the challenges ahead before permitting QD use with human beings.

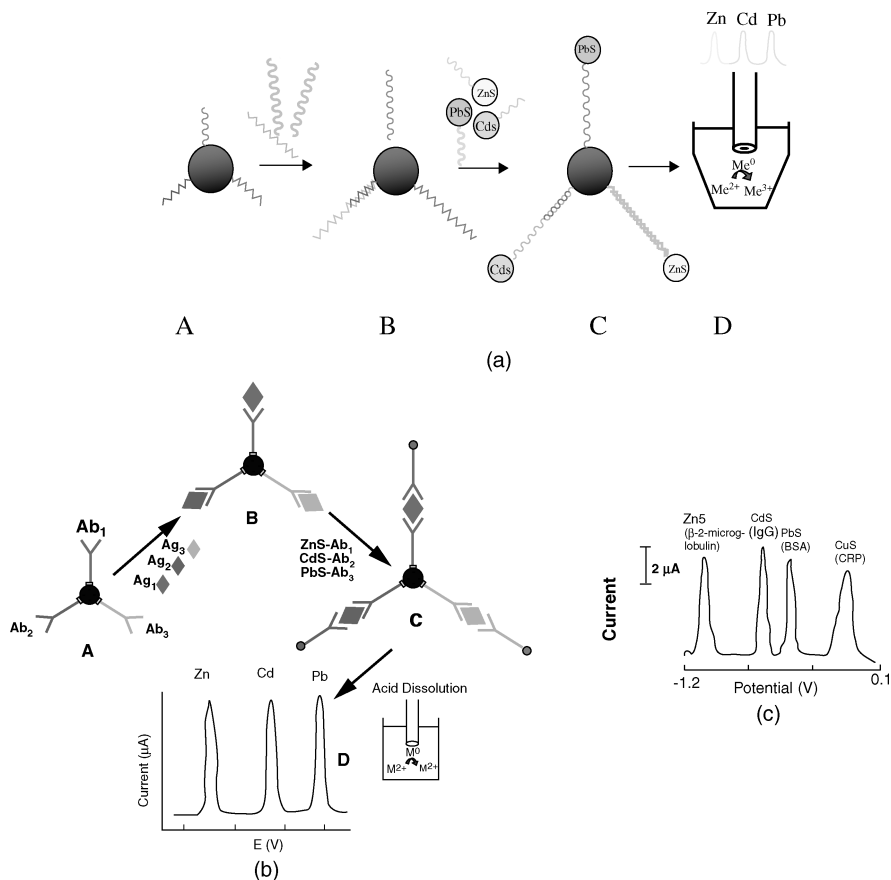


FIGURE 11.5 (a) Multitarget electrical DNA detection protocol based on different inorganic colloid nanocrystal tracers: (A) introduction of probe-modified magnetic beads; (B) hybridization with the DNA targets; (C) second hybridization with the QD-labeled probes; (D) dissolution of QDs and electrochemical detection. (b) Multiprotein electrical detection protocol based on different inorganic colloid nanocrystal tracers: (A) introduction of antibody-modified magnetic beads; (B) binding of the antigens to the antibodies on the magnetic beads; (C) capture of the nanocrystal-labeled secondary antibodies; (D) dissolution of nanocrystals and electrochemical stripping detection. (c) Immunoassay stripping voltammograms for a sample mixture containing 100 ng/mL antigen targets (β_2 -microglobulin, IgG, BSA, C reactive protein) in the presence of ZnS-anti- β_2 -microglobulin, CdS-anti-IgG, PbS-anti-BSA, and CuS-polyclonal anti-human C_{reactive} protein tags, respectively. [(a) From ref. 116, with permission. Copyright © 2003 American Chemical Society. (b,c) From ref. 117, with permission. Copyright © American Chemical Society.]

REFERENCES

1. Weiss S. Fluorescence spectroscopy of single biomolecules. *Science*. 1999;283:1676–1683.
2. Hotz CZ. Applications of quantum dots in biology: an overview. *Methods Mol. Biol.* 2005;303:1–17.
3. Vashist SK, Tewari R, Bajpai RP, Bharadwaj LM, Raiteri R. Review of quantum dot technologies for cancer detection and treatment. *J. Nanotechnol.* Online DOI: 102240/azojono0113 2006.
4. Bawendi MG, Steigerwald ML, Brus LE. The quantum mechanics of larger semiconductor clusters (“quantum dots”). *Annu. Rev. Phys. Chem.* 1990;41:477–496.
5. Bruchez M, Moronne M, Gin P, Weiss S, Alivisatos AP. Semi-conductor nanocrystals as fluorescent biological labels. *Science*. 1998;281:2013–2016.
6. Chan WCW, Nie SM. Quantum dot bioconjugates for ultrasensitive nonisotopic detection. *Science*. 1998;281:2016–2018.
7. Ekimov AI, Efros AL, Onushchenko AA. Quantum size effect in semiconductor microcrystals. *Solid State Commun.* 1985;56:921–924.
8. Borovitskaya E, Shur MS. *Quantum dots Selected Topics in Electronic and Systems*, Vol. 25. World Scientific, Singapore, 2002.
9. Howarth M, Takao K, Hayashi Y, Ting AY. Targeting quantum dots to surface proteins in living cells with biotin ligase. *Proc. Natl. Acad. Sci. USA*. 2005;102:7583–7588.
10. Maksym PA, Imamura H, Mallon GP, Aoki H. Review article: molecular aspects of electron correlation in quantum dots. *J. Phys. Condensed Matter*. 2000;12:R299–R334.
11. Kim SM. Review on recent development of quantum dots: from optoelectronic devices to novel biosensing applications. Razeghi M, Brown, GJ, eds. *Quantum Sensing: Evolution and Revolution from Past to Future*. *Proc. SPIE*. 2003;4999:423–430.
12. Medintz IL, Uyeda HT, Goldman ER, Mattoussi H. Quantum dot bioconjugates for imaging, labelling and sensing. *Nat. Mater.* 2005;4:435–446.
13. Parak WJ, Pellegrino T, Plank C. Labelling of cells with quantum dots. *Nanotechnology*. 2005;16:R9–R25.
14. Alivisatos AP, Gu W, Larabell C. Quantum dots as cellular probes. *Annu. Rev. Biomed. Eng.* 2005;7:55–76.
15. Rosenthal SJ, Wright DW, eds. *Nanobiotechnology Protocols*. Humana Press, Totowa, 2005.
16. Hardman R. A toxicologic review of quantum dots: toxicity depends on physicochemical and environmental factors. *Environ. Health Perspect.* 2006;114:165–172.
17. Rogach AL, Harrison MT, Kershaw SV, et al. Colloidally prepared CdHgTe and HgTe quantum dots with strong near-infrared luminescence. *Phys. Status Solidi B*. 2001;224:153–158.
18. Gaponik N, Talapin DV, Rogach AL, et al. Capping of CdTe nanocrystals: an alternative to organometallic synthetic routes. *J. Phys. Chem. B*. 2002;106:7177–7185.
19. Norris DJ, Sacra A, Murray CB, Bawendi MG. Measurement of the size dependent hole spectrum in CdSe quantum dots. *Phys. Rev. Lett.* 1994;72:2612–2615.

20. Hoheisel W, Colvin VL, Johnson CS, Alivisatos AP. Threshold for quasicontinuum absorption and reduced luminescence efficiency in CdSe nanocrystals. *J. Chem. Phys.* 1994;101:8455–8460.
21. Dabbousi BO, Rodriguez-Viejo J, Mikulec FV, et al. (CdSe)/ZnS core-shell quantum dots: synthesis and characterization of a size series of highly luminescent nanocrystallites. *J. Phys. Chem. B.* 1997;101:9463–9475.
22. Reiss P, Bleuse J, Pron A. Highly luminescent CdSe/ZnSe core/shell nanocrystals of low size dispersion. *Nano Lett.* 2002;2:781–784.
23. Sukhanova A, Devy J, Venteo L, et al. Biocompatible fluorescent nanocrystals for immunolabeling of membrane proteins and cells. *Anal. Biochem.* 2004;324:60–67.
24. Spahnel L, Haase M, Weller H, Henglein A. Photochemistry of colloidal semiconductors 20. Surface modification and stability of strong luminescing CdS particles.. *J. Am. Chem. Soc.* 1987;109:5649–5655.
25. Eychmuller A, Hasselbarth A, Katsikas L, Weller H. Fluorescence mechanism of highly monodisperse Q-sized CdS colloids. *J. Luminesc.* 1991;48–49:745–749.
26. Kortan AR, Hull R, Opila RL, et al. Nucleation and growth of cadmium selenide on zinc sulfide quantum crystallite seeds, and vice versa, in inverse micelle media. *J. Am. Chem. Soc.* 1990;112:1327–1332.
27. Tian Y, Newton T, Kotov NA, Guldi DM, Fendler JH. Coupled composite CdS–CdSe and core-shell types of (CdS)CdSe and (CdSe)Cds nanoparticles. *J. Phys. Chem.* 1996;100:8927–8939.
28. Hoener CF, Allan KA, Bard AJ, et al. Demonstration of a shell-core structure in layered CdSe–ZnSe small particles by x-ray photoelectron and Auger spectroscopies. *J. Phys. Chem.* 1992;96:3812–3817.
29. Eychmuller A, Mews A, Weller H. A quantum dot quantum well: CdS/HgS/CdS. *Chem. Phys. Lett.* 1993;208:59–62.
30. Mews A, Eychmuller A, Giersig M, Schoos D, Weller HJ. Preparation, characterization and photo-physics of the quantum dot quantum well system CdS/HgS/CdS. *Phys. Chem.* 1994;98:934–941.
31. Danek M, Jensen KF, Murray CB, Bawendi MG. Electrospray organometallic chemical vapor deposition: a novel technique for preparation of II–VI quantum dot composites. *Appl. Phys. Lett.* 1994;65:2795–2797.
32. Hines MA, Guyot-Sionnest P. Synthesis and characterization of strongly luminescing ZnS-capped CdSe nanocrystals. *J. Phys. Chem.* 1996;100:468–471.
33. Peng X, Schlamp MC, Kadavanich AV, Alivisatos AP. Epitaxial growth of highly luminescent CdSe/CdS core/shell nanocrystals with photostability and electronic accessibility. *J. Am. Chem. Soc.* 1997;119:7019–7029.
34. Song K, Lee S. Highly luminescent (ZnSe)/ZnS core-shell quantum dots: synthesis and Characterization. *Curr. Appl. Phys.* 2001;1:169.
35. Zhang CY, Ma H, Nie SM, Ding Y, Jin L, Chen DY. Quantum dot-labeled trichosanthin. *Analyst.* 2000;125:1029–1031.
36. Winter JO, Liu TY, Korgel BA, Schmidt CE. Recognition molecule directed interfacing between semiconductor quantum dots and nerve cells. *Adv. Mater.* 2001;13:1673–1677.
37. Kloepper JA, Kloepper JA, Mielke RE, et al. Quantum dots as strain- and metabolism-specific microbiological labels. *Appl. Environ. Microbiol.* 2003;69:4205–4213.

38. Mitchell GP, Mirkin CA, Letsinger RL. Programmed assembly of DNA functionalized quantum dots. *J. Am. Chem. Soc.* 1999;121:8122–8123.
39. Hanaki K, Momo A, Oku T, et al. Semiconductor quantum dot/albumin complex is a long-life and highly photostable endosome marker. *Biochem. Biophys. Res. Commun.* 2003;302:496–501.
40. Chen CC, Yet CP, Wang HN, Chao CY. Self-assembly of monolayers of cadmium selenide nanocrystals with dual color emission. *Langmuir.* 1999;15:6845–6850.
41. Jaiswal JK, Mattoussi H, Mauro JM, Simon SM. Long-term multiple color imaging of live cells using quantum dot bioconjugates. *Nat. Biotechnol.* 2003;21:47–51.
42. Sukhanova A, Venteo L, Devy J, et al. Highly stable fluorescent nanocrystals as a novel class of labels for immunohistochemical analysis of paraffin-embedded tissue sections. *Lab. Invest.* 2002;82:1259–1261.
43. Aldana J, Wang YA, Peng X. Photochemical instability of CdSe nanocrystals coated by hydrophilic thiols. *J. Am. Chem. Soc.* 2001;123:8844–8850.
44. Gerion D, Pinaud F, Williams SC, et al. Synthesis and properties of biocompatible water-soluble silica-coated CdSe/ZnS semiconductor quantum dots. *J. Phys. Chem. B.* 2001;105:8861–8871.
45. Wu X, Liu H, Haley KN, et al. Immunofluorescent labeling of cancer marker Her2 and other cellular targets with semiconductor quantum dots. *Nat. Biotechnol.* 2003;21:41–46.
46. Pellegrino T, Manna L, Kudera S. Hydrophobic nanocrystals coated with an amphiphilic polymer shell: a general route to water soluble nanocrystals. *Nano Lett.* 2004;4:703–707.
47. Petruska MA, Bartko AP, Klimov VI. An amphiphilic approach to nanocrystal quantum dot–titania nanocomposites. *J. Am. Chem. Soc.* 2004;126:714–715.
48. Ballou B, Lagerholm BC, Ernst LA, Bruchez MP, Waggoner AS. Noninvasive imaging of quantum dots in mice. *Bioconjugate Chem.* 2004;15:79–86.
49. Pathak S, Choi SK, Arnheim N, Thompson ME. Hydroxylated quantum dots as luminescent probes for in situ hybridization. *J. Am. Chem. Soc.* 2001;123:4103–4104.
50. Dubertret B, Skourides P, Norris DJ, Noireaux V, Brivanlou AH, Libchaber A. In vivo imaging of QDs encapsulated in phospholipid micelles. *Science.* 2002;298:1759–1762.
51. Mattoussi H, Mauro JM, Goldman ER, et al. Self-assembly of CdSe–ZnS quantum dot bioconjugates using an engineered recombinant protein. *J. Am. Chem. Soc.* 2000;122:12142–12150.
52. Chen Y, Rosenzweig Z. Luminescent CdS quantum dots as selective ion probes. *Anal. Chem.* 2002;74:5132–5138.
53. Wang Y, Herron N. Nanometer-sized semiconductor clusters: materials synthesis, quantum size effects, and photo-physical properties. *J. Phys. Chem.* 1991;95:525–532.
54. Jovin TM. Quantum dots finally come of age. *Nat. Biotechnol.* 2003;21:32–33.
55. Kim Y, Lillo AM, Steiniger SCJ, et al. Targeting heat shock proteins on cancer cells: selection, characterization, and cell-penetrating properties of a peptidic GRP78 ligand. *Biochemistry.* 2006;45:9434–9444.
56. Akerman ME, Chan WCW, Laakkonen P, Bhatia SN, Ruoslahti E. Nanocrystal targeting in vivo. *Proc. Natl. Acad. Sci. USA.* 2002;99:12617–12621.
57. Rosenthal SJ, Tomlinson I, Adkins EM, et al. Targeting cell surface receptors with ligand-conjugated nanocrystals. *J. Am. Chem. Soc.* 2002;124:4586–4594.

58. Hermanson GT. *Bioconjugate Techniques*. Academic Press, San Diego, CA, 1996.
59. Pinaud F, King D, Moore HP, Weiss S. Bioactivation and cell targeting of semiconductor CdSe/ZnS nanocrystals with phytochelatin-related peptides. *J. Am. Chem. Soc.* 2004;126:6115–6123.
60. Goldman ER, Anderson GP, Tran PT, Mattooussi H, Charles PT, Mauro JM. Conjugation of luminescent quantum dots with antibodies using an engineered adaptor protein to provide new reagents for fluoroimmunoassays. *Anal. Chem.* 2002;74:841–847.
61. Dahan M, Levi S, Luccardini C, Rostaing P, Riveau B, Triller A. Diffusion dynamics of glycine receptors revealed by single-quantum dot tracking. *Science*. 2003;302:442–445.
62. Mansson A, Sundberg M, Balaz M, et al. In vitro sliding of actin filaments labelled with single quantum dots. *Biochem. Biophys. Res. Commun.* 2004;314:529–534.
63. Dahan M, Laurence T, Pinaud F, et al. Time-gated biological imaging by use of colloidal quantum dots. *Opt. Lett.* 2001;26:825–827.
64. Cheong WF, Prah SA, Welch AJ. A review of the optical properties of biological tissues. *IEEE J. Quantum Electron.* 1990;26:2166–2185.
65. Ntziachristos V, Bremer C, Weissleder R. Fluorescence imaging with near-infrared light: new technological advances that enable in vivo molecular imaging. *Eur. Radiol.* 2003;13:195–208.
66. Lacoste TD, Michalet X, Pinaud F, Chemla DS, Alivisatos AP, Weiss S. Ultrahigh-resolution multicolor colocalization of single fluorescent probes. *Proc. Natl. Acad. Sci. USA.* 2000;97:9461–9466.
67. Michalet X, Pinaud F, Lacoste TD, et al. Properties of fluorescent semiconductor nanocrystals and their application to biological labeling. *Single Mol.* 2001;2:261–276.
68. Pinaud F, Michalet X, Margeat E, Moore HP, Weiss S. *Single molecule fluorescence imaging of raft associated GPI-anchored receptors in live cells with semiconductor nanocrystals*. Presented at the Minerva–Gentner Symposium on Optical Spectroscopy of Biomolecular Dynamics, Banz, PL Germany, 2004.
69. Hohng S, Ha T. Near-complete suppression of quantum blinking in ambient conditions. *J. Am. Chem. Soc.* 2004;126:1324–1325.
70. Mahtab R, Harden HH, Murphy CJ. Temperature- and salt-dependent binding of long DNA to protein-sized quantum dots: thermodynamics of “inorganic protein”–DNA interactions. *J. Am. Chem. Soc.* 2000;122:14–17.
71. Larson D, Williams RM. Water-soluble quantum dots for multiphoton fluorescence imaging in vivo. *Science*. 2003;300:1434–1436.
72. Parak WJ, Boudreau R, Gros Le M, et al. Cell motility and metastatic potential studies based on quantum dot imaging of phagokinetic tracks. *Adv. Mater.* 2002;14:882–885.
73. Mikulec FV, Kuno M, Bennati M, Hall DA, Griffin RG, Bawendi MG. Organometallic synthesis and spectroscopic characterization of manganese-doped CdSe nanocrystals. *J. Am. Chem. Soc.* 2000;122:2532–2540.
74. Hu J, Li LS, Yang W, Manna L, Wang LW, Alivisatos AP. Linearly polarized emission from colloidal semiconductor quantum rods. *Science*. 2001;292:2060–2063.
75. Bailey RE, Nie SM. Alloyed semiconductor quantum dots: tuning the optical properties without changing the particle size. *J. Am. Chem. Soc.* 2003;125:7100–7106.
76. Alivisatos AP. Semiconductor clusters, nanocrystals, and quantum dots. *Science*. 1996;271:933–937.

77. Alivisatos AP. Nanocrystals: building blocks for modern materials design. *Endeavour*. 1997;21:56–60.
78. Efros AL, Rosen M. The electronic structure of semiconductor nanocrystals. *Annu. Rev. Mater. Sci.* 2000;30:475–521.
79. Murray CB, Kagan CR, Bawendi MG. Synthesis and characterization of monodisperse nanocrystals and close-packed nanocrystal assemblies. *Annu. Rev. Mater. Sci.* 2000;30:545–610.
80. Qu L, Peng X. Control of photoluminescence properties of CdSe nanocrystals in growth. *J. Am. Chem. Soc.* 2002;124:2049–2055.
81. Kippeny T, Swafford LA, Rosenthal SJ. Semiconductor nanocrystals: a powerful visual aid for introducing the particle in a box. *J. Chem. Educ.* 2002;79:1094–1100.
82. Yu WW, Qu L, Guo W, Peng X. Experimental determination of the extinction coefficient of CdTe, CdSe, and CdS nanocrystals. *Chem. Mater.* 2003;15:2854–2860.
83. Kulzer F, Kummer S, Matzke R, Bräuchle C, Basché T. Single-molecule optical switching of terylene in p-terphenyl. *Nature*. 1997;387:688–691.
84. Dickson RM, Cubitt AB, Tsien RY, Moerner WE. On/off blinking and switching behaviour of single molecules of green fluorescent protein. *Nature*. 1997;388:355–358.
85. Pawley JB, Centonze VE. Practical laser-scanning confocal light microscopy: obtaining optimal performance from your instrument. In Celis JE.; ed. *Cell Biology: A Laboratory Handbook*. Academic Press, San Diego, CA, 1994, PP. 44–64.
86. Goldmann ER, Clapp AR, Anderson GP, et al. Multiplexed toxin analysis using four colors of quantum dot fluororeagents. *Anal. Chem.* 2004;76:684–688.
87. Makrides SC, Gasbarro C, Bello JM. Bioconjugation of quantum dot luminescent probes for western blot analysis. *Biotechniques*. 2005;39:501–506.
88. Mattheakis LC, Dias JM, Choi YJ, et al. Optical coding of mammalian cells using semiconductor quantum dots. *Anal. Biochem.* 2004;327:200–208.
89. Rosenthal SJ. Bar-coding biomolecules with fluorescent nanocrystals. *Nat. Biotechnol.* 2001;19:621–622.
90. Han M, Gao X, Su JZ, Nie S. Quantum dot-tagged microbeads for multiplexed optical coding of biomolecules. *Nat. Biotechnol.* 2001;19:631–635.
91. Lagerholm BC, Wang M, Ernst LA, et al. Multicolor coding of cells with cationic peptide coated quantum dots. *Nano Lett.* 2004;4:2019–2022.
92. Bentolila LA, Weiss S. Biological quantum dots go live. *Phys. World*. 2003;16:23–24.
93. Uren RF. Cancer surgery joins the dots. *Nat. Biotechnol.* 2004;22:38–39.
94. Alivisatos P. The use of nanocrystals in biological detection. *Nat. Biotechnol.* 2004;22:47–52.
95. Chan WCW, Maxwell DJ, Gao X, Bailey RE, Han M, Nie S. Luminescent QDs for multiplexed biological detection and imaging. *Curr. Opin. Biotechnol.* 2002;13:40–46.
96. Niemeyer CM. Nanoparticles, proteins, and nucleic acids: Biotechnology meets materials science. *Angew. Chem. Int. Ed. Engl.* 2001;40:4128–4158.
97. Leatherdale CA, Woo WK, Mikulec FV, Bawendi MG. On the absorption cross section of CdSe nanocrystal quantum dots. *J. Phys. Chem. B.* 2002;106:7619–7622.
98. Nirmal M, Dabbousi BO, Bawendi MG, et al. Fluorescence intermittency in single cadmium selenide nanocrystals. *Nature*. 1996;383:802–804.

99. Efros AL, Rosen M. Random telegraph signal in the photoluminescence intensity of a single quantum dot. *Phys. Rev. Lett.* 1997;78:1110–1113.
100. Kuno M, Kuno M, Fromm DP, Hamann HF, Gallagher A, Nesbitt DJ. Nonexponential ‘blinking’ kinetics of single CdSe quantum dots: a universal power law behavior. *J. Chem. Phys.* 2000;112:3117–3120.
101. Koberling F, Mews A, Basché T. Oxygen-induced blinking of single CdSe nanocrystals. *Adv. Mater.* 2001;13:672–676.
102. Van Sark WGJHM, Frederix PLTM, Bol AA, Gerritsen HC, Meijerink A. Blueing, bleaching, and blinking of single CdSe/ZnS quantum dots. *Chem. Phys. Chem.* 2002;3:871–879.
103. Derfus AM, Chan WCW, Bhatia SN. Probing the cytotoxicity of semiconductor quantum dots. *Nano Lett.* 2004;4:11–18.
104. Ouellette J. Quantum dots for sale. *Ind. Phys.* 2003;14.
105. Li YX, Chen JL, Zhu CQ, et al. Preparation and application of cysteine-capped ZnS nanoparticles as fluorescence probe in the determination of nucleic acids. *Spectrochim. Acta A.* 2004;60:1719–1724.
106. Willner I, Patolsky F, Wasserman J. Photoelectrochemistry with controlled DNA-linked CdS-nanoparticle arrays. *Angew. Chem. Int. Ed.* 2001;40:1861–1864.
107. Willner I, Willner B. Functional nanoparticle architectures for sensoric optoelectronic and bioelectronic applications. *Pure Appl. Chem.* 2002;74:1773–1783.
108. Wang J, *Stripping Analysis*. VCH, New York, 1985.
109. Wang J, Liu GD, Polsky R, Merkoci A. Electrochemical stripping detection of DNA hybridization based on cadmium sulfide nanoparticle tags. *Electrochem. Commun.* 2002;4:722–726.
110. Zhu NN, Zhang AP, He PG, Fang YZ. Cadmium sulfide nanocluster-based electrochemical stripping detection of DNA hybridization. *Analyst.* 2003;128:260–264.
111. Zhu NN, Zhang AP, He PG, Fang YZ. DNA hybridization at magnetic nanoparticles with electrochemical stripping detection. *Electroanalysis.* 2004;16:1925–1930.
112. Zhu NN, Zhang AP, He PG, Fang YZ. Lead sulfide nanoparticles as oligonucleotide label for electrochemical stripping detection of DNA hybridization. *Electroanalysis.* 2004;16:577–582.
113. Milica TN, Mirjana IC, Vesna V, Olga IM. Transient bleaching of small lead sulfide colloids: influence of surface properties. *J. Phys. Chem.* 1990;94:6390–6396.
114. Jiang L, Chen X, Yang WS, et al. A kind of CdS nanocluster with free carboxyl groups on its surface. *Chem. J. Chin. Univ.* 2001;22:1397–1399.
115. Wang J, Liu GD, Jan MR, Zhu QY. Electrochemical detection of DNA hybridization based on carbon-nanotubes loaded with CdS tags. *Electrochem. Commun.* 2003;5:1000–1004.
116. Wang J, Liu GL, Merkoci A. Electrochemical coding technology for simultaneous detection of multiple DNA target. *J. Am. Chem. Soc.* 2003;125:3214–3215.
117. Liu GD, Wang J, Kim J, Jan MR, Collins GE. Electrochemical coding for multiplexed immunoassays of protein. *Anal. Chem.* 2004;76:7126–7130.
118. Liu G, Lee TMH, Wang J. Nanocrystal-based bioelectronic coding of single nucleotide polymorphisms. *J. Am. Chem. Soc.* 2005;127:38–39.

Nanoparticles and Inductively Coupled Plasma Mass Spectroscopy–Based Biosensing

ARBEN MERKOÇI

ICREA and Nanobioelectronics and Biosensors Group, Institut Català de Nanotecnologia, Barcelona, Spain

ROZA ALLABASHI

University of Natural Resources and Applied Life Sciences, Vienna, Austria

ALFREDO DE LA ESCOSURA-MUÑIZ

Nanobioelectronics and Biosensors Group, Institut Català de Nanotecnologia, Barcelona, Spain, and Instituto de Nanociencia de Aragón, Universidad de Zaragoza, Zaragoza, Spain

- 12.1 ICP-MS and application possibilities
 - 12.1.1 Principle of the method
 - 12.1.2 Applications of ICP techniques
- 12.2 Detection of metal ions
- 12.3 Detection of nanoparticles
- 12.4 Analysis of metal-containing biomolecules
- 12.5 Bioanalysis based on labeling with metal nanoparticles
 - 12.5.1 Protein detection
 - 12.5.2 DNA detection
- 12.6 Conclusions

12.1 ICP-MS AND APPLICATION POSSIBILITIES

Inductively coupled plasma mass spectrometry (ICP-MS) is a well-known method for trace element analysis in the environmental and geochemical fields; it is more and more embraced by researchers in other areas, because of its sub-parts-per-trillion

detection limits and multi-element, multi-isotope capability. The semiconductor, biomedical, food, nuclear and pharmaceutical industries have all found applications for this technology.

12.1.1 Principle of the Method

Figure 12.1(a) is a schematic of the ICP-MS. A minute quantity of sample is ionized in a conventional ICP torch [Figure 12.1(b)] and the resulting charged species are analyzed by a magnetic and/or electric field, depending on the type of instrument. The study of ion trajectories in the analyzer tube under vacuum allows determination of the mass/charge ratio [1]. The spectra produced in this way, which are remarkably simple compared with conventional ICP spectra, consist of a simple series of isotope peaks. These spectra are used for quantitative measurements based on calibration curves, often with an internal standard. Analysis can also be performed by the isotope dilution technique [2].

The inductively coupled plasma (ICP) is a very aggressive ion source. Because the source operates at temperatures of 7000 K, virtually all molecules in a sample are broken up into their component atoms. In ICP a radio-frequency (RF) signal is fed into

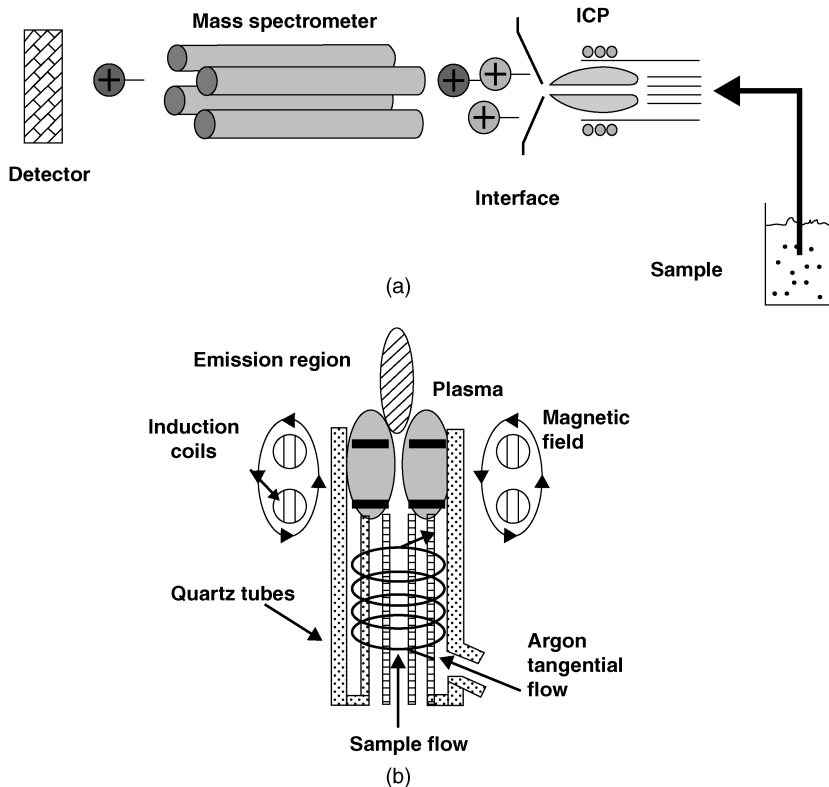


FIGURE 12.1 (a) ICP-MS and (b) ICP torches.

a tightly wound water-cooled coil, where it generates an intense magnetic field. In the center of this coil is a specially made glass or quartz plasma torch where the plasma is formed. The plasma is generated in the argon gas by “seeding” the argon with a spark from a Tesla unit. When the spark passes through the argon gas, some of the argon atoms are ionized and the resulting cations and electrons are accelerated toward the magnetic field of the RF coil. Through a series of inelastic collisions between the charged particles (Ar^+ , and electrons) and neutral argon atoms, a stable high-temperature plasma is generated. The concentrations of electrons, Ar^+ , and neutral species in the plasma very quickly reach equilibrium, after which the plasma will remain “lit” as long as the RF field is maintained and there is a constant supply of argon gas in the plasma.

Sampling and Ionization The plasma torch is designed to allow the sample to be injected directly into the heart of the plasma. The sample consists of a fine aerosol, which can come from any number of sources, including nebulized liquids and ablated solids. As the sample aerosol passes through the plasma, it collides with free electrons, Ar^+ , and neutral argon atoms. The result is that any molecules present initially in the aerosol are quickly broken down completely to charged atoms. These are usually in the M^+ state, although a few M^{2+} are also formed. Some of these charged atoms will recombine with other species in the plasma to create both stable and metastable molecular species (e.g., MAr^+ , M_2^+ , MO^+). Many of these molecular species will be positively charged and will also be transmitted into the mass analyzer along with the charged atoms (M^+ and M^{2+}).

Mass spectrometry (MS) is perhaps the most widely applicable of all of the analytical tools available to the scientist in the sense that this technique is capable of providing information about (1) the qualitative and quantitative composition of both organic and inorganic analytes in complex mixtures, (2) the structures of a wide variety of complex molecular species, (3) isotopic ratios of atoms in samples, and (4) the structure and composition of solid surfaces [2].

A mass spectrum is obtained by converting components of a sample into rapidly moving gaseous ions and separating them on the basis of their mass-to-charge ratios. This can be realized in various ways. The following types of mass spectrometers are available:

- *Magnetic sector analyzer.* This type of analyzer employs a permanent magnet or an electromagnet to cause the beam from the ion source to travel in a circular path of 180° , 90° , or 60° . Ions of different mass can be scanned by varying the field strength of the magnet or the accelerating potential between two slits. The ions passing through the exit slit of the magnetic sector fall on a collector electrode, resulting in an ion current that is amplified and recorded [2].
- *Double-focusing spectrometer.* The term *double focusing* is applied to mass spectrometers in which the directional aberrations and the energy aberrations of a population of ions are simultaneously minimized. Double focusing is usually achieved by the use of carefully selected combinations of electrostatic and magnetic fields [2].

- *Time-of-flight analyzer.* In time-of-flight (TOF) instruments, positive ions are produced periodically by bombardment of the sample with brief pulses of electrons, secondary ions, or laser-generated photons. The accelerated particles then pass into a field-free drift tube about 1 meter in length. Because all ions entering the tube have the same kinetic energy, their velocities in the tube must vary inversely to their masses. Typical flight times are 1 to 30 μs [2].
- *Ion trap analyzer.* An ion trap is a device in which gaseous anions or cations can be formed and confined for extended periods by electric and/or magnetic fields [2]. The most common ion trap consists of a doughnut-shaped ring electrode supplied with RF voltage and capped with two end-cap electrodes. Ions enter the end cap and oscillate in the trap. The stability of the oscillating ions is determined by the frequency and voltage supplied to the ring and the m/z value of the ion. Increasing the RF amplitude causes ions of increasing m/z to destabilize and leave the trap, where they are detected [3].
- *Quadrupole mass analyzer.* It is the most compact and widely used mass spectrometer in the market. For that reason its functioning principle is explained in detail below. The quadrupole mass analyzer (see Figure 12.2) consists of four cylindrical rods onto which is applied both an RF and a dc electric field. The four rods are arranged so that they form two pairs, one in the X -plane and one in the Y -plane.

As ions enter a quadrupole, they begin to oscillate in both planes. In such a system the lower m/e ions will be destabilized in the quadrupole whenever the alternating (RF) component of the electric field exceeds the direct (dc) component. In that case the lower m/e ions will quickly be thrown out of the quadrupole and will not reach the detector. This mode of operation makes an effective low-mass filter. If the direct component exceeds the alternating component, the reverse process is happening. High m/e ions become unstable, and this makes an effective high mass filter. The quadrupole mass analyzer is a very fast and efficient system.

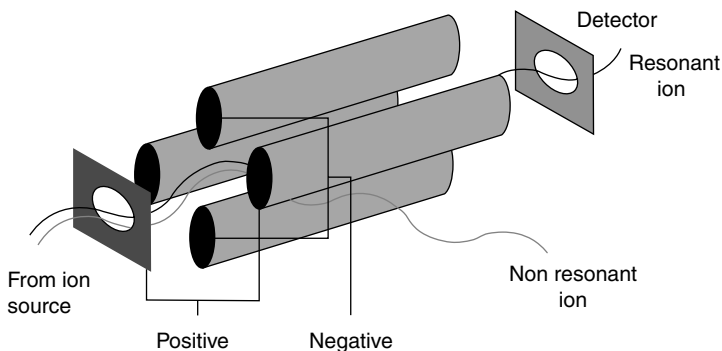


FIGURE 12.2 Quadrupole mass analyzer.

12.1.2 Applications of ICP Techniques

The ICP has had a major impact in analytical atomic spectrometry because of its multielement capabilities. On its own the plasma is not particularly element selective. The property of producing excited atomic and ionic species efficiently from most samples in various forms allows access to most elements of the periodic table. The selectivity of a plasma is brought about by coupling either optical (mono- or polychromator) or mass spectrometric (quadrupole filter) detectors [3].

Selectivity of the ICP method can be extended if a separation technique is employed as part of a sample introduction system. Gas and liquid chromatographic systems effectively coupled with ICP, resulting in an element-specific detector. Their combined analytical power becomes greater, allowing element speciation studies (e.g., the chemical form of the element to be performed). When the impressive separation obtained with capillary electrophoresis, in terms of speed and resolution, is combined with the element-specific ICP-MS, a potentially powerful analytical tool is obtained [3].

Wilson and Brinkman [4] have reviewed the possibilities for multiple hyphenation of liquid chromatography (LC) and spectroscopy techniques. According to these authors, the ICP-MS enables sensitive, selective, and quantitative detection of particular atoms present in the molecules, thereby providing additional information. While LC-DAD-ICP-MS provides the simplest hyphenated system involving ICP-MS, the greatest benefits arise when these are also capable of providing molecular data (e.g., TOF-MS) [4]. The combination of LC, ICP-MS, and MS has been reviewed by Wind and Lehmann [5], who described this hyphenation as “an emerging analytical dream team in the life sciences.”

ICP-MS has become a widely used method for isotopic measurements. The measurement of Hg isotopes by multicollector inductively coupled plasma-mass spectrometry (MC-ICP-MS) is now sufficiently precise and sensitive that it is potentially possible to develop the systematics of Hg isotopic fractionation. This provides an opportunity to evaluate the utility of Hg isotopes in identifying source processes, transport mechanisms, and sinks [6].

Plasma spectrometry has found widespread application in the analysis of environmental samples. This technique offers excellent sensitivity for most element, with detection limits in the low part per trillion range. Metals and nonmetals may be analyzed, offering the analyst flexible tools for trace elements, which are often difficult to determine. The sensitivity of ICP-MS is far greater than that of ICP-AES (atomic emission spectrometry), by up to three orders of magnitude for many elements. The ability to perform both semiquantitative and fully quantitative analyses is also an attractive feature of ICP-MS [3].

Atomic spectrometric techniques have been employed in geochemical analysis for many decades. Methods such as x-ray fluorescence spectrometry (XRF), optical emission spectrometry (OES), and atomic absorption spectrometry (AAS) belong to the widely used method for the determination of major and trace elements in geological samples, despite their known limitations. Development of the ICP, initially as an excitation source for optical emission spectrometry, rekindled

interest in emission spectrometric methods and had an early impact on geochemical analysis in the 1970s, when commercial ICP-AES instruments became available. Its multielement capability, good sensitivity for many geological significant elements, and the relatively good precision stemming from a more stable source counterbalanced the fact that it required liquid samples. Over the next 20 years it became established as a major analytical technique in the earth sciences. The subsequent development of ICP-MS, with its even greater and more uniform sensitivity for many elements, together with its ability to determine individual isotopes, heralded a second explosion of interest in ICP spectrometry among earth scientists [3].

Plasma spectrometry has many applications in food science and is used in the analysis of a wide range of types of sample in the food chain. Although several different plasma methods have been used, the most commonly encountered are ICP-AES and ICP-MS (together with hyphenated techniques based on these methods). Of the two, ICP-AES has the lower running costs, better tolerance to total salt content in test solutions, and less severe matrix effects compared to ICP-MS [3,7], but spectral overlap can be a problem. Some of the advantages of ICP-MS include fewer spectral interferences, improved sensitivity, and a wider dynamic range, with the ability to acquire isotopic information rapidly. The wide dynamic concentration range and speed of measurement makes this a particularly powerful tool of surveillance, legislative, and emergency work [3].

12.2 DETECTION OF METAL IONS

ICP-MS has been used extensively as a rapid and accurate instrumental technique for determinations of platinum group elements (PGEs) and gold. Methods based on ICP-MS have been important in analyses of many types of samples, especially of geological materials containing very low concentrations of these elements [8–11]. During the period covered in the review of Barefoot [12] (1998–2002), analytical methods based on ICP-MS have been improved and widened in scope by the introduction of new magnetic sector (or high-resolution) spectrometers and laser ablation (LA) sampling. Detection limits attainable for PGEs and Au using magnetic sector instruments in analytical procedures cited here are as low as 0.01 to 0.02 pg/g; instruments have a dynamic range of up to nine orders of magnitude. In this review, some applications of the technique to analysis of PGEs and gold in minerals, nodules, meteorites, ice, sediments, airborne particulates, and reference materials are described. A number of publications discuss the ICP-MS determination of gold and PGEs in geological samples after fire assaying, with or without tellurium coprecipitation [13–17]. Pyrzynska [18] discussed in her work the recent development in sample pretreatment on achieving high sensitivity, accuracy, and interference-free determination of gold by ETAAS, ICP-OES, and ICP-MS. Most of the proposed separation/preconcentration methods utilizing solid sorbents generally require strong acid mixtures as eluents. Alternatively, this

process may be carried out through the sorption of complexed analyte and elution with organic solvent.

Direct solid sampling—laser ablation ICP-MS—is very useful, as it avoids not only wet decomposition but also the risk of contamination during sample preparation, and it increases the power of detection [13]. This technique was applied for gold determination in geological matrices [18,19] for the characterization of precious artifacts and several monetary gold ore sources [20].

Other authors report as to the use of ICP-MS on the determination of human exposure by gold (among other trace elements) through hair [20], blood [21,22], urine [23], or human milk [24] analysis. These authors use magnetic sector field inductively coupled plasma mass spectrometry for milk analysis as an advanced instrumentation compared to conventional ICP-MS. This method is able to separate spectral overlaps from the analyte signal. Moreover, superior detection limits in the picogram per liter range can be obtained with such magnetic-sector field instruments. Therefore, this is the first study to report the concentrations of the elements Ag, Au, Pt, Sc, Ti, and V in human milk. Concentrations of Au showed large variations in human milk that might be associated with dental fillings and jewelry.

The use of ICP-MS and its performance for the determination of trace elements in seawater is also reported in the literature. Pozebon et al. [25] compare two flow injection systems (FI) for online separation and preconcentration of Cu, Cd, Pb, Bi, Au, Ag, As(III), and Se(IV) in seawater and determination by ICP-MS. Dressler et al. [26] propose and optimize an online preconcentration system for Au, Ag, Te, and U for the determination of Ag, Te, U, and Au in waters and in biological samples by FI-ICP-MS.

12.3 DETECTION OF NANOPARTICLES

Nowadays, there is a great interest for quantification of nanoparticles (NPs) because of their interesting applications in several fields, such as nanobiotechnology processes. Several enzyme, DNA, or protein-based sensing systems have been reported to use NPs as labels or transducing platforms. Gold nanoparticles (AuNPs), in particular, are excellent candidates for bioconjugation with interest for biosensing applications.

Electrochemical detection is an attractive way to determine these NPs, due to the inherent advantages that the electrochemical techniques offer in terms of selectivity sensitivity and the low cost of analysis. However, in most cases, a previous dissolution using toxic acids is required, so alternative routes are needed. In this way, Pumera et al. [27] have reported a strategy for the direct electrochemical detection of AuNPs, without previous dissolving, that opened the way to the use of these techniques for further applications.

Several optical methods are also ideally suited for NPs characterization. The atomic force microscope (AFM) [28,29] offers the capability of three-dimensional

visualization and both qualitative and quantitative information on many physical properties, including size, morphology, surface texture, and roughness. Statistical information, including size, surface area, and volume distributions, can be determined as well. Transmission electron microscopy (TEM) [30] has also been used for this purpose. However, although shown advantages, the techniques mentioned cannot be used for analytical quantification of NPs.

Thus, novel alternatives for NPs quantification are being required. In this context, ICP-MS is being shown to be an interesting alternative. Nevertheless, although ICP-MS is known as one of the most powerful methods for trace element analysis, the possibilities of this technique on the quantification of NPs have not yet been deeply explored. In this way, single-particle-counting ICP-MS was reported by Degueldre et al. to be a successful technique for determination of Au [31] and Te [32] in colloid samples. The signal induced by the flash of ions due to the ionization in the plasma torch was measured by the mass spectrometer without interference. The peak distributions recorded were analyzed as a function of particle size for different colloid suspensions.

Helfrich et al. [33] reported on the success of online coupling high-performance liquid chromatography (HPLC) in reversed-phase or alternatively gel electrophoresis, with a quadrupole ICP-MS for size characterization of AuNPs from 5 to 20 nm under the following instrumental operating conditions: RF power of 1300 W and plasma, auxiliary, and nebulizer gas flows of 15.5, 1.1, and 1.2 L/min, respectively. The results showed good agreement compared with complementary methods such as dynamic light scattering (DLS) and TEM.

One of the most important challenges in this field is to achieve direct determination of AuNPs in colloid solutions by ICP-MS without previous digestion or dissolution, avoiding the use of the hazardous reagents used in most of the studies reported, and reducing the analysis time. In this way, Allabashi et al. [34] have recently reported a direct and simple ICP-MS method for the determination of AuNPs, with particle sizes ranging from 5 to 20 nm and suspended in aqueous solutions using a quadrupole ICP-MS with an RF power of 1250 W and plasma, auxiliary, and nebulizer gas flows of 15.25, 1.275, and 0.89 L/min. The results showed no significant difference compared to determination of the same AuNPs after digestion, as claimed in the earlier literature. The limit of quantification of the method obtained was 0.15 $\mu\text{g/L}$ Au(III), which corresponds to 4.40×10^9 AuNPs/L, considering spherical AuNPs 15 nm sized. Spike recovery experiments also showed that the sample matrix was a significant factor influencing the accuracy of the measurement. The effect of NP size on the ICP-MS signal was also studied, and only significant differences due to the chemical environment (and not to AuNP size) were found. A scheme of the processes involved in the ICP-MS analysis of AuNPs with and without previous gold dissolution is shown in Figure 12.3.

Due to its analytical performance, the ICP-MS method may have significant applications in the bioanalytical field, where NPs are used as labels of biomolecules, allowing sensitive and selective bioanalysis.

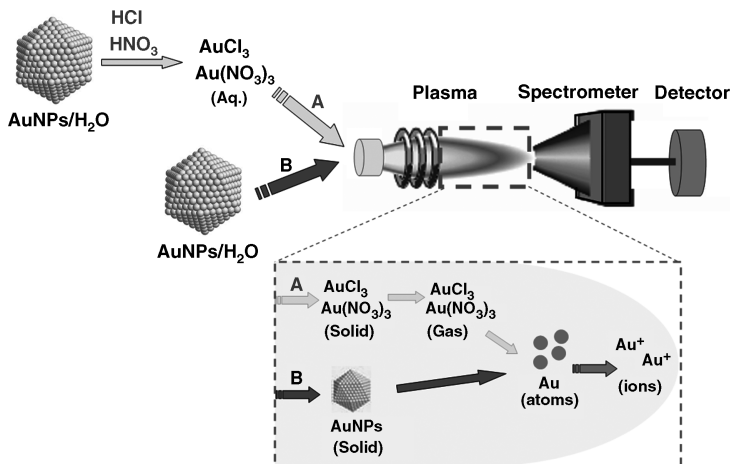


FIGURE 12.3 Processes involved in the ICP-MS analysis of AuNPs (A) with and (B) without previous gold dissolution. (From ref. 34. with permission).

12.4 ANALYSIS OF METAL-CONTAINING BIOMOLECULES

Elemental analysis is a successful tool for the quantization of metal-containing proteins [35,36]. For a long time it was accepted that if a biologically active molecule does not ligate or incorporate a metal atom, it should be analyzed by another means. For example, organic mass spectrometry (e.g., electrospray), a complementary technique of ICP-MS, has been a method of choice for protein identification and phosphorylation site analysis. Despite a limited set of building blocks, biologically active molecules exhibit an incredible variety of functionality, reactivity, and structural complexity. This is especially true for proteins and peptides, which are (in their inconceivable diversity) still polymers of the same monomer molecules in different combinations, making specific characterization of individual proteins difficult. In addition, there are numerous vital proteins present in cells in trace amounts. Therefore, these molecules represent a significant challenge for any analytical method, including ICP-MS, for which speciation capabilities are still very restricted. Most proteins, and therefore also the resulting peptides, naturally contain covalently bound tags, such as phosphorus, sulfur, and selenium. These elements can be used for both the qualitative detection and the quantification of proteins or peptides without the need for chemical derivatization procedures, provided that their stoichiometry within the compounds targeted is known. Thus, dramatic improvements in the detection of phosphorus and sulfur in biological samples, which enables determination of the state of phosphorylation of proteins, is another focus of ICP-MS applications.

In this context several authors have coined the concept of hetero (element) tagged proteomics, which includes the study of a proteome in which analytical information is acquired by complementary application of elemental mass spectrometry utilizing the

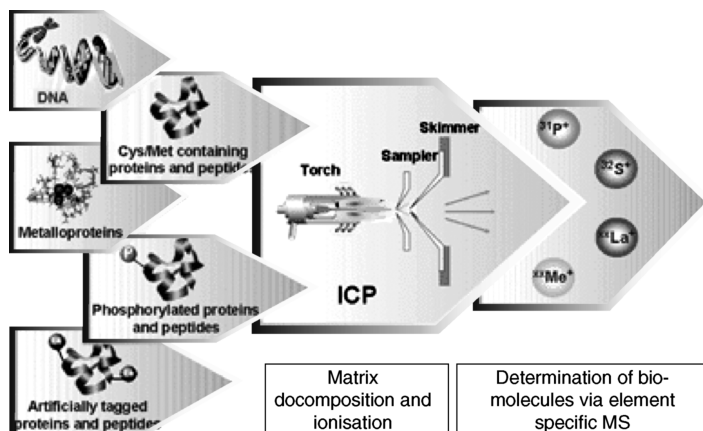


FIGURE 12.4 Reduction of sample complexity using a 7000K inductively coupled argon plasma (ICP) as an ion source. The ICP allows matrix decomposition and shows a compound-independent response, especially when using low flow sample introduction systems allowing the qualitative and quantitative determination of selected biomolecules via either natural or artificial (hetero-) element labels. (From ref. 39, with permission from the Royal Society of Chemistry.)

presence of a heteroatom (S, P, Se, I, lanthanide, element-coded NPs) in a protein or introduced via controlled chemical labeling, especially for fast screening and quantification purposes [37–39]. It is well known that ICP-MS cannot give much information about the structural characterization and final identification of a biomolecule containing an ICP-MS-detectable element, due to the fact that all structural information is lost as a result of its high temperatures (7000 K). But at the same time, this drawback represents the main strength of ICP-MS, since the result is a drastic reduction in sample complexity. Prange and Pröfrock [39] have illustrated this (Figure 12.4). The same authors schematized a typical proteomic workflow from the sample to the final protein identification in several fields, as shown in Figure 12.5.

12.5 BIOANALYSIS BASED ON LABELING WITH METAL NANOPARTICLES

12.5.1 Protein Detection

There are many methods for protein analysis in general, and between these, those based on tagging strategies that can provide analysis using different physical methods of detection are having continuous growth. The recent development of metal-tagged antibodies makes possible the involvement of atomic spectroscopy for protein analysis. Recent developments in ICP-MS have shown the potential to expand the “toolbox” of this technique for protein analysis via the use of several existing immunoassay platforms. An *immunoassay* can be described as a technique for the detection and quantification of a specific protein (antigen) by using reactions with complementary antibodies. The strong affinity of antigen–antibody interactions forms

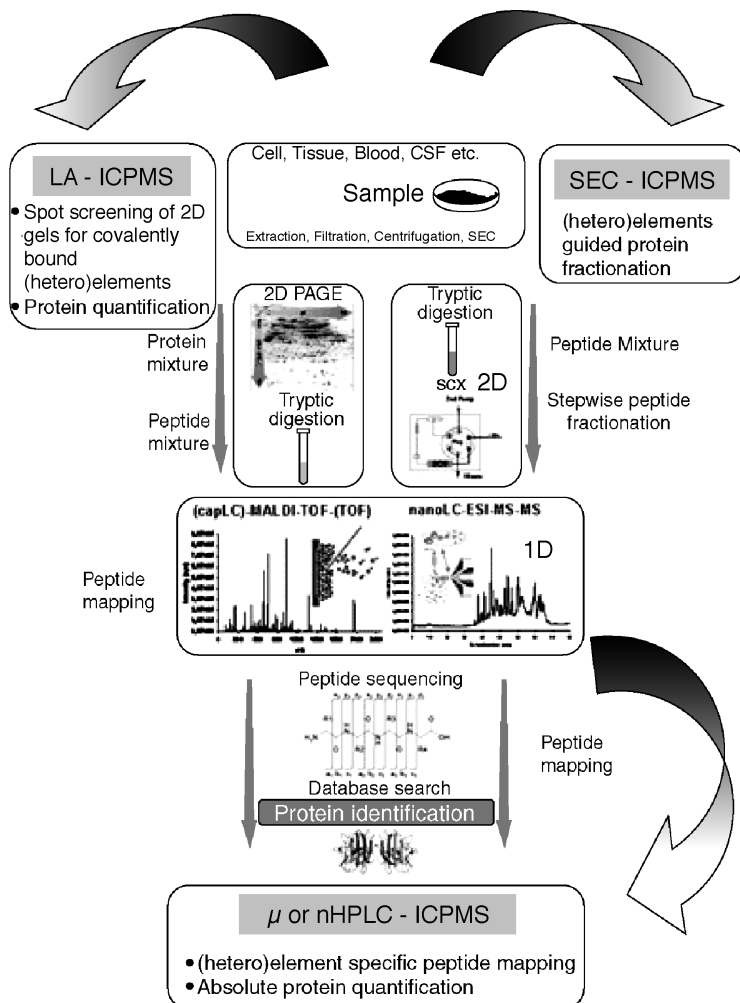


FIGURE 12.5 Most prominent fields of application for the complementary use of ICP-MS within a typical proteomic workflow (either gel-based or gel-free). It includes a multidimensional sample fractionation, (hetero-) element specific screening of two-dimensional gel separations using LA-ICP-MS, (hetero-) element specific peptide mapping using capillary- or nano-LC hyphenated to ICPMS. In particular, the latter also allows absolute protein quantification. (From ref. 39, with permission from the Royal Society of Chemistry.)

largely through noncovalent bonds and conformational fits. The high specificity and reactivity of the antigen–antibody interaction allows for many biotechniques, including (1) the separation and purification of antigens of interest through immobilized complementary antibodies, (2) the visualization of specific cellular proteins and structures through fluorescent conjugated antibodies, and (3) immunoassays or the quantization of a particular antigen through enzyme- or fluorescent-linked antibodies (in which the outcome of an enzymatic or fluorometric reaction is proportional to the amount of antigen present).

ICP-MS measurements of the atomic composition of a metallic-based tag (i.e., NPs) conjugated to a biologically active material, for example, an antibody molecule, offer new opportunities for protein analysis. The mass-to-charge ratio of the metal contained in the tag provides the potential for multianalyte detection using different elements and isotopes conjugated to different antibodies.

ICP-MS has analytical characteristics that are complementary to the conventional protocols applied so far for protein analysis based on labeling using metal-based compounds including NPs. Of special merit are the sensitivity, large dynamic range, independence of the sample matrix, and a large number of elements and isotopes that can be determined simultaneously. Combining these attributes with the specificity of immunoreaction offers a new approach to the proteomic challenge. The premise of ICP-MS-linked immunoassays is straightforward. Antigens of interest are reacted with complementary metal/nanoparticle-tagged antibodies, physically separated from nonreacting proteins, and then the atomic composition of the tag conjugated to the antibody is measured to determine the antigen concentration of the sample. Clearly, the sensitivity of the method is a linear function of the number of atoms of a given isotope in the tag. It is also clear that accurate quantization demands that the number of atoms in similar tags has a narrow distribution that would require the use of equal-size NPs. Further, multiple antibodies can be labeled with distinguishable element tags (as elements, isotopes, or in unique combinations; preferably those that occur at naturally low levels), potentially allowing simultaneous determination of multiple antigens provided that the immunochemical conditions are favorable and the reactions are independent.

The benefits of ICP-MS-linked immunoassays over the conventional immuno-methods can be summarized as follows: (1) the analysis of the tag is performed directly, eliminating the need of a substrate chelator; (2) biological impurities or contaminants do not affect elemental analysis results; (3) nonspecific background is not a function of time, unlike ELISAs, in which the background depends on the incubation time; (4) immediate acidification of the sample reacted allows for long-term storage before analysis; and (5) detection limits are improved linearly with multiple tagging isotopes.

NPs are especially attractive for quantization in these assays, because of their uniform size and significant number of atoms per conjugate. Colloidal gold or extremely small gold clusters (less than 2 nm in diameter) are used extensively to visualize protein structure in the cell and to detect receptor–ligand binding by electron microscopy. Gold-containing tags are obviously convenient for elemental analysis and have dominated the first attempts to utilize this technique. There is also the possibility of increasing the signal response yet further by using silver enhancement. Elemental analysis (employing electrothermal atomic absorption spectrometry, ICP-MS) of colloidal gold and conjugated gold clusters was summarized earlier. The limits of detection for colloidal gold in ICP-MS are much lower than those of P and S, due to an absence of interferences and a lower first ionization potential. These gold cluster antibody conjugates can also be used successfully in multitarget assays. Simultaneous analysis requires several distinguishable tags, the choice of which is still limited but is nevertheless sufficient for a variety of applications.

For example, gold-tagged antibodies and ligands are used routinely in the localization of cellular proteins using colloidal gold in electron microscopy [40,41] and have been analyzed successfully by ICP-MS [42,43]. These tags contain either colloidal gold or small gold clusters (less than 2 nm in diameter). This is an advantage when using ICP-MS for detection, as the elemental nanoparticles used are of uniform size and contain a significant number of atoms per conjugate. In addition, there is the option of increasing the Au signal response even further by using silver enhancement.

Zhang et al. [44] described a study of atomization of NPs by ICP-MS and developed a novel nonisotopic immunoassay by coupling a sandwich-type immunoreaction to ICP-MS. The goat anti-rabbit immunoglobulin G (IgG) labeled with colloidal gold NPs served as an analyte in ICP-MS for the indirect measurement of rabbit anti-human IgG. Matrix effect studies showed that the gold signal was not sensitive to the organic matrix. The samples were introduced at an uptake rate of 1.4 mL/min into the plasma under the following operation conditions: RF power of 1100 W (operating frequency 40 MHz) and plasma, auxiliary, and nebulizer argon flows of 15, 1.2, and 1 L/min, respectively. A relatively good correlation was obtained between the method proposed and ELISA assay. A scheme showing sandwich-type immunoreaction is shown in Figure 12.6. The method opened the way to the potential of the ICP-MS-based nonisotopic immunoassay method for the simultaneous determination of biological analytes of interest, by labeling different types of inorganic NPs.

In the same year, Baranov et al. [45] described several novel ICP-MS-linked immunoprecipitation assays using both nanogold and lanthanide-tagged antibodies in which some commonly used immunoaffinity separation techniques (i.e., centrifugal filtration, gel filtration, protein A Sepharose affinity, and ELISA) were coupled successfully to ICP-MS to detect and accurately quantify specific concentrations of target proteins in complex biological samples after acidic digestion in 10% HCl/0.1% HF. The RF plasma source used was a free-running (nominal frequency 40 MHz)

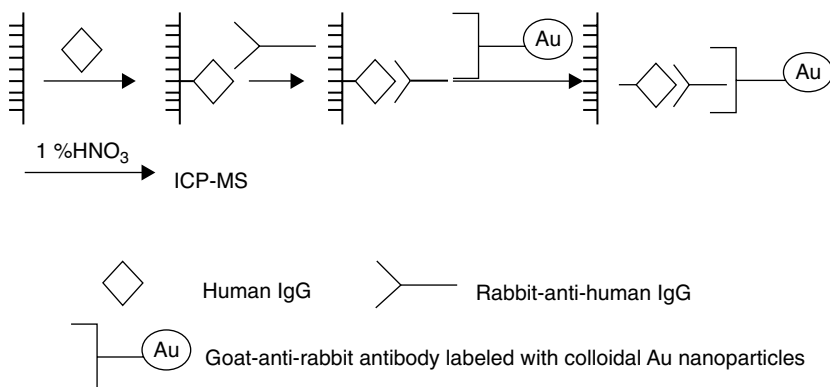


FIGURE 12.6 Sandwich-type immunoreaction using colloidal gold labels and final detection by ICP-MS. (From ref. 44, with permission.)

ICP 1400 W, with plasma, auxiliary, and nebulizer argon flows of 15, 1.2, and 1.02 L/min, where the sample was introduced at 0.5 mL/min. In this way, levels of target proteins as low as 0.1 to 0.5 ng/mL were obtained.

The same group [46] reported a method using distinguishable commercial element-tagged antibodies (AuNPs-IgG: nanoprobe, and EuIgG: Perkin-Elmer) that allowed discriminant detection with an ICP-MS, providing a sensitive and accurate means of determining the concentrations of specific proteins in complex mixtures. Two protein targets were analyzed simultaneously in each sample (IgG and FLAG-BAP in one sample and FLAG-BAP and GST-Smad2 in the other) after acidic digestion in 10% HCl/0.1% HF under the same operational conditions as those used in previous work. They obtained a linear response to both proteins in each sample for a concentration range of 2 to 100 ng/mL using a sample size of 0.5 mL. These results opened the way to possible simultaneous multiple protein quantification in complex biological samples.

Baranov et al. [47] also achieved purification and determination of the dissociation constant for an antibody-antigen complex using AuNPs as labels and the gel-filtration chromatography technique for separation and ICP-MS for detection, after dissolving the complex in 10% HCl/0.1% HF (Figure 12.7).

In the same work, these authors used AuNP-conjugated goat antibodies/anti-human Fab' (Fab'-nanoAu, No. 2053: Nanoprobes) to detect a protein, Smad2. This

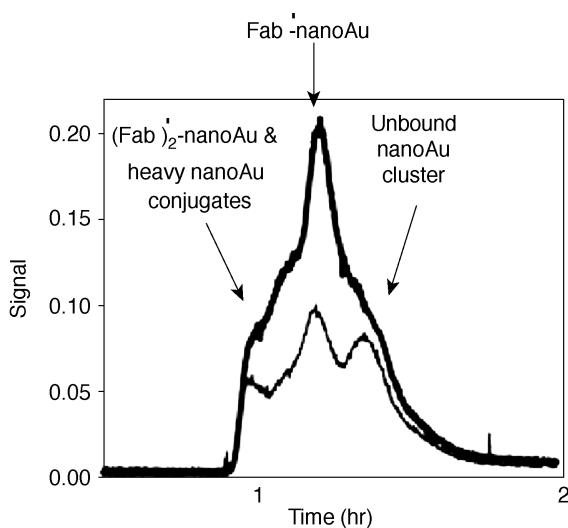


FIGURE 12.7 Results of size-exclusion filtration of two different stocks of Fab'-nanoAu with ICP-MS used as an elemental detector. Signal (the Y-axis) represents the $^{197}\text{Au}/(^{191}\text{Ir} + ^{193}\text{Ir})$ ratio. (From ref. 47, with permission from the Royal Society of Chemistry.)

protein is present endogenously at low levels in C2C12 cells and is expressed at detectable levels in other types of cells (COS cells) only when they have been transfected with an expression vector coding for the Smad2 protein. After the immunological reaction, the cells were digested using concentrated HCl, and an aliquot of the digest was then added to a 10% HCl solution before ICP-MS measurement, under operational conditions similar to those detailed in previous work. The difference between transfected and control cell lines was observed using a low-uptake sampling system to minimize the sample size and reduce the number of cells required (Figure 12.8).

More recently, the same authors [48] developed a novel application of ICP-MS-linked metal-tagged immunophenotyping which has great potential for highly multiplexed proteomic analysis. Expression of an intracellular oncogenic cell surface antigen, human stem cell factor receptor, and integrin receptor was investigated using model human leukemia cell lines. Antigens to which specific antibodies were available and distinguishably tagged were determined simultaneously, or multiplexed. Commercial conjugated AuNP-antimouse IgG (NMI No. 2001), as well as other commercially available lanthanide tags labeled with secondary antibodies [Perkin-Elmer: Eu-N1-anti-rabbit: Delfiar No. AD0082; Tb-N1-streptavidin (StrAv-Tb: Delfiar No. AD0047); Sm-N1-streptavidin (StrAv-Sm: Delfiar No. AD0049)] enabled a four-plex assay assuming that the primary antibodies were not cross-reactive. The tags were analyzed in the ICP-MS (RF power: 1400 W; plasma, auxiliary, and nebulizer argon flows: 17, 1.2, and 0.95 L/min) after dissolving in concentrated HCl (34%).

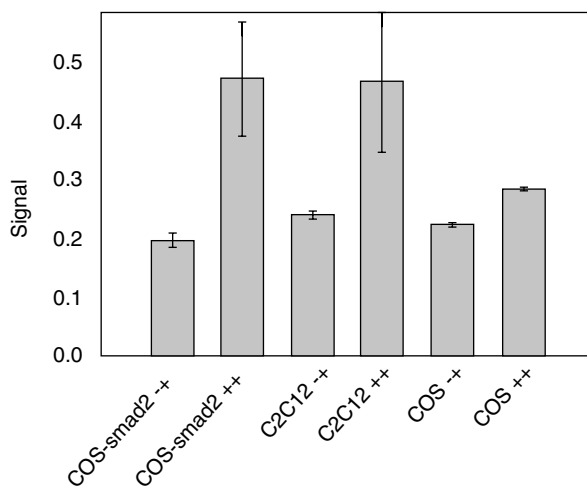


FIGURE 12.8 Results of detection of exogenous Smad2 protein in transfected COS cells and endogenous Smad2 in C2C12 cells in 60 mm plate format. — +, Negative control, probed with anti-rabbit Fab'-Au only; ++, probed with both rabbit anti-Smad2 antibody and anti-rabbit Fab'-Au. Signal (the Y-axis) represents the $^{197}\text{Au}/(^{191}\text{Ir} + ^{193}\text{Ir})$ ratio. (From ref. 47, with permission from the Royal Society of Chemistry.)

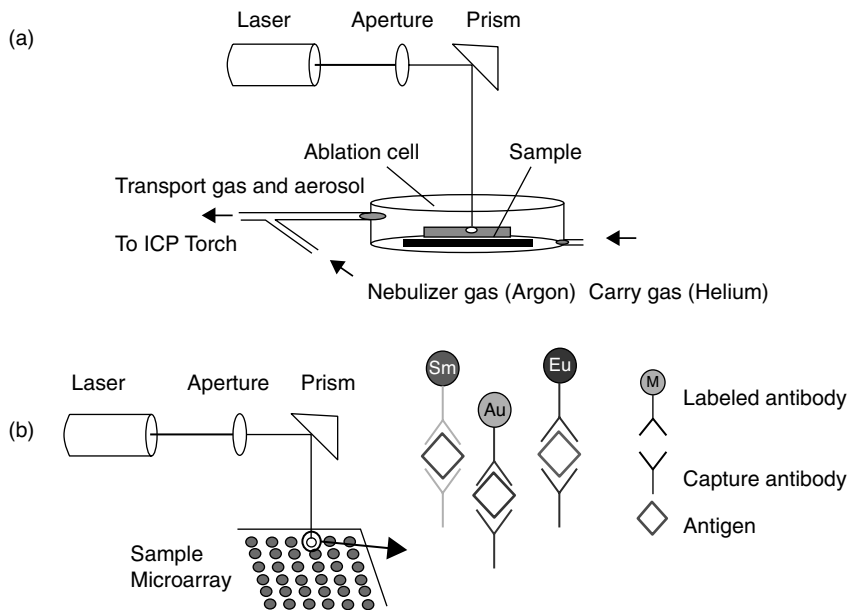


FIGURE 12.9 (a) Laser ablation system; (b) laser ablation sampling for detecting multiple analytes on each spot of a microarray. (From ref. 49, with permission.)

As has been explained, in most cases it is necessary to dissolve the elemental tags before introducing them to the plasma source, thus making it impossible to use this technique for microarray detection. For this reason, Hu et al. [49] recently proposed an alternative for the detection of multiple proteins, consisting of an immuno-microarray on a polyethylene substrate using AuNPs as well as Sm^{3+} and Eu^{3+} as labels and final detection by laser ablation ICP-MS. A scheme of the laser ablation system used in this work is shown in Figure 12.9.

Following this procedure, they detected α -fetoprotein IgG (AFP), carcinoembryonic antigen (CEA), and human IgG, used as model proteins, with detection limits of 0.20, 0.14, and 0.012 ng/mL, respectively.

Another interesting application has been reported by Sundstrom et al. [50]. They labeled *in vitro* antibodies anti-proteins expressed by the T lymphocytes with monocrystalline iron oxide NPs (MIONs) and then intracellular incorporation of MIONs was determined by ICP-MS, after microwave digestion in 5% HNO_3 . This study could provide important information on disease-related patterns of lymphocyte homing in nonhuman primate models of AIDS.

12.5.2 DNA Detection

The same fundamentals and properties explained for proteins can be utilized to detect DNA hybridization events, through the detection of the NPs used as labels by ICP-MS. Merkoçi et al. [51] have used AuNPs modified with anti-mouse IgG to trace

oligonucleotides carrying a c-myc peptide. They developed two strategies to detect the NP tracer: a dot-blot format and ICP-MS. In both cases, oligonucleotide–peptide conjugates were first applied to a nitrocellulose membrane using a manifold attached to a suction device. After immobilization of the oligonucleotide by ultraviolet radiation, the samples were incubated with an anti-c-myc monoclonal antibody. In the ICP-MS strategy case it was followed by incubation with the secondary antibody (anti-mouse IgG) conjugated to AuNPs and their ICP-MS detection after dissolving, obtaining a limit of detection for peptide-modified DNA of 0.2 pmol. A scheme of this assay is shown in Figure 12.10.

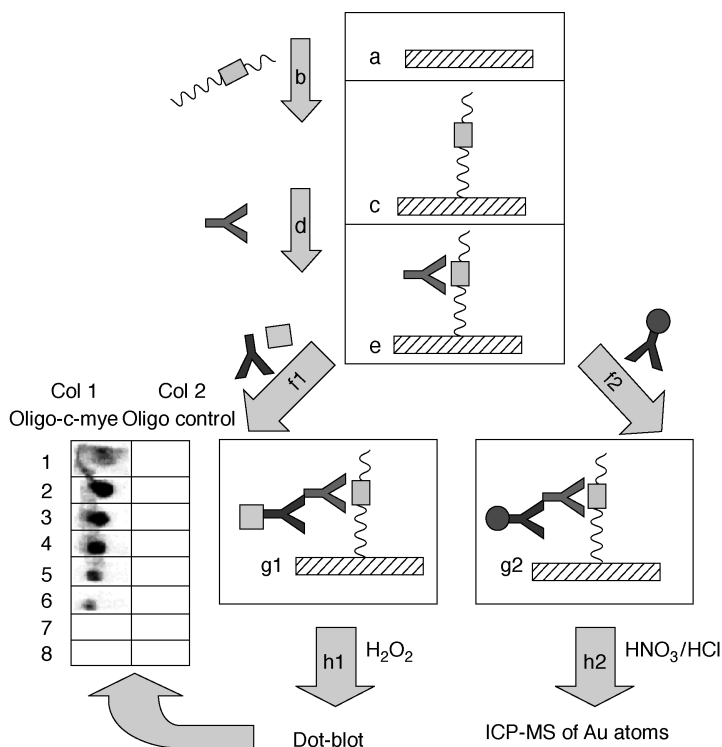


FIGURE 12.10 Assay protocol proposed by Merkoçi et al. The nitrocellulose membrane (a) was introduced into the dot-blot manifold. The oligonucleotide carrying c-myc peptide (b) is immobilized over the membrane (c). It reacts overnight with the anti-c-myc (d). The immobilized oligonucleotide (e) is then treated: 1. According to the dot-blot assay, it reacts first with the anti c-myc and goat antimouse HRP-conjugate antibody (f1) and is then developed (h1) following the ECL (Amersham) protocol and being exposing to x-ray film. 2. According to the ICPMS-linked assay it reacts for an hour with goat anti-mouse colloidal Au (f2) and then dissolved (h2) and detected by ICPMS. Also shown in that figure are autoradiography of the oligonucleotide with peptide c-myc (column 1) and the oligonucleotide without peptide (column 2 blank). Amounts of oligonucleotide–peptide conjugates: 8 (1); 4 (2); 2 (3); 1 (4); 0.5 (5); 0.25 (6); 0.125 (7); 0 (8) μg of oligonucleotide per dot. (From ref. 51, with permission.)

An interesting application of NP labeling of nucleic acids for enhanced ICP-MS detection has recently been reported by Kerr and Sharp [52]. It is well known that ^{31}P detection by ICP-MS has problems of polyatomic interferences (e.g., $^{14}\text{N}^{16}\text{O}^1\text{H}$, $^{16}\text{O}_2$), due to the fact that ^{31}P has a high first ionization potential (10.5 eV), which results in incomplete ionization (35%). These authors have successfully avoided this problem by labeling oligonucleotides containing a biotin functionality with a commercial AuNP–streptavidin conjugate (Nanoprobes) and then achieving subsequent separation and analysis by high-performance liquid chromatography–inductively coupled plasma mass spectrometry (HPLC-ICP-MS) after acidic dissolution. The polyatomic interferences problem is avoided thanks to the fact that the biomolecule signal is greatly enhanced by the higher sensitivity for ^{197}Au compared with ^{31}P and the presence of approximately 86 gold atoms per oligonucleotide.

12.6 CONCLUSIONS

ICP-MS, a well-known sensitive and accurate technique for trace element analysis, is being offered as an excellent tool for the detection of metal-based nanoparticles. The detection offered is quite sensitive and the possibility exists of detecting different types of nanoparticles simultaneously. The analytical performance of the direct ICP-MS detection of gold nanoparticles suspension reported may be extended to the analysis of other nanoparticles in aquatic media or other samples, including biological fluids, where the direct detection of nanoparticles should be of interest.

Few applications related to the use of gold nanoparticles to sense proteins or DNA have been reported. Taking into consideration the variety of applications of nanoparticles as signaling tags for DNA assays, immunoassays, or even cell detection, it is clear that ICP-MS can stand next to several other optical and electrochemical techniques as an alternative tool for biosensing applications.

Nanoparticles-based bioassays usually require dissolving the nanobioconjugates prior to ICP-MS detection. This dissolving process is required to separate the nanoparticles from the immobilization platforms (i.e., polymer surface, membranes, etc.) before their introduction in the ICP-MS detection system. Depending on the immobilization platforms used, the dissolving step can be eliminated. The use of microparticles (i.e., polymeric particles, etc.) as immobilization platforms so as to allow introduction of the whole conjugate (particles serving as immobilization platforms connected to biomolecules, such as DNA hybrids or immunosandwiches labeled with nanoparticles) into the ICP-MS detection system would shorten the detection time and cost of ICP-MS analysis.

The extension of ICP-MS in bioanalytical applications for the simultaneous determination of various biomolecules through labeling with different types of inorganic nanoparticles (including quantum dots such as CdS, PbS, and ZnS) is an interesting research field yet to be explored.

Combining the inherent sensitivity of ICP-MS of heavy metals with the amplification routes offered in several DNA and immunodetection systems introduces opportunities for further improvement of nanoparticles-based ICP-MS bioassays.

Acknowledgments

We wish to acknowledge MEC (Madrid) for projects MAT2008-03079/NAN and Consolider Nanobiomed and the Juan de la Cierva scholarship (A. de la Escosura).

REFERENCES

1. Rouessac F, Rouessac A. *Chemical Analysis: Modern Instrumental Methods and Techniques*, 4th ed. Wiley-VCH, New York, 1998.
2. Skoog DA, Leary JJ. *Principles of Instrumental Analysis*, 4th ed. Saunders College Publishing, Philadelphia, 1992.
3. Hill SJ. *Inductively Coupled Plasma Spectrometry and Its Applications*. Sheffield Academic Press, Poole, UK, 1999.
4. Wilson I, Brinkman UA. Hype and hyphenation: multiple hyphenation of column liquid chromatography and spectroscopy. *Trends Anal Chem.* 2007;26:847–854.
5. Wind M, Lehmann WD. Element and molecular mass spectrometry: an emerging analytical dream in the life sciences. *J. Anal. At. Spectrom.* 2004;19:20–25.
6. Ridley WI, Stetson SJ. A review of isotopic composition as an indicator of the natural and anthropogenic behavior of mercury. *Appl. Geochem.* 2006;21:1889–1899.
7. Barnes RM. Advances in inductively coupled plasma mass spectrometry: human nutrition and toxicology. *Anal. Chim. Acta.* 1993;283:115–130.
8. Jin X, Zhu H. Determination of platinum group elements and gold in geological samples with ICP-MS using sodium peroxide fusion and tellurium co-precipitation. *J. Anal. At. Spectrom.* 2000;15:747–751.
9. Sharara NA, Wilson GC, Rucklidge JC. Platinum-group elements and gold in Cu–Ni-mineralized peridotite at Gabbro Akarem, Eastern Desert, Egypt. *Can. Mineral.* 1999;37:1081–1097.
10. Hinchey JG, Wilton DHC, Tubrett MN. A LAM-ICP-MS study of the distribution of gold in arsenopyrite from the Iodestar prospect; Newfoundland, Canada. *Can. Mineral.* 2003;41:353–364.
11. Pitcairn IK, Warwick PE, Milton JA, Teagle DAH. Method for ultra-low-level analysis of gold in rocks. *Anal. Chem.* 2006;78:1290–1295.
12. Barefoot RR. Determination of platinum group elements and gold in geological materials: a review of recent magnetic sector and laser ablation applications. *Anal. Chim. Acta.* 2004;509:119–125.
13. Gros M, Lorand JP, Luguët A. Analysis of platinum group elements and gold in geological materials using fire assay and Te coprecipitation; the NiS dissolution step revisited. *Chem. Geol.* 2002;185:179–190.
14. Juvonen R, Lakomaa T, Soikkeli L. Determination of gold and the platinum group elements in geological samples by ICP-MS after nickel sulphide fire assay: difficulties encountered with different types of geological samples. *Talanta.* 2002;58:595–603.
15. Oguri K, Shimoda G, Tatsumi Y. Quantitative determination of gold and the platinum group elements in geological samples using improved NiS fire-assay and tellurium coprecipitation with inductively coupled plasma–mass spectrometry (ICP-MS). *Chem. Geol.* 1999;157:189–197.

16. Huffman EL, Clark JR, Yeager JR. Gold analysis: fire assaying and alternative methods. *Explor. Mining Geol.* 1998;7:155–160.
17. Figueiredo AMG, Enzweiler J, Sarkis JES, Jorge APS, Shibuya EK. NAA and UV laser ablation ICP-MS for platinum group elements and gold determination in NiS fire assay buttons: a comparison between two methods. *J. Radioanal. Nucl. Chem.* 2000;244:623–625.
18. Pyrzynska K. Recent developments in the determination of gold by atomic spectrometry techniques. *Spectrochim. Acta B.* 2005;60:1316–1322.
19. Campbell AJ, Humayun M. Trace element microanalysis in iron meteorites by laser ablation ICP-MS. *Anal. Chem.* 1999;71:939–946.
20. D'Ilio S, Violante N, Senofonte O, Caroli S. Occupational exposure of goldsmith workers of the area of Rome to potentially toxic metals as monitored through hair analysis. *Microchem. J.* 2000;67:343–349.
21. Heitland P, Koester HD. Biomonitoring of 37 trace elements in blood samples from inhabitants of northern Germany by ICP-MS. *J. Trace Elem. Med. Biol.* 2006;20:253–262.
22. Begerow J, Turfeld M, Dunemann L. Determination of physiological palladium, platinum, iridium and gold levels in human blood using double focusing magnetic sector field inductively coupled plasma mass spectrometry. *J. Anal. At. Spectrom.* 1997;12:1095–1098.
23. Begerow J, Sensen U, Wiesmüller GA, Dunemann L. Internal platinum, palladium and gold exposure in environmentally and occupationally exposed persons. *Int. J. Hyg. Environ. Med.*, 1999;202:411–424.
24. Krachler M, Prochaska T, Koellensperger G, Rossipal E, Stingeder G. Concentrations of selected trace elements in human milk and in infant formulas determined by magnetic sector field inductively coupled plasma–mass spectrometry. *Biol. Trace Elem. Res.* 2000;76:97–112.
25. Pozebon D, Dressler VL, Curtius AJ. Comparison of the performance of FI-ICP-MS and FI-ETV-ICP-MS systems for the determination of trace elements in sea water. *Anal. Chim. Acta.* 2001;438:215–225.
26. Dressler VL, Pozebon D, Curtius AJ. Determination of Ag, Te, U and Au in waters and in biological samples by FI-ICP-MS following on-line coprecipitation. *Anal. Chim. Acta.* 2001;438:235–244.
27. Pumera M, Aldavert M, Mills C, Merkoçi A, Alegret S. Direct voltammetric determination of gold nanoparticles using graphite–epoxy composite electrode. *Electrochim. Acta.* 2005;50:3702–3707.
28. Jiang P, Xie S, Pang S, Gao H. The combining analysis of height and phase images in tapping-mode atomic force microscopy: a new route for the characterization of thiol-coated gold nanoparticle film on solid substrate. *Appl. Surf. Sci.* 2002;191:240–246.
29. Collins JA, Xirouchaki C, Palmer RE, Heath JK, Jones CH. Clusters for biology: immobilization of proteins by size-selected metal clusters. *Appl. Surf. Sci.* 2004;226:197–208.
30. Chen H, Wang Y, Wang Y, Dong S, Wang E. One-step preparation and characterization of PDDA-protected gold nanoparticles. *Polymer.* 2006;47:763–766.
31. Degueldre C, Favarger PY, Wold S. Gold colloid analysis by inductively coupled plasma–mass spectrometry in a single particle mode. *Anal. Chim. Acta.* 2006;555:263–268.

32. Degueldre C, Favarger PY. Thorium colloid analysis by single particle inductively coupled plasma–mass spectrometry. *Talanta*. 2004;62:1051–1054.
33. Helfrich A, Brüchert W, Bettmer J. Size characterisation of Au nanoparticles by ICP-MS coupling techniques. *J. Anal. At. Spectrom.* 2006;21:431–434.
34. Allabashi R, Stach W, de la Escosura-Muñiz A, Liste-Calleja L, Merkoçi A. ICP-MS: a powerful technique for quantitative determination of gold nanoparticles without previous dissolving. *J. Nanopart. Res.* 2009; In print DOI 10.1007/s11051-008-9561-2.
35. Inagaki K, Mikuriya N, Morita S, et al. Speciation of protein-binding zinc and copper in human blood serum by chelating resin pre-treatment and inductively coupled plasma mass spectrometry. *Analyst*. 2000;125:197–203.
36. Wang J, Houk RS, Dreesen D, Wiederin DR. Speciation of trace elements in proteins in human and bovine serum by size exclusion chromatography and inductively coupled plasma–mass spectrometry with a magnetic sector mass spectrometer. *J. Biol. Inorg. Chem.* 1999;4:546–553.
37. Szpunar J. Advances in analytical methodology for bioinorganic speciation analysis: metallomics, metalloproteomics and heteroatom-tagged proteomics and metabolomics. *Analyst*. 2005;130:442–465.
38. Sanz-Medel A. From metalloproteomics to heteroatom-tagged proteomics. *Anal. Bioanal. Chem.* 2005;381:1–2.
39. Prange A, Pröfrock D. Chemical labels and natural element tags for the quantitative analysis of biomolecules. *J. Anal. At. Spectrom.* 2008;23:432–459.
40. Bendayan M. Worth its weight in gold. *Science*. 2001;291:1363–1365.
41. Hainfeld JF, Robinson JM. New frontiers in gold labeling: symposium overview. *J. Histochem. Cytochem.* 2000;48:459–460.
42. Andreu EJ, Martin de Llano JJ, Moreno I, Knecht E. A rapid procedure suitable to assess quantitatively the endocytosis of colloidal gold and its conjugates in cultured cells. *J. Histochem. Cytochem.* 1998;46:1199–1201.
43. Martin de Llano JJ, Andreu EJ, Pastor A, de la Guardia M, Knecht E. Electrothermal atomic absorption spectrometric diagnosis of familial hipercolesterolemia. *Anal. Chem.* 2000;72:2406–2413.
44. Zhang C, Zhang Z, Yu B, Shi J, Zhang J. Application of the biological conjugate between antibody and colloid Au nanoparticles as analyte to inductively coupled plasma mass spectrometry. *Anal. Chem.* 2002;74:96–99.
45. Baranov VI, Quinn Z, Bandura DR, Tanner SD. A sensitive and quantitative element-tagged immunoassay with ICPMS detection. *Anal. Chem.* 2002;74:1629–1636.
46. Quinn ZA, Baranov VI, Tanner SD, Wrana JL. Simultaneous determination of proteins using an element-tagged immunoassay coupled with ICP-MS detection. *J. Anal. At. Spectrom.* 2002;17:892–896.
47. Baranov VI, Quinn ZA, Bandura DR, Tanner SD. The potential for elemental analysis in biotechnology. *J. Anal. At. Spectrom.* 2002;17:1148–1152.
48. Ornatsky O, Baranov VI, Bandura DR, Tanner SD, Dick J. Multiple cellular antigen detection by ICP-MS. *J. Immunol. Methods*. 2006;308:68–76
49. Hu S, Zhang S, Hu Z, Xing Z, Zhang X. Detection of multiple proteins on one spot by laser ablation inductively coupled plasma mass spectrometry and application to immuno-microarray with element-tagged antibodies. *Anal. Chem.* 2007;79:923–929.

50. Sundstrom JB, Mao H, Santoianni R, et al. Magnetic resonance imaging of activated proliferating rhesus macaque T cells labeled with superparamagnetic monocrystalline iron oxide nanoparticles. *J. Acquired Immune. Defic. Syndr.* 2004;35:9–21.
51. Merkoçi A, Aldavert M, Tarrasón G, Eritja R, Alegret S. Toward an ICPMS-linked DNA assay based on gold nanoparticles immunocoupled through peptide sequences. *Anal. Chem.* 2005;77:6500–6503.
52. Kerr SL, Sharp B. Nano-particle labelling of nucleic acids for enhanced detection by inductively-coupled plasma mass spectrometry (ICP-MS). *Chem. Commun.* 2007; 4537–4539.

NANOSTRUCTURED SURFACES

Integration Between Template-Based Nanostructured Surfaces and Biosensors

WALTER VASTARELLA

ENEA C.R. Casaccia, Rome, Italy

JAN MALY

Department of Biology, University of J.E. Purkyne, Usti nad Labem, Czech Republic

MIHAELA ILIE

Department of Applied Electronics and Information Engineering, LAPI, Universitatea Politehnica București, Bucharest, Romania

ROBERTO PILLOTON

ENEA C.R. Casaccia, Rome, Italy

13.1 Introduction

13.2 Nanosphere lithography

13.2.1 Basic principles of nanosphere lithography

13.2.2 Preparation of the colloidal mask

13.2.3 Plasma modifications and lithography

13.2.4 Combination of NSL and other lithographic approaches

13.2.5 Application of NSL for sensor biointerfaces

13.3 Nanoelectrodes ensemble for biosensing devices

13.3.1 Electrochemical and electroless deposition of nanomaterials via templates

13.3.2 Gold nanoelectrode ensembles

13.3.3 Nanoelectrode ensemble for enzyme-based biosensors

13.4 Concluding remarks

13.1 INTRODUCTION

Nanostructured materials have proven to be a powerful tool in new technologies as well as in basic research, due to their very peculiar properties at the nanometer size scale. Many studies and publications have demonstrated, or are based on, the assumption that optical, mechanical, photocatalytic, or electronic properties of nanosize surfaces changes drastically with respect to those of bulk materials [1–22]. Electrochemical sensing and biosensing constitute research fields where nanotechnologies have been used successfully especially in using metal and carbon nanosize materials with high surface/volume ratios [9–14].

The synthesis via template represents a convenient procedure which in many cases has strongly simplified the production of such surface-confined nanoscale materials as nanoparticles, nanowires, and nanotubes. This method is based essentially on the simple but effective idea that the pores or cavities of the host supports can be used as templates to address and control the growth of specific materials (i.e., metals, semiconductors, biological compounds, and polymer chains).

The utilization of templates in producing novel nanomaterials goes back to the early 1980s. Pioneering works were ascribed to authors involved in the preparation of different metallic nanostructures [23–40], but the method was soon extended to a large number of substrates and applications.

In this chapter we focus on the following nanomaterials, which rely on template synthesis: nanostructure ordered surfaces prepared by nanosphere lithography (NSL) and metal nanoelectrode ensembles (NEEs) assembled into porous membranes. Apart from the theoretical approach, attention is paid to the integration of nanoelectrode ensembles with disposable screen-printed devices, which represent an interesting example of practical biosensing applications. Features and advantages of such devices with respect to comparable macroscopic systems are described and future perspectives are noted.

13.2 NANOSPHERE LITHOGRAPHY

13.2.1 Basic Principles of Nanosphere Lithography

The major issue in the development of nanoscale-ordered biointerfaces is the method of precise positioning of nanoobjects in periodic or aperiodic patterns. A nanostructured biointerface is usually obtained by selective anchoring of biomolecules through chemical bounds to nanopatterned substrate. Apart from conventional patterning techniques (e.g., electron-beam lithography), such substrates can be prepared conveniently by a low-cost alternative technique called *nanosphere lithography* (NSL). This technique makes use of self-assembling processes of nanometer-scale spherical particles onto a large area of planar substrate followed by several different steps of plasma etching and deposition processes, in this way creating polymeric or metallic nanostructures with relevant applications to biointerfaces. This bottom-up method is rather old, originally developed as a “natural lithography” technique for replicating submicroscopic

patterns [41]. Recently, it has undergone rapid development, showing many applications in various fields where large numbers of periodical nanosized features are often required, such as nanopattern definition in a variety of biological investigations, such as cell adhesion studies [42–46], fabrication of nanostructured biointerfaces for bioanalytical devices (biosensors) [47–50], and preparation of catalytically active surfaces [51,52]. The main advantages of the method, which are the driving force of its development, are the ability to control the size, shape, and coverage of particles independently over large areas (cm^2), the low cost and simplicity of preparation without a need for both complex equipment and strict operating conditions (e.g., clean rooms). This is possible due to the pure self-assembly nature of the process, where the resulting structures are preprogrammed in their molecular and colloidal behavior. The properties of the materials thus prepared depend on the tailored interactions between the molecular building blocks and substrate, which make this method highly flexible.

The common principle of NSL is quite simple (Figure. 13.1). Usually, colloidal nanoparticles are deposited on a planar surface by a self-assembling process mostly in

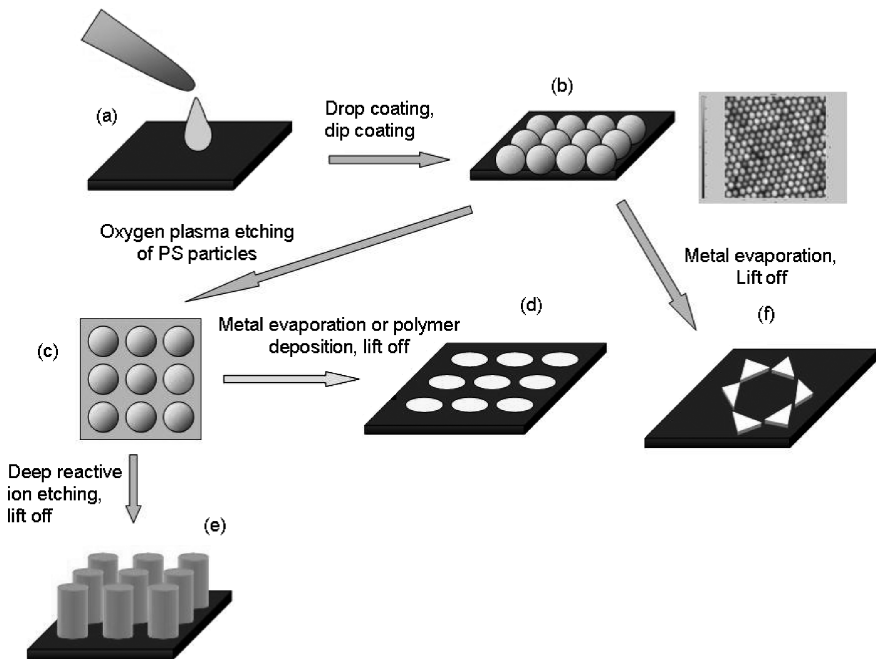


FIGURE 13.1 Basic principles of nanosphere lithography. (a) Solution of spherical nanoparticles is drop or dip coated on the flat base substrate surface; (b) after evaporation of solvent, the hexagonal two-dimensional array is formed spontaneously; (c) on the right side: AFM image of a 200-nm polystyrene monolayer; by oxygen plasma etching, the size of polystyrene particles can be decreased; (d) metal or polymer may be deposited in the interstitial area, providing sievelike structure after lift-off of polystyrene nanoparticles; (e) by deep reactive ion etching, nanopillars of the same material as base substrate can be prepared; (f) metal nanoparticle triangles may also be prepared by metal evaporation over the structure (b) and subsequent lift-off (f).

the form of monolayer. The resulting ordered array of nanoparticles (colloidal mask) is used as a template for various subsequent plasma etching and/or deposition processes. After selective plasma processing, the remaining colloidal mask is removed by means of a lift-off process which results in a nanopatterned surface consisting of regular spots with physicochemical and/or topographical properties which differ from those of an original planar surface. Such a surface can be used further for selective immobilization of various biomolecules by covalent attachment to the exposed surface and preparation of the final nanostructured biointerface. There are several key parameters, whose variation influences the properties of the resulting nanostructure. These include (1) nanoparticle properties (material, size, charge), (2) physicochemical properties of planar surface, (3) methodologies for mask self-assembly (drop casting, spin coating, etc.), (4) postassembling modification of a colloidal mask (e.g., plasma etching, selective patterning), and (5) plasma processing and development of the final nanostructured surface (i.e., etching, metal or polymer deposition, etc.). The main variations and their influence on the NSL process are discussed below.

13.2.2 Preparation of the Colloidal Mask

A huge variety of submicrometer particles in colloidal suspensions can be used for the preparation of a lithographic colloidal mask, varying in the type of material from which they are made, their dimensions, and the surface charge. Usually, they have a spherical or quasispherical shape, with controllable dimensions within the nanometric range. Due to their frequent use in many application fields, they are readily available on a commercial base. Colloids can be synthesized in a number of materials, including polymers (e.g., block copolymers, dendrimers) [53–55], metals (e.g., gold, platinum, palladium), semiconductors (quantum dots), or metal–polymer nanocomposites [56–58]. Among the others, polystyrene (PS) nanoparticles are frequently employed for NSL [59–63] since they can be synthesized monodispersed and with a wide range of surface chemistries and charges. Although they are available with a diameter smaller than 100 nm, silica nanoparticles are used primarily in this dimension range, due to their low size dispersion [60,64]. The selection of appropriate colloids is crucial for successful nanopattern generation, as are surface charge and particle size. Dispersion is also an important factor, since it influences the frequency of defects in the array obtained.

The colloidal mask is usually self-assembled on a planar base substrate that is patterned. The physicochemical properties of the surface are tailored according both to the needs of the final application and the special requirements of the lithographic process. Properties such as wettability and surface charge help the formation of an ordered colloidal template because they influence the solvent evaporation process and substrate–particle interaction. Conductive [59], insulating [52], optically transparent [47,52,65], or other types of materials can be used as the base substrate. Most frequently, glass or silicon [59–61,64,66] covered with thin metal layers [59,64], metal oxides [60], or with various types of polymers [64,66,67] have been exploited. Self-assembled spin-coated or plasma-polymerized thin films may be

prepared on base substrate [63,68,69]. Since the final nanopattern is obtained primarily through a plasma etching process, the etching rate of the base substrate has to be equal to or higher than that of the colloidal mask; otherwise, a pattern can not be transferred.

Colloidal nanoparticles are dispersed on the substrate in appropriate solution and are self-assembled electrostatically into two-dimensional crystalline structures as the solvent evaporates. The driving forces of the assembly (i.e., electrostatic particle–particle and particle–substrate interactions, hydrodynamic interactions, and diffusion) result in a hexagonally ordered nanostructure with the particles separated by an average distance [Figure 13.1(b)]. The space between particles can be adjusted by changing several conditions or particle–substrate properties, influencing the assembling forces. The ionic strength of the colloidal solution influences the range of repulsive interparticle electrostatic interactions [70]. With decreasing salt concentration, the interparticle repulsion forces increase, resulting in longer particle distances and decreased saturation coverage [60]. The ionic strength of the colloidal solution is therefore a simple way to control the interparticle distance in the colloidal mask. Similarly, other factors, such as the pH of the solution [71], particle and surface charges [71,72], and particle size [73], play an important role in the self-assembling process and must be controlled to obtain a reproducible pattern.

Several methods are used to spread colloids onto the base substrate. Probably the simplest approach is drop casting, where the solution of particles is simply added drop wise onto the base substrate. While the solvent evaporates, the colloids remain on the substrate surface. Since during evaporation the capillary forces between the particles dominate during evaporation, they can be arranged in different geometrical configurations to minimize the space and the free energy of the system. Therefore, the rate of the solvent evaporation controls the degree of order in the pattern [74,75]. Other methods of deposition are represented by sedimentation [76], electrodeposition [77], or spin coating [78,79]. Due to the parallel nucleation events of self-assembling, most of these methods inevitably lead to imperfections in the two-dimensional structures. Normally, the assembled defect-free area obtained is no larger than several square micrometers. Variation of nanoparticle size (polydispersion) alters electrostatic repulsion between individual pairs of colloidal particles, thus introducing dislocations [75].

Recently, an alternative form of colloidal lithography has been presented [60] in which charged particles adsorb randomly onto an oppositely charged surface. The randomness of the initial process of adsorption causes a uniformity of array over a large surface area without imperfections and dislocations. Additionally, dip coating as a sequential assembly process may be used for the fabrication of perfect, defect-free arrays over a large area [64], due largely to the well-controlled drying front (i.e., liquid meniscus) and other conditions, such as particle concentration and ionic strength. Contrary to previous methods, capillary forces are identified as the basis of the assembly process, which does not require any specific chemistry on either the template or the particles. Therefore, this method is generic and allows a wide choice of both support and particle materials.

13.2.3 Plasma Modifications and Lithography

Following the primary process of ordered nanosphere layer formation, the nanopatterns obtained can be used for biological investigations without further modifications [80,81], or, more frequently, various postassemble processes are performed (e.g., dry etching or coating) to modify the geometry of periodic two-dimensional colloidal mask or to pattern the base substrate. As an example, reactive oxygen plasma treatment is frequently used to modify the polystyrene particle size [61,82]. The ordered pattern becomes more *open*, since the particle size decreases. By variation of plasma exposure time, different sievelike structures can be prepared from the same template [Figure 13.1(c) to (f)]. Apart from size, the shape of particles becomes slightly ellipsoidal, due to the unequal plasma abrasion [60]. These structures are characterized by larger interstitial area compared to the original mask, which may be useful for the preparation of circular nanoposts, columns, or wells with chemical and topographical properties different from those of the base substrate.

Lithographic processing utilizing, reactive ion etching (RIE), for example, makes it possible to produce modified colloidal-derived nanotopographies [42,60,83]. Here, the assembled colloidal monolayer serves as a mask and protects the underlying base substrate, except the interstitial area between the individual particles, from etching. As a result, nanopillars with colloidal particle diameters can be prepared by etching the base substrate [46,84–87]. The dimensions and pillar profile are determined by etch time, gas, pressure, and mask integrity. Other geometric bodies formed on the colloidal lithographic mask may be hemispherical protrusions [42,88], cups [89], nanowells [90–92] or rings [93–95].

Apart from RIE lithography, a colloidal mask is often used for selective deposition of various materials, predominantly metals (e.g., silver, aluminum, nickel). After the lift-off procedure, when the colloidal monolayer is removed, a metal mask reflecting the interstices of the close-packed colloids assembled in hexagonal or triangular lattice arrangements is manufactured. Besides metals, various polymers (e.g., plasma polymerized) can be overlaid on the mask, leading to the homogeneous surface chemistry of patterned features after removing the template nanoparticles [45,62,83]. This allows further modifications of defined chemical patterns and decoration with other functional molecules, biomolecules (proteins, DNA), or nanoparticles [83,96]. A final step that follows exposure of the mask to RIE is performed to remove the colloidal mask. Mostly, wet chemical etching methods are employed in which particles are removed due to the combined effects of chemical etch and a net repulsive interaction between the particle and the surface. Short-time sonication usually helps the dissolution of the mask [97].

13.2.4 Combination of NSL and Other Lithographic Approaches

Despite the many advantages that NSL provides, there are some limitations in terms of the flexibility to produce different patterns (e.g., shape and size, spacing between features, addressability of individual units). Therefore, hybrid approaches in fabrication that combine the self-assembly principle of NSL with conventional lithography

are actively conducted to address these issues [98]. Successful attempts are reported where photolithography [99,100] or electrostatic fields [101] are used to pattern regions of particles. Here, conventional lithography or other patterning techniques are commonly used for the fabrication of micro(nano)-structured base substrates where the self-assembly of colloidal particles is directed to selected areas having certain chemical or topographic properties. As an example, a combination of colloidal particle self-assembly and interference lithography has been presented [64]. Poly(methyl methacrylate) (PMMA) layers spin-coated on chromium (36 nm)- or SiO₂ (100 nm)-coated silicon wafers has been used for line/space and hole pattern fabrication, with periods in the range 40 to 100 nm by a grating-based interferometer. Gold (50 and 15 nm) and silica (50 nm) particles in aqueous suspensions were self-assembled on PMMA by dip-coating. The difference in wettability (hydrophobic–hydrophilic contrast) between the polymer lines and the underlying surface affects the selective assembly of the particles.

Due to its simple fabrication and low cost, a combination of NSL and soft lithography has the potential of many future applications. Recently, a novel method entitled microcontact particle stripping was introduced [59] which combines the use of an elastomeric stamp as a basic component of microcontact printing with colloidal lithography. The simple procedure is based on contact between the elastomeric stamp and substrate modified by monolayer of preadsorbed polystyrene particles. Particles from contact regions are removed. The remaining colloidal particles unaffected in noncontact regions can be further used as a lithographic mask. This method has been applied successfully with particles in the size range 50 to 500 nm, whereas the spacing of the particles is a multiple of their diameters (from 1.5 to 4). Other methods that use microcontact printing are based on patterning of self-assembled monolayers (SAMs), which further facilitate a selective deposition of colloidal particles on chemically patterned surfaces [102,103].

A promising direction by which some limitations (e.g., configuration disorders, spacing of individual colloids) of classical NSL can be overcome is the self-assembly of block copolymers instead of colloidal particles, which has been used for fabrication of periodic arrays with sub-100-nm features [104,105]. Block copolymer lithography is, in fact, a fast-growing field with many interesting applications. As in NSL, the driving force for nanostructuring using these polymers is the self-assembly. Due to the enormous flexibility in chain properties and the behavior, various nanopatterns may be prepared which are normally inaccessible for NSL. In this chapter we show only a few interesting examples of the method. Readers who are interested in more details should follow one of the recent reviews in this field [106,107]. An advantage of amphiphilic diblock copolymers, such as polystyrene(*x*)-block-poly(2-vinylpyridine)(*y*) [PS(*x*)-*b*-P2VP(*y*)] is that under suitable conditions (e.g., solubilized in toluene), they form core–shell micellar structure, which enables selective dissolution of the metal precursor salts and after the chemical reduction step, generation of mono-dispersed metal particles. Block micelles of copolymers containing gold nanoparticles have been used for self-assembly on glass substrate [108]. After exposure to hydrogen plasma, gold particles remain on the substrate surface in hexagonal patterns, whereas the polymer has been removed. The spacing between

individual gold particles is setup by the properties of the diblock copolymer used. Similarly, combination of block copolymer and electron beam lithography has been used for fabrication of various periodic and nonperiodic patterns of Au nanoparticles, separated by distances not normally obtained by pure self-assembly [109].

13.2.5 Application of NSL for Sensor Biointerfaces

13.2.5.1 Biointerfaces Based on Protein Nanoarrays Application of colloidal lithography in the fabrication of nanostructured surfaces for biosensors and related biointerfaces is still in its infancy, but several representative examples of applications indicate the possible directions of future developments. Apart from biosensor interfaces, colloidal-derived nanotopographies currently under investigation show great promise in the control of cell growth and adhesion to surface, altering gene regulation or inflammatory response [43,46,110,111], which may bring new interesting properties of functional medical devices (e.g., implants or tissue-engineered constructs) [112]. Despite their importance, these applications are not reviewed in this chapter. The interested reader should follow recent reviews in the field [74].

A key achievement regarding the generation of sensor biointerfaces using colloidal lithography is the ability to bind sensing biomolecules selectively on patterned areas and to retain their natural active conformation and favorable orientation. Once the molecule is selectively immobilized on nanoarrayed substrate, it can be used in many detection strategies, most frequently optical and electrochemical, to detect the analyte of interest. Recently, several attempts have been performed to show this possibility. Chemically nano-patterned surfaces with biologically relevant end groups such as carboxylic groups and antifouling poly(ethylene glycol) (PEG) functionalities have been prepared by the combination of NSL and plasma-deposited functional polymeric layers [68]. Plasma-enhanced chemical vapor deposition (PE-CVD) is a low-pressure low-temperature process that permits the creation of thin films on a large variety of substrates with selectable chemical functionality, stability, density, and coverage of the films deposited. Here, a thin and negatively charged (carboxylic groups) hydrophilic plasma-polymerized acrylic acid (PAA) film has been deposited on solid support using a glow discharge created from acrylic acid vapor. After assembling a two-dimensional colloidal mask pattern of negatively charged polystyrene beads (diameter 200 to 1000 nm) by a dip-coating method, oxygen plasma etching has been carried out, resulting in the creation of PAA nanodomes. Following plasma deposition of the PEG-like coating (protein-resistant layer) and mask dissolution in an ultrasonic bath, bovine serum albumin (BSA) has been immobilized selectively on a PAA layer using standard conjugation chemistry.

Similarly, a horse spleen ferritin nanopattern has been prepared by selective protein deposition on gold cylindrical disks (20 nm high, 120 nm in diameter) covered by a SAM of hydrophobic thiols [113]. The pattern has been obtained by oxygen plasma etching of a polystyrene particle mask assembled on a silicon wafer and covered by a thin layer of gold. Nonspecific binding of ferritin on the exposed silicon surface has been protected by selective deposition of a PLL-PEG (PLL backbone and PEG side

chain) amphiphilic copolymer monolayer. Another investigation has described the collagen adsorption on model substrate exhibiting controlled topography and surface chemistry [88]. Substrates were prepared by gold deposition onto silicon wafers (smooth substrate) and onto a support with nanoscale protrusions created by colloidal lithography (rough substrate) and by subsequent functionalization with CH_3 (hydrophobic) or OH (hydrophilic) groups. Based on their results, authors concluded that while the amount of collagen adsorbed is affected only by the surface chemistry, the supramolecular organization is controlled by both surface chemistry and topography.

A simple approach to functional protein array production which is based on self-assembling of polymer templates and proteins has recently been developed [114,115]. To create arrays of protein nanostructures with defined spacing, monodisperse latex spheres have been coated with the desired protein (BSA, proteins A and G) and deposited on a mica (001) or gold (111) surface. After drying, latex particles are displaced to expose periodic arrays of immobilized proteins, which remain attached to the surface and maintain the order and periodicity of the latex scaffold. The morphology and diameter of protein nanostructures thus prepared are tunable by setting up the protein/latex ratio and the diameter of latex spheres [114]. Similarly, lysozyme periodic nanostructures have been prepared on silicon by NSL, retaining their full activity [115]. Another interesting approach based on self-assembling properties of diblock copolymers has been introduced [116]. It has been shown that chemical heterogeneity of self-assembled hexagonal polystyrene-*b*-poly(vinylpyridine) (PS-PVP) diblock copolymer micelles on flat surfaces can be exploited successfully as a template for protein self-assembling in specific polymer nanodomains, thus creating a high-density ordered protein array. The properties of the array may be tuned easily by the size of the underlying diblock copolymer. To show the possible exploitation of such a nanoarray in biosensor applications, various proteins have thus been immobilized and their activity screened [117]. By immobilizing proteins [e.g., horse radish peroxidase (HRP), mushroom tyrosinase, bovine immunoglobulin G, and green fluorescent protein], the authors found that they retain their catalytic activity over three months and that their binding behavior is not affected by surface immobilization on the diblock copolymer template.

Despite the fact that the potentiality of NSL or block copolymer lithography for protein arraying has been shown in several attempts, little work has been done to screen the biological functionality of proteins in arrays thus prepared. As an example, adsorption of fibrinogen on a substrate with nanoscale pits and the ability to bind unstimulated platelets selectively have been investigated [118]. Colloidal lithography has been used to create a high density of nanometer-sized pits (40 nm in diameter, 10 nm in depth) in continuous thin metallic film vapor-deposited overtop electrodes of quartz crystal microbalance (QCM) sensors or on silicon wafers. Multidomain protein human fibrinogen was adsorbed on a structured and planar surface as a control sample due to its similarity in pit size. The ability of fibrinogen molecules to bind specifically to receptors in platelet membranes has been correlated with both nanoscale chemistry and surface topography. No specific binding of unstimulated platelets during the initial phase of interaction was observed on fibrinogen bound to flat surfaces with homogeneous surface chemistry. On the contrary, fibrinogen bound at topographically

structured surfaces (both chemically homogeneous and chemically patterned surfaces) exhibited significant specific platelet binding. Authors speculate that the conformation or orientation of fibrinogen molecules is altered at surfaces that have nano-topography on the length scale of the individual molecules. The altered orientation or conformation on nano-structured surfaces may make binding sites available to the fibrinogen molecule, which can bind to membrane receptors on unstimulated platelets.

The assembly of single biomolecule arrays, where nanostructured surfaces are able to accept only a single biomolecule at an individual binding site, with definable spacing and orientation and created on a large sample area, is an interesting challenge because such surfaces may show a molecularly defined environment for cell culture studies and optimal sensing properties in biosensors [119–121]. Recently, the preparation of such an array has been shown [108,121] using nanostructured gold dot patterns prepared by micellar diblock copolymer lithography, discussed earlier in the chapter. Gold nanoclusters with a defined diameter (ca. 6 nm) and lateral spacing of 30, 96, and 160 nm have been prepared on glass, and the interstices between them have been modified with monomolecular film of mPEG–triethoxysilane to prevent non-specific binding of proteins. Afterward, gold nanodots have been modified with short thiol-nitrilotriacetic (NTA) chelator molecule. Also, recombinant proteins (Agrin, N-cadherin) that carry a 6 histidine ($6 \times \text{His}$) tag have been immobilized in an oriented manner through a specific NTA–His tag and their presence detected by primary and secondary fluorescence-labeled antibodies, as well as by atomic force microscopy (AFM). As result, up to 70% of gold particles creating the nanopattern have been modified with only a single functional biomolecule at molecularly defined density and locations. Due to the generality of the immobilization method, identical arrays can be prepared for every biomolecule available.

All these examples show that nanotopography can influence the structure and functionality of adsorbed proteins significantly when correct dimensions and topography are established. Similarly, as observed for immobilization of biomolecules on nanoparticles with smaller dimensions [122,123], it turns out that the smaller interaction area between the nanostructured surface and the biomolecule can affect the secondary structure to a lesser extent than can a planar surface. Therefore, the natural activity and functionality of protein is retained to a high degree. In an ideal case, the nanostructured element has dimensions similar to the dimensions of an immobilized biomolecule [62,118,121].

13.2.5.2 Biointerfaces for Localized Surface Plasmon Resonance Biosensors

One of the most interesting features of nanostructured layers of metals are their unusual optical properties, which can be used for the fabrication of ultrasensitive surface plasmon–based biosensors. Noble-metal nanoparticles normally exhibit a strong ultraviolet–visible (UV–vis) adsorption due to the resonance between the collective excitation of conduction electrons and incident photon frequency [47,48]. This phenomenon is known as *localized surface plasmon resonance* (LSPR). Due to the extremely large molar extinction coefficients (about $3 \times 10^{11} \text{ M}^{-1}/\text{cm}$) [124,125], intense signals can be obtained using spectroscopic methods, which predetermines

their use as optical sensors and biosensors [47,48,126,127]. Based on the theoretical model of Mie [128], the intensity of the LSPR spectrum depends on a number of parameters, such as nanoparticle radius, material, dielectric constant, and interparticle spacing [129,130]. A common effort in the field is to find synthetic routes of nanoparticle fabrication in order to tune and precisely control their plasmonic properties. The simplest and most common approach is based on reduction of metal salts in solution, which results in the colloidal suspension of metal nanoparticles. Highly sensitive LSPR biosensors have been realized based on the change of absorption UV–vis maxima upon interparticle coupling. Complementary DNA colorimetric sensing has been shown in which the change in color is observed when nanoparticles are brought together by the hybridization event [131–133]. The limits of detection (LOD) reach femtomoles of the target oligonucleotide, which is almost 100-fold lower than that of a conventional fluorescence assay [131].

Despite its sensitivity and simple procedure, the principal disadvantage of solution-based LSPR nanoparticle biosensing is the nonspecific, irreversible, and difficult-to-quantify particle aggregation [48]. Therefore, to easily overcome most of the difficulties, surface-confined nanoparticle arrays may be employed for biosensing purposes instead of colloidal suspensions. NSL has been used successfully to structure surface-confined triangular silver nanoparticles by metal deposition over a polystyrene nanosphere mask on a glass substrate [47,48]. The silver nanodots (100-nm in-plane and 51-nm out-of-plane width) have been modified with SAM from a mixture (3 : 1) of 1-octanethiol (1-OT) and 11-mercaptoundecanoic acid (MUA) and further with biotin through a zero-length coupling agent on carboxylate groups. The maximum of observed plasmon resonance ($LSPR_{\lambda_{max}}$) increased (red shift) at each modification step: from 561 nm up to 609 nm after the final modification step. To simulate antibody–antigen binding as one of the possible future applications of such optical biosensors, the calibration curve for streptavidin [47] and antibiotin [134] binding has been obtained as a function of the red shift of $LSPR_{\lambda_{max}}$. The LOD calculated from the response curve has been lower than 1 pM for streptavidin and 100 pM for antibiotin with 27 nm and 38 nm of maximal plasmon peak shift for each case. It was also shown that by changing the shape, size, and material composition of a metal layer it is possible to tune the sensing capability of LSPR sensors [135,136]. By immobilization of mannose on silver triangles, the carbohydrate binding protein (concanavalin A) has been used to track the response sensitivity as the function of height of silver nanodots [137]. Results show that the overall response of the nanosensor increases with decreasing nanoparticle height.

Apart from metal nanodots, nanoring structures represent a high potential to surface plasmon sensing at a nanometer scale. This is due mainly to their tunable plasmon resonances and the large empty volume, which provides more spaces for molecular attachment [95,138]. A low-cost method of producing large-area-ordered metal nanoring arrays based on NSL has been presented [95]. Close-packed SAMs of polystyrene monodisperse spheres were formed on silicon substrate by a spin-coating method. A layer of gold was sputtered onto a colloidal mask on a vertical incidence, followed sequentially by reducing the gold-capped polystyrene spheres from the topside by ion polishing. The inner diameters, wall thickness, and wall height of gold

nanorings have been tuned by the size of PS spheres and by the process parameters of RIE, sputtering, and ion polishing. Such tuning of metal nanoring structures leads to fine and flexible controlling of plasmon resonances of the nanorings [95].

Recent efforts in optical-device fabrication based on LSPR detection have stimulated the development of sensitive, simple, and label-free detection of a wide range of analytes in medical diagnostic, environmental, and chemical analysis. The key factor that influences its further development is the ability to precisely control and tune the parameters of an optically active metal array. Although novel approaches have also emerged, NSL lithography belongs to one of the simplest methods, by which such surfaces can be efficiently prepared and studied. Therefore, its further development in this field can be envisioned.

13.3 NANOELECTRODES ENSEMBLE FOR BIOSENSING DEVICES

13.3.1 Electrochemical and Electroless Deposition of Nanomaterials via Templates

13.3.1.1 Nanoporous Membranes The pores of filtration membranes represent a simple case of structural heterogeneity, whereby the discontinuity in the solid phase operates the selection for species with specific dimensional requirements. Deposition of nanomaterials can be carried out into the nanopores of ultrafiltration membranes with uniform, cylindrical, or prismatic pores of particular size.

Nowadays, chemical sieve materials, such as glass matrices with nanostructured channels, zeolites, or nanoporous proteins, are available worldwide. Many research groups involved in synthetic routes by means of nanoporous templates make use of commercially available ultrafiltration membranes. Owing to the rather limited number of pore sizes and pore density of commercial products (e.g., from Anopore, Nuclepore, or Synkera Technologies Inc.), other authors prefer to prepare their own templates in order to customize the geometric features.

Chapter 15 is dedicated to reviewing the methods and materials selected for nanopore fabrication. This part is dedicated specifically to applications of alumina and track-etched polymeric membranes as host templates for the synthesis of nanosized material.

Alumina membranes with regular pore distribution can generally be formed by electrooxidation of aluminum substrates (high-purity aluminum sheets) in acidic electrolytes using a two-electrode cell. Cathode is generally made of aluminum, lead, platinum or stainless steel [139–142]. The resulting structure of the porous oxide film consists of a uniform array of parallel alumina cells packed hexagonally, with a nearly cylindrical shape of the pores, high pore density, and low diameter size distribution. The hexagonal self-order of the pores was justified by the presence of repulsive forces and the volumetric expansion associated with the anodization process [143–145]. By appropriate selection of the electrochemical process conditions, such as applied potential/current density, treatment time, concentration of the electrolyte mixture, and temperature of the treatment, it has been possible to tune at will the size and aspect

ratio of the pores, preparing films with different thicknesses, pore densities, and pore diameters from 5 to 1000 nm [144,146–152]. It was verified experimentally that:

- The thickness of the porous alumina increases linearly from 0.1 μm to 10 μm with anodization time at a given voltage and temperature.
- The pore spacing varies regularly with the applied potential, typically in electrolytic solution of 25% sulfuric acid or phosphoric acid, or 15% sulfuric acid at a fixed temperature.
- The pore density and pore diameter are linearly correlated under controlled conditions [153].

According to some authors [154], obtain high-quality membranes, aluminum should be pretreated in concentrated acid and plenty of distilled water to show well-polished mirrorlike surfaces. During pore formation, aluminum is coated by a relatively thin nonporous insulating oxide layer; therefore, the anode material surface is not exposed directly to the solution. Several strategies and procedures to separate the unoxidized foil from the porous oxide layer have also been proposed. We leave it to readers to peruse the literature [155–158] to follow the progressive efforts in improving the support quality.

Alternatively to brittle and rather rough alumina or silica membranes, nanoporous polymeric membranes prepared by the track-etch method can be used as templates of high flexibility and smoothness, often very stable in acids as well as in organic solvents and biologically inert. Such membranes can be produced with a relatively wide range of pore diameters. Poly(ethylene terephthalate) (PET), polycarbonate (PC), polyimide (Kapton), polypropylene, poly(vinylidene fluoride), and CR-39 (allyl diglycol carbonate) membranes were already used for this purpose [159]. Because of its high sensitivity to tracking and the mild conditions required for sensitization, PC is the foremost material used for preparing commercial track-etched membranes (Osmonics or Whatman), with pore diameters ranging from as small as 10 nm to as large as 10 μm and pore densities between 10^7 and 10^9 pores/cm².

To prepare such templates, damage tracks in the polymer film are created with high-energy particles (atoms or ions) and a treatment time that finally influence the number of tracks and the resulting pores. Afterward, the tracks are exposed to an alkaline etching solution, resulting in porous membranes whose dimensions depend strictly on both the etching time and the solution composition [160,161]. Depending on the etching conditions, typical pores with symmetrical cylindrical or cigarlike shape can generally be produced. Under conditions of asymmetric etching (i.e., by treating one side of an ion-irradiated sample with an etchant), conical pores have been produced [162–164] on PC or PET membranes.

Track-etched membranes have a much lower pore density (on the order of 10^9 pores/cm²) than the alumina membranes (10^{11} pores/cm²); therefore, the former are more suitable as templates for producing low-density nanomaterials. The case of nanoelectrode ensembles is discussed in the following sections as an example whereby a relatively low density is required. A limitation of track-etched membranes is related

solely to their production techniques, which do not generate uniform products. As a matter of fact, unless special and accurate procedures are accomplished, the resulting pores in PC membranes are not always parallel to each other, presenting an irregular shape and random spatial distribution.

13.3.1.2 Deposition of Metals in Porous Templates Deposition of metals has been attempted successfully on alumina, silica, and track-etched polymer membranes in a variety of ways. Metal deposition has been accomplished electrochemically in the pores of the membrane, on the side that has been treated with a conductive layer (typically, 100 to 1000 nm) [165–182]. This approach is based on the assumption that template membranes are robust enough to tolerate hard treatment, such as plasma or vacuum deposition. In such experiments, the coated pre-sputtered thin layer is connected to a copper wire and set into an electrochemical cell, where the template membrane acts as the cathode and an external counter electrode acts as the anode. The deposition can be carried out both under galvanostatic or potentiostatic conditions. Literature data report gold electrodeposition into alumina, mica, or PC templates in the form of nanowires or nanorods [183–186], as well as deposition of silver, cobalt, nickel, copper, and rhodium nanowires [187–189], iron nanotubes, or cigar-shaped nanoparticles into polymers [168,190], and palladium, platinum, and tin nanoparticles or single-crystal nanowires into both alumina and PC [191–193]. In the case of a track-etched PC membrane, it was verified that addition to the plating solution of 1 to 2% gelatin generally improves the hydrophilic properties of the membrane with an effective increase in the reproducibility of electrodeposition [166]. Metal sputtering was first necessary to create the conductive layer. The subsequent process is based on the progressive growth and filling of the pores, from the bottom metallic layer toward open ends of the pores, which normally results in solid rather than hollow nanostructures (i.e., formation of nanowires or fibers, not tubes) [153,194,195]. Alternative to the deposition of single metal in the form of continuous nanowires, segmented nanoparticles or composed multilayered nanofibers with different metals can be created as well. In the latter case, the growth of nanofibers consisting of the same metal of the conductive layer is in some way limited by the electrodeposition of a second metal. The original metal foundation is etched away in a following treatment, leaving the nanoparticles composed of the second metal in the pores of the template. Such a formation must be performed with a removable metal instance (e.g., silver is attached by nitric acid) that acts as a foundation for the metal to be deposited in the second step [196,197].

Most experimental methods for the electroless deposition of metals in the form of nanostructures involve the presence of chemical reducing agents to plate the material from a solution onto a surface. The low kinetics of the homogeneous electron transfer from the reducing agent to the metal requires a catalyst, which should be applied to the surface to be coated to accelerate the reaction rate. The thickness of the metal film deposited can be controlled by modulating the plating time. The principles of electroless deposition into templates have been exemplified in the case of gold deposition by Menon and Martin for the fabrication of nanotubes or nanoelectrode ensembles [25]; the specific case is described and discussed extensively in the following sections.

Different from the electrochemical procedure, the electroless methods with templates allow for the deposition of metal layer into the activated sites on the pore walls without requiring a conducting layer. Nanomaterials tend to grow progressively from the pore walls toward the center of the cavity. For this reason, stopping the deposition at relatively short times, hollow metallic nanostructures can be generated into the template. In fact, it was observed experimentally that the production of gold nanotubes is realized, decreasing as much as possible the size of the metal grains that constitute the walls: for example, working at a pH condition of around 8.0 in the deposition bath [153].

After completion of the metal deposition, the template membranes can be used in the original form, containing nanostructured metal, or alternatively, they can be dissolved to leave arrays of nanowires or nanotubes attached at one end to a conductive electrode. In the former case, it is possible to obtain separation membranes with metallized nanopores that enable chemical functionalization of metal for different purposes: One of the most diffused examples in surface chemistry for biosensing applications utilizing thiol chemistry [196,198]. As will be shown in the following discussion, metal nanowires need to be deposited and kept inside the membrane to obtain a continuous ensemble of nanoelectrodes.

If the resulting objects of the deposition are going to be free nanostructures in the form of nanowires, nanotubes, or nanocones, their separation from the host membrane is required. Nanomaterials may be separated from track-etched template by dissolving the latter in a suitable organic solvent: PC membranes are soluble in dichloromethane, and PET in 1,1,1,3,3,3-hexafluoro-2-propanol. Alumina-ceramic membranes are shown to be soluble in strong alkali solution (such as KOH or NaOH), whereas polymers can also be etched by oxygen plasma treatment [25,153,168]. A criterion for the selection of the most suitable template may sometimes lie on the compatible matching between the metal to be deposited and the agent able to remove the membrane. Other *hybrid* deposition techniques, including metals and composites into host templates, are not investigated further in this chapter. It is the case of the chemical deposition of carbon-gold composite nanotubes in alumina templates by impregnation with a solution of diluted hydrogen tetrachloroaurate (HAuCl_4) and acetone as reducing agent [197], as well as the intriguing synthesis of nanoparticle nanotubes inside the pore walls of silane-treated alumina, according to a self-assembly mechanism [199], or the formation of gold nanotubes by RF sputtering of gold into nanoporous template [200].

13.3.1.3 Characterization of Nanomaterials in Porous Templates The characterization of such nanostructures can be done by several instrumental techniques, including spectrophotometry (optical features are useful for defining the shape and spatial distribution of the nanostructures), voltammetry, optical microscopy, atomic force microscopy (AFM), and scanning (SEM) or transmission electronic microscopy (TEM).

SEM or TEM analyses (and to a lesser extent, microthomy analyses) are typically used in morphological characterization of nanostructured materials obtained by template synthesis. The image resolution generally tends to improve as the nanomaterial

is separated from the host membrane. In this case microscopic investigations have shown curious mushroom shapes, or spaghetti-like metallic nanostructures after removing the PC membrane with the suitable organic solvents [25,168,171]. TEM and high-resolution TEM images of nanostructures were also obtained even without removal of the membrane, owing to the transparency of PC to electron beams, although possible interactions between the beam and the polymer can generate distortions and artifacts [25,153,201].

13.3.2 Gold Nanoelectrode Ensembles

The gold electrode has often been used as a transducer in electrochemical biosensors for several good reasons. One of the most intriguing characteristics, which is important in using functionalized surfaces for biosensing purposes, is the tendency to form self-assembled monolayers or deposited multilayers through thio- or amino-coordinate derivatives.

Nanoelectrode ensembles (NEEs), fabricated by growing metal nanowires or fibers into the pores of a template, are nanotechnology tools that actually find application in a variety of fields, ranging from electroanalysis to sensors and electronics. Here we describe the synthesis of gold nanowires into PC membranes with controlled pore size using an electroless deposition method. The density of the template nanopores determines the number of nanodisks per total surface (pores/cm²) and, correspondingly, the average distance between the nanowires, as the basic elements of NEEs.

The production of gold NEEs described here is based on the pioneering work of Martin's group [25], recently modified in order to optimize the resulting product and to obtain a well defined-nanostructure for the specific application. In brief, the electroless plating of gold NEEs consists of three main steps:

1. *Sensitization* with Sn²⁺ solution. PC is first kept for 2 hours in methanol, then immersed for 45 minutes in a solution of 0.026 M SnCl₂ and 0.07 M trifluoroacetic acid in equimolar mixture of methanol and water as the solvent; as reported previously, track-etched PC membranes are preferred for NEE fabrication over alumina membranes because of their smaller pore densities and their lower fragility.
2. Reduction of Ag⁺ to produce discrete silver nanoparticles. After accurate rinsing with methanol, the sensitized membrane is immersed for 10 minutes in 0.029 M Ag [(NH₃)₂]NO₃ at controlled pH.
3. Galvanic displacement of silver particles and reduction of gold. The membrane is immersed into the gold plating bath, which contains a commercial solution of 7.9 × 10⁻³ M Na₃Au(SO₃)₂ (e.g., Oromerse Part B, from Technics Inc.), 0.127 M Na₂SO₃, and 0.625 M formaldehyde; after 15 hours of electroless deposition, an additional 0.2 mL of formaldehyde is added to continue the deposition for an additional 9 hours; after that the membrane is rinsed with water, immersed in 10% HNO₃ to eliminate any surface traces of tin or silver, and dried in an oven at 150°C to stabilize the resulting deposition. It was already observed that depending on the mechanism of growth of such nanostructures into the pores, at short plating

times only gold nanotubes are formed, whereas complete filling of the pores to accomplish gold nanowires requires 24 hours or more of electroless plating [25]. Another interesting observation is that the deposition velocity decreases when performing the overall process at a temperature between 0 and 5°C. The original synthetic route was tested during the last years by varying the treatment time or the reagent concentration for surface activation both in SnCl₂ solution and in ammoniacal AgNO₃ for silver nanoparticle deposition. Basically, the key step of the synthetic procedure results in immersion of the membrane in a gold plating solution. Gold nanotubes or nanocones [162,163,196,202,203] were also fabricated by adopting a different treatment time under buffered controlled conditions (pH 10). From our practical experience, even AuCl₄⁻ as a precursor can be used instead of the commercial solution of Na₃Au(SO₃)₂: after 24 hours of immersion at 4°C, gold NEEs in the nanopores of track-etched PC membrane (nominal pore size 30 nm, thickness 10 μm, pore density 6 × 10⁸ pores/cm²) were created successfully. Both the front and rear sides of the membrane are coated with a thin gold layer.

13.3.2.1 Morphological Features of Gold Nanoelectrode Ensembles

SEM observations such as the one reported in Figure 13.2 show the successful formation of gold nanowires in PC membranes with a narrow size distribution and a mean diameter of 30 nm, adopting the synthetic method described above. A SEM model (JEOL JSM-5510) was used for the characterization of nanowires reported in Figure 13.2. The microscope is equipped with an Oxford Instrument EDS 2000 microanalysis detector and software for the elementary analysis. No sample coating was required for SEM observations. The image was obtained after peeling away the metal layer grown over the front side of the template membrane. Nanodisks emerging from the template are clearly visible from the figure, with the typical fading lines

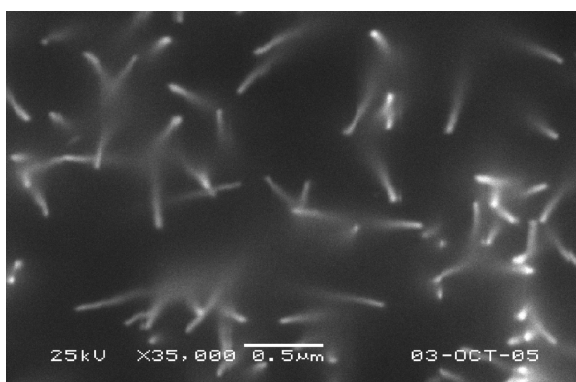


FIGURE 13.2 SEM image of gold nanoelectrode ensemble grown into polycarbonate nanoporous membrane (from Unipore), according to the electroless procedure; nominal pore size: 30 nm; pore density: 6 × 10⁸ pores/cm²; the scanning electron microscope was the JEOL JSM-5510 low-vacuum model.

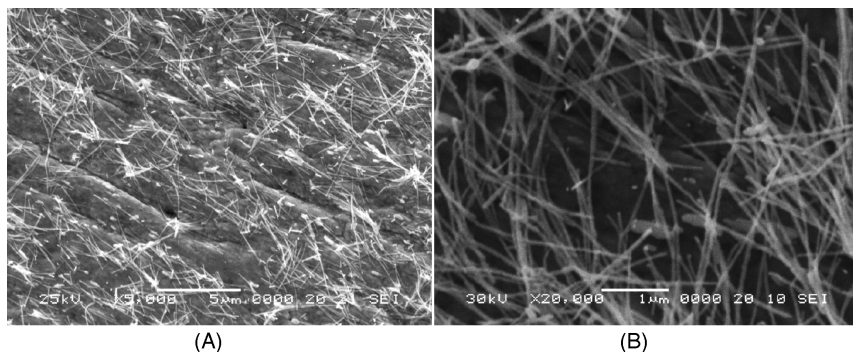


FIGURE 13.3 SEM image of gold nanoelectrode ensemble by electroless synthesis after dissolution of the polycarbonate template membrane (from Unipore) with dichloromethane. Images taken at two different magnifications: (A) energy beam, 25 kV; scale bar, 5 μm ; magnification; 5×10^4 ; (B) energy beam: 30 kV, scale bar: 1 μm , magnification: 2×10^5 . The Scanning electron microscope was the JEOL JSM-5510 low-vacuum model.

behind them representing traces of the nanofibers that grew inside the membrane. The observation of such traces is possible for two main reasons: First, the PC membrane is partially transparent to the electron beam; and second, the nanofibers are not perfectly aligned parallel to the surface as a consequence of the membrane production procedure [25,153,166]. The density of deposited nanowires can be calculated approximately from a sample microscopy image, taking into account a defined area of investigation. For instance, since an area of $9 \mu\text{m}^2$ is considered in Figure 13.2, a nanowire density of around 6 pores/ μm^2 has been inferred. Such a value is perfectly in accord with the declared pore density of commercial membrane, confirming that the process of filling pores with gold had been accomplished successfully. NEE can be used either as a platform for immobilization of biomolecules (i.e., including nanostructures into the host membrane) or as a free-standing assembly of very small ultramicroelectrodes confined in a rather small space. In the former configuration higher mechanical stability is accomplished, owing to the presence of the membrane; hence this is the preferred configuration for biosensing purposes. On the contrary, after membrane dissolution, a simultaneous process of nanowires or fiber self-aggregation and folding down takes place, with a possible partial loss of their electrochemical properties. Figure 13.3 shows two SEM images at different magnifications of gold nanostructures (mean diameter size of 50 nm) after dissolution of the template membranes with dichloromethane. Bundles of nanowires or disordered nanosized structures are still visible on the treated surface instead of free-standing aligned gold nanofibers.

13.3.2.2 *Electrochemical Features of Gold Nanoelectrode Ensembles*

An accurate description of the electroanalytical and kinetic behavior of NEE is beyond the scope of this chapter, but readers are referred to work of Ugo and moretto [153], an updated and complete treatment of such objects, including evaluation of the main

geometrical parameters involved, their relationships with current responses, and the corresponding electroanalytical equations. We will simply review briefly the general concepts with respect to the behavior of NEE.

NEE can exhibit three distinct voltammetric response regimes, depending on the scan rate and reciprocal distance between the nanoelectrode elements, which is a function of the pore density of the template. The total overlap regime occurs when radial diffusion boundary layers of each single nanodisk overlap totally (a small distance between nanoelectrodes), a pure radial regime occurs when the nanoelectrodes behave independently (higher scan rates, larger distances between nanoelectrodes), and a linear regime occurs when the nanoelectrodes behave as isolated planar electrodes [25]. It was demonstrated that for electroanalytical applications the total overlap regime is the most advantageous because of the higher faradaic/capacitive current ratio [153,204,207], which was calculated to be higher than the ratio of conventional electrodes (CGE) to the comparable geometrical area. This concept is reported as

$$\left(\frac{I_F}{I_C}\right)_{\text{NEE}} = 10^2 \div 10^3 \left(\frac{I_F}{I_C}\right)_{\text{CGE}} \quad (13.1)$$

where I_F is the faradaic current and I_C is the double-layer charging current. The numerator of both ratios can be calculated from the Randles–Sevcik equation:

$$I_F = 2.69 \times 10^5 n^{3/2} A_{\text{geom}} D^{1/2} C_b \nu^{1/2} \quad (13.2)$$

where n is the number of electrons involved in the process, A_{geom} the geometric area of the ensemble, D the diffusion coefficient, C_b the bulk concentration of redox substance, and ν the scan rate of the voltammetric cycle. The denominators for nanostructured and conventional electrodes depend, respectively, on the active and geometric areas of the ensemble. Indicating the ratio between active and geometric areas as [207]

$$f = \frac{A_{\text{act}}}{A_{\text{geom}}} \quad (13.3)$$

the application of Randles–Sevcik equation on both the systems results in a coefficient f spanning from 10^{-3} to 10^{-2} , which means that for NEEs, detection limits are at least two orders of magnitude lower than those of regular electrodes. The I_F/I_C ratios or, alternatively, the coefficient f are useful to discriminate the good NEEs for electrochemical biosensing applications from the bad ones [205,207,209].

In our laboratory, the total overlap diffusion regime was observed at gold NEEs fabricated from commercial PC track-etched membranes of 30- and 50-nm pore diameter. The large number of NEEs which were prepared according to the electroless procedure were selected on the basis of the electroanalytical response and the agreement between theoretical and experimental values [153]. For this purpose, a reversible redox probe with a known diffusion coefficient must be studied at defined experimental conditions (e.g., measuring the current peaks in CV at a fixed scan rate and potential step). The theoretical ratio, $(I_F/I_C)_{\text{theor}}$, depending on

well-defined equations was compared with the experimental one, $(I_F/I_C)_{\text{exp}}$. Values must be in accordance with a tolerance of 5%.

As a redox substance, α -(ferrocenylmethyl)trimethylammonium cation was selected, analogously with previous work [153,204,207], because of its well-known behavior. Cyclic voltammograms in 10^{-2} M NaNO₃ as supporting electrolyte alone and in 10 μ M of redox probe were recorded. It was calculated that NEEs satisfying the foregoing criteria are not more than 50% of the overall NEEs prepared in the laboratory.

The reachable potential window for gold NEEs was studied previously [25,206] both in the negative limit, which is influenced by the hydrogen evolution reaction and therefore depends on the solution pH, and in the positive potential range, which is given by the formation of gold oxide. The NEEs used at low analyte concentrations (typically, from 10 μ M to lower than 1 nM) gave a peak faradaic current down to a few picoamperes. By operating with suitable electronic amplification levels, at pH around 7 and micromolar analyte concentrations, a potential window of gold NEEs was found between -750 and $+800$ mV vs. an Ag/AgCl reference electrode [153]. Such a wide electroactivity range as well as the high sensitivities of NEEs to electron transfer kinetics are interesting characteristics that are being exploited in highly sensitive analytical techniques, such as in trace metal determinations and the observation of species with perfectly reversible and fast electrochemical behavior. To the best of our present knowledge, the electrochemical features of the metal nanomaterials, excepting gold grown in nanoporous templates, have not been so deeply investigated. In addition to applications for trace electroanalysis with well-known reversible redox probes, such as ferrocene derivatives or ruthenium complexes, NEEs were used in CV at micromolar concentration levels of more complex redox systems such as organic mediators or methylviologen or heme-protein cytochrome c [204,206,207].

13.3.2.3 Deposition of Nanoelectrode Ensembles on Substrates So far, a limited number of publications report the attempt to assemble NEE in handy electrodes for use in an electrochemical cell or in flow injection analysis (FIA) systems. Early assembly based on gold nanoelectrodes consisted of a copper tape that was attached directly to the upper gold layer, acting as electrical connections. After insulating this multilayer configuration, a hole was punched into the upper piece of insulating tape to define a geometric area, A_{geom} , of 7.0 mm² [25,204,207]. Recently, partial modifications have been carried out to improve the electrical connection between copper and NEE: The copper tape was attached on the lower layer, which completely covers the rear side of the host membrane. The upper gold layer was peeled away from the membrane and an insulator with a 7.0-mm² hole was attached [204,208,209].

In our laboratories, gold nanowires have been coupled with a carbon screen-printed electrode (SPE) to give a novel, rapid tool for disposable biosensors, defined as a nanoelectrode ensemble on a screen-printed substrate (NEE/SPS). The NEE/SPS preparation is aimed at combining the advantage of the electroanalytical sensitivities deriving from the nanosized properties with the feasibility and versatility of screen printing technology in fabrication of easy-to-use sensors [210–212].

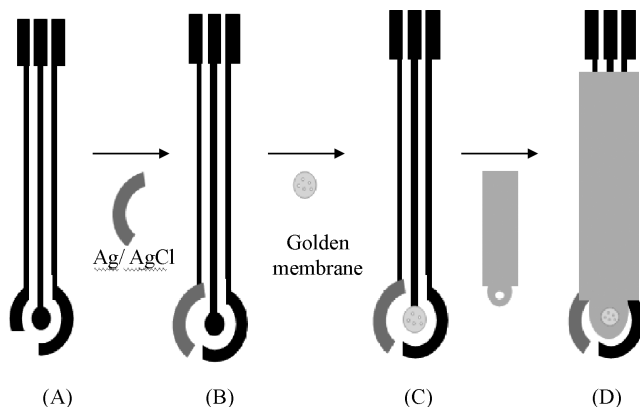


FIGURE 13.4 Sequence of NEE/SPS preparation: (A) carbon graphite tracks and contact pads by screen printing; (B) Ag–AgCl paste deposition for reference electrode; (C) deposition on the working of the NEE-based membrane; (D) dielectric paste screen printing. (From ref. 198, with permission.)

For the preparation of SPEs, conducting and insulating inks were printed on poly (vinylchloride) substrate using a HT10 Fleischle screen-printing machine [198,212]. Silver and carbon–graphite pastes for the conducting paths and the working electrode, Ag/AgCl for the reference electrode, and dielectric pastes were purchased from Gwent Electronics Materials Ltd. (www.g-e-m.com).

To assemble gold nanoelectrodes containing membranes with screen-printed substrates, the upper gold layer was first peeled away from the front side of an NEE membrane, leaving the gold nanodisks exposed on the surface. The rear side has been soaked into a wet graphite ink pad; then the inked membrane has been gently deposited onto the graphite WE of a plastic homemade screen-printed substrate [198]. As commonly used in screen-printing procedures, the device has been accomplished by printing both the insulator and the reference electrode layer. Figure 13.4 shows the described above novel screen-printing sequence for the production of disposable NEE/SPS. In each case, an active working electrode area of 2.5 mm^2 is defined by the insulator geometry. Also, NEE/SPS were tested with α -(ferrocenylmethyl)trimethylammonium cation by CV at different scan rates and different concentrations. Typical voltammetric patterns of such a redox tracer on NEE/SPS recorded at 100 mV/s showed quasireversible behavior with an anodic peak (I_p) at $150 \pm 10 \text{ mV}$ and a cathodic peak at $-20 \pm 1 \text{ mV}$ [198]. According to the characteristic of nanoelectrodes under total overlap diffusional regime, peak currents of the redox probe were 2 orders of magnitude higher than in the case of conventional macro-electrodes.

13.3.3 Nanoelectrode Ensemble for Enzyme-Based Biosensors

13.3.3.1 State of the Art Selective, sensitive, and accurate quantification of a specific analyte or group of analytes is the key requirement in many areas of analytical and bioanalytical chemistry, such as for clinical, agricultural, and environmental

analysis, as well as in the food and beverage industries. To be used as a reliable analytical tool complementarily with traditional chemical methodologies (such as colorimetric, spectroscopic, chromatographic, or hyphenated methods), biosensors must provide high performance levels with good accuracy, precision, and long-term stability for simple, rapid, online or in situ measurements.

The very promising feature of gold nanoelectrodes applied for electrochemical biosensors is their enhanced current sensitivity, as described in previous sections and expressed in equation (13.1). The sensitivity ratio between NEEs and conventional macroelectrodes with comparable geometric area and materials has already been indicated as the discriminating parameter in the selection of nanostructures for biosensing applications. This might result in a lowering of the detection limit during the bioanalytical monitoring of a specific analyte.

On the other hand, as shown in the following discussion of results, this advantage arising from the nanoparticles properties is not always maintained when biochemical immobilization is performed on the electrochemical probe. The complexity of structures such as proteins, cells or biomimic compounds, and the multiple layers accumulated on the original surface, are the characteristics that limit the resulting performance of electrochemical biosensors based on such nanoparticles.

NEEs were already used as a working probe on a copper, glassy, or carbon–glassy electrode for the detection of various substances. The model system used for preliminary investigation in a reliable electrochemical biosensing device was the enzyme glucose oxidase (GOx), whose structure and biochemical properties are well known. In recent work, gold NEEs were treated with ultraviolet–ozone and ethanol to remove any oxide deposit before the monolayer assembly, Then the surface was treated with thiols to form a SAM, and successively with coupling agents for enzymatic immobilization. After treatment with 3-mercaptopropionic acid and 2-mercaptoethylamine as thiol compounds, the functionalized surface was immersed, respectively, in glutaraldehyde (GA) in phosphate buffer solution (PBS) and a mixture of imides at pH 3.5 [213]. Two different flow detectors with a commercial glassy carbon working electrode were utilized for the amperometric detection of β -glucose with an injection loop of 100 and 20 μ L, respectively. After the optimization of the electrochemical and flow parameters, the authors compared the amperometric FIA response in terms of sensitivity, reproducibility, and stability for both GOx-based biosensors, distinguishing between the two different covalent immobilization of the enzyme (i.e., using glutaraldehyde and succinimide as coupling systems). A linear dependence of glucose on the signal in the analytical concentration range 0.2 to 30 mM was detected, even in the presence of interfering substances [214].

13.3.3.2 Nanoelectrode Ensemble on Screen Printed–Based Biosensors Our contribution to the development of biosensors based on nanoscale material relies on a combination of screen-printed substrates and gold NEEs, resulting in NEE/SPS biosensing devices, as reported previously and illustrated in Figure 13.4. The aim of this preliminary work was to evaluate the specific response to a target substrate after immobilization of the corresponding enzyme on NEE/SPS. GOx (from *Aspergillus niger*; specific activity of 198 units/mg solid) was again used as a biochemical model

system to test the feasibility of the sensing probe. The analytical performance of NEE/SPS-based biosensors tested under FIA conditions was evaluated and compared to that of unmodified carbon or conventional gold electrodes on which GOx is immobilized at a fixed concentration.

For this purpose a homemade flow cell was used for the characterization of NEE/SPS and successively for the amperometric detection of glucose with a GOx-based biosensor. The microcell was depicted and described in our previous work [198] and was provided with a peristaltic pump (Gilson Minipuls 3) to propel solution along a flow injection system, with a 115- μ L sample loop injection valve and volume (Omnifit, Cambridge, England). All reagents, supporting electrolyte solutions, and buffer carriers were prepared from deionized water (Synergy 185 apparatus from Millipore). All the other analytical-grade chemicals and solvents were used without further purification. Voltammetric and amperometric measurements, performed under batch and FIA conditions, respectively, were conducted with the Autolab potentiostat PGSTAT10. Two experimental methodologies [198] were chosen for the immobilization of GOx on a gold element that can be simplified as described below.

Covalent Immobilization of Protein In the former device the sequence is based on three main steps (Figure 13.5). First, 3-amino-mercaptopropionic acid, also called cysteamine (CYS), was assembled on gold nanodisks either electrochemically (20 s of 21-mM CYS growth at +800 mV vs. internal reference electrode) or chemically (after immersing the NEE/SPS in a solution of 21 mM CYS for 16 hours). The electrochemical deposition of CYS has already been demonstrated to be much faster and more effective on pure gold electrode than on other materials, resulting in electrochemically deposited multilayers (EDMs) [215] on whose upper surfaces are available terminal amino groups ($=\text{NH}_2$). For this reason, GA (12.5 % v/v, 1 hour of immersion) was chosen as the coupling agent in the second step, followed by accurate buffer washing to remove the excess GA. Finally, buffered GOx solution (6 mg/mL) was dropped on the activated surface and left to dry, allowing for the formation of a covalent bond between the primary amine groups of the enzyme and the carbonyl group of GA. The resulting sensor was washed and stored overnight at 4°C before being assayed. In the following discussion this sensor configuration is referred to as GOx/EDM/NEE/SPS.

Parallel Immobilization of Protein and Deposition of Conductive Polymer In this device, spatial patterning of the enzyme on PC membrane with conductive wires on gold nanoelectrodes has been carried out. In this way, direct electron transfer from the red-ox site of the enzyme to the electrode along the conductive polymer multilayer will be accomplished. As depicted in the sequence shown in Figure 13.6, first, conducting cables of polyaniline (PANI) were deposited electrochemically by cyclic voltammetry from -0.4 to +1.0 V, using as a precursor 50-mM aniline solution in diluted sulfuric acid (0.5 M) [198]. The growth of PANI wires on the gold nanostructures can be realized after a few cycles, analogous to that demonstrated on golden macroelectrode and other surfaces [216–218]. The active surface was immersed in a solution of 10% v/v aminopropyltriethoxysilane (APTES), to obtain a

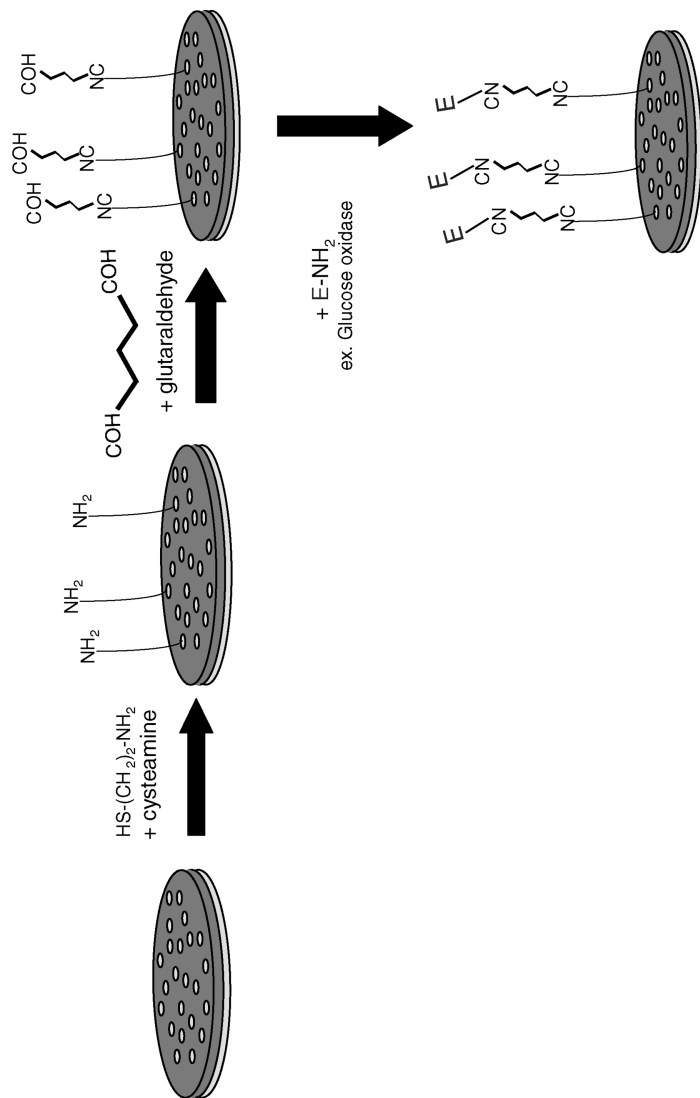


FIGURE 13.5 Covalent enzymatic immobilization via cysteamine (3-aminomercaptopropionic acid) and glutaraldehyde on gold nanoelectrode ensemble/screen-printed substrates; the distance of the gold nanodisks and the dimensions of the objects are not in scale.

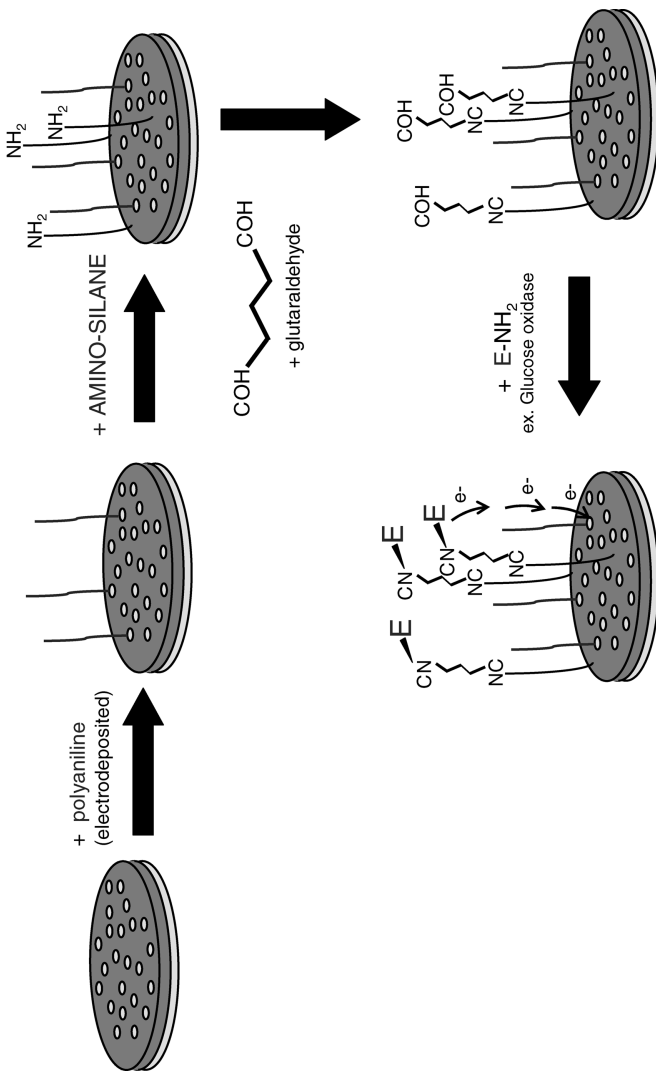


FIGURE 13.6 Enzymatic immobilization (via aminopropyl triethoxysilane/glutaraldehyde) on a polycarbonate membrane with parallel electrodeposition of conductive polyaniline (red wires) on gold nanoelectrodes; the distance and dimensions of the objects are not in scale.

terminal amino group onto the part of the membrane that is not gold-covered, then washed carefully with PBS (pH 6.8). The resulting surface was treated with GA (12.5% v/v) and again washed with PBS to remove the unbound GA. At this step, free carbonyl groups facing the PC surface are ready to react with the terminal amino groups of the enzyme. Freshly prepared GOx-buffered solution (6 mg/mL) was dropped on the activated surface and left to be covalently bound. In the following this sensor configuration is referred to discussion as GOx/PANI/NEE/SPS [198].

The effectiveness of the electrodeposition of multilayers of CYS was proven by the cyclic voltammograms and the corresponding oxidation peaks centered at approximately +800 mV vs. internal Ag/AgCl reference electrode, which decreases after a few scans in the case of both gold SPEs [215] and gold NEE/SPS [198]. Chronoamperometry current response corresponding to the oxidation of CYS on the surface was therefore carried out at +800 mV vs. internal Ag/AgCl pseudo-reference electrode. As shown in Table 13.1, the average peak for CYS grown on NEE/SPS is compared with CYS deposited on gold screen-printed probes, applying the oxidation potential of +800 mV vs. platinum reference electrode in a two-electrode configuration. The current signal for CYS deposited on NEE/SPS is two orders of magnitude lower than in the case of gold macroelectrodes obtained by galvanic deposition [column (a) of Table 13.1]. On the other hand, considering the active area, taking into account the gold nanodisk density and the area of a single nanodisk, calculations of current density show higher values for nanostructured assembly [column (e) of Table. 13.1, where current density is expressed in mA/cm²]. Two different diameters

TABLE 13.1 Mean Peak Currents for the Electrochemical Oxidation of Cysteamine for Several NEE Assemblies Using a Commercial Gold Electrode, Conventional NEE, and NEE/SPS^a

Electrode Probe	(a) Peak Current I_p (μ A)	(b) Geometric Area (cm ²)	(c) Conversion Factor	(d = bxc) Active Area (cm ²)	(e = a/d) Current Density (mA/cm ²)
Au	625.0	0.143	1.1330 ^b	1620.00 $\times 10^{-4}$	3.86
Au NEE [25,204,209]					
Pore diameter 30 nm	0.5	0.071	0.0042 ^c	3.07 $\times 10^{-4}$	1.66
Pore diameter 50 nm	0.5	0.071	0.0118 ^c	5.95 $\times 10^{-4}$	0.60
Au NEE/SPS [98]					
Pore diameter 30 nm	1.5	0.025	0.0042 ^c	1.08 $\times 10^{-4}$	14.15
Pore diameter 50 nm	1.5	0.025	0.0118 ^c	2.10 $\times 10^{-4}$	5.09

^aTwo different pore diameters (therefore, diameters of a single nanoelectrode) are considered. Cysteamine oxidation performed at +800 mV vs. Pt in a two-electrode configuration.

^bDimensionless, rugosity factor = A_r/A_g , the ratio between the real and the geometric surface areas of the gold electrode used [198].

^cDimensionless, f = fractional area = A_d/A_g , the ratio between active and geometric areas of NEEs, calculated assuming a pore diameter of 30 nm as reported by the producer, or a pore diameter of 50 nm, the mean value calculated from SEM measurements.

of a single nanoelectrode, depending on the pore diameter size of the host template, have been considered in such an evaluation.

13.3.3.3 Analytical Performance of NEE/SPS-Based Biosensors In both sensor configurations the flow injection conditions described above were optimized experimentally for the highest current signal. The working flow rate (0.4 mL/min) and buffer pH (6.8) were fixed in both cases by using a homemade flow-through detection cell and 115- μ L sample loop injection valve.

An unmodified NEE/SPS did not respond to glucose, confirming that a specific oxidation of the substrate/analyte at the gold surface did not occur. Since the best signal/noise ratio was achieved within the range +550/650 mV [198], an applied potential value of +600 mV vs. reference electrode was chosen for such sensors in all subsequent experiments.

In Table 13.2 the analytical performance of our sensor configurations (both GOx/EDM/NEE/SPS and PANI/GOx/NEE/SPS) is summarized while comparing such performances with those of an available reliable biosensing device for glucose detection [214] based on gold NEE (renamed GOx/GA/MPE/NEE in Table 13.2). An analog comparison has been made under flow conditions with a biosensor for glucose based on a commercial ceramic screen-printed electrode (BVT Technologies, Czech Republic), adopting one of the immobilization procedures for GOx on a golden working probe (herein indicated as GOx/CYS/Au SPE).

The linearity of response were found to be 1.0×10^{-4} M to 3.1×10^{-2} M ($r^2 = 0.993$) for GOx/EDM/NEE/SPS and 1.0×10^{-4} M to 2.0×10^{-2} M ($r^2 = 0.998$) for PANI/GOx/NEE/SPS. It is interesting to observe that the lower limits are always

TABLE 13.2 Analytic Performance of Four Gold-Based Biosensor Configurations for the Detection of Glucose

	GOx/GA/ MPE/NEE ^a	GOx/EDM/ NEE/SPS ^b	PANI/GOx/ NEE/SPS ^c	GOx/CYS/ Au SPE ^d
Range explored (mM)	Not reported	0.0075–31	0.019–20	0.2–20
Linearity range (mM)	Up to 30	0.1–31	0.1–20	1–20
Sensitivity (nA/mM ⁻¹)	110	35	18	0.9
Reproducibility (%) ^e	3.7 ($n = 38$)	3.9 ($n = 35$)	4.4 ($n = 35$)	14.2 ($n = 28$)
Detection limits (mM)	0.20	0.15	0.15	1.00
$K_{m(\text{app})}$ (mM)	13.7	14.9	8.9	Not measured
Shelf stability (days)	Not reported	20	15	2

^aEnzyme covalently immobilized on gold nanoelectrodes by means of a mercapto-compound coupling agent [214].

^bEnzyme covalently immobilized via cysteamine electrodeposited multilayers and glutaraldehyde on a gold nanoelectrode ensemble sensor.

^cEnzyme covalently immobilized via aminopropyltriethoxysilane and glutaraldehyde, with polyaniline grown on gold nanodisks.

^dEnzyme covalently immobilized via electrodeposited cysteamine on a commercially available gold screen printed electrode (BVT Technologies, Czech Republic).

^e0.5 mM glucose injected n times.

within the analytical range for glucose monitoring in a blood sample. At higher glucose concentration values, saturation of enzymatic active sites probably takes place. The linearity can be estimated by using the Michaelis–Menten equation with nonlinear curve fitting: Apparent constants of 14.9 and 6.9 mM were obtained for GOx/EDM/NEE/SPS and PANI/GOx/NEE/SPS; respectively. These values are, as expected significantly lower than those of the native enzyme [219].

Sensitivity (the slope of the calibration curve) and LOD by the Zund Meier method [220] as well as operational and shelf stability are reported in Table 13.2 according to the international definitions recommended [221,222]. The long-term stability in FIA conditions achieved for PANI/GOx/NEE/SPS biosensor suggests that chemical covalent immobilization of enzymes on the surface took place. This observation is an encouraging result in assessing the specific reaction between the silane-derivative compound and PC and, consequently, the selective addressable immobilization of proteins only onto the polymer part of the membrane.

The amperometric FIA responses were also compared for both sensors at the concentration level 0.5 mM glucose. The plots have been normalized in terms of the current peak height for both sensor configurations; the PANI/GOx/NEE/SPS sensor showed a faster response, which depends on a more effective charge transfer to the electrode along the PANI wires (for a graph, see ref. 198). In each case, when using PANI wires with covalent immobilization of GOx, performance improved in terms of the linear dynamic range, reproducibility (4.4% of relative standard deviations), and LOD.

Finally, it is worth noting that a comparison of the features of bare NEE or NEE/SPS (usually selected by their performances operating in CV) with those of the enzyme-based NEE or NEE/SPS biosensors under amperometric flow measurements are meaningless. As mentioned earlier, the effect of nanostructured surface properties in terms of a high signal/background ratio requires further investigation whenever the same nanosized component is implemented in a more complex configuration such as that of biosensing devices. The combination of diffusion pathways at the NEE and flow lines under the constrained geometry of a thin-layer flow detection cell should be envisaged as well.

13.4 CONCLUDING REMARKS

A remarkable example of the integration of nanotechnology and electrochemical biosensors is the NEE enzymatic-based biosensor, in which nanoelectrode ensembles synthesized by templates are deposited on several supports. Implementation of a novel disposable device based on a nanoelectrode ensemble on screen-printed substrate has been shown. In this way, the well-known advantages of nanostructured material properties (e.g., high sensitivity) have been coupled with the typical features of thick-film technology in screen-printing production, such as disposability, flexibility, and durability of the product under flow injection conditions. The electroanalytical properties of NEEs have been studied extensively and considered as a basis for the realization of NEE/SPS-based biosensors. Exploitation of nanosized surfaces to enlarge the range of such possibilities is discussed, especially for the enhanced

signal/background ratio of the gold nanoelectrode assembly (from two to three orders of magnitude higher than that of a conventional macroelectrode with a comparable geometric area).

Immobilization techniques of a model protein (e.g., glucose oxidase) have been presented in association with the formation of self-assembled monolayers and electrochemical-deposited multilayers. The concept of reversible, oriented, and addressable immobilization of special proteins on specific parts of the active sensing surface has been also recalled.

Simple enzyme immobilization on gold NEE and NEE/SPS by means of commonly used coupling agents or, more specifically, parallel immobilization of enzyme on the polymeric part of the membrane and polyelectrolyte on gold nanostructures has been carried out. The latter solution has been extended in some applications for third-generation biosensors, in which a mediatorless detection is required, thanks to the possibility of achieving a direct electron transfer between red–ox proteins and modified gold nanoelectrodes through the conducting polymer cables. A model protein was used to show the feasibility of such an approach to activate the surface with a specific biomolecule for the detection of an analyte or a class of analytes in many electrochemical biosensing applications, such as in the food or beverage industries or for environmental and clinical analyses.

Furthermore, the perspective of efficient parallel immobilizations on metal areas and polymeric parts opens the way to multifunctional electrochemical devices with different customized sensitive elements at different points in the same sensor. Multi-parametric electrochemical detection for simultaneous analysis at low cost may be designed insofar as successful and reliable scientific results will be accompanied by the industrial scale-up of such devices.

REFERENCES

1. (a) Nalwa HS, ed. *Handbook of Nanostructured Biomaterials and Their Applications in Nanobiotechnology*. American Scientific Publishers; Valencia, CA, 2005. (b) Guozhong Cao. *Nanostructures and Nanomaterials: Synthesis Properties and Applications* Imperial College Press. London. 2004.
2. Nirmal M, Norris DJ, Kuno M, Bawendi MG, Efros AL, Rosen M. Observation of the dark exciton in CdSe quantum dots. *Phys. Rev. Lett.* 1995;75(20):3728–3731.
3. Alivisatos AP. Perspectives on the physical chemistry of semiconductor nanocrystals. *J. Phys. Chem.* 1996;100(31):13226–13239.
4. Alivisatos AP. Nanocrystals: building block for modern materials design. *Endeavour.* 1997;21(2):56–60.
5. Smalley RE, Yakobson BI. The future of fullerenes. *Solid State Commun.* 1998;107(11):597–606.
6. Bruchez M, Moronne M, Gin P, Weiss S, Alivisatos AP. Semiconductor nanocrystals as fluorescent biological labels. *Science.* 1998;281(5385):2013–2016.
7. Williamson AJ, Zunger A. InAs quantum dots: predicted electronic structure of free-standing versus GaAs-embedded structures. *Phys. Rev. B.* 1999;59(24):15819–15824.

8. Zhong CJ, Zheng WX, Leibowitz FL. Electrode nanomaterials self-assembled from thiolate encapsulated gold nanocrystals. *Electrochem. Commun.* 1999;1(2):72–77.
9. Dubertret B, Calame M, Libchaber AJ. Single mismatch detection using gold-quenched fluorescent oligonucleotides. *Nat. Biotechnol.* 2001;19(4):365–370.
10. Zhang B, Liu C, Cheng HM, Cai QK. Progress in carbon nanotubes filled with foreign substances. *New Carbon Mater.* 2003;18(3):174–180.
11. Lu Q, Moore JM, Huang G, et al. RNA polymer translocation with single-walled carbon nanotubes. *Nano Lett.* 2004;4(12):2473–2477.
12. Guan WJ, Li Y, Chen YQ, Zhang XB, Hu GQ. Glucose biosensor based on multiwall carbon nanotubes and screen printed carbon electrodes. *Biosens. Bioelectron.* 2005;21(3):508–512.
13. Vastarella W, Nicastrì R. Enzyme/semiconductor nanoclusters combined systems for novel amperometric biosensors. *Talanta.* 2005;66:627–633.
14. Gouma P, Kalyanasundaram K, Bishop A. Electrospun single-crystal MoO₃ nanowires for biochemistry sensing probes. *J. Mater. Res.* 2006;21(11):2904–2910.
15. Reches M, Gasit E. Molecular self-assembly of peptide nanostructures: mechanism of association and potential uses. *Curr. Nanosci.* 2006;2(2):105–111.
16. Zhang HM, Quan X, Chen S, Zhao HM. Fabrication and characterization of silica-titania nanotubes composite membrane with photocatalytic capability. *Environ. Sci. Technol.* 2006;40(19):6104–6109.
17. Bavykin DV, Friedrich JM, Walsch FC. Protonated titanates and TiO₂ nanostructured materials: synthesis, properties, and applications. *Adv. Mater.* 2006;18(21):2807–2824.
18. Avouris P, Chen J. Nanotube electronics and optoelectronics. *Mater. Today.* 2006;9(10):46–54.
19. Ago H, Uchimura E, Saito T, et al. Mechanical immobilization of *HeLa* cells on aligned carbon nanotube array. *Mater. Lett.* 2006;60(29–30):3851–3854.
20. Corzilius B, Gembus A, Weiden N, Dinse KP, Hata K. EPR characterization of catalyst-free SWNT and N–C-60 based peapods. *Phys. Status Solidi B.* 2006;243(13):3273–3276.
21. Ponce-de-Leon C, Bavykin DV, Walsch FC. The oxidation of borohydride ion at titanate nanotube supported gold electrodes. *Electrochem. Commun.* 2006;8(10):1655–1660.
22. Chen L, Lu GX. Direct electrochemistry and electroanalysis of hybrid film assembled by polyelectrolyte–surfactant polymer, carbon nanotubes and hemoglobin. *J. Electroanal. Chem.* 2006;597(1):51–59.
23. Penner RM, Martin CR. Preparation and electrochemical characterization of ultramicroelectrode ensembles. *Anal. Chem.* 1987;59(21):2625–2630.
24. Cheng IF, Martin CR. Ultramicrodisk electrode ensembles prepared by incorporating carbon paste into a microporous host membrane. *Anal. Chem.* 1988;60(19):2163–2165.
25. Menon VP, Martin CR. Fabrication and evaluation of nanoelectrode ensembles. *Anal. Chem.* 1995;67(13):1920–1928.
26. Martin CR, Mitchell DT. *Electroanalytical Chemistry: A Series of Advances*, Vol. 21. Marcel Dekker, New York, 1999.
27. Martin CR, Mitchell DT. Nanomaterials in analytical chemistry. *Anal. Chem.* 1998;70(9):322A–327A.

28. Alkawlawi D, Liu CZ, Moskovits M. Nanowires formed in anodic oxide nanotemplates. *J. Mater. Res.* 1994;9(4):1014–1018.
29. Li J, Moskovits M, Haslett TL. Nanoscale electroless metal deposition in aligned carbon nanotubes. *Chem. Mater.* 1998;10(7):1963–1967.
30. Davydov DN, Haruyama J, Routkevitch D, Statt BW, Ellis D, Moskovits M, Xu JM. Nonlithographic nanowire-array tunnel device: fabrication, zero-bias anomalies, and Coulomb blockade. *Phys. Rev. B.* 1998;57(21):13550–13553.
31. Li J, Papadopoulos C, Xu JM, Moskovits M. Highly ordered carbon nanotube arrays for electronics applications. *Appl. Phys. Lett.* 1999;75(3):367–369.
32. Preston CK, Moskovits M. Optical characterization of anodic aluminum oxide films containing electrochemically deposited metal particles. *J. Phys. Chem.* 1993;97 (32):8495–8503.
33. Routkevitch D, Bigioni T, Moskovits M, Xu JM. Electrochemical fabrication of CdS nanowire arrays in porous anodic aluminum oxide templates. *J. Phys. Chem.* 1996; 100(33):14037–14047.
34. Ji CX, Searson PC. Synthesis and characterization of nanoporous gold nanowires. *J. Phys. Chem. B.* 2003;107(19):4494–4499.
35. Lewandowski EP, Searson PC, Stebe KJ. Orientation of a nanocylinder at a fluid interface. *J. Phys. Chem. B.* 2006;110(9):4283–4290.
36. Searson PC, Cammarata RC, Chien CL. Electrochemical processing of metallic nanowire arrays and nanocomposites. *J. Electron. Mater.* 1995;24(8):955–960.
37. Whitney TM, Jiang JS, Searson PC, Chien CL. Fabrication and magnetic properties of arrays of metallic nanowires. *Science.* 1993;261(5126):1316–1319.
38. Liu K, Nagodawithana K, Searson PC, Chien CL. Perpendicular giant magnetoresistance of multilayered Co/Cu nanowires. *Phys. Rev. B.* 1995;51(11):7381–7384.
39. Liu K, Chien CL, Searson PC, Kui YZ. Structural and magneto-transport properties of electrodeposited bismuth nanowires. *Appl. Phys. Lett.* 1998;73(10):1436–1438.
40. Liu K, Chien CL, Searson PC. Finite-size effects in bismuth nanowires. *Phys. Rev. B.* 1998;58(22):14681–14684.
41. Deckman HWD, Dunsmuir JH. Natural lithography. *Appl. Phys. Lett.* 1982;41:377–379.
42. Hanarp P, Sutherland DS, Gold J, Kasemo B. Nanostructured biomaterials surfaces prepared by colloidal lithography. *Nanostruct. Mater.* 1999;12:429–432.
43. Hulteen JC, Van Duyne RP. Nanosphere lithography: a materials general fabrication process for periodic particle array surfaces. *J. Vacuum Sci. Technol. A.* 1995;13(3):1553–1558.
44. Andersson AS, Olsson P, Lidberg U, Sutherland D. The effects of continuous and discontinuous groove edges on cell shape and alignment. *Exp. Cell Res.* 2003;288:177–188.
45. Andersson AS, Backhed F, von Euler A, Richter-Dahlfors A, Sutherland D, Kasemo B. Nanoscale features influence epithelial cell morphology and cytokine production. *Biomaterials.* 2003;24:3427–3436.
46. Dalby MJ, Riehle MO, Sutherland DS, Agheli H, Curtis ASG. Morphological microarray analysis of human fibroblasts cultured on nanocolumns produced by colloidal lithography. *Eur. Cells Mater.* 2005;9:1–8.
47. Haes AJ, van Duyne RP. A nanoscale optical biosensor: sensitivity and selectivity of an approach based on the localized surface plasmon resonance spectroscopy of triangular silver nanoparticles. *J. Am. Chem. Soc.* 2002;124:10596–10604.

48. Haes AJ, Hall WP, Chang L, Klein WL, van Duyne RP. A localized surface plasmon resonance biosensor: first steps toward an assay for Alzheimer's disease. *Nano Lett.* 2004;4:1029–1034.
49. Haynes CL, Van Duyne RP. Nanosphere lithography: a versatile nanofabrication tool for studies of size-dependent nanoparticle optics. *J. Phys. Chem. B.* 2001;105(24):5599–5611.
50. McFarland AD, Van Duyne RP. Single silver nanoparticles as real-time optical sensors with zeptomole sensitivity. *Nano Lett.* 2003;3:1057–1062.
51. Cheng S, Lu S, Li C, Chang Y, Huang C, Chen H. Fabrication of periodic nickel silicide nanodot arrays using nanosphere lithography. *Thin Solid Films.* 2006;494(1–2):307–310.
52. Bhaviripudi S, Reina A, Qi JF, Kong J, Belcher AM. Block-copolymer assisted synthesis of arrays of metal nanoparticles and their catalytic activities for the growth of SWNTs. *Nanotechnology.* 2006;17:5080–5086.
53. Yang Z, Huck WT, Clarke SM, Tajbakhsh AR, Terentjev EM. Shape-memory nanoparticles from inherently non-spherical polymer colloids. *Nat. Mater.* 2005;4:486–490.
54. Ng V, Lee YV, Chen BT, Adeyeye AO. Nanostructure array fabrication with temperature-controlled self-assembly techniques. *Nanotechnology.* 2002;13:554–558.
55. Ray MA, Kim H, Jia L. Dynamic self-assembly of polymer colloids to form linear patterns. *Langmuir.* 2001;21:4786–4789.
56. Sonvico F, Dubernet C, Colombo P, Couvreur P. Metallic colloid nanotechnology, applications in diagnosis and therapeutics. *Curr. Pharm. Des.* 2005;11:2095–2105.
57. Laurent G, Felidj N, Lau Truong S, et al. Imaging surface plasmon of gold nanoparticle arrays by far-field Raman scattering. *Nano Lett.* 2005;5:253–258.
58. Schlotterbeck U, Aymonier C, Thomann R, et al. Shape-selective synthesis of palladium nanoparticles stabilized by highly branched amphiphilic polymers. *Adv. Funct. Mater.* 2004;14:999–1004.
59. Andersson A, Glasmästar K, Hanarp P, Seantier B, Sutherland DS. Patterning colloidal monolayer films using microcontact particle stripping. *Nanotechnology.* 2007;18(20):205–303.
60. Hanarp P, Sutherland DS, Gold J, Kasemo B. Control of nanoparticle film structure for colloidal lithography. *Colloids Surf. A.* 2003;214(1–3):23–26.
61. Silván MM, Hernández MA, Costa VT, Palma RJM, Duarte JMM. Structured porous silicon submicrometer wells grown by colloidal lithography. *Europhys. Lett.* 2006;76(4):690–695.
62. Yap F, Zhang Y. Protein and cell micropatterning and its integration with micro/nanoparticles assembly. *Biosens. and Bioelectron.* 2007;22(6):775–778.
63. Yap FL, Zhang Y. Assembly of polystyrene microspheres and its application in cell micropatterning. *Biomaterials.* 2007;28(14):2328–2338.
64. Juillerat F, Solak HH, Bowen P, Hofmann H. Fabrication of large-area ordered arrays of nanoparticles on patterned substrates. *Nanotechnology.* 2005;16(8):1311–1316.
65. Nath N, Chilkoti A. A colorimetric colloidal gold sensor to interrogate biomolecular interactions in real-time on a surface. *Anal. Chem.* 2002;74:504–509.
66. Städler B, Solak HH, Frerker S, et al. Nanopatterning of gold colloids for label-free biosensing. *Nanotechnology.* 2007;18(15):155–306.

67. Satriano C, Messina G, Carnazza S, Guglielmino S, Marletta G. Bacterial adhesion onto nanopatterned polymer surfaces. *Mater. Sci. Eng. C*. 2006;26(5–7):942–946.
68. Valsesia A, Mezziani T, Bretagnol F, Colpo P, Leccone G, Rossi F. Plasma assisted production of chemical nano-patterns by nano-sphere lithography: application to bio-interfaces. *J. Phy. D*. 2007;40(8):2341–2347.
69. Dalby MJ, Riehle MO, Sutherland DS, Agheli H, Curtis ASG. Changes in fibroblast morphology in response to nano-columns produced by colloidal lithography. *Biomaterials*. 2004;25(23):5415–5422.
70. Norman J, Desai T. Methods for fabrication of nanoscale topography for tissue engineering scaffolds. *Ann. Biomed. Eng.* 2006;34(1):89–101.
71. Antelmi DA, Spalla O. Adsorption of nanolatex particles to mineral surfaces of variable surface charge. *Langmuir*. 1999;15:7478–7489.
72. Serizawa T, Kamimura S, Akashi M. Electrostatic adsorption of polystyrene particles with different surface charges onto the surface of an ultrathin polymer film. *Colloids Surf. A*. 2000;164:237–245.
73. Serizawa T, Takeshita H, Akashi M. Electrostatic adsorption of polystyrene nanospheres onto the surface of an ultrathin polymer film prepared by using an alternate adsorption technique. *Langmuir*. 1998;14:4088–4094.
74. Yang SM, Jang SG, Choi DG, Kim S, Yu HK. Nanomachining by colloidal lithography. *Small*. 2006;2:458–475.
75. Wood M. Colloidal lithography and current fabrication techniques producing in-plane nanotopography for biological applications. *R. Soc. Interface*. 2007;4(12):1–17.
76. van Blaaderen A, Ruel R, Wiltzius P. Template-directed colloidal crystallization. *Nature*. 1997;285:321–324.
77. Bailey RC, Stevenson KJ, Hupp JT. Assembly of micropatterned colloidal gold thin films via microtransfer molding and electrophoretic deposition. *Adv. Mater.* 2000;12:1930–1934.
78. Xia D, Brueck SRJ. A facile approach to directed assembly of patterns of nanoparticles using interference lithography and spin coating. *Nano Lett*. 2004;4:1295–1299.
79. Xia D, Biswas A, Li D, Brueck SRJ. Directed self-assembly of silica nanoparticles into nanometer-scale patterned surfaces using spin-coating. *Adv. Mater.* 2004;16:1427–1432.
80. Wood MA, Meredith DO, Owen GHR, Richards RG, Riehle MO. Utilising atomic number contrast for FESEM imaging of colloidal nanotopography underlying biological cells. *Nanotechnology*. 2005;16:1433–1439.
81. Wood MA, Wilkinson CDW, Curtis ASG. The effects of colloidal nanotopography on initial fibroblast adhesion and morphology. *IEEE Trans. Nanobiosci.* 2006;5(1):20–31.
82. Haginoya C, Ishibashi M, Koike K. Nanostructure array fabrication with a size-controllable natural lithography. *Appl. Phys. Lett.* 1997;71:2934–2936.
83. Denis FA, Hanarp P, Sutherland DS, Dufrene YF. Nanoscale chemical patterns fabricated by using colloidal lithography and self-assembled monolayers. *Langmuir*. 2004;20:9335–9339.
84. Wood MA, Riehle M, Wilkinson CDW. Patterning colloidal nanotopographies. *Nanotechnology*. 2002;13:605–609.

85. Lewis PA, Ahmed H. Nanopillars formed with a colloidal gold etch mask. *J. Vac. Sci. Technol. B.* 1999;17:3234–3239.
86. Lewis PA, Ahmed H, Sato T. Silicon nanopillars formed with colloidal particle masking. *J. Vac. Sci. Technol. B.* 1998;16:2938–2941.
87. Cheung CL, Nikoli RJ, Reinhardt CE, Wang TF. Fabrication of nanopillars by nanosphere lithography. *Nanotechnology.* 2006;17(5):1339–1343.
88. Denis FA, Hanarp P, Sutherland DS, Dufrene YF. Fabrication of nanostructured polymer surfaces using colloidal lithography and spin-coating. *Nano Lett.* 2002;2:1419–1425.
89. Werdinius C, Osterlund CL, Kasemo B. Nanofabrication of planar model catalysts by colloidal lithography: Pt/ceria and Pt/alumina. *Langmuir.* 2003;19:458–468.
90. Prikulis J, Hanarp P, Olofsson L, Sutherland DS, Kall M. Optical spectroscopy of nanometric holes in thin gold films. *Nano Lett.* 2004;4:1003–1007.
91. Whitney AV, Myers BD, van Duyne RP. Sub-100 nm triangular nanopores fabricated with the reactive ion etching variant of nanosphere lithography and angle-resolved nanosphere lithography. *Nano Lett.* 2004;4:1507–1511.
92. Jiang P, McFarland MJ. Wafer-scale periodic nanohole arrays templated from two-dimensional nonclose-packed colloidal crystals. *J. Am. Chem. Soc.* 2005;127:3710–3711.
93. Aizpurua J, Hanarp P, Sutherland DS, Kall M, Bryant GW, de Abajo FJG. Optical properties of gold nanorings. *Phys. Rev. Lett.* 2003;90(5):057401.
94. Hovis JS, Boxer SG. Patterning barriers to lateral diffusion in supported lipid membranes by blotting and stamping. *Langmuir.* 2000;16:894–897.
95. Zheng Y, Wang S, Huan A, Wang Y. Fabrication of large area ordered metal nanoring arrays for nanoscale optical sensors. *J. Non-Cryst. Solids.* 2006;352(23–25):2532–2535.
96. Michel R, Reviakine I, Sutherland D, et al. A novel approach to produce biologically relevant chemical patterns at the nanometer scale: selective molecular assembly patterning combined with colloidal lithography. *Langmuir.* 2002;18:8580–8586.
97. Qin K, Li Y. Mechanisms of particle removal from silicon wafer surface in wet chemical cleaning process. *J. Colloid Interface Sci.* 2003;261:569–574.
98. Brétagnol F, Ceriotti L, Valsesia A, et al. Fabrication of functional nano-patterned surfaces by a combination of plasma processes and electron-beam lithography. *Nanotechnology.* 2007;18(13):135303.
99. Nakagawa M, Oh SK, Ichimura K. Photopatterning and visualization of adsorbed monolayers of bis(1-benzyl-4-pyridinio)ethylene moieties. *Adv. Mater.* 2000;12:403–407.
100. Bale M, Turner AJ, Palmer RE. Fabrication of ordered arrays of silicon nanopillars at selected sites. *J. Phys. D.* 2002;35:L11–L14.
101. Fudouzi H, Kobayashi M, Shinya N. Assembling 100 nm scale particles by an electrostatic potential field. *J. Nanopart. Res.* 2001;3:193–200.
102. Aizenberg J, Braun PV, Wiltzius P. Patterned colloidal deposition controlled by electrostatic and capillary forces. *Phys. Rev. Lett.* 2000;84:2997–3000.
103. Himmelhaus M, Takei H. Self-assembly of polystyrene nano particles into patterns of random-close-packed monolayers via chemically induced adsorption. *Phys. Chem. Chem. Phys.* 2002;4:496–506.
104. Park MC, Chaikin PM, Register RA, Adamson DH. Large area dense nanoscale patterning of arbitrary surfaces. *Appl. Phys. Lett.* 2001;79:257–259.

105. Kim SO, Solak HH, Stoykovich MP, Ferrier NJ, De Pablo JJ, Nealey PF. Epitaxial self-assembly of block copolymers on lithographically defined nanopatterned substrates. *Nature*. 2003;424:411.
106. Segalman RA. Patterning with block copolymer thin films. *Mater. Sci. Eng. R*. 2005;48:191–226.
107. Hamley IW. Nanostructure fabrication using block copolymers. *Nanotechnology*. 2003;14:R39–R54.
108. Glass R, Moller M, Spatz JP. Micellar nanolithography. *Nanotechnology*. 2003;14:1153–1160.
109. Glass R, Arnold M, Cavalcanti-Adam E, et al. Block copolymer micelle nanolithography on non-conductive substrates. *New J. Phys.* 2004;6:101–117.
110. Arnold M, Cavalcanti-Adam E, Glass R, et al. Activation of integrin function by nanopatterned adhesive interfaces. *Chem. Phys. Chem.* 2004;5:383–388.
111. Cavalcanti-Adam E, Micoulet A, Blummel J, Aurenheimer J, Kessler H, Spatz JP. Lateral spacing of integrin ligands influences cell spreading and focal adhesion assembly. *Eur. J. Cell Biol.* 2006;85:219–224.
112. Curtis AS. The potential for the use of nanofeaturing in medical devices. *Expert Rev. Med. Dev.* 2005;2:293–301.
113. Agheli H, Malmstrom J, Larsson E, Textor M, Sutherland D. Large area protein nanopatterning for biological applications. *Nano Lett.* 2006;6(6):1165–1171.
114. Li JR, Henry GC, Garno JC. Fabrication of nanopatterned films of bovine serum albumin and staphylococcal protein A using latex particle lithography. *Analyst*. 2006;131(2):244–250.
115. Cai Y, Ocko B. Large scale fabrication of protein nanoarrays based on nanosphere lithography. *Langmuir*. 2005;21(20):9274–9279.
116. Kumar N, Parajuli O, Hahm J. Two-dimensionally self-arranged protein nanoarrays on diblock copolymer templates. *J. Phys. Chem. B*. 2007;111(17):4581–4587.
117. Kumar N, Parajuli O, Dorfman A, Kipp D, Hahm J. Activity study of self-assembled proteins on nanoscale diblock copolymer templates. *Langmuir*. 2007;23(14):7416–7422.
118. Sutherland DS, Broberg M, Nygren H, Kasemo B. Influence of nanoscale surface topography and chemistry on the functional behaviour of an adsorbed model macromolecule. *Macromol. Biosci.* 2001;1:270–273.
119. Silva GA. Neuroscience nanotechnology: progress, opportunities and challenges. *Nat. Rev. Neurosci.* 2006;7:65–74.
120. Busch K, Tampe R. Single molecule research on surfaces: from analytics to construction and back. *Mol. Biotechnol.* 2001;82:3–24.
121. Wolfram T, Belz F, Schoen T, Spart JP. Site-specific presentation of single recombinant proteins in defined nanoarrays. *Biointerphases*. 2007;2(1):44–48.
122. Vertegel AA, Siegel RW, Dordick JS. Silica nanoparticle size influences the structure and enzymatic activity of adsorbed lysozyme. *Langmuir*. 2004;20:6800–6807.
123. Lundqvist M, Sethson I, Jonsson BH. Protein adsorption onto silica nanoparticles: conformational changes depend on the particles' curvature and the protein stability. *Langmuir*. 2004;20:10639–10647.
124. Link S, El-Sayed MA. Spectral properties and relaxation dynamics of surface plasmon electronic oscillations in gold and silver nanodots and nanorods. *J. Phys. Chem. B*. 1999;103(40):8410–8426.

125. El-Sayed MA. Some interesting properties of metals confined in time and nanometer space of different shapes. *Acc. Chem. Res.* 2001;34(4):257–264.
126. Hirsch LR, Jackson JB, Lee A, Halas NJ, West JL. A whole blood immunoassay using gold nanoshells. *Anal. Chem.* 2003;75(10):2377–2381.
127. Haes AJ, Van Duyne RP. Silver nanoparticles behave as ultrasensitive biosensors. *Laser Focus World.* 2003;39:153–156.
128. Kreibig U, Vollmer M. *Optical Properties of Metal Clusters*, Vol. 25. Springer Verlag, New York, 1995;p. 532.
129. Zhang X, Whitney AV, Zhao J, Hicks EM, van Duyne RP, Richard P. Advances in contemporary nanosphere lithographic techniques. *J. Nnosci. Nanotechnol.* 2006;6(7):1920–1934.
130. Haynes CHL, McFarland AD, Smith MT, Hulteen JC, van Duyne RP. Angle-resolved nanosphere lithography: manipulation of nanoparticle size, shape, and interparticle spacing. *J. Phys. Chem. B.* 2002;106(8):1898–1902.
131. Taton TA, Mirkin CA, Letsinger RL, Scanometric DNA array detection with nanoparticle probes. *Science.* 2002;289(5485):1757–1760.
132. Storhoff JJ, Elghanian R, Mirkin CA, Letsinger RL. Stability of DNA-modified gold nanoparticles. *Langmuir.* 2002;18(17):6666–6670.
133. Elghanian R, Storhoff JJ, Mucic RC, Letsinger RL, Mirkin CA. Selective colorimetric detection of polynucleotides based on the distance-dependent optical properties of gold nanoparticles. *Science.* 1997;227(5329):1078–1081.
134. Riboh JC, Haes AJ, McFarland AD, Yonzon CR, Van Duyne RP. A nanoscale optical biosensor: real time immunoassay and nanoparticle adhesion. *J. Phys. Chem. B.* 2003;107:1772–1780.
135. Haynes CL, Van Duyne RP. Nanosphere lithography: a versatile nanofabrication tool for studies of size-dependent nanoparticle optics. *J. Phys. Chem. B.* 2001;105:5599–5601.
136. Haes AJ, Zou S, Schatz GC, Van Duyne RP. A nanoscale optical biosensor: the long range distance dependence of the localized surface plasmon resonance of noble metal nanoparticles. *J. Phys. Chem. B.* 2004;108:109–116.
137. Yonzon CR, Stuart DA, Zhang X, McFarland AD, Haynes CL, Van Duyne RP. Towards advanced chemical and biological nanosensors: an overview. *Talanta.* 2005;67(3):438–448.
138. Hanarp P, Käll M, Sutherland DS. Optical properties of short range ordered arrays of nanometer gold disks prepared by colloidal lithography. *J. Phys. Chem. B.* 2003;107:5768–5772.
139. Foss JCA, Hornyak GL, Stockert JA, Martin CR. Template synthesized nanoscopic gold particles- optical spectra and the effects of particle size and shape. *J. Phys. Chem.* 1994;98(11):2963–2971.
140. Hornyak GL, Phani KLN, Kunkel DL, Menon VP, Martin CR. Fabrication, characterization and optical theory of aluminum nanometal nanoporous membrane thin film composites. *Nanostruct. Mater.* 1995;6(5–8):839–842.
141. Patermarakis G. Transport phenomena inside the pores involved in the kinetics and mechanism of growth of porous anodic Al₂O₃ films on aluminium. *J. Electroanal. Chem.* 1996;404(1):69–76.
142. Zhang ZB, Gekhtman D, Dresselhaus MS, Ying JY. Processing and characterization of single-crystalline ultrafine bismuth nanowires. *Chem. Mater.* 1999;11(7):1659–1665.

143. Masuda H, Hasegawa F, Ono S. Self-ordering of cell arrangement of anodic porous alumina formed in sulfuric acid solution. *J. Electrochem. Soc.* 1997;144(5):L127–L130.
144. Cheng GS, Zhang LD, Zhu XG, Chen SH, Li Y, Zhu Y, Fei GT. Synthesis of orderly nanostructure of crystalline GaN nanoparticles on anodic porous alumina membrane. *Nanostruct. Mater.* 1999;11(3):421–426.
145. Mozalev A, Poznyak A, Mozaleva I, Hassel AW. The voltage–time behaviour for porous anodizing of aluminium in a fluoride-containing oxalic acid electrolyte. *Electrochem. Commun.* 2001;3(6):299–305.
146. Brumlik CJ, Menon VP, Martin CR. Template synthesis of metal microtubule ensembles utilizing chemical, electrochemical, and vacuum deposition techniques. *J. Mater. Res.* 1994;9(5):1174–1183.
147. Hoyer P, Masuda H. Electrodeposited nanoporous TiO₂ film by a two-step replication process from anodic porous alumina. *J. Mater. Sci. Lett.* 1996;15(14):1228–1230.
148. Shawaqfeh AT, Baltus RE. Growth kinetics and morphology of porous anodic alumina films formed using phosphoric acid. *J. Electrochem. Soc.* 1998;145(8):2699–2706.
149. Cheng GS, Zhang LD, Zhu Y, et al. Large scale synthesis of single crystalline gallium nitride nanowires. *Appl. Phys. Lett.* 1999;75(16):2455–2457.
150. Shawaqfeh AT, Baltus RE. Fabrication and characterization of single layer and multilayer anodic alumina membrane. *J. Membrane. Sci.* 1999;157(2):147–158.
151. Bocchetta P, Sunseri C, Bottino A, et al. Asymmetric alumina membranes electrochemically formed in oxalic acid solution. *J. Appl. Electrochem.* 2002;32(9):977–985.
152. Piao Y, Lim H, Chang JY, Lee WY, Kim H. Nanostructured materials prepared by use of ordered porous alumina. *Electrochim. Acta.* 2005;50(15):2997–3013.
153. Ugo P, Moretto LM. Metal deposition. In Zoski CG, ed. *Handbook of Electrochemistry*. Elsevier Science, Amsterdam, 2007, pp. 678–709.
154. Hornyak GL, Patrissi CJ, Martin CR. Fabrication, characterization, and optical properties of gold nanoparticle/porous alumina composites: the nonscattering Maxwell–Garnett limit. *J. Phys. Chem. B.* 1997;101(9):1548–1555.
155. Furneaux RC, Rigby WR, Davidsons AP. Porous films and methods forming them. U.S. patent 4,687,551, 1987.
156. Parpaleix T, Laval JM, Majda M, Bourdillon C. Potentiometric and voltammetric investigations of H₂/H⁺ catalysis by periplasmic hydrogenase from *Desulfovibrio gigas* immobilized at the electrode surface in an amphiphilic bilayer assembly. *Anal. Chem.* 1992;64(6) 641–646.
157. Mozalev A, Magaino S, Imai H. The formation of nanoporous membranes from anodically oxidized aluminium and their application to Li rechargeable batteries. *Electrochim. Acta.* 2001;46(18):2825–2834.
158. Tian M, Xu S, Wang JG, et al. Penetrating the oxide barrier in situ and separating freestanding porous anodic alumina films in one step. *Nano Lett.* 2005;5(4):697–703.
159. Harrell CC, Lee SB, Martin CR. Synthetic single nanopore and nanotube membranes. *Anal. Chem.* 2003;75(24):6861–6867.
160. Trautman C, Bruchle W, Spohr R, Vetter J, Angert N. Pore geometry of etched ion tracks in polyimide. *Nucl. Instrum. Methods Phys. Res. B.* 1996;111(1–2):70–74.
161. Apel P. Track etching technique in membrane technology. *Radiat. Meas.* 2001; 34(1–6):559–566.

162. Scopece P, Baker LA, Ugo P, Martin CR. Conical nanopore membranes: solvent shaping of nanopores. *Nanotechnology*. 2006;17(15):3951–3956.
163. Apel PY, Korchev YE, Siwy Z, Spohr R, Yoshida M. Diode-like single ion track membrane prepared by electro-stopping. *Nucl. Instrum. Methods Phys. Res. B*. 2001;184(3):337–346.
164. Siwy Z, Apel P, Baur D, et al. Preparation of synthetic nanopores with transport properties analogous to biological channels. *Surf. Sci*. 2003;532:1061–1066.
165. Masuda H, Tanaka H, Baba N. Preparation of microporous gold film by two step replicating process using anodic alumina as template. *Bull. Chem. Soc. Jpn*. 1993;66(1):305–311.
166. Kautek W, Reetz S, Pentzien S. Template electrodeposition of nanowire arrays on gold foils fabricated by pulsed-laser deposition. *Electrochim. Acta*. 1995;40(10):1461–1468.
167. Schönenberger C, van der Zande BMI, Fokkink LGJ, et al. Template synthesis of nanowires in porous polycarbonate membranes: electrochemistry and morphology. *J. Phys. Chem. B*. 1997;101(28):5497–5505.
168. Tian M, Wang JU, Kurtz J, Mallouk TE, Chan MHW. Electrochemical growth of single-crystal metal nanowires via a two-dimensional nucleation and growth mechanism. *Nano Lett*. 2003;3(7):919–923.
169. Zhao Y, Guo YG, Zhang YL, Jiao K. Fabrication and characterization of highly ordered Pt nanotubule arrays. *Phys. Chem. Chem. Phys*. 2004;6(8):1766–1768.
170. Fukunaka Y, Motoyama M, Konishi Y, Ishii R. Producing shape-controlled metal nanowires and nanotubes by an electrochemical method. *Electrochem. Solid State Lett*. 2006;9(3):C62–C64.
171. Karim S, Toimil-Molares ME, Maurer F, et al. Synthesis of gold nanowires with controlled crystallographic characteristics. *Appl. Phys. A*. 2006;84(4):403–407.
172. Gelves GA, Lin B, Sundararaj U, Haber JA. Low electrical percolation threshold of silver and copper nanowires in polystyrene composites. *Adv. Funct. Mater*. 2006;16(18):2423–2430.
173. Gelves GA, Murakami ZTM, Krantz MJ, Haber JA. Multigram synthesis of copper nanowires using ac electrodeposition into porous aluminium oxide templates. *J. Mater. Chem*. 2006;16(30):3075–3083.
174. Evans P, Hendren WR, Atkinson R, et al. Growth and properties of gold and nickel nanorods in thin film alumina. *Nanotechnology*. 2006;17(23):5746–5753.
175. Lee UH, Lee JH, Jung DY, Kwon YU. High-density arrays of platinum nanostructures and their hierarchical patterns. *Adv. Mater*. 2006;18(21):2825–2828.
176. Xu LP, Yuan ZH, Zhang XG. Fabrication of multi-level branched metal nanowires by AAO template electrodeposition. *Chin. Sci. Bull*. 2006;51(17):2055–2058.
177. Ohgai T, Enculescu I, Zet C, et al. Magnetosensitive nickel nanowires fabricated by electrodeposition into multi- and single-ion track templates. *J. Applied Electrochem*. 2006;36(10):1157–1162.
178. Kazeminezhad I, Barnes AC, Holbrey JD, Seddon KR, Schwarzacher W. Templated electrodeposition of silver nanowires in a nanoporous polycarbonate membrane from a nonaqueous ionic liquid electrolyte. *Appl. Phys. A*. 2007;86(3):373–375.
179. Han S, Chen HY, Chen CC, Yuan TN, Shih HC. Characterization of Ni nanowires after annealing. *Mater. Lett*. 2007;61(4–5):1105–1108.

180. Xu XJ, Fei GT, Wang XW, Jin Z, Yu WH, Zhang LD. Synthetic control of large area, ordered silver nanowires with different diameters. *Mater. Lett.* 2007;61(1):19–22.
181. Penner RM. Metal deposition. In Zoski CG, ed. *Handbook of Electrochemistry*. Elsevier Science, Amsterdam, 2007pp. 673–677.
182. Zhu JT, Jiang W. Fabrication of conductive metallized nanostructures from self-assembled amphiphilic triblock copolymer templates: nanospheres, nanowires, nanorings. *Mater. Chem. Phys.* 2007;101(1):56–62.
183. Williams WD, Giordano N. Fabrication of 80-Å metal wires. *Rev. Sci. Instrum.* 1984;55 (3):410–412.
184. Brumlik CJ, Martin CR, Tokuda K. Microhole array electrodes based on microporous alumina membranes. *Anal. Chem.* 1992;64(10):1201–1203.
185. van der Zande BMI, Böhmer MR, Fokkink LGJ, Schönenberger C. Colloidal dispersions of gold rods: synthesis and optical properties. *Langmuir.* 2000;16(2):451–458.
186. Zhang XY, Zhang LD, Lei Y, Zhao LX, Mao YQ. Fabrication and characterization of highly ordered Au nanowire arrays. *J. Mater. Chem.* 2001;11(6):1732–1734.
187. Piraux L, Dubois S, Demoustier-Champagne S. Template synthesis of nanoscale materials using the membrane porosity. *Nucl. Instrum. Methods Phys. Res. B.* 1997;131 (1–4):357–363.
188. Chiriac H, Moga AE, Urse M, Óvári TA. Preparation and magnetic properties of electrodeposited magnetic nanowires. *Sens. Actuators A.* 2003;106(1–3):348–351.
189. Verbeeck J, Lebedev OI, Van Tendeloo G, Cagnon L, Bougerol C, Tourillon G. Fe and Co nanowires and nanotubes synthesized by template electrodeposition: A HRTEM and EELS study. *J. Electrochem. Soc.* 2003;150(10):E468–E471.
190. Tourillon G, Pontonnier L, Levy JP, Langlais V. Electrochemically synthesized Co and Fe nanowires and nanotubes. *Electrochem. Solid State Lett.* 2000;3(1):20–23.
191. Zheng MJ, Li GH, Zhang XY, Huang SY, Lei Y, Zhang LD. Fabrication and structural characterization of large-scale uniform SnO₂ nanowire array embedded in anodic alumina membrane. *Chem. Mater.* 2001;13(11):3859–3861.
192. Platt M, Dryfe RAW, Roberts EPL. Electrodeposition of palladium nanoparticles at the liquid–liquid interface using porous alumina templates. *Electrochim. Acta.* 2003;48(20–22):3037–3046.
193. Platt M, Dryfe RAW, Roberts EPL. Structural and electrochemical characterisation of Pt and Pd nanoparticles electrodeposited at the liquid/liquid interface. *Electrochim. Acta.* 2004;49(22–23):3937–3945.
194. Tian ML, Wang JG, Snyder J, et al. Synthesis and characterization of superconducting single-crystal Sn nanowires. *Appl. Phys. Lett.* 2003;83(8):1620–1622.
195. Wang JG, Tian ML, Mallouk TE, Chan MHW. Microstructure and interdiffusion of template-synthesized Au/Sn/Au junction nanowires. *Nano Lett.* 2004;4(7):1313–1318.
196. Jirage KB, Hulteen JC, Martin CR. Effect of thiol chemisorption on the transport properties of gold nanotubule membranes. *Anal. Chem.* 1999;71(21):4913–4918.
197. Göring P, Pippel E, Hofmeister H, Wehrspohn RB, Steinhart M, Gösele U. Gold/carbon composite tubes and gold nanowires by impregnating templates with hydrogen tetrachloroaurate/acetone solutions. *Nano Lett.* 2004;4(6):1121–1125.
198. Vastarella W, Della Seta L, Masci A, et al. Biosensors based on gold nanoelectrode ensembles and screen printed electrodes. *Int. J. Environ. Anal. Chem.* 2007;87 (10–11):701–714.

199. Lahav M, Sehayek T, Vaskevich A, Rubinstein I. Nanoparticle nanotubes. *Angew. Chem. Int. Ed.* 2003;42(45):5575–5579.
200. Barreca D, Gasparotto A, Maragno C, Tondello E. Synthesis of gold nanotubes by sputtering of gold into porous materials. *J. Nanosci. Nanotechnol.* 2005;5(11):1883–1886.
201. Liu J, Duan JL, Toimil-Molares E, et al. Electrochemical fabrication of single-crystalline and polycrystalline Au nanowires: the influence of deposition parameters. *Nanotechnology.* 2006;17(8):1922–1926.
202. Li NC, Yu SF, Harrell CC, Martin CR. Conical nanopore membranes: preparation and transport properties. *Anal. Chem.* 2004;76(7):2025–2030.
203. Demoustier-Champagne S, Delvaux M. Preparation of polymeric and metallic nanostructures using a template-based deposition method. *Mater. Sci. Eng. C.* 2001;15:(1–2):269–271.
204. Brunetti B, Ugo P, Moretto LM, Martin CR. Electrochemistry of phenothiazine and methylviologen biosensor electron transfer mediators at nanoelectrode ensembles. *J. Electroanal. Chem.* 2000;491(1–2):166–174.
205. Crowley TA, Ziegler KJ, Lyons DM, et al. Synthesis of metal and metal oxide nanowire and nanotube arrays within a mesoporous silica template. *Chem. Mater.* 2003;15(18):3518–3522.
206. Ugo P, Pepe N, Moretto LM, Battagliarin M. Direct voltammetry of cytochrome c at trace concentrations with nanoelectrode ensembles. *J. Electroanal. Chem.* 2003;560:51–58.
207. Moretto LM, Pepe N, Ugo P. Voltammetry of redox analytes at trace concentrations with nanoelectrode ensembles. *Talanta.* 2004;62(5):1055–1060.
208. De Leo M, Kuhn A, Ugo P. 3D-Ensembles of gold nanowires: preparation, characterization and electroanalytical peculiarities. *Electroanalysis.* 2007;19(2–3):227–236.
209. Pereira FC, Moretto LM, De Leo M, Boldrin Zanoni MV, Ugo P. Gold nanoelectrode ensembles for direct trace electroanalysis of iodide. *Anal. Chim. Acta.* 2006;575(1):16–24.
210. Savage J, In Holmes PJ, Loasby RG, eds. *Handbook of Thick Film Technology.* Electrochemical Publications, Port Erin, Isle of Man, UK, 1976; p. 50.
211. White NM. Thick film technology. In Prudenziati M ed. *Thick Film Sensors: Handbook of Sensors and Actuators.* Elsevier, Amsterdam, 1994; p. 3.
212. Vastarella W, Lanza B, Masci A, Pilloton R. Screen printed electrodes for biosensor application: reproducibility, sensitivity and stability. In Di Natale C, D’Amico A, Martinelli G, Carotta MC, Guidi V, eds. *Proceedings of the 9th Italian Conference on Sensor and Microsystems,* Ferrara, Italy, Feb. 8–11, 2004, World Scientific, Singapore, 2005; p. 19.
213. Delvaux M, Demoustier-Champagne S. Immobilisation of glucose oxidase within metallic nanotubes arrays for application to enzyme biosensors. *Biosens. Bioelectron.* 2003;18(7):943–951.
214. Delvaux M, Demoustier-Champagne S, Walcarius A. Flow injection amperometric detection at enzyme-modified gold nanoelectrodes. *Electroanalysis.* 2004;16(3):190–198.
215. Maly J, Ilie M, Foglietti V, et al. Continuous flow micro-cell for electrochemical addressing of engineered bio-molecules. *Sens. Actuators B.* 2005;111–112:317–322.

216. Zotti G, Cattarin S, Comisso N. Electrodeposition of polythiophene, polypyrrole and polyaniline by the cyclic potential sweep method. *J. Electroanal. Chem.* 1987;235 (1–2):259–273.
217. Andrade GD, Aguirre MJ, Biaggio SR. Influence of the first potential scan on the morphology and electrical properties of potentiodynamically grown polyaniline films. *Electrochem. Acta.* 1998;44(4):633–642.
218. Chowdhury AN, Ferdousi S, Islam MM, Okajama T, Ohsaka T. Arsenic detection by nanogold/conducting polymer-modified glassy carbon electrodes. *J. Appl. Polym. Sci.* 2007;104(2):1306–1311.
219. (a) Swoboda B, Massey V. Properties of native glucose oxidase *J. Biol. Chem.* 1965;240:2209. (b) Rodriguez-Nogales JM. Kinetic behaviour and stability of glucose oxidase entrapped in liposomes. *J. Chem. Tech. Biotechnol.* 2004;79(1):72–78.
220. Meier PC, Zund RE. Statistical methods in analytical chemistry. In Winefordner JD, ed. *Chemical Analysis*, vol. 123. Wiley, New York, 1993, p. 87.
221. Thevenot DR, Toth K, Durst RA, Wilson GS. Electrochemical biosensors: recommended definitions and classification. *Biosens. Bioelectron.* 2001;16(1–2):121–131.
222. Thevenot DR, Toth K, Durst RA, Wilson GS. Electrochemical biosensors: recommended definitions and classification. *Anal. Lett.* 2001;34(5):635–659.

Nanostructured Affinity Surfaces for MALDI-TOF-MS–Based Protein Profiling and Biomarker Discovery

R. M. VALLANT, M. RAINER, M. NAJAM-UL-HAQ, R. BAKRY, C. PETTER, N. HEIGL, G. K. BONN, and C. W. HUCK

Institute of Analytical Chemistry and Radiochemistry, Leopold-Franzens University, Innsbruck, Austria

- 14.1 Proteomics and biomarkers
- 14.2 MALDI in theory and practice
 - 14.2.1 Surface-enhanced laser desorption/ionization
 - 14.2.2 Material-enhanced laser desorption/ionization
- 14.3 Carbon nanomaterials
 - 14.3.1 Derivatized diamond
 - 14.3.2 Modified CNT
 - 14.3.3 Derivatized fullerenes
- 14.4 Near-infrared diffuse reflection spectroscopy of carbon nanomaterials
 - 14.4.1 NIR characterization of C₆₀ fullerenes
 - 14.4.2 NIR characterization of nanocrystalline diamond

14.1 PROTEOMICS AND BIOMARKERS

Proteomics is a research field related to the measurement and characterization of proteins. Proteins are polymeric organic substances composed of amino acids (called *residues*), which are covalently bound, through peptide bonds, forming stable conformations. They are not completely rigid structures, as they can swap among the related structures through conformational changes, thus performing unique functions.

Their role in biological systems can be better understood if their structures are completely revealed. Various robust and reliable analytical techniques are employed for analyzing and tracking the distinctive proteins and an attempt is made to quantify them for their further use in clinical proteomics.

Biomarkers are entities that help in early detection and diagnosis of a disease. The quest for diagnostic markers at the early stage of any disease can prevent complications generated in terms of curing and prevention [1]. The identification of biomarker candidates is carried out by different strategies involving the peptide and protein mass fingerprinting, enzymatic digestions, and peptide sequencing through mass spectrometric analysis. The classical approach for discovering disease-associated proteins continues to be two-dimensional polyacrylamide gel electrophoresis (2D-PAGE) [2]. Although 2D-PAGE is unchallenged in its ability to resolve thousands of proteins, it is laborious, requires large quantities of protein, lacks critical reproducibility standards from one laboratory to another, and is not easily converted into a diagnostic test. Recent advances in mass spectrometry (MS) and multidimensional liquid chromatography (MDLC), combined with tandem mass spectrometry (MS/MS) [3], offer an alternative to or an interface with two-dimensional electrophoresis for the simultaneous detection and identification of multiple protein species. The proteolytic digest mixture is producing better sequence coverage when separated chromatographically before carrying out the MS/MS, as the contents can suppress or overlap each other. The peptide mass fingerprints of a protein are characteristic and when compared to databases result in identification. Therefore, the surface-enhanced laser desorption/ionization (SELDI) or material-enhanced laser desorption/ionization (MELDI) techniques developed recently are handier in this regard. The more peptide peaks in a digest mixture, the better the protein sequence coverage. There are also other approaches, including serum protein profiling, which assign distinctive proteins between control and cancerous serum and identification of overexpressed genes from libraries built from either normal or cancerous samples [4]. Early detection and diagnostics can be achieved if the changes in cancer-related proteome are understood, leading to biomarker discoveries [5]. The proteomics approaches must also focus on the functions of cells, in terms of protein interactions, modifications, and activities on the course of a particular disease [6].

There is, however, a need to develop new methodologies and to improve existing systems in terms of their selectivity, sensitivity, and specificity. The identification of proteins from peptide mass fingerprinting can lead to disease markers, as the leakage of these biomarkers from the cell into the bloodstream is a response of the body when it is in a diseased state [7]. The new bioanalytical methods, combined with mass spectrometric detection of biomarkers, holds promise of providing diagnostic and prognostic information for cancer and other disease-related biological fluids.

14.2 MALDI IN THEORY AND PRACTICE

Mass spectrometry is one of the most important physical methods in analytical chemistry today. A particular advantage of mass spectrometry over other molecular

spectroscopic methods, is its high sensitivity, down to the zeptomole level [8]. That is why MS is one of the few methods that is entirely suitable for the identification of trace amounts of biological substances. The further development of MS instrumentation, combined with optimized sample preparation and purification steps, has led to a dramatic increase in accessible mass range, resolution, and sensitivity, which made it possible to analyze macromolecules such as proteins.

Laser desorption/ionization (LDI) MS, which involves the desorption of molecules through a laser beam, was introduced in the 1960s. The first experiments were carried out by placing a thin film of sample on a metal surface and irradiating it with a pulsed laser. The results of this technique were rather disappointing at first, because ions could only be detected with very low signal intensities and below 1000 Da. Strong fragmentation also took place, which is a very disturbing factor in the field of MS. As a result, this method was unsuitable for larger molecules such as proteins, DNA, and RNA.

The end of the 1980s saw in a big breakthrough the introduction of matrix-assisted laser desorption/ionization (MALDI) MS by Karas and co-workers [9,10]. They used an ultraviolet (UV) laser to investigate the effect of laser energy on UV-absorbing organic materials. Moreover, they discovered that the embedding of samples in a matrix consisting of organic compounds that have high absorbance in the same wavelength of the laser beam results in an increase in signal intensity and a decrease in fragmentation. This can be carried out by mixing the analyte solution with a small amount of aromatic acid (the matrix) and allowing it to dry on a MALDI sample support (target) (see Figure 14.1). The target is inserted into a vacuum lock and transferred into a vacuum chamber (ion source). The matrix ionizes the analyte molecules and absorbs the UV light of short laser pulses, causing the explosion, or desorption, of the crystalline matrix–analyte mixture. The charged analyte molecules are accelerated in the mass spectrometer and are detected after passing through the time-of-flight tube. Since their speed is a simple function of their mass, the time of flight can be converted into molecular mass information. The great advantage of this system is simple application with very high sensitivity and the possibility of detecting compounds of low abundance in a very broad mass range.

After the desorption process the ionized peptides are accelerated in an electric field by high-voltage grids. All ions are accelerated to the same kinetic energy level to

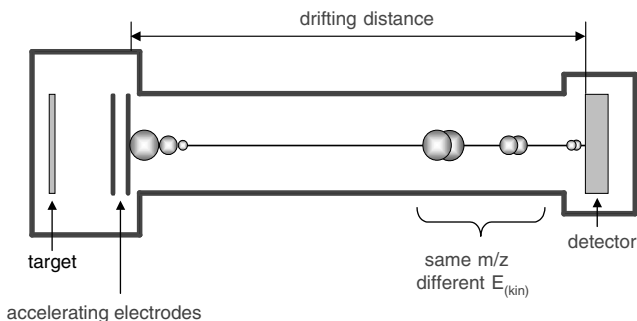


FIGURE 14.1 The linear mass analyzer represents a powerful feature of the time-of-flight mass spectrometer in its simplest instrumental design.

ensure that all ions of identical mass move at the same speed. The accelerated ions are then introduced into a high-vacuum flight tube (field-free drift region) and continue to fly until they reach the detector. Since light ions reach the detector earlier than do heavy ions, recorded flight times are used to calculate the mass-to-charge (m/z) ratio of ion masses. Resolution and mass accuracy are thus dependent on the time window in which ions of the same mass reach the detector. This is for the large part determined by the start velocity distribution. When one of the ion packets reaches the time-of-flight tube a precise time measurement is initiated, and when the individual sample components reach the detector the time is measured.

An impressed voltage first accelerates the gaseous ions that are created by the laser shot. After passing through the acceleration voltage U , the kinetic energy E_{kin} of the ions is

$$E_{\text{kin}} = \frac{mv^2}{2} = zeU \quad (14.1)$$

where m is the mass of the ion, v the velocity after the acceleration voltage, z the charge number of the ion, and e the elementary charge. The ions, with velocity v , then reach a field-free drift distance of length L . The time t needed for the ions to cross this distance is

$$T = \frac{L}{v} \quad (14.2)$$

When inserting equation (14.2) into equation (14.1), m/z can be solved:

$$\frac{m}{z} = \frac{2eU}{L^2} t^2 \quad (14.3)$$

Here it can be seen that m/z is proportional to t^2 . When the flight time that an ion needs to cross a distance L is known, a direct statement of the mass belonging to this ion can be made.

Pulsed extraction and reflector tubes are used to minimize and correct the start velocity distribution, respectively. During pulsed extraction, the voltage of the acceleration grid is switched on with a time delay of a few hundred nanoseconds from the laser impulse. Once the acceleration grid voltage is applied, ions with a higher start velocity will be farther away from the target than slower ions and receive a smaller portion of kinetic energy. For example, a slow ion that has traveled 1% of the distance obtains 99% of the potential, whereas a fast ion might have traveled 15% and will obtain only 85%. Pulsed extraction greatly reduces start velocity distribution and improves resolution in the reflector mode.

Reflector tubes are used to reverse the drift direction of the ions in an electric counter field (Figure 14.2). Ions of the same mass but higher start energy drift deeper into the reflector before being reflected and fly a greater distance before they reach the detector. In this way, they catch up with the slower-moving ions at a certain point after the reflector. The detector is located at this focusing point.

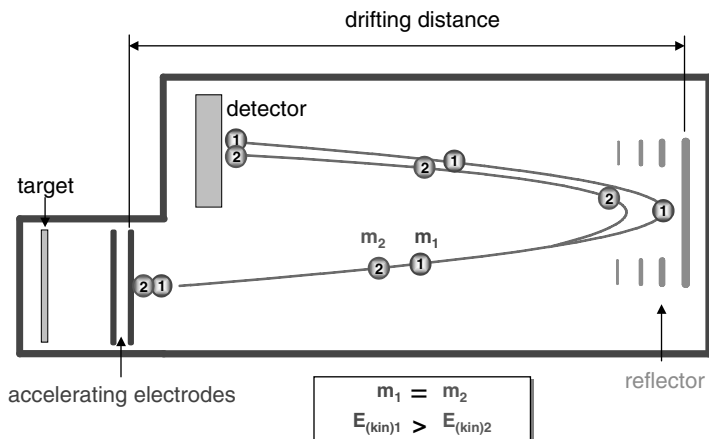


FIGURE 14.2 Reflector time-of-flight mass analyzer.

Reflector tubes greatly enhance resolution up to the isotope level by correcting start velocity distribution and prolonging the flight time. Although use of the reflector mode results in higher resolution, reflection reduces sensitivity and high-molecular-weight polypeptides can only be detected in the linear mode.

14.2.1 Surface-Enhanced Laser Desorption/Ionization

Surface-enhanced laser desorption/ionization (SELDI) is an approach introduced by Hutchens and Yip in 1993 [11]. It encompasses two major subsets of MS technology: surface-enhanced neat desorption (SEND) and surface-enhanced affinity capture (SEAC). SEAC involves the derivatization of a sample-bearing surface that is used to capture analytes that were analyzed directly by laser desorption/ionization (LDI)-MS with the addition of MALDI matrix material. SEND is a method in which a molecule with LDI matrix properties is incorporated onto the LDI probe surface, which means that there is no need for further addition of matrix solution. In contrast to MALDI, where the sample surface is not derivatized and merely presents the substrate for the analytes, a SEAC probe surface plays an active role in the extraction, fractionation, cleanup, and/or amplification of the sample of interest. Today, the SEAC or SEND targets or ProteinChip arrays are distributed by Ciphergen Biosystems Inc. (Fremont, California). They incorporate the full range of surface properties, extending from broad binding characteristics of classical chromatographic media, such as IMAC, ion exchange, and reversed phase, to more specific biomolecular affinity probes, such as antibodies, receptors, enzymes, and DNA. Chromatographic surfaces are typically used for projects ranging from the identification of disease biomarkers to the study of biomolecular interactions. Array fractionation is normally performed by exposure of the biological media to the chromatographic surface, followed by washing steps of successive sample spots.

14.2.2 Material-Enhanced Laser Desorption/Ionization

The discovery and utility of new high-throughput methods based on different materials and chemical derivatizations for protein profiling of complex analytes leading toward biomarkers, for early detection and diagnosis of a disease, is an ongoing field. However, the complexity of biofluids, especially the most commonly used blood serum with suppressing nonvolatile salts, is hindering the analytical tools employed [12]. The complexity of samples can be reduced by implementing the screening techniques. The focus here includes the development, optimization, and application of a material-based approach, termed MELDI-MS (material-enhanced laser desorption ionization mass spectrometry) [13], which not only involves the various functionalities, but also emphasizes the morphology (i.e., porosity or particle size of the carrier material).

The materials investigated in the MELDI approach involve carbon nanomaterials: nanotubes [14], nanofibers, C₆₀ fullerenes, diamond layer [15] (diamond powder), cellulose, silica [16], and poly(glycidyl methacrylate/divinylbenzene) [17,18]. The serum contents are bound through different affinities, such as immobilized metal ion affinity chromatography (IMAC) and reversed phase (RP) on nanocrystalline diamond, nanotubes, and fullerenes. The advantages compared to other LDI-MS methodologies lie in the nature of support materials in addition to the functionalities added. The aim of the MELDI-MS approach is to screen biofluids such as serum and explore the distinctive peaks among healthy and diseased samples, which can then be employed as diagnostic markers after their authentic validations. Multiplexed protein pattern analysis based on the material morphology, physical characteristics and chemical functionalities provides a multitude of protein patterns. The contents can be eluted from MELDI materials, separated by μ -LC and identified through MS/MS, according to the top-down proteomics workflow depicted in Figure 14.3.

Serum peptides and proteins from human serum samples were enriched on derivatized materials and mass fingerprints were obtained directly through MALDI/TOF-MS. The main focus in MELDI technique is to use different derivatized materials to generate characteristic mass fingerprinting patterns and compare them for normal and diseased samples. The MELDI approach based on these derivatized carrier materials is meant to increase the number of proteins bound and resultantly to use them in basic biological research, leading toward marker search. The marker entities are also normally at very low concentrations (low ng/mL) in serum [19], and highly sensitive methods are required to bind them effectively from the biosamples. The sensitivity is improved by designing the sample preparation protocols, the purity of matrices, the target plates, and the overall sensitivity of the instruments. The recorded spectra have been proven to be specific for each carrier material. The diversity in the physical characteristics of these derivatized materials is responsible to get improved sensitivity, specificity, capacity, and a broad range of information compared to the conventional screening methods, without prior albumin or immunoglobulin depletion, and can be adapted to a liquid-handling robotic system for routine analysis. This approach includes the built-in desalting step for serum protein profiling and is sensitive

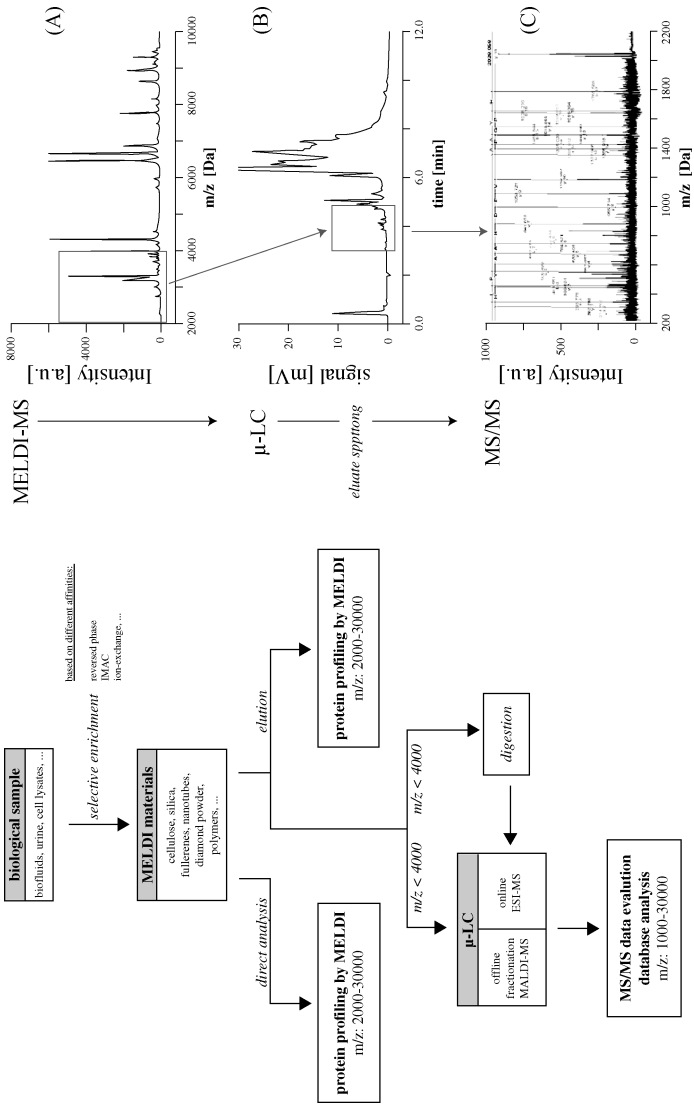


FIGURE 14.3 Workflow as a combination of MELDI, solvent-selective elution, and μ-LC-MALDI/MS or μ-LC-ESI/MS for the investigation of proteins and peptides from biofluids: (A) MELDI-MS; (B) μ-LC; (C) MS/MS.

enough to detect peptides and proteins down to the level where biomarkers could exist in biofluids.

The types of amino acid residues and their side chains forming the proteins decide about their interactions toward the specific affinity. A protein can exhibit more than one affinity at a time, depending on the nature of amino acids. The reversed-phase materials favor proteins possessing the more hydrophobic nonpolar contents of amino acids, whereas ion exchange (cation and anion) favors the charged (positively or negatively) side chains of amino acids constituting the proteins. Conversely, their elution after binding toward the support materials depends on their interactions. For instance, on RP supports, an organic solvent such as acetonitrile carries out the elution of nonpolar hydrophobic contents. Purification and prefractionation through the MELDI approach can begin with a starting complex material such as serum, cell lysate, or tissue and can lead toward their identification, post-translational modifications, and functions.

To investigate the applicability of MELDI, materials are checked for reproducibility of derivatization and sample preparation with human serum samples. Upon comparison of these carbon IMAC supports, the protein profiles are quite specific to each material. Due to the same surface functionality used for all carrier materials (e.g., copper-loaded IDA), some peaks in the resulting mass fingerprints exhibited the same m/z values; however, upon closer examination of the individual profiles in the respective MELDI spectra, noteworthy differences are found. The absence and presence of some peaks emphasize the differences in net hydrophilicity and hydrophobicity of these materials after derivatizations. The diversity in physical and chemical characteristics, hydrophobic and hydrophilic characters of the derivatized materials, are responsible for the improved sensitivity, specificity, capacity, and broad range of information content of resulting spectra.

Material characteristics such as nanostructuring, particle size, surface area, hydrophilicity, and hydrophobicity contribute to the nature of bindings of serum contents. So the success of this technique depends significantly on the adsorbent nature of material used for serum enrichment. During the evaluation process of various functionalized carrier materials, it is found that not all the materials provide the same mass fingerprints. As in earlier MELDI studies, cellulose carrier materials of different shapes result in unique peak patterns, 8 to 10 μm being the most effective size range, in the sense of number and signal intensity of resulting peaks [13]. As the particle size increases to 20 to 30 μm , or the shape changes from spherical to fibrous, the efficiency decreases tremendously, suggesting that fibrous and large spherical cellulose particles are not adequate for MELDI. Furthermore, the porosity of MELDI supports investigated influences the binding properties and appearance of the resulting mass spectra. Pore size thus has to be selected carefully, as porosity has a great impact on the desorption process and consequently, on the mass spectra obtained. For instance, narrow-pore silica particles (6 nm) do not provide adequate MS traces.

The MELDI approach also involves the addition of matrix (energy-absorbing substance); however, the sensitivity is improved overall in the case of certain MELDI materials, such as like carbon nanotubes and fullerenes, due to their known energy absorbing tendencies. The MELDI technique covers both direct analysis by laser

irradiation of the material, loaded with peptides and proteins, or the elution of bound contents, followed by subsequent MALDI analysis. The MELDI support particles do not affect the spectral patterns in terms of background signals.

However, care must always be taken to employ the standard investigated protocols of MELDI for reproducibility, fixing of biomarkers, and avoiding the false positives because of various proteolytic activities going on in the biofluids. The ability of this method is already proven by a comprehensive study analyzing hundreds of serum samples with the aim to distinguish prostate cancer from nonprostate cancer samples [13]. Using this method it was possible to differentiate these two groups with a high probability of more than 90%. In addition, focus is laid on sample collection and storage condition to avoid biases and methodological errors, since it was shown that they alter the serum peptidome significantly [20]. The sample preparation protocols are further optimized, and incubation times are reduced to few minutes. To strengthen the robustness and to control the MELDI platform, all steps, from sample preparation to extraction, sample spotting, and MS analyses, are fully automated.

14.3 CARBON NANOMATERIALS

The nanomaterials are regarded as potential candidates in many categories of scientific fields, including biosensors, biomedical, drug delivery, and biomarker research. The miniaturized nanoparticles are composed of the microscopic grains, which are constituted of atoms and provide the opportunity to work in three dimensions at very minute scale. The reason behind is based on the fact that the characteristics are altered when dimensions (size and shape) are brought to nano levels, which offer unique applications in comparison to the same bulk material. Their thermal, optical, and electrical properties make them a candidate in analytical devices. The fragility of the nanomaterials at the nanoscale is reduced to make them mechanically stable, hard, and very reactive. They can attain the various forms or shapes as existing tubes, wires, fibers, or dots. The nanometer-sized polymeric dendrimers are also grown in layers. The nanomaterials are interfaced and integrated to many analytical techniques, such as mass spectrometry. The overall sensitivity and utility as support phases are enhanced, due to their energy-transferring capabilities. Nanomaterials are incorporated in the ionization methods in matrix-free LDI-MS [21] and matrix-assisted LDI-MS. Tanaka reports the first use of cobalt nanopowder for surface-assisted laser-desorption/ionization (SALDI-MS) in the analysis of proteins [22]. Broader matrix-free application is reported for DIOS (desorption ionization on porous silicon). In 1999 it was introduced for analyzing low-molecular-mass compounds [23]. The gold nanoparticles with 2- to 5-nm sizes are also reported to support the desorption ionization (DI) phenomenon [24]. Metals and metal oxides of titanium and tungsten in their particle forms dispersed in paraffin or glycerol are also employed for LDI-MS [25].

Carbon, with its variety of different configurations and allotropes in nature, has received more and more attraction in the last decade [26]. Carbon nanomaterials such as diamond, carbon nanotubes and fullerenes are selected in this regard as carrier supports, because of their higher surface/volume ratios, expanded nanostructures,

higher potential binding sites, and sensitivities. They have a strong role in the recent past in certain biological applications coupled to desorption/ionization. The sample supports for use in matrix-free LDI-MS are graphite [27], carbonnanotubes [28], fullerenes [29] or amorphous carbon [30]. The graphite powder is reported to be packed in GELoader tips for desalting and concentration of peptide mixtures prior to LDI-MS [31]. Carboxylated and aminated diamond particles have been used to concentrate and purify the proteins and DNA oligonucleotides [32]. The modified diamond, carbon nanotubes, and fullerenes are acting as small chromatographic interfaces for preconcentration and screening of biofluids. Blood serum samples are used for preliminary testing and evaluation of these derivatized materials for protein profiling. The unique properties were exploited for manipulating these nanomaterials to construct an interface for protein profiling.

Under all elements carbon has found a very special place in the periodic table, due to the fact that it forms very stable expanded structures that are covalently bound. Due to the strong delocalization of the valence electrons, the bondings between metals are weaker than those of carbon. Other nonmetals, such as nitrogen and oxygen, build extremely strong bindings among each other so that a pair production of electrons takes place, minimizing the free energy (compare the explosive nature of many nitrogen compounds). Carbon combines these two extremes: It can establish strong bonds with itself as well as with two, three, or four other binding partners.

Elemental carbon occurs in the form of diamond and graphite, and when it is impure (the amorphous form), we call it coal. In the case of diamond, every carbon atom is sp^3 hybridized and covalently bound to four other carbon atoms, whose binding arms point to the corners of a tetrahedron, having an angle of 109° between each arm, resulting in its unique structure. In graphite every carbon atom is sp^2 hybridized and covalently bound to three other carbon atoms, forming a plain of continuous hexagons between which relatively weak van der Waals forces act. Next to these two crystalline structures, a new carbon modification with a spherical network exists which was isolated in 1990: the buckminsterfullerenes.

Fullerenes differ from the other two allotrope forms of carbon, diamond and graphite, mainly by their molecular character. They don't form two- or three-dimensional expanded structures but closed molecular systems, with a sp^2 -hybridized carbon as a common building block. In contrast to graphite and diamond, they are soluble in various solvents, which is important for chemical manipulation. Fullerenes consist of pentagons and hexagons. The pentagons are responsible for the bend and the unique football structure. The easiest available fullerene is the I_h -symmetrical C_{60} . The next-best stable homolog known is the D_{5h} symmetric C_{70} , followed by the higher fullerenes C_{76} , C_{78} , C_{84} , C_{90} , C_{94} , and C_{96} . The Euler theorem demands that every closed, spherical network of penta- and hexagons exist of exactly 12 pentagons. In such networks all pentagons are completely surrounded by hexagons when there are at least 60 corner points. Therefore, fullerenes smaller than C_{60} are unstable. The isolated pentagons play a crucial role in the stability of the molecule. Here we speak of the isolated pentagon rule (IPR) [33]. Some interesting physical properties of diamond, graphite, and C_{60} are shown in Table 14.1.

TABLE 14.1 Diamond, Graphite, and C₆₀ Comparison

	Diamond: Cubic	Graphite: Hexagonal	C ₆₀ : Face-Centered Cubic
Density (g/cm ³)	3.30	2.27	1.65
Lattice constant (Å)	3.513	$a = 2.456$ $b = 6.696$	14.15
C–C length (Å)	1.54	1.42	1.455
C=C length	—	—	1.391
Standard heats of formation (kcal/mol)	0.4	0.0	0.9
Bulk modulus (GPa)	1200	207	18(174)
Melting point (K)	3700	3800	Sublm. 800
Index of refraction	2.42	—	2.2 (600 nm)
Conductivity	Insulator	Conductor	Semi conductor
Naturally occurring deposit	Kimberlite	Pegmatite	Shungite
Location	S. Africa	Sri Lanka	Russia
Crystal formation	Octahedral	Tubular	Hexagonal, cubic
Name meaning	“Invincible”	“To write”	Named after architect
Isothermal volume compressibility (cm ² /dyn)	0.18×10^{-12}	2.7×10^{-12}	6.9×10^{-12}

14.3.1 Derivatized Diamond

Diamond is a material that shows properties such as high stiffness, thermal conductivity, optical transparency range, physicochemical stability, erosion resistance, and inertness [34]. The transparency is covered over a broad range from the far-ultraviolet (UV) to the far-infrared (IR). Diamond is coated and utilized in form of surfaces, and the surface properties are different from the bulk properties. Diamond is found with different types, from natural single crystal to CVD ultrananocrystalline (UNCD). The different forms of CVD-deposited diamond can be categorized as ultrananocrystalline, polycrystalline, and single crystal [35]. UNCD contains about 95% sp³ carbons, 2 to 5 nm in size, separated by high-energy grain boundaries.

Natural diamond is found most often in crystalline form in pure cubic structures of sp³-bonded carbon atoms. The diamond crystal has face-centered cubic lattice structure, with a basis of two atoms. The growth of diamond from molten material in case of natural and synthetic diamond produces cubic structures, as they are stable due to the lower internal energies. Because of the large amount of energy needed to break numbers of covalent bonds, diamond has a high melting point (2820 K).

The four outer electrons of each carbon atom in diamond are localized between the atoms, which makes the movement of electrons very restricted and thus is electrically insulating in its purest forms. However, it is good conductor of heat because the electrons in covalent bonds are mutually shared and heat can be dissipated easily. In addition, due to its large stability to many chemical agents and to its biocompatibility, diamond appears as an attractive candidate material in several applications [36]. Nanocrystalline diamond (NCD) coatings on various substrates have created an

interest in biological applications during recent times. The investigation of morphology, surface termination, and the possibilities for biofunctionalization of NCD are important tasks.

Hydrogen-terminated diamonds possess high p-type conductivity (high negative electron affinity) whereas oxygen-terminated diamonds are insulating. The conductivity of H-terminated NCD is affected by the adsorbents from atmosphere. NCD can be doped so as to vary the conductivity of films, which can be more effective in LDI-MS sensitivity. The oxygen-terminated surface can be terminated as C—O—C, carbonyl group, or hydroxyl group. Hydrogen terminations on NCD are obtained automatically in a CVD process, as methane and hydrogen gases are used during growth [37]. In addition, H-terminated surfaces are hydrophobic and O-terminated surfaces are hydrophilic. However, the hydrophobicity and hydrophilicity do not greatly influence the surface topography. The extent of hydrophobicity and hydrophilicity are characterized by measuring the shape and contact angles of the liquid drops placed on the surfaces. Consequently, selective adsorption of biomolecules such as proteins on diamond material due to van der Waals and/or electrostatic forces is possible using selective fabrication of hydrophobic and hydrophilic regions on diamond substrates [38].

14.3.1.1 Immobilized Metal Ion Affinity Chromatography The main focus is laid around the affinity termed immobilized metal ion affinity chromatography (IMAC), introduced by Porath et al. in 1975 [39]. NCD is derivatized as IMAC support material to screen peptides and proteins specific to this affinity from human serum samples. The specific bindings of his-tagged proteins enable the enrichment, which reduces the complexity of serum. However, one can still argue about highly abundant proteins such as albumin (50 to 60 mg/mL), which can limit the material capacity. IMAC supports can be loaded with a range of metal ions, depending on their nature of interaction with peptides and proteins. It is proposed that proteins possess around 2% histidine [2-amino-3-(3*H*-imidazol-4-yl)propanoic acid], and only half are exposed to the surface for effective bindings to loaded Cu^{2+} ions [40]. The statement is supported through studies carried out on binding constants with histidine residues [41]. The binding potential of side chains of proteins with histidine residues is very high, as only one histidine exposed on the protein is enough to bind with Cu^{2+} [42].

14.3.1.2 Preparation of NCD–IMAC Supports Diamond surfaces coated with titanium were derivatized [43] so as to develop new surfaces for serum profiling. The derivatization was performed by having a thin layer of glycidyl methacrylate (GMA) on an NCD surface in an inert chamber equipped with a quartz window. The illumination was performed by UV light under a constant flow of nitrogen. Afterward, the derivatized chip was washed with deionized water to remove the physically adsorbed molecules, and then immersed in iminodiacetic acid (IDA) solution.

In general terms, diamond is considered a stable material; however, when diamond is coated as a layer, it misses one neighboring atom in the lattice structure and offers dangling bonds pointed outward. These bonds provide high-reactivity sites for terminations, as they are at higher energy configurations and lower the stability by

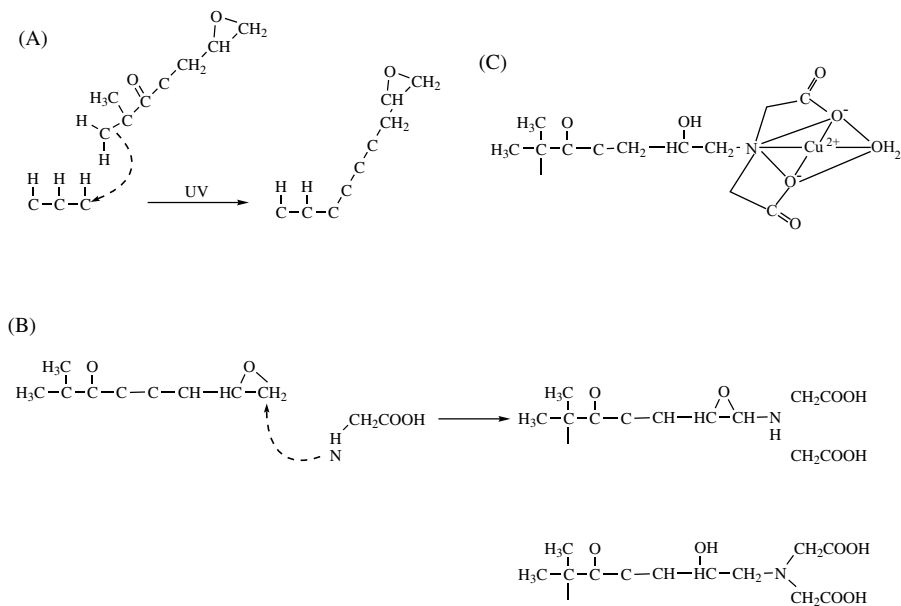


FIGURE 14.4 (A) Nucleophilic attack of π -electrons on partially positive carbon of hydrogen-terminated NCD surface; (B) mechanism of epoxide opening of GMA with IDA on an NCD surface under basic conditions (pH 10); (C). Cu^{2+} loading on chelating ligand, IDA to be employed as an IMAC support for protein profiling.

joining available atoms during reactions. The C—H bond in hydrogen-terminated surfaces has a polar character due to the difference in electronegativity of carbon and hydrogen atoms.

Functionalization on the diamond surface is carried out by a UV-assisted photochemical process. The mechanism is based on the nucleophilic attack on a positively charged $\text{C} \delta^+$ of a C—H bond. The mechanism of this nucleophilic addition reaction is shown in Figure 14.4(A). The nucleophilic attack happens when shorter-wavelength UV radiations excite the electron-hole pairs across the bandgap (5.48 eV for diamond). The necessity of UV light for nucleophilic attack can be attributed to the free energy released due to the recombination of electron-hole pairs, which is quite high for diamond (i.e., 5.48 eV).

The attachment of GMA to hydrogen-terminated NCD surfaces is followed by the derivatization with IDA in strongly basic conditions to open up the epoxide group through the mechanism shown in Figure 14.4 (B). The high strain of epoxide ring makes it susceptible to nucleophilic attack. The IDA nucleophilic nitrogen attacks the least-hindered carbon and make a transition complex, stabilized by ionic charges, followed by IDA attachment. Copper (Cu^{2+}) is loaded on metal-chelating iminodiacetic acid (IDA), as shown in Figure 14.4(C).

Cu^{2+} belongs to the intermediate metal ions and has a coordinating potential toward nitrogen, sulfur, and oxygen. Cu^{2+} , particularly, binds the amino acids of

peptides and proteins at N-terminals at pH greater than 8 [44]. The binding entities to the IMAC materials belong to histidine-tagged proteins, as sulfur-containing cysteines are quite less on the boundaries of proteins. The mechanism of interaction is based on the specific interaction of the imidazole side chain of histidine with chelated Cu^{2+} .

XPS measurements are carried out to analyze the diamond surface to assess the elements present. The survey spectrum reveals the presence of elements (i.e., carbon, oxygen, and nitrogen) at the surface. A composition of 88.4% carbon, 9.9% oxygen, and 1.7% nitrogen is calculated from the peak intensities. If Ti is also taken into account for the quantification, a concentration of 0.3% is calculated, reducing the C fraction to 88.0%. The small Ti intensity shows that this element is present at the interface between the substrate and the adsorbate layer. Direct proofs for the presence of chemistry carried out on the diamond surface are the nitrogen signals in the survey spectra, which originate from the addition of IDA by opening of epoxide group of GMA (Figure 14.5). As a result, chelating ligand, IDA, is covalently attached by reaction between the epoxide and the primary amine of IDA.

The N 1s peak appears at 400 eV, which is exactly the representative binding energy (BE) for such nitrogen functionalities [45]. Also in the survey spectra, the Ti 2p peak is evident, which is from titanium substrate, indicating that the diamond surface is not fully closed. In the C 1s signal measured in high-resolution mode, several peaks can be identified by fitting Gauss–Lorentzian functions to the experimental data. Four different binding states of carbon can be identified, labeled C1 to C4 in Figure 14.6. The binding energies are determined to be 284.2, 284.9, 285.8, and 288.3 eV, respectively. Peaks C1 and C2 are characteristic of C–C and C–H bonds, respectively. However, the assignment to specific bonds in this binding energy region is ambiguous [46], since C–H and C–C bonds of various characters contribute to the C 1s intensity. Therefore, no precise assignment to a specific bond type can be made for the C1 and C2 peaks. C3 has binding energies typical for C–O groups (alcohols, ethers), whereas C4 is the BE region where carbonyl bonds appear.

14.3.1.3 Protein Profiling on IMAC–NCD Surfaces An IMAC–NCD surface is checked for reproducibility of the method developed for serum protein profiling from mass range of 2 to 10 kDa, shown in Figure 14.7. The spectra are also recorded at higher masses of 10 to 20 and 20 to 80 kDa, to check the efficacy and that the results produce a number of peaks in this mass range, as shown in Figure 14.8. The spectrum is also recorded at the higher mass range 20 to 80 kDa. The NCD-derivatized surface is the binding number of proteins in this mass range, depicted in Figure 14.9.

Conclusively, NCD surfaces have enough docking sites to hold and bind a huge number of proteins in a broad range of masses, from 2 to 80 kDa. The advantage of NCD surfaces for recording the high-mass proteins lies in the fact that there is no additive added to the analyte solutions, which can aid the desorption of those proteins. Normally, the nonionic and zwitterionic surfactants are added to increase the detection of higher mass proteins [47]. They are believed to avoid or minimize the adsorption

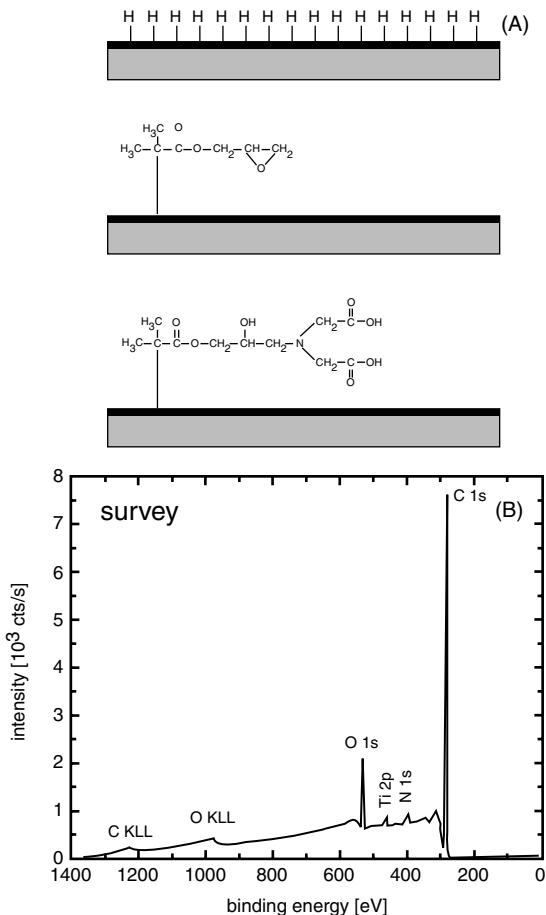


FIGURE 14.5 Chemical steps to derivatize an NCD surface. (A) Photochemical attachment of GMA followed by IDA derivatization; (B) XPS survey spectra of a derivatized diamond surface showing the elements as C 1s, O 1s, and N 1s.

losses of proteins and stabilize them [48]. However, these ionic surfactants can suppress the MALDI signals, which is why they must be removed prior to MALDI-MS analysis.

The success of these diamond surfaces over a longer period of time depends entirely on achieving and maintaining enduring bonds between the chemical functionalities of the linkers and the diamond surface. The IMAC supports can be stored stably for longer period of times without losing their functionalities and efficacies. The stability periods can be extended over years if they are kept at 4°C under proper storage conditions.

The introduction of MELDI as a profiling technique provides a sensitive, multiplexed protein pattern analysis approach, offering accurate and reproducible

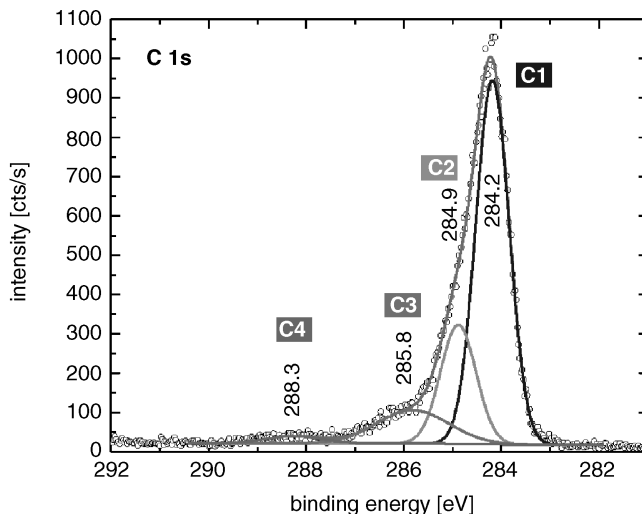


FIGURE 14.6 C 1s energy window high-resolution XPS spectra, showing peaks at 284.2, 284.9, 285.8, and 288.3 eV characteristic of the diamond surface and functionalities.

MS traces that can be useful for wide-ranging applications. The protein profiles emerged out of the derivatized carbon nanomaterials (diamond, carbon nanotubes, and fullerenes) are reproducible up to norms and resulting broad information from range of these materials can widen up the horizons for biomarker research. The potential bonding sites are enhanced due to the expanded nanostructures and higher surface areas of carbon nanomaterials. The materials are derivatized as IMAC support material and characterized through various analytical techniques. The protein mass fingerprints are characteristic for every serum sample on every material. These carbon materials with developed protocols are thus a domain of central importance for the search of distinctive markers.

14.3.2 Modified CNT

The discovery of multiwalled carbon nanotubes (MWNTs) by Iijima in 1991 [49] and of single-walled carbon nanotubes (SWNTs) by Iijima and Bethune et al. in 1993 [50] has given rise to a new important material, designated to be used in nanotechnology. Nanotubes are composed entirely of sp^2 -hybridized bonds having a diameter in the range 1 to about 50 nm and a length between 1 and about 20 μm . Their unique optical, electrical, thermal, and chemical properties have caused great research interest, and their effective biocompatibility has provided an opportunity to use this material in many biological applications, especially in the field of bioanalytics. Recently, functionalized carbon nanotubes (CNTs) were used successfully as energy-absorbing MALDI matrices for the study of micro- as well as macromolecules [51–54]. They have been shown to absorb laser light (ultraviolet, infrared) and to be excellent conductors of electricity, which is crucial for the energy transfer and dissipation

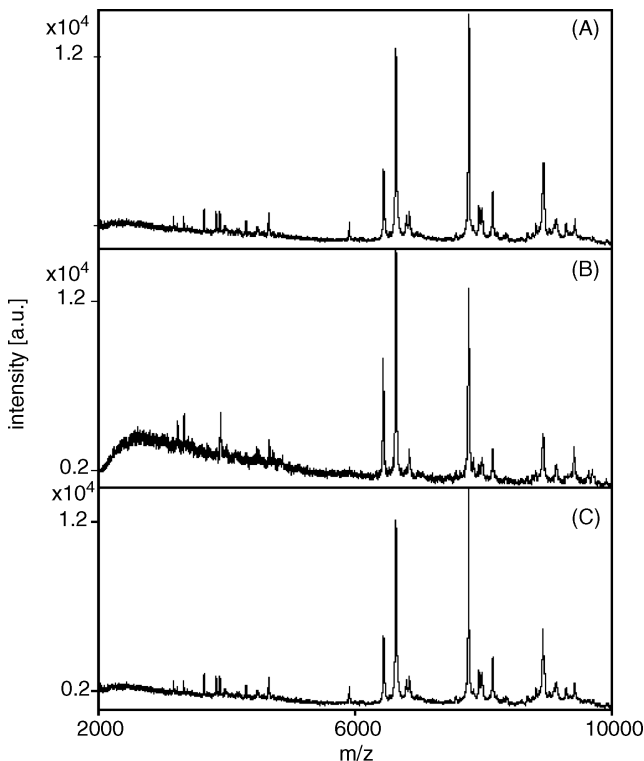


FIGURE 14.7 Reproducibility of serum mass fingerprinting on IMAC-NCD with MALDI/TOF-MS. The spectra in A, B, and C are recorded with standard serum at three different times in a linear mode.

efficiency during desorption and ionization. These outstanding advantages of CNTs have provided an opportunity to use this material for the specific binding of biomolecules followed by their subsequent mass spectrometric analysis by employing them as MELDI carriers. This was demonstrated for iminodiacetic acid (IDA)-modified CNTs by synthesizing CNT-IDA-Cu²⁺ support material. The main aim of employing CNT derivatives in MELDI MS was to provide a rapid and sensitive material for protein profiling, creating a basic platform for further identification of disease markers from a variety of biological samples.

14.3.2.1 Derivatization of Carbon Nanotubes The derivatization of CNTs is a three-step procedure. In the first step the carboxylic groups, which are obtained after oxidizing with nitric acid [55,56], are chlorinated with thionyl chloride [57]. In a further step the resulting acid chlorides were aminated with iminodiacetic acid. Finally, the CNTs were loaded with copper(II) ions. During this loading step IDA forms a bidentate complex with the Cu(II) ions. The steps of CNT-IDA-Cu²⁺ derivatization are shown in Figure 14.10.

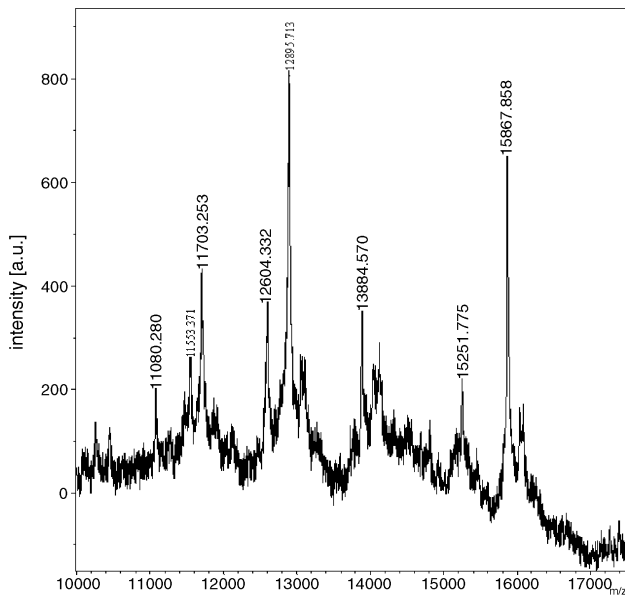


FIGURE 14.8 Serum mass fingerprint on IMAC-NCD with MALDI/TOF-MS. The spectrum is recorded in the mass range 10 to 20 kDa with standard serum in linear mode.

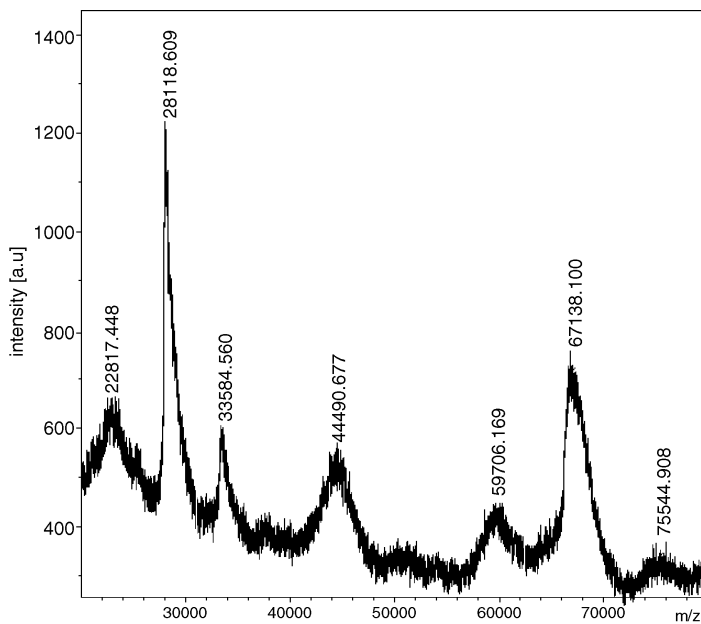


FIGURE 14.9 Serum mass fingerprint on IMAC-NCD with MALDI/TOF-MS. The spectrum is recorded in the mass range 20 to 80 kDa with standard serum in the linear mode.

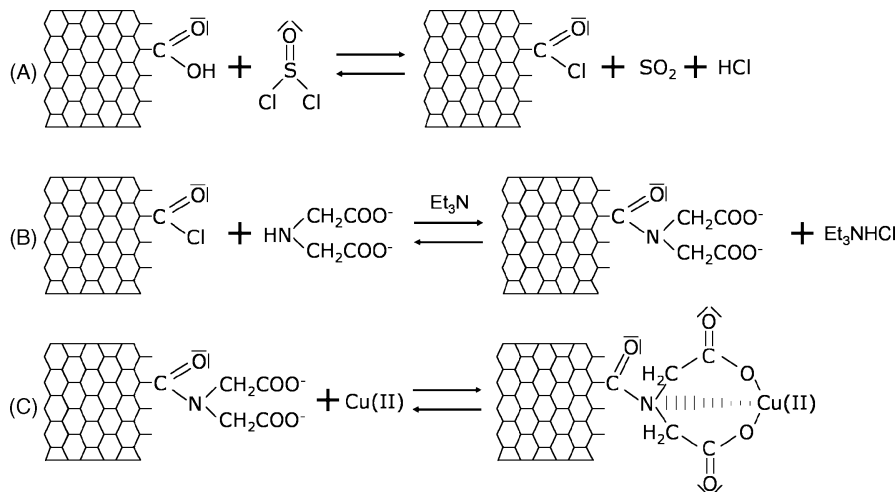


FIGURE 14.10 Derivatization scheme of carbon nanotubes. Oxidized CNTs are reacted with thionyl chloride (A) followed by the attachment of iminodiacetic acid under alkaline conditions (B) and copper loading (C).

14.3.2.2 Characterization of Carbon Nanotubes

Field Emission Microscopy Field emission microscopy (FEM) plays a major role in understanding the structure of solid surfaces. FEM pictures are derived from the emission of electrons under the influence of a high electrostatic field from a metal or semiconductor into vacuum at a CNT's surface. High vacuum is extremely prominent in field emission experiments, as it has an extreme surface sensitivity to change the emission pattern. As demonstrated in Figure 14.11, the FEM photographs of underivatized and IDA-derivatized CNTs are depicted. Unmodified CNTs and CNT-IDA-Cu²⁺ have different morphology and arrangement. The derivatization process leads to no serious shortening of the CNTs but makes them thicker and swollen in diameter.

Copper Capacity Study The relatively high copper capacity (~1 mmol/mg CNT) of CNTs, which can be determined quantitatively by atomic absorption spectrometry (AAS), makes this material an attractive support for studies in MELDI. Normally, it is difficult to chelate proteins out of serum samples in the mass range 10 to 40 kDa, but CNT-IDA-Cu²⁺ support material exhibits quite a reasonable affinity for high-molecular-weight proteins. Moreover, CNT-IDA-Cu²⁺ is a good material to bind serum albumin. This is in accordance with other literature, where it was demonstrated that IMAC has excellent affinity specifically to serum albumin [58,59].

Infrared The successful derivatization of CNTs can, furthermore, be confirmed by recording comparative IR spectra as illustrated in Figure 14.12. The materials termed A, B, C, and D are IDA-modified CNTs from different batches to check the reproducibility of derivatization features. There is a clear difference between

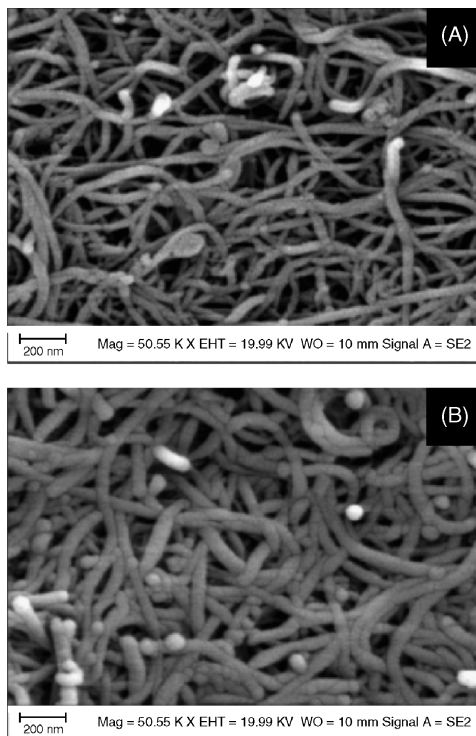


FIGURE 14.11 Field emission microscope pictures of (A) underivatized and (B) derivatized carbon nanotubes at 50 times magnification. The carbon nanotubes were mounted directly on the stub using an adhesive prior to microscopic inspection. A base pressure of less than 10^{-10} mbar needed to be maintained during the experiments.

the untreated and the four IDA-treated nanotube materials. The distinctive band appearing at approximately 2300 cm^{-1} is due to the tertiary amine created by IDA. The unmodified CNTs do not show any deflection band at this wave number.

Batch-to-batch reproducibility was assured and shown in Figure 14.13. The spectra generally show the same mass pattern, but there are minor differences in intensity which can be attributed to differences resulting from sample preparation and recrystallization of matrix, which further influence the desorption and ionization process of the MS. Regarding their applicability, CNT-IDA- Cu^{2+} show high efficiency as carrier materials in the high mass range 10 to 40 kDa and provide satisfactory results in the lower mass range 1 to 5 kDa.

14.3.3 Derivatized Fullerenes

In 1966, Jones [60] assumed that a graphite layer would close to a hollow ball if he were able to add some pentagons between the hexagons. The first publication in which a C_{60} molecule was described was written by Eiji Osawa in Japanese. In 1970 he

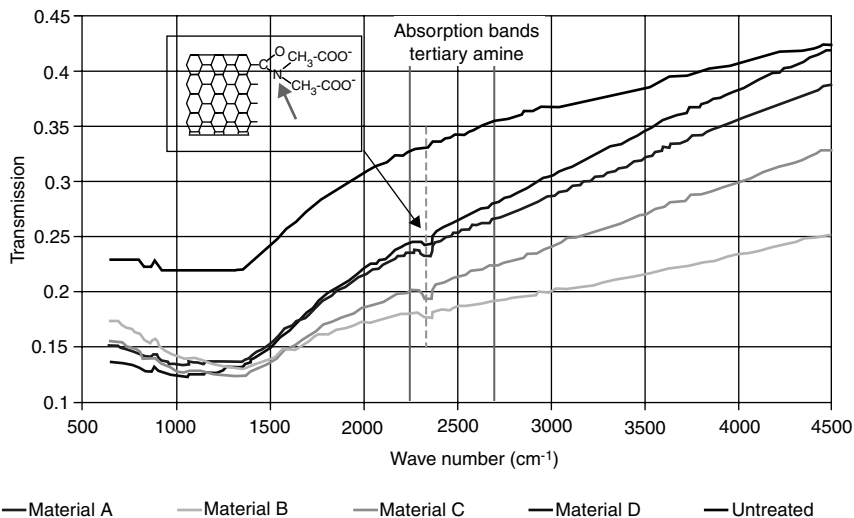


FIGURE 14.12 Infrared spectra of untreated and treated CNTs recorded by ATR-FTIR (attenuated total reflection–fourier transform infrared) spectrometer (Bruker Vector 22, Germany) in the range 500 to 4500 cm^{-1} . The derivatized CNTs were suspended in water and filtered over a cellulose acetate filter ($0.2\text{ }\mu\text{m}$). After the filter was dried, the respective “buckypaper” was removed from the filter manually and brought in to record the IR spectra.

published the theory that a molecule of this structure could be stable [61]. Assumptions of the existence of molecular carbon allotropes were mentioned in other works, but not until 1984 did this idea receive experimental support [62]. The first fullerene was created by Kroto and Smaley in 1985 by laser evaporation of graphite [63]. They gave the new substance class the name of the American engineer and architect Buckminster Fuller, whose dome-shaped constructions obey a similar assembly principle. The preparative isolation of this new carbon allotrope was first attained in 1990 by the group of Krätschmer [64]. In the meantime, the production of fullerenes is done by the evaporation of graphite in an arc using an electrical resistance heater at temperatures up to 6000°C in an inert gas atmosphere. Mostly helium with optimized pressure is used. They can also be manufactured by heating carbon black with an optimized flame [65–67]. Afterward, the carbon black gets extracted with organic solvents (e. g., toluene, resulting in a yield of 10 to 15% fullerenes); the amount of C_{60} is greatest, 80%, whereas C_{70} has a yield of 15%, the rest being the higher fullerenes up to C_{94} [68,69]. The fullerene mixture won through this procedure is separated by column chromatography on aluminum oxide using a hexane–toluene mixture as mobile phase. The best results for the purification are nevertheless achieved using flash chromatography on silica gel–activated carbon with toluene as mobile phase [70,71].

14.3.3.1 C_{60} Characteristics The absorption spectra of C_{60} and C_{70} [72] show strong absorbance between 190 and 410 nm, C_{60} having its absorption maximum at

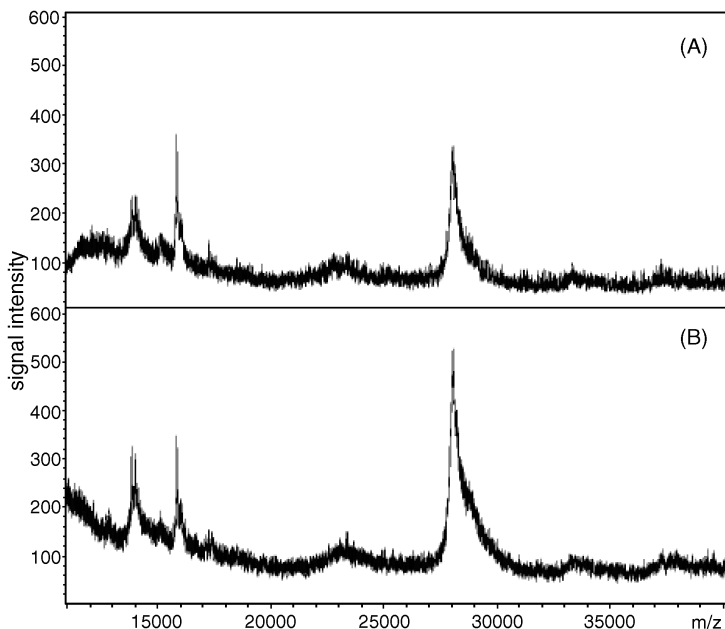


FIGURE 14.13 Serum protein profiles of CNT-IDA-Cu²⁺ recorded by MALDI/TOF-MS in the mass range 10 to 40 kDa by averaging 180 laser shots. Samples were analyzed in a MALDI-TOF/TOF spectrometer (Ultraflex, Bruker Daltonics) in the linear mode using a UV nitrogen laser (337 nm). Sinapinic acid was used as the matrix substance.

340 nm. They also absorb visible light, giving them their unique violet (C₆₀) and red (C₇₀) color. Saturation of one or more double bonds in the case of an addition reaction leads to a change in the chromophore and results in a characteristic change of the absorption spectrum. Another unique phenomenon of fullerenes is due to their conjugated electron system; they can absorb a lot of energy, making them a potential substance that can be used as a matrix. Fullerenes have the ability to fly even without the influence of an acidic group, as shown in Figure 14.14, where a fullerene dissolved in toluene is spotted on a stainless steel target without a matrix and excited via a laser. In comparison, a protein is not able to fly without an ionization process.

14.3.3.2 Derivatization Reaction of C₆₀ Fullerene derivatives have become the current focus of research and play an important role in biological and material science [73]. One of the most important methods for C₆₀ functionalization involves the formation of methanofullerenes. These consist of the C₆₀ fullerene cage, a cyclopentane ring, and one or more carboxylic functionalities. Several methods for the synthesis of these methanofullerenes are known:

1. Thermal addition of diazo compounds, followed by thermo or photolysis [74]
2. Addition of free carbenes to C₆₀ [75]

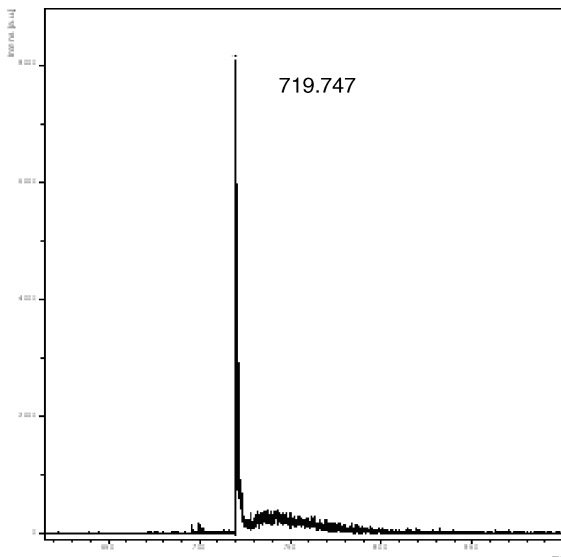
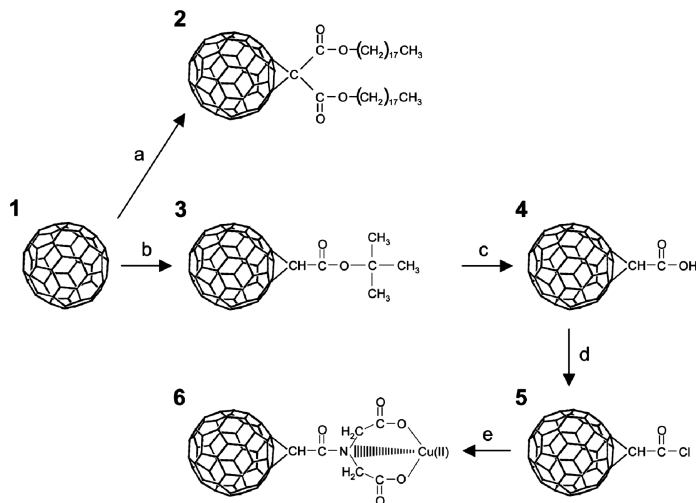


FIGURE 14.14 C_{60} MALDI spectrum recorded without a matrix; 400 shots added.

3. Reactions that proceed by an addition–elimination mechanism [76]
4. Reaction of sulfonium ylides with C_{60}

The first method always produces a mixture of [5,6]-open fulleroids and [6,6]-closed methanofullerenes. Pure [6,6]-methanofullerenes are obtained only after tedious isomerizations. The other three reactions give pure methanofullerenes. The reaction of C_{60} with diethyl brommalonate and a base such as DBU (1,8-diazabicyclo [5.4.0]undec-7-en) is a special case when looking at reactions with metal-organic compounds. α -halogen-CH-acidic compounds for diethyl brommalonate, for example, react in the presence of a base with C_{60} to cyclopropane derivatives [77]. The mechanism of the reaction is as follows: After deprotonation of the α -halogen-ester, a nucleophilic attack on C_{60} follows. A stable, intermediate carbanion is built and simultaneously, a cyclopropane ring is formed through loss of the bromide [78,79]. This is called the Bingle reaction. The reaction scheme shown in Figure 14.15 represents three MELDI materials: RP-[60]fullerene (**2**) [60]fullerenoacetic acid (**4**) and IDA-[60]fullerene (**6**) beginning with fullerenes (**1**).

The main focus is to utilize the derivatized fullerenes such that peptides and proteins can be effectively bound with the surface and analyzed by MALDI/TOF-MS in order to get mass fingerprints. The advantage of this method is the ability to effectively resolve polypeptides and peptides smaller than 20 kDa, which are normally very difficult to monitor. In this phenomenal approach, the derivatized fullerenes comprehensively measure proteins in biological samples like serum, allowing rapid identification of the differences between the control serum and cancer patient serum.



	name	empirical formula	mass [g/mol]	CAS	conditions	solvent
a	di(12-iodododecyl)propanedionate	$C_{39}H_{76}O_4$	609.03	16832-90-7	R.T. 12h	toluene
b	t-butyl(dimethylsulfuranylidene)acetate	$C_9H_{16}OS$	160.28	58719-71-4	R.T. 8h	toluene
c	p-toluenesulfonic acid monohydrat	$C_7H_6O_3S \cdot H_2O$	190.22	6192-52-5	reflux 8h	toluene
d	thionyl chloride	$SOCl_2$	118.97	7719-09-7	reflux 8h	-
e	iminodiacetic acid	$C_4H_7NO_4$	133.10	142-73-4	reflux 8h	THF
1	buckminsterfullerene	C_{60}	720.64	99685-96-8		
2	RP-[60] fullerene	$C_{99}H_{74}O_4$	1329.75	193271-96-4		
3	t-butyl [60]fullerenoacetate	$C_{68}H_{10}O_2$	834.068	311336-89-7		
4	[60]fullerenoacetic acid	$C_{62}H_2O_2$	778.00	155116-19-1		
5	[60]fullerenoacetyl chloride	$C_{62}HO_2Cl$	811.96	-		
6	IDA-[60]fullerene	$C_{66}H_7NO_5$	893.03	-		

FIGURE 14.15 Reaction scheme of fullerene derivatives used as MELDI materials.

The MELDI spectra were compared with the standard serum in terms of the binding trends of peptides and proteins toward various functionalities on fullerenes. As expected, the bound biomolecules show a distinct difference, especially in the mass range 2 to 7 kDa, as shown in Figure 14.16. [60] Fullerenoacetic acid [Figure 14.16(B)] shows a higher capacity than RP-[60] fullerene [Figure 14.16(B)] and Cu(II)-IDA-[60] fullerenes [Figure 14.16(C)] in this particular low mass range. The differences in the binding nature of these functionalized fullerenes continue when the spectra are recorded from 10 to 20 kDa, as shown in Figure 14.16(D)–(F). In this relatively higher mass range the spectra quality parameters and the binding abilities are much improved for Cu(II)-IDA-[60]fullerenes [Figure 14.16(F)]. This is in accordance to the values obtained from the Langmuir study described below, where the capacity of lysozyme was measured. Therefore, it can be inferred that [60]fullerenoacetic acid is better than Cu(II)-IDA-[60] fullerenes for binding relatively small mass peptides and proteins. This phenomenon of diversity in binding nature is helping to widen the range of information from biofluids when data are analyzed as a combined picture by bioinformatics.

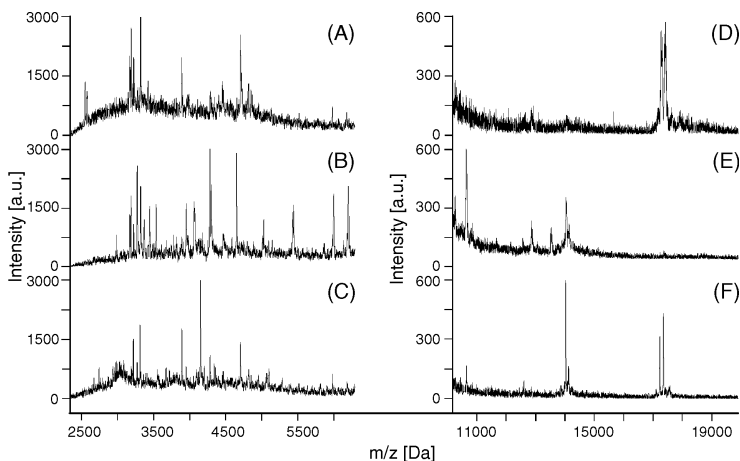


FIGURE 14.16 Influence of fullerene derivatization on a MELDI protein profile pattern in the m/z range 2300 to 6300 (A–C) and 10,200 to 20,000 (D–F); (A, D) dioctadecyl methano[60] fullerene; (B, E) [60]fullerenoacetic acid; (C, F) Cu(II)-IDA-[60]fullerene. Conditions: Bruker Ultraflex MALDI-TOF/TOF, each spectrum: addition of 350 shots, matrix: SA. Sample: diluted human serum.

14.3.3.3 Identification of Low-Abundance, Low-Mass (Peptidic) Serum Constituents As mentioned earlier, proteins and peptides in the low-mass range are most likely to be discovered as biomarkers [80]. Therefore, it was a goal of this work to study the low-mass MELDI spectra in more detail. Another reason to pay more attention to the low-mass range is the fact that one can easily identify peptides in the range 3000 to 4000 Da with MALDI-MS/MS without precedent digestion.

As shown in Figure 14.17, [60]fullerenoacetic acid shows the highest amount of substances in the low-mass range from m/z 1000 and to m/z 4000. For the fragmentation process to take place successfully, the parent ion peak has to be very intensive. Direct measurement of the MELDI material, however, resulted in a too-low parent ion peak intensity, making it impossible for a fragmentation process.

The next step was to analyze the eluted peptides via standard MALDI-MS, hoping to gain in signal intensity. This study showed that the adsorption of serum peptides and proteins on fullerene derivatives is, to a great extent, reversible. This can be seen by comparing the MELDI spectrum gained by a direct MALDI analysis of the incubated particles with the spectrum of the elution.

In the case of [60]fullerenoacetic acid, all bound proteins are able to be eluted; in the case of RP-[60]fullerenes, most of the proteins are eluted. Although the signal intensity increased when analyzing the eluted peptides and proteins, it was still not possible to get a promising fragmentation for the peptide identification. The reason for this could be that the peptides and proteins in this low mass range show m/z values that are very close together, which makes it difficult for only one parent ion to pass through the gating and be lifted for fragmentation.

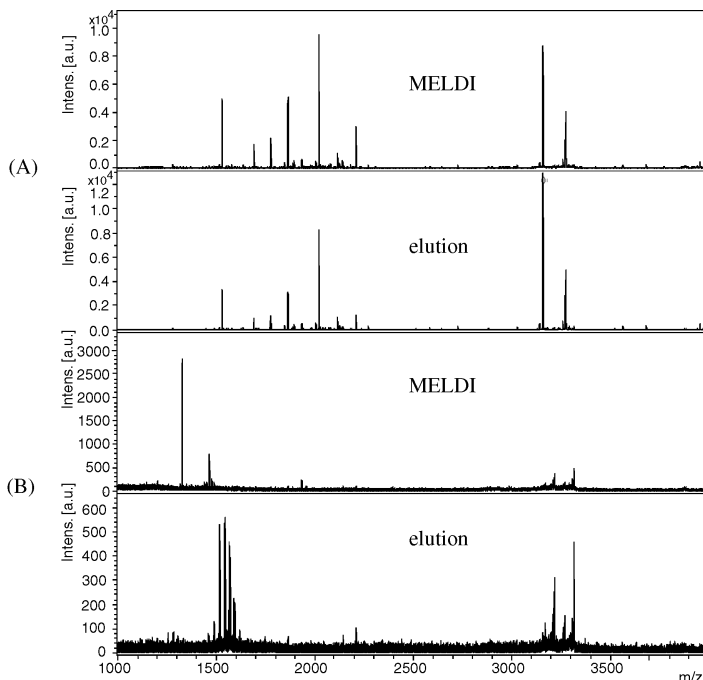


FIGURE 14.17 Comparison of the MELDI spectra of (A) [60]fullerenoacetic acid and (B) RP-[60]fullerene.

Fractionation processes was necessary to preconcentrate and separate the peptides. This was achieved successfully using a μ HPLC system equipped with a novel monolithic styrene capillary using RP conditions. Separation of the eluates from RP-[60]fullerenes and [60]fullerenoacetic acid is not represented. The chromatograms show the presence of a large variety of peptides, which it was possible to separated. The [60]fullerenoacetic acid has many more proteins. This goes hand in hand with the information gathered from the MELDI and elution spectrum. The combination of binding low-molecular-weight serum constituents to MELDI material with subsequent μ -LC separation of the elution gives a simple, effective, and informative method for estimation of the occurrence of peptides in the low-mass range.

To simplify and to increase the quality of the serum separation and the peptide identification, an automated target spotting of the chromatographic runs was performed. This was carried out on a anchor chip target using thin-layer HCCA preparation with angiotensin I ($M_r = 1296.489$) and ACTH 18–39 ($M_r = 2464.20$) as internal standard. For both cases, 100 fractions were spotted in this way and analyzed using an automated MALDI-MS run. The hundreds of spectra obtained by the automated MALDI-MS analysis were overlaid. When comparing the untreated peptide elution spectrum in Figure 14.18 (A) with the treated peptide elution spectrum in Figure 14.18 (C), the impact of a μ LC separation with the subsequent fractionation of the eluted peptides becomes clear.

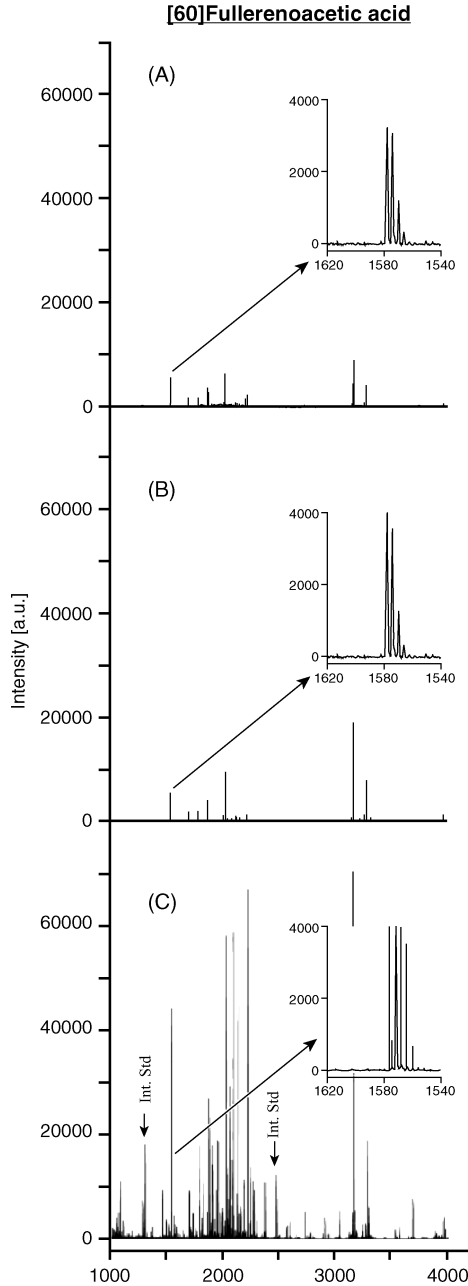


FIGURE 14.18 Representation of the low-molecular-mass work flow of human serum enriched on [60]fullerenoacetic acid: (A) MELDI mass spectra; (B) MALDI spectra of the eluate before LC separation; (C) MALDI spectra after LC separation. Bruker Ultraflex MALDI-TOF/TOF, each spectrum: addition of 400 shots, matrix: HCCA, m/z : 1000 to 4000. Sample: diluted human serum.

The increase in intensity and number of mass signals is immense. The isotopic resolution (R) and signal-to-noise ratio (S/N) of one selected mass signal are proof of this point. At the first stage, where direct particle irradiation of the loaded MELDI material took place, the isotopic resolution (R) and signal-to-noise ratio (S/N) were 6119 and 102.5, respectively. In the second stage, where MALDI measurement of the eluted peptides was performed, a slight improvement in the isotopic resolution (R) and the signal-to-noise ratio (S/N) was achieved: $R = 6675$ and $S/N = 139.8$. A successful MALDI spectrum with a high isotopic resolution (R) and a high signal-to-noise ratio (S/N), which makes MS/MS analysis possible, was achieved in the third stage. Here R has a value of 14516 and S/N , 450.7. Matrix suppression effects and a disturbing interference in the laser energy, which could be caused by the MELDI material, could be the cause of the comparatively ineffective detection of low-mass compounds experienced in the first stage. The reason for the comparatively poor MALDI spectrum of the second stage could be explained by taking into consideration suppression of low concentrated species at the expense of high abundant masses. All these negative effects are diminished by high-resolution separation and simultaneous fractionation in terms of target spotting, making MS/MS analysis possible.

14.3.3.4 MS/MS Analysis Tandem mass spectrometers operate by using the separation of ions as a first fractionation step. To induce fragmentation, these ion fractions are dissociated by passing them through a neutral gas where collisions can occur. These fragments are a family of subset ions generated from the original parent ion. Using a computerized analysis method the m/z value of the subset daughter ions can be used to determine the structure of the parent ion. In protein analysis the parent ions are whole proteins or peptides built of amino acid chains of varying length which have characteristic m/z fingerprints. The mass spectra obtained by the fragments, which consist of a limited number of m/z bands due to the relatively short combinations of the 20 amino acids, can be sequenced by automated inspection. These automated inspections involve bioinformatics tools, which enable fast, reliable data processing of the mass spectrometric analysis obtained. This can only be done by comparing MS data with the data from a database. This step in proteomics is very important for the identification of proteins and peptides.

14.4 NEAR-INFRARED DIFFUSE REFLECTION SPECTROSCOPY OF CARBON NANOMATERIALS

To shorten turnaround time in the lab, simple, robust, fast, and at best, noninvasive analytical methods are implemented for analyzing materials. Nanostructured materials especially often need elaborate techniques to characterize the physical and chemical nature of the samples. Therefore, near-infrared diffuse reflection spectroscopy (NIRS) is used to prove implemented derivatization steps and/or surface modifications. The fact that NIR spectra reflect both the chemical and physical nature of the sample often causes offset, wave number, and baseline shifts. Physical effects especially, such as crystallinity, particle size/shape, morphology, and composition,

have a considerable effect on the spectra that can be recorded, whether in transmission, diffuse reflection, or transfection mode [81,82]. The characteristic of diffuse reflected light of an irradiated sample is dependent on light scattering within its layers. The absorption (k) and scattering coefficient (s) are related to a sample's physicochemical properties. The higher s is, the lower the penetration of the radiation into the sample, and the lower effects of k will influence the characteristic of the spectra. The distinctive broad and overlapping NIR bands cannot always be attributed unambiguously to specific absorptions. Therefore, statistical methods, multivariate data analysis (MVA), and chemometrics have contributed tremendously to elucidating NIR spectral data and creating useful models for quantifying and qualifying specimens [83–87].

Visual spectra interpretations and band assignments play an important role, particularly for comparison of pure materials and rather complex spectra mixes [88]. In this context the designation for a stretching mode is written as ν , and for a bending mode, δ is used. For the first overtone the vibrational mode is preceded by $2\times$ and the second overtone by $3\times$.

14.4.1 NIR Characterization of C_{60} Fullerenes

The fact that the C=C bond does not show a dipole or deviating masses makes fullerenes a very weak absorber in the near-infrared. In contrast to that covalent bond, long-chain saturated alkanes linked to functional groups show strong absorption signals in the NIR that can be allocated to implemented surface modifications (Figure 14.19).

In the case of C_{60} -epoxysilica, intense absorptions appear at 4394 cm^{-1} and 5263 cm^{-1} due to a combination of a $\nu(\text{O-H}) + \nu(\text{C-C})$ vibration and the C=O stretching first overtone. The C_{60} -aminosilica shows characteristic bands at 4329 cm^{-1} and 4359 cm^{-1} corresponding to the $\nu(\text{C-H}) + \delta(\text{C-H})$ combination

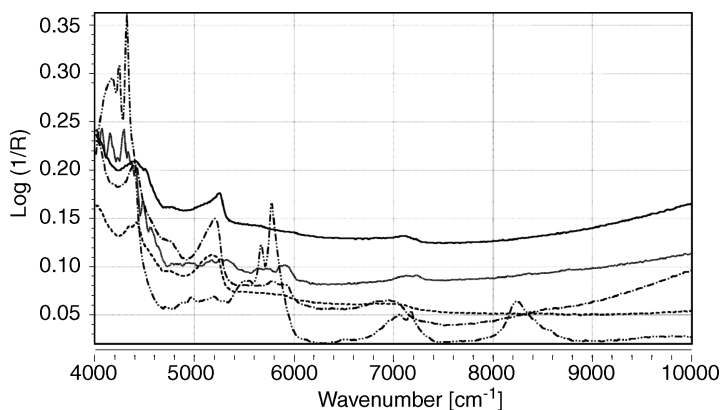


FIGURE 14.19 Averaged NIR spectra (100 scans) of five species of derivatized fullerenes: C_{60}^- epoxy silica (—), C_{60} (.....), IMAC: IDA-[60]fullerene (-·-·-·-); C_{60} -aminosilica (-----), dioctadecylmethano[60]fullerene (-----).

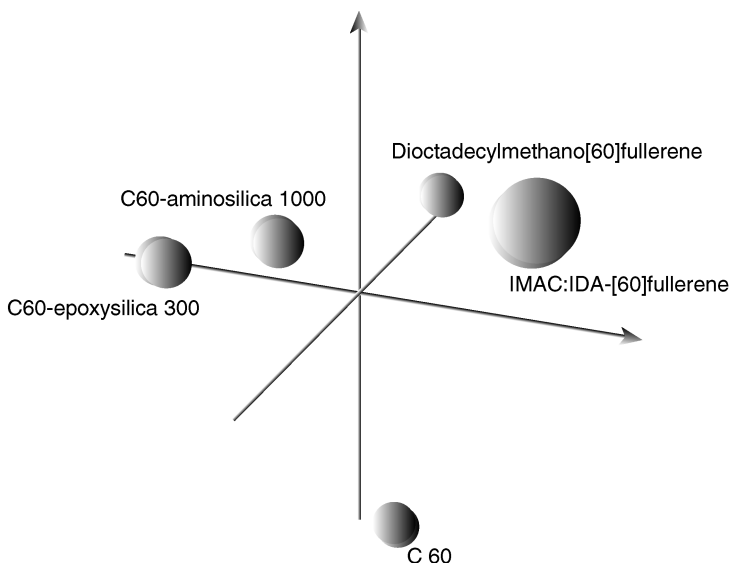


FIGURE 14.20 Three-dimensional score plot of five differently modified fullerenes. The plot shows the classification of every sample into a single cluster. This model is used to predict surface modifications of unknown samples or to prove implemented derivatization steps. Wave-number range: 4440 to 9000 cm^{-1} , 100 scans, $T = 23^\circ\text{C}$, first derivative, seven factors.

vibration. A representative absorption at 4739 cm^{-1} could be assigned to $\nu(\text{N-H})$ $\delta(\text{N-H})$ vibration. The spectrum of dioctadecylmethano[60]-fullerene shows several absorptions at 4252 , 4329 , 7057 , and 7100 cm^{-1} [$\nu(\text{C-H}) + \delta(\text{C-H})$] due to existing methylene groups. The C-H stretching first overtone absorptions are placed at 5666 and 5784 cm^{-1} , and the absorption at 8244 cm^{-1} corresponds to the $3 \times \nu(\text{C-H})$ vibration, respectively. As shown in the IMAC:IDA-[60]-fullerene spectra the band at 4292 cm^{-1} could be assigned to the $\nu(\text{C-H}) + \delta(\text{C-H})$ vibration whereas the $2 \times \nu(\text{C-H}) + \delta(\text{C-H})$ mode is placed at 6948 cm^{-1} . The $\nu(\text{N-H})$ $\delta(\text{N-H})$ was found at 4740 cm^{-1} , the $2 \times \nu(\text{C=O})$ at 5208 cm^{-1} , and the $2 \times (\text{C-H})$ at 5784 cm^{-1} . Due to the distinctly characteristic features of different states of derivatization, qualitative analyses can be implemented within seconds. The classification ability of the established cluster model (Figure 14.20) provides the possibility to perform go/no-go analyses that save a lot of time in daily lab work.

14.4.2 NIR Characterization of Nanocrystalline Diamond

The most notable point about nanocrystalline diamond is its outstanding characteristic to specifically bind different biological fluids onto its surface. The diamond surface can either be H- or O-terminated, resulting in a hydrophobic or hydrophilic surface. In that way the success for further derivatisation is dependent on the type of termination. Typically, x-ray photoelectron spectroscopy (XPS) is implemented for differentiation

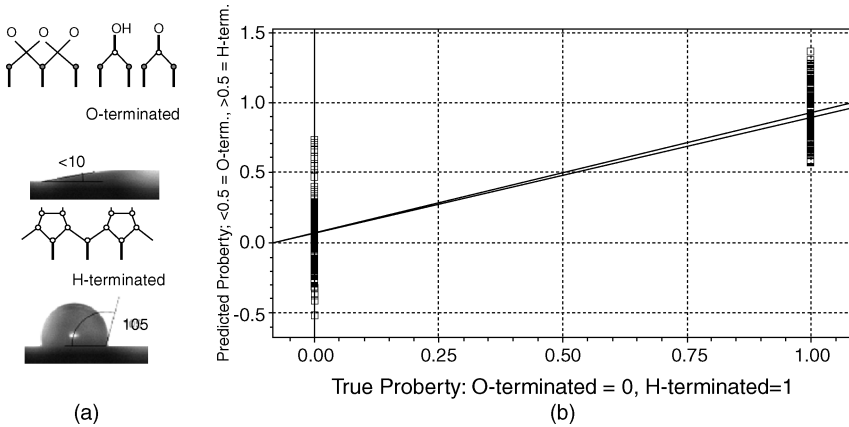


FIGURE 14.21 Calculated vs. expected properties for the determination of H- and O-terminated nanocrystalline diamond surfaces; nitrogen atmosphere, wave-number range 4596 to 9996 cm^{-1} , 1000 scans, $T = 23^\circ\text{C}$, five factors.

and detection of different terminated surfaces. Unfortunately, this method presents itself as time consuming and elaborate. Therefore, 400 spectra from H- and O-terminated NCD surfaces were recorded in diffuse reflection mode. The aim is to differentiate and classify the terminated surfaces noninvasively and as fast as possible. For that purpose, spectra were recorded under a nitrogen atmosphere in order to prevent hydrogen bonding of water molecules to the surface. Ten measurements presenting the average of 10 scans each were conducted on 20 H-terminated and 20 O-terminated diamond wafers. A full-spectrum two-point PLS calibration model was calculated; H-terminated spectra were marked as “1,” O-terminated as “0” (Figure 14.21). The calibration wave-number range was set from 4596 to 9996 cm^{-1} , and the original reflection spectra were used without further pretreatment for calculation. Finally, this model allowed predicting the H- or O-termination with a precision of 80%.

NIRS turned out to be a well-suited method for characterization of the active sites on carbon surfaces. This noninvasive and rapid analyzing technique is even highly suitable for characterizing materials regarding its physical parameters as shown for particle- and pore-size determinations [89]. Although near-infrared spectroscopy is dependent on reliable and often elaborate reference techniques, as soon as the calibration model is validated, NIRS can be implemented as a supplementary method.

REFERENCES

1. Seibert V, Ebert MPA, Buschmann P. Advances in clinical cancer proteomics: SELDI-ToF-mass spectrometry and biomarker discovery. *Brief Funct Genom. Proteom.* 2005;4:16–26.

2. Hardt M, Thomas LR, Dixon SE, et al. Toward defining the human parotid gland salivary proteome and peptidome: identification and characterization using 2D SDS-PAGE, ultrafiltration, HPLC, and mass spectrometry. *Biochemistry*. 2005;44:2885–2899.
3. Koomen JM, Li D, Xiao LC, et al. Direct tandem mass spectrometry reveals limitations in protein profiling experiments for plasma biomarker discovery. *J. Proteome Res*. 2005;4:972–981.
4. Yousef GM, Polymeris ME, Yacoub GM, et al. Parallel overexpression of seven kallikrein genes in ovarian cancer. *Cancer Res*. 2003;63:2223–2227.
5. Lee CJ, Ariztia EV, Fishman DA. Conventional and proteomic technologies for the detection of early stage malignancies: markers for ovarian cancer. *Crit. Rev. Clin. Lab. Sci*. 2007;44:87–114.
6. Irish JM, Kotecha N, Nolan G.P. Mapping normal and cancer cell signaling networks: towards single-cell proteomics. *Nat. Rev. Cancer*. 2006;6:146–155.
7. Marvin LF, Roberts MA, Fay LB. Matrix-assisted laser desorption/ionization time-of-flight mass spectrometry in clinical chemistry. *Clin. Chim. Acta*. 2003;337:11–21.
8. Andren PE, Emmett MR, Caprioli RM. Micro-electrospray: zeptomole/attomole per microliter sensitivity for peptides. *J. Am. Soc. Mass Spectrom*. 1994;5:867–869.
9. Karas M, Hillenkamp F. Laser desorption ionization of proteins with molecular masses exceeding 10,000 daltons. *Anal. Chem*. 1988;60:2299–2301.
10. Karas M, Bahr U, Hillenkamp F. UV laser matrix desorption/ionization mass spectrometry of proteins in the 100,000 dalton range. *Int. J. Mass Spectrom. Ion Process*. 1989;92:231–242.
11. Keough T. Tandem mass spectrometry methods for definitive protein identification in proteomics research. *Electrophoresis*. 2000;21:2252–2265.
12. Kaufman J, Jaber AJ, Stump MJ, Simonsick WJ, Wilkins CL. Interference from multiple cations in MALDI-MS spectra of copolymers. *Int. J. Mass Spectrom*. 2004;234:153–160.
13. Feuerstein I, Najam-ul-Haq M, Rainer M, et al. Material enhanced laser desorption/ionization (MELDI) a new protein profiling tool utilizing specific carrier materials for TOF-MS analysis. *J. Am. Chem. Soc. Mass Spectrom*. 2006;17:1203–1208.
14. Najam-ul-Haq M, Rainer M, Schwarzenauer T, Huck CW, Bonn GK. Chemically modified carbon nanotubes as material enhanced laser desorption ionisation (MELDI) material in protein profiling. *Anal. Chim. Acta*. 2006;561:32–39.
15. Najam-ul-Haq M, Rainer M, Huck CW, et al. Chemically modified nano crystalline diamond layer as material enhanced laser desorption ionisation (MELDI) surface in protein profiling. *Curr. Nanosci*. 2006;2:1–7.
16. Trojer L, Stecher G, Feuerstein I, Bonn GK. Cu(II)-loaded iminodiacetic acid/silica particles for protein profiling of human serum samples using surface-enhanced affinity capture: support porosity effects. *Rapid Commun. Mass Spectrom*. 2005;19:3398–3404.
17. Rainer M, Najam-ul-Haq M, Huck CW, et al. Ultra fast mass fingerprinting by high-affinity capture of peptides and proteins on derivatized poly(glycidyl methacrylate/divinylbenzene) for the analysis of serum and cell lysates. *Rapid Commun. Mass Spectrom*. 2006;20:2954–2960.
18. Rainer M, Najam-ul-Haq M, Bakry R, Huck CW, Bonn GK. Mass spectrometric identification of serum peptides and proteins employing derivatized poly(glycidyl-methacrylate/divinyl-benzene) particles for selective immobilization and enrichment. *J. Proteome Res*. 2007;6:382–386.

19. Merrell K, Southwick K, Graves SW, Esplin MS, Lewis NE, Thulin CD. Analysis of low-abundance, low-molecular-weight serum proteins using mass spectrometry. *J. Biomol. Technol.* 2004;15:238–248.
20. Banks RE, Stanley AJ, Cairns DA, Barrett JH, Clarke P, Thompson D, Selby PJ. Influences of blood sample processing on low-molecular-weight proteome identified by surface-enhanced laser desorption/ionization mass spectrometry *Clin. Chem.* 2005; 51:1637–1649.
21. Guo Z, Ganawi AAA, Liu Q, He L. Nanomaterials in mass spectrometry ionisation and prospects for biological application. *Anal. Bioanal. Chem.* 2006;384:584–592.
22. Tanaka K, Waki H, Ido Y, Akita S, Yoshida Y, Yoshida T. Protein and polymer analyses up to m/z 100,000 by laser ionization time-of-flight mass spectrometry. *Rapid Commun. Mass Spectrom.* 1988;2:151–153.
23. Wei J, Buriak JM, Siuzdak, G. Desorption-ionization mass spectrometry on porous silicon. *Nature.* 1999;399:243–246.
24. McLean JA, Stumpo KA, Russell DH. Size-selected (2–10 nm) gold nanoparticles for matrix assisted laser desorption ionization of peptides. *J. Am. Chem. Soc.* 2005;127: 5304–5305.
25. Yuan MJ, Shan Z, Tian BZ, Tu B, Yang PY, Zhao DY. Preparation of highly ordered mesoporous $\text{WO}_3\text{-TiO}_2$ as matrix in matrix-assisted laser desorption/ionization mass spectrometry. *Micropor. Mesopor. Mater.* 2005;78:37–41.
26. Gruen DM. Nanocrystalline diamond films. *Annu. Rev. Mater. Sci.* 1999;29:211–259.
27. Kim HJ, Lee JK, Park SJ, Ro HW, Yoo DY, Yoon DY. Observation of low molecular weight poly(methylsilsesquioxane)s by graphite plate laser desorption/ionization time-of-flight mass spectrometry. *Anal. Chem.* 2000;72:5673–5678.
28. Ren S, Zhang L, Cheng Z, Guo Y. Immobilized carbon nanotubes as matrix for MALDI-TOF-MS analysis: applications to neutral small carbohydrates. *J. Am. Soc. Mass Spectrom.* 2005;16:333–339.
29. Hopwood FG, Michalak L, Alderdice DS, Fisher KJ, Willett GD. C_{60} -assisted laser desorption/ionization mass spectrometry in the analysis of phosphotungstic acid. *Rapid Commun. Mass Spectrom.* 1994;8:881–885.
30. Kalkan AK, Fonash SJ. Carbon/Nafion[®] nanocomposite thin films as potential matrix-free laser desorption-ionization mass spectroscopy substrates. *Mater. Res. Soc. Symp. Proc.* 2003;788:595–600.
31. Larsen MR, Cordwell SJ, Roepstorff P. Graphite powder as an alternative or supplement to reversed-phase material for desalting, and concentration of peptide mixtures prior to matrix-assisted laser desorption/ionization-mass spectrometry. *Proteomics.* 2002; 2:1277–1287.
32. Kong XL, Huang LCL, Hsu CM, Chen WH, Han CC, Chang HC. High-affinity capture of proteins by diamond nanoparticles for mass spectrometric analysis. *Anal. Chem.* 2005;77:259–265.
33. Kroto HW. The stability of the fullerenes C_n , with $n = 24, 28, 32, 36, 50, 60$ and 70 . *Nature.* 1987;329:529–531.
34. Bigelow LK, D'Evelyn MP. Role of surface and interface science in chemical vapour deposition diamond technology. *Surf. Sci.* 2002;500:986–1004.
35. Butler JE. Chemical vapor deposited diamond: maturity and diversity. *Electrochem. Soc. Interface.* 2003;12:22–26.

36. Specht CG, Williams OA, Jackman RB, Schoepfer R. Ordered growth of neurons on diamond. *Biomaterials*. 2004;25:4073–4078.
37. Toshiki T, Osamu H, Shintaro I, Shoji N, Masanori N, Yasumichi M. Reactivity of the hydrogen atoms on diamond surface with various radical initiators in mild condition. *Diamond Relat. Mater.* 2002;11:1360–1365.
38. Tachiki M, Kaibara Y, Sumikawa Y, et al. Diamond nanofabrication and characterization for biosensing application. *Phys. Status Solidi A*. 2003;199:39–43.
39. Porath J, Carlsson J, Olsson I, Belfrage G. Metal chelate affinity chromatography, a new approach to protein fractionation. *Nature*. 1975;258:598–599.
40. Klapper MH. The independent distribution of amino acid near neighbor pairs into polypeptides. *Biochem. Biophys. Res. Commun.* 1977;78:1018–1024.
41. Arnold FH. Metal-affinity separations: a new dimension in protein processing. *Nat. Biotechnol.* 1991;9:151–156.
42. Sulkowski E. The saga of IMAC and MIT. *BioEssays*. 1989;10:170–175.
43. Yang W, Auciello O, Butler JE, et al. DNA-modified nanocrystalline diamond thin-films as stable, biologically active substrates. *Nat. Mater.* 2002;1:253–257.
44. Andersson L, Sulkowski E. Evaluation of the interaction of protein alpha-amino groups with M II by immobilized metal ion affinity chromatography. *J. Chromatogr. A*. 1992;604:13–17.
45. Ip J, Nguyen TP, Le RP. An x-ray photoelectron spectroscopy study of the interface formed between ITO, and 4,4'-bis(4-dimethyl amino styryl)benzene based light emitting diode. *Synth. Met.* 2003;138: 107–111.
46. Fink A, Widdra W, Wurth W, et al. Core-level spectroscopy of hydrocarbons adsorbed on Si (100)-(2×1): a systematic comparison. *Phys. Rev. B*. 2001;64:0453081–0453089.
47. Meetani MA, Voorhees KJ. MALDI mass spectrometry analysis of high molecular weight proteins from whole bacterial cells: pretreatment of samples with surfactants. *J. Am. Chem. Soc. Mass Spectrom.* 2005;16: 1422–1426.
48. Arnott D, Oconnell KL, King KL, Stults JT. An integrated approach to proteome analysis: identification of proteins associated with cardiac hypertrophy. *Anal. Biochem.* 1998;258:1–18.
49. Iijima S. Helical microtubules of graphitic carbon. *Nature*. 1991;354:56–58.
50. Bethune DS, Kiang CH, de Vries MS, et al. Cobalt catalyzed growth of carbon nanotubes with single atomic layer walls. *Nature*. 1993;363:605–607.
51. Ren SF, Zhang L, Cheng ZH, Guo YL. Carbon nanotubes as matrix for MALDI-TOF-MS analysis: applications to neutral small carbohydrates. *J. Am. Chem. Soc. Mass Spectrom.* 2005;16:333–339.
52. Chen WY, Wang LS, Chiu HT, Chen YC, Lee CY. Carbon nanotubes as affinity probes for peptides and proteins in MALDI MS analysis. *J. Am. Chem. Soc. Mass Spectrom.* 2004;15:1629–1635.
53. Ugarov MV, Egan T, Khabashesku DV, Schultz JA, Peng H, Khabashesku VN, Furutani H, Prather KS, Wang HWJ, Jackson SN, Woods AS. MALDI matrices for biomolecular analysis based on functionalised carbon nanomaterials. *Anal. Chem.* 2004;76:6734.
54. Xu S, Li Y, Zou H, Qiu J, Guo Z, Guo B. Carbon nanotubes as assisted matrix for laser desorption/ionization time-of-flight mass spectrometry. *Anal. Chem.* 2003;75:6191–6195.

55. Ko FH, Lee CY, Ko CJ, Chu TC. Purification of multi-walled carbon nanotubes through microwave heating of nitric acid in a closed vessel. *Carbon*. 2005;43:727–733.
56. Liu J, Rinzler AG, Hongjie D, et al. Fullerene pipes. *Science*. 1998;280:1253–1256.
57. Chen J, Hamon MA, Hui H, et al. Solution properties of single-walled carbon nanotubes. *Science*. 1998;282:95–98.
58. O'Brien SM, Thomas Owen RT, Peter DJ. Non-porous magnetic chelator supports for protein recovery by immobilized metal affinity adsorption. *J. Biotechnol.* 1996;50:13–25.
59. Odabasi M, Uzun L, Denizli A. Porous magnetic chelator support for albumin adsorption by immobilized metal affinity separation. *J. Appl. Polym. Sci.* 2004;93:2501–2510.
60. David EH. Dreams in a charcoal fire predictions about giant fullerenes and graphite nanotubes. *Philos. Trans. R. Soc. London Ser. A.* 1993;343:9–18.
61. Osawa E. Superaromaticity. *Kagaku*. 1970;25:854–863.
62. Haymet ADJ. C₁₂₀ and C₆₀: Archimedean solids constructed from sp² hybridized carbon atoms. *Chem. Phys. Lett.* 1985;122:421–424.
63. Kroto HW. C₆₀-buckminsterfullerene: the heavenly sphere that fell to Earth. *Angew. Chem.* 1992;104:113–133.
64. Kraetschmer W, Lamb LD, Fostiropoulos K, Huffman DR. Solid C₆₀: a new form of carbon. *Nature*. 1990;347:354–358.
65. Osterodt J, Zett A, Voegtle F. Fullerenes by pyrolysis of hydrocarbons and synthesis of isomeric methanofullerenes. *Tetrahedron*. 1996;52:4949–4962.
66. Gerhardt P, Loeffler S, Homann H. Polyhedral carbon ions in hydrocarbon flames. *Chem. Phys. Lett.* 1987;137:306–310.
67. Pope CJ, Marr JA, Howard JB. Chemistry of fullerenes C₆₀ and C₇₀ formation in flames. *J. Phys. Chem.* 1993;97: 11001–11013.
68. Schmalz TG, Seitz WA, Klein DJ, Hite GE. Sixty-carbon-atom carbon cages. *Chem. Phys. Lett.* 1986;130:203–207.
69. Diederich F, Ettl R, Rubin Y, Whetten RL, Beck RAM. The higher fullerenes: isolation and characterization of C₇₆, C₈₄, C₉₀, C₉₄, and C₇₀O, an oxide of D_{5h}-C₇₀. *Science*. 1991;252:548–551.
70. Scrivens WA, Bedworth PV, Tour JM. Purification of gram quantities of C₆₀: a new inexpensive and facile method. *J. Am. Chem. Soc.* 1992;114:7917–7919.
71. Scrivens WA, Cassell AM, North BL, Tour JM. Single column purification of gram quantities of C₇₀. *J. Am. Chem. Soc.* 1994;116:6939–6940.
72. Ajje H, Alvarez MM, Anz SJ, et al. Characterization of the soluble all-carbon molecules C₆₀ and C₇₀. *J. Phys. Chem.* 1990;94:8630–86333.
73. Diederich F, Isaacs L, Philp D. Syntheses, structures, and properties of methanofullerenes. *Chem. Soc. Rev.* 1994;23:243–255.
74. Smith AB, Strongin RM, Brard L, et al. 1,2-Methanobuckminsterfullerene (C₆₁H₂), the parent fullerene cyclopropane: synthesis and structure. *J. Am. Chem. Soc.* 1993;115: 5829–5830.
75. Vasella A, Uhlmann P, Waldraff CAA, Diederich F, Thilgen C. Glycosylidencarbenes: 9. Fullerene sugar: preparation of an enantiomerically-pure, spiro-bound C-glycoside of C₆₀. *Angew. Chem.* 1992;104:1383–1385.
76. Bingel C. Cyclopropanation of fullerenes. *Chem. Ber.* 1993;126:1957–1959.

77. Dettman J. *Fullerene Die Buckyballs erobern die Chemie*. Birkhäuser Verlag, Basel, Switzerland, 1994.
78. Bingel C. Cyclopropanation of fullerenes. *Chem. Ber.* 1993;126:1957–1959.
79. Bingel C, Schiffer H. Biscyclopropanation of C₇₀. *Liebigs Ann.* 1995;8:1551–1553.
80. Bakhtiar R, Nelson R.W. Electrospray ionization and matrix-assisted laser desorption ionization mass spectrometry: emerging technologies in biomedical sciences. *Biochem. pharmacol.* 2000;59:891–905.
81. Hanssen LM, Snail KA. Integrating spheres for mid- and near-infrared reflection spectroscopy. In *Handbook of Vibrational Spectroscopy*, Vol. 3. Wiley, Chichester, UK, 2002.
82. Dahm DJ, Dahm KD. *Interpreting Diffuse Reflectance and Transmittance*. NIR Publications, Chichester, UK, 2007.
83. Massart DL, Vandeginste BGM, Deming SN, Michotte Y, Kaufman L. *Chemometrics: a Textbook*. Elsevier, Amsterdam, 1988.
84. Kowalski BR, ed. *Chemometrics: Mathematics and Statistics in Chemistry*. Proceedings of the NATO Advanced Study Institute on Chemometrics: Mathematics and Statistics in Chemistry, Sept. 12–23, 1983, Italy. D. Reidel, Dordrecht, The Netherlands, 1984.
85. Martens H, Martens M. *Multivariate Analysis of Quality: An Introduction*. Wiley, Chichester, UK, 2001.
86. Brereton RG. *Chemometrics: Data Analysis for the Laboratory and Chemical Plants*. Wiley, Chichester, UK, 2003.
87. Esbensen KH. *An Introduction to Multivariate Data Analysis and Experimental Design*, 5th ed. Camo, Esbjerg, Denmark, 2004.
88. Weyer LG, Lo SC. Spectra–structure correlations in the near-infrared. In *Handbook of Vibrational Spectroscopy*, Vol. 3. Wiley, Chichester, UK, 2002.
89. Heigl N, Petter CH, Rainer M, et al. Review: near infrared spectroscopy for polymer research, quality control and reaction monitoring *J. Near Infrared Spectrosc.* 2007;15 (5):269–282.

NANOPORES

Biosensing with Nanopores

IVAN VLASSIOUK

Department of Physics and Astronomy, University of California, Irvine, California

SERGEI SMIRNOV

Department of Chemistry and Biochemistry, New Mexico State University, Las Cruces,
New Mexico

- 15.1 Nanoporous materials in sensing
- 15.2 Nanochannel and nanopore fabrication
 - 15.2.1 Nanochannels
 - 15.2.2 Nanopores
 - 15.2.3 Nanopore- and nanochannel-diameter tuning
 - 15.2.4 Self-assembled nanopores and nanochannels
- 15.3 Surface modification chemistry
- 15.4 Nonelectrical nanoporous biosensors
- 15.5 Electrical nanoporous biosensors
- 15.6 Summary

15.1 NANOPOROUS MATERIALS IN SENSING

Most analytical instruments, including those used in biochemical applications, are designed to differentiate molecules by their properties with respect to a certain quality: (e.g., mass, mass/charge ratio, mobility), or use a more complicated approach, such as identification of spectroscopic features. As a result, the instruments become relatively sophisticated and expensive. A major goal of the fast-growing field of biosensor technologies is to create inexpensive and robust methods for detecting (sensing) particular biomolecules or organisms instead of characterizing every species in the sample [1,2]. To expedite the analysis and minimize the human factor, numerous analytes need to be detected simultaneously and the sensors interfaced to a computer.

The simplicity of the interface determines cost and durability. Optical sensors (fluorescence and absorption) are very popular because of their high sensitivity and ability to be employed without a computer. On the flip side, when integration of optical methods with other techniques is necessary, it would require their interfacing with computer, which can be quite expensive. Thus, one has to search for the most direct approach to transfer identification of the analyte presence into an electrical signal (i.e., design an electrical sensor). One very powerful realization of this approach is in the form of an electrochemical sensor, where each analyte produces a unique response, usually appearing due to a faradaic current at the same or different electrodes. However, the need for a potentiostat introduces complications in implementing this method, especially when a number of different analytes are to be detected in parallel on a single sensor chip.

Recently there has been a significant growth of interest in nanoporous membranes and nanopores as conduits mimicking biological channels and as platforms for biosensor design. Life depends on the ability of organisms to transport molecules and ions selectively across membranes for a large variety of metabolic and signaling purposes. For example, the transmission of nerve impulses depends on ionic currents generated by the controlled release of ions across membranes. Mimicking such biological control of material transport between aqueous phases using synthetic nanoporous membranes and nanofluidic channels is an interesting scientific challenge with applications in medicine, materials science, fuel cells, analytical chemistry, and sensors.

For example, sensors may be based on changes in ion conductance across membranes induced by the interaction of proteins, DNA, or small molecules with nanopores. Dramatic increases in the surface/volume ratio in nanoporous materials enhance the significance of interaction between solutes and the surface. Single-nanopore sensors can be used to detect single biomolecules, whereas nanoarrays allow parallel sensing of numerous analytes. Biosensors based on nanopore arrays and single nanopores show promising new features reviewed here. Methods for nanopore fabrication using different materials are reviewed, and the advantages of each scheme, including surface modification, are discussed.

15.2 NANOCANNEL AND NANOPORE FABRICATION

Various applications of nanochannels dictate different requirements for material properties and nanopore geometry. Synthetic nanopores can be fabricated via either bottom-up or top-down approaches. The former is achieved using self-assembly and is usually represented by nanopore arrays. In the latter, it is convenient to distinguish between nanopores with high aspect ratios or nanochannels and those with low aspect ratio or nanopores.

15.2.1 Nanochannels

In the majority of fabrication techniques, silicon and silica (SiO_2) are the materials of choice because of the methods developed in the semiconductor industry, the high

stability of these materials, the easy chemical surface modification, and the biochemical inertness. Various lithographic techniques lie at the heart of the following top-down fabrication methods.

The most straightforward process of nanochannel fabrication comes from micro-channel technology [3] but emphasizes further decrease in dimensions. A typical scheme is presented in Figure 15.1(A). First, a substrate is patterned using photo or electron beam lithography. Then the patterned substrate is etched to the desired depth defining the height of the nanochannel and bonded with another flat substrate that produces the top part of the nanochannel. Numerous reports [4–8] demonstrate routine fabrication of nanochannels 70 nm to 1 μm in height, 50 μm wide, and >1 mm long for ionic conductivity experiments.

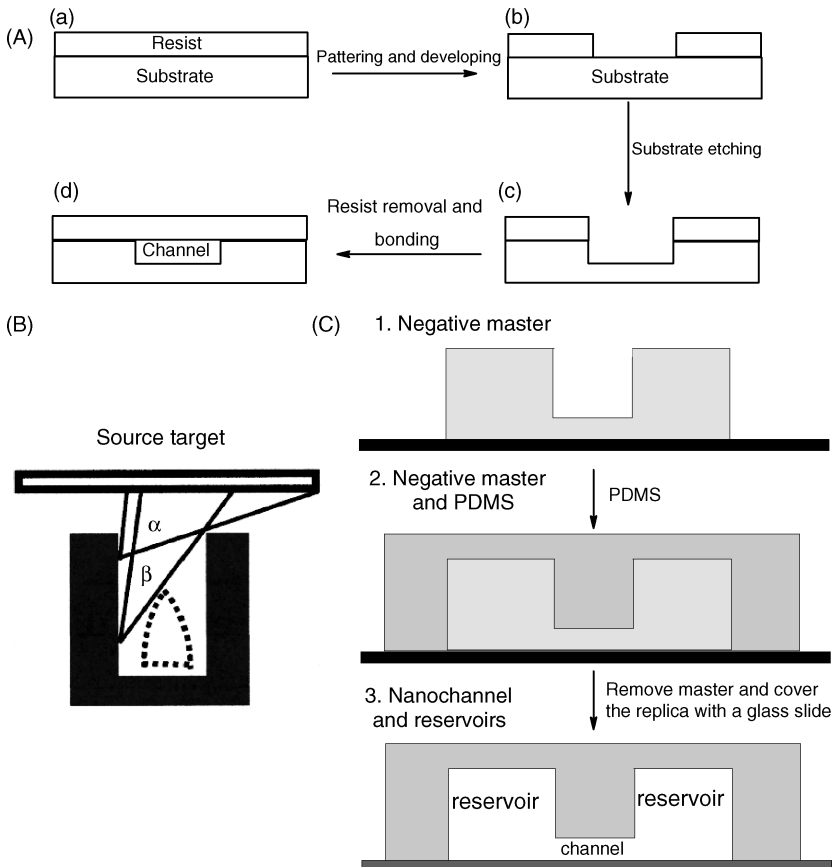


FIGURE 15.1 (A) Outline of a typical nanochannel fabrication procedure; (B) formation of nanochannels by sputtering the ceiling on the top of previously formed trenches; (C) fabrication of nanochannels from polymer (PDMS) using a negative replica approach. [(B) From ref. 15, with permission.]

Smaller pore heights can be achieved by reversing the order of sacrificial layer removal, as shown by Majumdar's group at Berkley, who followed the technique developed by Turner et al. [9] and Bhusari et al. [10]. The nanochannels can be produced with heights of less than 5 nm and lengths as great as 1.5 mm. Instead of resist removal at the site where the nanochannel is going to be built [Figure 15.1(A)], a bump formed lithographically from sacrificial material (Si) with silica deposited on top formed the nanochannel walls. Subsequently, core Si was etched away, forming the nanochannel. This approach allows construction of more complex structures with built-in gate electrodes. Karnik et al. [11,12] demonstrated this technique on a device with nanochannels 30 nm high, about 1 μm wide, and more than 20 μm long.

Nanochannels with cross sections in the nanometer range in both directions can also be constructed using various methods. Majumdar's group used a method similar to the one described above, in which they first synthesized silica nanowire [13] and integrated it into a microfluidic system, then covered it with SiO_2 and etched silicon away to form a long, truly one-dimensional nanochannel. The inner diameters of such channels can be varied from 10 to 100 nm [11,14].

A completely different approach to nanochannel fabrication was reported by Stephen Chou's group at Princeton (they actually fabricated an addressable array of nanochannels) [15,16]. First, an array of nanofluidic channels with trenches about 55 nm in depth was fabricated using nanoimprint lithography. The trenches were sealed by sputtering or electron-beam evaporation of silica at different angles [Figure 15.1(B)] to form nanochannels. The sidewalls of trenches shaded the bottom from exposure to incoming material, and thus the majority of sputtered Si was deposited on the top to leave nanoporous voids and channels. This approach assures effective shrinkage and sealing of the nanochannels while making a ceiling of thickness less than 10 nm.

One of the cheapest and most convenient methods of producing nanochannel devices was proposed by Saleh and Sohn [17]. The method first requires fabrication of a negative master replica of the nanochannel and reservoirs by photo or electron-beam lithography. Then the replica is filled with poly(dimethylsiloxane) (PDMS), which is subsequently cured and bonded to the glass substrate, forming an entire ready-to-use structure in a short period of time [Figure 15.1(C)]. However, PDMS is a hydrophobic material, and even after exposure to oxygen, plasma can regain hydrophobicity, which hinders its use for nanochannels of small dimensions.

Another major class of artificial nanochannel is lithography-free and offers structures of cylindrical and conical shape. For the latter, the pore diameter on one side (tip) is smaller than that on the other side (base) [see Figure 15.2(A)]. Note that for a high-enough divergence angle, the voltage drop for electrolyte flowing through such a nanochannel occurs primarily at the tip, and thus this type of structure can be considered nanoporous.

The oldest and arguably the most widely used technique for this type of nanochannels fabrication is latent track etching [18]. At the core of the fabrication process lies the irradiation of polymeric films by heavy ions and subsequent etching of damaged tracks [Figure 15.2(B)]. Commonly used polycarbonate filters are made this way. The density of nanochannels is determined by the flux of irradiating ions.

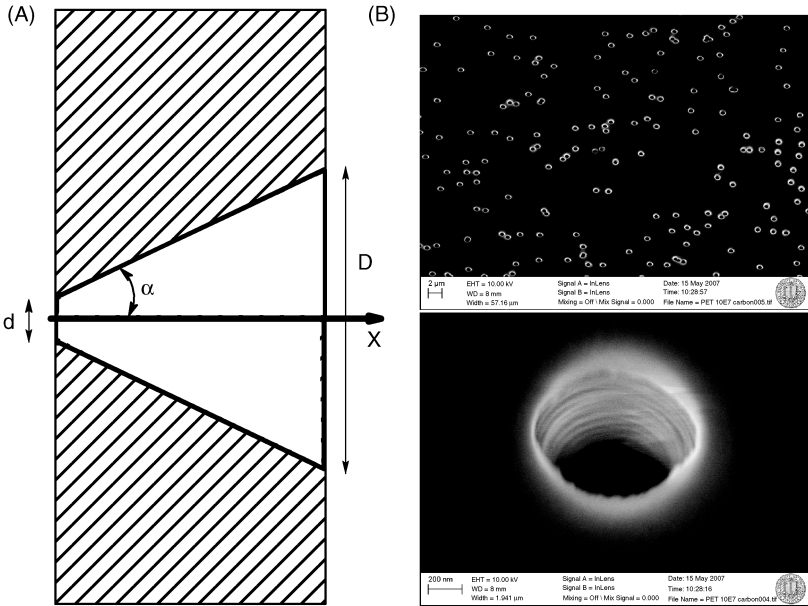


FIGURE 15.2 (A) Conical nanochannel/nanopore with d and D being the tip and the base diameter, respectively; (B) nanopores prepared by latent track etching.

Irradiation with a single ion results in formation of a single damaged track and thus a single nanochannel after track etching [19]. The shape and dimensions of such nanochannels are controlled by the etching conditions [20–22]. Nanopores with the smallest openings, on the order of 2 nm, are readily available [22]. The length of the pores is defined by the thickness of irradiated films and usually ranges from 5 to 20 μm .

Fabrication of nanochannel arrays using latent track techniques is relatively easy except for the need of a nuclear facility to perform irradiation. Single-ion irradiation is currently available only at GSI in Darmstadt, Germany. These complications encourage the search for other possibilities for similar fabrication techniques.

Another lithography-free technique was introduced by Karhanek et al. [23], who were able to fabricate quartz nanochannels about 50 nm in diameter. A force applied to a quartz capillary during heating results in the capillary's elongation and simultaneous decrease in radius. Using this procedure, nanochannels with diameters of about 50 nm can be fabricated. Despite the relatively large diameters, such nanopipettes show electrochemical properties similar to those of conical nanochannels prepared by a track-etching technique [24]. Wu et al. [25] reported fabrication of nanochannels in Apiezon via shrinking of larger holes by laser heating. This method allows fabrication of sub-100-nm single channels. White's group in Utah has made conical nanopores with sealed electrode inside for electrochemical detection [26]. This was achieved by electrochemical etching of sharp platinum wire sealed in a glass capillary. Careful polishing of the capillary exposes the platinum wire end and allows subsequent

etching to reveal a conically shaped glass nanochannel with a radius of 15 to 100 nm. However, the lack of feedback control during nanochannel fabrication using techniques proposed by Karhanek et al. and Zhang et al. can be seen as a drawback compared to the track-etching technique.

Crooks' group at Texas A&M proposed a radically different method [26]. They embedded a single multiwall carbon nanotube (MWNT) in epoxy and the resulting block was microtomed to produce membranes containing single slices with MWNT of about 65 nm internal radius sealed in the epoxy. The length of MWNT nanochannel is defined by the microtome precision and hardness of the epoxy. The usual length was around 1 μm .

The lithography-free techniques seem to be more attractive during the research stage because their fabrication does not require access to a clean room. However, future mass production and further integration of such structures with nanofluidic devices would probably be problematic, due to the uncertainty in the nanochannel location. The investigations have to be extended in both directions, but the issues of compatibility and integration need to be addressed for successful applications.

15.2.2 Nanopores

Nanopores are convenient for electrical detection of single molecules (biological or otherwise), due to their size. Since all dimensions are small, only a single molecule can occupy the nanopore and thus be detected without interference from other molecules. This feature reveals a broad range of possible applications, as well as a interesting physical phenomena (see, e.g., a nice review by Dekker [27]). For these reasons, this field is growing so fast that by the time of this publication, some new developments may have emerged.

The first breakthrough came from Golovchenko's group at Harvard [29]. They developed the ion beam sculpting technique, which allowed fabrication of single nanopores in Si_3N_4 membrane with nanometer control [30]. The authors preformed a cavity on the opposite side of the substrate with the intention of slowly etching away (ablating) the front part under an Ar^+ beam and create a nanopore. The counting of Ar^+ ions passing through the nanopore provide feedback for very precise monitoring of the pore radius. To their surprise, they found that a competing process, lateral material transport on the surface sputtered by the Ar^+ beam, deposited preferentially at the pore walls and made the pore diameter smaller. As happens frequently in science, unforeseen results observed in experiments sometimes work better than the original idea. The authors realized that under their experimental conditions of low flux of ions, even large pores formed by a feed-controlled ion beam shrink via lateral diffusion and redeposition of material [Figure 15.3(A)] and suggested that the effect could be used for fabrication of nanopores with diameters down to 1 nm.

Dekker's group in the Netherlands discovered a similar approach using a more convenient irradiation source, TEM [31]. They created nanopores about 10 nm in diameter by a TEM focused beam and observed similar shrinkage of the pore. Again, the shrinkage occurs upon irradiation with a lower flux of electrons that is insufficient to ablate the substrate and only heats it up. The force that drives the nanopore to shrink,

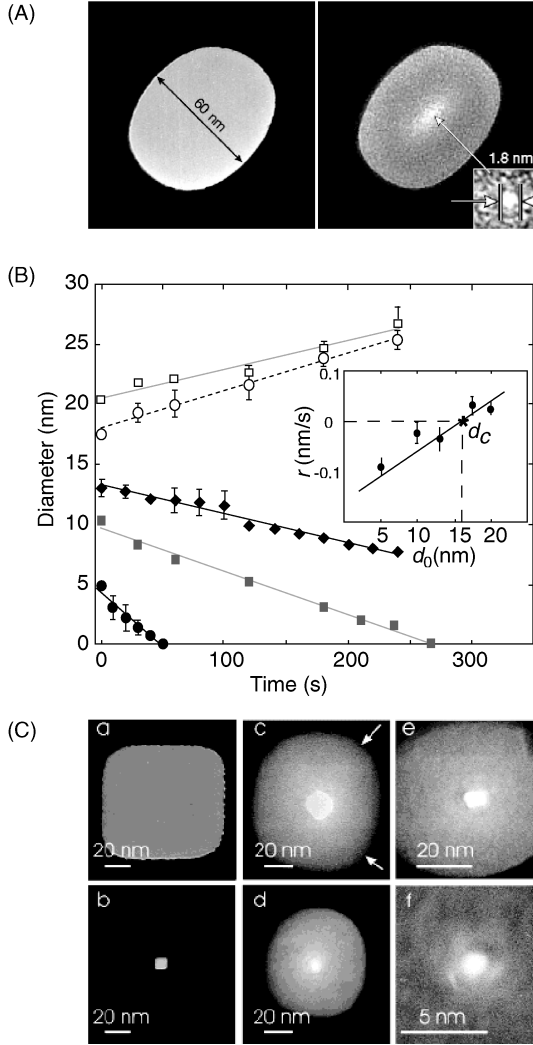


FIGURE 15.3 (A) Closing of a large 60-nm nanopore to smaller 1.8-nm pore using the approach of Li et al. (B) Nanopore expansion or contraction dynamics a function of the initial nanopore diameter, d_0 , in 50-nm-thick SiN. The different symbols represent different d_0 values at $t = 0$. The average diameter is displayed as a function of time. The inset depicts the rate of contraction or expansion as a function of d_0 . (C) Decrease of a nanopore diameter (in Si_3N_4) by atomic-layer deposition of Al_2O_3 . TEM images of nanopores before (top row), and after ALD (bottom row). [(A) from ref. 29, (B) from ref. 32, and (C) from ref. 33, with permission.]

the surface tension, can lead to different outcomes, depending on the initial pore radius r for different thicknesses h of the substrate film. The change in free energy compared with an intact sheet is

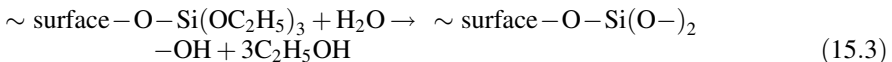
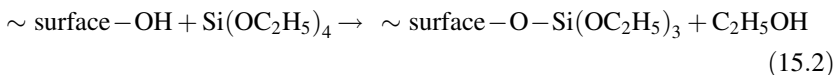
$$\Delta F = \gamma\Delta A = 2\pi\gamma(rh - r^2) \quad (15.1)$$

where γ is the surface tension of the liquid and ΔA is the change in surface area. Pores with radius $r < h/2$ can lower their surface free energy by reducing r (shrinking), whereas pores with larger radii, $r > h/2$, grow in size. TEM provides visual feedback for monitoring the nanopore dimensions. This work has opened a possibility for many scientific groups around the world to fabricate such pores. Kim et al. [32] observed that in their SiN films the critical radius was not $h/2$ but $h/6$ [see Figure 15.3(B)] and ascribed this discrepancy to a noncylindrical pore shape. They also demonstrated that nanopore arrays can be made easily using this approach.

All these techniques for single-nanopore production are relatively expensive, but the cost can be cut significantly if it were possible to shrink larger-diameter pores, which can be prepared using a combination of photolithography and etching techniques.

15.2.3 Nanopore- and Nanochannel-Diameter Tuning

Surface tension-induced shrinkage of nanopores occurs nonuniformly and thus has limited control or, in the case of long nanochannels lacks it completely. Atomic-layer deposition (ALD) offers a controllable uniform method for surface modification in which the nanochannel surface can be altered to introduce another material and/or can be shrunk as a result of the increased thickness of the layer deposited. The technique is based on sequential reactions of two chemicals passivating the surface-active groups in two steps, as shown for silica layer formation:



The reactions are self-limiting; each stops after completion of a single monolayer, only to become reactive toward the alternate chemical in the second step, and so on. In reaction (15.3), two of the hydrolyzed ethoxy groups are dehydrated simultaneously by linking neighboring Si atoms via a Si-O-Si bond. Similar alternation of two chemicals allows formation of other thin solid films, such as TiO₂, Al₂O₃, and V₂O₅. The approach is used for the modification of surface properties as well as for the diameter reduction of nanopores [33] [Figure 15.3(C)] and nanochannels, [34,35]. Due to self-limiting chemistry and atomic precision, the decrease in nanopore diameter can be calculated from the number of ALD cycles, which eliminates the need for feedback.

The atomic precision of ALD has the drawback of being slow. A number of methods have been suggested to expedite or modify the process. For example, Danelon et al. [36] employed a low-energy electron beam to “decompose” adsorbed tetraethylorthosilicate on the surface of nanopores to form an SiO_2 deposit. Real-time visual feedback was provided by SEM, and it was claimed that the reaction proceeded with the monolayer resolution (similar to ALD) necessary for controllable nanopore shrinkage. However, the role of the electron beam in the reaction was not apparent since there was no dependence on electron flux and the presence of water made it possible for slow simultaneous reactions such as reactions (15.2) and (15.3).

Sol–gel chemistry offers a quick way to form a silica layer with relatively good accuracy. Charles Martin’s group effectively demonstrated this method on narrowing nanochannel diameter in membranes as well as for synthesis of stand-alone silica nanotubes [37,38]. Applicability of this method to very small pores, below 10 nm in diameter, is limited due to difficulty in controlling the thickness of deposited sol–gel.

Charles Martin’s group also perfected the process of electroless deposition of metals inside polymeric nanopores as a way of narrowing the pore diameter [39]. They demonstrated that the initial 30-nm-diameter track-etched nanopores in polycarbonate membranes can be narrowed down to as small as 1 nm using high-pH electroless gold plating.

15.2.4 Self-Assembled Nanopores and Nanochannels

Growing porous metal oxide films on metals by anodization has been known for a few decades. Under the appropriate conditions defined by suitable competition between metal oxidation and metal ion dissolution, anodization can result in the formation of hexagonally arranged nanoporous oxide films. Anodization of aluminum has been studied most extensively (see, e.g., refs. 40–42) and perfected so that the desired dimensions—with diameters from 10 nm to 200 nm and lengths up to hundreds of micrometers—can easily be achieved. The structure of a typical porous array is sketched in Figure 15.4(A). Different electrolytes are optimal for particular ranges of anodization voltages and can contain various acids: sulfuric, oxalic, and phosphoric acids being the most typical. The pore diameters D_p and interpore intervals D_c (and thus the surface densities of pores) are proportional to the anodization voltage [see Figure 15.4(B) and (D)]. The dependencies can be approximated as $D_p/V_a \sim 1.2 \text{ nm/V}$ and $D_c/V_a \sim 2.5 \text{ to } 2.8 \text{ nm/V}$ [43–45], with some variations in different electrolytes. The growth rate depends exponentially on the anodization voltage. Figure 15.4(C) illustrates the high quality of the hexagonal structure of the such membranes. Dissolution of the underlying metal (in CuCl_2 or HgCl_2) and the barrier layer (in phosphoric acid) releases stand-alone membranes. Treatment in phosphoric acid also widens the pores. If pore narrowing is required instead, it can be achieved by ALD or sol–gel, as described above, or by using a hydrothermal treatment [46], which causes formation of a bottleneck near the pore mouth with a characteristic diameter on the order of a few nanometers. Surprisingly, such hydrothermal shrinkage does not occur for free-standing membranes [46].

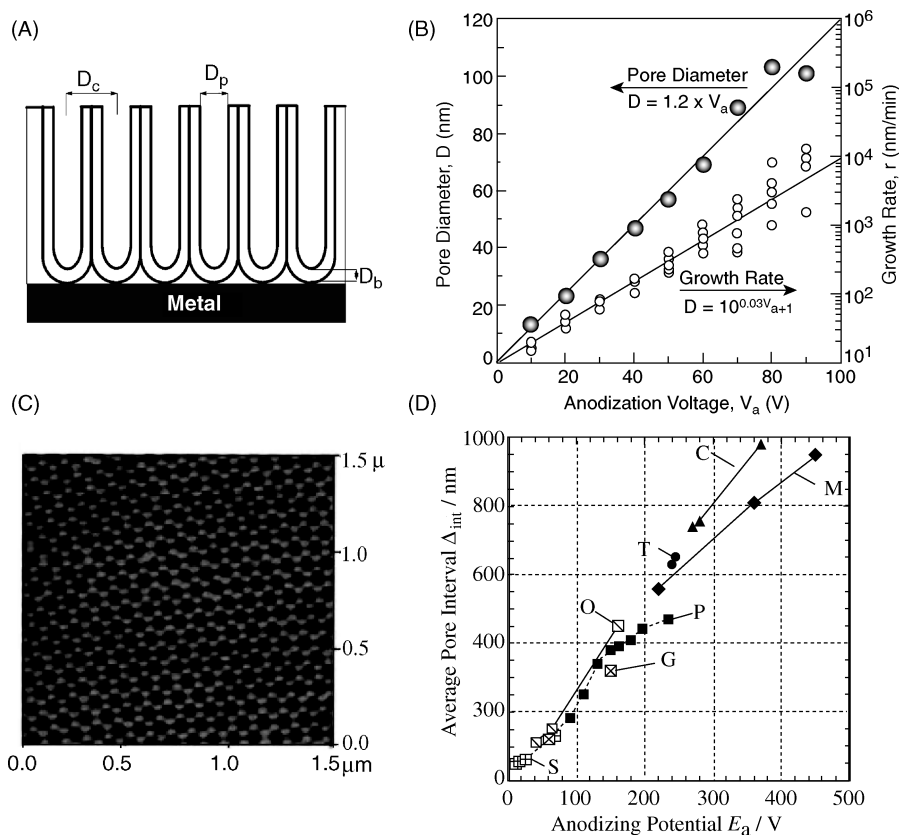


FIGURE 15.4 (A) Typical structure of nanoporous oxide film (D_c inter-pore interval; D_p pore diameter; D_b thickness of a barrier layer); (B) relationship between pore diameter and growth rate of anodized aluminium oxide layer and anodization voltage; (C) AFM image of aluminum anodized in oxalic acid at 40 V; (D) effects of anodizing potential on the inter-pore interval Δ_{int} of porous alumina films in sulfuric (S), oxalic (O), glycolic (G), phosphoric (P), tartaric (T), malic (M), and citric (C) acid solutions. [(B) From ref.43, (C) from ref. 40, and (D) from ref. 42, with permission.]

Other metals can also be anodized with formation of nanoporous membranes. In the majority of cases, HF acid is required in the anodization solution for formation of nanoporous oxide film. Significant advances in this field are due to the efforts of Patrik Schmuki's group from University of Erlangen–Nuremberg, Germany. They optimized anodization conditions for the anodization of titanium, yielding exceptionally well-defined TiO_2 nanotubes [47] with diameters of 30 to 60 nm and lengths exceeding 5 μm . Nanoporous tantalum oxide films were also prepared by Sieber and Schmuki [48] and Singh et al. [49] In the latter case, exceptionally uniform stand-alone membranes of 35 to 100 nm thickness were prepared. Similarly good results were achieved with WO_3 and ZrO_2 self-organized nanoporous films [50,51].

Formation of porous silicon by anodization differs from the methods described above for two reasons: (1) doped porous silicon is conductive, which is not the case for metal oxide films; and (2) formation of silicon dioxide does not accompany pore growth during anodization. In other words, Si is etched rather than anodized. This etching also does not produce hexagonally arranged pores, and the pore structure is wildly dependent on the conditions. Typically, aqueous and/or ethanol solutions of HF are used for anodization [52]. The resulting pores can have a rich branching structure, depending on the anodization conditions.

Instead of drilling or anodizing/etching pores in a solid material, one can assemble blocks into a porous structure. This approach is represented in the last class of nanoporous material discussed here: opals and reverse opals [53]. Opals can be formed by sedimentation of colloids from solution under gravitation force. The colloids are usually polymeric or silica spheres with diameters ranging from few hundred to a few thousands of nanometers. The voids between them become pores of size determined by the diameter of colloidal spheres. Fabrication of reverse opals adds another step, in which the voids between spheres are filled with a different material and the colloidal particles are removed.

15.3 SURFACE MODIFICATION CHEMISTRY

Building a biosensor usually (but not necessarily) requires introduction of a recognition element. This is achieved by surface modification of the nanochannel walls. Chemical modification of nanopores is similar to functionalization of solid flat surfaces. However, due to the hindered diffusion inside nanopores and larger surface area, one should account for some differences in the procedure. We present only commonly used surface modification techniques and discuss the peculiarities due to nanoporous structures. Thorough reviews of biomolecule conjugations and surface modifications may be found elsewhere [54, 55].

Generally, surfaces do not have groups suitable for direct linkage with a desired molecule. The first step in modification of such surfaces is their activation with a self-assemble monolayer that has an appropriate headgroup for further linkage. The nanochannels made from materials having surface hydroxide groups, e.g., SiO₂, TiO₂, and Al₂O₃, can be modified by well-known silane chemistry (Figure 15.5). Similar methods can be applied to oxidized surfaces as Si₃N₄ and polymers.

The surface density of hydroxyls on oxide surfaces is on the order 4 to $5 \times 10^{14} \text{ cm}^{-2}$. The surface density of the silanes in the monolayer is usually smaller, due to the steric difficulties coming from unreacted methoxy groups (Figure 15.5). For a flat SiO₂ surface, densities of silanes are reported to be 2 to $3 \times 10^{14} \text{ cm}^{-2}$ [56,57]. The density can be increased to be close to that of hydroxyls by using double silanization separated by the hydrolysis of unreacted methoxy groups after the first step [58].

Different purposes dictate different functional silane groups. Alkyl- and amine-terminated silanes are the major types of silanes used for modifications. In the absence of water, silanization is supposed to be a self-terminating reaction. Thus, diffusion

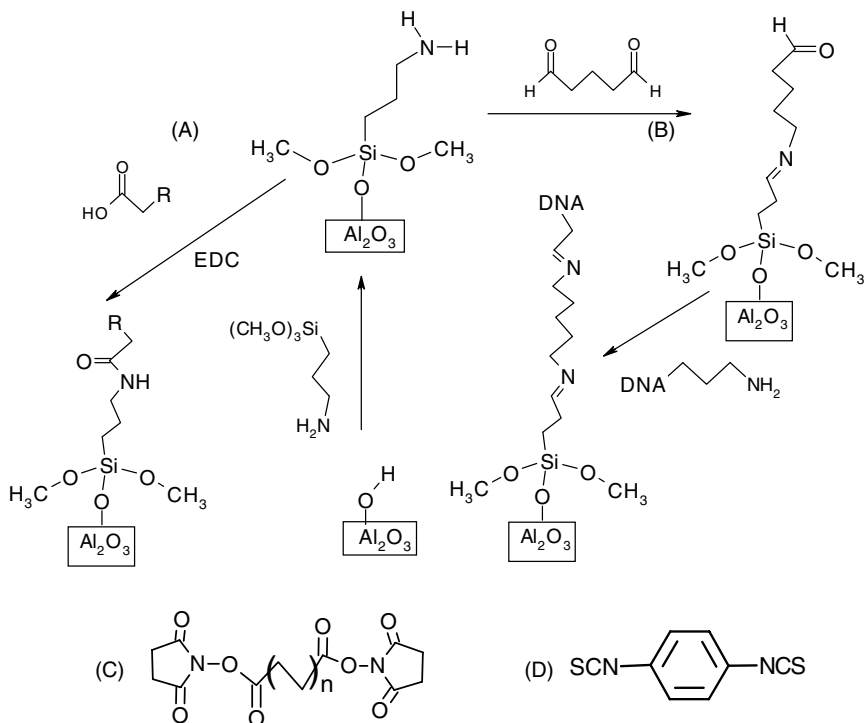


FIGURE 15.5 Typical schemes for immobilization of carboxyl (A) and amine (B) terminated molecules on the surface of oxides. Both start by amination with aminoalkoxysilane followed by either (A) amide formation using EDC coupler or (B) activation with glutaraldehyde and reaction with another amine. Other homofunctional cross-linkers, such as disuccinimidyl (C) and 1,4-phenylene diisothiocyanate (D) can also be used.

inside the nanopore and larger surface area, which is hindered compared to that on a flat surface can be overcome by an extended reaction time and/or by excess reagents. In reality this approach has an optimal duration, due to difficulty in controlling small water impurities, which can result in a runaway from surface polymerization when trialkoxysilanes and trichlorosilanes are used. Better results are reported with dialkoxysilanes [57]. Hydrophobic silanes have been used to decrease silica nanochannel surface charge [4], and to influence the wettability of alumina membranes [59–61] and silica nanotubes [62,63]. Introduction of amine-terminated silane provides an opportunity for further modification (Figure 15.5). Single silica nanopores [64,65], single nanochannels [66,67], alumina membranes [35,68,69,72], and reverse opals [74] are aminated easily.

Silanization of nanochannels with diameters above 10 nm can be carried out without apparent difficulty by dipping the sample into a silane solution in a dry organic solvent with subsequent rinsing and baking. However, nanopores with diameters below 5 nm tend to clog, requiring modification of the silanization procedure.

It was found that in situ modification or silanization with voltage applied across the nanopore during silanization prevents clogging and allows more reproducible outcomes [65]. The stability of the silane monolayer must also be taken into consideration for nanochannel functionalization. It was shown that silanes containing primary or secondary amines are not stable on a nanoporous alumina membrane surface [35]. Amines have a pK_a value close to 9 and thus increase local pH, which results in breakage of the Al–O–Si bond when in an aqueous environment for extended periods of time. Deposition of thin SiO₂ films on nanoporous alumina by ALD assures stability of amine-containing silane on the surface [35].

Activated by amines, nanochannels and nanopores can easily be modified with desired molecules using various cross-linking methodologies [55]. For example, immobilization of biomolecules containing primary amines can be realized by homofunctional cross-linkers that are reactive toward amines. However, hindered diffusion inside nanochannels must be taken into consideration when side reactions such as hydrolysis of the intermediate can occur. In fact, to our knowledge, the popular disuccinimidyl [Figure 15.5(C)] and its water-soluble analog sulfodisuccinimidyl cross-linkers were never employed successfully in nanochannel modifications. We found that this to be due to fast hydrolysis (ca. 10 minutes) of NHS ester in aqueous solutions. Hydrolysis can be avoided by using organic solvents, but this is useless because of the insolubility of many biomolecules in such solvents. Thus, other cross-linking molecules are generally used. For example, the 1,4-phenylene diisothiocyanate [Figure 15.5(D)] cross-linker, which is less susceptible to hydrolysis, was employed for immobilization of aminated DNA on the aminated nanopore walls [64]. Glutaraldehyde (Figure 15.5) was used for immobilization of aminated DNA on nanoporous alumina membranes [46,68,69].

If the molecule of interest has an NHS ester attached, hydrolysis can be ignored when an excess of reagent is used. For example, nanochannels were modified with biotin–NHS ester from aqueous solutions [66,70]. When the desired molecule is soluble in organic solvents, convenient and reproducible modification using NHS–ester can also be achieved. Biotin and different dyes have been immobilized on the nanochannel surfaces using this approach [35,73]. The surface density of immobilized molecules is not readily measurable for single nanochannels. An array of nanopores (a membrane) and flat surfaces allows such measurement using ultraviolet or infrared (UV or IR) spectra. For example, 21-mer single-stranded DNA was immobilized on the alumina nanopore surface using glutaraldehyde with a surface density of $4 \times 10^{12} \text{ cm}^{-2}$ [68].

When the surface and desired molecule have amine and carboxyl groups, respectively (or vice versa), EDC (1-ethyl-3-(3-dimethylaminopropyl)carbodiimide hydrochloride) linker can be used (Figure 15.5) [55]. EDC can be employed in both aqueous and organic solutions (such as ethanol). Coupling of EDC to a carboxyl group yields a highly reactive intermediate, which reacts eagerly with primary amines to form an amide bond. Unlike disuccinimidyl, EDC is a heterofunctional linker and the reaction is carried out in one step (mixing all reagents together). EDC hydrolysis in aqueous solutions is overcome by its excess. Cross-linking that results

in immobilization of desired molecules was employed by many researchers for nanochannel sensors. For example, we utilized it for immobilization of hydrophobic carboxylic acids and spiropyran molecules on the aminated alumina nanochannels [60,72]. Track-etched nanopores in various polymers have carboxylic groups on the surface which can be coupled to amines using EDC as well [75].

Well-known thiol chemistry can be used to modify metallic surfaces of nanochannels. Martin and co-workers deposited gold on track-etched polymer membranes walls with subsequent immobilization of a variety of molecules, such as DNA [76], proteins, antibodies [77], and carboxylic acids [78]. Even though thiol chemistry appears attractive due to easy realization, stability of the Au–S bond is known to be weak, which makes it problematic for use in long-term applications.

15.4 NONELECTRICAL NANOPOROUS BIOSENSORS

Although this is not the main purpose of this chapter, we felt that it would be educational to demonstrate that there exist other than electrical realizations for the use of nanoporous materials in biosensors. Alumina membranes have good transparency in the visible range, especially when they are wet, but they can be employed for optical detection even in the UV and IR regions. For example, at 260 nm (the maximum absorption wavelength of unmodified DNA) the optical density of commercial membranes from Whatman is below 2, which provides up to 2 units of OD in the dynamic range of absorbance measurements for captured molecules. Because of the long (60 μm) and narrow (ca. 200 nm diameter) pores, the effective surface is increased by a factor of about 10^3 , which is sufficient for easy detection of even short DNA strands [68]. Figure 15.6 demonstrates UV and IR absorption spectra of immobilized 21-mer-long DNA strands on such membranes before and after hybridization with a complementary target DNA strand (21-mer for UV and 41-mer for IR). In both cases, no tagging of DNA was necessary. The clear increase in absorption reduces to the original value after denaturing with urea. The process can be repeated numerous times without significant loss of single-stranded DNA covalently bound to the surface, as illustrated by the inset. Denaturing can also be achieved by heating the DNA duplex above its melting temperature, which for surface-bound DNA is very close to the melting temperature measured in solution. Note that the IR spectrum is limited to the transparency window above 1400 cm^{-1} . Lower-frequency vibrations are masked by absorption and scattering by the alumina membrane, but absorption due to OH bending, carbonyl, carboxyl, amide, and ring stretching near 1600 to 1700 cm^{-1} , and R–H stretching above 2600 cm^{-1} are easily observed and can be quantified in sensor applications.

These modified membranes can also be employed as affinity filters to capture from solution single-stranded nucleic acid oligomers of a desired sequence. We have shown that complementary DNA can be filtered with over 80% efficiency using a single passage through such a modified filter. From a mixture where it was present at 1/20 compared to other DNA, 85% was bound on the filter and >95% of that was eluted after denaturing [68].

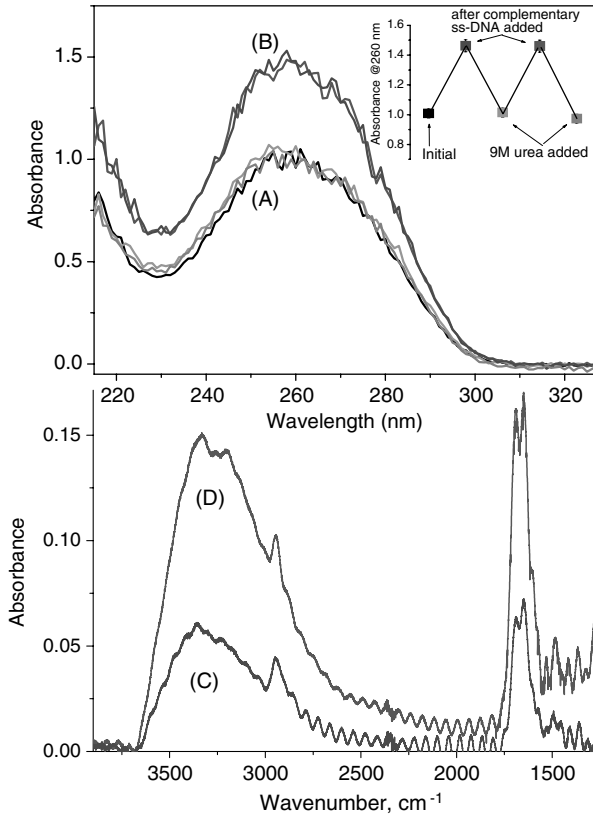


FIGURE 15.6 Variation of UV and IR absorption from DNA immobilized inside membranes before (A,C) and after (B,D) hybridization with complementary strand. The inset demonstrates reproducibility of hybridization/denaturing. (From ref. 68.)

High-cross-section density of molecules on the surface due to the longer path length in nanopores can be similarly advantageous in fluorescence-based sensors used in biochips and DNA chips [73,79]. The enhancement can be further improved and simplified by leaving the anodized membrane on the Al substrate and by taking advantage of its mirrorlike reflection. Figure 15.7 demonstrates that fluorescently labeled streptavidin provides almost an order-of-magnitude greater fluorescence when it binds to the biotin-decorated surface of a nanoporous membrane about 450 nm deep on the top of an Al underlayer [73]. With proper care, an additional increase can be achieved, due to the effects arising from optical interference in the resulting dielectric layer [80]. To gain maximum benefit, one should properly address the interference for both absorption and fluorescence spectra. Optical methods of detection using single nanochannels are not popular, due to the bulkiness of the equipment required and the difficulty of integration. However, monitoring fluorescence over the entire nanochannel cross section upon analyte binding to the nanochannel walls has been demonstrated [70].

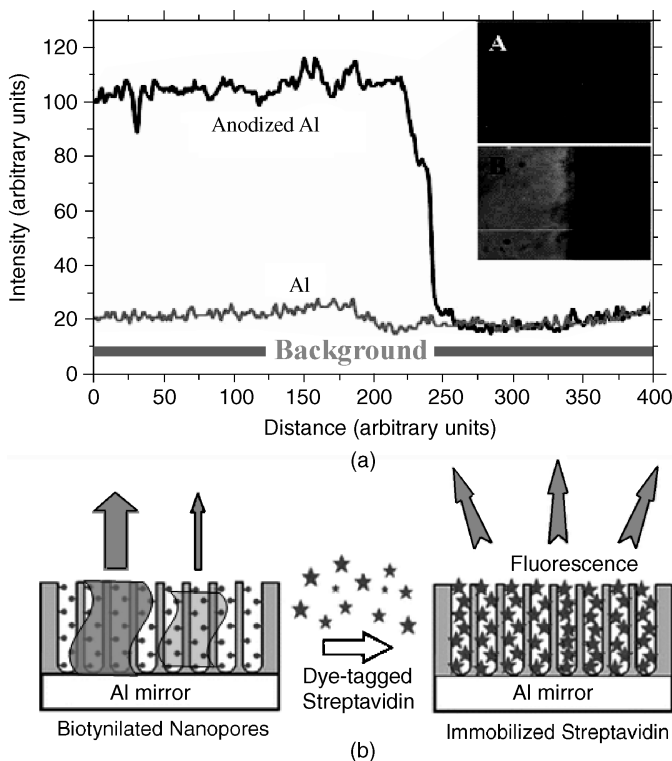


FIGURE 15.7 (a) Overlay of the fluorescence intensity profiles for the images in the inset: of anodized aluminum edge (B) and of metallic Al edge (A). Both films are modified with biotin and incubated with 15- μ M streptavidin. (b) Fluorescence enhancement arising from increased optical path length and reflection from underlying Al mirror. The arrows and the waves emphasize that interference additionally affects the intensity for thin membranes. [(a) From ref. 73, with permission.]

15.5 ELECTRICAL NANOPOROUS BIOSENSORS

For “human-free” analysis, any signal should eventually be transformed into an electrical signal. Thus, it would be convenient to eliminate intermediate stages and design an electrical detection scheme. A very promising and popular realization of such a scheme is based on the field or charge effect, where binding of charged analytes to the surface of one- or two-dimensional semiconductors depletes the conductive region of charge carriers and thus alters its electrical resistance.

We and others have been exploring an alternative approach in which ionic conductance through the nanoporous membranes (rather than the free carrier conductance in a semiconductor) is altered as a result of specific analyte binding. Similar effects can be realized on single nanochannels and nanopores. The attractive characteristic of this approach is that the analytes are label-free (unlike in fluorescence DNA and protein chips). The simplest detection scheme stipulates either dc or

ac conductance measurements with no gating or reference potential (i.e., no potentiostat). This detection scheme can utilize a standard input/output computer interface such as a USB port, and thus would be easily accessible for manipulation. In the ac mode, it is advantageous to have purely resistive impedance at the frequency of detection to facilitate simultaneous (parallel) detection of multiple analytes in the same sample.

First, we discuss different mechanisms [81] for altering ionic conductance through nanochannels and their arrays (membranes), each of which can be utilized in such electrical sensors. Specifics of detection with single nanopores is also discussed. We have identified at least four mechanisms of ionic conductance variation, illustrated schematically in Figure 15.8.

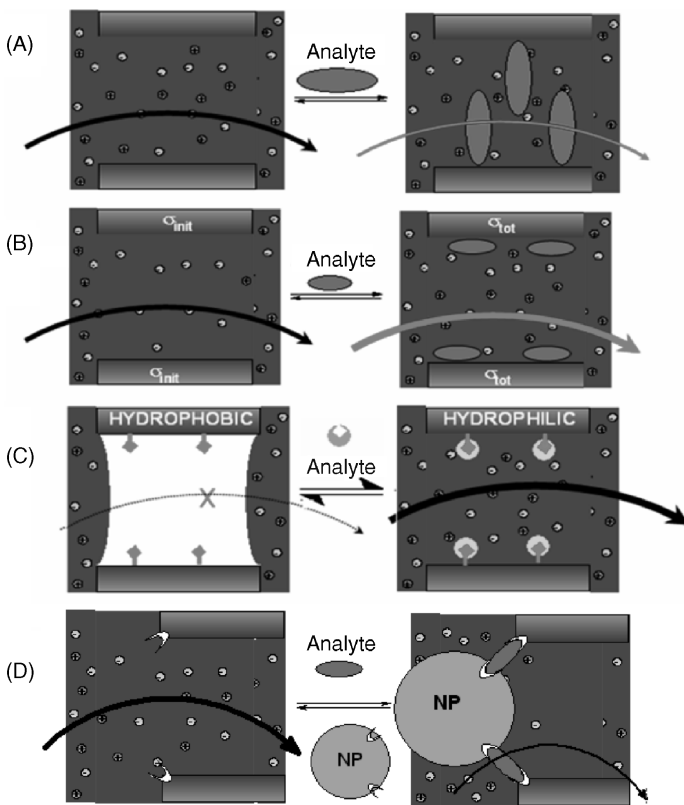


FIGURE 15.8 Four mechanisms affecting the ionic conductance through nanopores: (A) volume exclusion by bound analytes hinders ionic current; (B) at low ionic strengths, the surface charge from bound analytes depletes the nanopore of ions of the same charge, either increasing or decreasing the conductance depending on the total change of σ ; (C) surface tension difference between water and originally dry hydrophobic surface can be decreased by specific binding of hydrophilic analytes, thus allowing electrolyte penetration and electrical shortening of the gap; (D) analyte molecules bind nanoparticles (NP) to the pore mouth to block the pore. (From ref. 81, with permission.)

The *volume-exclusion mechanism* is suitable for analytes whose sizes are comparable to the nanochannel diameter. This condition is not always easy to realize, but the advantage of this method is that it can be used at various ionic strengths. At low ionic strengths, the outcome can be ambiguous because of interference with the surface charge mechanism, but at high ionic strength, the signal is independent of the analyte's charge.

We demonstrated this principle in sensing DNA oligomers using two schemes. First, we employed redox species (ferrocyanine and ruthenium hexamine) to monitor changes in conductance through commercial membranes modified with DNA. The signal was detected by cyclic voltammetry at a noble electrode [69]. Conductance and the corresponding CV amplitude decrease when surface-bound single-stranded DNA is hybridized with a complementary DNA oligo (see Figure 15.9). No changes were observed with a noncomplementary DNA that does not hybridize. The effect is observed only in the 20-nm-diameter pores of the membrane and not in the 200-nm pores (chosen by the membrane side). The effect is indeed due to volume exclusion because its sign and amplitude do not depend on the ion charge—they are the same for negatively charged ferrocyanine as for positively charged $\text{Ru}(\text{NH}_3)_6^{2+/3+}$. The effect (signal ratio) does not depend on the ionic strength between 0.1 and 1.0 M of KCl. However, the density of surface-immobilized DNA affects dramatically the response to hybridization (see Figure 15.9). The reason for this is the same as that for the observation of a signal with only narrow pores and not with 200-nm pores. When the pore diameter is comparable with the DNA length, its resistance is affected more by DNA binding. Similarly, with increasing amounts of DNA in the pores, the contribution of pore resistance becomes more important than that of charge transfer at the electrodes.

Therefore, the key to increasing the sensitivity is in (1) decreasing pore diameters (raising pore resistance), (2) increasing the surface concentration of DNA, and (3) minimizing resistance at the electrodes. There is a relatively simple approach to raising the pore resistance of alumina membranes by hydrothermal treatment (boiling) after anodization [46]. The Bode plot (of impedance Z vs. ac frequency) shown in Figure 15.10 offers insight into the behavior in such membranes:

$$Z = R_s + \frac{R_p}{\sqrt{1 + jR_p\omega C_p}} + \frac{1}{\sqrt{j\omega C_{ox}}} \quad (15.4)$$

Before boiling, the pore resistance (R_p in the inset) of the membrane with 60-nm-diameter pores from anodization is too small to be recognized because of the dominating contribution of the capacitance from the oxide layer (C_{ox}) on the Al electrode (curve a). Hydrothermal treatment (boiling) shrinks the pores to a much smaller effective diameter of about 2 nm (see Figure 15.11) and changes the Bode plot appearance dramatically. Now both pore resistance and capacitance can be recognized, and for frequencies between 10 and 1000 Hz, the contribution due to pore resistance dominates. Because R_p becomes so large, it can be monitored successfully even when the electrode resistance is high, that is, the need for low charge transfer resistance at the electrode is not as critical and signal detection simplifies to measuring ac impedance at around 100 Hz and with the electrolyte (ionic) resistance alone.

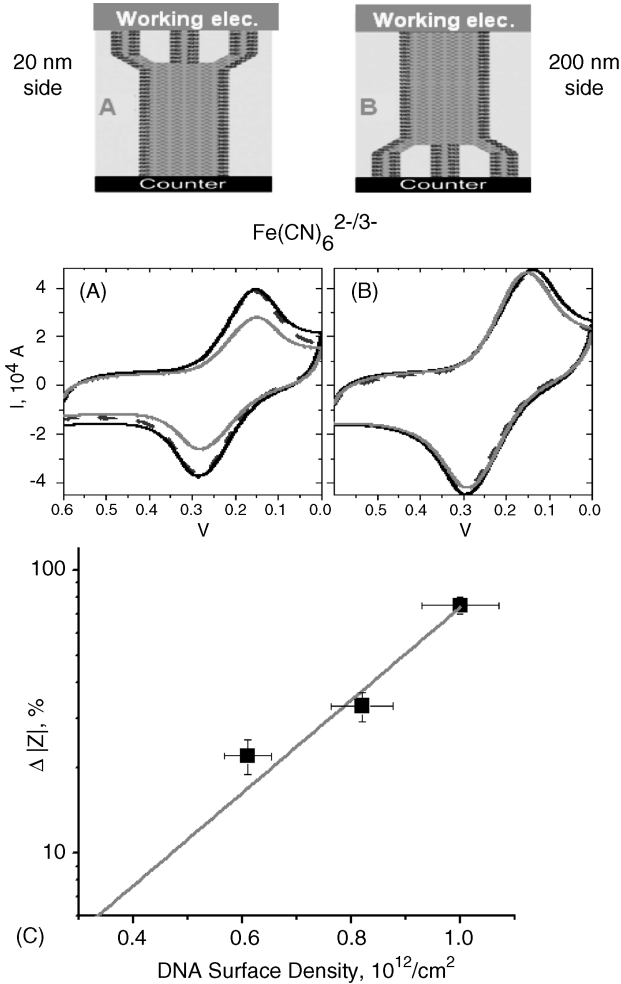


FIGURE 15.9 CV signal of $\text{Fe}(\text{CN})_6^{2-/3-}$ at 20 nm (A) and 200 nm (B) side of a nanoporous membrane modified with 21-mer DNA oligomers before (black) and after hybridization (gray) with complementary DNA strands. C) The relative increase of the impedance upon full hybridization depends strongly on the initial surface density of DNA. The gray line helps guide the eye. (From ref. 69, with permission.)

Figure 15.10 illustrates the fact that, indeed, R_p is sensitive to DNA binding in this range and increases by almost 50% upon hybridization with complementary DNA. The disadvantage of increasing R_p is that it is too high both before and after hybridization, which reduces its applicability for microchip applications where miniature (micrometer-sized) membranes are preferred.

The same method can be used with nanochannels and nanopores. A system based on a single conical nanopore covered with a gold layer can serve as an example for this type of sensor [77]. Interestingly enough, authors reported almost complete ionic

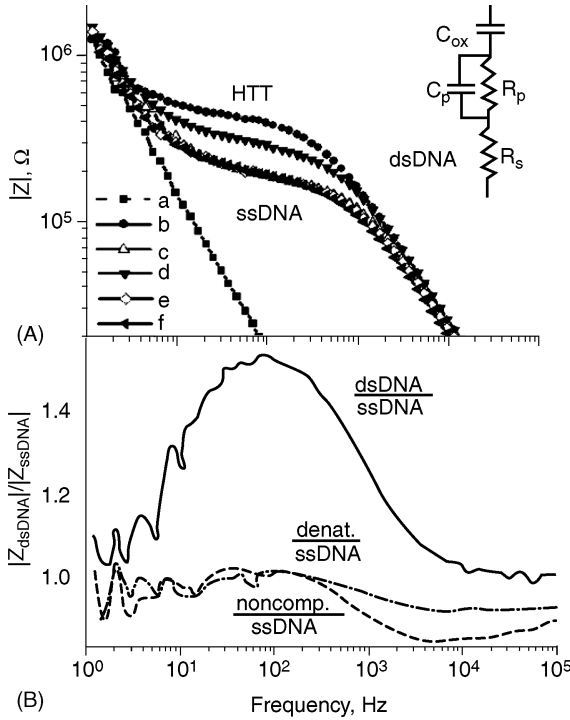


FIGURE 15.10 (A) Impedance Bode plot for nanoporous alumina membrane and its equivalent scheme: a, untreated membrane; b, after hydrothermal treatment (HTT); c, HTT membrane after immobilization of ssDNA; d, after hybridization with complementary ssDNA; e, after dehybridization with urea; f, with a noncomplementary ssDNA; (B) relative changes of the impedance after exposing to complementary and noncomplementary ssDNA targets. (From ref. 46, with permission.)

current blockage upon binding of several proteins, (e.g., streptavidin, immunoglobulin, ricin) to a nanopore of about 5 nm diameter.

The *surface charge mechanism* is very similar conceptually to the field effect in the electrical conductance of semiconductors, but in reverse—with depletion of the ionic carriers inside the nanochannel rather than electrons. The effect is pronounced at low ionic strengths when the surface charge on the pore walls (with the density σ) cannot be compensated for by the electrolyte with bulk concentration $[C]$. When the bulk concentration of electrolyte $[C]$ is small;

$$[C]_{\text{inside}} \sim \frac{4\sigma}{FD_{\text{pore}}} > [C] \tag{15.5}$$

where D_{pore} is the pore diameter and F is Faraday’s constant, the surface charge dictates the ion concentrations inside the nanochannel. The resulting conductance of the nanochannel becomes independent of the bulk electrolyte concentration [4].

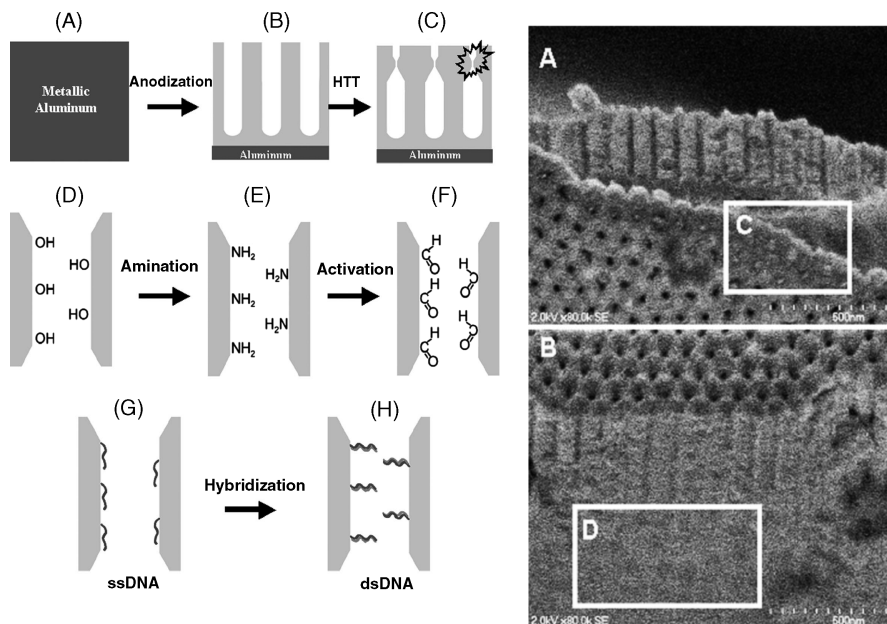


FIGURE 15.11 Construction and modification of hydrothermally treated nanoporous membrane and its SEM micrographs: the top view (A) and side view (B) show the shrunk pore zone (labeled as C and D regions) developed inside the porous structure. (From ref. 46, with permission).

Because of the low ionic strength needed to achieve this condition, pore resistance exceeding that of the electrolyte outside the pore, $R_{\text{pore}} > R_{\text{electrolyte}}$, is easier to accomplish with a long single nanochannel rather than with multiple short nanochannels in parallel, as in nanoporous membranes. Even for modest surface charge densities, $\sigma \sim 0.01 \text{ e/nm}^2$, and a relatively large pore diameter $D_{\text{pore}} \sim 200 \text{ nm}$, the condition (15.4) can be achieved at concentrations of $[C] \sim 3 \times 10^{-4} \text{ M}$. To fulfill electroneutrality, the nanochannel is filled predominantly with ions charged opposite to that of the surface wall. Binding of analytes to the walls can change their charge and thus the ionic conductance through the channel. The sign of the effect depends on the change in the total surface charge density and can appear either as an increase or a decrease in the nanochannel resistance induced by binding of the (charged) analyte. The analyte charge can be regulated by solution pH. It should be noted that unlike the volume-exclusion regime, binding of charged analytes alters the conductance even if the overall cross section of the nanopore is unchanged. Moreover, even a decrease in the effective nanopore cross section can lead to an overall conductance increase.

No direct experiments have been published with the claim of employing the surface charge effect as a biosensing element. However, numerous publications provide solid proof for its applicability. For example, a single nanochannel modified with uncharged biotin shows a significant increase in conductance upon charged streptavidin

binding [66]. Since DNA is a highly charged molecule, the charge effect could be employed successfully for DNA sensing. It was shown that the flux of anions through a gold nanopore array modified with uncharged peptide nucleic acid (PNA) decreases upon hybridization with complementary DNA [82].

Blocking nanopores with nanoparticles is a seemingly attractive approach presuming a significant ionic current variation by appropriately sized nanoparticles. Unfortunately, it does not live up to expectations, even though it seems so appropriate for the macro world. Although, such “blocking” can be physically realized, the electrical blocking is never perfect, especially if a discriminative response based on the specific interaction on the linker (between the particle and the pore) is required. Lee et al. [83] demonstrated that blocking of single nanopores by charged nanoparticles can be achieved electrophoretically, but even then the current drop was only about 50%, which was attributed to the balance of electrostatic and entropic forces that hold the particle to the pore opening. Blocking the nanochannels via ‘gluing’ nanoparticles to them by bioanalyte also results in similarly small contrast of ionic current. If the particles are smaller than the pore diameter, the effect can be larger. Then we would attain results similar to the volume-exclusion mechanism but with less convenience.

Many complications with electrode polarization can be eliminated if the membranes’ ionic resistance change is more dramatic. *Hydrophobicity switching* offers such a possibility. This mechanism requires surface modification with mixed monolayers that consist of both hydrophobic molecules and triggering or receptor molecules, which respond to either physical or chemical stimuli. Initially, when the surface tension difference between water and the pore surface $\Delta\gamma$ is such that the surface is hydrophobic (the contact angle for water is greater than 90° on that surface), the pores are dry and nonconductive. If the surface becomes more hydrophilic (the contact angle drops below 90°) due to physical stimuli or analyte binding, water or electrolyte can enter the pores and shorten them electrically. The resistance ratio between hydrophobic and hydrophilic membranes can exceed seven orders of magnitude and thus is very attractive for sensor applications.

Physical stimuli such as light and pressure are easier to employ, and elucidate the peculiarities of this mechanism. An optically active spiropyran molecule is less polar in its ground-state spiro form. After excitation by UV light, it is transformed into zwitterion (polar) merocyanine, which renders the surface more hydrophilic (see Figure 15.12) [72]. Irradiation by visible light switches spiropyran back to the spiro form. Modification of the membrane surface with a mixture of aliphatic and spiropyran moieties, gradually transforms it from hydrophobic to somewhat hydrophilic upon increasing the portion of spiropyran. However, when the latter is in the merocyanine (excited) form, this transition occurs at a lower concentration of the dye. In the range of intermediate concentrations, one can switch the membrane from its nonconductive dry state to a highly conductive form by means of UV irradiation [72] as shown in Figure 15.13. Notably, irradiation with visible light, which transforms the dye back into its spiro form, does not recover the high membrane resistance. The membrane remains filled with water because the dry state is not achievable by spontaneous dewetting for pore diameters greater than 5 nm, due to a high activation barrier. Membrane drying can be used to recover the dry state. The maximum effect observed

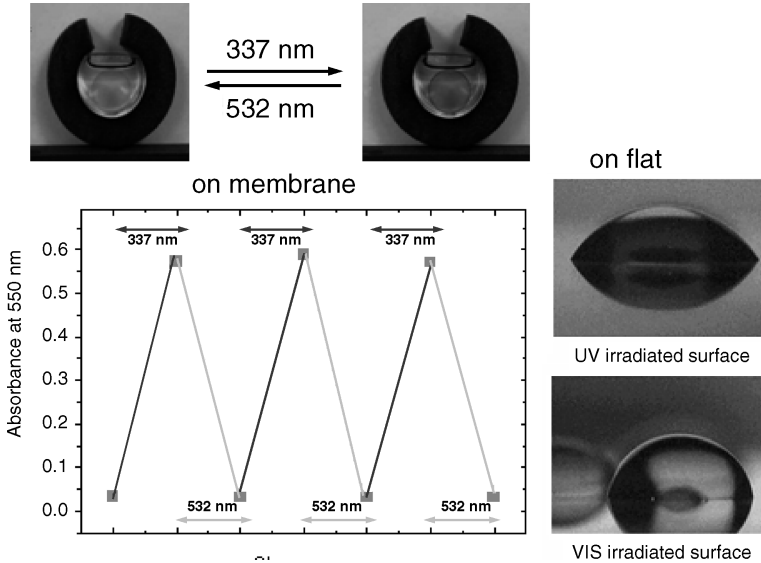


FIGURE 15.12 UV irradiation turns spiropyran into the colored merocyanine form (top) rendering surface more hydrophilic (right). Visible irradiation recovers properties. Cycling of these properties can be repeated numerous times (center). (From refs. 71 and 72, with permission.)

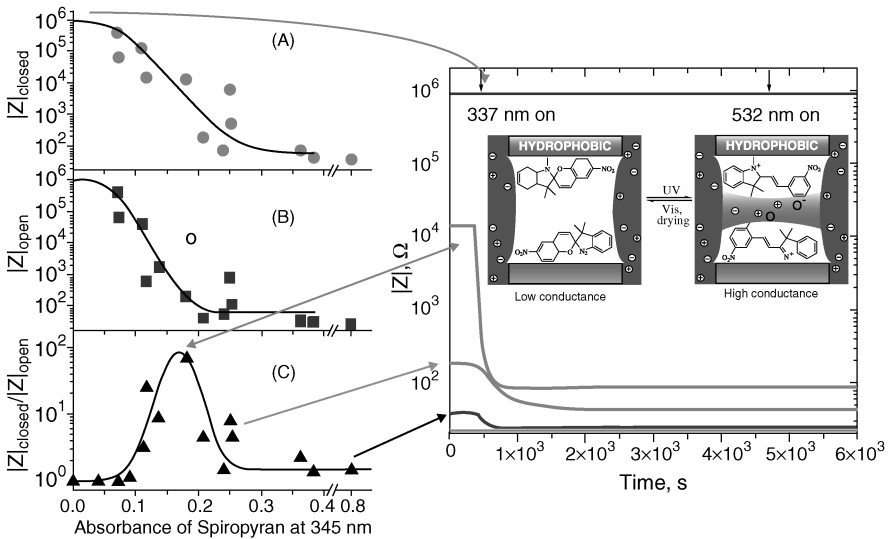


FIGURE 15.13 Dependence of the membrane resistance on the relative amount of spiropyran in the hydrophobic monolayer for its (A) spiro (visible irradiation) and (B) merocyanine (after UV) forms; (C) effect of light irradiation on the membrane resistance change. (From ref. 72, with permission.)

in this optical nanovalve, as measured via the resistance change, is almost two orders of magnitude—more than enough for a good sensor, although it could be improved further.

The effect is partially diminished by the intrinsic surface wall conductance of the hydrophobic membranes, which is sensitive to the type and the quality of the organic modifier [60]. The resistance can vary by more than five orders of magnitude—even when water does not intrude into the pores—because of surface hydroxyls and other water sensitive/ionizable groups of the linkers. Because of this, various hydrophobic modifiers also differentiate membranes by their ability to withstand strong acids, which typically can survive $\text{pH} < 1$ after modification. Ways to minimize the undesired effect of hydrophobic membrane conductance by proper surface modification have since been formulated.

Conductance of hydrophobic membranes via surface groups is also observed [84] in studying the pressure dependence of water intrusion into purely hydrophobic membranes (Figure 15.14). The external hydrostatic pressure at which water intrudes into nanopores depends on their diameter and the surface energy difference between water and the surface:

$$\Delta P = P_{\text{ext}} - P_{\text{int}} > \frac{4\Delta\gamma}{D_{\text{pore}}} \quad (15.6)$$

Commercial 20-nm membranes have the nominal diameter indicated on one side for only about 2% of its total thickness, while the remaining part has 200-nm-nominal-diameter pores. Compared to one with just 200-nm pores, a 20-nm/200-nm membrane has a broad range of pressures at which its pores are not fully filled with water and thus the activation barrier for their dewetting is low. Indeed, a recovery of resistance upon pressure release is observed to be greater than in 200-nm membranes, but its value is still less than 100%. The effect is important for proper design of electrical sensors based on the hydrophobicity switching effect, which we believe is the most promising realization of a biochemical sensor with nanoporous membranes.

Steinle et al. [59] observed a resistance decline with small concentrations of amphiphiles on similarly prepared hydrophobically modified nanoporous membranes. They stipulated that such membranes can be employed as sensors for amphiphilic drugs. We observe a similar effect but at higher concentrations of amphiphiles that are close to their critical micellar concentrations [85] (see Figure 15). Specific interactions such as that of biotin–streptavidin, on the other hand, are strong enough to switch hydrophobicity permanently at low concentrations of analytes (Figure 15.15).

Single nanochannels and nanopores have a number of advantages over nanochannel arrays. Smaller dimensions make it possible to operate with less analyte. As a consequence, single channels should provide lower detection limits. Moreover, single nanopores are set uniquely because of new avenues for data collection based on electrical pulses from single-molecule translocation through the nanopore.

Translocation through a single nanopore can be viewed as a nano version of the Coulter counter and is a straightforward realization of the volume-exclusion

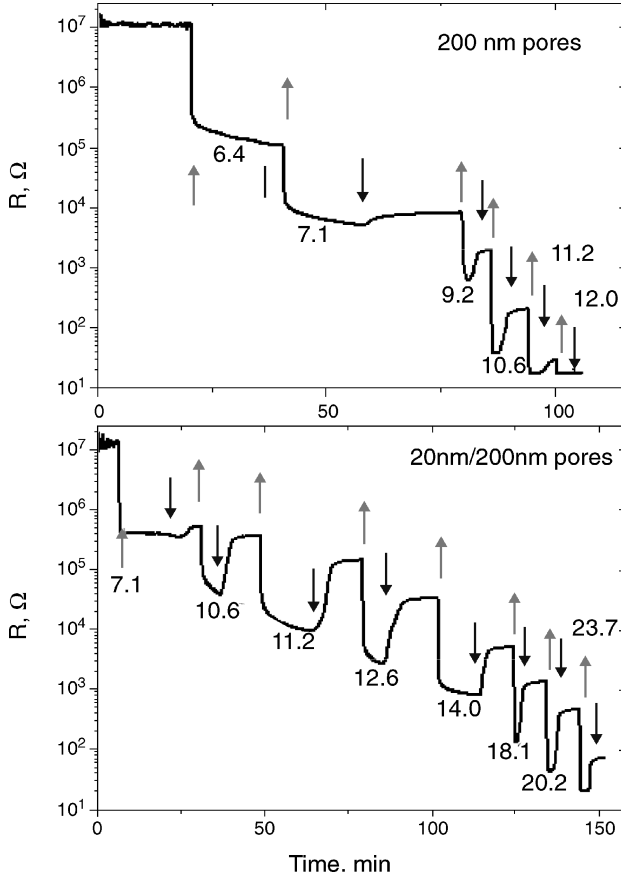


FIGURE 15.14 Ionic resistance of fluorinated nanoporous membranes as a function of applied pressure (in bar): 200 nm diameter pores and 20 nm on the top of 200 nm differ not only by the range of pressure intrusion but also by the resistance recovery after releasing pressure. (From ref. 84, with permission).

mechanism, without the need for specific analyte binding on the surface. The seeming feasibility of this method to sequence single DNA molecules (Figure 15.16) has triggered enormous interest in this area. The first experimental data were obtained a decade ago using biological (α -hemolysin) nanopores for detection of DNA [86]. Synthetic nanopores allowed greater control of their dimensions, which boosted the use of this phenomenon for translocation not only of DNA [87] and other molecules [88] but of nanoparticles as well [28]. The events are registered as pulses of the ionic current drop due to a molecule's occupation of the pore. At high concentrations of electrolyte, DNA translocation through a nanopore induces transient decrease in the ionic current. However, at low ionic strengths, the effect can be opposite, due to highly charged DNA dragging along additional counterions, with subsequent increase in ionic conductance (analogous to the surface charge effect discussed above) [14]. The

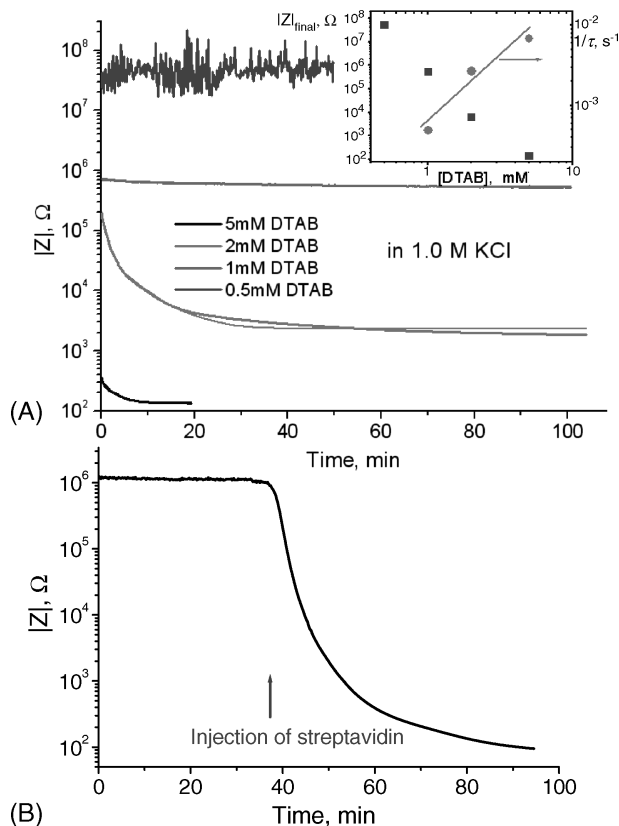


FIGURE 15.15 (A) Hydrophobically modified 200-nm pore diameter membrane by octylsilane is dry and nonconductive. Its ionic resistance drops from about $5 \times 10^7 \Omega$ to less than 200Ω in a narrow range of amphiphile (DTAB) concentrations. The pores open up for electrolyte intrusion only at concentrations exceeding its CMC of about 0.05 mM. The inset shows variations of the final resistance and the relaxation rate, as a function of [DTAB]. (B) Similarly modified 200-nm-pore-diameter membrane with a mixed hydrophobic monolayer of biotin–octylsilane responds to injection of streptavidin by dropping resistance to less than 200Ω . [(A) From ref. 85, with permission. (B) From unpublished results of I. Vlasiouk.]

length of DNA and its two forms, double stranded (ds) and single stranded (ss), are the two obvious features one can get from an analysis of the pulse duration and its amplitude. This is not sufficient to identify the sequence of DNA molecules constructed from four different bases.

The two existing solutions to that problem utilize ssDNA hybridization with a complementary strand and employ such complementary strands either immobilized in the pore [64] or supplied in solution [89]. In the former case, a pore diameter of a few nanometers appears to translocate complementary strands faster than noncomplementary but does it more frequently [64]. The technique cannot be expanded easily

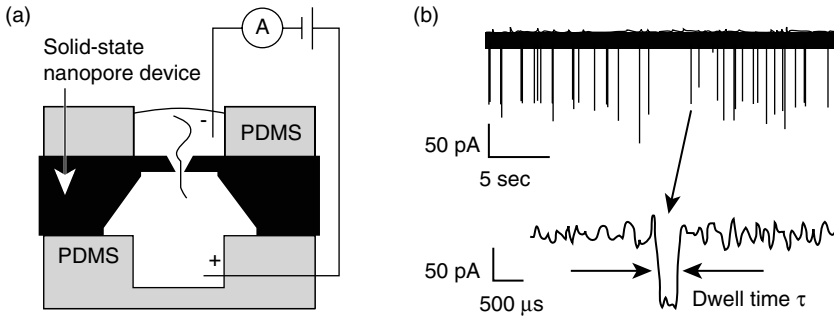


FIGURE 15.16 (a) DNA molecule passing through the nanopore; (b) ion current blockage events with 11.5-kbp double-stranded DNA translocating through 10-nm nanopore. Single pulse represents one DNA passing through the nanopore. (From ref. 87, with permission.)

to longer DNA. In the latter, the sequence of a long ssDNA can be recovered from statistical analysis of pulse shapes of the same ssDNA consecutively hybridized with short oligonucleotides of different sequences—greater ionic current decline for the dsDNA portion [89].

Ultimately, one would like to read out one base of a ssDNA at a time. If the nanopore's dimensions are comparable to the size of individual nucleotides, the ionic current through the nanopore could be modulated by the different bases that occupy the nanopore. Thus, a current vs. time plot should possess the information about the identity of the DNA molecule that is passed through the nanopore (Figure 15.16B). It was realized that the straightforwardly measured ionic current does not provide a signal sufficient for unambiguous DNA sequencing. The DNA translocates too fast—a single base occupies the nanopore for as little as $1\ \mu\text{s}$ under typical experimental conditions. For that time period, the number of ions passing through, for example, an α -hemolysin pore is approximately 100. Four bases do not differ enough in volume to beat the fluctuations in the number of ions located in the nanopore [28]. DNA translocation can be slowed by an order of magnitude by adjusting different experimental parameters, such as solution viscosity, temperature, and ionic strength [90]. However, this approach leads to a decrease in ionic current and results in a lower signal/noise ratio. Attaching DNA to a bead enables better control of DNA translocation time using optical tweezers [91], a technique currently used for force measurements. As was pointed out, single-base precision control over the DNA location inside the nanopore is a very challenging task.

Recently, a number of theoretical groups started exploring the possibility of direct electrical detection of ssDNA sequences using nanopore technology. At least two methods have been proposed. The first one is based on placing two electrodes on the nanopore and measuring the electrical tunneling current between those electrodes. Every DNA base located between those electrodes would influence the tunneling electrical current differently, thus providing information about the particular DNA base located between the electrodes [92]. This approach would overcome the limitation of ionic currents, due to the much higher electrical tunneling current.

Another idea is based on capacitive sensing, where each base influences the capacitance of the nanopores, with two electrodes placed on top and bottom of the nanopore [93]. It is likely that this approach would enable counting of the number of bases since every nucleotide is charged. However, discrimination between bases is a very challenging problem because one needs to distinguish between differences in bases' conductance.

15.6 SUMMARY

We realize that it would be next to impossible to provide a thorough and up-to-date review on the use of nanoporous materials in biosensing. Even by focusing on electrical detection schemes, we have probably missed many interesting papers. We see our task here as a rather biased recollection of our past, present, and possibly future interests in terms of physicochemical phenomena related to nanoporous materials. Through this approach, our goal has been to expand our understanding of nature so that we could mimic it in new biomedical applications. We are particularly excited that there are numerous ways to appreciate and utilize these phenomena, and their exploration should bring wonderful scientific discoveries.

REFERENCES

1. Mirkin CA. The beginning of the small revolution. *Small*. 2004;1:14–16.
2. Lieber CM, Wang ZL. Functional nanowires. *MRS Bull*. 2007;32:99–104.
3. Henry C. S. ed. *Microchip Capillary Electrophoresis*. Humana Press, Totowa, NJ, 2006.
4. Stein D, Kruithof M, Dekker C. Surface-charge-governed ion transport in nanofluidic channels. *Phys. Rev. Lett*. 2004;93(3):035901.
5. van der Heyden FHJ, Bonthuis DJ, Stein D, Meyer C, Dekker C. Power generation by pressure-driven transport of ions in nanofluidic channels. *Nano Lett*. 2007;7(4):1022–1025.
6. van der Heyden FHJ, Stein D, Besteman K, Lemay SG, Dekker C. Charge inversion at high ionic strength studied by streaming currents. *Phys. Rev. Lett*. 2006;96:224502.
7. van der Heyden FHJ, Stein D, Dekker C. Streaming currents in a single nanofluidic channel. *Phys. Rev. Lett*. 2005;95:116104.
8. Plecis A, Schoch RB, Renaud P. Ionic transport phenomena in nanofluidics: experimental and theoretical study of the exclusion-enrichment effect on a chip. *Nano Lett*. 2005;5(6):1147–1155.
9. Turner SW, Perez AM, Lopez A, Craighead HG. Monolithic nanofluid sieving structures for DNA manipulation. *J. Vac. Sci. Technol. B*. 1998;16(6):3835.
10. Bhusari D, Reed HA, Wedlake M, Padovani AM, Allen SAB, Kohl PA. Fabrication of air-channel structures for microfluidic, microelectromechanical, and microelectronic applications. *J. Microelectromech. Syst*. 2001;10:400.
11. Karnik R, Fan R, Yue M, Li D, Yang P, Majumdar A. Electrostatic control of ions and molecules in nanofluidic transistors. *Nano Lett*. 2005;5(5):943–948.

12. Karnik R, Castelino K, Majumdar A. Field-effect control of protein transport in a nanofluidic transistor circuit. *Appl. Phys. Lett.* 2006;88:123114.
13. Fan R, Wu Y, Li D, Yue M, Majumdar A, Yang P. Fabrication of silica nanotube arrays from vertical silicon nanowire templates. *J. Am. Chem. Soc.* 2003;125:5254.
14. Fan R, Karnik R, Yue M, Li D, Majumdar A, Yang P. DNA Translocation in inorganic nanotubes. *Nano Lett.* 2005;5(9):1633–1637.
15. Cao H, Yu Z, Wang J, et al. Fabrication of 10nm enclosed nanofluidic channels. *Appl. Phys. Lett.* 2002;81(1):174–176.
16. Tegenfeldt JO, Prinz C, Cao H, et al. The dynamics of genomic-length DNA molecules in 100-nm channels. *Proc. Nat. Acad. Sci. USA.* 2004;101(30):10979–10983.
17. Saleh OA, Sohn LL. An artificial nanopore for molecular sensing. *Nano Lett.* 2003; 3(1):37–38.
18. Spohr R, *Ion Tracks and Microtechnology: Principles and Applications*, View. eg, Braunschweig, Germany, 1990.
19. Apel PY, Korchev YE, Siwy Z, Spohr R, Yoshida M. Diode-like single-ion track membrane prepared by electro-stopping. *Nuc. Instrum. Methods Phys. Res. B.* 2001;184:337–346.
20. Apel PY, Blonskaya IV, Dmitriev SN, Orelovich OL, Presz A, Sartowska BA. Fabrication of nanopores in polymer foils with surfactant-controlled longitudinal profiles. *Nanotechnology.* 2007;18:305302.
21. Fleischer RL, Price PB, Walker RM. *Nuclear Tracks in Solids*. University of California Press, Berkeley, CA; 1975.
22. Siwy ZS. Ion-current rectification in nanopores and nanotubes with broken symmetry. *Adv. Funct. Mater.* 2006;16(6):735–746.
23. Karhanek M, Kemp JT, Pourmand N, Davis RW, Webb CD. Single DNA molecule detection using nanopipettes and nanoparticles. *Nano Lett.* 2005;5(2):403–407.
24. Umehara S, Pourmand N, Webb CD, Davis RW, Yasuda K, Karhanek M. Current rectification with poly-l-lysine-coated quartz nanopipettes. *Nano Lett.* 2006;6(11): 2486–2492.
25. Wu S, Park SR, Ling XS. Lithography-free formation of nanopores in plastic membranes using laser heating. *Nano Lett.* 2006;6(11):2571–2576.
26. Zhang B, Zhang Y, White HS. The nanopore electrode. *Anal. Chem.* 2004;76:6229–6238.
27. Dekker C. Solid-state nanopores. *Nat. Nanotechnol.* 2007;2:209.
28. Ito T, Sun L, Crooks RM. Simultaneous determination of the size and surface charge of individual nanoparticles using a carbon nanotube-based coulter counter. *Anal. Chemi.* 2003;75:2399–2406.
29. Li J, Stein D, McMullan C, Branton D, Aziz MJ, Golovchenko JA. Ion-beam sculpting at nanometer length scales. *Nature.* 2001;412:166–169.
30. Stein DM, McMullan CJ, Li J, Golovchenko JA. Feedback-controlled ion beam sculpting apparatus. *Rev. Sci. Instrum.* 2004;75(4):900–905.
31. Storm AJ, Chen JH, Ling XS, Zandbergen HW, Dekker C. Fabrication of solid-state nanopore with single-nanometer precision. *Nat. Mater.* 2003;2:537–540.
32. Kim MJ, Wanunu M, Bell DC, Meller A. Rapid fabrication of uniformly sized nanopore and nanopore arrays for parallel dna analysis. *Adv. Mater.* 2006;18(23):3149–3153.

33. Chen P, Mitsui T, Farmer DB, Golovchenko J, Gordon RG, Branton D. Atomic layer deposition to fine-tune the surface properties and diameters of fabricated nanopores. *Nano Lett.* 2004;4(7):1333–1337.
34. Cameron MA, Gartland IP, Smith JA, Diaz SF, George SM. Atomic layer deposition of SiO₂ and TiO₂ in alumina tubular membranes: pore reduction and effect on surface species on gas transport. *Langmuir.* 2000;16:7435–7444.
35. Szczepanski V, Vlasiouk I, Smirnov S. Stability of silane modifiers on alumina nanoporous membranes. *J. Membrane Sci.* 2006;281:587–591.
36. Danelon C, Santschi C, Brugger J, Vogel H. Fabrication and functionalization of nano-channels by electron-beam-induced silicon oxide deposition. *Langmuir.* 2006;22:10711.
37. Mitchell DT, Lee SH, Trofin L, et al. Smart nanotubes for bioseparations and biocatalysis. *J. Am. Chem. Soc.* 2002;124:11864.
38. Gasparac R, Kohli P, Mota MO, Trofin L, Martin CR. Template synthesis of nano test tubes. *Nano Lett.* 2004;4(3):513–516.
39. Jirage KB, Hulteen JC, Martin CR. Nanotubule-based molecular-filtration membranes. *Science.* 1997;278:655–658.
40. Li F, Zhang L, Metzger RM. On the growth of highly ordered pores in anodized aluminum oxide. *Chem. of Mater.* 1998;10:2470–2480.
41. Diggle JW, Downie TC, Goulding CW. Anodic oxide films on aluminum. *Chem. Rev.* 1969;3:365.
42. Chu SZ, Wada K, Inoue S, Isogai M, Katsuta Y, Yasumori A. Large-scale fabrication of ordered nanoporous alumina films with arbitrary pore intervals by critical-potential anodization. *J. Electrochem. Soc.* 2006;153(9):B384–B391.
43. Ohgai T, Gravier L, Hoffer X, et al. Template synthesis and magnetoresistance property of Ni and Co single nanowires electrodeposited into nanopores with a wide range of aspect ratios. *J. Phys. D.* 2003;36:3109–3114.
44. Keller F, Hunter MS, Robinson DL. Structural features of oxide coatings on aluminum. *Electrochem. Soci.* 1953;100:411–419.
45. O'Sullivan JP, Wood GC. Morphology and mechanism of formation of porous anodic films on aluminium. *Proc. R. Soc. London Seri. A.* 1970;317(1531):511–543.
46. Takmakov P, Vlasiouk I, Smirnov S. Hydrothermally shrunk alumina nanopores and their application to dna sensing. *Analyst.* 2006;131:1253–1248.
47. Macak JM, Tsuchiya H, Taveira L, Aldabergerova S, Schmuki P. Smooth anodic TiO₂ nanotubes. *Angew. chem. int. ed. engl.* 2005;44(45):7463–7465.
48. Sieber IV, Schmuki P. Porous tantalum oxide prepared by electrochemical anodic oxidation. *J. Electrochem. Soci.* 2005;152(9):C639–C644.
49. Singh S, Greiner MT, Kruse P. Robust inorganic membranes from detachable ultrathin tantalum oxide films. *Nano Lett.* 2007;7(9):2676–2683.
50. Tsuchiya H, Macak JM, Sieber I, Schmuki P. Self-organized high-aspect-ratio nanoporous zirconium oxides prepared by electrochemical anodization. *Small.* 2005;1(7):722.
51. Tsuchiya H, Macak JM, Sieber I, et al. Self-organized porous WO₃ formed in NaF electrolytes. *Electrochem. Commun.* 2005;7:295.
52. Canham L. ed. *Properties of Porous Silicon.* INSPEC, Institution of Electrical Engineers, London, 1997.
53. Xia Y, Gates B, Yin Y, Lu Y. Monodispersed colloidal spheres: old materials with new applications. *Adv. Mater.* 2000;12(10):693.

54. Blalock E.M. ed. *A Beginner's Guide to Microarrays*. Kluwer Academic, Dordrecht, The Netherlands, 2003.
55. Hermanson GT. *Bioconjugate Techniques*. Academic Press, New York, 1996.
56. Krasnoslobodtsev A, Smirnov S. Surface assisted intermolecular interactions in self-assembled coumarin submonolayers. *Langmuir*. 2001;17:7593–7599.
57. Moon JH, Shin JW, Kim SY, Park JW. Formation of uniform aminosilane thin layers: an imine formation to measure relative surface density of the amine group. *Langmuir*. 1996;12:4621–4624.
58. Krasnoslobodtsev A, Smirnov S. Effect of water on silanization of silica by trimethoxysilanes. *Langmuir*. 2002;18:3181–3184.
59. Steinle ED, Mitchell DT, Wirtz M, Lee SB, Young VY, Martin CR. Ion channel mimetic micropore and nanotube membrane sensors. *Anal. Chem*. 2002;74:2416–2422.
60. Vlassiok I, Rios F, Vail SA, Gust D, Smirnov S. Electrical conductance of hydrophobic membranes or what happens below the surface. *Langmuir*. 2007;23(14):7784–7792.
61. Ku AY, Ruud KA, Early TA, Corderman RR. Evidence of ion transport through surface conduction in alkylsilane-functionalized nanoporous ceramic membranes. *Langmuir*. 2006;22(20):8277–8280.
62. Jayaraman K, Okamoto K, Son SJ, et al. Observing capillarity in hydrophobic silica nanotubes. *J. Am. Chem. Soc*. 2005;127(49):17385–17392.
63. Okamoto K, Shook CJ, Bivona L, Lee SB, English DS. Direct observation of wetting and diffusion in the hydrophobic interior of silica nanotubes. *Nano Lett*. 2004;4(2):233–239.
64. Iqbal SM, Akin D, Bashir R. Solid-state nanopore channels with DNA selectivity. *Nat. Nanotechnol*. 2007;2:243–248.
65. Wanunu M, Meller A. Chemically modified solid-state nanopores. *Nano Lett*. 2007;7(6):1580–1585.
66. Karnik R, Castelino K, Fan R, Yang P, Majumdar A. Effects of biological reactions and modifications on conductance of nanofluidic channels. *Nano Lett*. 2005;5(9):1638–1642.
67. Wang G, Zhang B, Wayment JR, Harris JM, White HS. Electrostatic-gated transport in chemically modified glass nanopore electrodes. *J. Am. Chem. Soc*. 2006;128:7679–7686.
68. Vlassiok I, Krasnoslobodtsev A, Smirnov S, Germann M. 'Direct' detection and separation of dna using nanoporous alumina filters. *Langmuir* 2004;20:9913–9915.
69. Vlassiok I, Takmakov P, Smirnov S. Sensing DNA hybridization via ionic conductance through a nanoporous electrode. *Langmuir*. 2005;21:4776–4778.
70. Karnik R, Castelino K, Duan C, Majumdar A. Diffusion-limited patterning of molecules in nanofluidic channels. *Nano Lett*. 2006;6(8):1735–1740.
71. Rosario R, Gust D, Hayes M, Jahnke F, Springer J, Garcia AA. Photon-modulated wettability changes on spiropyran-coated surfaces. *Langmuir*. 2002;18:8062–8069.
72. Vlassiok I, Park C-D, Vail SA, Gust D, Smirnov S. Control of nanopore wetting by a photochromic spiropyran: a light-controlled valve and electrical switch. *Nano Lett*. 2006;6(5):1013–1017.
73. Takmakov P, Vlassiok I, Smirnov S. Application of anodized aluminum in fluorescence detection of biological species. *Anal. Bioanal. Chem*. 2006;385:954–958.
74. Newton MR, Bohaty AK, Zhang Y, White HS, Zharov I. pH- and ionic strength-controlled cation permselectivity in amine-modified nanoporous opal films. *Langmuir*. 2006;22:4429–4432.

75. Vlassioux I, Siwy Z. Nanofluidic diode. *Nano Lett.* 2007;7(3):552–556.
76. Harrell CC, Kohli P, Siwy Z, Martin CR. DNA–nanotube artificial ion channels. *J. Am. Chem. Soc.* 2004;126(48):15646–15647.
77. Siwy Z, Trofin L, Kohli P, Baker LA, Trautmann C, Martin CR. Protein biosensors based on biofunctionalized conical gold nanotubes. *J. Am. Chem. Soc.* 2005;127(14):5000–5001.
78. Siwy Z, Heins E, Harrell CC, Kohli P, Martin CR. Conical-nanotube ion-current rectifiers: the role of surface charge. *J. Am. Chem. Soc.* 2004;126(35):10850–10851.
79. Kang M, Trofin L, Mota MO, Martin CR. Protein capture in silica nanotube membrane 3-d microwell arrays. *Anal. Chem.* 2005;77:6243–6249.
80. Cunin F, Schmedake TA, et al. Biomolecular screening with encoded porous-silicon photonic crystals. *Nat. Mater.* 2002;1:39–41.
81. Smirnov S, Vlassioux I, Rios F, Takmakov P, Gust D. Smart nanoporous membranes. *ECS Trans.* 2007;3(26). *Bioelectronics, Biointerfaces, and Biomedical Applications*; 2:23–29.
82. Jagerszki G, Gyurcsanyi RE, Hoffer L, Pretsch E. Hybridization-modulated ion fluxes through peptide–nucleic-acid-functionalized gold nanotubes: a new approach to quantitative label-free DNA analysis. *Nano Lett.* 2007;7(6):1609.
83. Lee S, Zhang YH, White HS, Harrell CC, Martin CR. Electrophoretic capture and detection of nanoparticles at the opening of a membrane pore using scanning electrochemical microscopy. *Anal. Chem.* 2004;76(20):6108–6115.
84. Vlassioux I, Rios F, Takmakov P, Smirnov S. Water confinement in hydrophobic nanopores: pressure induced wetting and drying. In preparation.
85. Rios F, Smirnov S. Another view on hydrophobic nanopores' interaction with amphiphiles. In preparation.
86. Kasianowicz JJ, Brandin, Branton D, Deamer DW. Characterization of individual polynucleotide molecules using a membrane channel. *Proc. Nat. Acad. Sci. USA.* 1996;93(24):13770–13773.
87. Storm AJ, Storm C, Chen J, Zandbergen H, Joanny J-F, Dekker C. Fast DNA translocation through a solid-state nanopore. *Nano Lett.* 2005;5(7):1193–1197.
88. Heins EA, Siwy ZS, Baker LA, Martin CR. Detecting single porphyrin molecules in a conically shaped synthetic nanopore. *Nano Lett.* 2005;5(9):1824–1829.
89. Ling XS, Bready B, Pertsinidis A. Methods for hybridization-assisted nanopore sequencing of nucleic acids. USPTO patent WO2007041621.
90. Fologea D, Uplinger J, Thomas B, McNabb DS, Li J. Slowing DNA translocation in a solid-state nanopore. *Nano Lett.* 2005;5(9):1734–1737.
91. Keyser UF, van der Does J, Dekker C, Dekker NH. Optical tweezers for force measurements on DNA in nanopores. *Rev. Sci. Instrum.* 2006;77:105105/1–105105/9.
92. Lagerqvist J, Zwolak M, Di Ventra M. Fast DNA sequencing via transverse electronic transport. *Nano Lett.* 2006;6(4):779–782.
93. Gracheva ME, Xiong A, Aksimentiev A, Schulten K, Timp G, Leburton J-P. Simulation of the electric response of DNA translocation through a semiconductor nanopore-capacitor. *Nanotechnology.* 2006;17:622–633.

INDEX

- Acetylcholine, 30
Acetylcholinesterase-choline oxidase, 30
Acrylamide, 298
Acrylic acid (AA), 304
Actin, 311
 filaments, 320
Active sites, 9
Adsorption, 217
 physical, 13
Affinity tags, 51
Affymetrix Human U133A2.0 GeneChip
 platform, 325
Agarose gel electrophoresis (AGE), 308
Aggregation, 154, 306
AIBN, 301
Alloy, 153
5-Amino-1-pentanol, 307
bis-Aminopropyl PEG linker, 311
Amperometric, 178. *See also* Biosensors,
 amperometric; Electrodes, amperometric
 enzyme; Immunosensor, amperometric
Amplification, T7, 325
Anchor-probe self-assembly scheme, 49
Anodic aluminum oxide (AAO) template, 41
Anodic stripping voltammetry, 347. *See also*
 Differential pulse anodic stripping
 voltammetry
Antibody(ies), 18, 154, 200. *See also* Her-2,
 anti-Her-2 antibodies; IgG
 antitopoI, 318
 mouse anticycline E, 316
 murine anti-p-gp, 315
Antibody-antigen, 51
Antigen(s), *see also* Prostate-specific antigen;
 Prostate-specific membrane antigen
 (PSMA)
 nuclear, 311
Apoenzymes, 53
Aptamer(s), 159, 205

Arginine-glycine-aspartic acid (RGD), 313
Array(s), 24, 25. *See also* CNT, arrays; Gold,
 nanoparticle arrays; Gold, nanotube
 arrays; Microarray(s); Multiwalled
 carbon nanotubes, MWCT tower arrays;
 Nanoarrays
 vertical, 7. *See also* CNT, arrays, vertical
 vertically aligned, 13
 well-ordered silver, 118
Arrested precipitation, 207
Ascorbic acid, 29, 228
Atom, artificial, 341
Atomic force microscopy, 106, 308
AuNPs, 178, 361
Auxotrophic expression, 47
Avidin, 217

Bacillus thuringiensis, 228
Bamboo-like, 6
Band gap, 201
Barcodes, 307, 324
Barcoding, 225
Basal-plane, 4, 8, 9, 21. *See also* Graphite,
 pyrolytic, basal-plane
Bathochromic shifts, 214
Bead agglutination, 314
Benzoyl peroxide, 300
Bioanalysis, 13, 364
Biocompatibility, 108, 178, 256, 262
Biocompatible, 334
Bioconjugation, 305
Bioelectroanalysis, 13, 14
Biomacromolecules, 100
Biomarkers, 421
Bioprobe, 200
Biorecognition, 324
 element, 200
Biosensing, 20, 29, 182, 459
 applications, 372

- Biosensor(s), 13, 17–21, 25, 28–30, 178, 200, 459, 460, 469, 472, 474
- amperometric, 104
 - DNA, 21
 - electrochemical, 25
 - electrochemical, 21, 23, 25, 100, 178, 345
 - enzyme-based, 399
 - glucose, 28, 29, 106
 - optical, 20
- Biotechniques, 365
- Biotin, 237
- Biotin-streptavidin, 50
- Biotinylated goat anti-human IgG, 311
- Blinking, 341
- Block copolymers, 293
- Bovine serum albumin (BSA), 22, 230, 231, 299, 311, 316
- Bradford assay, 311
- Branched polymers, 294
- Brucine, 7
- n*-Butyl methacrylate, 302
- Cancer cell, *see* Cell
- Capsule deformation, 261
- Capsules, uptake of, 259, 261
- Carbon, *see also* CNT, carbon paste; Electrode(s), carbon paste
- amorphous, 430
 - fiber, 9
 - nanomaterials, 429
 - paste, 26
 - powder, 9, 23
- Carbon nanotube(s), 3, 9, 18, 20–22, 100, 430.
- See also* CNT(s); Multiwalled carbon nanotubes; Single-walled carbon nanotubes
 - paste electrodes, 13
 - powder microelectrode, 103
- Carboxyl groups, 16
- surface, 13
- Carboxylic acid groups, 22
- Carotid artery, 317
- Cascade Blue, 320
- Caspase-1, 237
- Catalysis, 178
- Catalytic, 18
- activity, 101
- Catechol, 7, 30, 228
- Catechine, 30
- CdSe, 294
- CdSe-CdS, 294
- CdTe QDs, 297
- Cd-ZnS, 293
- Cell(s)
- cancer
 - lysates, 115
 - human breast cancer cell line SK-BR-3, 310
 - multi-drug-resistant MCF7r breast adenocarcinoma, 315
- detection, 372
- receptors, 18
- metastatic, 313
- human bone marrow mesenchymal stem, 325
- 3T3 mouse fibroblast, 320
- Centrifugal microfluidics, 322
- Charge driven encapsulation, 296
- Chemically modified, 14
- Chemical modification, 14
- Chemical vapor deposition, 6, 25
- Chemosensing, 166
- Chitosan, 230
- Chromoionophore, 320
- Chronoamperometry, 179
- Chymotrypsin, 237
- “Click” chemistry, 44
- CNT(s), 3–15, 17, 20–30. *See also* Carbon nanotube(s); Gold nanoparticle, gold nanoparticle -CNT hybrids; Multiwalled carbon nanotubes; Single-walled carbon nanotubes
- arrays, 108
 - immobilization sites on, 42
 - vertical, 24
 - carbon paste, 23
 - electrode(s), 101
 - modified, 9, 12, 13, 20, 27, 30
 - paste, 30
 - well-aligned, 104
 - modified, 9
- Coiled-coil, 54
- Collagenase, 237
- Colloidal stability, 305
- Conductometric, 182
- Confocal imaging, 303
- Confocal microscopy, 302
- Core-shell, 292, 337
- nanocrystals, 205
 - particles, 307
 - structures, 153
- Cortisol, 237
- Covalent attachment, 22
- Covalent functionalization, 21
- Covalent modification, 21
- Cranial window, 317
- Cross-linked latex, 305
- Cyclic voltammetry, 179

- Cy3, 314
 DL-CYSTEINE, 299
 Cysteine acrylamide, 301
 Cytochrome *c*, 7, 23
 Cytotoxicity, 142, 262, 268, 270
- Decay rate
 nonradiative 215
 radiative, 215
- Delivery, 248, 250, 262–264, 267, 270.
 See also Drug delivery
 intracellular delivery, 301
- Dendrimers, 294, 429
- Deposition, 390. *See also* Electroless, deposition
- Desorption, 212
- Diamond, 431
- Didecyl-*p*-ethylbenzylmethylammonium chloride (DEMAC), 302
- Didecyl-*p*-vinylbenzylmethylammonium chloride (DVMAC), 301
- Dielectric medium, 149, 165
- Diethylenetriamine (DETA), 295
- Differential pulse anodic stripping voltammetry (DPASV), 188
- Differential pulse voltammetry (DPV), 179
- Diffusion domain approximation, 8
- Dimercaptosuccinic acid, 300
- N*-(3-Dimethylaminopropyl)-*N'*-ethylcarbodiimide hydrochloride (EDAC), 316
- Dip pen nanolithography, 57
- DMF, 296
- DNA, 21, 22, 25–27, 155, 168, 178, 218.
 See also Biosensors, DNA;
 Hybridization, DNA
 detection, 110, 370
 DNA-topoisomerase I (topoI), 319
 microarray analysis, 169
 ssDNA probes, 320
- Dopamine, 29, 228
- Doping, 297
- Double-labeling approach, 309
- DPASV, 188
- DPV, 179
- Drop coating, 23
- Drude theory, 144
- Drug delivery, 317
- DVB, 298
- Dynamic light scattering (DLS), 308
- EDC, 43, 293
- Edge-plane, 4, 8, 9
 defects, 8, 9, 13
 step defects, 8
- edge-plane-like, 10
 defects, 5
 defect sites, 6
 sites, 11, 15
 nanobands, 9
 sites, 9
- Effective mass approximation, 209
- Electrical conductivity, 108
- Electroactive, 12
 sites, 8, 10, 11
- Electroactivity, 179
- Electroanalysis, 7, 10, 13, 14, 17
 bioelectroanalysis, 13, 14
- Electroanalytical, 13
- Electrocatalysis, 12
- Electrocatalytic, 7–9, 11, 12, 23,
 24, 29
- Electrochemical, *see also* Biosensor(s), DNA,
 electrochemical; Biosensor(s),
 electrochemical; Immunosensors,
 electrochemical; Sensors,
 electrochemical
 genosensor, 114
 sensing, 23
 transducer(s), 19, 23
- Electrochemical impedance spectroscopy, 113,
 184
- Electrochemistry, *see also* Nanoelectrochemistry
 direct, 105
- Electrode(s), *see also* Carbon nanotube, paste
 electrodes; CNT(s), electrode(s);
 CNT(s), paste electrode; Multiwalled
 carbon nanotubes, microelectrode;
 Multiwalled carbon nanotubes, MWCNT
 (s), paste electrodes; Nanoelectrodes
 amperometric enzyme, 20, 21
 carbon paste, 23, 29, 101
 modified 29
 composite, 105
 enzyme, 106
 glassy carbon, 23, 26, 28–30, 103
 modified, 26, 27
 graphite, 8, 9, 13
 graphitic, 9
 graphitic carbon, 8
 ion-selective microelectrodes
 (ISE), 186
 modified, 29
 spatially heterogeneous, 8
 vertically aligned, 24
- Electroless, 390
 deposition, 392
- Electron-beam lithography, 117

- Electron transfer, 8, 9, 21, 23–27
 direct, 20, 106
 enhanced, 103
 kinetics, 105
- Electrostatic, 300
 interactions, 299
- Emulsion polymerization, 297
- Encapsulation, in situ, 300
- Encoded beads, 300
- Encoding, 343. *See also* Optical, encoding
- Endocytosis, 310, 316
- Environmental
 applications, 25
 hazards, 30
- Environmental scanning electron
 microscopy, 108
- Enzyme, *see* Biosensors, enzyme-based;
 Electrode(s), amperometric enzyme;
 Electrode(s), enzyme; Sensors,
 enzymatic
- Escherichia coli*, 226
- Estrogen, 155
- Exciton, 208
- Extravasate, 313
- FACS, 322
- Ferrocene (Fc)-capped gold nanoparticle/
 streptavidin conjugates, 115
- FITC-labeled, 321
- Flow cytometer, 321
- Flow cytometry, 321
- Fluorescein, 237
- Fluorescence, 200, 335
 fluorescence correlation spectroscopy
 (FCS), 308
 fluorescence (or Förster) resonant energy
 transfer (FRET), 314
 in situ hybridization, 225
 quenching, 304
- Fluorescent, *see also* Proteins, fluorescent
 emission profiles, 324
- Fluorophores, 202, 335
 acceptor, 314
- Folic acid receptors, 316
- FRET, 217
 FRET-based QD-containing systems, 314
- Fullerenes, 430, 440
- Fullerenoacetic acid, 445
- Functional groups, 7
- Galactose, 7
- Gene, *see also* Housekeeping genes
 expression, 321
 gene-specific oligonucleotide probes, 324
 identification, 324
- Glassy carbon (GC), 7, 16, 26. *See also*
 Electrode(s), glassy carbon
- Glucose, 7, 18, 20, 23, 25, 27–29, 161. *See also*
 Biosensor(s), glucose; Sensors, glucose
 glucose oxidase, 22–25, 28
- Gold, *see also* Nanoelectrodes, gold nanoelectrode
 ensembles
 colloidal, 366
 nanotube arrays, 117
- Gold nanoparticle(s), 27, 100, 178, 361
 AuNPs, 178, 361
 gold nanoparticle -CNT hybrids, 112
 nanoparticle arrays, 111
- Graphite, 8, 9, 13, 15, 16, 23, 26. *See also*
 Electrode(s), graphite; Electrode(s),
 graphitic
 powder, 15, 17
 pyrolytic,
 basal-plane, 9
 BPPG, 9, 28
 highly ordered, 8
- Halothane, 11, 12
- HeLa, 316
- Heme group, 105
- Hepatitis A, 323
- Hepatitis B, 226, 323
 surface antigen, 323
- Hepatitis C, 226, 323
 virus nonstructural protein 4, 323
- Her-2, 310
 anti-Her-2 antibodies, 310
 HER2 locus, 227
- Heterobifunctional linker, 310
- Hexadecylamine, 301
- High dilution, 306
- High-voltage arc discharge, 6
- HIV, 323
 glycoprotein 41, 323
- H₂O₂, 300
- Horseradish peroxidase, 7, 23, 27
- Horseradish peroxide, 22
- Housekeeping genes, 325
- HRTEM, 180
- Human oncogene p53, 226
- Human serum albumin (hSA), 311
- Hybridization, 25–27, 320. *See also*
 Fluorescence, in situ hybridization; RNA,
 cRNA, probe-cRNA hybridization
 assays, 230
 DNA 114, 370

- Hydrazine, 11, 12
 Hydrodynamic radius, 214, 308
 Hydrodynamic volume, 293
 Hydrogen interaction, 160
 Hydrogen peroxide(s), 7, 11, 12, 23, 24, 28–30, 160
 Hydrophobic interactions, 297, 307
N-Hydroxysuccinimide ester, 294
 NHS, 43
- Identification, 445
 IgG, 227, 229, 311
 anti-immunoglobulin G, 300
 goat antimouse IgG, 310
 Imaging, 317
 applications, in vivo, 311
 Immobilization
 oriented, 45
 parallel, 401
 Immunoactivity, 113
 Immunoassay(s), 113, 154, 225, 364.
 See also Inductively coupled
 plasma mass spectrometry,
 ICP-MS-linked immunoassays
 Immunomagnetic assay, 227
 Immunoreaction, 366
 Immunosensors, 186
 amperometric, 109
 electrochemical, 114
 Inductively coupled plasma mass
 spectrometry, 355
 ICP-MS, 355
 ICP-MS-linked immunoassays, 366
 Insulin, 7
 Integrin $\alpha_v\beta_3$, 313
 Internal standard, 356
 Intracellular delivery, 301
 Intracellular studies, 294
 Ionization, 357
 Ion selective, 320. *See also*
 Electrode(s), ion-selective
 microelectrodes (ISE)
- Isocyanate coupling, 304
 Isotope dilution, 356
- Kras point mutations, 234
 K₂S₂O₈, 300
- Label, 167, 336. *See also* Nanolabels
 labeling, 301. *See also* Metal Nanoparticle(s),
 labeling with
 Lab-on-a-chip, 321
 Laccase, 29
- Lactic acid, 228
 Laser Doppler velocimetry, 308
 Latex bead, 168
 Layer-by-layer, 256–258
 assembly, 21
 deposition, 299
 (LBL) films, 108
 Leaching, 298
 Leaky vasculature, 313
 Leucine-zipper, 232
 Ligand(s), *see also* Thiol, ligands
 chromism, 215
 exchange, 212, 254, 255
 ligand-exchange mechanism, 166
 oligomeric phosphine, 304
 polymerizable, 301
 polymerizable phosphine, 302
 Lithography, 141. *See also* Dip pen
 nanolithography; Electron-beam
 lithography; Nanosphere
 lithography (NSL)
 soft, 385
 Localized surface plasmon resonance
 (LSPR), 388
 Longitudinal mode, 160
 Long-pass filter, 322
 Luminescence, 200. *See also*
 Photoluminescence
 Lycurgus cup, 148
- Macroporous, 297
 Magnetic, *see also* Nanoparticle(s), magnetic;
 Quantum dot(s) (QD(s)), magnetic
 QD-composite
 beads, 114, 188, 231
 particle, 168
 Material enhanced laser desorption/
 ionization, 426
 MELDI, 426
 Matrix-free LDI-MS, 430
 Maxwell equations, 144
 Medical diagnostic(s), 25
 Melamine beads, 319
 Melamine formamide, 296
 Melt curves, 218
 Membranes
 alumina, 470–472, 476, 478
 polymeric, 391
 track-etched, 391
 Mercaptopropanoic acid, 299
 3-Mercaptopropionic acid, 294
 Mercaptopropyltris(methyloxy)silane
 (MPS), 305

- 3-Mercaptotrimethoxysilane, 297
- Metal
- cation, 162
 - containing biomolecules, 363
 - impurities, 12
 - ions, 360
 - metal-tagged, 364
- Metal nanoparticle(s), 12, 13, 27, 29, 110
- catalysts, 11
 - labeling with, 364
- Methacryloxypropyltrimethoxysilane, 302
- 2-[Methoxy(polyethyleneoxy)propyl]trimethoxysilane (PEOS), 306
- Micelles, 295. *See also* Quantum dot(s) (QD(s)), QD compound micelles (QDCMs)
- lipid, 223
- Microanalysis, 303
- Microarray(s), 120, 225. *See also* DNA, microarray analysis
- Microcapsules, 296
- Microcontact particle stripping, 385
- Microemulsion, 207, 301
- Microfluidic chip, 321. *See also* Centrifugal microfluidics
- poly(dimethylsiloxane) (PDMS), 323
- Microparticle, 230. *See also* Polystyrene microparticles
- Microperoxidase, 22
- Microspheres, 231. *See also* Polystyrene microspheres
- Microtubule fibers, 311
- Mie, 147
- Mixed monolayer, 106
- Molecular beacon, 236
- Molecular wires, 24
- molecular wiring, 53
- Monodisperse, 304, 306
- Monomeric phosphine, 303
- Morphine, 7
- MS/MS analysis, 448
- Multianalyte detection, 366
- Multiphoton microscopy, 317
- Multiplexed analysis, 202
- Multiplexed bioanalysis, 123
- Multiplexing, 323
- multiplexing biomolecules, 54
- Multiwalled carbon nanotubes, 4. *See also*
- Carbon nanotube(s); CNT(s);
 - Single-walled carbon nanotubes
- microelectrode, 102
 - MWCNT(s), 4–6, 9, 11–15, 26–29
 - paste electrodes, 26
 - MWCT tower arrays, 108
- Murine anti-p-gp antibodies, 315
- Nafion, 23, 27–30
- Nanoarrays, 13
- Nanobands, 8, 9
- Nanochannel(s), 460–464, 466, 467, 469, 470–480, 482
- Nanocomposite film, 106
- Nanocomposites, 305. *See also* Quantum dot(s) (QD(s)), QD-polyisoprene nanocomposites
- Nanconnector, 106
- Nanocrystal, *see also* Core-shell, nanocrystals
- semiconductor, 334
 - tracers, 123
- Nanodevice, 178
- Nanoelectrochemistry, 178. *See also* Electrochemistry
- Nanoelectrode(s), 24
- ensemble, 390, 396, 398
 - gold nanoelectrode ensembles, 395
- Nano- γ -Fe₂O₃, 316
- Nanoforests, 24, 25, 27
- Nanohybrid films, 106
- Nanolabels, 189
- Nanomaterials, 20, 100, 178, 333. *See also*
- Carbon, nanomaterials
- Nanomedicine, 142
- Nano-optodes, 319
- Nanoparticle(s), 12, 28, 29, 140, 248–259, 261–270, 333, 361. *See also* Gold nanoparticle(s); Metal nanoparticle(s); Nanotube, and nanoparticle hybrid materials; Platinum nanoparticles; Silver nanoparticles
- colloidal, 249, 250, 253, 383
 - composite, 305
 - heatable, 250
 - magnetic, 248–250, 252, 262, 265
 - NPs, 361
 - QDs and Fe₃O₄, 297
 - semiconductor, 248–251, 260, 262
- Nanoplugs, 11
- Nanopore(s), 390, 459, 460, 463–467, 469–475, 477–480, 482, 483, 485, 486
- Nanoreactors, 104
- Nanorod, 150
- Nanoscience, 333
- Nanosensor, 178
- Nanosphere lithography (NSL), 380
- Nanospheres, polymeric, 303
- Nanostructures, 20
- Nanotechnology, 100

- Nanotube, *see also* Gold, nanotube arrays and nanoparticle hybrid materials, 104
- Nanowells, well-oriented, 117
- Near-infrared diffuse reflection spectroscopy (NIRS), 448
- Nernst equation, 14
- Neurotransmitters, 102
- NHS, 43
- N*-Hydroxysuccinimide ester, 294
- Nicotinamide adenine dinucleotide, 7
- Nitric oxide, 7
- Noncovalent functionalization, 21
- Nucleic acid(s), 18, 22, 25, 200
- Octylamine, 293
- n*-Octyltriethoxysilane, 305
- Oligonucleotides, 216
- Optical, 19. *See also* Biosensor(s), optical codes, 297
- detection, 20
- encoding, 320
- transducers, 19
- Organophosphorous hydrolase, 30, 228
- Organosilane, 220
- Oscillator strength, 210
- Overpotential, 8, 104
- Oxidative degradation, 301
- Paraoxon, 228
- Particle-in-a-box, 209
- Particles, heatable, 249
- Passive targeting, 313
- PCR, *see also* Polymerase chain reaction
- PCR amplicons, 231
- quantitative PCR (qPCR), 325
- PDEA, 43
- PEG, 293. *See also* bis-Aminopropyl PEG linker; Poly(ethylene glycol)
- pH, 14
- sensing, 13
- sensor, 15
- Phenol, 30
- Phosphatidyl choline, 295
- Phosphatidylethanolamine, 295
- Phospholipid, 295
- Photobleaching, 202, 312, 342
- Photodiode detector, 323
- Photoluminescence, 202. *See also* Luminescence
- Photoluminescent (PL), 293
- Photooxidation, 214
- Photostability, 345
- Physical adsorption, 13
- Physisorbing, 13
- Physisorption, 23
- Piezoelectric, 19, 20
- transducers, 19
- pKa, 14–16
- values, 14, 15, 17
- Plasmonics, 139
- Platinum nanoparticles, 29
- Poly(allylamine hydrochloride) (PAH), 297, 300
- Polyamidoamine (PAMAM), 294
- Polyaniline, 401
- Polyanion, 297
- Poly(butyl acrylate), 294
- Polycation, 297
- Polycondensation, 305
- Polydispersity, 304
- Polyelectrolytes, 118, 299. *See also* Polymer(s), polyelectrolyte
- capsules, 249, 250, 256–260, 262–268, 270
- Poly(ethylacrylate), 294
- Poly(ethylene glycol), 217
- Poly(ethylene oxide) (PEO), 295
- Poly(ethylenimine) (PEI), 294
- Polyhistidine, 216
- Poly(*N*-isopropylacrylamide) (PNIPAM), 316
- Poly(maleic anhydride-alt-1-octadecene), 293
- Polymer(s), 18. *See also* Membranes, polymeric; Nanospheres, polymeric; Quantum dot(s) (QD(s)), discrete QD(s), discrete QD-polymer composites; Quantum dot(s) (QD(s)), QD-encoded polymer beads; Quantum dot(s) (QD(s)), QD-polymer composites; Quantum dot(s) (QD(s)), QD-polymer composites that contain a plurality of QDs
- amphiphilic 222, 293. *See also* Quantum dot(s) (QD(s)), discrete QD(s), coated in amphiphilic polymers
- beads that contain a plurality of QDs, 314
- block copolymers, 293
- tri-block copolymer, 312
- branched, 294
- coating(s), 212, 255
- conductive, 401
- encapsulation, 294
- matrix, 297
- polyelectrolyte, 256, 257, 259
- shell, 304
- Polymerase chain reaction, 115.
- See also* PCR
- Polymerization reaction, in situ, 311
- Poly(methacrylic acid), 294
- Polyphenoloxidase, 30

- Poly (sodium 4-styrenesulfonate), 300
- Polystyrene microgels, 298
- Polystyrene microparticles, 224
- Polystyrene microspheres, 297
- Poly(styrene sulfonate), 300
- Poly(vinylpyrrolidone) (PVP), 297
- Potassium persulfate, 305
- Potentiometric, 186
- potentiometric stripping analysis (PSA), 182
- Potentiometry, 187
- Prostate-specific antigen, 227
- Prostate-specific membrane antigen (PSMA), 312
- Protein(s), 157
- analyses, 178
 - conformational changes in, 158
 - detection, 364
 - fluorescent, 342
 - green fluorescent (GFP), 342
 - GFP-expressing epithelial cells, 318
 - p*-glycoprotein transmembrane transporter (*p*-gp), 315
 - maltose-binding, 217, 314
 - metallothionein, 21
 - profiling, 434
 - protein A, 229
 - transmembrane tyrosine kinase receptor, 310
- Pyrolysis, 206
- Qbeads, 324
- Quadrupole mass analyzer, 358
- Quantification, 324
- Quantum confinement, 201
- effect, 334
- Quantum dot(s) (QD(s)), 13, 100, 200, 291. *See also*
- CdTe QDs; FRET, FRET-based QD-containing systems; Nanoparticle(s), QDs and Fe₃O₄; Polymer(s), beads that contain a plurality of QDs
 - discrete QD(s)
 - coated in amphiphilic polymers, 310
 - discrete QDs in micelles, 309
 - discrete QD-polymer composites, 308
 - magnetic QD-composite, 316
 - magnetic QD-containing beads, 316
 - QD compound micelles (QDCMs), 296
 - QD-encoded polymer beads, 320
 - QD/Fe₃O₄-containing silica particles, 316
 - QD-polyisoprene nanocomposites, 305
 - QD-polymer composites, 293
 - QD-polymer composites that contain a plurality of QDs, 308
 - QD-polystyrene particles, 297
 - QD-silica conjugates, 306
 - quantum dot-composite, 293
- Quantum size effect, 335
- Quantum yield, 205, 317
- Quenching, 228, 296. *See also* Fluorescence, quenching
- self-quenching, 297
- Radical initiators, 300
- Radio frequency, 356
- Raisin-bun, 306
- Resonance light scattering (RLS), 311
- RNA, 181
- cRNA, 324
 - probe-cRNA hybridization, 324
 - miRNA, 226
- Salmonella typhimurium*, 226
- Sandwich assays, 226
- Scanning electrochemical microscopy, 120
- Scanning near-field optical microscopy (SNOM), 318
- Scattering, 147
- Screen-printing, 399
- screen-printed electrode, 398
 - screen-printed substrate, 398
- Self-assembly, 381
- Semiconductivity, 108
- Semiconductor, 209. *See also* Nanoparticles, semiconductor
- material, 334
- Sensing, 248, 250, 262, 341.
- See also* Electrochemical, sensing; pH, sensing
- Sensitivity ratio, 400
- Sensors, 13. *See also* Immunosensors; Nanosensor; pH, sensor
- electrochemical, 19
 - enzymatic, 112
 - glucose, 18, 28
 - particulate, 319
- Sentinel lymph node (SLN) mapping, 313
- Silane co-monomers, 305
- Silanes, functionalized, 306
- Silanization, 255, 256
- Silica, *see also* Quantum dot(s) (QD(s)), QD/Fe₃O₄-containing silica particles; Quantum dot(s) (QD(s)), QD-silica conjugates
- coatings, 212
 - encapsulation, 305
 - shell, 224, 298
 - spheres, 306

- Silver nanoparticles, 120, 153, 157, 158, 161, 165–167, 389, 394, 395
- Simultaneous measurement, 105
- Single-molecule spectroscopy, 230
- Single nucleotide polymorphisms, 225
- Single-walled carbon nanotubes, 4, 102. *See also*
Carbon nanotube(s); CNT(s);
Multiwalled carbon nanotubes
single CNT, 121
SWCNT(s), 4, 9, 11, 15, 20, 27, 29
SWNT field effect transistors, 109
SWNT forests, 109
- Size exclusion chromatography (SEC), 308
- SLN branches, 313
- Sodium poly(styrene sulfonate), 297
- Solid-state detection, 184
- Solvent accessibility, 47
- Solvent evaporation technique, 305
- Spatially heterogeneous, 8. *See also* Electrode(s),
spatially heterogeneous
- Spinal muscular atrophy, 235
- Square wave voltammetry (SWV), 184
- Step defects, 8. *See also* Edge-plane, step defects
- Stöber method, 221
- Stöber process, 305
- Streptavidin, 227, 311
- Stripping analysis, 180. *See also* Potentiometric,
potentiometric stripping analysis (PSA)
- Succinimide coupling, 294
- Sulfamethazine, 226
- Surface, *see also* Carboxyl groups, surface
degradation, 296
modification, 212, 254, 256
plasmon band, 138
plasmons, 249
surface-enhanced affinity-capture (SEAC), 425
surface-enhanced laser desorption/ionization
(SELDI), 425
surface-enhanced neat desorption (SEND), 425
surface plasmon resonance, 139, 248
- Suspension, 301
- Systemic sclerosis, 319
- Tetanus, 323
- Tetraethylorthosilicate (TEOS), 305
- Thioalkyl acids, 212
- Thioglycolic acid, 299
- Thiol, 294
ligands, 212
- Thrombin, 237
thrombin-binding aptamer, 228
- Titania-coated, 307
- Total overlap diffusion, 397
- Toxicity, 256, 261, 262, 318, 336.
See also Cytotoxicity
- Tracking, 341
- Transduction element, 200
- Transforming growth factor- β 1, 325
- Transmission electron microscopy (TEM),
180, 295
- Trialkoxysilane, 306
(Trihydroxysilyl) propylmethylphosphonate, 306
- Trioctylphosphine oxide (TOPO), 292
- Tufts, 311
- Tumor
marker, 109
vasculature, 317
xenografts, 312
- Tyrosinase, 30
- Ultramicrotronic, 302
- Ultrasonication, 301
- Ultrasonic irradiation, 305
- Uric acid, 7
- UV-vis, 140
- Voltammetric, 178
voltammetric techniques, 183
- Voltammetry, *see also* Anodic stripping
voltammetry; Cyclic voltammetry;
Differential pulse anodic stripping
voltammetry (DPASV); Differential
pulse voltammetry (DPV); Square wave
voltammetry (SWV)
- Wide-type p53, 115
- Working electrode, 180
- Xenopus cells, 312
- Zeta potential, 308
- Zinc sulfide, 292